Volume 13 • No 1 • 2025 • p-ISSN: 2410-9355 • e-ISSN: 2307-549X

ARO

The Scientific Journal of Koya University

2.1

WoS IMPACT FACTOR

Journal Citation Reports
Clarivate
2025

www.koyauniversity.org

ARO-The Scientific Journal of Koya University

ARO, meaning "Today" in Hewramí Kurdish, is an esteemed international scientific journal proudly published by Koya University with the following identifiers: p-ISSN: 2410-9355, e-ISSN: 2307-549X, and DOI: 10.14500/2307-549X. As a reputable open-access peer-reviewed journal, ARO is dedicated to publishing original scientific research, global news, and insightful commentary. Recognized for its impact in the academic community, ARO Journal has been awarded an Impact Factor by WoS-ESCI and covers diverse areas of Multidisciplinary Sciences, welcoming both original research articles and review articles. Notably, ARO Journal is committed to providing free access to its content and proudly boasts the absence of both APC (Article Processing Charges) and ASC (Article Submission Charges) fees.

ARO Executive Publisher

ARO Editor-in-Chief

ARO Co-Editor-in-Chief

ARO Editorial Board

ARO takes pride in its robust and dedicated Editorial Board, comprising a distinguished twelve-member Senior Executive Editorial Board and a dynamic six-member Associate Editorial Board, both instrumental in shaping journal policies and ensuring editorial excellence. Additionally, ARO benefits from a highly esteemed Board of Reviewing Editors, consisting of over 250 prominent scientists from diverse fields. Their invaluable expertise and rigorous peer-review process contribute to the high standards and credibility of ARO, making it a leading platform for disseminating original scientific research, global news, and insightful commentary. The ARO editorial group consists of: Senior Executive Editors and Editorial Advisory Board.

Senior Executive Editors

Editorial Advisory Board

This Issue Reviewers

ARO is a distinguished online open access scientific journal that releases hard copies biannually. All published articles are freely accessible online under the Creative Commons Attribution License (CC-BY-NC-SA 4.0). It is important to note that the responsibility for the content lies solely with the authors and not with ARO or Koya University.

ARO the Scientific Journal Office

Koya University, University Park
Danielle Mitterrand Boulevard, Koya KOY45
Kurdistan Region - F.R. Iraq

E-mail: aro.journal@koyauniversity.org
url: aro.koyauniversity.org

June 2025

ARO

The Scientific Journal of Koya University

Vol XIII, No 1(2025)

Contents

ARO Editorial Words

Scaling New Heights: ARO Achieves 2.1 Impact Factor

Dear Esteemed Readers,

We are thrilled to share extraordinary news with our academic community: on June 18, 2025, ARO-The Scientific Journal of Koya University achieved a remarkable 2.1 Impact Factor from Web of Science (Clarivate Analytics). This exceptional milestone represents a 75% increase from our previous Impact Factor of 1.2, demonstrating our journal's accelerating influence and growing recognition in the global research community.

This outstanding achievement reflects the exceptional quality of scholarship published in ARO and underscores the dedication of our authors, reviewers, editorial board members, and the entire Koya University community. Each article, every peer review, and all collaborative efforts have contributed to this tremendous success, positioning ARO as an increasingly influential platform for groundbreaking research in the Kurdistan Region of Iraq and across international boundaries.

Reaching a 2.1 Impact Factor in such a relatively short time is a testament to our journal's commitment to publishing rigorous, innovative, and impactful research. This achievement validates our vision of creating a world-class scholarly platform that contributes meaningfully to global scientific discourse. We are particularly proud that ARO continues to serve as a vital conduit for regional research to reach international audiences while maintaining the highest standards of academic excellence.

As we celebrate this milestone, we recognize that it marks not an endpoint but a launching pad for even greater achievements. We remain committed to continuous improvement in all aspects of our operations: expanding our thematic scope to embrace emerging research areas, refining our peer review processes to ensure the highest quality standards, and fostering an even more dynamic and inclusive academic community around ARO.

We extend our deepest gratitude to our authors who entrust us with their groundbreaking research, to our reviewers whose rigorous evaluation ensures the integrity and excellence of our published work, and to our editorial board members whose expertise and guidance continue to elevate ARO's standing in the scholarly community. Your unwavering commitment has been instrumental in achieving this remarkable Impact Factor.

We invite researchers from all disciplines to join us in this exciting journey. Submit your innovative work, engage with our growing academic community, and help us build on this momentum as we continue to enhance ARO's reputation and impact.

We look forward to an even more successful future and invite you to be part of ARO's continuing story of excellence and impact.

With warm regards,

Dilan M. Rostam
Editor-in-Chief

Mohammed H. S. Zangana
Executive Publisher

Dilan M. Rostam, Salah I. Yahya, Fahmi F. Muhammad, Wali M. Hamad, Jorge Correia, Fouad Mohammed, Jacek Binda, Nadhir Al-Ansari, Howri Mansurbeg, Tara F. Tahir, Yazen A. Khaleel, Mohammad Gh. Faraj and Sahar B. Mahmood.
Executive Editorial Board Members

Predictive Logistic Models for Off-Street Parking Policy: Controlling Traffic Volume and Movement

Nahla H. Alaswadko†

Department of Civil Engineering, College of Engineering, University of Duhok,
Duhok, Kurdistan Region – F.R. Iraq

Abstract—**The land in city centers is typically used for commercial and industrial purposes, leading to increased traffic congestion. To promote more efficient, sustainable, and accessible land use in city centers, it is necessary to manage incoming traffic flow and travel demands effectively. This can be achieved by implementing appropriate parking policies, which should be predicted carefully to avoid adverse effects on human and economic activities. A case study is conducted in Duhok city, Iraq, aims to estimate the potential responses of city center travelers to reasonable off-street parking restriction policies. Real data were gathered through interviews with a quantitative sample of drivers to assess their reactions to two policies: Increasing parking fees and reducing available parking spaces. The study examines central parkers' socio-demographic and travel characteristics, including origin, trip purpose, timing, parking duration, search time, payment, income, age, and car occupancy. The study presents the results of two binary logistic models used to estimate the probability of implementing new parking policies to alleviate traffic congestion and improve movement. The findings suggest that travelers are more inclined to change their mode of transportation or travel time of day rather than altering their destination or canceling their trip. The findings contribute to the ongoing discourse on sustainable urban development and offer practical solutions for addressing the complex challenges associated with traffic volume and movement control in developing cities. This study aims to contribute to the growing body of knowledge on sustainable urban transportation planning and offer practical recommendations for transportation authorities.**

Index Terms—**City center traveler, Logistic model, Parker travelling decision, Parking policy, Response modeling.**

I. INTRODUCTION

To develop suitable sustainable transportation programs in any area, parking policies have an extremely influential role and an effective logic that help road planners and traffic policemen control traffic congestion and transport demand (Fahmy, Nazareth and Dyck, 2021, Kim, 2024). Historically, central areas have been opposed to applying such parking constraint policies due to the belief that urban access is considered essential to the economic achievement of any city center area (Chen, et al., 2021, Mei, et al., 2017 and Nieuwkoop, Axhausen and Rutherford, 2016). The city center traffic congestion problem is often aggravated due to many reasons, such as drivers spending too much time searching for parking spaces and thereby congesting the roads. Furthermore, the total number of parking spaces available has a critical effect on the traffic volume that could reach the central area, and the distribution of these spaces can have an effective impact on the movement of traffic within the city center. Obviously, expanding the number of parking spaces is considered a short-term solution to parking space shortages and traffic congestion problems and may attract additional travelers and create more congestion problems. Therefore, parking can be successfully managed by applying some forms of policies in terms of travel demand management strategies, which include parking cost, parking time limit, taxes, parking spatial distribution, and controlling the number of available parking spaces (Patel, et al., 2023, Wang, et al., 2024). However, parking charge and supply policies are the most actual approaches that affect parker travel decisions, which, in turn, are vital for the regular operation of the traffic volume in any city center (Mei, et al., 2017, Moeinaddinia, et al., 2013, Shiftan and Burd-Eden, 2000). To apply such suitable parking restriction policies in the city center, it is imperative to recognize how travelers are more likely to respond to such new and different parking policies (Nieuwkoop, Axhausen and Rutherford, 2016). Several studies have mentioned that increasing parking supply can help to reduce the parking impedance; still, it can also increase the traffic congestion in and around the area due to more travelers that use their private cars than public transportation to reach the CBD (Franco, 2017, Dowling, et al., 2017, Goulias, et al., 2016, Guo, 2013, Gallo, D'Acierno and Montella, 2011, Manville and Shoup, 2005). A study was conducted by Ding and Yang (2020) to predict travelers' responses to high parking charges using logit models. They adopted a method to predict the consequences of different parking pricing strategies on mode choice responses for various travelers' trip purposes. The higher price is specified due to travel time inconsistency,

---

ARO-The Scientific Journal of Koya University
Vol. XIII, No. 1 (2025), Article ID: ARO.11851. 9 pages
DOI: 10.14500/aro.11851
Received: 07 October 2024; Accepted: 08 January 2025
Regular research paper; Published: 01 February 2025
†Corresponding author's e-mail: nahla.alaswadko@uod.ac

which has sound effects on transport policy when applying such new or different parking pricing strategies.

Recent studies on city center parking policies emphasize the need for reform to address inefficiencies, environmental concerns, and social inequities. Donald Shoup's work remains central to these discussions, particularly through his influential publications. His studies highlight the economic, environmental, and urban design consequences of traditional parking policies. Shoup studied how factors including parking time, car occupancy, walking speed, and the value of saving time spent walking affect parking. Furthermore, he underlines that effective parking policies can contribute to more vibrant, equitable, and environmentally friendly cities. Policymakers are encouraged to adopt dynamic pricing, reduce parking minimums, and invest in alternative transportation to create sustainable urban environments (Shoup, 2005, Shoup, 2018, Yoka, 2018, Shoup, 2024).

Furthermore, to sidestep additional traffic congestion and parking demand in the city center of many developed countries, the concept of a park-and-ride policy has been implemented. This concept has been presented by many researchers as a multimodal and intermodal transport policy that aims to rearrange the parking areas from the most valuable and economically important city center urban zones to the bordering areas, even though it proposes such alternative plans for travelers to save time and money. However, the park-and-ride policy might be applicable when the study area is large and there is a manageable, accessible, and virtuous scheduling public transport system (Ortega, Tóth and Péter, 2021, Molan and Simićević, 2018, Yan, Levine and Marans, 2018, Shen, et al., 2017, Zhang, Wang and Sun, 2016, Dijk and Parkhurst, 2014, Aros-Vera, Marianov and Mitchell, 2013, Habib, Mahmoud and Coleman, 2013, Zhang, Wang and Yan, 2009, Syed, Golub and Deakin, 2009, Meek, Ison and Enoch, 2008).

The motivation behind this research lies in the growing need for sustainable urban mobility solutions. With increasing urbanization and the accompanying traffic challenges, understanding and implementing effective parking policies can significantly contribute to reducing congestion and enhancing quality of life in cities. This study aims to estimate binary logistic models to evaluate parking users' responses to two main parking restrictions: an increase in parking prices and a decrease in accessible parking spaces, which will increase parking search time. Duhok city center in the Kurdistan region in the north of Iraq is the case study for this investigation. Its distinct geographic location has caused a lot of transportation to be executed through the city and led to a high density of people and vehicles in its city center. In addition to that, during the past decade, this city has experienced an exceptionally high growth rate in population and vehicles due to people migrating from other cities in Iraq. In 2012, an improvement was carried out in the city center road network by changing the traffic direction of its road links. Consequently, road network efficiency to serve traffic was increased by a slightly decreased volume/capacity ratio, increased average traffic speed, and decreased delay time (Abdullah, 2013). However, so far, no parking restriction policies have been applied to reduce its traffic congestion and to shift people to use public transportation, as there are about 15 routes of public transportation in Duhok city (Khalid, 2011). According to a recent study conducted by Al-Ani (2021), it was determined that the peak hour volume ranges between 3470 and 7250 vehicles per hour, and the estimated level of service is F for Duhok city center routes. This service level indicated that the route operations are with extremely low speeds, adverse signal progression, and high delay. In fact, Duhok city center is now at a stage where it is required to implement such practical parking policies, and there is a need to evaluate the possible effects of such policies without affecting its vitality due to such observable traffic congestion problems, as shown in Fig. 1. This study stands out for its innovative use of SPSS software to develop predictive logistic models for parking policies, with a specific case study of Duhok city center. By analyzing real-world data, it offers localized insights into optimizing parking systems and reducing traffic congestion. The findings emphasize the scalability of such predictive models for developing cities, bridging the gap between theory and actionable urban policy recommendations. In addition, the study provides a roadmap for dynamic pricing and traffic volume control strategies that enhance urban mobility. The remainder of this paper is organized as follows: Section II describes the methodology and data used for modeling requirements. Section III presents the modeling approach used to develop logistic regression models to predict the relationship between the response of parkers to parking policies and the characteristics of parking users. Section IV presents the findings of this study and discusses the implications and potential applications of the results.

II. Methodology for Modeling Requirements

A. Survey of the City Center Area

A Parking Inventory Survey was undertaken to supply all the necessary, information related to parking in Duhok city center, located in the Kurdistan Region of Iraq, as shown in Fig. 2. On-street parking inventory was carried out and indicated that traffic policemen restricted travelers to using on-street spaces. However, very few spaces are available for very specific times of day. These spaces are free of charge and for about 5–10 min only; otherwise, there is a fine applied (USD $25). There are 28 off-street parking locations

Fig. 1. Traffic congestion problem in the study area.

(surface lots, multistory garages, and underground garages), with a total of 4,350 parking spaces in the study area (Fig. 2). Only 35% of these parking locations are public, and the rest are private, all with unrestricted parking duration.

B. Questionnaires Survey of the City Center Travelers

The possible responses to parking restriction policies of city center-bound travelers were carried out by a questionnaire survey. For an interview survey design purpose, the sample size calculator program was utilized to find out the required number of respondents to be interviewed to acquire statistically significant results for developing response models, where this sample size is reflecting the target population of the study area (SSC, 2023). The program is based on two main measures that are relevant to the accuracy of the data and represent the confidence interval and level.

The population size in this study is the number of vehicle spaces in the selected study area, which are 4,350 vehicle parking spaces. Hence, the required representative sample size to be interviewed for the CBD area is 354 respondents based on a 5% confidence interval and a 95% confidence level. The regular proportion of parking spaces used per day (parking space turnover) in Duhok city center was roughly 5.8 vehicles per space per day (Aswad, 2003). Therefore, the number of vehicles occupying parking spaces was expanded to 25,230 (4350 × 5.8) vehicles, which was considered the actual population size, and then the required sample of parking users became 378 respondents. A total of 380 parking users were interviewed in the city center area and were asked a number of inquiries related to their trip, as presented in Table I. In addition, the stated performance part of the survey included the two main questions that drivers have been asked for their probable responses to: Increasing parking fees and decreasing available parking spaces to increase the time to find a parking space.

Fig. 2. Off-street parking facilities in the study area (Duhok city center).

III. Modeling Approach

At present, there are two vital approaches that are being used to develop models in the field of transportation: deterministic and probabilistic modeling approaches. However, the latter models are considered more accurate as they deliberate uncertainties that are related to the explanatory variables (Shtayat, et al., 2022, Justo-Silva, Ferreira and Flintsch, 2021, Abaza, 2021). One of the more common and simple probabilistic models is the binary logistic regression model, which is used for binary classification and to assess the probability of binary responses using one or more predictors. This probability permits that the occurrence of a possibility of such a factor increases the likelihood of a given

TABLE I
Explanatory Variables for Asking Travelers About Their Trip

Explanatory variables	Choices
Origin (region)	
Time needed to arrive	a. 5 min to 15 min b. 15 min to 30 min c. More than 30 min
Driver age	a. Younger than 35 years b. Older than 35 years
Driver income	a. Less than (USD $ 500) b. Between (USD $ 500 and 1000) c. More than (USD $ 1000)
Trip purpose	a. Work b. Shopping c. Other purposes
Expected parking time (duration)	a. Less than 1 h b. Between (1 and 3) h c. More than 3 h
Type of parking payment	a. Paid c. Not paid (free)
Number of person in the car	
Time spent searching for a parking space	a. Less than 10 min b. Between (10 and 20) min c. More than 20 min
Time needed to walk from the parking location to a terminal place	a. Less than 10 min b. Between (10 and 20) min c. More than 20 min
What is your probable response if the parking cost is increased?	a. Not change b. Shift to using public transportation, taxi, or walking c. Switch time of day d. Alter terminal e. Change the trip
What is your probable response if the number of parking spaces is decreased?	a. Not change b. Shift to using public transportation, taxi, or walking c. Switch time of day d. Alter terminal e. Change the trip

outcome by a particular factor. This will help to develop a response model that presents the probability of output in terms of the input variable(s) (Alaswadko, 2016, Wuensch, 2014). In this study, the binary logistic regression model was utilized to predict the probability that a traveler to the city center will change their travel routines according to applying two parking policies: decreasing parking availability and/or increasing parking cost. The logistic regression models were developed to predict the relationship between each of the above two variables, which were considered the predicted variable or dependent variable (the response of parkers to parking policies) and the predictors or independent variables (the characteristics of parking users).

A. Characteristics of Parking Users

Parker Trip Origin and Time Needed to Reach the City Center: The origins of travelers' trips were divided into eight zones. The majority of parking users entered the city center from zones 2 and 1, which are about 20% and 22%, respectively. The lower percentages of parkers were entered from zones 6 and 7. These results indicated that the higher percent of travelers' origins were from the west side of Duhok city and the lower percent were from the east side. The travelers' responses indicated that 57% of drivers needed only 5–15 min to reach their terminal place in the city center. This is followed by 35% of drivers needing 15–30 min, which means that the majority of drivers had a short trip to reach their terminal place.

Parker Age and Income: Drivers were asked about their age within two categories, as some people were not ready to respond about their exact age. The age categories were <35 years or more than 35 years. It was found that slightly over half of the respondents were aged more than 35 years. This means that the study area almost attracts equally many drivers, both older than 35 years and younger than 35 years. The sample was comprised of 58 percent of average drivers' incomes, which were between USD $500 and $1,000; 34% were less than USD $500; and only 8% were more than USD $1,000.

Parker Trip Purpose, Duration, and Type of Parking Payment: Parkers that were destined for the study area were divided into three types according to their purposes, including working trips, shopping trips, and other reasons for trips. The sample consisted of 41% of work trips, which is the highest percentage; 24% of shopping trips; and 35% of other trips. 28% of the respondents were expected to stay in the city center for less than an hour, which was expected to be a short stay, wherase 33% were between an hour and 3 h, and the rest of the respondents were expected to stay for more than 3 h. The last two groups were people who had come to work and expected to have a long stay in the city center. Parking payments were classified as free parking and non-free parking (meaning the driver paid for parking). Only 64% of respondents were paid for parking their cars, and the rest were not paid. Where these latter respondents were parked was mostly in illegal parking spaces. This indicates that the driver could take more time to find available free parking spaces. More than 70% of the worker's trips have long trip duration, whereas less than 10% of non-worker trips have long trip duration, as shown in Fig. 3. Furthermore, the figure shows the classification of parkers' trip purpose by parking payment. The figure shows that the sample was nearly equally divided between paid and non-paid parking. This reflects that there are many illegal parking spaces that drivers can utilize to park their cars in the city center.

Number of People in the Car, Searching Time, and Time Spent: It was found that about 49% of the drivers drove alone, and 25% of the drivers had only one passenger in the car. The rest had more than one passenger in the car. The majority of respondents (90%) spent <10 min searching for parking spaces. This could be due to the high number of available parking spaces in the study area. In addition, 89% of travelers can reach their terminal in <10 min after parking their cars. Out of 380 respondents, 337 of them show short walking time, and only 43 of them show long walking time.

B. Response of Parkers to Parking Policies

Increase in parking cost

Fig. 4 presents the results of stated responses to an increase in parking cost and shows that 47% of users would never discontinue coming into the city center, no matter how much parking it will cost. About 36% of parking users would shift to using public transport. However, there are a small number of parkers who chose the other options.

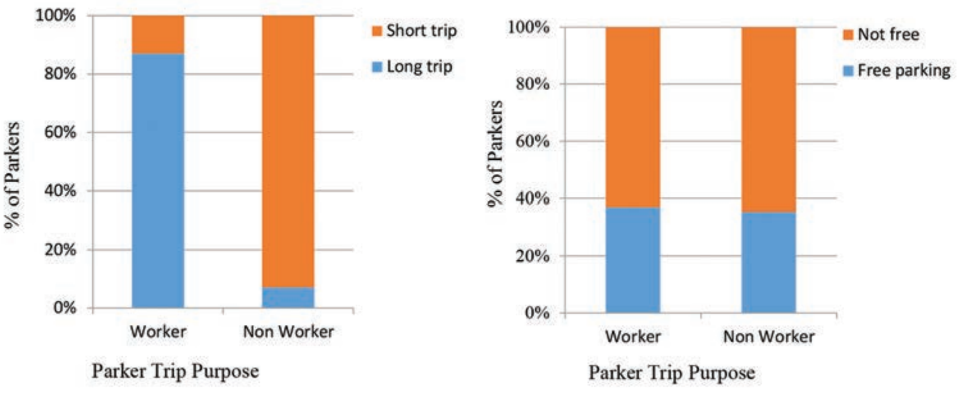

Fig. 3. Classifications of parkers' trip purposes by trip duration and parking payment.

These results indicate that increasing parking costs can be a good policy to reduce traffic congestion. A virtuous parking policy encourages people to shift modes of travel, use public transport facilities, or switch the time of day. These options will lead to decreased traffic congestion without decreasing the number of travelers to the city center (i.e., not reducing the vitality of the city center); they will also discourage people from canceling their trips to the city center. Therefore, the travelers' travel decisions were categorized into two groups. First, the positive change, which comprises no changes in travelers' travel decisions or changes in mode or time of day, Second, the negative change, which comprises alterations in terminal locations or canceling the trips, Fig. 4 also shows that the percentage of parkers who responded to the positive change was higher than the negative change. This indicated that the increase in parking prices would not significantly affect the attractiveness of the central area.

Decrease in parking supply

Fig. 5 shows that the percentage of users that would continue coming into the city or shift to using public transport was significantly higher than other options. This indicates that the percentage of parkers who responded to positive change was higher than the percentage of parkers who responded to negative change. Therefore, these results specify that the policy of decreasing parking supply can be a good policy to reduce traffic congestion without affecting the vitality of the center and causing travelers to move out of the city center.

C. Binary Logistic Models

Binary logistic regression models were estimated to predict the probability that parkers to the city center will change their travel behaviors according to applying the two suggested parking policies. The analysis process was conducted using the Statistical Package for the Social Sciences (SPSS) (SPSS, 2023). The two categorized travelers' travel decisions (positive and negative changes) were considered dependent variables to predict the probability of applying parking policies. The logit link function of the odds in logistic regression is signified by (υ) and serves as the dependent variable for the model. In a binary regression model, the logit is the natural logarithm of the odds that a circumstance arises for a specific event (Justo-Silva, Ferreira and Flintsch, 2021, Huang, et al., 2019, Alaswadko, et al., 2019, Alaswadko, 2017, Wuensch, 2014). In this study, the event is applying parking policies due to positive changes in parking users' behavior. The general form of this model is described below (1 and 2):

$$\upsilon = \ln [\text{odds (positive change)}] \qquad (1)$$

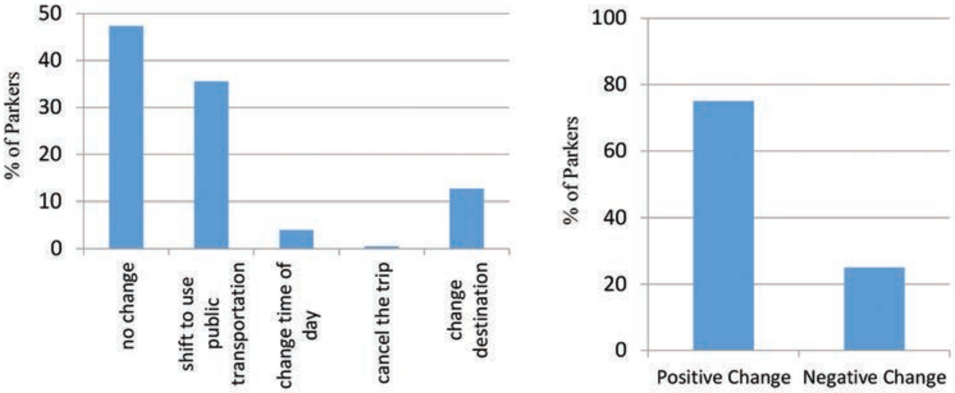

Fig. 4. Stated responses to the increase in parking costs.

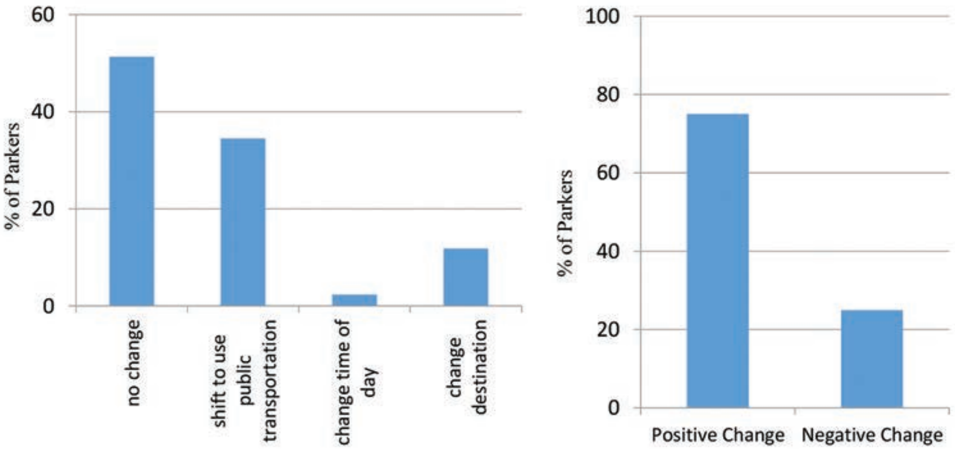

Fig. 5. Stated responses to a decrease in parking supply.

TABLE II
The Results of the Predicted Binary Model Increase Parking Costs

Explanatory variables	Coefficients (β)	Standard error	Wald	df	Sig. p-value*	Odds ratio	95% confidence interval limits	
							Lower limit	Upper limit
Intercept	1.817	0.785	5.363	1	0.021	6.152		
Trip origin	−0.134	0.070	3.723	1	0.049	0.874	0.763	1.002
Arrival time	−0.394	0.191	4.260	1	0.039	0.675	0.464	0.980
Income	−2.073	0.275	56.615	1	0.000	0.126	0.073	0.216
Trip purpose	0.340	0.153	4.916	1	0.027	1.405	1.040	1.898
Parking payment	0.836	0.269	9.662	1	0.002	2.306	1.362	3.905
Time searching	1.119	0.395	8.019	1	0.005	3.062	1.411	6.641

*: All variables are statistically significant (p<0.05) at 95% of confidence level

$$\upsilon = ln\ [\frac{probability\ of\ positive\ change}{probability\ of\ negative\ change}] \quad (2)$$

Where: ln is the natural logarithm: The probability of positive change of parkers' travelling decision can be obtained by the predicted log-odds using the following formula (3):

$$\text{The probability of positive change } = \frac{1}{1+exp\ (-\upsilon)} \quad (3)$$

The log-odds (υ) can be determined from the linear combination of contributed predictors.

Binary model for an increase in parking cost

The results of the binary logistic regression model for the sample used herein are shown in Table II. The second column in the table presents the estimated coefficient (B) for each variable. It can be seen that all variables are not included in the model because the insignificant variables are eliminated based on significant values ($p < 0.05$). The model is statistically significant, and each included variable has a significant coefficient with an odd ratio (exp B) value, which is an amount of the range in event odds resulting from a unit change in the variable within the lower and upper limits of the 95% confidence interval (Hosmer and Lemeshow, 2013). The constant value (i.e., intercept) is the predicted probability of positive change when the effects of all other variables in the model are assessed at zero. Accordingly, see (4):

The predicted probability of positive change is

$$= \frac{1}{1+exp\ (-\upsilon)} = \frac{1}{1+exp\ (-1.817)} = 0.86 \quad (4)$$

Consequently, about 86% of respondents within the city center were expected to see positive changes in parking users' behavior during the period of the study. Nonetheless, the average probability of negative changes was 14% ([1–0.86] × 100). The odds of positive changes were defined as the ratio of the probability of positive changes over the probability of negative changes. In that regard, the odds for positive changes were 6 (0.86/0.14), that is, the odds of positive changes in parkers' travel decisions with an increase in parking costs were 6 to 1. The effect of each variable, as shown in Table II, is as follows: Trip origin has a negative significant coefficient value and indicates that people coming from the west side of Duhok city are more likely to change their travel decision. Time needed to arrive has a negative significant coefficient value and indicates that people who have a long trip to reach their terminal are more likely to change their travel decision. Income has a negative significant coefficient value and indicates that travelers with more income are less likely to change their behaviors when parking prices increase. Trip purpose has a positive significant coefficient value and indicates that non-worker travelers are more likely to change their behaviors than worker travelers. Parking payment has a positive significant coefficient value and indicates that those who paid for parking are more likely to change their travel decisions as they are the most likely to need parking. Time needed for searching a park has a positive significant coefficient value and indicates that those who spend more time searching a park are more likely to change their travel decision. The developed logistic model can be evaluated by testing classification accuracy. The aptitude of the model to correctly forecast positive changes in parkers travel decisions due to applying the suggested policies is tested using cross-tabulation analysis. The frequency distribution of the estimated and observed changes in travel decisions due to such applied policies is displayed as a table in matrix format (Wuensch, 2014). Hence, to evaluate the success rate of the predicted logistic model, the numbers of respondents that are being correctly or incorrectly anticipated are determined. The cross-tabulation table shown in Table III is used to evaluate the accuracy of the estimated model and shows that 75% of the observed respondents are correctly assigned to the probability of applying the policy of increasing parking costs.

TABLE III
Correctly Estimated Results of the Predicted Binary Model to Increase Parking Costs

Observed	Estimated		
	Increase parking cost		Percentage correction
	No change	Change	
Increase parking cost			
No change	140	39	78.2
Change	55	145	72.5
Overall percentage			75.2

TABLE IV
The Results of the Predicted Binary Model to Decrease Parking Supply

Explanatory variables	Coefficients (β)	Standard error	Wald	df	Sig. p-value*	Odds ratio	95% confidence interval limits	
							Lower limit	Upper limit
Constant	0.288	0.797	0.131	1	0.018	1.334		
Origin	−0.142	0.068	4.420	1	0.036	0.867	0.759	0.990
Arrival time	−0.491	0.195	6.353	1	0.012	0.612	0.418	0.897
Age	−0.757	0.258	8.579	1	0.003	0.469	0.283	0.779
Income	−0.951	0.254	14.001	1	0.000	0.386	0.235	0.636
Trip purpose	0.442	0.153	8.310	1	0.004	1.556	1.152	2.102
Parking payment	1.363	0.266	26.257	1	0.000	3.908	2.320	6.582
Time searching	0.944	0.383	6.079	1	0.014	2.571	1.214	5.445

*: All variables are statistically significant ($p<0.05$) at 95% of confidence level

TABLE V
Correctly Estimated Results of the Predicted Model to Decrease Parking Supply

Observed	Estimated		
	Decrease parking supply		Percentage correction
	No change	Change	
Decrease parking supply			
No change	150	45	76.9
Change	53	131	71.2
Overall percentage			74.1

Binary model for decrease in parking supply

Table IV demonstrates the results of the binary logistic regression model for the responses of decreasing parking supply. The significant coefficients are the same as in the increasing cost model and have the same signs. However, the driver's age is also significant and has a negative coefficient, indicating that younger people are more likely to change their manners. The constant value is the predicted probability of positive change when the effects of all other variables in the model are assessed to be zero. Hence, the predicted probability of a positive change for a decrease in parking costs is 0.57. Thus, about 57% of respondents within the city center were expected to see positive changes in parking users' behavior during the study period. Even so, the probability of negative changes was 43% ([1–0.57] × 100). Therefore, the odds for positive changes over negative changes were 1.3 (0.57/0.43), that is, the odds of positive changes in parkers' travel decisions with decreasing parking supply were 1.3–1. For evaluating the model's accuracy, Table V shows the accuracy of the estimated model and demonstrates that 74% of the observed respondents are correctly assigned to the probability of applying the policy of decreasing parking supply.

IV. Conclusions and Anticipated Recommendations

In urban areas worldwide, managing traffic volume and movement is an ongoing challenge with significant implications for city infrastructure, environmental sustainability, and quality of life. Predictive logistic models have emerged as powerful tools in this domain, offering the ability to forecast and optimize parking policies to efficiently control traffic volume and movement. This case study explores the application of predictive logistic models to addressing parking policy challenges within urban environments. By leveraging data-driven insights and advanced analytical techniques, cities can proactively design and implement parking policies that mitigate congestion, reduce emissions, and enhance the overall urban experience. Through a detailed examination of real-world scenarios and outcomes, this study sheds light on the efficacy of predictive logistic models in shaping parking strategies and optimizing traffic management efforts. The majority of users entering Duhok city center from the west require a short time to reach their destination. They typically have average incomes, are on work-related trips, drive alone, pay for parking, spend a short time searching for parking spaces, have long durations of stay, and can reach their destination within a short walking distance. The percentage of parkers who respond positively to an increase in parking costs is higher than that of those who respond negatively, indicating that increasing parking prices would not significantly affect the attractiveness of the central area. Similarly, the percentage of parkers who respond positively to a decrease in parking supply is higher than that of those who respond negatively, suggesting that reducing parking supply could effectively reduce traffic congestion without diminishing the vitality of the center or causing travelers to move out of the city center. Individuals with longer trip times to reach their destination are more open to changing their travel decisions. Moreover, travelers with higher incomes are typically less inclined to accept changes in their activities due to parking restrictions. Non-workers are more likely to change their behavior than workers, whereas those who pay for parking are more likely to alter their travel decisions, increasing their need for parking. In addition, individuals who spend more time searching for parking are more likely to change their travel plans, and younger people are more likely to do so than older individuals. Seventy-five percentages of observed respondents are correctly assigned to the probability of applying the policy of increasing parking costs, whereas 74% are correctly assigned to the probability of applying policies to decrease parking supply. This study recommends implementing the presented parking policies to reduce traffic congestion in Duhok city center. The benefits of these policies include reducing travel time, lowering costs for some users, improving city center amenities, boosting economic activities, decreasing air pollution, reducing energy consumption, increasing productive land use, and decreasing the necessity to expand roads. Through a comprehensive review of existing literature and empirical evidence, this case study aims to contribute to the growing body of knowledge on sustainable urban transportation planning and offer practical recommendations for policymakers, city planners, and transportation authorities.

REFERENCES

Abaza, K.A., 2021. Optimal novel approach for estimating the pavement transition probabilities used in Markovian prediction models. *International Journal of Pavement Engineering*, 23, 8.

Abdullah, P.H., 2013. *The Development of a Trip Assignment Algorithm to Improve Traffic Flow in Duhok City*. M.Sc. Thesis Submitted to the Faculty of Engineering and Applying Science, University of Duhok, Duhok, Iraq.

Al-Ani, N., 2021. *Study of Strategic Plan to Establish a Bus Transportation System in Duhok City Using ITSAs*. M.Sc. Thesis, Technical College of Engineering, Duhok Polytechnic University, Kurdistan Region, Iraq.

Alaswadko, N., 2016. *Deterioration Modelling of Granular Pavements for Rural Arterial Roads*. Thesis (PhD). Swinburne University of Technology, Melbourne, Australia.

Alaswadko, N., Hassan, R., Meyer, D., and Mohammed, B., 2019. Probabilistic prediction models for crack initiation and progression of spray sealed pavements. *International Journal of Pavement Engineering*, 20(1), pp.1-11.

Alaswadko, N.H., 2017. Prediction modelling approach for crack progression of heavy duty flexible pavements. *Journal of Duhok University*, 20(1), pp.307-318.

Aros-Vera, F., Marianov, V., and Mitchell J.E., 2013. P-hub approach for the optimal park-and-ride facility location problem. *European Journal of Operational Research*, 226, pp.277-285.

Aswad, N.H., 2003. *Parking Characteristics Study and their Effect in Dohuk City Center*. In: M.Sc. Thesis Submitted to College of Engineering, University of Salahaddin, Erbil, Iraq.

Chen, X., Yin, R., An, Q., and Zhang, Y., 2021. Modeling a distance-based preferential fare scheme for park-and-ride services in a multimodal transport network. *Sustainability*, 13, p.2644.

Dijk, M., and Parkhurst, G., 2014. Understanding the mobility transformative qualities of urban park and ride polices in the UK and the Netherlands. *International Journal of Automotive Technology and Management*, 14(3/4), pp.246-270.

Ding, L., and Yang, X., 2020. The response of urban travel mode choice to parking fees considering travel time variability. *Advances in Civil Engineering Journal*, 2020, p.8969202

Dowling, C., Fiez, T., Ratliff, L., and Zhang, B., 2017. How much urban traffic is searching for parking? In: *Computers and Society*. Oxford University Press, Oxford.

Fahmy, A., Nazareth, F., and Dyck, M., 2021. *Parking Policy for Sustainable, Accessible Communities. University of British Columbia, Social Ecological Economic Development Studies (SE EDS) Sustainability Program, April 2021*.

Franco, S.F., 2017. Downtown parking supply, work-trip mode choice and urban spatial structure. *Transportation Research Part B Methodological*, 101, pp.107-122.

Gallo, M., D'Acierno, L., and Montella, B., 2011. A multilayer model to simulate cruising for parking in urban areas. *Transport Policy*, 18, pp.735-744.

Goulias, K., Davis, A.W., Lee, J., Lundberg, A., and Mcbride, E., 2016. Behavioural micro-dynamics of car ownership and travel in the Seattle metropolitan region from 1989 to 2002. *European Journal of Transport and Infrastructure Research*, 16(4), pp.735-753.

Guo, Z., 2013. Does residential parking supply affect household car ownership? the case of new york city. *Journal of Transport Geography*, 26(1), pp.18-28.

Habib, K., Mahmoud, M., and Coleman J., 2013. Effect of parking charges at transit stations on park-and-ride mode choice: Lessons learned from stated preference survey in Greater Vancouver, Canada. *Transportation Research Record: Journal of the Transportation Research Board*, 2351(1), pp.163-170.

Hosmer, D.W., and Lemeshow, S., 2013. *Applied Logistic Regression*. 3rd ed. Wiley, New York, Hoboken.

Huang, K., Liu, Z., Zhu, T., Kim, I., and An, K., 2019. Analysis of the acceptance of park-and-ride by users: A cumulative logistic regression approach. *Journal of Transport and Land Use*, 12, pp.637-647.

Justo-Silva, R., Ferreira, A., and Flintsch, G., 2021. Review on machine learning techniques for developing pavement performance prediction models. *Sustainability* (*Switzerland*), 13, p.5248.

Khalid, S.W., 2011. *Characteristics and Performance of Public Transit Bus in Duhok City*. In: M.Sc. Thesis Submitted to College of Engineering, University of Salahaddin, Erbil, Iraq.

Kim, S., Tak, Y., Barmpounakis, M., and Geroliminis, N., 2024. Monitoring Outdoor Parking in Urban Areas with Unmanned Aerial Vehicles. *IEEE Transactions on Intelligent Transportation Systems*, 99, pp1-14.

Manville, M., and Shoup, D., 2005. Parking, people, and cities. *Journal of Planning and Development*, 131, pp.233-245.

Meek, S., Ison, S., and Enoch, M., 2008. Role of bus-based park and ride in the UK: A temporal and evaluative review. *Transport Reviews*, 28(6), pp.781-803.

Mei, Z., Lou, Q., Zhang, W., Zhang, L., and Shi, F., 2017. Modelling the effects of parking charge and supply policy using system dynamics method. *Journal of Advanced Transportation*, 2017, p.6463586.

Moeinaddinia, M., Asadi-Shekaria, Z., Ismailb, C.R., and Shaha, M.Z., 2013. A practical method for evaluating parking area level of service. *Land Use Policy*, 33, pp.1-10.

Molan, V., and Simićević, J., 2018. Park-and-ride system: Urban parking management policy. *International Journal for Traffic and Transport Engineering*, 8(4), pp.426-445.

Nieuwkoop, R., Axhausen, K.W., and Rutherford, T.F., 2016. A traffic equilibrium model with paid-parking search. *Journal of Transport Economics and Policy (JTEP)*, 50, pp.262-286.

Ortega, J., Tóth, J., and Péter, T., 2021. Planning a park and ride system: A literature review. *Future Transp*, 1, pp.82-98.

Patel, A., Tiwari, V., Ojha, M., and Vyas, O.P., 2023. Ontology-based detection and identification of complex event of illegal parking using SPARQL and description logic queries. *Chaos, Solitons and Fractals*, 174, pp.113774.

Shen, X., Chen, F., Su1, B., Che Q., and Ya, J., 2017. Optimization of park-and-ride system: A case study of Shunyi in Beijing. *Advances in Mechanical Engineering*, 9(8), pp.1-8.

Shiftan, Y., and Burd-Eden, R., 2001. Modeling the response to parking policy. *Journal of Transportation of Research Record*, 1765(1), pp.27-34.

Shoup, D., 2005. *The High Cost of Free Parking*. The American Planning Association, Planners Press, Chicago.

Shoup, D., 2018. *Parking and the City*. Routledge, New York.

Shoup, D., 2024. Parking benefit districts. *Journal of Planning Education and Research*, 44(4), pp.2154-2166.

Shtayat, A., Moridpour, S., Best, B., Rumi, S., 2022. An overview of pavement degradation prediction models. *Journal of Advanced Transportation*, 2022, p.7783588.

SPSS, 2023. *IBM SPSS Statistics for Windows. Version 25.0*. IBM Corp, Armonk, NY.

SSC, 2023. *Sample Size Calculator*. Available from: https://www.surveysystem.com/sscalc.htm [Last accessed on 2023 Oct 15].

Syed, S., Golub, A., and Deakin, E., 2009. Response of regional rail park-and-ride users to parking price changes: System wide results and a detailed study of two stations. *Transportation Research Record: Journal of the Transportation Research Board*, 2110, pp.155-162.

Wang, H., Zhu, S., Long, Z., Chen, M., and Gao, R., 2024. Reducing Traffic Congestion through Parking Pricing Policy: A System Dynamics Simulation. Available from: https://www.ssrn4764731

Wuensch, K.L., 2014. *Binary Logistic Regression with SPSS*. Available from: https://core.ecu.edu/psyc/wuenschk/mv/multreg/logistic-spss.pdf [Last accessed on 2023 Oct 21].

Yan, X., Levine, J., and Marans, R., 2018. The effectiveness of parking policies to reduce parking demand pressure and car use. *Transport Policy Journal*, 73, pp.41-50.

Yoka, R., 2018. *Shoup's Parking and the City Highlights Parking Reform*. International Parking and Mobility Institute. Available from: https://www.parking-mobility.org [Last accessed on 2024 Dec 20].

Zhang, L., Wang, Y.P., and Sun J., 2016. The sightseeing bus schedule optimization under park and ride system in tourist attractions. *Annals of Operations Research*, 273, pp.587-605.

Zhang, R., Wang, L.P., and Yan, Z.B., 2009. Park-and-ride demand analysis and parking pricing: A case study of shanghai in rail transit park-and-ride operation. *Urban Transport of China*, 2, pp.13-18.

A Comprehensive Review of Facial Beauty Prediction Using Multi-Task Learning and Facial Attributes

Ali H. Ibrahem[1†] and Adnan M. Abdulazeez[2]

[1]Department of IT, Technical College of Informatics - Akre, Akre University for Applied Sciences,
Kurdistan Region – F.R. Iraq

[2]Technical College of Engineering, Duhok Polytechnic University,
Kurdistan Region – F.R. Iraq

***Abstract*—Beauty multi-task prediction from facial attributes is a multidisciplinary challenge at the intersection of computer vision, machine learning, and psychology. Despite the centrality of beauty in human perception, its subjective nature—shaped by individual, social, and cultural influences—complicates its computational modeling. This review addresses the pressing need to develop robust and fair predictive models for facial beauty assessments by leveraging deep learning techniques. Using facial attributes such as symmetry, skin complexion, and hairstyle, we explore how these features influence perceptions of attractiveness. The study adopts advanced computational methodologies, including convolutional neural networks and multi-task learning frameworks, to capture nuanced facial cues. A comprehensive analysis of publicly available datasets reveals critical gaps in diversity, biases, and ground truth annotation for training effective models. We further examine the methodological challenges in defining and measuring beauty, such as data imbalances and algorithmic fairness. By synthesizing insights from psychology and machine learning, this work highlights the potential of interdisciplinary approaches to enhance the reliability and inclusivity of automated beauty prediction systems.**

***Index Terms*—Convolutional neural network, Facial beauty prediction, Facial attractiveness, Human rater.**

I. Introduction

Studies in different fields such as biology, philosophy, psychology, and art have tried to quantify beauty and challenged many aspects of esthetics and facial analysis. Face beauty assessment using computer vision is a relatively novel topic of study with a broad range of applications, including plastic surgery, the cosmetic industry, and facial photographs beautician (Bougourzi, et al., 2023). Facial beauty prediction (FBP) is a multi-paradigm computation problem that aims to develop human-like models for automatically assessing facial attractiveness. Recent studies have explored the use of multi-task learning (MTL) and transfer learning (TL) are robust techniques that can significantly reinforce the performance of FBP models. By leveraging these methods, researchers can build more strong and accurate systems that can capture complex facial attributes and their interplay. Combining these methods allows for better generalization across tasks and datasets, making them particularly useful in scenarios, such as motor imagery signal classification (Xie, et al., 2023). A diagram of the classification model of facial image attractiveness based on the TL approach is shown in Fig. 1. The diagram typically includes some key stages: preprocessing, feature extraction, and classification. In the preprocessing stage, facial images are normalized and augmented to enhance the dataset's diversity and robustness. During the training stage, a pre-trained convolutional neural network (CNN), such as VGG16 or ResNet50, is employed for feature extraction. This pre-trained model, initially trained on a large dataset, such as ImageNet, is fine-tuned on the attractiveness classification task by replacing its top layers with a new fully connected layer specific to the new task. The model learns to map the extracted features to attractiveness scores. In the testing stage, the fine-tuned model evaluates the unseen facial images to predict their attractiveness, demonstrating its generalization capabilities. The performance is then assessed using metrics such as accuracy and precision. The advancement of the model is enhancing predictive accuracy through MTL, which integrates task and feature correlations for effective knowledge sharing and moving beyond the traditional or classical handcrafted features for achieving an end-to-end optimization using deep learning. Moreover, the synthesis highlights the transformative potential of these models across applications in healthcare, cosmetics, social media, and more. The integration of 3D modeling and dynamic datasets could further refine predictions, offering more personalized and context-aware assessments.

ARO-The Scientific Journal of Koya University
Vol. XIII, No. 1 (2025), Article ID: ARO.11850. 12 pages
Doi: 10.14500/aro.11850
Received: 07 October 2024; Accepted: 01 January 2025
Regular review paper; Published: 01 February 2025
†Corresponding author's e-mail: ali.hikmat@auas.edu.krd

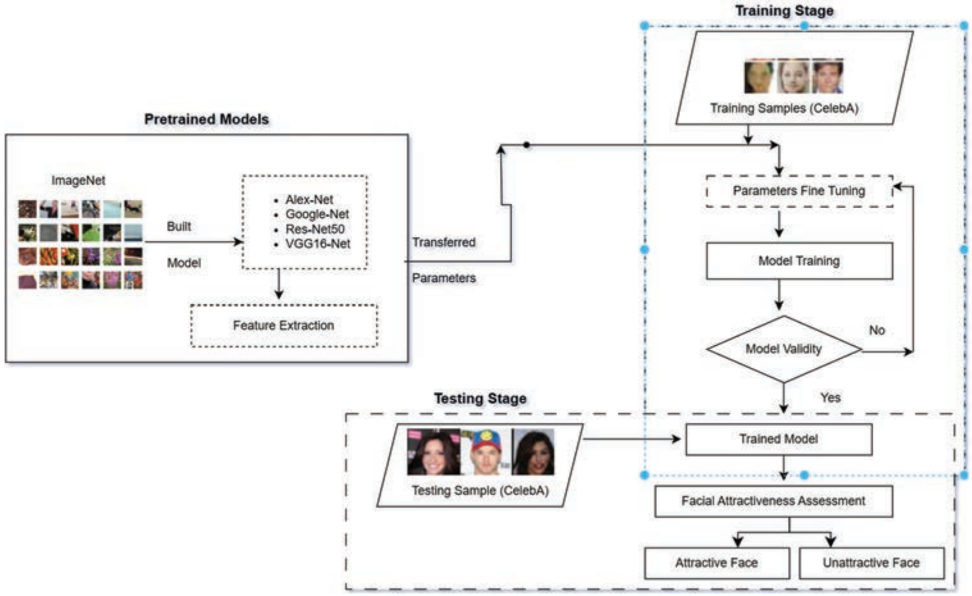

Fig. 1. The classification model of facial image attractiveness based on transfer learning path (Saeed, Abdulazeez and Ibrahim, 2022).

In the context of MTL, various paths have been proposed to facilitate knowledge sharing between tasks. These paths can be largely categorized into three groups based on the relationship between tasks or features. These approaches take into account both task relationships and trait correlations. While the max-margin method excels in discrimination, the Bayesian method offers greater flexibility in combining rich prior information (Taherkhani, et al., 2021).

Incorporating task relationships during training: This approach considers the relationships between tasks during the training phase. For example, one method treats the MTL challenge as a multi-label classification problem, utilizing prior knowledge of closely related labels. The model uses a max-margin multi-label formulation and integrates correlation-based interactions between labels into the prediction loss function.

Discovering common feature structures: Methods falling into this category target to identify common feature structures shared across all tasks or explore related features that are common among them. Such as a non-parametric Bayesian model is proposed to learn a commonly hidden space for all related tasks. This shared subspace captures the relationships between tasks, where each task's parameters (e.g., weight vectors in linear Support vector Machine SVM) are explained as a linear combination of basis tasks forming the latent shared subspace.

Recent way considering both tasks and feature correlations: The third category includes recent models, such as the max-margin method and Bayesian method.

From FBP to Personalized Facial Beauty assessment, the objective is to develop a model that can estimate facial attractiveness as accurately as humans. Traditional approaches often trust geometric features or global appearance descriptors (such as Color Histograms, Local Binary Patterns, Histograms of Oriented Gradients [HOG], and Gabor Filters) to learn FBP. However, these handcrafted attributes heavily rely on heuristic rules. With the remarkable success of deep learning, FBP can now be optimized using (CNNs) in an end-to-end manner. It's significant to note that most existing FBP methods are designed to learn esthetics at the population level (Lin, et al., 2023).

Currently, Artificial Intelligence (AI) and image improvement, receiving and quantifying beauty remains an interrogation able yet fascinating pursuit. This literature review shows the landscape of beauty multi-functional predictions grounded in face attributes analysis. With the proliferation of deep learning methodologies, researchers have investigated leveraging facial features to predict different sides of beauty, including attractiveness, age, gender, and ethnicity. This review begins by studying the foundational theories of beauty perception, encompassing both evolutionary and cultural perspectives. It proceeds to discuss the methodologies employed in beauty prediction models, encompassing feature extraction, dataset curation, and algebraic frameworks for instance CNNs and generative adversarial networks (GANs) (Cowen, et al., 2021).

Furthermore, this review investigates the implications and applications of beauty multi-task predictions across diverse domains, including cosmetics, healthcare, and social media. It highlights the potential societal impacts, ethical considerations, and biases inherent in beauty prediction algorithms. Moreover, it reviews the challenges faced in developing universal standards of beauty and the implications for inclusivity and diversity. Finally, this review outlines some future directions for research in this field, emphasizing the need for interdisciplinary collaboration, robust evaluation metrics, and transparency in algorithmic decision-making. By synthesizing insights from psychology, computer vision, and sociology, this literature review aims to provide a comprehensive overview of the current state and prospects of beauty multi-task predictions based on face attributes. The current literature review is structured according to the following. First, the datasets and image rating systems critical for training beauty prediction models are introduced. Second, several related works offering a comparative analysis of key results are highlighted. Finally, a conclusion and future directions for research, emphasizing the necessity for ethical and inclusive advancements in beauty prediction systems are presented.

II. Facial Beauty Dataset and Image Rating

The establishment of a definitive standard for beauty remains challenging due to its subjective nature. Therefore, FBP lacks extensively accepted authoritative data, making the construction of large-scale databases difficult. This section reviews the datasets commonly used in FBP studies, emphasizing their strengths, limitations, and the diversity they provide. An ideal dataset should encompass a range of attributes, including gender and age for the diversity of facial images. However, the available datasets often lack diversity, limiting model generalizability. For rating methods, facial images are typically annotated with beauty scores using human raters. The accuracy of these ratings significantly impacts the training of beauty prediction models. Despite the studies suggesting that facial beauty is a universal concept that can be learned through machine learning, establishing a definitive standard for beauty remains challenging due to the subjective nature of individual judgments. Consequently, FBP lacks widely accepted authoritative data, making the construction of large-scale databases difficult. A diverse range of attractiveness is essential for datasets used in facial image beauty research, which underscores the importance of selecting an appropriate face database for optimal model performance. Facial images can be sourced from the Internet, digital cameras, 3D scanners, existing facial image databases, and computer-generated images. Furthermore, these images must be evaluated using various rating methods. They are then labeled with beauty scores to establish the ground truth for the learning process and validate the model (Gan, et al., 2020).

A. Facial Images Databases

An ideal database should encompass a diverse array of facial images, representing all beauty levels across different genders, ages, races, poses, and expressions. In addition, it is essential for the dataset to include both ends of the facial attractiveness spectrum, featuring both highly attractive and very unattractive faces, to provide a comprehensive representation of the concept of beauty (Mu, 2013). However, due to privacy concerns, the majority of datasets are not publicly accessible. In addition, landmarks are critical for evaluating the geometry cue, which is lacking in some of the benchmarks (Aarabi, et al., 2001). The majority of existing datasets are relatively small (Eisenthal, Dror and Ruppin, 2006; Gunes and Piccardi 2006). Moreover, they are neutral (postures, expression, attractiveness), insufficiently diverse, and most of them are limited for female facial beauty (Altwaijry and Belongie 2013; Kalyta, et al., 2022).

Gender is an important factor in facial beauty analysis, with many facial databases primarily focusing on female subjects. These datasets often yield better results in beauty classification than those centered on male subjects. This discrepancy may be due to the relative simplicity of analyzing and computing beauty in female faces compared to male faces. Consequently, researchers frequently use images of females or a mix of both genders in their studies, whereas datasets comprising exclusively male images are less common (Ahmadimehr and Moridani 2020). Due to the absence of datasets that meet the specific conditions required for (FBP), such as considering diverse attractiveness levels, particularly extremes of attractiveness and unattractiveness, researchers have resorted to using general face recognition datasets cited in references (Schmid, Marx and Samal. 2008), as well as facial expression datasets from (Xu, et al., 2018) for their FBP studies especially in the initial stages. The limitations posed by variations in facial posture and expression are critical factors that can constrain both dataset availability and model performance. Consequently, existing FBP databases predominantly consist of frontal face images with neutral expressions.

In spite of the rarity of facial image datasets especially designed for FBP and related tasks, several well-known face datasets are mostly used as benchmarks for this purpose as shown in Table I. Gray, et al. (2010) carried out the first attempt to address the issue of facial feature landmark localization and imposing stringent limits on training samples by building a large number of FBP database of 2056 females known as Hot or Not HotorNot. It is a very difficult dataset since the images are under unconstrained conditions on the background, expression, position, lighting, race and age with no use of landmarks, as well as the problem of predicting the locations of landmark features sufficiently. The same notion was also used for constructing a benchmark called the Large-Scale Asian Facial Beauty Database LSAFBD (Zhai, et al., 2016), which comprised 20,000 labeled images of gender and 80,000 unlabeled ones. However, both datasets are based on apparent features only and are not accessible publicly.

Most prediction performances of facial esthetic are fulfilled on nearly small facial datasets through employing conventional machine learning or shallow network learning methods (Zhai, et al., 2020). As a result, small datasets often lead to overfitting during the training of the model. This makes the prediction model less effective. In addition to this, datasets that are built under specific computational constraints limit the performance and flexibility of the model. This complicates the comparisons between models that are developed with various methodologies. For example, the widely-used FBP databases the South China University of Technology SCUT-FBP5500 (Zhai, et al., 2020) and the South China University of Technology SCUT-FBP (Xie, et al., 2015) have produced promising results in many researches. However, SCUT-FBP is made up of only 500 Asian female faces, restricting the performance of models trained on this data. Conversely, the SCUT-FBP5500 dataset, though relatively large, has limitations in terms of lighting, blurriness, and positioning, which can

TABLE I
FBP DATASET BENCHMARKS

Database Name	References	Year	Size	Gender	Age	Landmark	Ethnicity	Pose	Expression	Beauty score
Celeb A	Saeed and Abdulazeez, 2022	2022	200K	F/M	Different	5	Different	Different	Different	2
LFWA Labeled Faces the Wild Attributes	Fan, et al., 2019	2019	13,233	F/M	Different	N/A	Different	Different	Different	N/A
RAF-DS	Zheng, et al., 2024	2024	29672	F/M	Different	68	Diverse	Almost frontal	Different	N/A
CASIA-WebFace	Sekhar, et al., 2024	2024	500000	F/M	Different	68	Diverse	Diverse	Different	N/A
M2B	Nguyen, et al., 2013	2021	1240	F	19-40	N/A	Western/Eastern	Different	Different	10
HotorNot	Xu, et al., 2018	2018	2056	F	18-40	N/A	Diverse	Almost frontal	Different	10
Beauty 799	Chen, Xu and Zhang, 2014	2014	799	F	N/A	98	Diverse	Frontal	Almost Neutral	3
SCUT-FBP	Xie, et al., 2015	2015	500	F	N/A	84	Asian	Frontal	Neutral	5
LSAFBD	Gan, et al., 2023	2023	20000	F/M	Different	5	Asian	Almost frontal	Different	5
SCUT-FBP5500	Lebedeva, Guo and Ying, 2022	2022	5500	F/M	15–60	86	Asian/Caucasian	Frontal	Neutral	5
MEBeauty	Lebedeva, Guo and Ying, 2022	2022	2550	F/M	Different	N/A	Diverse	Different	Different	10
CFD	Gan, et al., 2023	2023	597	F/M	17–65.	86	Diverse	Almost frontal	Different	7
SCface	Grgic, Delac and Grgic, 2011	2011	4160	F/M	Different	N/A	Diverse	Different	Neutral	N/A

impact the effectiveness of attractiveness prediction models (Lebedeva, Guo and Ying, 2021). Moreover, researchers have shown that the SCUT-FBP5500 dataset has an imbalanced distribution of beauty scores, potentially influencing correlation analyses. Another public dataset, the CelebFaces Attributes dataset Celebrity Attributes (CelebA) (Liu, et al., 2015), contains over 200,000 images with 40 attribute annotations, including attractiveness. Despite its extensive range of poses and backgrounds, CelebA is mostly utilized in computer vision tasks such as face recognition, detection, component localization, editing, and synthesis. While it has been frequently employed for facial beauty classification, its binary beauty scores (attractive and unattractive) simplify computation but may not fairly evaluate beauty. The range of beauty scores affects considerably the fairness of beauty assessment. This makes the establishment of robust ground truth fundamental for both learning and model validation processes.

Real-world Affective Faces Dataset (RAF-DS) consists of over 30,000 facial images annotated with different expressions and facial attributes. It was labeled through crowdsourcing, variation, and ensuring high reliability. While primarily designed for expression recognition tasks in FBP (Zheng, et al., 2024). The Surveillance Cameras Face database (SCface) (Grgic, Delac and Grgic, 2011) includes 4,160 facial images captured by surveillance cameras in real-world conditions. The database contains images of 130 individuals taken from diverse angles and with low quality to simulate surveillance scenarios. SCface serves as a crucial resource for face recognition tasks in challenging environments, for example, scenarios with varying distances and inconsistent lighting conditions.

Chinese Academy of Sciences Institute of Automation WebFace (CASIA-WebFace) dataset provided by the Chinese Academy of Sciences Institute of Automation, consists of around 494,000 facial pictures belonging to 10,575 different individuals. It is primarily created for use in face recognition research and encompasses images obtained from the web spanning various conditions such as pose, expression, and lighting. This diversity makes it an excellent choice for training and evaluating face recognition algorithms, although its primary focus is not on beauty evaluation (Sekhar, et al., 2024). In Gan, et al. (2023), the Chicago Face Database is a thorough collection of images showcasing faces with a variety of demographic characteristics, such as age, ethnicity, and gender. It offers precise evaluations on aspects, such as attractiveness, trustworthiness, and other social traits, which enhances its utility for research in social perception and facial features analysis. This dataset is commonly employed in psychological with behavioral studies, emphasizing social sciences instead of computational beauty forecasting.

Recently, a Multi-Ethnic (ME Beauty) dataset consists of 2,550 in-the-wild facial images of both males and females, named ME Beauty (Lebedeva, Guo and Ying, 2022), has been introduced and is expected to become a prominent resource for further study in facial beauty assessment. However, the personalized nature of FBP may be influenced by the relatively considerable number of raters. Existing facial datasets primarily concentrate on static features. To address dynamic FBP, Weng, et al. (2021) developed the first Video-based Facial Attractiveness Prediction (VFAP) dataset, which includes 1,430 short video clips of facial performances from TikTok. Variations in beauty scores may take place because of using likes, comments, and forward as indicators of attractiveness. In addition to this, the gender distribution in TikTok's facial performance videos is uneven which makes the beauty rankings of male faces less easily explained in comparison to those of female faces.

The challenges outlined in this review necessitate innovative computational approaches, which are discussed in the next section. Building on the dataset limitations mentioned in the previous section. Researchers have developed sophisticated computational methods to enhance FBP systems. For Deep Learning, techniques such as CNNs enable the end-to-end optimization of beauty prediction, leveraging features such as facial symmetry and texture. Regarding MTL, integrating auxiliary tasks, such as age or gender prediction, MTL frameworks enhance the robustness of beauty prediction models. These methods demonstrate the potential to advance beauty prediction systems, setting the stage for a deeper exploration of related works.

III. Related Works

The related work is divided into three parts mainly: CNN, MTL, and Machine learning. This section synthesizes findings from the available research, highlighting contributions to FBP while identifying gaps for future studies. For the comparison of computational approaches, the Studies using CNN architectures, such as VGG16, EfficientNetV2B0, and ResNet50, balance computational cost against predictive performance. Lightweight models prioritize efficiency but may compromise precision. Challenges and future directions indicate key limitations include dataset biases, overfitting, and subjective beauty standards. Addressing these requires improved dataset diversity, advanced multimodal methods, and fairness-aware models.

A. CNN

Saeed and Abdulazeez (2021). Advanced deep learning techniques, particularly deep CNNs (DCNN), have been employed to assess facial attractiveness – a task shaped by subjectivity and cultural influences. Challenges in this domain include the lack of comprehensive datasets encompassing diverse attributes such as age, gender, culture, ethnicity, and facial expressions, as well as the absence of standardized evaluation metrics for FBP systems. Despite their relevance in areas, such as beauty product recommendations and cosmetic procedures, FBP studies face hurdles, such as limited datasets, resource constraints, and inconsistent assessment criteria. Current approaches address data scarcity through semi-supervised learning, data augmentation, and GANs. Developing diverse datasets and incorporating 3D facial models, along with varied rating methods, can enhance predictive accuracy and foster further advancements, paving the way for future research in FBP technologies.

Favorskaya and Pakhirka (2023) Introduced an innovative multi-task CNN for age-group classification enhanced by auxiliary tasks such as the identification of gender and facial expression analysis. The model features three interconnected CNN branches sharing initial feature extraction layers with relatively straightforward architectures. Different from the traditional approaches, the age-group classification task is framed as a ranking problem rather than a regression, improving prediction accuracy. Tested on five Internet Movie Database (IMDB), University of Tennessee, Knoxville Face Dataset UTKFace, and Morphological MORPH II—the model outperformed Densely Connected Convolutional Networks (DenseNet) and queeze-and-Excitation Networks (SENet), achieving a mean accuracy of 96.8% for age-group ranges (18–25), (26–40), and (41–65). This work highlights the benefits of leveraging auxiliary attributes and demonstrates the potential of MTL in facial analysis. The study overlooks substantial challenges such as dataset imbalance, real-world applicability, and the inclusion of diverse facial attributes, all of which can impact the robustness and fairness of the model.

Gao, et al. (2018) addressed facial attractiveness prediction (FAP) using a deep MTL strategy. The proposed model considers both texture and shape (geometric landmarks) by incorporating two tasks: predicting attractiveness scores and localizing fiducial landmarks. A lightweight CNN is designed to learn these tasks effectively, even with limited training data. Evaluated on the SCUT-FBP dataset, the method achieves a correlation score of 0.92, demonstrating its efficacy. Furthermore, the model outperforms several cutting-edge approaches and reliably compares facial images pre- and post-make-up or beautification. This research highlights the advantages of a MTL framework for precise and efficient facial beauty analysis.

B. MTL

Another study (Savchenko, 2021) introduced an innovative training pipeline for compact CNNs, achieving cutting-edge performance in recognizing facial expressions and attributes across various datasets. Utilizing MTL and pre-training on the extensive Visual Geometry Group Face (VGGFace2) dataset, the method enhances resilience to face extraction and alignment challenges. The models, trained on tightly cropped faces, deliver high accuracy, impressive speed, and a small footprint, making them ideal for mobile devices. Although the models perform exceptionally well, reliance on conventional classifiers (e.g., SVMs, random forests) slightly limits their accuracy below state-of-the-art levels. This study highlights the potential of lightweight architectures for efficient decision-making in practical scenarios. The robustness to face extraction and alignment is stated, but the potential limitations or challenges of relying on cropped faces without margins are not addressed. Moreover, the discussion on challenges specific to emotion recognition is limited.

Fan, et al. (2019) presented an innovative MTL framework for predicting face attributes, focusing on a smile and gender recognition tasks. The architecture addresses the challenges of conventional MTL models by integrating attention modules into task-specific layers, enabling the model to learn disentangled representations for predicting face attributes through softmax layers. Experiments on the LFWA and FotW both datasets demonstrate the model's superior performance over traditional MTL architectures and state-of-the-art methods. Future directions include expanding the model to additional face feature tasks, applying attention mechanisms to other layers, and exploring dynamic weighting methods to enhance predictive capabilities. The research gap lies in the limited scope of tasks (smile and gender), static task relationships, and restricted application of attention mechanisms to task-specific layers. In addition, the scalability, dynamic weighting, and generalizability of the model across diverse datasets are unexplored. The research issue focuses on enhancing MTL frameworks to dynamically model task dependencies, generalize across varied attributes, and improve computational efficiency.

The 2M BeautyNet, a multi-input multi-task network designed for FBP is conducted by Gan, et al. (2020). The network prioritizes beauty prediction as its core task while leveraging gender recognition as a secondary task through multi-task TL to boost performance. By transferring pre-trained network parameters across datasets, the model enhances accuracy. It employs a multi-task loss automatic learning strategy to balance contributions from each task, preventing dominance by any single task. After training, a random forest classifier replaces the softmax classifier for improved results. Experimental findings on the SCUT FBP5000 with LSFBD databases show the model achieves an FBP accuracy of 68.23%, surpassing alternative approaches. Future enhancements include exploring additional tasks for MTL, integrating local information, and accounting for other factors influencing facial beauty. This methodology shows promise for applications in esthetic surgery, cosmetic recommendations, and facial beautification, but the research shows encouraging outcomes in forecasting facial attractiveness and fails to consider the influence of various demographic characteristics, such as gender, age, or the inclusion of 3D facial traits, which could improve the adaptability and practical use in real-world scenarios of the model.

Another study by Lin, et al. (2021) described an innovative multi-task network that is created to simultaneously identify faces and forecast facial characteristics (such as gender and age). Instead of treating face detection and attribute prediction as two separate tasks, the study has merged them into a unified model. It has also introduced an optimization technique based on noise estimation to dynamically adjust the weights of multi-task losses, enhancing task equilibrium. Experiments conducted on the CelebA dataset demonstrate that this approach achieves an excellent performance in terms of both accuracy and speed.

C. Machine Learning

Lebedeva, Guo and Ying (2023) focus on the personalized evaluation of facial attractiveness, aiming to accommodate the unique beauty preferences of individuals. Unlike conventional models that predict universal beauty norms, the proposed method uses meta-learning to capture shared beauty preferences during meta-training and adapts to new individuals with minimal data in the meta-testing phase. Tests on a diverse dataset of facial attractiveness – varying in age, ethnicity, gender, and expression – demonstrate the technique’s ability to discern individual preferences and outperform current models in personalized scenarios. Future research can explore alternative machine learning techniques to enhance accuracy with limited annotated samples, investigate 3D FAP, utilize active learning to optimize data, and integrate the approach into recommender systems to address cold-start issues. The main point of the research is evaluating personalized facial attractiveness. However, it is experiencing difficulties in managing scarce labeled data, incorporating diverse cultural preferences, and ensuring efficient scalability for practical applications such as recommendation systems. Bridging these deficiencies can improve forecast accuracy, address cold-start problems, and allow for effective deployment. Machine-learning methods are applied to explore the impact of facial geometric attributes on attractiveness and emotional interpretation, focusing on changes after rhinoplasty. Analysis of data from 42 patients using multivariate regression revealed that increased nasolabial and nasofrontal angles correlated with greater attractiveness. Neural networks proved most effective in recognizing facial expressions, emphasizing the importance of mouth, eyebrows, and eye shape in emotion identification. These results suggest that highlighting these geometric features in rhinoplasty can enhance esthetic outcomes. Furthermore, findings from emotion classification support an improved version of the Facial Action Coding System, demonstrating its reliability in linking facial structure and emotions. The research highlights the role of data-driven approaches in shaping plastic surgery practices (Štěpánek, Kasal and Mestak, 2018). In addition, Zhang, Xiao and Lu (2018) inducted models to predict and enhance facial attractiveness. The Geometric + Principal Component Analysis Network (Geo + PCANet) model uses geometric features from facial landmarks to estimate beauty indices closely aligning with human assessments. Skin esthetics are improved with multi-level median filtering, while facial geometry is refined using the moving least squares technique. In addition, an average facial beautification model is proposed to enhance overall appearance. The findings validate the efficacy of these approaches, though challenges remain, particularly in the computational efficiency of skin enhancement. Future work will focus on refining these methods for greater practical applicability. The objective of this research is to create effective, scalable models that incorporate sophisticated neural structures for enhanced and computationally efficient facial beautification. Nevertheless, the issue of the study is rooted in depending on the geometric attributes and neglecting investigation into deep learning approaches to improve beauty prediction and enhancement (Lin, et al., 2023) focuses on personalized FBP (PFBP), aiming to predict individual esthetic preferences from a few personalized images. Different from the traditional models that generalize facial attractiveness, PFBP treats each user as a distinct meta-task within the Few-Shot Learning (FSL) framework. The proposed MetaFBP framework includes a universal feature extractor to identify common esthetic traits and a high-order predictor that adapts swiftly to personal preferences, overcoming issues of slow adaptation and overfitting in traditional methods. Experiments on newly created PFBP benchmarks show the effectiveness of the framework, confirming its ability to make accurate, user-specific beauty predictions. The study also discusses the limitations of conventional FSL methods and introduces a learning-to-learn mechanism designed for faster and more effective adaptation in PFBP tasks.

The review of some research on FBP, which investigates dataset, attributes, algorisms, challenges, future directions, strengths, and metrics is presented in Table II. The comparative analysis of the computational approaches for predicting beauty judgments using facial attributes reveals several strengths, such as the high accuracy and scalability of methods, including multi-task TL, which benefits from shared learning frameworks. Furthermore, models, including ShadowFace3D showcase robustness and generalization through diverse datasets and novel integrations of geometry and texture. However, limitations persist, including data insufficiencies and ethnic and gender biases, which hinder model fairness and inclusivity. Moreover, advanced CNNs may encounter problems such as overfitting and significant computational requirements. Research gaps contain the lack of various datasets, particularly for features, such as hairstyles, smiles, and 3D geometries, and a reliance on one-dimensional inputs without multi-modal integration. Future directions should prioritize enhancing data diversity, integrating multimodal approaches, exploring advanced attention mechanisms for feature enhancement, and developing subjectivity-aware models to better reflect human perceptions of beauty. Furthermore, investigating cross-cultural esthetics through region-specific data collection will provide deeper insights into the variability of beauty standards. By comparing these approaches, this section underlines the necessity of interdisciplinary solutions to enhance FBP systems.

The review provides a critical assessment of methodologies used for predicting facial beauty by examining the trade-offs in CNN architectures and dataset biases. CNN studies, such as those utilizing VGG16 or ResNet50, often balance complexity and computational cost against performance. Conversely, lightweight models prioritize efficiency but may compromise on precision. Dataset biases are a significant concern, as many lack diversity in ethnicity, age, and gender, leading to generalized models across various populations. The review underscores challenges such as overfitting from small datasets, imbalanced beauty score distributions, and subjective beauty judgments influenced by cultural factors. To identify effective approaches, the review explores how TL, data augmentation, and MTL can address dataset limitations and enhance model robustness. It is highly necessary to stress the importance of incorporating varied datasets, rectifying imbalances, and utilizing fairness metrics to comprehensively assess models. This critical synthesis aims to guide future research toward more inclusive and efficient beauty prediction systems.

Traditional machine learning methods, such as SVR and KNN, leverage handcrafted features like geometric landmarks and global descriptors. While computationally efficient, these approaches struggle with capturing complex relationships in large-scale datasets. Techniques such as local binary patterns, Gabor filters, and HOG focus on specific visual patterns but require extensive preprocessing and are sensitive to variations in lighting and pose. MTL improves model performance by incorporating auxiliary tasks, such as gender recognition, to enable robust feature sharing; however, it requires careful balancing of tasks and dataset preparation. GANs contribute by simulating esthetic transformations, including facial symmetry enhancements, though they are computationally demanding and complex to train. PFBP utilizes meta-learning frameworks like FSL to adapt models to individual preferences, promoting inclusivity but presenting scalability challenges. Advances in dataset diversity, with datasets like MEBeauty and RAF-DS, address demographic variations and biases, aligning outputs with inclusive beauty standards. These developments demonstrate a shift from rule-based approaches to adaptive, data-driven systems, enhancing generalization and fairness in beauty prediction tasks. This review synthesizes an understanding from computer vision, psychology, and ML to provide a comprehensive overview of FBP. It emphasizes the significance of various datasets, ethical considerations in developing inclusive beauty prediction models, and fairness in algorithmic decisions.

IV. Conclusion and Future Directions

This review has provided a comprehensive synthesis of computational methodologies for predicting beauty judgments from facial attributes, addressing the interplay between individual, social, and cultural factors. By leveraging deep learning frameworks, feature extraction techniques, and ensemble models, significant progress has been made in automating beauty predictions. The work underscores the importance of diverse and robust datasets, detailing their limitations and the challenges they introduce, such as data variation, subjective judgments, and algorithmic biases. One of the major contributions of this review is its integration of interdisciplinary perspectives – spanning psychology, and sociology, with computer vision – to present a holistic understanding of beauty prediction. It emphasizes how advancements in transfer and MTL have propelled the field, enabling nuanced modeling of complex facial attributes. Moreover, the synthesis highlights the transformative potential of these models across applications in healthcare, cosmetics, social media, and more. Despite these advances, there remains a critical need for addressing the ethical and societal implications of beauty algorithms, particularly concerning inclusivity and fairness across cultural contexts. The integration of 3D modeling and dynamic datasets could further refine predictions, offering more personalized and context-aware assessments. Future research should prioritize developing datasets that encompass greater demographic diversity and employ active learning techniques to mitigate biases. In addition, collaborative efforts between fields – incorporating ethics, computational sciences, and the arts – could redefine the standards and applications of beauty prediction models. Innovations in model interpretability, explainability, and user-centric design are essential for fostering trust and expanding the real-world utility of these algorithms. This review serves as a foundation for advancing beauty prediction, urging the community to adopt transparent, inclusive, and multidisciplinary approaches in the journey ahead.

TABLE II
THE SUMMARY OF FACIAL BEAUTY COMPUTATIONAL MODELS THAT UTILIZED FEATURES-BASED APPROACHES

References	Categories and description	
Gan, et al., 2020	Dataset	LSFBD and SCUT-FBP5500
	Attributes	Gender and Skin
	Algorithm	Random Forest Classifier.
	Limitations	How to establish a versatile, effective multi-input multi-task network that merges local information and other elements that affect facial beauty.
	Future Direction	How to establish a versatile, effective multi-input multi-task network that merges local information and other elements that affect facial beauty.
	Strengths	Use of multi-task transfer learning in 2M BeautyNet, improving facial beauty prediction by leveraging knowledge from related tasks for better performance.
	Metrics	Accuracy up to 68.23%
Panić, Marjanović, and Bezdan, 2024	Dataset	diverse
	Attributes	Age
	Algorithm	CNN
	Limitations	Dataset Composition, and Bias Across Ethnic Groups.
	Future Direction	Use pre-trained CNN models, particularly VGG19, which are further fine-tuned aiming at the prediction of age.
	Strengths	Focus on Bias means addresses the critical issue of ethnic bias in facial age prediction models, supporting fairness and inclusivity.
	Metrics	Mean Absolute Error (MAE): 7.946 tested on African faces. 7.677 tested on Asian faces.
Cao, et al., 2020	Dataset	SCUT-FBP5500
	Attributes	All Facial Attributes
	Algorithm	CNN
	Limitations	Designing active Network. Attention Mechanism. Significance Distribution among features. To address this, the paper presents a joint spatial-wise and channel-wise attention (SCA) block. This approach helps exploit inner correlations among features and leads to a better representation of facial features.
	Future Direction	The improvement of Network Structures and Multimodal methods: integrating the prediction of facial beauty with other modalities, such as voice or body language
	Strengths	Utilization of Deep Learning and Scalability
	Metrics	• (MAE): 0.2595; Root-Mean-Square Error (RMSE) = 0.3397 Root-Mean-Square Error (RMSE)) = 0.8570
Chen, et al., 2021	Dataset	CelebHair
	Attributes	Hairstyle
	Algorithm	CNNs and Spatial Transformer Network (STN).
	Limitations	The initial challenge that is highlighted in the abstract is the absence of appropriate hairstyle-related datasets that are necessary for improving the recommendation application hairstyle.
	Future Direction	The hairstyle try-on experience needs to be refined for users through employing Interface GAN.
	Strengths	Creation of a new large-Scale database
	Metrics	Accuracy=85.45%
Moridani, et al., 2023	Dataset	Most Beautiful Women Faces (MBWFs).
	Attributes	All Facial Attributes
	Algorithm	K-Nearest Neighbors (KNN). Support Vector Regression (SVR).
	Limitations	Beauty Subjectivity and Feature Extraction.
	Future Direction	Future researches need to be done to improve attractive models through exploring more features. This results study is useful for the industry, modeling, and marketing of beauty, where ranking attractiveness is significant.
	Strengths	Human-like Evaluation that's mean The method mimics human judgment, achieving alignment together with human perceptions of facial beauty prediction.
	Metrics	Coefficient of determination (R2) =0.9902. RMSE=0.0056. and Mean Absolute Percentage Error (MAPE) =0.0856.
Gao, et al., 2018	Dataset	SCUT-FBP database
	Attributes	All Facial Attributes
	Algorithm	CNN
	Limitations	Inadequate Label Information, Overfitting, and intricacy of facial features.
	Future Direction	It is suggested that the proposed deep multi-task learning that is based on a prediction model joint with landmark localization is effective for Facial Attractiveness Prediction.
	Strengths	Getting better accuracy and attribute generalization.
	Metrics	Correlation=0.92

TABLE II
(CONTINUED)

References	Categories and description	
Yuan, et al., 2024	Dataset	University of Tennessee, Knoxville Face Dataset (UTKFace dataset).
	Attributes	Age, Gender, and Race
	Algorithm	CNN
	Limitations	The Imbalance of data search for means treatment imbalanced database where certain features may be underrepresented.
	Future Direction	Both Enhanced data augmentation as well as improved model architectures implies designing more efficient model architectures to deal with the intricacy and improve performance.
	Strengths	Outweigh in employing uncertainty-based weighting in MTL enhancing the precise and equitable estimation of different facial attributes.
	Metrics	Age=64.74, Gender=90.91, and Race=79.98
Jamoliddin and Yoo, 2022	Dataset	UTKFace dataset
	Attributes	Age as well as Gender
	Algorithm	CNN
	Limitations	Limited Dataset: Small-scale CNNs often lack access to extensive, diverse datasets. This leads to overfitting and poor generalization to new data. To Ensure sufficient variability in the training data is indispensable for the enhancement of model robustness.
	Future Direction	Improving Accuracy seeks to Enhance the performance of the model with advanced architectures or additional data.
	Strengths	Strength lies in its efficient employ of a small-scale CNN construction to achieve accurate gender and age classification, balancing performance and computational cost.
	Metrics	F1 Score=0.90
Vahdati and Suen, 2021	Dataset	SCUT-FBP5500
	Attributes	All Facial Attributes
	Algorithm	CNN
	Limitations	The complexity of the Model as well as partiality and balance.
	Future Direction	Improving both model architecture and addressing subjectivity.
	Strengths	Innovative use of multi-task and multi-stream CNN To forecast facial attractiveness by thoroughly examining each facial feature and its impact.
	Metrics	Accuracy: 95%; Correlation Coefficient: 0.9; F1 Score: 0.9
Xiao, et al., 2021	Dataset	ShadowFace3D
	Attributes	All facial attributes
	Algorithm	CNN
	Limitations	3D Data complexity. Dataset Availability means There could be a shortage of large, high-quality 3D facial datasets annotated with attractiveness ratings that can limit model training and generalization.
	Future Direction	Investigate how our deep learning network interprets facial attractiveness by employing geometric as well as textural features. To figure out cross-cultural esthetics, more various data will be collected. Beauty3DFaceNet and ShadowFace3D will be used for applications, such as enhancing 3D facial attractiveness.
	Strengths	Fusion of deep geometry and texture features using Beauty3DFaceNet, enabling accurate and comprehensive 3D facial attractiveness prediction.
	Metrics	Pearson correlation coefficient=0.742
Wang, et al., 2017	Dataset	Morphological (MORPH II). CelebA. LFWA.
	Attributes	Age, gender, and race.
	Algorithm	CNN
	Limitations	Heterogeneity of Attributes indicates that facial attributes, such as gender, age, and expressions vary noticeably in terms of characteristics and data needs. This requires various information for the accuracy prediction.
	Future Direction	Examine both illumination and pose normalization methods and automatic attribute category grouping approach as well for efficient attribute prediction.
	Strengths	Strength lies in its application of deep multi-task learning to jointly predict diverse facial attributes, enhancing efficiency besides accuracy through shared attribute learning.
	Metrics	Accuracy: Age: 85.3, Gander: 98, and Race: 96.6
Yin, et al. 2020	Dataset	LFW, WIDER FACE, Queen's University Machine Learning - Surveillance Face Dataset (QUML-SurvFace), and SCface datasets.
	Attributes	All Facial Attributes
	Algorithm	Feature Adaptation Network (FAN)
	Limitations	Disentanglement learning feature and adaptation feature. By first disentangling the face features into identity and non-identity components, it facilitates our adaptation network to require both feature-level and image-level similarity regularizations. This framework is appropriate for both paired and unpaired training,
	Future Direction	The main aim is to learn the features of robust identity for FR. These features are used to produce a normalized face with enhancement facial details and neutral Pose Illumination Expression (PIE).
	Strengths	Normalizes and improves face recognition performance in opposed surveillance scenarios.
	Metrics	LFW Accuracy=95.2%, QMULAccuracy=70.88%, and SCface=90.3

TABLE II
(Continued)

References	Categories and description	
Sagonas, et al., 2016	Dataset	Diverse
	Attributes	N/A
	Algorithm	Constrained Local Mod (CLM) and Coarse-to-Fine Auto-Encoder Networks (CFAN)
	Limitations	Authors compare their approaches with other state-of-the-art. They do so by applying, in many cases, completely different databases for training compared to the ones that the other methods were originally trained on.
	Future Direction	Robustness to Lighting and Quality Variations mean enhancing the robustness of detection algorithms to varying illumination conditions and image qualities and enhanced Datasets as well.
	Strengths	Providing an overall benchmark database and evaluation framework, advancing the development and comparison of strong face alignment algorithms under real-world conditions
	Metrics	Accuracy=95.8%
Savchenko, 2021	Dataset	UTKFace, Affective Facial Expressions Network Dataset) AffectNet(, Acted Facial Expressions in the Wild (AFEW), and Video-based Group-level Affect and Face Dataset) VGAF datasets(
	Attributes	Age and Gender
	Algorithm	CNN, Support Vector Machines (SVM), and Random forests.
	Limitations	Handling variability in data means handling variations in real-world data's occlusions, stances, illumination, and face expressions. In addition, the efficiency of models indicates that there must be a balance in models in terms of both computing efficiency and intricacy so as to be used on tools that have constrained resources.
	Future Direction	Improved Model Efficiency hints focusing on the creation of more efficient lightweight models that involve less computational power when maintain high accuracy. Enhanced MTL indicates Further explore and refine MTL approaches to enhance the simultaneous recognition of facial expressions and attributes.
	Strengths	Its use of lightweight neural networks with MTL to effectively and accurately recognize facial expressions and attributes simultaneously.
	Metrics	Accuracy: 94.0% on the AffectNet dataset Accuracy: 88.7% on the CelebA dataset.
Liang, et al., 2017	Dataset	SCUT-FBP
	Attributes	Eyes, lips, and overall symmetry
	Algorithm	Support vector regression (SVR)
	Limitations	Constraints of Asian Female face on the SCUT-FBP dataset
	Future Direction	Construct a large-scale benchmark database in a later study.
	Strengths	Use of region-aware scattering convolution networks to capture detailed and localized facial features, enhancing the accuracy of FBP.
	Metrics	PC=0.83
Mao, et al., 2020	Dataset	CelebA. And LFWA datasets
	Attributes	All Facial Attributes
	Algorithm	Deep Multi-task Multi-label CNN, (DMM-CNN)
	Limitations	The study investigates difficulties such as handling data imbalance.
	Future Direction	Improving model accuracy seeks to Enhancing the CNN architecture or examining new strategies so as to make the accuracy of facial attribute classification in better shape.
	Strengths	Its use of a deep multi-task, multi-label CNN architecture, enabling accurate classification of multiple facial attributes simultaneously by leveraging shared attribute learning.
	Metrics	Mean accuracy CelebA=91.70% and Mean accuracy LFWA=86.56%
Rohani, Farsi and Mohamadzadeh, 2023	Dataset	IMDB-WIKI (Internet Movie Database) and GENKI-4K datasets
	Attributes	Smile, age, and gender
	Algorithm	CNN
	Limitations	About features have fewer samples, causing bias with suboptimal performance.
	Future Direction	Develop architectures to share knowledge while preserving task accuracy.
	Strengths	Employing deep multi-task convolutional neural networks to efficiently classify multiple facial features, leveraging shared representations for improved performance and efficiency.
	Metrics	Smile accuracy=96.63 Gender accuracy=93.20 Age accuracy=68.92

REFERENCES

Aarabi, P., Hughes, D., Mohajer, K., and Emami, M., 2001. The Automatic Measurement of Facial Beauty. In: *2001 IEEE International Conference on Systems, Man and Cybernetics. e-Systems and e-Man for Cybernetics in Cyberspace (Cat. No. 01CH37236)*. IEEE.

Ahmadimehr, S., and Moridani, M.K., 2020. Evaluating facial attractiveness through proportions analysis based on geometric features. *Journal of Image Processing & Pattern Recognition Progress*, 7(2), pp.20-26.

Altwaijry, H., and Belongie, S., 2013. Relative Ranking of Facial Attractiveness. In: *2013 IEEE Workshop on Applications of Computer Vision (WACV)*. IEEE.

Bougourzi, F., Dornaika, F., Barrena, N., Distante, C., and Taleb-Ahmed, A., 2023. CNN based facial aesthetics analysis through dynamic robust losses and ensemble regression. *Applied Intelligence,* 53(9), pp.10825-10842.

Cao, K., Choi, K.N., Jung, H., and Duan, L., 2020. Deep learning for facial beauty prediction. *Information*, 11(8), p.391.

Chen, F., Xu, Y., and Zhang, D., 2014. A new hypothesis on facial beauty perception. *ACM Transactions on Applied Perception*, 11(2), pp.1-20.

Chen, Y., Zhang, Y., Huang, Z., Luo, Z., and Chen, J., 2021. CelebHair: A New Large-scale Dataset for Hairstyle Recommendation Based on CelebA. In: *International Conference on Knowledge Science, Engineering and Management.* Springer.

Cowen, A.S., Keltner, D., Schroff, F., Jou, B., Adam, H., and Prasad, G., 2021. Sixteen facial expressions occur in similar contexts worldwide. *Nature*, 589(7841), pp.251-257.

Eisenthal, Y., Dror, G., and Ruppin, E., 2006. Facial attractiveness: Beauty and the machine. *Neural Computation*, 18(1), p.119-142.

Fan, D., Kim, H., Kim, J., Liu, Y., and Huang, Q., 2019. Multi-task learning using task dependencies for face attributes prediction. *Applied Sciences*, 9(12), p.2535.

Favorskaya, M.N., and Pakhirka, A.I., 2023. Age-Group Estimation of Facial Images Using Multi-task Ranking CNN. In: I*nternational KES Conference on Intelligent Decision Technologies*. Springer.

Gan, J., Jiang, K., Tan, H., and He, G., 2020. Facial beauty prediction based on lighted deep convolution neural network with feature extraction strengthened. *Chinese Journal of Electronics*, 29(2), pp.312-321.

Gan, J., Luo, H., Xiong, J., Xie, X., Li, H., and Liu, J., 2023. Facial beauty prediction combined with multi-task learning of adaptive sharing policy and attentional feature fusion. *Electronics*, 13(1), p.179.

Gan, J., Xiang, L., Zhai, Y., Mai, C., He, G., Zeng, J., Bai, Z., Labati, R., Piuri, V., and Scotti, F., 2020. 2M BeautyNet: Facial beauty prediction based on multi-task transfer learning. *IEEE Access*, 8, pp.20245-20256.

Gan, J., Xie, X., Zhai, Y., He, G., Mai, C., and Luo, H., 2023. Facial beauty prediction fusing transfer learning and broad learning system. *Soft Computing*, 27(18), pp.13391-13404.

Gao, L., Li, W., Huang, Z., Huang, D., and Wang, Y., 2018. Automatic Facial Attractiveness Prediction by Deep Multi-task Learning. In: *2018 24th International Conference on Pattern Recognition (ICPR*). IEEE.

Gray, D., Yu, K., Xu, W., and Gong, Y., 2010. Predicting Facial Beauty Without Landmarks. In: *Computer Vision-ECCV 2010: 11th European Conference on Computer Vision. Proceedings, Part VI 11*. Springer, Heraklion, Crete, Greece.

Grgic, M., Delac, K., and Grgic, S., 2011. SCface-surveillance cameras face database. *Multimedia Tools and Applications,* 51, pp.863-879.

Gunes, H., and Piccardi, M., 2006. Assessing facial beauty through proportion analysis by image processing and supervised learning. *International Journal of Human-computer Studies*, 64(12), pp.1184-1199.

Jamoliddin, U., and Yoo, J.H., 2022. Age and gender classification with small scale cnn. *The Journal of the Korea Institute of Electronic Communication Sciences*, 17(1), pp.99-104.

Kalyta, O., Krakb, I., Barmaka, O., Wojcikd, W., and Radiuk, P., 2022. Method of Facial Geometric Feature Representation for Information Security Systems. In: 3rd *International Workshop on Intelligent Information Technologies & Systems of Information Security.* Khmelnytskyi, Ukraine.

Lebedeva, I., Guo, Y., and Ying, F., 2021. Transfer learning adaptive facial attractiveness assessment. *Journal of Physics: Conference Series*, 1922, p.012004.

Lebedeva, I., Guo, Y., and Ying, F., 2022. MEBeauty: A multi-ethnic facial beauty dataset in-the-wild. *Neural Computing and Applications*, 34, pp.14169-14183.

Lebedeva, I., Guo, Y., and Ying, F., 2023. Personalized facial beauty assessment: A meta-learning approach. *The Visual Computer*, 39(3), pp.1095-1107.

Liang, L., Xie, D., Jin, L., Xu, J., Li, M., and Lin, L., 2017. Region-aware Scattering Convolution Networks for Facial Beauty Prediction. In: *2017 IEEE International Conference on Image Processing (ICIP*). IEEE.

Lin, L., Shen, Z., Yin, J.L., Liu, Q., Yu, Y., and Chen, W., 2023. MetaFBP: Learning to Learn High-Order Predictor for Personalized Facial Beauty Prediction. In: *Proceedings of the 31st ACM International Conference on Multimedia.*

Lin, Y., Zhibin, G., Zhang, S., Li, L., and Huang, L., 2021. Multi-Task Network and Optimization for Face Detection and Attribute Analysis. In: *2021 IEEE International Conference on Artificial Intelligence and Computer Applications (ICAICA*). IEEE.

Liu, Z., Luo, P., Wang, X., and Tang, X., 2015. Deep learning face attributes in the wild. In: *Proceedings of the IEEE International Conference on Computer Vision*. IEEE.

Mao, L., Yan, Y., Xue, J.H., and Wang, H., 2020. Deep multi-task multi-label CNN for effective facial attribute classification. *IEEE Transactions on Affective Computing*, 13(2), pp.818-828.

Moridani, M.K., Jamiee, N., and Saghafi, S., 2023. Human-like evaluation by facial attractiveness intelligent machine. *International Journal of Cognitive Computing in Engineering*, 4, pp.160-169.

Mu, Y., 2013. Computational facial attractiveness prediction by aesthetics-aware features. *Neurocomputing*, 99, pp.59-64.

Nguyen, T.V., Liu, S., Ni, B., Tan, J., Rui, Y., and Yan, S., 2013. Towards decrypting attractiveness via multi-modality cues. *ACM Transactions on Multimedia Computing, Communications, and Applications*, 9(4), p.28.

Panić, N., Marjanović, M., and Bezdan, T., 2024. Ethnic representation matters: Investigating bias in facial age prediction models. *Mathematics*, 12(15), pp.1-30.

Rohani, M., Farsi, H., and Mohamadzadeh, S., 2023. Deep multi-task convolutional neural networks for efficient classification of face attributes. *International Journal of Engineering*, 36(11), pp.2102-2111.

Saeed, J.N., Abdulazeez, A.M., and Ibrahim, D.A., 2022. FIAC-Net: Facial Image Attractiveness Classification based on Light Deep Convolutional Neural Network. In: *2022 Second International Conference on Computer Science, Engineering and Applications (ICCSEA*). IEEE.

Saeed, J.N., and Abdulazeez, A.M., 2021. Facial beauty prediction and analysis based on deep convolutional neural network: A review. *Journal of Soft Computing and Data Mining*, 2(1), pp.1-12.

Saeed, J.N., and Abdulazeez, A.M., 2022. 2D Facial Images Attractiveness Assessment Based on Transfer Learning of Deep Convolutional Neural Networks. In: *2022 4th International Conference on Advanced Science and Engineering (ICOASE*). IEEE.

Sagonas, C., Antonakosa, E., Tzimiropoulosb, G., Zafeirioua, S., and Pantic, M., 2016. 300 faces in-the-wild challenge: Database and results. *Image and Vision Computing*, 47, pp.3-18.

Savchenko, A.V., 2021. Facial Expression and Attributes Recognition Based on Multi-task Learning of Lightweight Neural Networks. In: *2021 IEEE 19th International Symposium on Intelligent Systems and Informatics (SISY*). IEEE, pp.119-124.

Schmid, K., Marx, D., and Samal, A., 2008. Computation of a face attractiveness index based on neoclassical canons, symmetry, and golden ratios. *Pattern Recognition*, 41(8), pp.2710-2717.

Sekhar, J.C., Joel Josephson, P., Chinnasamy, A., Maheswari, V., Sankar, V., and Kalangi, R.R., 2024. Automated face recognition using deep learning technique and center symmetric multivariant local binary pattern. *Neural Computing and Applications*, pp.1-19.

Štěpánek, L., Kasal, P., and Mestak, J., 2018. Evaluation of Facial Attractiveness for Purposes of Plastic Surgery Using Machine-learning Methods and Image

Analysis. In: *2018 IEEE 20th International Conference on e-Health Networking, Applications and Services*. IEEE.

Taherkhani, F., Dabouei, A., Soleymani, S., Dawson, J., and Nasrabadi, N.M., 2021. Tasks structure regularization in multi-task learning for improving facial attribute prediction. arXiv preprint arXiv:2108.04353.

Vahdati, E., and Suen, C.Y., 2021. Facial beauty prediction from facial parts using multi-task and multi-stream convolutional neural networks. *International Journal of Pattern Recognition and Artificial Intelligence*, 35(12), p.2160002.

Wang, F., Han, H., Shan, S., and Chen, X., 2017. Deep Multi-task Learning for Joint Prediction of Heterogeneous Face Attributes. In: *2017 12th IEEE International Conference on Automatic Face & Gesture Recognition (FG 2017*). IEEE.

Weng, N., Wang, J., Li, A., and Wang, Y., 2021. Two-stream Temporal Convolutional Network for Dynamic Facial Attractiveness Prediction. In: *2020 25th International Conference on Pattern Recognition (ICPR)*. IEEE.

Xiao, Q., Wu, Y., Wang, D., Yang, Y.L., and Jin, X., 2021. Beauty3DFaceNet: Deep geometry and texture fusion for 3D facial attractiveness prediction. *Computers & Graphics*, 98, pp.11-18.

Xie, D., Liang, L., Jin, L., Xu, J., and Li, M., 2015. Scut-fbp: A Benchmark Dataset for Facial Beauty Perception. In: *2015 IEEE International Conference on Systems, Man, and Cybernetics*. IEEE.

Xie, Y., Wang, K., Meng, J., Yue, J., Meng, L., Yi, W., Jung, T.P., Xu, M., and Ming, D., 2023. Cross-dataset transfer learning for motor imagery signal classification via multi-task learning and pre-training. *Journal of Neural Engineering*, 20(5), p.056037.

Xu, L., Xiang, J., and Yuan, X., 2018. CRnet: Classification and Regression Neural Network for Facial Beauty Prediction. *In: Pacific Rim Conference on Multimedia*. Springer, Cham.

Xu, M., Chen, F., Li, L., Shen, C., Lv, P., Zhou, B., and Ji, R., 2018. Bio-inspired deep attribute learning towards facial aesthetic prediction. *IEEE Transactions on Affective Computing*, 12(1), pp.227-238.

Yin, X., Tai, Y., Huang, Y., and Liu, X., 2020. Fan: Feature Adaptation Network for Surveillance Face Recognition and Normalization. In: *Proceedings of the Asian Conference on Computer Vision.*

Yuan, H., He, Y., Du, P., and Song, L., 2024. *Multi-Task Learning Using Uncertainty to Weigh Losses for Heterogeneous Face Attribute Estimation*. [Preprint].

Zhai, Y., Huang, Y., Xu, Y., Gan, J., Cao, H., Deng, W., Labati, R.D., Piuri, V., and Scotti, F., 2020. Asian female facial beauty prediction using deep neural networks via transfer learning and multi-channel feature fusion. *IEEE Access*, 8, pp.56892-56907.

Zhai, Y., Huang, Y., Xu, Y., Zeng, J., Yu, F., and Gan, J., 2016. Benchmark of a Large Scale Database For Facial Beauty Prediction. In: *Proceedings of the 1st International Conference on Intelligent Information Processing.*

Zhang, B., Xiao, X., and Lu, G., 2018. Facial beauty analysis based on features prediction and beautification models. *Pattern Analysis and Applications*, 21, pp.529-542.

Zheng, K., Tian, L., Li, Z., Li, H., and Zhang, J., 2024. Incorporating eyebrow and eye state information for facial expression recognition in mask-obscured scenes. *Electronic Research Archive*, 32(4), pp.2745-2771.

Extraction of Nickel Oxide from Spent Catalyst for Environmentally Safe Disposal

Fakhri H. Ibraheem[1†], Heaven E. Mahmoud[1], Dunya I. Saleh[1], Jahfer M. Smail[2], Hawbash H. Karim[2], and Faten A. Chaqmaqchee[2]

[1]Department of Chemical Engineering, Faculty of Engineering, Koya University,
Danielle Mitterrand Boulevard, Koya KOY45, Kurdistan Region – F.R. Iraq

[2]Department of Physics, Faculty of Science and Health, Koya University,
Danielle Mitterrand Boulevard, Koya KOY45, Kurdistan Region – F.R. Iraq

Abstract*—Molecular sieves are used in various industries, especially petroleum and gas processing plants, as catalysts. These materials are in contact with crude oil products. After several operational years, these materials' activities were reduced to a non-feasible level called spent molecular sieve. Tens of tons are disposed of annually from oil and gas companies in Iraq. The paper aims to determine the kinds and amounts of toxic materials carried by the nickel oxide sulfur bed spent catalyst and then submit the suitable treatment methods, such as leaching by water, base solution, and acid solution. A radioactive test was first done to ensure the material was free from the radioactivity array. The material was tested for nickel oxide concentration after each step of treatment. It was found that the leaching by water reduces the content by 4.5% during 24 h of leaching and 15.5% after 7 days. The leaching by alkaline sodium hydroxide 10% concentration solution reduces the content by 7% during 24 h and 14.3% after 7 days. The 10% hydrochloric acid concentration solution leaching reduces the nickel content by 10.8 during 24 h and 65.7 after 7 days. Leaching by acid solution is more efficient in the extraction of nickel oxide. The treatment method novelty is to be carried out at reasonable temperatures with high metal extraction efficiency. The research results achieved this goal of attaining extraction at an easily achievable temperature of 70°C with a relatively good extraction rate higher than 65%.

***Index Terms*—Extraction process, Nickel base catalyst, Sulfur bed, Safe disposal, Spent molecular sieve.**

I. Introduction

Molecular sieves are auxiliary materials for chemical reactions. They are engineered to contain a high internal surface area, which helps speed up the completion of chemical reactions. Their internal design contains spaces and precise channels for transferring the reaction materials and results (Naydenov, 2003). It can absorb materials, conduct chemical reactions on its interfacial surface area, and then adsorb the reaction products. It can absorb gases and liquids based on molecular size and polarity (Rezaei, 2015) and (Naydenov, 2003). The diameter of the pores is between 0.3–2.0 nm, like a zeolite molecular sieve (ZMS) (Flanigen, 2001). ZMS is a crystalline metal aluminosilicate with a three-dimensional interconnecting silica and alumina tetrahedral network (Banerjee, et al., 2022). It has been used in industrial applications for over 60 years, mainly as a highly efficient adsorbent for separation processes in the gas or liquid phase (Gleichmann, Unger and Brandt, 2016). They contain tiny pores of a precise and uniform size and are primarily used as adsorbents for gases and liquids. Five angstroms molecular sieves dry natural gas (Mafra and Klinowski, 2013). The absorbed gases or liquid molecules are smaller than the effective diameter of their pores. It can exchange ionic species with variable and adaptable selectivity. They have properties that are related to the particular structure of their framework (Meier and Uytterhoeven, 1973). These catalysts have specific life and are discarded due to their deactivation due to coke deposition on their surface. Disposal of spent catalysts is problematic as they fall under hazardous industrial waste (Oza and Patel, 2012). Thus, producing an efficient reaction takes a limited amount of time. Then, it becomes inefficient and feasible, called the "Spent Molecular Sieve" (SMS), as shown in Fig. 1 for the desulfurization unit. Therefore, it is a hazardous waste, and its disposal is considered an extremely crucial issue, subject to strict legislation (Marafi and Rana, 2017). Iraq has no regulation for the safe limits of pollutants in SMS. In the Kurdistan Region, more than 100 tons of these spent materials are purged in different types and shapes (spheres, bars, and tubes) in <6 years (Zangana, et al., 2017). A fixed bed reactor does the desulfurization unit in the Sulymanea Refinery in the North of Iraq. Usually, one bed will be under regeneration while the others are under operation. The catalyst is based on nickel and nickel oxide Fig. 1. The operating temperature, space velocity, and physical condition affect its efficiency and life (Petrov, 2002). The nickel oxide acted as a chemical reagent combined with the sulfur in the

ARO-The Scientific Journal of Koya University
Vol. XIII, No. 1 (2025), Article ID: ARO.11889. 5 pages
DOI: 10.14500/aro.11889
Received: 06 November 2024; Accepted: 29 December 2024
Regular research paper; Published: 01 February 2025

†Corresponding author's e-mail: fakhri.ibraheem@koyauniversity.org

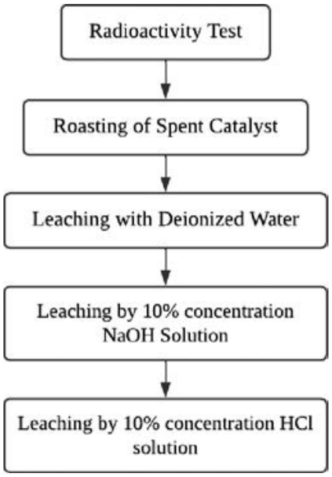

Fig. 1. Treatment process of spent Nickel catalyst.

oil to produce nickel sulfide. The amount of desulfurization depended on the contact time (Abu Bakar, et al., 2009). The oxidation of nickel sulfide with air produced nickel sulfate, which had no activity as a desulfurization agent. The nickel or its compounds remove sulfur as hydrogen sulfide or may be reagents according to the following reactions:

$$Ni_{\square}O_{\square} + 3RHS + 4H_{\square} \rightarrow 4H_{\square}O + 3NiS + 3RH$$

Various methods treated spent catalysts, and the products were tested to determine their activity as desulfurization catalysts or whether they are suitable for disposal or use in another industry. The large quantities of these materials accumulated in Iraq present an environmental challenge because they contain heavy elements. These materials are often associated with oil extracted from deep underground, which may result in contamination with other, more toxic substances, including those with potential radioactive activity. This situation necessitates increased scientific research to identify safe and effective treatment methods. In addition, there is a need for legislation that establishes environmental limits for dangerous pollution levels and outlines proper treatment procedures.

In the USA, the disposal and treatment of spent catalysts and molecular sieves are subject to the Resource Conservation and Recovery Act (RCRA) regulations and EPA restrictions for land treatment and disposal of solid wastes (EPA, 2024). In some instances, stability treatment before land-filling may be required. The disposal is done either by solidification, capsulation, or landfill. This work aims to determine the efficient extraction process and solution for Nickel from the Sulfur bed spent catalyst.

II. Materials and Methods

First, spent catalyst samples were radiologically tested to determine whether they were contaminated with radioactive materials and if they were safe for handling. Then, a chemical analysis laboratory test was performed to determine their composition. The treatment starts with heating the samples to a high temperature of 400°C to remove all the volatile organic materials. The Nickel from the spent catalyst is extracted using different solutions in three steps of the leaching process (Marafi and Stanislaus, 2003). The leaching is done by deionized water, a 10% solution of sodium hydroxide alkaline solution NaOH, and a 10% concentration of hydrochloric acid solution by HCl acid. The leached spent catalyst was analyzed chemically using an X-ray fluorescence (XRF) system (Faris, et al., 2022). The following block diagram, Fig. 1, has been adopted to treat this waste, which was based on the characteristics of the oils passing through it across different layers of the earth and at various depths. This may have exposed it to contact with many polluting materials, some of which may be radioactive.

Five samples, each weighing 200 g, were roasted to ensure the accuracy of the results. The weight loss observed ranged from 1.95 to 2.05 g, indicating a 1% difference. Two calibrated weighing scales were used for this process. For the extraction procedure, samples weighing 200 g were tested. To enhance the reliability of the results, the extraction experiments were conducted twice, and lab tests were performed using XRF. The samples were ground and pressed into molds to form a suitable shape for testing. Statistical analysis was conducted on only two samples from each extraction case (water, base, and acid). The percentage of element concentrations showed close agreement between the two experiments, with a 3% difference in $NiO_{\square}$ concentration for water and base and a 5% difference in the case of acid extraction.

A. Radioactivity Test

A 1-kg sample was ground to a uniform size of <2 mm. It was then packed in a one-liter Marinelli beaker and sealed for 4 weeks to achieve secular equilibrium among the radium isotopes in the sample before proceeding with gamma-ray spectrometric analysis. A gamma-ray spectrometry system equipped with a high-purity germanium (HPGe) detector was utilized for this analysis (Reguigui, 2014)(Reguigui, 2014). It is the most widely used technique for measuring and analyzing the radioactivity of environmental samples. It is impossible to handle, transfer, and treat spent catalysts without ensuring they are radioactivity-free for safety precautions. This gives us an accurate vision of the safe ways to dispose of or bury them and the depths required. Knowledge of the radionuclide distribution is necessary because it provides helpful information for observing the natural environmental radioactivity and associated external exposure resulting from primary gamma radiation based on geological and geographical conditions (Smail, Ahmad and Mansour, 2021).

Furthermore, if they are radiation-free, the horizon is broader for searching for their uses in other industries.

The technique determined 226Ra, 232Th, and 40K activity levels. Table I compares the safe standard limits of activity concentration with the actual measurements of the samples, expressed in becquerel per kilogram (Bq/kg).

The gamma spectrum shape Fig. 2. shows the scattering of the beams.

TABLE I

Concentration Activity of the Sample Based on Different Standard Element Levels

Nuclear radiation element	Standard safe limit (Bq/Kg)	Actual sample reading (Bq/Kg)
^{226}Ra	35	11.16±0.33
^{232}Th	30	5.3±0.1
^{40}K	400	73.63±2.2

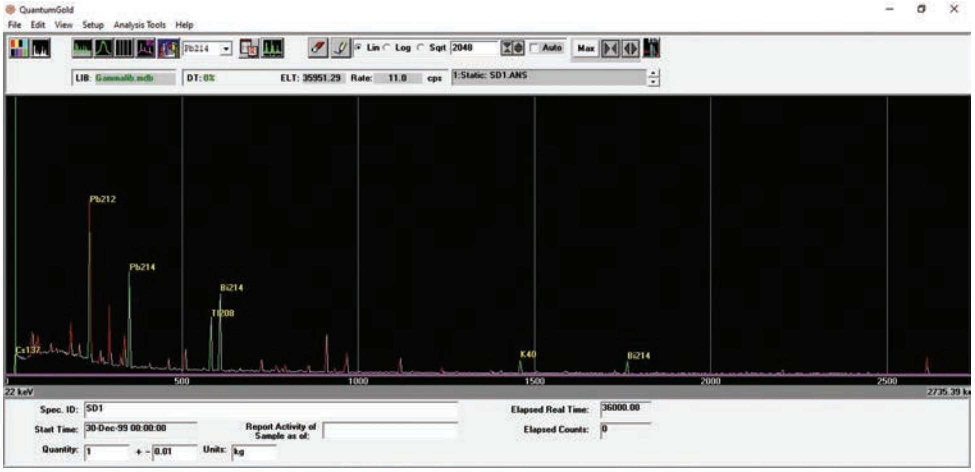

LIB: Gammalib.mdb

DT: 0%

ELT: 35951.29 Rate: 11.0 cps

1:Static: SD1.ANS

Spec. ID: SD1

Start Time: 30-Dec-99 00:00:00

Report Activity of Sample as of:

Quantity: 1 + - 0.01 Units: kg

Elapsed Real Time: 36000.00

Elapsed Counts: 0

Fig. 2. Gamma spectrum test.

B. Roasting of Samples

A sample weighing 200 g was gradually heated in an electrical furnace to 400°C for two h. Most light hydrocarbons are volatilized during heating, leaving the catalyst nearly free of organic matter. The spent catalyst was left inside the switched-off furnace overnight for natural cooling to room temperature. The weight loss (Δw) measured for five samples ranged between 0.97% and 1%. The roasting process is essential for two reasons:

1. It removes the accumulated carbon deposits on the catalyst's surface, preventing the macro channels from closing. This allows the solvent to penetrate more effectively, enhancing its interaction with the metal.
2. It cleans out any build-up in the internal pores, increasing the available surface area for interaction between the acid and the metal.

C. Leaching Experiments for Recovery of Metals

The leaching process was conducted in three stages. The samples were analyzed using an XRF system to evaluate their composition changes.

Leaching with Deionized Water

It is the first step of the leaching process, where the roasted samples are immersed in warm distilled water at 70°C in a water bath for 24 h to 7 days. The warm aqueous medium positively affects the speed of movement of molecules inside the catalyst to the outside during the extraction process.

Leaching by Alkaline Solution

A 10% sodium hydroxide (NaOH) solution was prepared. Samples from the initial leaching step were immersed in the warm alkaline solution at 70°C for 24 h to 7 days. The samples were washed and dried in preparation for the next leaching step.

Leaching by Acid Solution

A 10% concentration of acid HCl solution was prepared. The samples from the second leaching step are immersed in the warm acid solution at 70^{o}C for 24 h to 7 days.

III. Results and Discussions

The laboratory tests referred to alumina oxide (Al□O□) and silicon oxide (SiO□), which are the main components of catalyst support. These are stable components and don't affect the different extraction processes. The catalyst active sites are Nickel and Nickel Oxide. Different extraction processes reduce their concentration. The composition of the samples before and after treatment is tested and shown in Table II.

1. Fig. 3. illustrates the reduction profile of NiO□ when using various types of leaching solutions over different leaching durations. Leaching with a 10% hydrochloric acid (HCl) solution demonstrates effective extraction capabilities. The extraction time significantly influences efficiency; for instance, leaching with the HCl solution for 7 days enhances efficiency to over three times achieved in just 24 h.

Leaching with water reduces NiO□ by 4.5% after 24 h and 15.5% after 7 days. Leaching with a 10% NaOH solution reduces NiO□ by 7.3% after 24 h and 14.2% after 7 days. Leaching with a 10% HCl solution reduces NiO□ by 10.8% after 24 h and 65.7% after 7 days.

A literature review reveals (Miazga and Mulak, 2008) indicated that nickel extraction from a benzene hydration catalyst achieved an efficiency of 74% at 60°C using a 35% HCl solution after 45 minutes. (Aras and Ağaçayak, 2017) studied the leaching of nickel from ore and found experimentally that the optimum leaching conditions were

TABLE II
XRF ANALYSIS OF SOLID SAMPLES BEFORE AND AFTER DIFFERENT TREATMENT PROCESSES

Status	Ni (mg/L)	S	Al (mg/L)	Si (mg/L)
Before treatment (raw spent catalyst)	87.6	1.11	4.95	3.17
After 24 h of leaching by water	83.7	0.0308	0.199	0.492
After 7 days of leaching by water	74.04			
After 24 h of leaching by alkaline solution	81.2	0.0151	-	0.182
After 7 days of leaching by alkaline solution	75.15			
After 24 h, leaching by acid solution	78.1	0.360	4.95	2.69
After 7 days, leaching by acid solution	30.04			

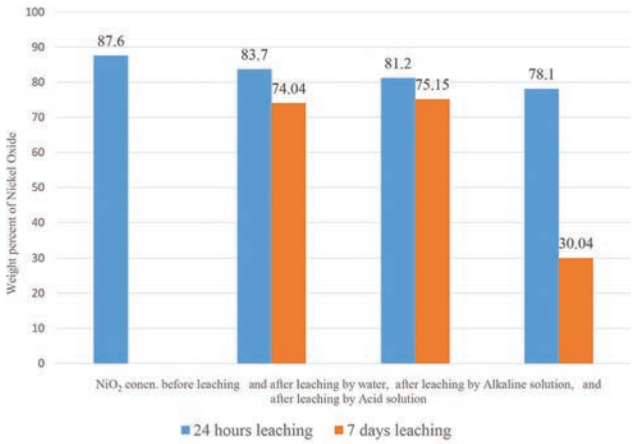

Fig. 3. Nickel concentration for spent catalyst before and after the leaching process.

70°C and 35% HCl concentration for 6 h, which extracted 90.66%. Cano, et al. (2016) investigated nickel extraction with a nitric acid solution, achieving 85% efficiency at temperatures between 25°C and 65°C for 30 to 120 minutes with a 50% acid concentration. Therefore, our experiments suggest that higher extraction efficiency can be attained using a safer concentration of 10% HCl at 70°C, over 7 days.

2. Hydrochloric acid (HCl) is beneficial for metal extraction due to its selective reaction with elements like nickel in solid form. This extraction process requires a solvent to react with and dissolve the metal ions and/or compounds. The primary reaction for nickel extraction from both catalysts is as follows:

$$NiO + 2HCl \rightarrow NiCl_2 + H_2O$$

The reaction rate increases significantly because HCl can diffuse quickly into the surface of the solid spent catalyst. In contrast, the side reaction:

$$\alpha\text{-}Al_2O_3 + 6HCl \rightarrow 2AlCl_3 + 3H_2O$$

Proceeds very slowly, as α-Al_2O_3 is inert toward acids. Nevertheless, the overall reactions will occur rapidly when using HCl as the solvent (Miazga and Mulak, 2008). Most hydrocarbon gases with hydrogen sulfide (H_2S) are expected to be released from the spent catalyst after roasting to 400°C. The total weight loss percentage is from 0.97% to 1% of a 200 g sample. To ensure the accuracy of the data, five samples were tested. It was observed that bubbling and a visibly gaseous release, accompanied by a foul odor, occurred when the solutions were poured onto the roasting samples.

3. This research can have a practical industrial application. The design and installation of an industrial unit can be submitted using lab-scale data. The equipment can be designed to accommodate and modify temperature and mixing shape for any further future work. That features a silo for expired catalysts, a rotary furnace for roasting, tanks for acid preparation, and a simple reactor, which may utilize an electric heater or medium-pressure steam jacket. A stirred tank reactor can be employed, along with necessary handling equipment and pumps for the acid.

The feasibility of these projects includes many aspects, including:

A. Rid the oil facilities of the large accumulated quantities of these materials that pollute the environment and occupy ample space in the plant area, which can be used for more valuable purposes.
B. Extracting the valuable nickel element from surplus materials gives added value to the project.
C. Finding opportunities to use the material after extracting nickel from it in other industries, such as cement, since it contains pure silica and aluminum compounds.
D. Despite the fixed costs of establishing such a project, the above benefits can be compensated by an appropriate recovery period for the capital cost.
E. The actual cost of a treatment project cannot be known unless its production capacity is known. Given that the accumulated quantities of these materials in Iraq are spread across numerous oil projects in different Iraqi governorates and of various types, no accurate figures are available. It is, therefore, impossible to calculate the production capacity being treated daily. In addition, it is impossible to determine the costs of machines, equipment, operating materials, services, accessories, and transportation, making it impossible to conduct an actual economic feasibility study. Still, this can be done in the future through a separate study.

The environmental impact of implementing such a project includes the release of gaseous pollutants resulting from the burning of the material. Despite its relatively small quantities, it can be treated using the known dry and wet methods. The solid materials can be used in other industries since most are non-polluting silica and alumina compounds. The remaining acid can be recycled in a closed circuit.

IV. Conclusion

The Sulfur bed catalyst is based on Nickel Oxide. After 3 years of operation, its efficiency has begun to decline. Over several years of operation at the refinery, a significant amount of catalyst has been spent in the factory area, posing an environmental pollution risk. Since the materials are associated with petroleum extracted from several kilometers underground, conducting risk assessments on the spent catalyst is essential before metal extraction or disposal.

A standard radioactive testing method confirmed that the material is safe for handling. The chemical treatment involved three steps: extraction with distilled water, followed by treatment with a 10% sodium hydroxide (NaOH) solution, and finally, treatment with a 10% hydrochloric acid (HCl) solution. These processes were carried out over periods of 24 h and 7 days. The results indicate that the most effective extraction occurred with the acid solution over the 7 days.

V. Recommendation

Further research is needed to identify the most effective method for extracting nickel metal from its acidic solution, including the type of acid solution, extraction temperature, and time. At a specified percentage, we should also investigate the potential for reusing this material in other industries, such as cement. In addition, it is essential to study the safe disposal of spent catalysts and develop a standard regulation sheet that outlines their specifications. A realistic economic study for an industrial treatment project can be conducted after having information about its real materials' quantities and locations.

VI. Acknowledgment

We would like to thank Ms. Roza A. Fattah, Senior Engineer at Bazyan Petroleum Refinery, and Mr. Paymen Khaled, Soran University, for their support and cooperation.

References

Abu Bakar, W.W., Othman, Y., Young, R.A., and Toemen, S., 2009. The investigation of active sites on nickel oxide based catalysts towards the *in-situ* reactions of methanation and desulfurization. *Modern Applied Science*, 3(2), pp.35-43.

Aras, A., and Ağaçayak, T., 2017. Optimization of nickel extraction from lateritic ore in hydrochloric acid. *Selcuk University Journal of Engineering Sciences*, 5(3), pp.341-352.

Banerjee, D., Ganeshan, R., Rao, N., and Kumar, A., 2022. Novel analytical method for quality control of molecular sieves at manufacturing sites. *Research Journal of Material Science*, 10(1), pp.21-24.

Cano, J.R., Zamarripa, G.G.,Pedroza, F.R., Aguilar, M.D., Macías, A.H., and Vielma, A.C., 2016. Kinetics and statistical analysis of nickel leaching from spent catalyst in nitric acid solution. *International Journal of Mineral Processing*, 148, pp.41-47.

EPA. 2024. *Resource Conservation and Recovery Act (RCRA) Regulations.* EPA, USA.

Faris, N., Pownceby, M.I., Bruckard, W.J., and Chen, M., 2022. The direct leaching of nickel sulfide flotation concentrates-a historic and state-of-the-art review Part I: Piloted processes and commercial operations. *Mineral Processing and Extractive Metallurgy Review*, 44(6), pp.407-435.

Flanigen, E.M., editor. 2001. Zeolites and molecular sieves: An historical perspective. In: *Studies in Surface Science and Catalysis*. Vol. 137., Ch. 2. Elsevier, Amsterdam, pp.11-35.

Gleichmann, K., Unger, B., and Brandt, A., 2016. Industrial Zeolite Molecular Sieves, Claudia Belviso. In: *Zeolites-Useful Minerals*. Claudia Belviso, Germany.

Mafra, L., and Klinowski, J., 2013. Molecular sieves: Crystalline systems. In: Harris, R.K., Wasylishen, R., editors. *Encyclopedia of Magnetic Resonance.* Vol. 2. Wiley, United States, pp.89-108.

Marafi, M., and Ran, M.S., 2017. Refinery waste: The spent hydroprocessing catalyst and their metal recovery. *International Journal of Energy and Environmental Engineering*, 11(10), pp.918-922.

Marafi, M., and Stanislaus, A., 2003. Options and processes for spent catalyst Handling and Utilization. *Journal of Hazards Materials*, 101(2), pp.123-132.

Meier, W.M., and Uytterhoeven, J.B., 1973. Molecular sieves. Gould, R.F., editor. *Advances in Chemistry Series*. American Chemical Society, Belgium.

Miazga, B., and Mulak, W., 2008. Leaching of nickel from sent catalysts. *Physicochemical Problems of Mineral Processing,* 42, pp.177-184.

Naydenov, V., 2003. *Structured Molecular Sieves.* Doctoral Thesis. Luleå University of Technology, Luleå, Sweden.

Oza, R., and Patel, S., 2012. Recovery of nickel from spent Ni/Al2O3 catalysts using acid leaching, chelation and ultrasonication. *Research Journal of Recent Sciences*, 1, pp.434-443.

Petrov, L., 2002. Problems and challenges about accelarated testing of the catalytic activity of catalysts. In: Derouane, E.G., Parmon, V., Lemos, F., and Ribeior, F.R., Eds. *Principles and Methods for Accelerated Catalyst Design and Testing.* Vol. 69. Springer Nature, Bulgaria, pp.13-69.

Reguigui, N., 2014. *Gamma Ray Spectrometry Practical Information*. International Atomic Energy Agency (IAEA), Austria.

Rezaei, S., 2015. *Novel Adsorbents for Acid Gas Treatment in Process Streams.* Doctoral Thesis. University of Alberta, Canada.

Smail, J.M., Ahmad, S.T., and Mansour, H.H., 2021. Estimation of the natural radioactivity levels in the soil along the Little Zab River, Kurdistan Region in Iraq. *Journal of Radioanalytical and Nuclear Chemistry*, 331, pp.119-128.

Zangana, M.H., Ibraheem, F.H., Khaleel, S.I., and Al-Dahhan, M.H., 2017. *Recycling of spent Molecular Sieves from Oil and GAS Industry: North Gas Company As a Case Study.* IEEE, Iraq.

Dual-Band Power Divider with Wide Suppression Band: Artificial Intelligence Modeling for Performance Confirmation

Golshan Mohamadpour[1], Salman Karimi[1†] and Saeed Roshani[2]

[1]Department of Electrical Engineering, Lorestan University,
Khorramabad, Iran

[2]Department of Electrical Engineering, Kermanshah Branch, Islamic Azad University,
Kermanshah, Iran

***Abstract*—In this paper, a planar dual-band Wilkinson power divider (DWPD) with a triangular-shaped resonator is designed. This work stands out from existing designs by addressing key limitations in conventional power dividers, i.e., physical size, harmonic suppression, and insertion loss. The proposed triangular-shaped resonator has a compact size of 9.9 mm × 3.4 mm (0.26 λ_g × 0.09 λ_g), where λ_g is electrical wavelength at 5.9 GHz, and provides a wide suppression band from 7.1 GHz to 20.6 GHz with a 20 dB attenuation level. In the proposed DWPD structure, two triangular-shaped resonators are used in two branches. It works at 3.6 GHz and 5.5 GHz with <0.1 dB insertion loss at both operating bands. The input and output return losses and ports isolation parameters at both bands are better than 20 dB, which show good performance of the divider at operating bands. Besides the acceptable performance, the proposed DWPD provides a wide suppression band from 6.8 GHz to 20.5 GHz with more than 20dB attenuation level. In the divider design, the neural network is employed to model a triangular-shaped resonator. The proposed neural network has two outputs (S_{11} and S_{21}), and two hidden layers with eight neurons at each layer. The weights of each neuron are obtained using particle swarm optimization algorithms. The proposed neural network model has accurate results, and the mean relative error of the train and test data for both outputs is <0.1, which validates the accurate results of the proposed model.**

***Index Terms*—Dual band Wilkinson power divider, Harmonic suppression, Neural network, Resonator.**

I. Introduction

Power dividers are widely used component in microwave circuits and systems (Cheng and Law, 2008). This device divides input signals into two or more signals, and it is also a reciprocal device, so it can be used to combine power from output ports into the input port. A typical Wilkinson divider consists of two-quarter wavelength (λ/4) microstrip lines and a lumped 100 ohms' resistor between two lines in order to create port isolation. However, despite its wide applications, it has basic problems, which passes unwanted signals at other frequencies along with desired signal. In recent years, various designs are provided to remove undesirable harmonic.

Moreover, the typical divider operates only in a single band. Recently, various dual-band dividers are presented.

However, harmonic-suppressed dual-band dividers need high-tech and complex design. In (Srisathit, Chongcheawchamnan and Worapishet, 2003), (Wu, et al., 2005), and (Wu, et al., 2006), various dual-band power dividers based on open or short stubs and lumped elements are presented.

In (Srisathit, Chongcheawchamnan and Worapishet, 2003), a two-section transformer is used to create a dual-band divider, which has a simple structure but suffers from poor output ports isolation (S32) and poor output return losses (S22, S33). In (Wu, et al., 2005) and (Wu, et al., 2006), two dual bands divider are reported with lumped elements (L-C). The frequency response is improved in these dividers but they need extra fabrication process and frequency limitation due to applied lumped components.

As mentioned, the typical divider cannot suppress harmonics, but in the modern wireless communication systems, harmonics suppression is a necessary demand (Roshani, Roshani and Zarinitabar, 2019b), (Heydari and Roshani, 2017), (Liang and Xu, 2012), (Roshani, et al., 2018), therefore, several methods are introduced to overcome this drawback.

In many works, low pass filters (Mohammadi, et al., 2024), (Lotfi, Roshani and Roshani, 2020), and (Roshani, et al., 2016) and resonators (Heydari, Rostami and Roshani, 2019) and (Jamshidi, et al., 2019), are used to rejects unwanted harmonics. In these works, unwanted harmonics are successfully removed, but this method increases the insertion loss of the divider. Microstrip filters (Roshani, Dehghani, and Roshani, 2019a) are widely used in electronic systems

---

ARO-The Scientific Journal of Koya University
Vol. XIII, No. 1 (2025), Article ID: ARO.11945. 7 pages
DOI: 10.14500/aro.11945
Received: 13 December 2024; Accepted: 15 January 2025
Regular research paper; Published: 01 February 2025

†Corresponding author's email: karimi.salman@lu.ac.ir

to enhance the performance of both passive (Bavandpour, et al., 2021) and active devices by selectively passing desired frequency bands and suppressing unwanted signals. Their compact size, high efficiency, and ability to suppress harmonics make them integral to improving signal integrity and stability in applications such as wireless communications (Roshani, et al., 2023), radar, and satellite systems. In some other works, electromagnetic (EM) band gap cells (Lin, et al., 2007) and DGS (Woo and Lee, 2005) are used for harmonics suppression. Unfortunately, these methods need an extra fabrication process, which is undesirable. Lumped reactive components (external L and C), (MahdiAbadi, et al., 2024), (Pirasteh, Roshani and Roshani, 2020), (Huang, et al., 2010), (Wang, et al., 2014b), and (Wang, et al., 2014a) are used as other methods to overcome the presence of harmonics in the frequency response, which this approach is also undesirable for mass production environments.

Microstrip stubs, including open-ended or short-ended configurations, are widely used to suppress unwanted harmonics, as demonstrated in studies (Tang and Chen, 2016), (Wang, et al., 2017), (Cheng and Ip, 2010), and (Ahmed and Abbosh, 2015). These methods have a simple structure but suppress only a few harmonics.

Previously, several dividers with only harmonics suppression ability or dual band divider are designed and reported. However, previously only few dividers are designed, which have both properties of dual-band and harmonics suppression together.

In (Rostami and Roshani, 2018) a dual-band divider was designed at 0.9/1.8 GHz, which suppressed undesired signals from 3.1GHz to 10.6 GHz. In this work several lumped capacitors are used, restricting the operating frequency and also undesirable for mass production environments. In (Roshani, et al., 2022) a dual-band divider designed at 2.6/3.3 GHz, which only suppresses 3rd harmonics. This work exhibits a large insertion loss.

In recent years, artificial neural networks (ANN) are used to model and prediction of microwave device like divider as useful tools (Jamshidi, et al., 2020), (Yahya, et al., 2024), (Yahya, et al., 2022), and (Roshani, et al., 2021).

In this work, a harmonic suppressed Dual-band Wilkinson Power Divider (DWPD) is proposed using resonators, and the neural network models are used to model the desired parameters to improve the operation of resonators. The ADS simulator is used to simulate the resonator and divider, and also MATLAB R2017a is applied to model the proposed resonator with neural networks. The proposed Wilkinson power divider (WPD) stands out due to its unique design, incorporating triangular-shaped resonators and advanced neural network modeling. This innovative approach allows the divider to operate efficiently in two frequency bands while achieving outstanding harmonic suppression. It effectively filters out unwanted signals across a wide range, from 7.1 GHz to 20.6 GHz, with more than 20 dB attenuation, all while maintaining a compact and efficient design with minimal signal loss. The use of neural networks ensures precise modeling of the resonators, enhancing the overall accuracy and performance of the system, making it a highly effective solution for modern microwave applications.

II. Power Divider Design Process

This section describes the design process of the typical divider and the proposed divider.

A. Typical WPD

A typical divider, as shown in Fig. 1 is composed of three ports, one port as input and two ports as output. The input port is connected to output ports with two long quarter-wave lines. There is a lumped resonator between two output ports in order to provide port isolation. Input signal at port 1 is divided into two output ports. In the typical divider, undesired signals at higher frequencies are passed with desired signal without any suppression, which has undesirable effects on the original signal. In the modern power dividers, the divider should pass the original signal at operating frequency and eliminate higher frequencies.

The conventional Wilkinson divider inherently lacks the ability to suppress harmonics because its λ/4 transmission lines are designed to operate at a single frequency. These lines allow higher-order harmonics to pass through alongside the desired signal, leading to interference and signal distortion. This limitation becomes increasingly problematic in modern applications that demand high signal integrity across multiple bands.

Conventional Wilkinson dividers typically exhibit low insertion loss within their operating band due to their simple structure of λ/4 transmission lines, and this parameter is defined by S_{12}. However, their port isolation and return loss performance often degrade outside this narrow frequency range. Port isolation, defined by $S_{23,}$ is generally sufficient at the design frequency but is not optimized for dual-band or wideband operations. Similarly, return losses, measured at the input and output ports (S_{11}, S_{22}, and S_{33}), are acceptable in single-band applications but decline significantly for higher-order harmonics.

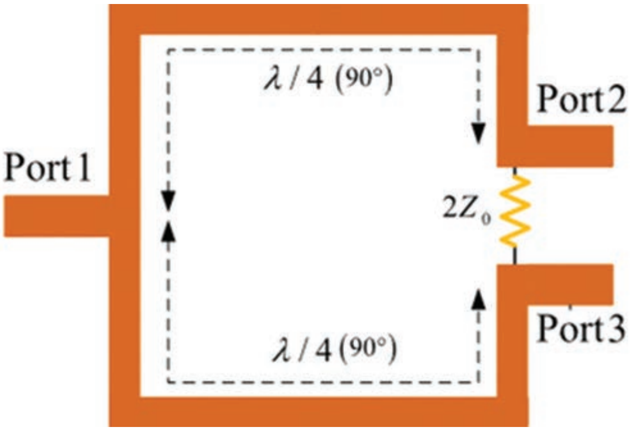

Fig. 1. Structure of a conventional Wilkinson power divider with λ/4 branches and a 100-ohm isolation resistor.

B. Proposed WPD Design

The block diagram of the proposed divider to suppress unwanted harmonics is depicted in Fig. 2. In this structure, two small resonators should be inserted in two branches of the typical divider. These resonators should pass the original signal at the operating frequency with low insertion loss and suppress other signals at higher frequencies.

In the proposed Wilkinson Divider design, which is illustrated in Fig. 2, the long conventional λ/4 branches are replaced with a novel structure that combines a resonator and two microstrip lines. These microstrip lines have an impedance of Z_1 and an electrical length of θ_1, resulting in a significantly smaller physical size compared to traditional λ/4 branches. This compact design not only reduces the overall footprint but also enhances harmonic suppression and operating efficiency. In addition, a lumped resistor, typically 100 ohms, is placed between Port 2 and Port 3 to ensure proper isolation between the output ports. This resistor plays a critical role in preventing signal interference and ensuring stable and reliable operation of the power divider across its intended frequency range.

C. Proposed Resonator Design

The structure of the proposed resonator, shown in (Fig. 3a), is designed to optimize performance by combining different impedance characteristics and stubs. It consists of three distinct sections: A central section and two outer sections. The central part of the resonator is designed with three high-low impedance sections, which create a balanced structure for impedance matching. This variation in impedance is essential for enhancing the performance of the resonator to operate efficiently over a range of frequencies, improving its overall performance in the system. In the two outer sections, long meandered lines are used. These meandering lines are loaded with rectangular shapes to further tune the resonance properties of the resonator. The meandered structure increases the effective length of the lines without occupying too much physical space, allowing for a compact design while still maintaining the desired electrical characteristics. The addition of rectangular shapes in these sections helps in controlling the resonant frequency and fine-tuning the response of the resonator. This combination of different impedance regions and the meandered line geometry ensures that the resonator can achieve the required resonance behavior while maintaining a compact and efficient design. Each section is chosen to contribute to the desired functionality and performance of the resonator in the proposed system. The proposed resonator is designed based on RT/Duroid substrate with $\varepsilon_r = 2.2$.

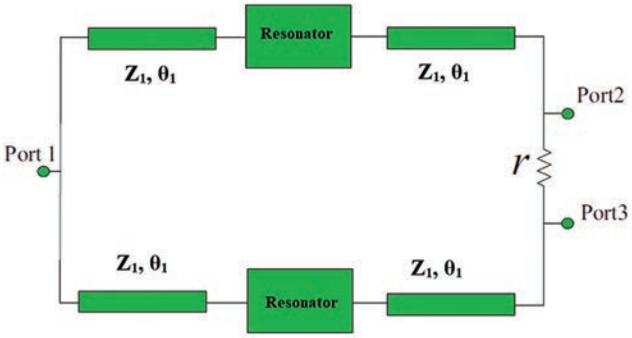

Fig. 2. Block diagram of the proposed dual-band Wilkinson power divider (WPD) with compact resonator-based branches.

The RT/Duroid substrate was chosen for its low dielectric constant and loss tangent, ensuring high performance at microwave frequencies. While it offers excellent signal integrity, its cost and scalability may pose challenges for large-scale production. Alternative materials could be considered for cost-sensitive applications in future work.

The compact size of the design inherently contributes to energy efficiency by reducing material usage and potentially lowering energy consumption during production. In addition, the enhanced performance and harmonic suppression can lead to more efficient operation in communication systems, indirectly reducing power waste.

The S-parameters of the designed resonator are depicted in (Fig. 3b) and phase curve of the proposed resonator is depicted in (Fig. 3c). As the results show, this resonator passes signals below 5.8 GHz with low insertion loss (IL) and provide wide rejection band from 7.1 GHz to 20.6 GHz with more than 20 dB suppression level.

III. Modeling of the Proposed resonator

The proposed resonator contains several high and low impedances, and making analysis and deriving closed-form equations for this structure is so difficult, therefore, an ANN model is provided for the proposed resonator.

The provided ANN model for the proposed resonator is depicted in Fig. 4. In the first step, inputs and outputs of the ANN model should be determined. For the designed resonator, the S_{11} and S_{12} are defined as the output of ANN model. In the resonators 4 parameters of W_1, L_1, $W_{2,}$ and L_2 have important effect on the response, so these four parameters and frequency are considered as 5 inputs of the ANN model. The applied resonator is designed using EM simulation in ADS software and required data of ANN model are extracted from EM simulation in ADS. An multi-layer perceptron (MLP) with two hidden layers is used for provided ANN model.

Model details, including the number of input/output neurons and hidden layers, number of epochs, and activation functions are listed in Table I.

The ANN model used in the design of the proposed WPD plays a crucial role in accurately modeling and optimizing the triangular-shaped resonators. This approach ensures a precise relationship between the resonator's physical dimensions and its electrical performance, making the design both efficient and reliable.

The ANN model is based on a MLP structure with two hidden layers, each containing eight neurons. The input layer accepts five parameters—frequency and the key geometric parameters of the resonator (W_1, W_2, L_1, and L_2)—whereas the output layer predicts the S-parameters S_{11} (input return

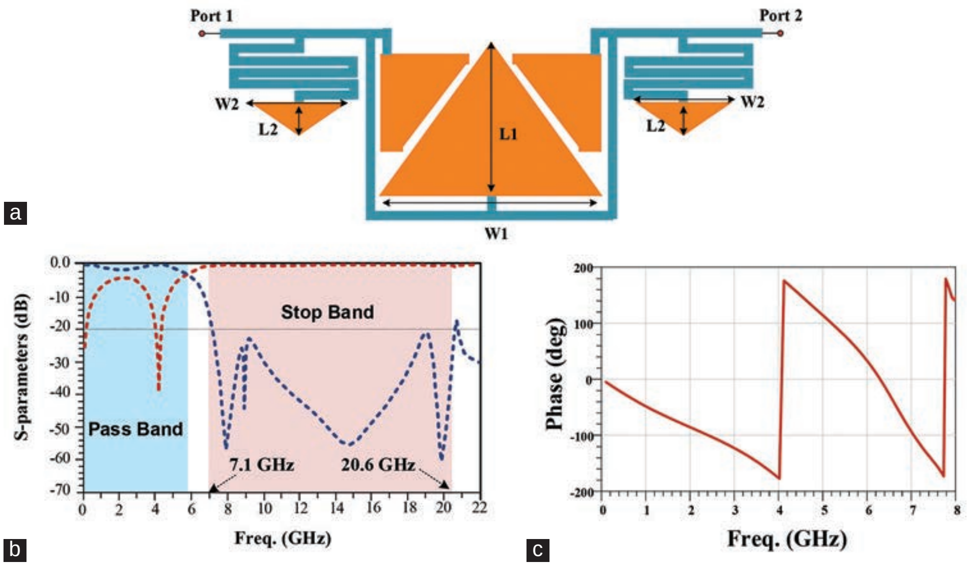

Fig. 3. Structure of the (a) proposed resonator, (b) S-parameters and (c) phase curve of resonator.

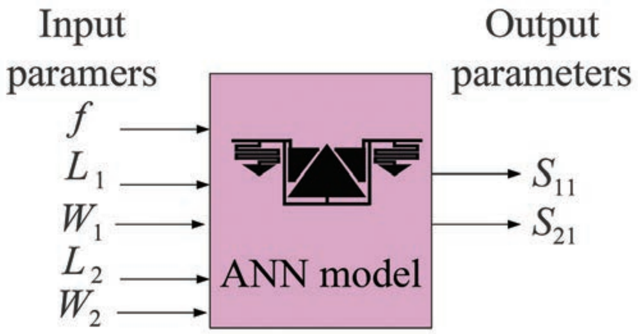

Fig. 4. The provided ANN model for proposed resonator.

loss) and S_{21} (insertion loss). This configuration allows the ANN to effectively handle the complex dependencies within the design.

The structure of the provided MLP model is illustrated in Fig. 5 as seen the proposed model has 2 hidden layers and each hidden layer has 8 neurons.

To train the model, EM simulation data generated using ADS software were utilized. The training process employed a particle swarm optimization (PSO) algorithm to fine-tune the weights of the network. The data were divided into 80% for training and 20% for testing, ensuring the ANN's ability to generalize to unseen configurations. The performance of the ANN was evaluated using metrics such as mean relative error (MRE) and mean absolute error (MAE), both of which remained below 0.1, indicating a high level of accuracy.

Using the ANN offered several advantages. It significantly reduced the time and computational effort required for iterative simulations, as the trained model could quickly predict the performance of various resonator configurations. This efficiency allowed for rapid exploration of design variations and enabled precise tuning to achieve wideband harmonic suppression with minimal insertion loss.

The MRE, which known, as MRE is determined (Willmott and Matsuura, 2005) in (1) as follow:

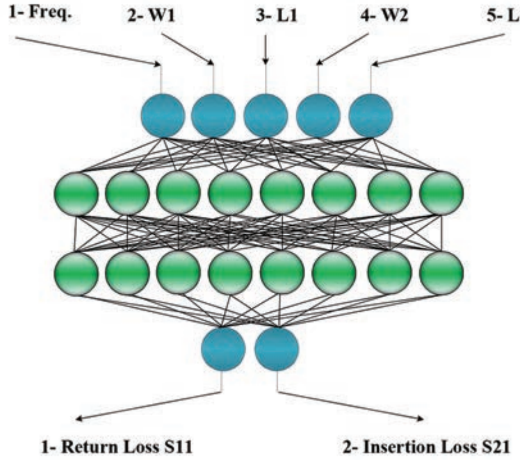

Fig. 5. Structure of the proposed multi-layer perceptron model with 2 hidden layers.

TABLE I
Provided MLP Model Details

Proposed model details	Specifications
MLP	Type of the artificial neural network
5	Number of neurons in the input layer
2	Number of hidden layers
8	Number of neurons in each hidden layer
2	Number of neurons in the output layer
500	Epochs number
Tansig	Activation functions

MLP: Multi-layer perceptron

$$MRE = \frac{1}{N} \sum_{i=1}^{N} \frac{\left| X_i(Exp) - X_i(Pred) \right|}{X_i(Exp)} \tag{1}$$

The MAE is defined (Armstrong and Collopy, 1993) in (2) as follow:

$$\mathrm{MAE} = \frac{1}{N} \sum_{i=1}^{N} \left| X_i(\mathrm{Exp}) - X_i(\mathrm{Pred}) \right|, \tag{2}$$

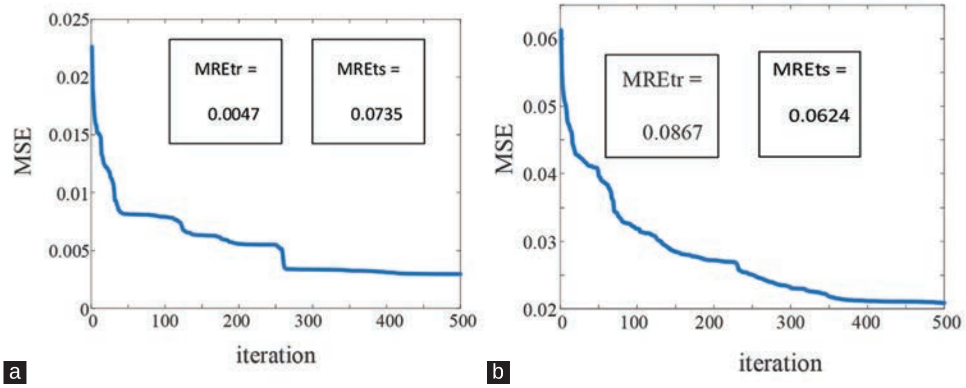

Fig. 6. Obtained value of mean absolute error and mean relative error errors for the (a) S_{11} and (b) S_{21} of the proposed model.

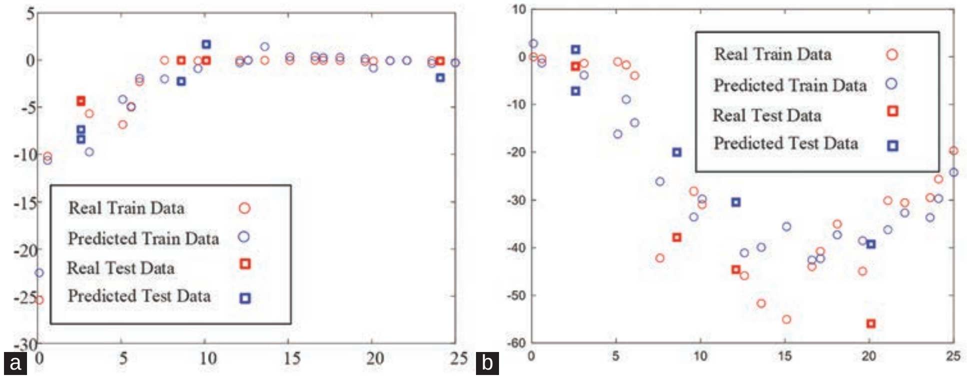

Fig. 7. Real, predicted and test results for the (a) S_{11} and (b) S_{21} of the presented multi-layer perceptron model of the proposed resonator.

The obtained values of MAE and MRE errors of the S_{11} and S_{21} for the provided MLP are listed in the Table II and shown in (Fig. 6a and b), respectively.

The real, predicted, and test results for the S_{11} and S_{21} of the presented MLP model of the proposed resonator are illustrated in (Fig. 7a and b). As results shown the predicted value of the proposed model are very similar to the real values.

The PSO algorithm is selected for the ANN model due to its simplicity, efficiency, and capability to handle complex optimization tasks. PSO operates by mimicking the behavior of natural swarms, where particles explore the solution space by updating their positions based on personal and global best solutions. This approach balances exploration and exploitation, making it well-suited for optimizing the weights and biases of the ANN, which predicts the resonator's S-parameters. Unlike traditional gradient-based methods, PSO effectively navigates non-linear, multi-dimensional spaces, avoiding local minima and achieving global optimization. Its application resulted in a highly accurate ANN model, with a MRE below 0.1, ensuring precise resonator modeling.

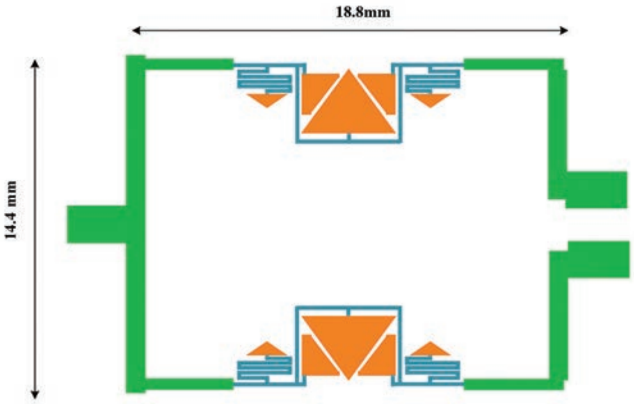

Fig. 8. Structure of the provided dual-band Wilkinson power divider.

TABLE II
OBTAINED VALUES OF MAE AND MRE ERRORS OF THE S11 AND S21 FOR THE PROPOSED MLP MODEL

MRE train error	MRE test error	MAE train error	MAE test error	Output
0.1007	0.0333	0.0735	0.0047	S11
0.2054	0.1103	0.0624	0.0867	S21

MRE: Mean relative error, MAE: Mean absolute error

IV. PROPOSED WPD

As mentioned in previous sections in the typical divider unwelcome signals at other frequencies are passed with desired signals, which have destructive effects on the main signal. Therefore, to improve the performance of the typical divider, two resonators are applied in the divider structure. The proposed resonator passes signals below 5.8 GHz with very low loss and provide wide rejection band from 7.1 GHz to 20.6 GHz with more than 20 dB suppression level. The structure of the proposed divider is depicted in Fig. 8. The provided DWPD is designed based on RT/Duroid substrate with $\varepsilon_r = 2.2$. The overall size of the proposed divider is

TABLE III
PERFORMANCE SUMMARY OF THE PROPOSED DUAL-BAND DIVIDER

Harmonic suppression (suppression level)	Ports isolation loss (dB)	Output return loss (dB)	Input return loss (dB)	Insertion loss (dB)	f_1/f_2 (GHz)
6.8–20.5 GHz (>20 dB)	31/26	34/25	27/21	0.04/0.08	3.6/5.5

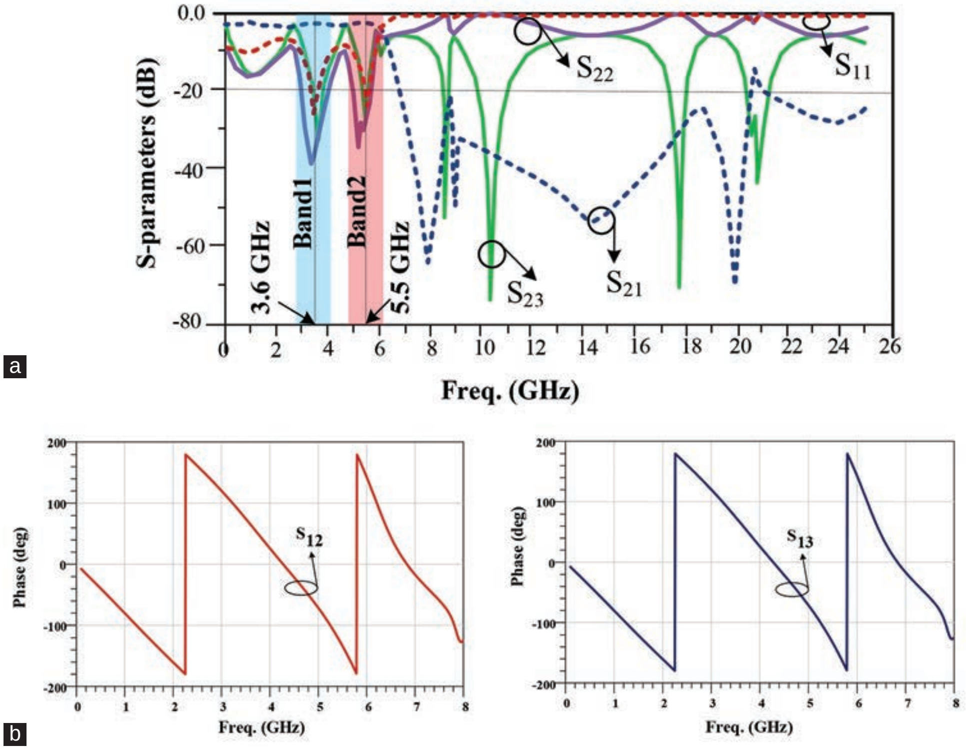

Fig. 9. Frequency response (a) and phase curves (b) of the provided dual-band Wilkinson power divider.

14.4 mm × 18.8 mm, which is equal to $0.23\lambda_g \times 0.31\lambda_g$, where λ_g is electrical wavelength at 3.6 GHz.

The frequency response of the provided DWPD is illustrated in (Fig. 9a). As seen proposed DWPD correctly works at 3.6 GHz and 5.5 GHz. The insertion losses at both operating bands are <0.1 dB. The input and output return losses at both operating bands are better than 20 dB, and better than 25 dB output port isolations are obtained for both operating bands. The results show that provided DWPD has good performance at both operating frequency bands. Also, the proposed dual-band divider has an excellent performance at higher frequencies. The proposed DWPD provides wide harmonics suppression band from 6.8GHz to 20.5GHz with more than 20 dB suppression level, which satisfactory overcome main drawback of the typical divider. The phase curves of the provided DWPD are depicted in (Fig. 9b).

The proposed WPD has the potential to bring exciting advancements to the field of microwave circuit design. It's particularly well-suited for modern applications like wireless communication systems, radar technologies, and signal processing, where maintaining signal quality and filtering out unwanted interference across multiple frequencies is essential.

A performance summary of the provided DWPD is listed in Table III. The results show the good performance of the proposed divider in operating bands and higher frequencies.

V. CONCLUSION

A DWPD is designed in this paper using triangular-shaped resonators and meandered lines. Applied resonator provides wide suppression band from 7.1 GHz to 20.6 GHz with 20dB attenuation level. The proposed DWPD works at 3.6 GHz and 5.5 GHz with <0.1 dB insertion loss at both operating bands. The input (S_{11}) and output return losses (S22, S33) and ports isolation (S23) parameters at both bands are better than 20dB, which show good performance of the divider at operating bands. The proposed DWPD not only has good performance at two operating bands, but also provides wide suppression band from 6.8 GHz to 20.5 GHz with more than 20dB attenuation level.

Moreover, applied resonator is modeled with neural network. The proposed neural network has two outputs (S_{11} and S_{21}), and two hidden layers with 8 neurons at each layer. The weights of each neuron are obtained using PSO algorithms. The proposed neural network model has accurate results and MRE for the train and test data for both outputs are <0.1, which validates the accurate results of the proposed model.

REFERENCES

Ahmed, U., and Abbosh, A., 2015. Modified Wilkinson power divider using coupled microstrip lines and shunt open-ended stubs, *Electronics Letters,* 51(11), pp.838-839.

Armstrong, J., and Collopy, F., 1993. Error measures for generalizing about forecasting methods: Empirical comparisons. *International Journal of Forecasting*, 8(1), 69-80.

Bavandpour, S.K., Roshani, S., Pirasteh, A., Roshani, S., and Seyedi, H., 2021. A compact lowpass-dual bandpass diplexer with high output ports isolation. *AEU-International Journal of Electronics and Communications,* 135, pp.153748.

Cheng, K.K.M., and Ip, W.C., 2010. A novel power divider design with enhanced spurious suppression and simple structure. *IEEE Transactions on Microwave Theory and Techniques,* 58(12), pp.3903-3908.

Cheng, K.K.M., and Law, C., 2008. A novel approach to the design and implementation of dual-band power divider. *IEEE Transactions on Microwave Theory and Techniques*, 56(2), pp.487-492.

Heydari, M., and Roshani, S., 2017. Miniaturised unequal Wilkinson power divider using lumped component elements. *Electronics Letters,* 53(16), pp.1117-1119.

Heydari, M., Rostami, P., and Roshani, S., 2019. Design of a modified wilkinson power divider with size reduction and harmonics suppression using triangle-shaped resonators. *Wireless Personal Communications*, 109(3), pp.1571-1579.

Huang, W., Liu, C., Yan, L., and Huang, K., 2010. A miniaturized dual-band power divider with harmonic suppression for GSM applications. *Journal of Electromagnetic Waves and Applications*, 24(1), pp.81-91.

Jamshidi, M., Lalbakhsh, A., Lotfi, S., Siahkamari, H., Mohamadzade, B., and Jalilian, J., 2020. A neuro-based approach to designing a Wilkinson power divider. *International Journal of RF and Microwave Computer-Aided Engineering*, 30(3), pp.e22091.

Jamshidi, M., Siahkamari, H., Roshani, S., and Roshani, S., 2019. A compact gysel power divider design using U-shaped and T-shaped resonators with harmonics suppression. *Electromagnetics*, 39(7), pp.491-504.

Liang, J.G., and Xu, H.X., 2012. Harmonic suppressed bandpass filter using composite right/left handed transmission line. *Journal of Zhejiang University Science C*, 13(7), pp.552-558.

Lin, C.M., Su, H.H., Chiu, J.C., and Wang, Y.H., 2007. Wilkinson power divider using microstrip EBG cells for the suppression of harmonics. *IEEE Microwave and Wireless Components Letters*, 17(10), pp.700-702.

Lotfi, S., Roshani, S., and Roshani, S., 2020. Design of a miniaturized planar microstrip Wilkinson power divider with harmonic cancellation. *Turkish Journal of Electrical Engineering and Computer Sciences*, 28(6), pp.3126-3136.

MahdiAbadi, S., Roshani, S., Parandin, F., and Roshani, S., 2024. Design of a miniaturized 90-degree quadrature hybrid coupler with harmonic suppression ability using π-shaped lumped elements. *Scientific Reports*, 14(1), pp.26489.

Mohammadi, N., Moloudian, G., Roshani, S., Roshani, S., Parandin, F., and Lalbakhsh, A., 2024. A Wilkinson power divider with harmonic suppression through low-pass filter for GSM and LTE applications. *Scientific Reports*, 14(1), pp.2429.

Pirasteh, A., Roshani, S., and Roshani, S., 2020. Design of a miniaturized class F power amplifier using capacitor loaded transmission lines. *Frequenz,* 74(3-4), pp.145-152.

Roshani, S., Dehghani, K., and Roshani, S., 2019a. A lowpass filter design using curved and fountain shaped resonators. *Frequenz*, 73(7-8), pp.267-272.

Roshani, S., Golestanifar, A., Ghaderi, A., Siahkamari, H., and Abbott, D., 2018. High performance microstrip low pass filter for wireless communications. *Wireless Personal Communications,* 99, pp.497-507.

Roshani, S., Hayati, M., Setayeshi, S., Roshani, S., and Mohamadpour, G., 2016. A miniaturized harmonic suppressed power amplifier integrated with lowpass filter for long term evolution application. *Analog Integrated Circuits and Signal Processing*, 89, pp.197-204.

Roshani, S., Jamshidi, M.B., Mohebi, F., and Roshani, S., 2021. Design and modeling of a compact power divider with squared resonators using artificial intelligence. *Wireless Personal Communications,* 117, pp.2085-2096.

Roshani, S., Koziel, S., Roshani, S., Hashemi Mehr, F.S., and Szczepanski, S., 2022. Design and implementation of a dual-band filtering Wilkinson power divider using coupled T-shaped dual-band resonators. *Energies*, 15(3), pp.1189.

Roshani, S., Koziel, S., Yahya, S.I., Chaudhary, M.A., Ghadi, Y.Y., Roshani, S., and Golunski, L., 2023. Mutual coupling reduction in antenna arrays using artificial intelligence approach and inverse neural network surrogates. *Sensors*, 23(16), pp.7089.

Roshani, S., Roshani, S., and Zarinitabar, A., 2019b. A modified Wilkinson power divider with ultra harmonic suppression using open stubs and lowpass filters. *Analog Integrated Circuits and Signal Processing*, 98(2), pp.395-399.

Rostami, P., and Roshani, S., 2018. A miniaturized dual band Wilkinson power divider using capacitor loaded transmission lines. *AEU-International Journal of Electronics and Communications,* 90, pp.63-68.

Srisathit, S., Chongcheawchamnan, M., and Worapishet, A., 2003. Design and realisation of dual-band 3 dB power divider based on two-section transmission-line topology. *Electronics Letters*, 39(9), pp.723-724.

Tang, C.W., and Chen, J.T., 2016. A design of 3-dB wideband microstrip power divider with an ultra-wide isolated frequency band. *IEEE Transactions on Microwave Theory and Techniques,* 64(6), pp.1806-1811.

Wang, X., Ma, Z., Yoshikawa, M., Kohagura, J., Tokuzawa, T., Kuwahara, D., and Mase, A., 2017. Mixed π type structure in W ilkinson power divider design with 3rd harmonic suppression. *Microwave and Optical Technology Letters,* 59(6), pp.1245-1248.

Wang, X., Sakagami, I., Mase, A., and Ichimura, M., 2014a. Trantanella Wilkinson power divider with additional transmission lines for simple layout. *IET Microwaves, Antennas and Propagation,* 8(9), pp.666-672.

Wang, X., Sakagami, I., Mase, A., and Ichimura, M., 2014b. Wilkinson power divider with complex isolation component and its miniaturization. *IEEE Transactions on Microwave Theory and Techniques*, 62(3), pp.422-430.

Willmott, C.J., and Matsuura, K., 2005. Advantages of the mean absolute error (MAE) over the root mean square error (RMSE) in assessing average model performance. *Climate Research*, 30(1), pp.79-82.

Woo, D.J., and Lee, T.K., 2005. Suppression of harmonics in Wilkinson power divider using dual-band rejection by asymmetric DGS. *IEEE Transactions on Microwave Theory and Techniques,* 53(6), pp.2139-2144.

Wu, L., Sun, Z., Yilmaz, H., and Berroth, M., 2006. A dual-frequency Wilkinson power divider. *IEEE Transactions on Microwave Theory and Techniques*, 54(1), pp.278-284.

Wu, L., Yilmaz, H., Bitzer, T., and Berroth, A.P.M., 2005. A dual-frequency Wilkinson power divider: For a frequency and its first harmonic. *IEEE Microwave and Wireless Components Letters,* 15(2), pp.107-109.

Yahya, S.I., Alameri, B.M., Jamshidi, M., Roshani, S., Chaudhary, M.A., Ijemaru G.K., Mezaal, Y.S., and Roshani, S., 2022. A new design method for class-E power amplifiers using artificial intelligence modeling for wireless power transfer applications. *Electronics,* 11(21), pp.3608.

Yahya, S.I., Zubir, F., Hussin, F.A., Chaudhary, M.A., Roshani, S., Sadeghin, J., Jizat, N.M., and Roshani, S., 2024. Design of a compact power splitter with improved performance for wireless applications using recurrent and feed forward neural networks inverted models. *IEEE Access*, 12, pp.117056-117071.

The Role of Immune Defense in *Serratia marcescens* Nosocomial Infections

Ihsan A. Raheem[1], Fatima R. Abdul[2] and Hanan T. Subhi[3†]

[1]Department of Medical Lab, College of Medical Techniques, Al-Farahidi University,
Baghdad, – F.R. Iraq

[2]Department of Biology, College of Science, Mustansiriyah University,
Baghdad – F.R. Iraq

[3]Department of Biology, Faculty of Science and Health, Koya University, Koya KOY45,
Kurdistan Region – F.R. Iraq

***Abstract*—Developing resistance mechanisms leads to various nosocomial infections caused by opportunistic bacteria. S*erratia marcescens* are well known to be opportunistic and are equipped with an armory of virulence factors against host immune response. The study aims to detect the immune defense in patients infected with multidrug-resistant *S. marcescens*. The study includes 132 clinical samples, including burn, wound, otitis media, and urinary tract infection (UTI) at several hospitals in Baghdad, Iraq. All isolates are identified by cultivation on MacConkey agar, nutrient agar, and blood agar, followed by biochemical tests and assessment with the VITEK 2 compact system. The isolates are tested for antibiotic susceptibility tests, interleukin-12 (IL12) levels, neutrophil ability to phagocytosis, and complement C3 and C4 levels. Out of 120 positive cultures, six isolates are identified as *S. marcescens*. The urine samples are the most isolated source and a higher level of antibiotic resistance was noticed in ampicillin and cefotaxime (100%), whereas a lower level is in imipenem. Stimulation (p = 0.005) provided a significant increase in IL-12 production. The infection with the *S. marcescens* stimulated the neutrophil's phagocytosis process compared with the control. The interplay role of virulence factors in *S. marcescens* influences its pathogenesis, antibiotic resistance, and immune response, particularly involving neutrophils and IL-12. Understanding these interactions is crucial for developing effective therapeutic strategies.**

***Index Terms*—Antibiotics susceptibility test, Interleukin-12, Neutrophil, Phagocytosis, *Serratia marcescens,* Virulence factors.**

I. Introduction

Serratia marcescens is a Gram-negative, facultative anaerobe and opportunistic bacteria related to several hospital-acquired infections, such as urinary tract, ocular lens, respiratory tract infections, wounds, septicemia, and osteomyelitis (Hsueh, 2020; Friedrich et al., 2021). Secreting a variety of inflammatory-promoting enzymes, serine protease 56-kDa is the most potent enzyme, known as serralysin, which causes keratitis, cleaves IgG and IgA, lysozyme, and triggers interleukin (IL)-6 and IL-8 (Jupatanakul et al., 2020). Being an Enterobacteriaceae member, this bacterium is widespread and possesses mechanisms for developing antibiotic resistance. It is generally documented that 1–2% of nosocomial infections affect the urinary tract, and 30–35% of asymptomatic patients with a history of instrumentation also get infections of the respiratory tract, surgical wounds, and soft tissues (Moles et al., 2019; Prado et al., 2021). A high fatality rate was associated with *S. marcescens* infections, despite limited epidemiological data, and nosocomial illnesses such as sepsis, meningitis, and endocarditis. The pathogenic isolates of *S. marcescens* often produce proteases, nucleases, lecithin, and hemolysin. A variety of strains exude prodigiosin pigment ranging from dark red color to pink indicating metabolic change over time (Sameer et al., 2023), the capacity to manufacture a beta-lactamase, which is the primary factor in the development of bacteremia and sepsis during hospitalization due to broad-spectrum antibiotic resistance (Tóth et al., 2020). Toll-like receptors (TLRs) and other receptors are used by immune cells (monocytes/macrophages and neutrophils) in response to pathogens such as bacteria, fungi, intracellular parasites, or viruses (IL-12) (Iain et al., 2023). Besides, neutrophils' role in innate immune responses shapes the host's immune defense (Bhor et al., 2021). Through CD41 Th1 cells, phagocytic cells are stimulated to release IL-12 in response to bacterial endotoxin. INF-gamma produced by IL12 controls how much IL-12 neutrophils and macrophages may secrete. IL-12 ties innate and adaptive immunity together. IL-12 and IFN- are produced in response to inflammation in an acute infection, but IL-12 production that is out of control causes septic shock syndrome and autoimmunity in a chronic infection (Ullrich et al., 2020). Therefore, the primary goal of this research is to understand how *S. marcescens* contributes to various clinical infections in Baghdad, Iraq by isolating, identifying,

ARO-The Scientific Journal of Koya University
Vol. XIII, No. 1 (2025), Article ID: ARO.11819. 8 pages
DOI: 10.14500/aro.119819
Received 12 September 2024; Accepted 12 January 2025
Regular research paper; Published 01 February 2025

†Corresponding author's e-mail: hanan.baker@koyauniversity.org

and detecting the major virulence factors, followed by the examination of neutrophils' ability to undergo phagocytosis as a marker for innate immunity and their relationship to immune-mediated diseases.

II. Materials and Methods

A. Isolation and Identification

Between June and November 2021, 132 clinical specimens, including otitis media, burn infections, infected wounds, and urinary tract infections (UTIs), were obtained at several hospitals in Baghdad province. The specimen collection followed the Tille (2022) protocol, which involved taking ear swabs by gently rotating the swab in the ear canal and collecting midstream urine and skin scrapes from wounds and burn infections in sterile containers. The specimen swabs were quickly transferred and cultured on the nutrient, blood, and MacConkey agar for biochemical and microbiological characterization. The biochemical test included catalase, oxidase, Voges-Proskauer, citrate utilization, indole production, motility, and sugar fermentation on MacConkey agar. A Gram stain, nutrient agar, and blood agar were used to characterize the isolates. The VITEK 2 compact system (BioMerieux, France) was used to validate the identification (Abhishek and Tanu, 2020).

B. Virulence Factors Detection

S. marcescens isolates' phenotypic virulence characteristics were examined to determine isolates' pathogenicity, biofilm-forming capacity, protease, beta-lactamase, lipase, urease, lecithinase, hemolysin, and motility (Abdul et al., 2019; Abhishek and Tanu, 2020; Tille, 2022).

C. Antibiotics Susceptibility Test

The disk diffusion method was used to determine the antibiotics susceptibility patterns for cefotaxime (CTX 30μg), azithromycin (AZM 30 μg), ampicillin (AMP 10 μg), piperacillin/tazobactam (TZP 110 μg), ceftazidime (CAZ 30 μg), ciprofloxacin (CIP 10 μg), amikacin (AK 30 μg), tobramycin (TOB 5 μg), gentamycin (GEN 10 μg), and imipenem (IPM 10 μg) (bioanalysis/Turkey). The results were interpreted according to the Clinical and Laboratory Standards Institute as described by (Priyanka et al., 2023).

D. Clinical Sample Collection

Blood samples were obtained from six patients infected with *S. marcescens*, and healthy individuals who served as the control group. Two tubes were prepared from each blood sample. The first tubes were used to test the neutrophils' phagocytosis capacity, and the second part of the blood samples yielded serum stored in a sterile container for laboratory testing.

E. Enzyme-Linked Immunosorbent (ELISA)

The assessment of plasma IL-12 levels using commercial ELISA kits is crucial for understanding the cytokine's role in various therapeutic contexts, commercial ELISA kits (IBL international IBL GMBH, Germany) following the manufacturer's instructions were applied to the plasma level of IL-12 patients. The kits' standard curves tested the cytokines' concentration, and the results detected were done in ng/ml. The data were examined in the median value, and each sample was run twice.

F. Evaluation of Neutrophil Activity

The nitro-blue tetrazolium (NBT) test is a widely utilized method for assessing the phagocytic capacity of neutrophils, particularly in various clinical contexts. This assay measures the ability of neutrophils to reduce NBT, indicating their functional status in phagocytosis and oxidative burst activity (Nurasyikin et al., 2022). Venous blood from healthy (control) and patients infected with *S. marcescens* was incubated with a solution of nitro blue-tetrazolium (NBT).

G. Complement Level Assessment

Single radial immunodiffusion (SRID) is a reliable technique for quantifying serum proteins, including complement components, using a small volume of serum. The method typically employs 5 μL of patient serum, as recommended by manufacturers, to ensure accurate results while optimizing sample usage. SRID accurately measures components C3 and C4, particularly at elevated concentrations. Endplates were used to create C3, and C4, the plate's lids were tightly closed after being slightly opened for 5 min to eliminate moisture droplets and left on the bench at room temperature for 48–72 h. The diameter of the immunological precipitation ring was measured to an adjacent 0.1 mm using a definite ruler (Ayano and Horiuchi, 2023).

H. Statistical Methods

Statistical analysis ANOVA was performed using the PROC MIXED model (SAS 8.2; SAS Institute, Cary, NC, USA). T-test was used to compare means of tests and controls. P-values indicate statistical significance if $p < 0.05$. To adjust the alpha (α) level, Bonferroni Correction was applied using an online calculator: https://www.statology.org/bonferroni-correction-calculator

III. Results and Discussion

In this study, *S. marcescens* was isolated from 6 (out of 132) clinical specimens. The organism was identified as a Gram-negative bacillus, catalase-positive, oxidase-negative, reacts positively in the Voges–Proskauer test, and utilizes citrate as a sole carbon source. *S. marcescens* colonies on nutrient and blood agar appeared circular with pink or red pigmentation, attributed to prodigiosin production. They did not ferment lactose on MacConkey agar and most of the isolates are pigment producers (66.7%) (Fig. 1).

Virulence factor secretion contributes to bacterial pathogenicity. Consequently, these bacteria produce various metabolites during infection. Table I and Fig. 2 show the virulence factors of isolates.

TABLE I
Virulence Factors of *S.* Marcescens Isolates in this Study

Isolated number of *S. marcescens*	Virulence factor							
	Motility	Hemolysis	Beta lactamase	DNase	Urease	Lipase	Lecithinase	Prodigiosin
1	+	+	+	+	+	+	-	+
2	+	+	+	-	+	-	-	+
3	+	+	+	+	-	-	-	+
4	+	+	+	+	+	-	+	-
5	+	+	+	+	-	-	-	-
6	+	+	-	-	-	+	-	+
%	100	100	83.3	66.7	50	33.3	16.63	66.7

S. marcescens: Serratia marcescens

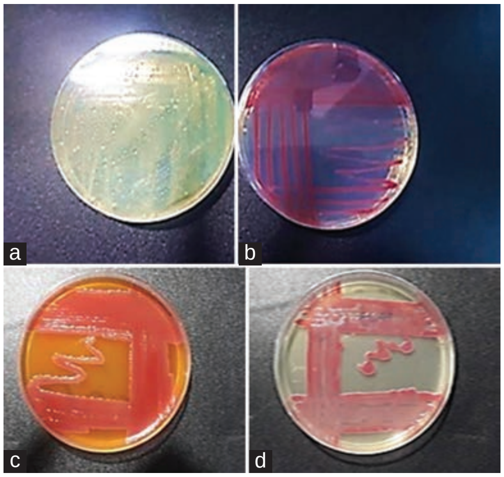

Fig. 1. S*erratia marcescens* colonies. (a) Non-producing a pigment on nutrient agar. (c) produces a red colony on blood agar. (b and d) The colonies are red because of a pigment (prodigiosin) produced by this organism on nutrient agar.

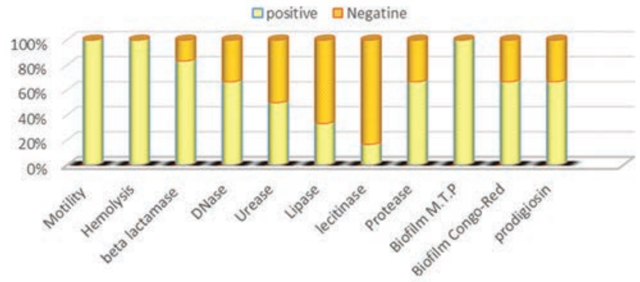

Fig. 2. Virulence factors percentage of *Serratia marcescens* isolates.

Notably, the strain that synthesized prodigiosin did not secrete lecithinase. The production of prodigiosin in *S. marcescens* is intricately regulated by various systems, notably the EnvZ/OmpR system, which responds to environmental stimuli. This multifaceted regulatory landscape encompasses metabolic pathways and biosynthetic processes, influencing pigment synthesis under specific conditions (Jia et al., 2022).

Another notable point was the strains producing urease with strong biofilm producers (see isolate numbers 1, 2, and 4 in Tables I and II). Clinical *S. marcescens* isolates demonstrate significant adaptive plasticity through urea-induced acyl-homoserine lactonase, particularly in response to environmental signals including urea and population density (quorum sensing). This adaptability allows the bacteria to regulate gene expression based on external cues (Tuttobene et al., 2024).

Protease activity is also linked to these cells' invasion and demise (Ferreira et al., 2020). All isolates produce hemolysin and are known to induce cytotoxicity and inflammatory mediator cell secretion. These substances can invade and kill HeLa cells and fibroblasts, degrade the complements (C1 and C5a) system, and increase vascular permeability (Ferreira et al., 2020). *S. marcescens* nuclease has both intracellular and extracellular degradation properties and is resistant to high temperatures (Cai et al., 2024). Lipase contributes to degrading host lipids by hydrolysis of triglycerides, providing fatty acids that can be utilized for energy, and growth, and may also disrupt cellular membranes, facilitating tissue invasion and immune evasion. Thus, supporting bacterial proliferation in host environments (Nwachukwu et al., 2017).

Despite the bacteria isolation rate was 4.6%, UTI samples occupied the first position in isolation (50%), followed by burns, wounds, and otitis media (16.63%) in each sample (Table III). The present results agreed with the local studies (Suhad et al., 2023; Sadeq and Neamah 2024) which noticed a higher incidence of urine and burns.

Most *S. marcescens* were isolated from female patients 4 (66.7%) compared with males 2 (33.3%) (Table IV). Females are exposed to more infections, such as UTIs, than males. This result contrasts with the finding by Ferreira et al. (2020), who found isolation incidences were more recurrent in males. That means the bacteria invade individuals that have the prevalent disease.

The prevalence of *S. marcescens* increased with age peaking at 50% in the age range of (36–55) since, the majority in this age range are workers, who may experience an accident at work. Some of them may also be immunocompromised, such as individuals with diabetes mellitus, and 30% of people with *S. marcescens* infection carry the bacterium in their intestines, which is the main reservoir for the bacteria (Ferreira's et al., 2020; Drummond et al., 2023). Regarding the third age group (36–55), most bacteria were isolated from their UTI specimen, wound, and burn swab (33.3% for each).

TABLE II
Capacity Biofilm Formation and Protease Production by *S. Marcescens*

Biofilm Congo-Red	Biofilm (M.T.P)	Protease by (mm) lysis diameter	Isolation source	Isolated number of *S. marcescens*
1	Wounds	-	S/0.395	+
2	UTI	16	S/0.273	+
3	burns	11	M/0.189	−
4	UTI	21	S/0.454	+
5	UTI	10	M/0.238	+
6	Otitis media	12	M/0.126	−
Control			0.114	
%		66.7	100	66.7

S=Strong biofilm forming,
M=Moderate biofilm forming
S. marcescens: Serratia marcescens

TABLE III
Number and Percentage of S. Marcescens Isolates According to Specimens' Type

Study groups	Total number of specimens	No. of *S. marcescens* isolated	(%)
UTI	55	3	50
burns	34	1	16.63
Wounds	25	1	16.63
Otitis media	18	1	16.63
Total	132	6	100

S. marcescens: Serratia marcescens

A. Virulence Factors

Evaluating the diameter of the lysis area on skim milk agar media, determined that five isolates were protease producers (or wells method). The lowest protease activity measured 10 mm in diameter, while the maximum activity measured 21 mm in diameter, was found in four isolates.

In the Microtitre Plate (M.T.P.), all *S. marcescens* isolates formed biofilm. In the quantitative assay results, three isolates exhibited moderate biofilm formation, whereas three isolates demonstrated significant biofilm formation. Out of all isolates tested, only 4 (66.7%) formed biofilms on Congo-red agar. The results are listed in Table II and Fig. 2.

The opportunistic traits such as colonization and antibiotic resistance are influenced by biofilm formation (Wu et al., 2024). Biofilm development allows the bacteria to thrive in challenging conditions and confer resistance to a wide antimicrobial treatment (Haidar et al., 2024). *S. marcescens* can produce biofilm associated with biotic or abiotic surfaces (Srinivasan et al., 2021). This ability has been linked to *Serratia*'s capacity to form colonies and endure in medical devices such as catheters and prostheses. In addition, the bacteria are able to attach to the host's epithelial cells through the production of biofilms (Weber et al., 2023).

Antibiotics susceptibility

All isolate susceptibility tests were conducted on 10 antibiotics: Ampicillin, cefotaxime, azithromycin, ceftazidime, piperacillin/tazobactam, ciprofloxacin, amikacin, tobramycin, gentamicin, and imipenem.

The data in Fig. 3 display a high-level resistance of *S. marcescens* medical isolates to the greatest number of antibiotics beneath the test. All isolates were resistant to ampicillin and cefotaxime, with notable resistance rates to amikacin (83.3%) and gentamicin (66.7%). The bacteria can acquire resistance genes encoded to aminoglycoside-modifying enzymes which inactivate amikacin and gentamicin (Tavares-Carreon et al., 2023). However, our results contrast with a systematic review meta-analysis, which shows no resistant strains against amikacin, while three strains out of 26 isolates were resistant (Zivkovic Zaric et al., 2023).

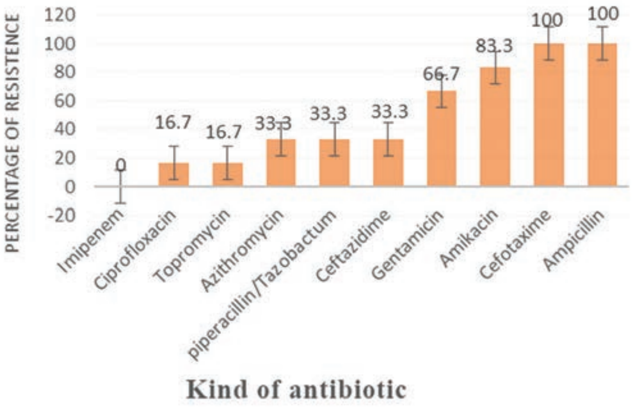

Fig. 3. Antibiotic resistance to *Serratia marcescens* isolates.

Ceftazidime, piperacillin/tazobactam, and azithromycin were recorded to be moderate resistance (33.3%) followed by tobramycin and ciprofloxacin (16.63%). The most effective drug from the carbapenem group was imipenem 100%. This finding is consistent with a local study (Abdul et al., 2022). However, the effectiveness of imipenem, particularly in the context of *S. marcescens* infections has been a topic of research and investigation. While imipenem is a potent carbapenem antibiotic, its efficacy can vary based on the resistance mechanisms present in the bacterial strains (Mughrabi et al., 2023).

Ampicillin, a member of the penicillin family, appeared to be highly resistant (100%); as a result, researchers found that *S. marcescens* possesses intrinsic ampicillin resistance (Gravrand et al., 2022). Increasing the production of AmpC beta-lactamase by Enterobacteriaceae is linked to treating infections with third-generation broad-spectrum cephalosporins (cefotaxime and ceftazidime). *S. marcescens* expresses extended-spectrum-lactamases (ESBLs) through a plasmid and is chromosomally encoded for the AmpC beta-lactamase (Hayashi et al., 2021): Third-generation cephalosporins and aztreonam hydrolyzed by ESBLs to treat the variety of infections, including UTIs. *S. marcescens* isolates showed a 49.4% resistance rate to third-generation cephalosporins, with 32.2% producing ESBLs (Radeva et al., 2022). Resistance levels in *S. marcescens* have been significantly enhanced in various clinical isolates, particularly within hospital environments (Xu et al., 2024). Mutant strains have emerged due to the combination of antibiotics used to treat severe Gram-negative infections, particularly the combination of cefotaxime and amikacin (Sharma et al., 2022).

B. Immunological Study

IL-12

The amount of IL-12 increases when a bacterial infection occurs in a room. In the course of our research, the IL-12 in wounds and UTIs with *S. marcescens* was examined. As presented in Fig. 4, IL-12 level was increased significantly in wounds and UTI patients compared to the normal control patients ([217.32 ± 48.9 pg/mL], and [81.65 ± 13.64 pg/mL; $p < 0.001$]). Certain patients who expected no treatment had a great level of IL-12. Nevertheless, based on the extensive deviation in IL-12 level, the individuals were divided into two collections: patients with a high IL-12 level, and healthy patients with an ordinary level. As shown in Fig. 4, levels of IL-12 in patients were significantly higher compared to the control with normal IL-12 levels ($p < 0.05$). Although there was a significant correlation between IL-12 levels, the levels in patients with wounds and UTIs contrasted with those in the control group. P-value (one-tailed) = 0.003765, p-value (two-tailed) = 0.007531, The *post hoc* test revealed significant results in each comparison, a $p < 0.02500$.

This interaction activates several signals and upregulates the expression of molecules involved in the presentation of Ag, and cytokines inflammatory mediators such as IL-12, TNF-gamma, and CCL2. Then, IL-12 promotes innate and adaptive immune responses by activating T and B cells and controlling the growth and differentiation of the Th1-type immune response (Ullrich et al., 2020). IL12 secretion fluctuates and is consistently produced at the beginning of an infection, where it then controls the production of other cytokines and upholds acquired immunity (Jiang et al., 2020). Cytokines are produced and matured during the immune system’s control of infections. IL12 is suppressed or activated by pathogen contacts with immune cells’ cytokine release, which regulates immunological responses and affects the development of infectious illnesses (Ullrich et al., 2020). Therefore, an increase in IL12 stimulates endosomes to destroy Gram-positive bacteria. This process is essential for effectively removing pathogens such as *Staphylococcus aureus* and *Mycobacterium tuberculosis* (Peignier et al., 2024).

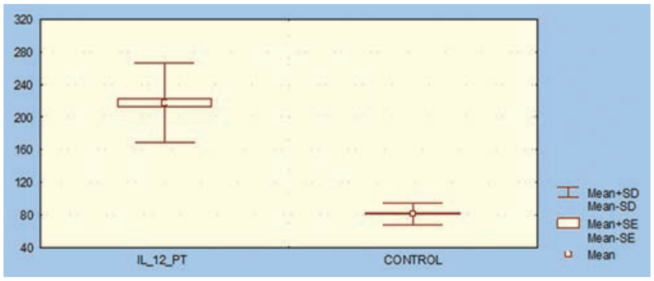

Fig. 4. Levels of interleukin-12 in patients compared with control

The bacterium hindered the innate immune response by employing a broad strategy of immune evasion. For instance, it secretes serralysin metalloprotease, which degrades adhesion molecules on immune cells, thereby inhibiting their ability to adhere and clear bacteria effectively and accelerating immune cell death through lipopolysaccharide and flagella. (Ishii et al., 2014; Vale de Macedo et al., 2021). This is due to IL12 secretion by *S. marcescens.*

Neutrophils phagocytic activity

In comparison to control groups, the findings revealed a statistically significant rise ($p < 0.05$) in the phagocytic action of polymorphonuclear neutrophils in *S. marcescens* infections. In burns infection, the average patient with positive cells was 9.72±*25.17 compared to the control 4.76±10.17, and the largest proportion of reduction in NBT was seen. The rate was lower in patients with otitis media infection 16.33±4.51 compared to control 5.03±10.67, as shown in Table V and Fig. 5.

This demonstrated that bacterial infections boosted the phagocytic action of polymorphonuclear cells in all groups. Neutrophils are known to take part in phagocytic activity, one of the immunological reactions that are non-specific and are triggered by the presence of foreign agents. The NBT dye reduction test is a cytochemical immunoassay revealing macrophages’ involvement in phagocytosis (Nurasyikin et al., 2022).

The metabolic alterations happen in neutrophils and monocytes after phagocytosis and are related to the decrease in NBT *in vitro* inside the phagocytic vacuole (Britt et al., 2022). It has been demonstrated that the neutrophil NBT-reduction test is a useful indicator of bacterial infection (Nurasyikin et al., 2022). Although neutrophil phagocytosis’s role removes pathogens, the initial anti-inflammatory cytokines secreting through neutrophil cells develop an immune paralysis response and hyperinflammatory response which lead to the insufficient removal of pathogens and subsequently cause septicemia (Kwok et al., 2023). Neutrophils account for

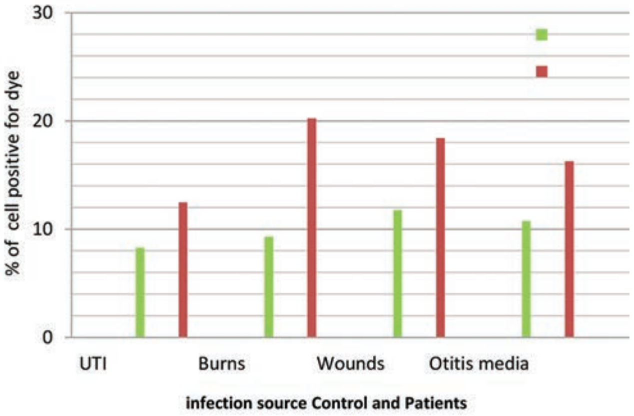

Fig. 5. Percentage of polymorphonuclear neutrophils in patients and control.

60%–80% of leukocyte cells rise tenfold during infections. Neutrophil membrane adhesion is reduced in response to bacteria endotoxin and hyperinflammatory cytokines secreted leading to inflammation of tissues and initial sepsis (Hortová-Kohoutková et al., 2020). The pro-inflammatory cytokines TNFα, IL-1β, IL-6, and IL-12 are secreted in response to Gram-negative bacteria infections through the outer membrane and LPS which TLR4 recognizes expressed on the neutrophil cell surface and trigger pro-inflammation signals (Ernst et al., 2021). Then the complement activates and recruits the neutrophils (Maqsood et al., 2024).

Patients' serum complements level (infected by S. marcescens)

As shown in Table VI the complements C3 and C4 levels in the serum of patients were 102.67±6.43, and 51.67±3.06, whereas the control levels of C3 and C4 were 85.33±5.03, 38.33±11.93, respectively. An increased level of complements in patients compared to control. Statistical analysis showed no significant differences; however, the *post hoc* test revealed that the means of the C3 and C4 tests were equal and significant. Complement levels are often significantly elevated after infection or injury (Rognes et al., 2021). The serum complements C3 and C4 are critical biomarkers for assessing complement pathways, diagnosing infectious diseases, and managing immune disorders. Their measurement provides insights into the functionality of the complement system, which plays a vital role in innate immunity and the pathogenesis of various diseases (Wang and Liu, 2021).

In addition, the classical pathway of complement activation plays a crucial role in enhancing the opsonization of bacteria, particularly through the binding of immunoglobulin IgM to bacterial surface molecules or extracellular material in biofilms. This process initiates complement activation, leading to the formation of C3 convertase, which cleaves C3 protein and facilitates opsonization (Pinto et al., 2024) (Table VI). These levels also revealed the state of the individual's innate immunity, especially C3 is the main element of the complement pathway, whereas C4 levels were increased. A drop in C3 is a reliable sign that a close, non-intrusive bacterial infection is forcing the complement system to use an alternative pathway (Tzoumas et al., 2021). Even though few studies have concentrated on immune responses to bacterial biofilm, the development of the biofilm plays a significant role in evading the host immune defense because it shields bacteria from antimicrobial peptides, neutrophil phagocytosis, complement deposition, and antibodies (Dong et al., 2022). The complement C3 controls the inflammatory response and macrophage phagocytosis (Bai et al., 2022). Moreover, the complement C4 expression is raised by lipopolysaccharide, IFNγ, and IL6 (Wang and Liu, 2021). The pathogens use different mechanisms to inhibit the innate immunity of the complement system, and the ability to do that reflects the bacteria's pathogenicity (Syed et al., 2020).

S. marcescens is an opportunistic pathogen that presents significant challenges in clinical environments due to its capability to evade host immune responses. The mechanisms

TABLE IV

Distribution of *Serratia marcescens* isolates according to patient's gender and age with specimen types

Ag group (Years)	Patient No	Gender		Study group			
		Male No.	Female No.	UTI No.	Wound No.	Burns No	Otitis media No.
≤20	1	-	1	1	-	-	-
21–35	1	-	1	1		-	-
36–55	3	1	2	1	1	1	-
>55	1	1	-	-	-	-	1
Total no. (%)	6 (100)	2 (33.3)	4 (66.7)	3 (50)	1 (16.63)	1 (16.63)	1 (16.636.7)

TABLE V

Percentage of Polymorphonuclear Neutrophils that Tested Positive for the Dye Nitro Blue Tetrazolium

Clinical source	Group	% cells positive for dye (mean±SD)	P-value	***Post hoc test*
UTI	Control	8.33±1.35	0.046	Non-significant
	Patients	*15.33±5.13		
Burns	Control	4.76±10.17	0.008	Significant
	Patients	9.72±*25.17		
Wounds	Control	1.15±10.67	0.011	Significant
	Patients	2.65±*18.00		
Otitis media	Control	5.03±10.67	0.220	Non-significant
	Patients	16.33±4.51		

*significance ($p<0.05$) comparison to the healthy

***Post hoc* P=0.0125

TABLE VI

Complements Level in *Serratia marcescens*-Infected Patient Sera

Complements	Patients' sera (M±standard deviation)	Control	P-value	**Post-hoc test*
C3 (mg/dL)	102.67±6.43	85.33±5.03	0.021 nonsignificant	Significant
C4 (mg/dL)	51.67±3.06	38.33±11.93	0.134 nonsignificant	Significant

**Post hoc* P=0.025

by which *S. marcescens* escapes immune detection are multifaceted, primarily involving its capsule polysaccharides, which play a crucial role in its virulence and survival during infections (Anderson et al., 2024).

IV. CONCLUSION

S. marcescent is one of the important causes of infections in hospitals, with the highest isolation rate depicting the pathogenicity of the isolates. The incidence was high among females, and the isolates were multi-resistant to most antibiotics and induced an inflammatory immune response, IL-12. The study showed that infection with a virulent bacterium stimulates the process of phagocytosis in neutrophil cells compared to the control.

ACKNOWLEDGMENT

The authors would like to express their gratitude to the; College of Health and Medical Technologies at Al-Farahidi University, the Department of Biology at Mustansiriyah University, and the Department of Biology at Koya University for their support.

REFERENCES

Abdul, F.R., Abbas, M.K., Rasool, K.H., and Raheem, I.A., 2022. The contribution of interleukin (17) in Iraqi patients with type I diabetes and positive agglutination sera with *Morganella morganii* antigens. *International Journal of Design and Nature and Ecodynamics*, 17(5), pp.767-772.

Abdul, F.R., Subhi, H.T., Taher, N.A., and Raheem, I., 2019. Activity of Iron oxide nanoparticles on bacterial biofilm formation. *International Journal of Pharmaceutical Sciences and Research*, 11(3), pp.1126-1130.

Abhishek, C., and Tanu, J., 2020. *Biochemical and Molecular Methods for Bacterial Identification*. Springer, Germany, pp.425-468.

Ayano, M., and Horiuchi, T., 2023. Complement as a biomarker for systemic lupus erythematosus. *Biomolecules*, 13(2), pp.367-367.

Bai, H., Mu, L., Qiu, L., Chen, N., Li, J., Zeng, Q., Yin, X., and Ye, J., 2022. Complement C3 regulates inflammatory response and monocyte/macrophage phagocytosis of *Streptococcus agalactiae* in a teleost fish. *International Journal of Molecular Sciences*, 23(24), p.15586.

Bhor, R., Rafati, S., and Pai, K., 2021. Cytokine saga in visceral leishmaniasis. *Cytokine*, 147, p.155322.

Britt, E.C., Lika, J., Giese, M.A., Schoen, T.J., Seim, G.L., Huang, Z., Lee, P.Y., Huttenlocher, A., and Fan, J., 2022. Switching to the cyclic pentose phosphate pathway powers the oxidative burst in activated neutrophils. *Nature Metabolism*, 4(3), pp.389-403.

Cai, J., Zhang, Y., Jiang, X., Hu, Y., and Chen, W., 2024. Thermally resistant nuclease in *Serratia marcescens* hinders PCR reactions and degrades PCR products. *Cell Biochemistry and Function*, 42(4), p.e4032.

Dong, J., Wang, W., Zhou, W., Zhang, S., Li, M., Li, N., Pan, G., Zhang, X., Bai, J., and Zhu, C., 2022. Immunomodulatory biomaterials for implant-associated infections: From conventional to advanced therapeutic strategies. *Biomaterials Research*, 26(1), p.72.

Drummond, S.E., Maliampuraka A., Jamdar A., Melly L., and Holmes S., 2023. *Serratia marcescens* causing recurrent superficial skin infections in an immunosuppressed patient. *Skin Health and Disease*, 3, p.e283.

Ernst, O., Khan, M.M., Oyler, B.L., Yoon, S.H., Sun, J., Lin, F.Y., Manes, N.P., MacKerell, A.D., Jr., Fraser, I.D.C., Ernst, R.K., Goodlett, D.R., and Nita-Lazar, A., 2021. Species-specific endotoxin stimulus determines toll-like receptor 4-and caspase 11-mediated pathway activation characteristics. *mSystems*, 6(4), p.e0030621.

Ferreira, R.L., Rezende, G.S., Damas, M.S.F., Oliveira-Silva, M., Pitondo-Silva, A., Brito, M.C.A., Leonardecz, E., De Góes, F.R., Campanini, E.B., Malavazi, I., Da Cunha, A.F., and Pranchevicius, M.D.S., 2020. Characterization of KPC-producing *Serratia marcescens* in an intensive care unit of a Brazilian tertiary hospital. *Frontiers in Microbiology*, 11, p.956.

Friedrich, I., Bodenberger, B., Neubauer, H., Hertel, R., and Daniel, R., 2021. Down in the pond: Isolation and characterization of a new *Serratia marcescens* strain (LVF3) from the surface water near frog's lettuce (*Groenlandia densa*). *PLoS One*, 16(11), p.e0259673.

Gravrand, V., Ariey, F., Terracol, L., Poupet, H., Doloy, A., Poyart, C., and Mammeri, H., 2022. Frameshift mutation (690delG) in cpxA contributes to the extensive drug resistance of a *Serratia marcescens* clinical isolate. *The Journal of Antimicrobial Chemotherapy*, 77(6), pp.1611-1616.

Haidar, A., Muazzam, A., Nadeem, A., Atique, R., Naveed, A., Sharif, J., Perveen, A., Fatima, H. R., and Samad, A., 2024. Biofilm formation and antibiotic resistance in *Pseudomonas aeruginosa*. *The Microbe*, 3, p.100078.

Hayashi, W., Yoshida, S., Izumi, K., Koide, S., Soga, E., Takizawa, S., Arakawa, Y., Nagano, Y., and Nagano, N., 2021. Genomic characterisation and epidemiology of nosocomial *Serratia marcescens* isolates resistant to ceftazidime and their plasmids mediating rare blaTEM-61. *Journal of Global Antimicrobial Resistance*, 25, pp.124-131.

Hortová-Kohoutková, M., Tidu, F., De Zuani, M., Šrámek, V., Helán, M., and Frič, J., 2020. Phagocytosis-inflammation crosstalk in sepsis: New avenues for therapeutic intervention. *Shock*, 54(5), pp.606-614.

Hsueh, K., 2020. Fevers and sepsis. In: Spec, A., Escota, G.V., Chrisler, C., and Davies, B., Eds. *Comprehensive Review of Infectious Diseases*. 1st ed. Elsevier, USA, p.181.

Iain, L., Hirschfeld, J., Kantarci, A., Wilensky, A., and Shapira, L., 2023. The role of the host-neutrophil biology. *Periodontology 2000*, 10.1111/prd.12490, pp.1-47.

Ishii, K., Adachi, T., Hamamoto, H., and Sekimizu, K., 2014. *Serratia marcescens* suppresses host cellular immunity via the production of an adhesion-inhibitory factor against immunosurveillance cells. *The Journal of Biological Chemistry*, 289(9), pp.5876-5888.

Jia, X., Zhao, K., Liu, F., Lin, J., Lin, C., and Chen, J., 2022. Transcriptional factor OmpR positively regulates prodigiosin biosynthesis in *Serratia marcescens* FZSF02 by binding with the promoter of the prodigiosin cluster. *Frontiers in Microbiology*, 13, p.1041146.

Jiang, H., Zhai, T., Yu, Y., Li, X., Gong, P., Zhang, X., Li, G., and Li, J., 2020. Delayed IL-12 Production by macrophages during *Toxoplasma gondii* infection is regulated by miR-187. *Parasitology Research*, 119(3), pp.1023-1033.

Jupatanakul, N., Pengon, J., Selisana, S.M.G., Choksawangkarn, W., Jaito, N., Saeung, A., Bunyong, R., Posayapisit, N., Thammatinna, K., Kalpongnukul, N., Aupalee, K., Pisitkun, T., and Kamchonwongpaisan, S., 2020. Serratia marcescens secretes proteases and chitinases with larvicidal activity against *Anopheles dirus*. *Acta Tropica*, 212, p.105686.

Kwok, A.J., Allcock, A., Ferreira, R.C., Cano-Gamez, E., Smee, M., Mentzer, A.J., Todd, J.A., and Knight, J.C., 2023. Neutrophils and emergency granulopoiesis drive immune suppression and an extreme response endotype during sepsis. *Nature Immunology*, 24(5), pp.767-779.

Maqsood, M., Suntharalingham, S., Khan, M., Ortiz-Sandoval, C.G., Feitz, W.J.C., Palaniyar, N., and Licht, C., 2024. Complement-mediated two-step NETosis: Serum-induced complement activation and calcium influx generate NADPH oxidase-dependent NETs in serum-free conditions. *International Journal of Molecular Sciences*, 25(17), p.9625.

Anderson, M.T., Himpsl, S.D., Kingsley, L.G., Smith, S.N., Bachman, M.A., and Mobley, H.L.T., 2024. *Infection characteristics among Serratia marcescens capsule lineages*. bioRxiv: The Preprint Server for Biology. https://doi.org/10.1101/2024.08.23.609398

Moles, L., Gómez, M., Moroder, E., Jiménez, E., Escuder, D., Bustos, G., Melgar, A., Villa, J., Del Campo, R., Chaves, F., and Rodríguez, J.M., 2019. *Serratia marcescens* colonization in preterm neonates during their neonatal intensive care unit stay. *Antimicrobial Resistance and Infection Control*, 8, p.135.

Mughrabi, A., Maamari, J., Philips, T., Alabbasi, A., Brooks, A., Nuriev, R., Zenkin, L., Jaber, B., and Nader, C., 2023. 2787. Carbapenem versus non-carbapenem based therapy for blood stream infection caused by *Serratia marcescens*: A multicenter, retrospective cohort study. *Open Forum Infectious Diseases*, 10(Suppl 2), p.S1232

Nurasyikin, Y., Yasin, N.M., Yousuf, R., Wahab, A.A., and Aziz, S.A., 2022. Comparison of neutrophil respiratory oxidative burst activity between flow cytometry using dihydrorhodamine (DHR) 123 and conventional nitroblue tetrazolium test (NBT). *Bangladesh Journal of Medical Science*, 21(3), pp.626-633.

Nwachukwu, E., Ejike, E.N., Ejike, B.U., Onyeanula, E.O., Chikezie-Abba, R.O., Okorocha, N.A., and Onukaogu, U.E., 2017. Characterization and optimization of lipase production from soil microorganism (*Serratia marcescens*). *International Journal of Current Microbiology and Applied Sciences*, 6(12), pp.1215-1231.

Peignier, A., Kim, J., Lemenze, A., and Parker, D., 2024. Monocyte-regulated interleukin 12 production drives clearance of *Staphylococcus aureus*. *PLOS Pathogens*, 20(10), p.e1012648.

Pinto, A.J., Chouquet, A., Bally, I., Thielens, N.M., Dumestre-Perard, C., Kunert, R., Gaboriaud, C., Ling, W.L.W., and Reiser, J.B., 2024. The Fc Fragment of Soluble IgMs Binds C1q to Activate the Classical Complement Pathway, While Inhibiting Complement-Dependent Cytotoxicity. bioRxiv: the preprint server for biology, 2024.07.10.602503.

Prado, L.C.D.S., Giacchetto Felice, A., Rodrigues, T.C.V., Tiwari, S., Andrade, B.S., Kato, R.B.,… & Soares, S.D.C., 2021. New putative therapeutic targets against Serratia marcescens using reverse vaccinology and subtractive genomics. *Journal of Biomolecular Structure and Dynamics*, 30, pp.1-16.

Priyanka, G., Vivek, H., Rath, R.S., Mohanty, A., Singh, P., and Rukadikar, A., 2023. Interpretation of antimicrobial susceptibility testing using European committee on antimicrobial susceptibility testing (EUCAST) and clinical and laboratory standards institute (CLSI) breakpoints: Analysis of agreement. *Cureus*, 15, p.e36977.

Radeva, S.D., Niyazi, D., Bojkova, M., Savova, D., and Stoeva, T., 2022. Resistance rates to 3rd generation cephalosporins and carbapenems in *Serratia marcescens* isolates obtained from various clinical samples from two Bulgarian hospitals. *Medical Sciences Forum,* 12(1), p.32.

Rognes, I.N., Pischke, S.E., Ottestad, W., Røislien, J., Berg, J.P., Johnson, C., Eken, T., and Mollnes, T.E., 2021. Increased complement activation 3 to 6 h after trauma is a predictor of prolonged mechanical ventilation and multiple organ dysfunction syndrome: A prospective observational study. *Molecular Medicine*, 27(1), p.35.

Sadeq, J.N., and Neamah, A.J., 2024. Comparative phenotypic and genotypic properties of *Serratia marcescens* isolates from clinical cases from human in AL-Diwaniyah Province, Iraq. *South Eastern European Journal of Public Health*, Volume XXV S1 pp.580-592.

Sameer, R.S., and Arun, P., 2023. Prodigiosin: An in-depth exploration of a bioactive compound from *Serratia* sp. *Current Bioactive Compounds,* 19, p.13.

Sharma, M.K., Rizvan, M., Ahmad, N., Jain, P., and Kumar, M., 2022. Treatment of MDR Gram-negative bacteria infections: Ongoing and prospective. *Journal of Pure and Applied Microbiology*, 16(3), pp.1575-1589.

Srinivasan, R., Santhakumari, S., Poonguzhali, P., Geetha, M., Dyavaiah, M., and Xiangmin, L., 2021. Bacterial biofilm inhibition: A focused review on recent therapeutic strategies for combating the biofilm mediated infections. *Frontiers in Microbiology*, 12, p.676458.

Suhad, A.A., Al-Kadmy, M.S.I., Sarah, N.A., and Hamzah, I.H., 2023. The predominance of virulence genes associated with multidrug-resistant *Serratia marcescens* isolated from urinary tract infections. *Reviews and Research in Medical Microbiology*, 35(3), pp.160-166.

Syed, S., Viazmina, L., Mager, R., Meri, S., and Haapasalo, K., 2020. Streptococci and the complement system: Interplay during infection, inflammation and autoimmunity. *FEBS Letters*, 594(16), pp.2570-2585.

Tavares-Carreon, F., De Anda-Mora, K., Rojas-Barrera, I.C., and Andrade, A., 2023. *Serratia marcescens* antibiotic resistance mechanisms of an opportunistic pathogen: A literature review. *PeerJ*, 11, p.e14399.

Tille, P.M., 2022. *Bailey and Scott's Diagnostic Microbiology*. 15th ed. Elsevier, Netherlands, pp.334-339.

Tóth, Á., Makai, A.L., Jánvári, L., Damjanova, I., Gajdács, M., and Urbán, E., 2020. Characterization of a rare bla$_{\text{VIM-4}}$ metallo-β-lactamase-producing *Serratia marcescens* clinical isolate in hungary. *Heliyon*, 6, p.e04231.

Tuttobene, M.R., Arango Gil, B.S., Di Venanzio, G., Mariscotti, J.F., Sieira, R., Feldman, M.F., Ramirez, M.S., and García Véscovi, E., 2024. Unraveling the role of UilS, a urea-induced acyl-homoserine lactonase that enhances *Serratia marcescens* fitness, interbacterial competition, and urinary tract infection. *mBio*, 15, p.e0250524.

Tzoumas, N., Hallam, D., Harris, C.L., Lako, M., Kavanagh, D., and Steel, D.H.W., 2021. Revisiting the role of factor H in age-related macular degeneration: Insights from complement-mediated renal disease and rare genetic variants. *Survey of Ophthalmology*, 66(2), pp.378-401.

Ullrich, K.A., Schulze, L.L., Paap, E.M., Müller, T.M., Neurath, M.F., and Zundler, S., 2020. Immunology of IL-12: An update on functional activities and implications for disease. *EXCLI Journal*, 19, pp.1563-1589.

Vale de Macedo, G.H.R., Costa, G.D.E., Oliveira, E.R., Damasceno, G.V., Mendonça, J.S.P., Silva, L.D.S., Chagas, V.L., Bazán, J.M.N., Aliança, A.S.D.S., Miranda, R.D.C.M.D., Zagmignan, A., Monteiro, A.D.S., and Nascimento da Silva, L.C., 2021. Interplay between ESKAPE pathogens and immunity in skin infections: An overview of the major determinants of virulence and antibiotic resistance. *Pathogens*, 10(2), p.148.

Wang, H., and Liu, M., 2021. Complement C4, infections, and autoimmune diseases. *Frontiers in Immunology*, 12, p.694928.

Weber, D.J., Rutala, W.A., Anderson, D.J., and Sickbert-Bennett, E.E., 2023. Biofilms on medical instruments and surfaces: Do they interfere with instrument reprocessing and surface disinfection. *American Journal of Infection Control*, 51(11), pp.A114-A119.

Wu, X., Wu, D., Cui, G., Lee, K.H., Yang, T., Zhang, Z., Liu, Q., Zhang, J., Chua, E.G., and Chen, Z., 2024. Association between biofilm formation and structure and antibiotic resistance in *H. pylori*. *Infection and Drug Resistance*, 17, pp.2501-2512.

Xu, Q., Zheng, B., Li, K., Shen, P., and Xiao, Y., 2024. A preliminary exploration on the mechanism of the carbapenem-resistance transformation of *Serratia marcescens in vivo*. *BMC Genomics*, 25(1), p.2.

Zivkovic Zaric, R., Zaric, M., Sekulic, M., Zornic, N., Nesic, J., Rosic, V., Vulovic, T., Spasic, M., Vuleta, M., Jovanovic, J., Jovanovic, D., Jakovljevic, S., and Canovic, P., 2023. Antimicrobial treatment of *Serratia marcescens* invasive infections: Systematic review. *Antibiotics* (*Basel)*, 12(2), p.367.

Gene Polymorphism of Antigen B Subunit 2 and Pathogenesis of Cystic Echinococcosis in Murine Model

Hadi M. Alsakee[1†], Hussein M. Abdulla[2] and Reshna K. Albarzanji[3]

[1]Department of Medical Microbiology, International University of Erbil,
Erbil, Kurdistan Region - F.R. Iraq

[2]Department of Medical Laboratory, Erbil Technical Medical Institute,
Erbil Polytechnic University,
Erbil, Kurdistan Region - F.R. Iraq

[3]Department of Microbiology and Physiology, College of Medicine, Hawler Medical University,
Erbil, Kurdistan Region – F.R. Iraq

***Abstract*—A complex genetic diversity among the causative agent, *Echinococcus granulosus*, is documented. Antigen B (AgB) is a major antigenic fraction of hydatid fluid and hydatid cyst tissues. This study aims to investigate the role of antigen B subunit 2 (*AgB2*) gene polymorphism in the pathogenesis of cystic echinococcosis (CE) in murine model. Ovine liver hydatid cysts are obtained from Erbil Slaughterhouse. Protoscoleces from each isolate are separated into two batches. First preserved at −20°C for molecular analysis whereas the second is used for experimental infection in mice. Parasite DNA was extracted, and *AgB2* genome was amplified and sequenced. The sequencing profile of six of the isolates (1, 2, 3, 5, 8, and 11) revealed a 100% analogy with *AgB2* gene of *E. granulosus* genotype G2. Minor sequence polymorphisms, 1.67%, are observed in one of the isolates, whereas remarkable DNA sequence polymorphisms are noticed in three of the isolates. The polymerase chain reaction (PCR) products sequencing profiles revealed 100% polymorphisms in four of the isolates in comparison with the source gene (AY569356.1), instead, those isolates reveal various degrees of analogy, 80.33%, 80.87–89.05%, and 89.36% to G1, G3, and G6, respectively. Polymorphic sequencing profile of the PCR-amplified product (250 bp) of *E. granulosus* clone EgB2G2v13 *AgB2* gene (Accession no.: AY569356.1) has no significant impact on the pathogenicity of the CE in murine model. To upgrade the diagnostic sensitivity rates of the immunological techniques, a mixture of native hydatid antigens containing AgB is recommended to be used in the ser-diagnosis of this infection.**

***Index Terms*—Antigen B subunit 2, cystic echinococcosis, *Echinococcus granulosus*, genotype G1, genotype G2, Tasmanian sheep strain.**

ARO-The Scientific Journal of Koya University
Vol. XIII, No. 1 (2025), Article ID: ARO.11837. 7 pages
DOI: 10.14500/aro.11837
Received: 28 September 2024; Accepted: 24 January 2025
Regular research paper; Published: 04 February 2025
†Corresponding author’s e-mail: hadi.alsakee@ue.edu.krd

I. INTRODUCTION

Cystic echinococcosis (CE) is a public health challenge caused by the larval stage of *Echinococcus granulosus* (Elmajdoub and Rahman, 2015) (Shirazi, et al., 2016) (Alsakee, 2023). Annual incidence is estimated to be approximately 188,000 new cases worldwide and contributes to 1,097,000 disability-adjusted life years (Shao, et al., 2023). The disease is cycled among carnivorous animals such as dogs, coyotes, and jackals, acting as definitive hosts, and herbivorous animals such as sheep, goats, cattle, camels, and deer, serving as intermediate hosts and harboring a cyst-forming stage, hydatid cyst. Man is accidentally infected following ingestion of *E. granulosus* eggs that shed with the infected dog’s excretions, and this later host is considered a dead end for the parasite (Patra, et al., 2021) (Hogea, et al., 2024).

Many intraspecific variations or strains within *E. granulosus* sensu lato have been recognized (Pal and BDutta, 2013) (Abbas, Al-Kappany and Al-Araby, 2016) (Babaei, et al., 2021). Those strain variations have been critically impacted upon the epidemiology of the disease, parasite transmission dynamics, life cycle pattern, host specificity, hydatid cyst growth rate within the intermediate hosts, pathogenicity, immunogenicity, and responsiveness to anthelmintics treatment, and even upon the diagnostic efficiency of the routinely used serological tests (Siyadatpanah, et al., 2019) (Macin, et al., 2021). So far, and based on the mitochondrial DNA, 10 strains (genotypes), namely G1-G10 and line strain of *E. granulosus* sensu lato, have been recognized. G1 is the common sheep strain, which is responsible for the majority of human cases worldwide; G2 (Tasmanian sheep strain), G3 (buffalo strain), G4 (horse strain), G5 (cattle strain), G6 (African camel strain), G7 (swine strain), G8 (cervid strain), G9 (Poland swine/human strain), and G10 (Eurasian reindeer strain), and recently another novel species, *E. felidis* isolated from lions, have also been added to those strains (Alvarez Rojas, Romig and Lightowlers, 2014) (Shariatzadeh, et al.,

2015) (Shahbazi, et al., 2020) (Mahdi, Al-Hamairy and Al-Rubaiey, 2020). Of those well-recognized strains of *E. granulosus*, G1, G2, G3, G5, G6, G7, G8, G9, and G10 are known to be infective to human beings. However, human susceptibility to the genotypes, G4, and lion strain has not been proven yet (Shahbazi, et al., 2020) (Utuk and Simsek, 2012). The predominant genotypes causing the bulk of the global burden of human infestation are *E. granulosus* s. (G1-G3) (Macin, et al., 2021) (Casulli, et al., 2022).

Humans get infected through ingestion of the parasite eggs either through direct contact with dogs and dog feces or consumption of vegetables or food and water contaminated with infected dog feces. Once ingested, the released oncospheres that emerge from the eggs will penetrate the small intestinal mucosa mechanically and by lytic action, getting access to the portal venous circulation, which provides access to the liver, lungs, and various other organs (Ün, Yaman and Erbaş, 2020).

Antigen B (AgB) is a major *E. granulosus* native antigenic fraction of hydatid fluid and hydatid cyst tissues. It is a substance of lipoprotein nature with a molecular weight of 60–120 kDa and resists temperatures of 100°C for 15 min without great alteration of its antigenicity. Genotype-specific AgB is likely to develop different immune responses in the host (da Silva, et al., 2018). Furthermore, (Lorenzo, et al., 2005) demonstrated that antigen B is a thermostable heteropolymorphic protein composed of several distinct but related 8 kDa subunits, encoded by a multigenic family, and it binds strongly to lipids and other hydrophobic compounds, suggesting its possible involvement in the process of lipid uptake or detoxification. (Sadjjadi, et al., 2022) revealed that the application of AgB extracted from only one genotype is not adequate to be used in the serodiagnosis of human CE. The cytokine expression in a host is significantly varied and could lead to both protective and/or immunopathological reactions. As revealed previously, at the time of cyst development, TH1 response, which is associated with increased levels of interferon-gamma (IFN-γ), could be detected, but if TH1 responses begin to damage the parasite, then the parasite starts to dominate TH2 response through the release of antigens that induce TH2-promoting cytokines such as interleukin (IL)-4 and IL-13 (Beyhan, Albayrak and Guven, 2022). TH1 is associated with protective immunity and produces IL-2, IL-12, tumor necrosis factor, and IFN-γ, whereas TH2 is associated with susceptibility to infection and pathogenicity and ensures the survival of the parasite within host tissues through the expression of the cytokines IL-4, IL-5, IL-6, IL-9, IL-10, and IL-13 (Zhang, et al., 2012) (Li, et al., 2019). Antigen B is thought to contribute to the switching of the immune response toward non-protective mechanisms as a part of the survival strategies of the parasite (Riganò, et al., 2001) (Riganò, et al., 2007). The application of antigen B, which originated from different strains of *E. granulosus* sensu stricto, individually or in combination, revealed various responses in the serodiagnosis of human CE that could be questionable for the presence of polymorphic genes that encode for the AgB fraction (Sarkari Shahriari, et al., 2013).

To the best of our knowledge so far, no studies concerning the role of antigen B subunit 2 (*AgB2*) gene polymorphisms in the pathogenesis of CE have been conducted. The current study aimed to investigate the association of *AgB2* gene polymorphisms from different isolates of *E. granulosus* metacestode and the pathogenesis of the infection in a murine model.

II. Materials and Methods

A. Source of Protoscoleces

Ovine liver hydatid cysts were collected from Erbil Governmental Slaughterhouse over a period from January 2024 to April 2024. The cysts were immediately delivered to the microbiology laboratory at the International University of Erbil for processing and separation of the protoscoleces in accordance with (Hassan, AL-Hadithi and Al-Sakee, 2016). Briefly, under aseptic conditions, the cysts were dissected, and the contents (hydatid fluid and hydatid sand) were aspirated and dispensed in a clean, sterile screw-capped test tube. Hydatid sand was allowed to stand for 20 min at room temperature, and the fluid was carefully removed. The precipitated protoscoleces were washed thrice with 0.15 M phosphate-buffered saline (pH 7.2) and assessed for viability by motility of flame cells and eosin (0.1%) exclusion test as described by Khoshnaw and Al-Sakee (Khoshnaw and Al-Sakee, 2022). For each isolate, two batches of protoscoleces were collected. First preserved in an equal volume of ethanol (70%) at −20°C for molecular analysis, whereas the second batch was used immediately in the *in vivo* study.

B. Molecular Analysis

Genomic DNA extraction

A commercially available kit from GeneAll® Exgene™ (South Korea) was used for the extraction of genomic DNA as recommended by the leaflet that was provided with the kit. Frozen, ethanol-fixed hydatid cyst tissue samples were allowed to thaw at room temperature (25°C–27°C) for 30 min before processing. Ethanol was removed by rinsing the hydatid tissue samples thrice with an equal volume of sterile distilled water in a 10 mL capacity sterile screw-capped centrifuge test tube. The concentration and purity of extracted genomic DNA were assessed by a Nano-Drop spectrophotometer. The samples that yield a purity of 1.8–2.0 were considered for amplification.

Polymerase chain reaction (PCR) and sequence analysis

A region of 250 bp of the *E. granulosus* clone EgB2G2v13 *AgB2* gene (Accession no.: AY569356.1), that was characterized previously by (Kamenetzky, et al., 2005) in a human hydatid cyst sample of G2 strain, was amplified using the following primers: F-5’ TCTCTCTTGCTCTCGTGGCT and R-5’ TTGCAGCTTCTGGCAAATGG 3’. The amplification protocol was carried out in accordance with (Sarkari Shahriari, et al., 2013). Briefly, the reaction was performed using mixtures of 0.3 μL of Taq polymerase (Ampliqon, Denmark) with 2.5 μL of 10X PCR buffer, 17.5 μL of deionized distilled water, 0.6 μL of $MgCl_2$, 0.7 μL (10 mM) of dNTP, 25 pmol of each primer, and 2 μL of DNA template, in a total volume of 25 μL. The PCR reactions involved an initial 3 min at 95°C denaturation step, followed by 35 cycles of 60 s at 95°C, 60 s at 56°C, and 90 s at 72°C, with a final incubation at 72°C for 3 min in a PCR ALPHA MAX Thermal Cycler (Alpha, United Kingdom). The PCR yields were subjected to agarose gel electrophoresis and ethidium bromide (BioBasic Canada INC, Canada) staining. The results were visualized by ultraviolet (UV) illumination at (240–366 nm) wavelength on a UV transilluminator, and the gel was documented with a Polaroid photo documentation camera. Amplified DNA bands were purified from the gel using the QIAquick Gel Extraction Kit (Qiagen, Germany), following the manufacturer's instructions. The purified amplicons were sequenced in both directions using forward and reverse primers by the ABI Prism Terminator Sequencing Kit (Applied Biosystem) at Humanizing Genomics Macrogen Inc., Seoul, South Korea. Sequence data were obtained from the National Center for Biotechnology Information (NCBI) database to characterize the parasite isolates AgB2. The AgB2 sequencing results were analyzed and compared with the relevant gene sequences deposited in GenBank using the basic local alignment search tool (BLAST). Chromatograms of the amplified region of *E. granulosus* clone EgB2G2v13 *AgB2* gene (Accession no.: AY569356.1) were interpreted using Finch TV software, while MEGA X software was used to edit the PCR product sequences.

C. In vivo Experiments

Experimental infection in murine model

Fourteen groups of Albino (BALB)/c mice (male and female) weighing 22–25 g were used in the *in vivo* experiments. Each group included six animals and was infected experimentally with the protoscoleces obtained from 14 isolated sheep liver hydatid cysts. Each mouse was injected with 2000 protoscoleces (viability >90%) in 200 μL of Phosphate-buffered saline pH 7.2. Ninety days later, all mice were anesthetized with 12.5 mg/kg xylazine (Interchemie, Netherlands) and 87.5 mg/kg ketamine (Cluj-Napoca, Romania) and dissected. Internal organs were inspected for developed hydatid cysts (Ma, et al., 2007) (Hassan, AL-Hadithi and Al-Sakee, 2016).

D. Ethical Consecrations

The study protocols were approved by the Research Ethics Committee in the College of Science, International University of Erbil (meeting code: 1, paper code: 1 on September 2nd, 2024), and the statement of the World Medical Association for animal use in biomedical research (https://www.wma.net/policies-post/wma-statement-on-animal-use-in-biomedical-research/) was followed for mice handling and management.

E. Statistical Analysis

The obtained data were interpreted by Statistical Package for the Social Sciences (version 25.0). The correlation coefficient (r) as well as analysis of the variance of two factors without replication was calculated between the size and number of the developed secondary hydatid cysts and *E. granulosus AgB2* gene. p ≤ 0.05 was considered statistically significant.

III. Results

Sixteen isolates of hydatid cysts (containing protoscoleces with viability >90%) that were obtained from infected sheep livers were subjected to genomic DNA extraction and PCR, targeting a region of 250 bp of the *E. granulosus* clone EgB2G2v13 *AgB2* gene, and sequenced (Fig. 1). The sequencing profile of the isolates revealed no polymorphisms (100% analogy) in the isolates 1, 2, 3, 5, 8, and 11, in comparison with the source gene (Genotype G2, AgB2 [Accession no.: AY569356.1]). To the best of our knowledge, this is considered the first record instance of *E. granulosus* genotype G2 in Erbil province. Minor sequence polymorphisms, 1.67%, were observed in isolate 9, whereas remarkable DNA sequence polymorphisms, 4.49%, 4.76%, and 6.41%, in isolates 7, 10, and 14, respectively, were observed. Furthermore, the PCR products sequencing profiles revealed 100% polymorphisms in four of the isolates (4, 6, 12, and 13) in comparison with the amplified region of the source (Accession no.: AY569356.1) (Table I); instead, those isolates revealed various degrees of identity to the previously published *E. granulosus* AgB genes on NCBI (Table II). Two of the 16 isolates revealed sequence profiles that did not match any previously published genes on the *NCBI* gene bank; therefore, those two isolates were excluded from the *in vivo* experiments.The results of the *in vivo* experiments revealed that the fourteen isolates that were used in the experimental infection of the mice exhibited various degrees of pathogenesis as reflected by the number and size of the developed hydatid cysts (Table I). The number of the developed hydatid cysts ranged from 12 ± 7.54 to 59.5 ± 67.71, with cyst size ranging from 18.67 ± 5.61 mm to 68 ± 23.27 mm. The highest number and largest size of cysts were detected in the mice group that was infected with isolate 10, in turn, exhibited 95.24% identity to the studied source (AY569356.1) (Table I). However, there was no significant (p = 0.6073, p = 0.7122) association between *E. granulosus* clone EgB2G2v13 *AgB2* gene polymorphisms and the number and size of the developed hydatid cysts.

Four of the studied isolates (4, 6, 12, and 13) revealed 100% sequence polymorphisms compared with the source

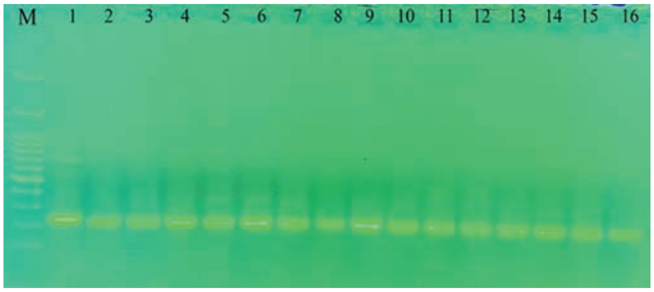

Fig. 1. Polymerase chain reaction-amplified *E. granulosus* antigen B subunit 2 gene fragments (250 bp) from 16 isolates (lanes 1–16). M: 100 bp DNA molecular weight ladder.

TABLE I
Correlation of Parasite Isolate Pathogenesis and Antigen B Subunit 2 (AgB2) Gene Polymorphism in Experimentally Infected Murine Model

Mice Group	Parasite Isolate	No. of Secondary Hydatid Cysts Mean±SD$^{\#}$	Size of Secondary Hydatid Cysts (mm) Mean±SD*	Identity to the Source (AY569356.1) (%)	Polymorphism (%)$^{*\#}$
1	1	12±7.54	19.2±9.73	100	0
2	2	20±12.84	21.33±13.89	100	0
3	3	25.75±8.95	29±8.9	100	0
4	4	15.5±10.55	18.67±5.61	0	100
5	5	25.5±10.55	34±8.58	100	0
6	6	28.75±12.36	35±6.22	0	100
7	7	25.6±15.58	36±5.83	95.51	4.49
8	8	28.75±14.0	43±11.01	100	0
9	9	33.5±30.59	47±7.02	98.33	1.67
10	10	59.5±67.71	68±23.27	95.24	4.76
11	11	27.83±14.0	35.67±28.93	100	0
12	12	25.6±8.08	25.33±13.31	0	100
13	13	26.5±9.32	32±13.57	0	100
14	14	31±18.57	35.33±14.79	93.59	6.41
		p=0.6073	p=0.7122		
		F=0.8571	F=0.7281		
		F crit=2.576	F crit=2.576		

*Correlation coefficient = −0.1155774 (association of the number of developed hydatid cyst and *AgB2*) gene polymorphism. #Correlation coefficient = −0.2962189 (association of size of developed hydatid cyst and *AgB2*) gene polymorphism

TABLE II
Basic Local Alignment Search Tool of the Isolates That Revealed 100% Polymorphisms Comparing With the Studied Source (AY569356.1)

Isolate	Polymorphisms (%)	Identity to genes other than the source on NCBI			Isolate country	Isolate strain	Host
		%	Accession no. (NCBI)	Gene			
4	100	89.36	MH243705.1	*E. canadensis* voucher C5B2 antigen B subunit 4 (*AgB/4*) gene	Iran	G6	Camel
		89.05	AY357112.1	*E. granulosus* clone EgB4.3 antigen B subunit 4 gene, exons I and II, and partial cds	Brazil	G3	Cow
		88.73	AY357111.1	*E. granulosus* clone *EgB4.2* antigen B subunit 4 gene, exons I and II, and partial cds	Brazil	G3	Cow
		88.69	LC781357.1	*E. granulosus* B4H2 EgAgB4 gene for antigen B subunit 4, partial cds	Turkey	?	Human
6	100	85.07	AY357111.1	*E. granulosus* clone *EgB4.2* antigen B subunit 4 gene, exons I and II, and partial cds	Brazil	G3	Cow
12	100	77.4	LC781357.1	*E. granulosus* B4H2 *EgAgB4* gene for antigen B subunit 4, partial cds	Turkey	?	Human
		77.05	LC781358.1	*E. granulosus* B4H3 EgAgB4 gene for antigen B subunit 4, partial cds	Turkey	?	Human
13	100	80.87	AY871034.1	*Echinococcus granulosus* antigen B2 (*AgB*) gene, AgB-K4 allele, and partial cds	Brazil	G3	Cow
		80.65	GU166201.1	*Echinococcus granulosus* isolate ZGA2-4 antigen B 2/1 (*AgB2/1*) gene, partial cds	Australia	?	Dog
		80.33	AY569344.1	*Echinococcus granulosus* clone EgB2G1v4 isolation-source cyst 2 antigen B subunit 2 (*AgB2*) gene, complete cds	Argentina	G1	Human
		79.76	LC780495.1	*Echinococcus granulosus B2H5* gene for antigen B, partial cds	Turkey	?	Human

NCBI: National Center for Biotechnology Information

gene; however, they revealed potential pathogenicity in the experimentally infected murine model at the same degree as the isolates (1, 2, 3, 5, 7, 8, 9, 10, 11, and 14) with highly identical gene sequences did. BLAST revealed that those aberrant isolates have various degrees of analogy with different clones of *AgB* genes that were isolated from different hosts in different countries (Table II).

IV. Discussion

Recent studies have demonstrated the rising rate of human CE worldwide (Yan, et al., 2018). In 2013, the World Health Assembly classified this zoonotic infection as one of the eight neglected zoonotic diseases (Nusrath, et al., 2013). The results revealed that the sequencing profile of the PCR-amplified product (250 bp) of the *E. granulosus* clone EgB2G2v13 *AgB2* gene (Accession no.: AY569356.1), that was previously characterized as *E. granulosus* genotype G2 (Accession number, AY569356.1) (Kamenetzky, et al., 2005), has shown extreme polymorphic sequence profiles. PCR product sequences of five (1, 2, 3, 5, 11) of the studied isolates revealed 100% mimicry with the selected source of the *E. granulosus AgB2* gene. This finding indicates the possible occurrence of the *E. granulosus* G2 strain in the Erbil province. Previous records in this regard revealed similar figures while using other genes of *E. granulosus*, such as NAD1, NAD2, and COX1, in hydatid cyst samples extracted from humans and sheep in Baghdad, Iraq, and in Riyadh, Saudi Arabia (Khalf, et al., 2014) (Metwally, et al., 2018). However, common sheep strain G1 is the predominated genotype of *E. granulosus* in almost all countries with endemicity of this zoonotic parasite (Ergin, Saribas and Yuksel, 2010) (Khalf, et al., 2014) (Spotin, et al., 2015) (Hamoo, Mustafa and Abdulraheem, 2019). In the present study, four of the studied isolates (4, 6, 12, and 13) revealed 100% variability in comparison with the studied source gene (Accession no.: AY569356.1). However, those isolates revealed polymorphic sequence profiles that matched with the parasite strains other than G2, including G1, G3, and G6, with analogy rates ranging between 80.33% and 89.36%. Similarly, high genetic diversity was reported worldwide (Khalf, et al., 2014) (Spotin, et al., 2015) (Kinkar, et al., 2017). Furthermore, various diagnostic sensitivity rates of immunological techniques using native hydatid antigens in the serodiagnosis of human CE have been reported by previously published data (Al-sakee, 2011) (Al-Olayan and Helmy, 2012) (Sadjjadi, et al., 2022) (Alsakee, 2023) could support the genetic diversity of the *E. granulosus* AgB that has been noticed in the present study.

A study carried out in Iran suggested that *E. granulosus* genotype G1 (the common sheep strain) is the most prevalent genotype in livestock and that genotype G2 (the Tasmanian sheep strain) is the second most common genotype in both cattle and sheep (Rostami Nejad, et al., 2012). The third most common genotype of *E. granulosus* is G3 (buffalo strain). This latter genotype of *E. granulosus* was mainly isolated from cattle, buffalo, and sheep, as well as from human cases with liver and lung involvement (Piccoli, et al., 2013) (Metwally, et al., 2018). In the present study, one of the isolates revealed 89.36% sequence analogy to *E. granulosus* genotype G6 (camel strain). Previous studies carried out in Iraq and Iran have demonstrated that G6, with proven infectivity to human beings, is predominant in those countries (Khalf, et al., 2014) (Ebrahimipour, et al., 2017).

The complex intraspecific genetic diversity within the cestode, *E. granulosus*, has obviously impacted the various characteristics of the parasite and parasite-host relationship, including parasite life cycle, host specificity, pathogenicity, host defense mechanisms, the disease process and prognosis, definitive diagnosis, and susceptibility to antihelminth drugs (Maglioco, et al., 2019) (Li, et al., 2019) (Babaei, et al., 2021) (Mardani, et al., 2021).

AgB, with significant immunological properties, constitutes approximately 10% of hydatid fluid (Siracusano, et al., 2008) and is synthesized and released by the hydatid cyst's germinal layer as well as by the germinated protoscoleces (Shirazi, et al., 2016). This hydatid antigenic fraction encoded by a gene family involves 10 unique genes of five subfamilies (EgAgB1-EgAgB5) expressed in different stages of the parasite (Sarkari Shahriari, et al., 2013). At present, similarly, a high level of AgB8 subunits 1 and 3 was observed in hydatid cyst samples isolated from humans and cattle (Esfedan, Sarkari, and Mikaeili, 2018). AgB is thought to be involved in crucial roles in the host-parasite relationship through disturbing both innate and adaptive immune responses, including disturbance of polymorphonuclear leukocyte chemotaxis and shifting the immune response toward a non-protective Th2 response that initiates a long-term chronic infection (Shirazi, et al., 2016).

In the present study, despite the studied isolates revealing various complexed polymorphic profiles in the amplified products of the *E. granulosus AgB2* gene (Accession no.: AY569356.1), the pathogenicity of the parasite did not significantly alter, and those findings might be explained by the significant levels of AgB that are expressed in all stages of *E. granulosus* throughout its life cycle, regardless of the parasite strain (Esfedan, Sarkari and Mikaeili, 2018) (Sadjjadi, et al., 2022). Furthermore, no significant alteration in the pathogenesis of the studied isolates might be attributed to both immunomodulation and lipid transport, contributing to the AgB in the host-parasite relationship (da Silva, et al., 2018).

V. Conclusion

The polymorphic sequencing profile of the PCR-amplified product (250 bp) of the *E. granulosus* clone EgB2G2v13 *AgB2* gene (Accession no.: AY569356.1) has no significant impact on the pathogenicity of CE in a murine model. *E. granulosus* genotype G2 is the common cause of CE in Erbil province, northern Iraq. To upgrade the diagnostic sensitivity rates of the immunological techniques, and due to the highly polymorphic genes that encode for AgB2, a mixture of native hydatid antigens containing AgB is recommended to be used in the serodiagnosis procedures for this infection.

References

Abbas, I.E.A., Al-Kappany, Y.M., and Al-Araby, M.A., 2016. Prevalence and molecular characterization of hydatid cyst isolates from cattle in Egypt. *Asian Journal of Animal and Veterinary Advances*, 11(12), pp.794-804.

Al-Olayan, E.M., and Helmy, H., 2012. Diagnostic value of different antigenic fractions of hydatid cyst fluid from camel and sheep in Kingdom of Saudi Arabia. *Journal of Saudi Chemical Society*, 16(2), pp.203-207.

Al-sakee, H.M.A., 2011. Immunological aspects of cystic echinococcosis in Erbil. *Zanco Journal of Medical Sciences*, 15(2), pp.1-9.

Alsakee, H.M.A., 2023. Diagnostic efficiency of heat shocked protoscoleces extract antigens for human cystic echinococcosis by ELISA. *Iraqi Journal of Science*, 64(1), pp.65-74.

Alvarez Rojas, C.A., Romig, T., and Lightowlers, M.W., 2014. *Echinococcus granulosus* sensu lato genotypes infecting humans--review of current knowledge. *International Journal for Parasitology*, 44, pp.9-18.

Babaei, Z., Taherkhani, R., Barazesh, A., Taherzadeh, M., Khorami, S., and Fouladvand, M., 2021. Genotyping and phylogenetic analysis of hydatid cysts isolated from livestock in Bushehr province, Iran. *Journal of Parasitic Diseases*, 45(1), pp.197-203.

Beyhan, Y.E., Albayrak, C., and Guven, I., 2022. IL-4, IL-10, TNF-α and IFN-γ cytokine levels in patients with cystic echinococcosis and fascioliasis. *Iranian Journal of Public Health*, 51(6), pp.1339-1347.

Casulli, A., Massolo, A., Saarma, U., Umhang, G., Santolamazza, F., and Santoro, A., 2022. Species and genotypes belonging to *Echinococcus granulosus* sensu lato complex causing human cystic echinococcosis in Europe (2000-2021): A systematic review. *Parasites and Vectors*, 15(1), p.109.

Da Silva, E.D., Cancela, M., Monteiro, K.M., Ferreira, H.B., and Zaha, A., 2018. Antigen B from *Echinococcus granulosus* enters mammalian cells by endocytic pathways. *PLoS Neglected Tropical Diseases*, 12(5), p.e0006473.

Ebrahimipour, M., Sadjjadi, S.M., Yousofi Darani, H., and Najjari, M., 2017. Molecular studies on cystic echinococcosis of camel (*Camelus dromedarius*) and report of *Echinococcus ortleppi* in Iran. *Iranian Journal of Parasitology*, 12(3), pp.323-331.

Elmajdoub, L.O., and Rahman, W.A., 2015. Prevalence of hydatid cysts in slaughtered animals from different areas of Libya. *Open Journal of Veterinary Medicine*, 5, p.1-10.

Ergin, S., Saribas, S., and Yuksel, P., 2010. Genotypic characterisation of *Echinococcus granulosus* isolated from human in Turkey. *African Journal of Microbiology Research*, 4(7), pp.551-555.

Esfedan, A.F., Sarkari, B., and Mikaeili, F., 2018. Genetic variability of antigen B8/1 among *Echinococcus granulosus* isolates from human, cattle, and sheep in Fars Province, Southern Iran. *Reports of Biochemistry and Molecular Biology*, 6(2), pp.164-169.

Hamoo, R.N., Mustafa, N.G., and Abdulraheem, S.A., 2019. Nad1 gene analysis of *Echinococcus granulosus* from sheep in Aqrah city, Iraq. *Iraqi Journal of Veterinary Sciences*, 33(2), pp.341-345.

Hassan, H., AL-Hadithi, T.S., and Al-Sakee, H.M., 2016. Experimental trial with a heat-shocked protoscolex extract as a vaccine candidate for protection against hydatid disease. *Turkish Journal of Parasitology*, 40(1), pp.1-8.

Hogea, M.O., Ciomaga, B.F., Muntean, M.M., Muntean, A.A., Popa, M.I., and Popa, G.L., 2024. Cystic echinococcosis in the early 2020s: A review. *Tropical Medicine and Infectious Disease*, 9(2), p.36.

Kamenetzky, L., Muzulin, P.M., Gutierrez, A.M., Angel, S.O., Zaha, A., Guarnera, E.A., and Rosenzvit, M.C., 2005. High polymorphism in genes encoding antigen B from human infecting strains of *Echinococcus granulosus*. *Parasitology*, 131(Pt 6), pp.805-815.

Khalf, M.S., Al-Faham, M.A., Al-Taie, L.H., and Alhussian, H.A., 2014. Genotyping of *Echinococcus granulose* in Samples of Iraqi Patients. *IOSR Journal of Pharmacy and Biological Sciences*, 9(3), pp.6-10.

Khoshnaw, K.J.S., and Al-Sakee, H.M.A., 2022. Cystic echinococcosis and host interleukin-2, interleukin-9 and interleukin-10 as biomarkers for evaluation of albendazole and praziquantel treatment in experimentally infected mice. *Indian Journal of Pharmaceutical Sciences*, 84, pp.246-254.

Kinkar, L., Laurimäe, T., Sharbatkhori, M., Mirhendi, H., Kia, E.B., Ponce-Gordo, F., Andresiuk, V., Simsek, S., Lavikainen, A., Irshadullah, M., Umhang, G., Oudni-M'rad, M., Acosta-Jamett, G., Rehbein, S., and Saarma, U., 2017. New mitogenome and nuclear evidence on the phylogeny and taxonomy of the highly zoonotic tapeworm *Echinococcus granulosus* sensu stricto. *Infection, Genetics and Evolution*, 52, pp.52-58.

Li, Z., Zhang, C., Li, L., Bi, X., Li, L., Yang, S., Zhang, N., Wang, H., Yang, N., Abulizi, A., Aini, A., Lin, R., Vuitton, D.A., and Wen, H., 2019. The local immune response during *Echinococcus granulosus* growth in a quantitative hepatic experimental model. *Scientific Reports*, 9(1), p.19612.

Lorenzo, C., Ferreira, H.B., Monteiro, K.M., Rosenzvit, M., Kamenetzky, L., García, H.H., Vasquez, Y., Naquira, C., Sánchez, E., Lorca, M., Contreras, M., Last, J.A., and González-Sapienza, G.G., 2005. Comparative analysis of the diagnostic performance of six major *Echinococcus granulosus* antigens assessed in a double-blind, randomized multicenter study. *Journal of Clinical Microbiology*, 43, pp.2764-2770.

Ma, X.M., Bao, G.S.H., Wan, J.M., Liao, D.J., Yin, S.H.F., Meng, X.Q., Zhou, G.K., Lu, X.M., and Li, H.Y., 2007. Therapeutic effects of *Sophora moorcroftiana* alkaloids in combination with albendazole in mice experimentally infected with protoscolices of *Echinococcus granulosus*. *Brazilian Journal of Medical and Biological Research*, 40(10), pp.1403-1408.

Macin, S., Orsten, S., Samadzade, R., Colak, B., Cebeci, H., and Fındık, D., 2021. Human and animal cystic echinococcosis in Konya, Turkey: Molecular identification and the first report of *E. equinus* from human host in Turkey. *Parasitology Research*, 120(2), pp.563-568.

Maglioco, A., Gentile, J., Barbery Venturi, M.S., Jensen, O., Hernández, C., Gertiser, M.L., Poggio, V., Canziani, G., and Fuchs, A.G., 2019. Detection of *Echinococcus granulosus* sensu lato infection by using extracts derived from a protoscoleces G1 cell line. *Parasite Immunology*, 41(12), p.e12674.

Mahdi, Z.M.S., Al-Hamairy, A.K., and Al-Rubaiey, H.M., 2020. Genotyping of *Echinococcus granulosus* isolates from human, sheep and cattles hydatid cysts in some central euphrates provinces, Iraq. *Medico-Legal Update*, 20(2), pp.570-575.

Mardani, P., Ezabadi, A.T., Sedaghat, B., and Sadjjadi, S.M., 2021. Pulmonary hydatidosis genotypes isolates from human clinical surgery based on sequencing of mitochondrial genes in Fars, Iran. *Journal of Cardiothoracic Surgery*, 16(1), p.167.

Metwally, D.M., Qassim, L.E., Al-Turaiki, I.M., Almeer, R.S., and El-Khadragy, M.F., 2018. Gene-based molecular analysis of COX1 in *Echinococcus granulosus* cysts isolated from naturally infected livestock in Riyadh, Saudi Arabia. *PLoS One*, 13(4), p.e0195016.

Nusrath, N.K., Khader Faheem, N., Syama Sundara Rao, B., and Raja Ram, G., 2013. The scenario of Hydatid cyst disease in epidemic areas of Andhra Pradesh-evaluation and analysis. *International Journal of Research and Development of Health*, 1, pp.120-128.

Pal, M., and Dutta, J.B., 2013. Echinococcosis -an emerging and re-emerging cyclozoonosis of global importance. *International Journal of Livestock Research*, 3(3), pp.5-12.

Patra, G., Ghosh, S., Behera, B., Bhattacharyay, P., Arya, R.S., Alam, S.S., and Maity, I., 2021. A brief review on Echinococcosis and its perspective in public health point of view. 32(6), pp. 23-45.

Piccoli, L., Bazzocchi, C., Brunetti, E., Mihailescu, P., Bandi, C., Mastalier, B., Cordos, I., Beuran, M., Popa, L.G., Meroni, V., Genco, F., and Cretu, C., 2013. Molecular characterization of *Echinococcus granulosus* in South-Eastern Romania: Evidence of G1-G3 and G6-G10 complexes in humans. *Clinical Microbiology and Infection*, 19(6), pp.578-582.

Riganò, R., Buttari, B., Profumo, E., Ortona, E., Delunardo, F., Margutti, P., Mattei, V., Teggi, A., Sorice, M., and Siracusano, A., 2007. *Echinococcus granulosus* antigen B impairs human dendritic cell differentiation and polarizes immature dendritic cell maturation towards a Th2 cell response. *Infection and Immunity*, 75(4), pp.1667-1678.

Riganò, R., Profumo, E., Bruschi, F., Carulli, G., Azzarà, A., Ioppolo, S., Buttari, B., Ortona, E., Margutti, P., Teggi, A., and Siracusano, A., 2001. Modulation of human immune response by *Echinococcus granulosus* antigen B and its possible role in evading host defenses. *Infection and Immunity*, 69(1), pp.288-296.

Rostami Nejad, M., Taghipour, N., Nochi, Z., Mojarad, E.N., Mohebbi, S.R., Harandi, M.F., and Zali, M.R., 2012. Molecular identification of animal isolates of *Echinococcus granulosus* from Iran using four mitochondrial genes. *Journal of Helminthology*, 86(4), pp.485-492.

Sadjjadi, S.F., Mohammadzadeh, T., Hafezi, F., and Sadjjadi, S.M., 2022. Evaluation of the ability of antigen B originated from *Echinococcus granulosus* sensu stricto and *E. canadensis* for the diagnosis of confirmed human cystic echinococcosis using ELISA. *Iranian Journal of Parasitology*, 17(3), pp.358-365.

Sarkari Shahriari, B., Biranvand, E., Sadjjadi, S.M., and Rahimi, H., 2013. Genetic variability of antigen B2 of human, sheep, goats, camel and cattle isolates of *Echinococcus granulosus* in Iran. *Iranian Journal of Parasitology*, 8(4), pp.545-551.

Shahbazi, A.E., Saidijam, M., Maghsood, A.M., Matini, M., Motavali Haghi, M., and Fallah, M., 2020. Genotyping of fresh and parafinized human hydatid cysts using nad1 and cox1 genes in Hamadan province, West of Iran. *Iranian Journal of Parasitology*, 15(2), pp.259-265.

Shao, G., Hua, R., Song, H., Chen, Y., Zhu, X., Hou, W., Li, S., Yang, A., and Yang, G., 2023. Protective efficacy of six recombinant proteins as vaccine candidates against *Echinococcus granulosus* in dogs. *PLoS Neglected Tropical Diseases*, 17(10), p.e0011709.

Shariatzadeh, S.A., Spotin, A., Gholami, S., Fallah, E., Hazratian, T., Mahami-Oskouei, M., Montazeri, F., Moslemzadeh, H.R., and Shahbazi, A., 2015. The first morphometric and phylogenetic perspective on molecular epidemiology of *Echinococcus granulosus* sensu lato in stray dogs in a hyperendemic Middle East focus, Northwestern Iran. *Parasites and Vectors*, 8(1), p.409.

Shirazi, S., Madani, R., Hoghooghi Rad, N., and Ranjbar Bahadori, S., 2016. Isolation and purification of *Echinococcus granulosus* antigen B from hydatid cyst fluid using three different methods. *Archives of Razi Institute*, 71(2), pp.103-108.

Siracusano, A., Riganò, R., Ortona, E., Profumo, E., Margutti, P., Buttari, B., Delunardo, F., and Teggi, A., 2008. Immunomodulatory mechanisms during *Echinococcus granulosus* infection. *Experimental Parasitology*, 119, pp.483-489.

Siyadatpanah, A., Anvari, D., Emami Zeydi, A., Hosseini, S.A., Daryani, A., Sarvi, S., Budke, C.M., Esmaeelzadeh Dizaji, R., Mohaghegh, M.A., Kohansal, M.H., Dodangeh, S., Saberi, R., and Gholami, S., 2019. A systematic review and meta-analysis of the genetic characterization of human echinococcosis in Iran, an endemic country. *Epidemiology and health*, 41, p.e2019024.

Spotin, A., Mahami-Oskouei, M., Harandi, M.F., Baratchian, M., Bordbar, A., Ahmadpour, E., and Ebrahimi, S., 2015. Genetic variability of *Echinococcus granulosus* complex in various geographical populations of Iran inferred by mitochondrial DNA sequences. *Acta Tropica*, 165, pp.10-16.

Ün, M., Yaman, S.S., and Erbaş, O., 2020. Hydatid cyst and treatment. *Demiroglu Science University Florence Nightingale Transplantation Journal*, 5(1-2), pp.70-78.

Utuk, A.E., and Simsek, S., 2012. Molecular characterization of the horse isolate of *Echinococcus granulosus* in Turkey. *Journal of Helminthology*, 87, pp.305-308.

Yan, B., Liu, X., Wu, J., Zhao, S., Yuan, W., Wang, B., Wureli, H., Tu, C., Chen, C., and Wang, Y., 2018. Genetic diversity of *Echinococcus granulosus* genotype G1 in Xinjiang, Northwest of China. *Korean Journal of Parasitology*, 56(4), pp.391-396.

Zhang, W., Wen, H., Li, J., Lin, R., and McManus, D.P., 2012. Immunology and immunodiagnosis of cystic echinococcosis: An update. *Clinical and Developmental Immunology*, 2012, p.101895.

Computational Study of Some Urolithin Derivatives-based Biomass Corrosion Inhibitors on the Fe (110), Cu(111) and Al(111) Surface

Rebaz A. Omer[†]

Department of Chemistry, Faculty of Science and Health, Koya University,
Koya, Kurdistan Region – F.R. Iraq

***Abstract*—Corrosion poses a significant economic and environmental burden, highlighting the need for sustainable corrosion inhibitors. This study investigates the potential of urolithin derivatives (UroE, UroM5, UroM6, and UroM7) as eco-friendly corrosion inhibitors for Fe(110), Cu(111), and Al(111) surfaces. The research uses density functional theory calculations and Monte Carlo (MC) simulations to compute quantum chemical parameters, Fukui function, and non-covalent interactions. The results show that compounds with strong hydrogen bonding interactions form more robust bonds with the metal surface, potentially leading to enhanced corrosion protection. UroM5 demonstrates superior stability and lower reactivity due to its high band gap energy. MC simulations reveal that the adsorption energies of urolithin derivatives on metal surfaces follow a trend: UroM5 > UroM6 > UroE > UroM7, suggesting a stronger binding affinity for these metals. Thermal characteristics, particularly Gibbs free energy, are also investigated. The results suggest that a temperature increase from 825 to 1000 K may induce a transition from physisorption to chemisorption for all chemicals on the metal surface. These comprehensive analyses provide valuable insights into the mechanism and efficiency of urolithin derivatives as corrosion inhibitors, paving the way for the development of novel and eco-friendly anti-corrosion materials.**

***Index Terms*—Urolithins, Density functional theory, Fukui function, Global reactivity, Monte Carlo simulations. Anti-Corrosion**

I. Introduction

The phenomenon of corrosion, which refers to the degradation of metals caused by their contact to corrosive substances such as acids, presents substantial economic and environmental challenges. The scope of this matter encompasses not just metals, but also non-metallic substances such as plastics, ceramics, concrete, and rubber (Predko, et al., 2021; Kareem, et al., 2024). Corrosion inhibitors may safeguard metals or alloys by altering their quantum chemical characteristics. Some corrosion inhibitors, for example, may adsorb onto the metal's surface and establish a protective barrier, preventing corrosive species from reaching the metal's surface. Researchers may discover new and more effective corrosion protection methods (Özbakır Işın, et al., 2020; İsen, et al., 2023, Koparir, et al., 2023). Historically, corrosion inhibitors have often used organic compounds that include heteroatoms (namely oxygen, nitrogen, phosphorus, and sulfur) and π-bonds. This is attributed to their capacity to create a protective coating on metal surfaces (El Aoufir, et al., 2017). The presence of this layer impedes the movement of oxygen and water, thereby impeding the corrosion mechanism caused by the disparity in potential energies between the metal and its corrosive derivatives. Corrosion inhibitors are sometimes included into paints to enhance their protective properties (Murthy and Vijayaragavan, 2014).

Corrosion inhibition has been extensively studied using both experimental and theoretical approaches. Weight-loss and electrochemical techniques are common experimental methods. Carbon steel, mild steel, copper, zinc, and aluminum are frequently investigated metals (Chen, et al., 2019, Hazani, et al., 2019, Guruprasad, et al., 2020, Tasić, et al., 2019, Uwiringiyimana, Joseph and ADams, 2016).

In recent years, research has focused on exploring "green corrosion inhibitors" as a sustainable alternative to potentially toxic organic substances. This approach leverages the inherent eco-friendliness of certain drugs, which often possess heterocyclic groups that effectively inhibit corrosion (Hameed, Abu-Nawwas and Shehata, 2013; Rani and Basu, 2012). In addition, the widespread availability and affordability of drugs make them attractive candidates for this application. Moreover, studies have shown that the effectiveness of organic corrosion inhibitors increases with higher concentrations (Uwiringiyimana, Joseph and ADams, 2016).

Rani and Basu (2012) attributed the efficacy of organic corrosion inhibitors to their high basicity, electron density, specific chemical structures, and physicochemical properties. To understand how these molecules inhibit corrosion, researchers have developed theoretical models

---

ARO-The Scientific Journal of Koya University
Vol. XIII, No. 1 (2025), Article ID: ARO.11828. 17 pages
DOI: 10.14500/aro.11828
Received: 19 September 2024; Accepted: 12 January 2025
Regular research paper; Published: 06 February 2025

[†]Corresponding author's e-mail: rebaz.anwar@koyauniversity.org

based on quantum mechanics. One such approach, the frontier molecular orbital theory, uses quantum mechanical calculations to investigate the corrosion inhibition potential of various drugs on metal surfaces, such as Fe(110), Cu(111), and Al(111) (Uwiringiyimana, Joseph and ADams, 2016; Rasul, et al., 2023).

Urolithins are bioactive phenolic compounds that originate as microbial metabolites from the consumption of pomegranate and certain berries. They belong to the 6H-dibenzo[b,d]pyran-6-one family and have gained significant scientific interest due to their diverse biological properties and potential health benefits. Among the natural urolithins identified, structural modifications primarily involve the hydroxyl and lactone groups, enabling researchers to explore their functional diversity. These modifications have led to the discovery of urolithin derivatives with enhanced biological activities, making them promising candidates for further investigation in therapeutic, industreal and nutritional applications (Xiangrong, Zhuanhong and Lei, 2023; Norouzbahari, et al., 2018).

This study employs density functional theory (DFT) and Monte Carlo simulations to evaluate the corrosion inhibition potential of urolithin derivatives (UroE, UroM-5, UroM-6, and UroM-7) see Fig. 1 on Fe(110), Cu(111), and Al(111) surfaces. By analyzing surface energies, HOMO-LUMO characteristics, and derived parameters such as electronegativity, hardness, softness, and charge transfer, the investigation aims to elucidate the corrosion inhibition mechanisms of these compounds. This research pioneers the exploration of urolithin derivatives as eco-friendly corrosion inhibitors for these metals, providing innovative insights into sustainable corrosion management.

II. COMPUTATIONAL STUDY

A. DFT

For the purpose of visualization, the molecular geometries of compounds S1–S8 were drawn out using GaussView 6.0 software to predict their potential for corrosion inhibition (Dennington, Keith and Millam, 2016). Gaussian 09, Revision D.01 was used to get optimal performance in the gas phase for these structures, (Frisch and Clemente) (Frisch et al., 2013) with the DFT/B3LYP/6-311++G(d,p) approach (Krishnan, et al., 1980, Becke, 1996, Frisch, Pople and Binkley, 1984). The HOMO, LUMO, and molecular electrostatic potential (MEP) surfaces were created using the optimized structures and GaussView 6.0 (Dennington, Keith and Millam, 2016, Omer, et al., 2024). The optimized and geometric structures of these molecules and calculated various parameters including energy gap(Ediff), global hardness (η), global softness (S), electronegativity (χ), chemical potential (μ), electrophilicity (ω), and nucleophilicity (ε), $\Delta E_{back\text{-}donation}$, reactivity, provide valuable insights into a molecule's stability, maximal amount of electronic charge (ΔN_{max}), and selectivity through the software as seen by Equations 1-10.

$$I = -E_{HOMO} \text{ and } A = -E_{LUMO} \tag{1}$$

$$\Delta E_{diff} = E_{LUMO} - E_{HOMO} \tag{2}$$

$$\chi_{inh} = \frac{E_{HOMO} + E_{LUMO}}{2} \tag{3}$$

$$\mu = -\frac{\left(E_{HOMO} + E_{LUMO}\right)}{2} \tag{4}$$

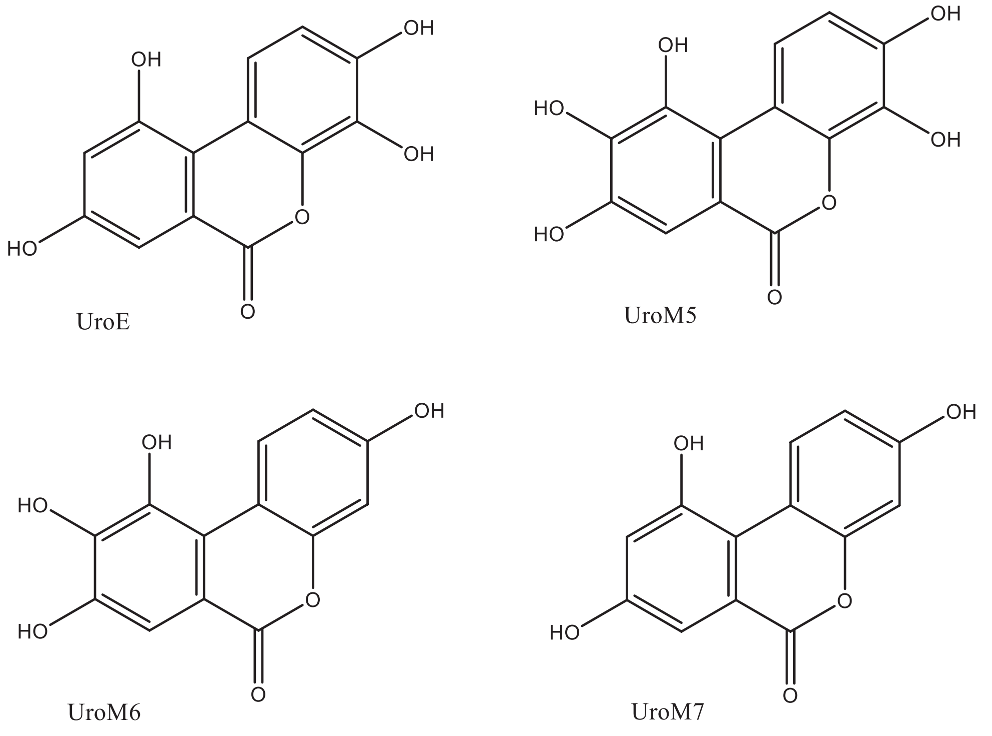

UroE

UroM5

UroM6

UroM7

Fig. 1. The chemical structures of the urolithin derivatives analyzed in this study.

$$\eta_{Inh} = \frac{\Delta E_{gap}}{2} \tag{5}$$

$$S = \frac{1}{2\eta_{inh}} \tag{6}$$

$$\omega_{inh} = \frac{\chi_{inh}^{2}}{2\eta_{inh}} \tag{7}$$

$$\Delta N = \frac{\phi_{Fe} - \chi_{inh}}{2\left(\eta_{Fe} + \eta_{inh}\right)} \tag{8}$$

$$\Delta \psi = -\frac{\left(\phi_{Fe} - \chi_{inh}\right)^{2}}{4\left(\eta_{Fe} + \eta_{inh}\right)} \tag{9}$$

$$\Delta E_{back-donation} = \frac{-\eta}{4} \tag{10}$$

When applied in this particular context, the symbols Φ_{Fe} and η_{Fe} represent the work function and absolute hardness of the iron (Fe) metal, respectively, with values of (Φ_{Fe} = 4.82) (Ech-Chihbi, et al., 2024), and the global hardness of Fe (η_{Fe}) theoretical values are η_{Fe} = 0 eV, assuming that IA = EA for metallic bulk atoms (Boughoues, et al., 2020).

B. Topological Parameters

The Monte Carlo simulations were carried out with the Adsorption Locator module within the Material Studio software. This computational setup employs the Metropolis algorithm to model the adsorption process (Gowers, et al., 2018). Each iteration consists of simulated annealing, executed over 50,000 steps. For energy evaluations and to search for equilibrium configurations, the COMPASSIII force field was applied (Sun, et al., 2016). To precisely assess electrostatic interactions, the Ewald method was implemented, achieving an accuracy of 10–5 kcal/mol (Nam, Gao and York, 2005).

III. Results and Discussion

A. Non-covalent Interactions (NCI) and Reduced Density Gradient (RDG) Analysis

NCI and RDG are novel methods for analyzing weak intermolecular interactions. The NCI index characterizes and evaluates the properties of weak interactions, while the RDG index supports the presence of non-covalent interactions. RDG is a fundamental dimensionless parameter that encompasses both the density and its initial derivative eq. (11). (Domingo, et al., 2002; Asath, et al., 2016; Boukabcha, et al., 2023; Asif, et al., 2023):

$$RDG(r) = \frac{1\left|\nabla \rho(r)\right|}{2\left(3\pi r^{2}\right)^{\frac{1}{3}} \rho^{\frac{4}{3}}(r)} \tag{11}$$

The Multiwfn program was used to generate the colorful RDG scatter plots (Lu and Chen, 2012). While the VMD program was used to create a visual illustration of the 3D isosurface (Humphrey, Dalke and Schulten, 1996). The visual representations of the two-dimensional RDG plots and the three-dimensional isosurface are shown in Fig. 2. The RDG scatter can be used to study the corrosion inhibition mechanism of all urolithins. The RDG scatter can be used to identify the regions of the metal surfaces (Fe(110), Cu (111), and Al (111) where the urolithins are adsorbing and to study the effect of the urolithins on the electron density of the metal surface. Red, blue, and green colors in RDG scatter plots for Urolithins can be used to study and predict their corrosion inhibition properties. The red color in RDG scatter plots indicates regions of high electron density. These regions are more likely to be involved in chemical reactions and thus more susceptible to corrosion. Urolithins (E, M5, M6, M7) that can effectively adsorb to the red regions of a metal surface are likely to be effective corrosion inhibitors. As well as the Blue color in RDG scatter plots indicates regions of low electron density. These regions are less likely to be involved in chemical reactions and thus less susceptible to corrosion. However, blue regions can still play a role in corrosion by providing a pathway for corrosive species to reach the more reactive red regions. Moreover, the Green color in RDG scatter plots is typically used to represent intermediate electron density regions. These regions may or may not play a role in corrosion (Saidj, et al., 2023; Boukabcha, et al., 2023). The positive sign of lambda (λ) indicates that the electrons are localized, while the negative sign of λ indicates that the electrons are delocalized. In the context of corrosion, the localized electrons are more likely to react with corrosive species and thus more susceptible to corrosion. Based on the results shown in Fig. 2, it is clear that the examined compounds exhibit a significant number of green and red spots. These visual characteristics can be attributed to the high prevalence of van der Waals interactions and the observed steric effects within the molecule. However, the greater number of blue spots indicates a higher number of strong hydrogen bonds throughout the entire compound. On the other hand, NCI-RDG scatter plots show red patches that correspond to strong repulsive forces inside aromatic rings. The green isosurface represents van der Waals (vdW) interactions involving hydrogen-hydrogen (H-H), nitrogen-hydrogen (N-H) bonds, and other associated interactions, which are somewhat weaker.

B. Topological Parameters

Atoms in molecules (AIM) analysis is a widely used method for identifying and describing non-covalent interactions within molecular systems, with a particular focus on intra- and intermolecular hydrogen bonds. AIM identifies and characterizes hydrogen bonds in molecular complexes by comprehensively analyzing electron density using topological methods (Tang and Zhu, 2021; Jumabaev, et al., 2023; Bader, 2010). We used the B3LYP methodology to compute the topological properties of bond critical points (BCPs), including the Laplacian of electron density, electron density, potential energy density, and ellipticity. Table I summarizes the calculations, and Fig. 3 shows the BCPs for the neutral and protonated states. Rozas, Alkorta and Elguero, 2000 classify hydrogen bonds as weak, medium, and strong based on the electron density and Hamiltonian at the BCP. Weak hydrogen bonds have a positive electron density and a positive Hamiltonian, and an interaction energy

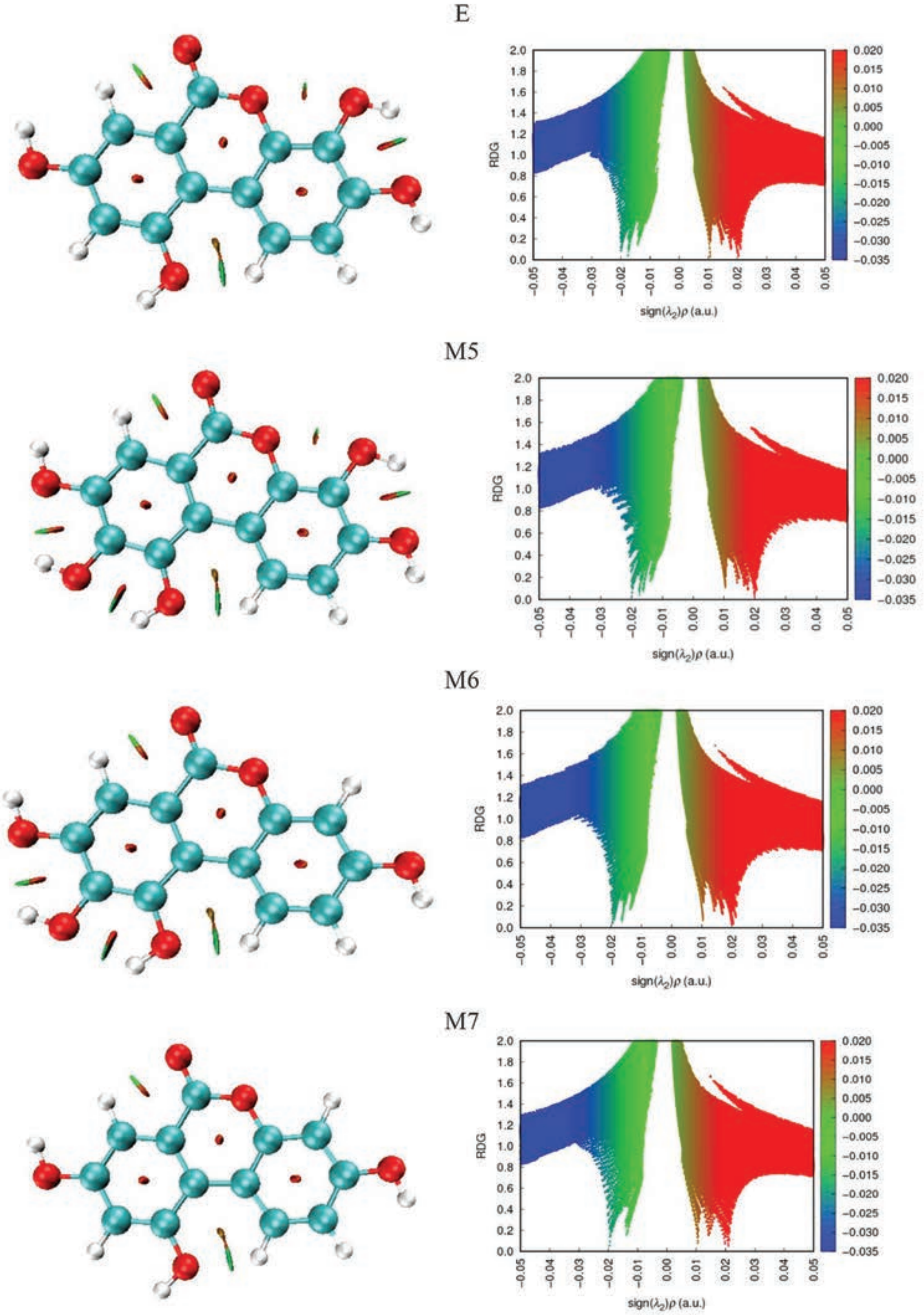

Fig. 2. Reduced density gradient and non-covalent interactions analysis for study compounds.

<12.0 kcal/mol. Medium hydrogen bonds have a positive second derivative of the electron density and a positive Hamiltonian, and an interaction energy between 12.0 and 24.0 kcal/mol. Strong hydrogen bonds have a negative electron density and a negative Hamiltonian, and an interaction energy >24.0 kcal/mol (Bader, 2010). According to Table I, all of the studied compounds have strong hydrogen-bonded interactions, except for Uro E, Uro M5, and Uro M6. Uro E has weak hydrogen-bonded interactions at O_2-H_{20}, Uro M5 has weak hydrogen-bonded interactions at O_3-H_{23} and O_2-H_{21}, and Uro M6 has weak hydrogen-bonded interactions at O_3-H_{24}, O_2-H_{21}, and O_2-H_{19}.

In conclusion, Uro E, Uro M5, Uro M6, and Uro M7 are all organic compounds that contain oxygen atoms. These atoms can form strong hydrogen bonds with the metal surface. When these compounds adsorb onto the metal surface, they form a layer that protects the metal from corrosion. Furthermore, Strong hydrogen bonds play a significant role in the topological parameters of a molecule and the corrosion inhibition efficiency of organic compounds. Compounds with strong hydrogen bonding interactions are more likely to form a strong bond with the metal surface and provide effective corrosion protection.

C. HOMO-LUMO

Comprehensive explanation of chemical reactivity characteristics such as HOMO-LUMO energy gap, chemical hardness, electronegativity, softness, chemical potential,

TABLE I

Topological Parameters (all in a.u) at the Bond Critical Point (bcp) of Title Compound (Electron Density [ρ(r)], Laplacian of Electron Density [$\nabla^2 \rho$(r)], and Ellipticity [e]), the Units of v, g, and h are in a.u., and Hydrogen Energy (ε) (kcal/mol)

Bonds	$\rho(r)$	$\nabla^2 \rho(r)$	ε	V	G	H	E
Uro E							
O_2–H_{20}	0.020	0.085	0.012	−0.014	0.018	0.003	4.538
C_{16}–H_{22}	0.278	−0.940	0.027	−0.315	0.040	−0.275	98.822
C_{19}–H_{23}	0.278	−0.941	0.028	−0.317	0.041	−0.276	99.359
C_{15}–H_{21}	0.281	−0.965	0.026	−0.317	0.038	−0.279	99.408
C_{12}–H_{20}	0.290	−1.022	0.023	−0.330	0.038	−0.293	103.694
O_3–H_{25}	0.362	−2.549	0.021	−0.773	0.068	−0.705	242.599
O_2–H_{24}	0.366	−2.537	0.022	−0.775	0.071	−0.705	243.285
O_4–H_{26}	0.365	−2.542	0.022	−0.776	0.070	−0.706	243.348
O_5–H_{27}	0.365	−2.545	0.022	−0.776	0.070	−0.706	243.478
Uro M5							
O_3–H_{23}	0.020	0.097	2.031	−0.017	0.021	0.004	5.355
O_2–H_{21}	0.019	0.081	0.014	−0.014	0.017	0.003	4.323
O_4–H_{25}	0.363	−2.546	0.022	−0.774	0.069	−0.705	242.780
O_5–H_{26}	0.362	−2.548	0.022	−0.773	0.068	−0.705	242.609
C_{12}–H_{20}	0.281	−0.967	0.024	−0.316	0.037	−0.279	99.194
O_3–H_{24}	0.359	−2.545	0.021	−0.768	0.066	−0.702	240.922
C_{13}–H_{21}	0.290	−1.021	0.023	−0.330	0.037	−0.292	103.439
C_{18}–H_{22}	0.278	−0.941	0.028	−0.317	0.041	−0.276	99.364
O_2–H_{23}	0.360	−2.539	0.021	−0.769	0.067	−0.702	241.256
Uro M6							
O_3–H_{24}	0.020	0.096	2.817	−0.017	0.020	0.004	5.295
O_2–H_{21}	0.019	0.080	0.010	−0.013	0.017	0.003	4.232
C_{12}–H_{20}	0.281	−0.966	0.024	−0.316	0.037	−0.279	99.219
O_3–H_{25}	0.359	−2.545	0.021	−0.768	0.066	−0.702	240.909
C_{13}–H_{21}	0.290	−1.025	0.016	−0.329	0.036	−0.292	103.116
O_6–H_{27}	0.366	−2.539	0.022	−0.777	0.071	−0.706	243.822
O_2–H_{24}	0.360	−2.538	0.021	−0.769	0.067	−0.702	241.147
C_{17}–H_{22}	0.281	−0.968	0.027	−0.316	0.037	−0.279	99.195
C_{18}–H_{23}	0.278	−0.939	0.029	−0.317	0.041	−0.276	99.416
O_4–H_{26}	0.364	−2.546	0.022	–	–	–	–
Uro M7							
O_2–H_{19}	0.020	0.083	0.008	−0.014	0.017	0.003	4.433
O_3–H_{25}	0.365	−2.542	0.022	−0.776	0.070	−0.706	243.367
C_{15}–H_{22}	0.278	−0.941	0.027	−0.315	0.040	−0.275	98.799
C_{12}–H_{20}	0.281	−0.965	0.026	−0.317	0.038	−0.279	99.396
C_{11}–H_{19}	0.290	−1.026	0.017	−0.330	0.037	−0.293	103.392
C_{17}–H_{23}	0.278	−0.939	0.029	−0.317	0.041	−0.276	99.418
O_5–H_{26}	0.366	−2.539	0.022	−0.777	0.071	−0.706	243.753
O_2–H_{24}	0.365	−2.537	0.022	−0.775	0.071	−0.705	243.248
C_{14}–H_{21}	0.281	−0.968	0.027	−0.316	0.037	−0.279	99.195

electrophilicity, nucleophilicity, proton affinity, electrons transported from inhibitor to metal surface, electron-donating ability, and electron-donating ability. Determines the quantum chemical parameters of the compounds in both gas and aqueous phases, with a focus on Uro E, Uro M5, Uro M6, and Uro M7, as detailed in Tables II and III. The results confirm that all the analyzed molecules exhibit effective corrosion inhibition properties. The main objective of this theoretical research is to anticipate the corrosion inhibition performance of the substance and its derived compounds. Quantum chemical computations are useful for researching the link between molecule structure and corrosion inhibition efficacy. The smaller the HOMO energy, the harder it is to remove electrons from the molecular structure, and hence the more resistant to oxidation the compound, and have a greater potential to be excellent inhibitors. In general, there is a link between LUMO energy and inhibitory action. Compounds with high levels of LUMO energy are more probable to be excellent inhibitors because they can receive electrons from other compounds (Özbakır Işın, et al., 2020). The HOMO-LUMO bandgap identifies the compound's last electric charge contact and is useful in describing chemical electrical transport features. Low energy band gap (ΔE) values suggest that the material is particularly effective at inhibiting, and resisting corrosion in acidic environments. Adsorption techniques help by influencing the transport mechanism by the adsorbed layer, while the low-lying LUMO level induces chargeback donation from the metallic material to the chemical molecule. The energy of LUMO stability raises the corrosion inhibitor's electro-accepting capacity (Sujatha and Lavanya, 2023; Korkmaz, et al., 2022). According to research, increasing the bandgap (Uro E, Uro M5, Uro M6, Uro M7) raises corrosion while decreasing it improves the material's resilience to corrosion. This is due to the fact that just a little amount of energy is required to ionize and remove an electron from the last molecular-occupied orbitals. According to our findings, as shown in Tables II and III, the energy gap of protonated molecules is usually lower than that of neutral molecules in aqueous and pas phases, since protonation gives a positive charge to the compounds. In all, a molecule with a smaller energy gap is more polarizable, with more chemical activity and poorer kinetic stability. Overall, the reduction in band gap energy with protonation is an essential phenomenon with several possible uses, and it increases the material's corrosion resistance. Here, one of the applications of protonated is more polarizable (Mamad, et al., 2023b; Hekim, Azeez and Akpinar., 2019; Hssain, 2022).

As the electronegativity value lowers, the electron donor of excellent inhibitors to the metal surface enhances corrosion inhibition ability. In general, electronegativity is the capacity of a chemical species to attract the chemical electron density toward itself. In this study, the maximal electronegativity investigated the gas phase in protonated or (χ protonated > χ neutral). Small electronegativity readings represent that the chemical is a good corrosion inhibitor, anti-corrosion inhibitor protonated < anti-corrosion inhibitor neutral. Here, electronegativity is the capacity of a chemical species to attract in protonated greater than neutral. The above data indicates that compounds with a high electronegativity value can't be used as useful corrosion inhibitors (Özbakır Işın, et al., 2020; Qader, et al., 2019; Yousif and Hanaa, 2021b).

Rises in inhibitory performance are inversely related to drops in electronegativity values because the inhibitor's atoms' ability to attract electrons decreases (Razali, et al., 2023). Hard compounds contain larger energy gaps, making them more chemical stable and less chemical reactive. Soft chemical compounds are more reactive than hard compounds because they can more readily donate electrons to an acceptor. According to energy gaps (Fig. 4), chemical stability, and reactiveness, the corrosion inhibition efficiency is ranked from highest to lowest: (Uro M6 > Uro M5 > Uro M7 > Uro E) using protonated/gas phase. Improving chemical hardness may be beneficial to corrosion resistance. As a result, the (Uro E) compound inhibitor that had higher ELUMO (-3.44 eV) and low energy gap (3.031 eV) was shown to have high softness (0.330 eV-1), and low hardness (1.516 eV) scores in the gas phase/protonated technique. This data indicate that the Uro E compound has a high kinetic no stability and a high molecular reactivity. Nucleophilicity and electrophilicity are theoretical chemistry characteristics that may be used to predict the chemical behavior of compounds,

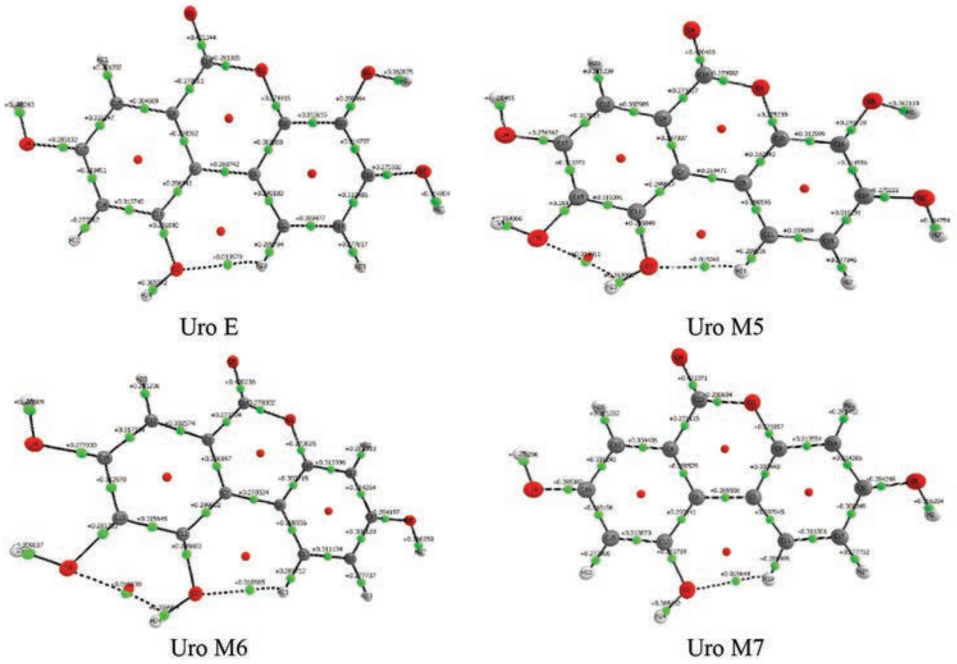

Uro E Uro M5

Uro M6 Uro M7

Fig. 3. Graph representation of neutral molecular state.

TABLE II
Quantum Chemical Parameters for Compound at Gas Phase

Neutral					Protonated			
Parameters	Uro E	Uro M5	Uro M6	Uro M7	Uro E	Uro M5	Uro M6	Uro M7
HOMO (eV)	−5.957	−5.978	−6.014	−5.986	−9.513	−9.446	−9.686	−9.734
LUMO (eV)	−1.871	−1.647	−1.707	−1.927	−6.671	−6.405	−6.473	−6.741
Ionization energy (eV)	5.957	5.978	6.014	5.986	9.513	9.446	9.686	9.734
Electron Affinity (eV)	1.871	1.647	1.707	1.927	6.671	6.405	6.473	6.741
Energy gap (eV)	4.086	4.331	4.307	4.059	2.842	3.041	3.213	2.993
Hardness (eV)	2.043	2.166	2.154	2.030	1.421	1.521	1.607	1.497
Softness (eV)-1	0.245	0.231	0.232	0.246	0.352	0.329	0.311	0.334
Electronegativity (eV)	3.914	3.813	3.861	3.957	8.092	7.926	8.080	8.238
Chemical potential (eV)	−3.914	−3.813	−3.861	−3.957	−8.092	−7.926	−8.080	−8.238
Electrophilicity (eV)	3.749	3.356	3.460	3.857	23.040	20.656	20.317	22.672
Nucleophilicity (eV)-1	0.267	0.298	0.289	0.259	0.043	0.048	0.049	0.044
Back-donation (eV)	−0.511	−0.541	−0.538	−0.507	−0.355	−0.380	−0.402	−0.374
Electron transfer ΔN	1.916	1.761	1.793	1.949	5.695	5.212	5.029	5.505

TABLE III
Quantum Chemical Parameters for Compound at Aqueous Phase

Parameters	Neutral				Protonated			
	Uro E	Uro M5	Uro M6	Uro M7	Uro E	Uro M5	Uro M6	Uro M7
HOMO (eV)	−5.981	−6.027	−6.053	−6.147	−6.471	−6.501	−6.620	−6.576
LUMO (eV)	−2.093	−1.866	−1.867	−2.053	−3.440	−3.230	−3.255	−3.432
Ionization energy (eV)	5.981	6.027	6.053	6.147	6.471	6.501	6.620	6.576
Electron Affinity (eV)	2.093	1.866	1.867	2.053	3.440	3.230	3.255	3.432
Energy gap (eV)	3.888	4.161	4.186	4.094	3.031	3.271	3.365	3.144
Hardness (eV)	1.944	2.081	2.093	2.047	1.516	1.636	1.683	1.572
Softness (eV)-1	0.257	0.240	0.239	0.244	0.330	0.306	0.297	0.318
Electronegativity (eV)	4.037	3.947	3.960	4.100	4.956	4.866	4.938	5.004
Chemical potential (eV)	−4.037	−3.947	−3.960	−4.100	−4.956	−4.866	−4.938	−5.004
Electrophilicity (eV)	4.192	3.743	3.746	4.106	8.102	7.237	7.245	7.964
Nucleophilicity (eV)-1	0.239	0.267	0.267	0.244	0.123	0.138	0.138	0.126
Back-donation (eV)	−0.486	−0.520	−0.523	−0.512	−0.379	−0.409	−0.421	−0.393
Electron transfer	2.077	1.897	1.892	2.003	3.270	2.975	2.935	3.183

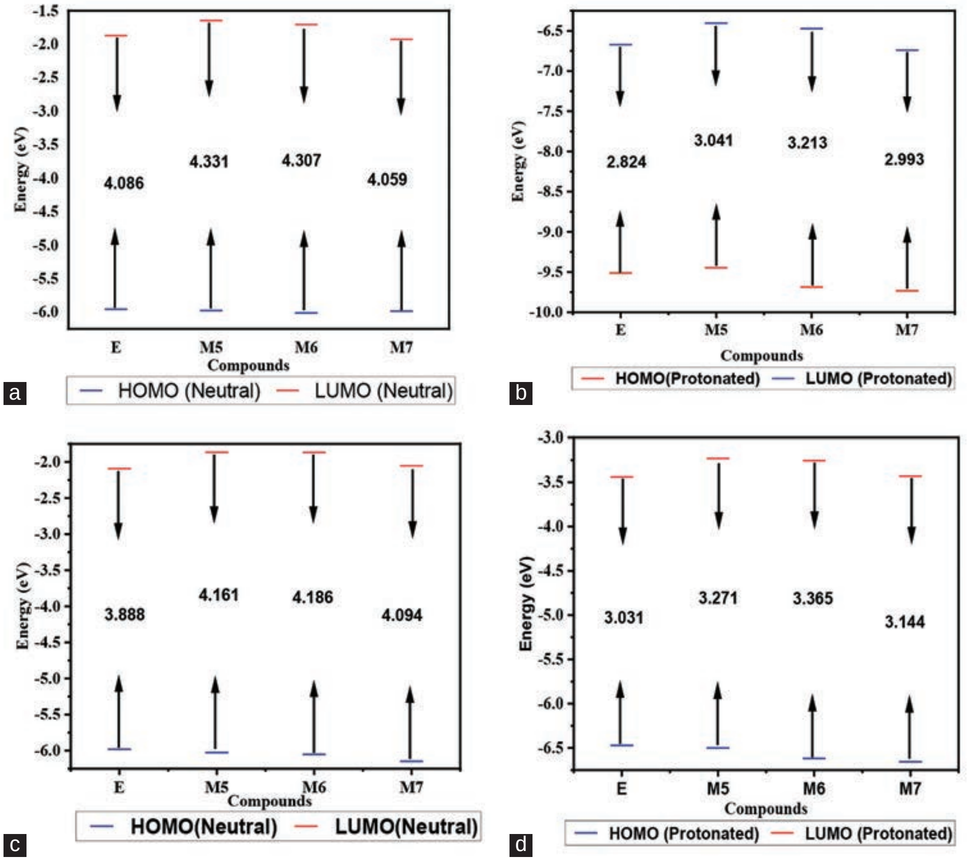

Fig. 4. Energy bandgap for all compounds (a) Neutral gas phase (b) Protonated gas phase (c) Neutral aqueous phase (d) Protonated aqueous phase.

and these values reflect their efficacy. It is vital to note that a molecular structure with a high nucleophilic value may effectively suppress corrosion inhibitors. In contrast, a material with a high electrophilic value provides no corrosion protection benefit. Nucleophiles are compounds that transfer an electron pair to form a connection with another chemical species, while electrophiles are electron-deficient compounds. The predicted ranking of corrosion inhibition effectiveness may be constructed by taking into account the nucleophilic and electrophilic values of the compounds investigated: Uro E > Uro M7 > Uro M5 > Uro M6 using the protonated method (Caid, et al., 2023). The electron transfer has an inverse relationship with the energy gap, implying that a greater value equates to a stronger corrosion inhibition capacity. According to the aqueous, and gas phases, the Uro E compound has the greatest electron transfer value, suggesting a large potential for electron release in the metals using neutral/protonated methods. The faster the electron transfer rate, the more probable corrosion will develop. Whenever the back donation of energy from a molecular structure to a metal is favored, it indicates that the inhibitor has a positive hardness and a negative back donation energy. The physical, and chemical interaction that occurs between inhibitors and the metal surfaces is influenced by the back-donation mechanism. According to this hypothesis, if back-donation from a molecule and electron transfer to the molecule happens simultaneously, the energy shift is proportional to the hardness of the molecules. The chemical contact between the molecule that inhibits and its chemical surface may be influenced by an electrical back-donation mechanism. When back-donation is < zero, or η > zero, The transfer of electrons from the molecular structure to the metal is favorable in terms of energy. The computed back-donation numbers in this study show a trend: ΔE b – d aqueous > ΔE b – d gas phase, because molecules of water are present in the aqueous technique (Qadr and Mamand, 2023). The protonated state has a negative influence on BG energy. Chemical stability, a change in the material's corrosion behavior, and peculiar corrosion inhibition difficulties are all directly tied to BG energy. Overall, increasing ionization energy, electron affinity, softness, and reducing the energy band gap may all increase corrosion resistance and inhibition. Protonated chemicals may be utilized to create coatings, inhibitors, and self-healing materials that protect metals against corrosion in a range of conditions.

D. MEP

Fig. 5 also depicts the MEP of (Uro E, Uro M5, Uro M6, Uro M7) compounds using the gas phase. The MEP is a useful tool for identifying the relative polarity of a molecular structure and whether or not certain regions in it have proton affinity or charge-regulated hard-hard interactions. The potential energy map (PEM) is a critical component in characterizing the arrangement of structural elements on a compound's surface. In color, PEM depicts the electrostatic potential surrounding a molecular structure. The electrostatic potential (ESP) Map may be affected by factors such as increased electron affinity, dipole moment, quantity of ionization, electronegativity, and electron density (Yıldız, et al., 2023). Increased ionization energy, electron affinity, softness, and a smaller energy band gap may all cause the (MEP) to become red. When electronegativity is high, an area of a molecule's electrostatic potential map becomes blue.

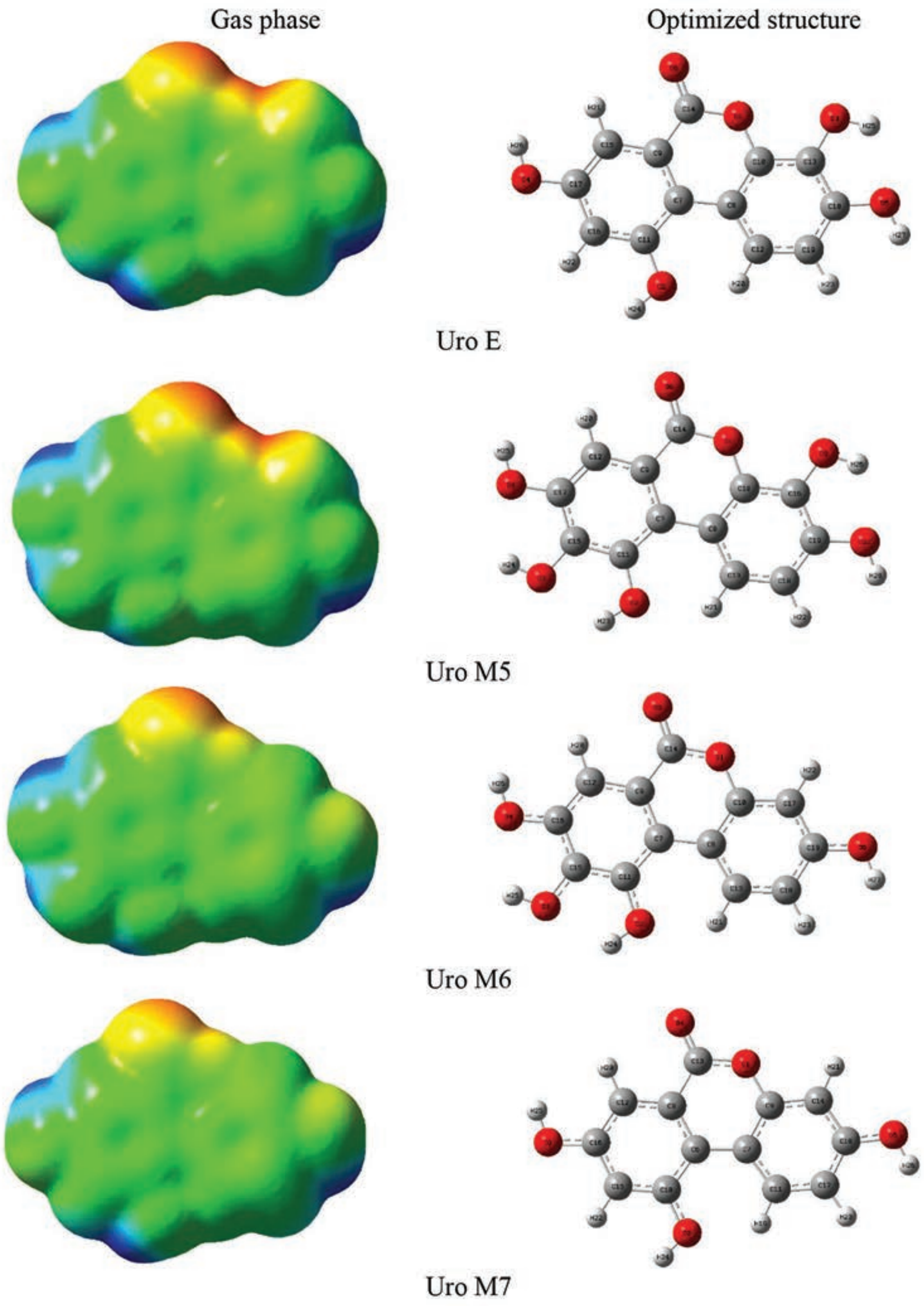

Fig. 5. Optimized molecular geometries and molecular electrostatic potential maps for all compounds.

Blue areas are more positively charged, have a lower electron density, and have a lower affinity for a proton. The existence of a red zone in a MEP map may be a strong predictor of corrosion resistance. Increase Positive charge (protonated) attracts electrons, which may aid in the formation of a protective layer on a metal's surface. Overall, the blue zone in a MEP map is a flexible tool for designing novel materials and catalysts with enhanced capabilities, as well as a strong instrument for advancing a broad variety of scientific subjects (Akman, et al., 2023; Mustafa and Mohammad, 2023).

E. Thermal Properties

The key thermodynamic parameters, enthalpy (ΔH), entropy (ΔS), Gibbs free energy (ΔG), and heat capacity (Cv) were computed for the investigated compounds using DFT with the 6-311++G(d,p) basis set. Calculations were performed in the gas phase at temperatures ranging from 100 K to 1000 K. Notably, the temperature dependence significantly affects the thermodynamic properties of the studied compounds (Arulaabaranam, et al., 2021; Fayomi, et al., 2021; Merdas, 2021). Our analysis using DFT revealed a consistent trend across all investigated compounds (E, M5, M6, and M7). As temperature increases from 25 K to 1000 K, most thermodynamic functions (enthalpy, entropy, and heat capacity) exhibit a positive correlation, indicating a rise in their values (Fig. 6). This behavior aligns with expectations as higher temperatures generally lead to increased molecular vibrations. However, Gibbs free energy (ΔG) shows an opposing trend, becoming increasingly negative with rising temperature. The positive enthalpy change (ΔH) observed throughout the temperature range signifies that the dissolution process for these molecules is endothermic, requiring an energy input (Abbaz, Bendjeddou and Villemin, 2018; Srivastavaa, et al., 2019; Yousif and Hanaa, 2021a). This suggests that dissolving these compounds is not a spontaneous process under the studied conditions. Increasing temperature may cause a change in the adsorption behavior of inhibitor molecules on metal surfaces, as shown by the trend in

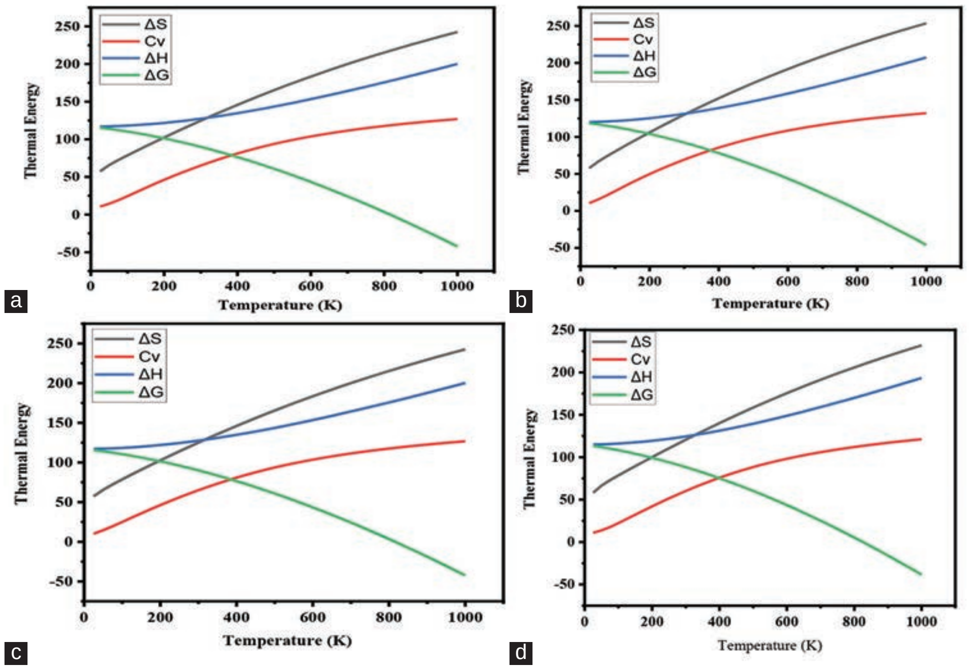

Fig. 6. Thermal properties for, (a) E compound, (b) M5 compound, (c) M6 compound, and (d) M7 compound.

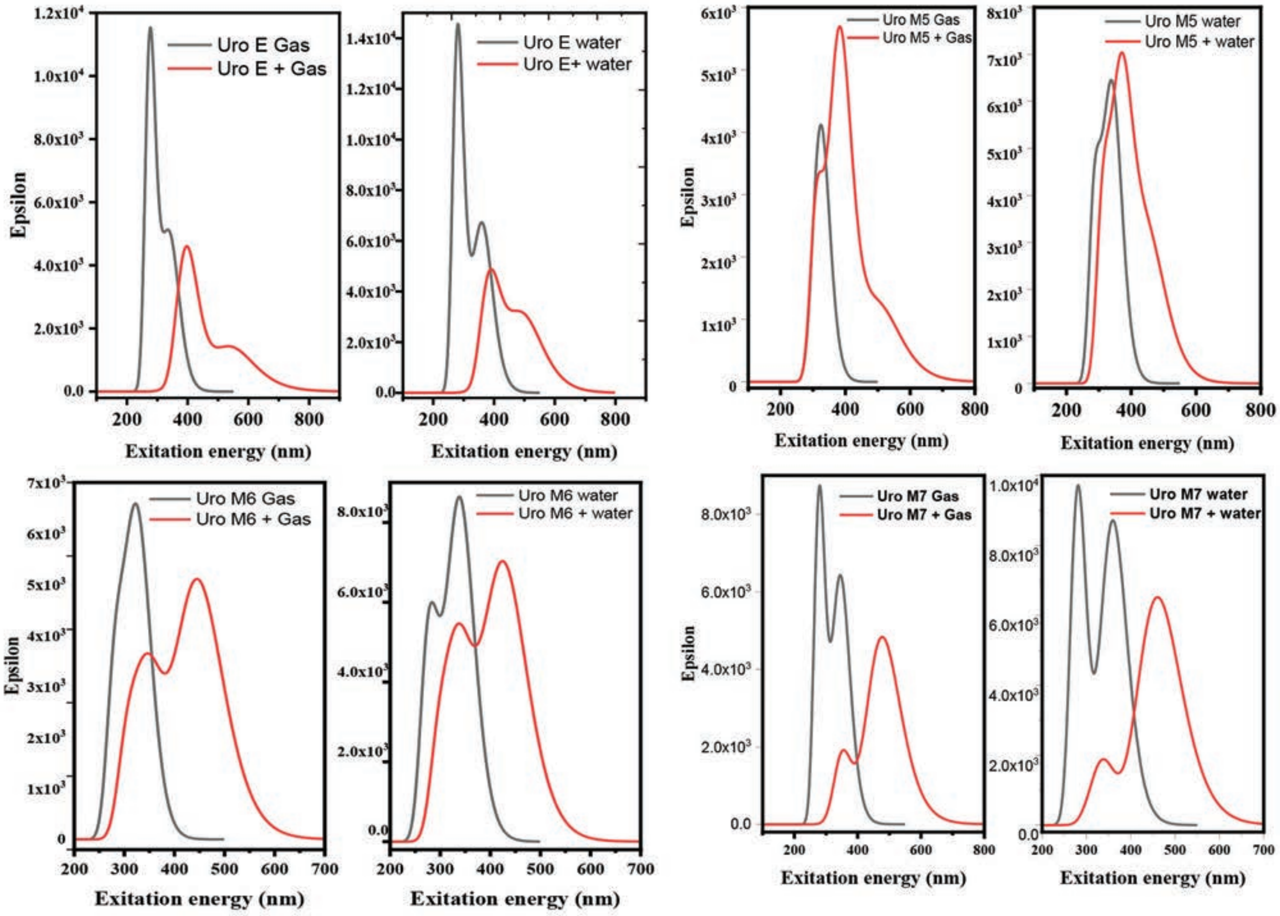

Fig. 7. Ultraviolet-visible analysis for all compounds in gas and aqueous phase.

TABLE IV
Fukui Functions at the Gas Phase

Atoms	Uro E			Uro M5			
	f_k^-	f_k^+	Δf	Atoms	f_k^-	f_k^+	Δf
O (1)	0.016	0.041	0.025	O (1)	0.015	0.04	0.025
O (2)	0.022	0.028	0.006	O (2)	0.021	0.028	0.007
O (3)	0.068	0.021	−0.047	O (3)	0.027	0.048	0.021
O (4)	0.062	0.043	−0.019	O (4)	0.049	0.034	−0.015
O (5)	0.073	0.03	−0.043	O (5)	0.077	0.023	−0.054
O (6)	0.058	0.108	0.05	O (6)	0.057	0.106	0.049
C (7)	0.018	0.05	0.032	C (7)	0.013	0.054	0.041
C (8)	0.031	0.002	−0.029	C (8)	0.032	0.000	−0.032
C (9)	0.018	0.039	0.021	C (9)	0.019	0.035	0.016
C (10)	0.026	0.002	−0.024	C (10)	0.028	0.005	−0.023
C (11)	0.03	0.022	−0.008	C (11)	0.03	0.02	−0.010
C (12)	0.045	0.017	−0.028	C (12)	0.033	0.046	0.013
C (13)	0.037	0.027	−0.01	C (13)	0.05	0.022	−0.028
C (14)	0.017	0.083	0.066	C (14)	0.015	0.081	0.066
C (15)	0.04	0.049	0.009	C (15)	0.025	0.079	0.054
C (16)	0.021	0.083	0.062	C (16)	0.04	0.029	−0.011
C (17)	0.031	0.02	−0.011	C (17)	0.037	0.025	−0.012
C (18)	0.056	0.031	−0.025	C (18)	0.022	0.02	−0.002
C (19)	0.022	0.02	−0.002	C (19)	0.058	0.033	−0.025
H (20)	0.049	0.031	−0.018	H (20)	0.043	0.053	0.010
H (21)	0.046	0.054	0.008	H (21)	0.051	0.032	−0.019
H (22)	0.048	0.066	0.018	H (22)	0.061	0.047	−0.014
H (23)	0.059	0.046	−0.013	H (23)	0.024	0.023	−0.001
H (24)	0.027	0.025	−0.002	H (24)	0.018	0.026	0.008
H (25)	0.024	0.02	−0.004	H (25)	0.022	0.022	0.000
H (26)	0.024	0.022	−0.002	H (26)	0.026	0.02	−0.006
H (27)	0.032	0.02	−0.012	O (27)	0.075	0.031	−0.044
				H (28)	0.033	0.02	−0.013

TABLE V
Fukui Functions at the Gas Phase

Atoms	Uro M6			Uro M7			
	f^-	f^+	Δf	Atoms	f-	f^-	Δf
O (1)	0.024	0.036	0.012	O (1)	0.026	0.041	0.015
O (2)	0.033	0.024	−0.009	O (2)	0.031	0.027	−0.004
O (3)	0.028	0.045	0.017	O (3)	0.069	0.043	−0.026
O (4)	0.052	0.032	−0.02	O (4)	0.068	0.109	0.041
O (5)	0.067	0.103	0.036	O (5)	0.078	0.037	−0.041
O (6)	0.077	0.036	−0.041	C (6)	0.025	0.051	0.026
C (7)	0.022	0.055	0.033	C (7)	0.038	0.00	−0.038
C (8)	0.045	−0.001	−0.046	C (8)	0.017	0.037	0.02
C (9)	0.019	0.037	0.018	C (9)	0.026	0.00	−0.026
C (10)	0.029	0.005	−0.024	C (10)	0.034	0.021	−0.013
C (11)	0.038	0.021	−0.017	C (11)	0.021	0.021	0.00
C (12)	0.04	0.043	0.003	C (12)	0.047	0.048	0.001
C (13)	0.02	0.026	0.006	C (13)	0.021	0.084	0.063
C (14)	0.024	0.09	0.066	C (14)	0.032	0.024	−0.008
C (15)	0.027	0.08	0.053	C (15)	0.023	0.083	0.06
C (16)	0.044	0.026	−0.018	C (16)	0.033	0.019	−0.014
C (17)	0.03	0.024	−0.006	C (17)	0.037	0.021	−0.016
C (18)	0.039	0.02	−0.019	C (18)	0.035	0.026	−0.009
C (19)	0.04	0.03	−0.01	H (19)	0.042	0.032	−0.01
H (20)	0.048	0.052	0.004	H (20)	0.05	0.054	0.004
H (21)	0.042	0.034	−0.008	H (21)	0.053	0.041	−0.012
H (22)	0.053	0.043	−0.01	H (22)	0.052	0.066	0.014
H (23)	0.06	0.049	−0.011	H (23)	0.059	0.048	−0.011
H (24)	0.025	0.023	−0.002	H (24)	0.028	0.025	−0.003
H (25)	0.02	0.026	0.006	H (25)	0.026	0.022	−0.004
H (26)	0.024	0.022	−0.002	H (26)	0.029	0.02	−0.009
H (27)	0.03	0.021	−0.009				

ΔG. As seen in Fig. 6, the observed positive ΔH values at lower temperatures align with endothermic physisorption, a weaker type of adsorption. Increasingly negative ΔG values at higher temperatures indicate chemisorption potential. Thermal energy may assist this transition by activating inhibitor molecules and metal surfaces to generate stronger chemical interactions. Since chemisorption protects against corrosion better than physisorption, this shift is essential for developing corrosion inhibitors. Thermal characteristics (Gibbs free energy), If the temperature rises from 825 to 1000 Kilven, all chemicals on the metal surface may chemisorption.

F. Ultraviolet (UV)-Visible Spectroscopy

UV spectroscopy is often used for quantitative and qualitative chemical analysis, as well as structural characterization (Salih, et al., 2023). The computed absorption spectrum shows that the maximum absorption wavelength corresponds to the transition of electrons from HOMO, LUMO. According bellow Fig. 7, the Gas phase and water solvent have been used to investigate the UV-visible of (Uro M6 > Uro M5 > Uro M7 > Uro E) compounds. The link between absorbance and corrosion resistance is complicated. In general, substances with a high absorbance are more prone to corrosion, while those with a low absorbance are able to resist corrosion. For evaluating the accuracy of peak location in the calculation of UV-visible wavelengths, the kind of basis set, and solvent is more important than the number of peaks. The greatest absorption wavelength parallels the chemical electronic shift from HOMO to LUMO molecular orbital, according to shifting and the absorption spectrum. The impact of neutral and protonated clearly has been studied based on peak location in the UV-visible, as illustrated in Fig. 7. When Uro E to M7 molecules are changed from neutral to protonated, their absorption of UV peak rises, as a result, increase positive charge (protonated).

G. Fukui functions

The Fukui Function gives information on the reactivity indices in a given system. For the highest Fukui function values, the atom exhibits a significant degree of reactivity. The Fukui functions from (Uro M6 > Uro M5 > Uro M7 > Uro E) have been calculated on the basis of B3LYP/6-311G++(d, p) level of theory, and the results are shown in Tables IV and V. The Fukui Functions ($f_k^-, f_k^+ f_k^0$) are computed using Mulliken population analysis charges of neutral, negative, and positive ions using equation (12-14). If (N) represents the number of electrons, then (N + 1) denotes an ion and (N – 1) denotes the system's cation (Caid, et al., 2023; Razali, et al., 2023).

$$f_k^+ = q\left(N+1\right) - q\left(N\right) \tag{12}$$

$$f_k^- = q\left(N\right) - q\left(N-1\right) \tag{13}$$

$$f_k^- \tag{14}$$

Furthermore, The Fukui function is a valuable tool for understanding the reactivity of molecules in corrosion inhibition. It helps identify regions within the inhibitor

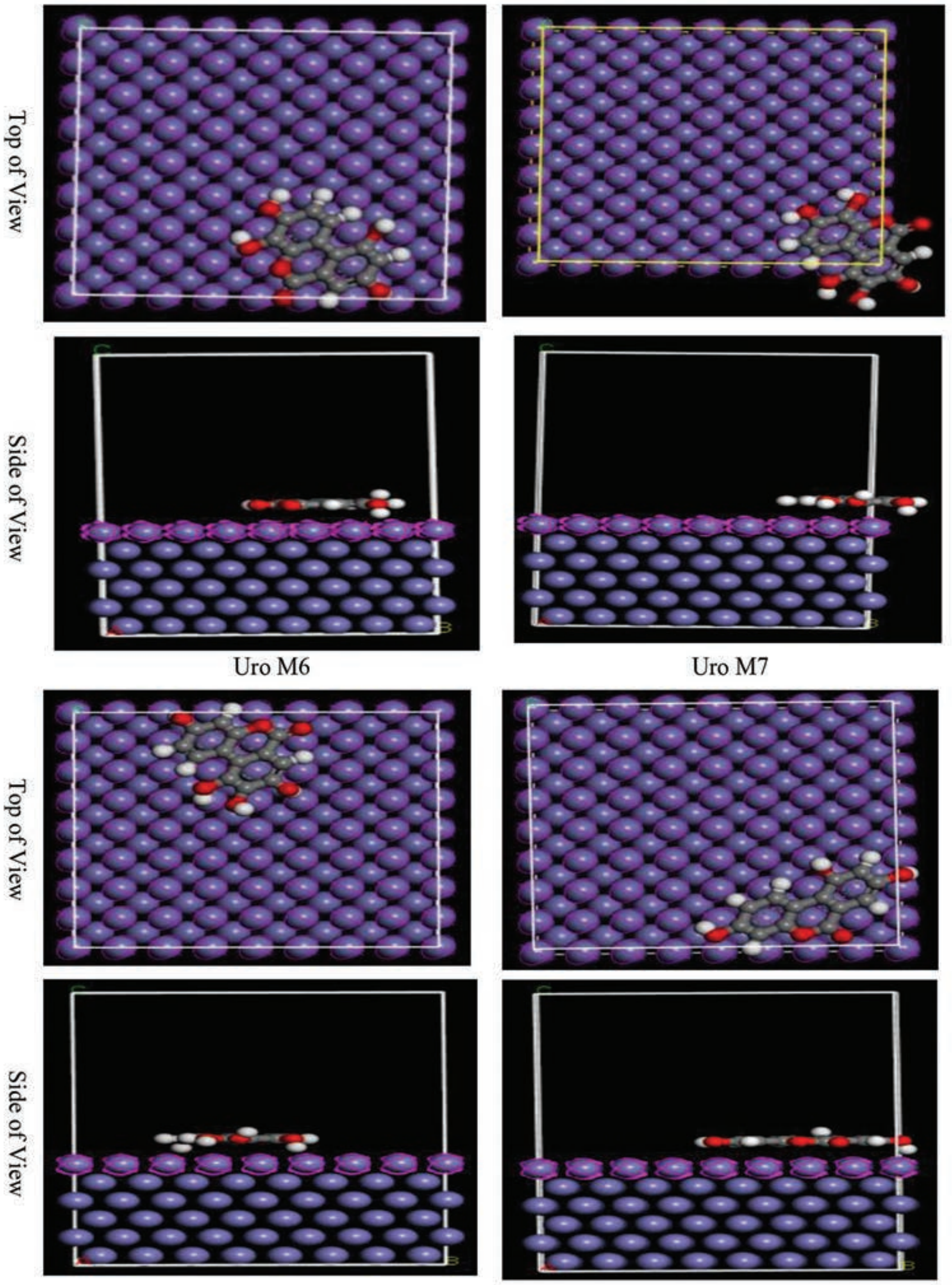

Fig. 8. The low-energy configurations for the adsorption of neutral forms of the study compounds on the Fe(110) surface were determined using Monte Carlo simulations.

molecule with enhanced electrophilic character (f_k^+). These regions, characterized by a higher Fukui function value, are more susceptible to attack by electron-rich species (nucleophiles). Conversely, the most nucleophilic atoms within the inhibitor molecule will exhibit the highest Fukui function value (f_k^-). During adsorption on a metal surface, the inhibitor molecule interacts with the metal through electron transfer. This electron transfer process influences the electronic density at both the nucleophilic and electrophilic sites on the inhibitor molecule. Therefore, the Fukui function analysis provides valuable insights into the potential adsorption sites on the metal surface. It essentially helps pinpoint which areas of the inhibitor molecule are more likely to interact and form bonds with the metal, ultimately determining the reactive sites during the adsorption process (Caid, et al., 2023; Fan, et al., 2022; Razali, et al., 2023). The condensed Fukui function serves as a helpful indicator of nucleophilic character within a molecule. Sites with a positive Fukui function ($\Delta f > 0$) are considered electrophilic, while those with a negative value ($\Delta f < 0$) are considered nucleophilic. Our analysis revealed that several atoms in the investigated compounds (Uro M6, Uro M5, Uro M7, and Uro E) exhibit significant nucleophilic character as shown in Table IV and V. Among the oxygen atoms analyzed, Uro M7 (O4) displayed the strongest nucleophilicity ((f_k^-) = 0.109), followed by Uro E (O6) ((f_k^-) = 0.108), Uro M5 (O6) ((f_k^-)= 0.106), and Uro M6 (O5) (f_k^-)= 0.103). This trend suggests that oxygen atoms within these molecules are generally more susceptible to nucleophilic attack compared

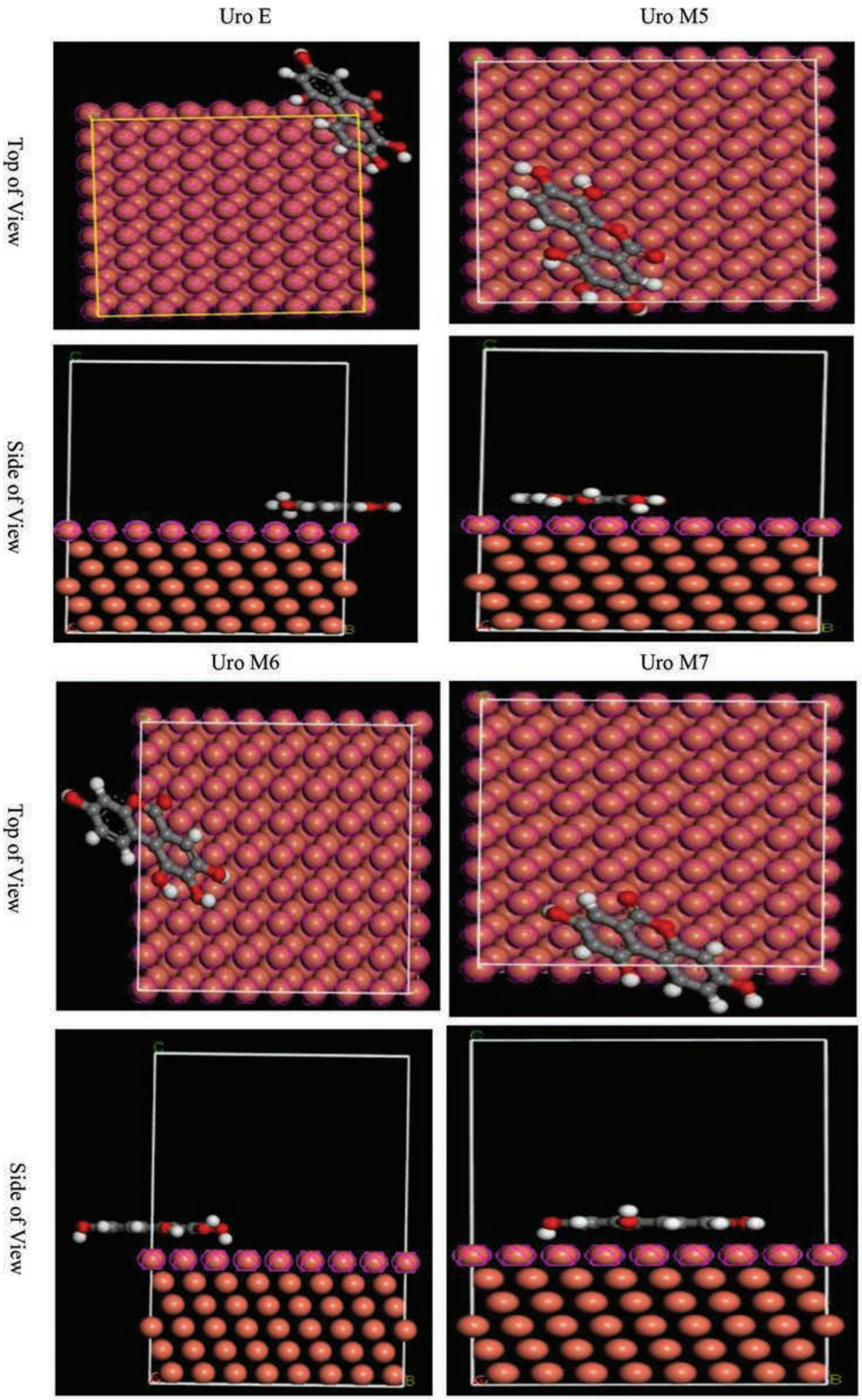

Fig. 9. The low-energy configurations for the adsorption of neutral forms of the study compounds on the Cu(111) surface were determined using Monte Carlo simulations.

to carbon and hydrogen atoms. The higher electronegativity (O: 3.44 > C: 2.55 > H: 2.20) and electron affinity of oxygen atoms contribute to their vulnerability toward nucleophiles. Oxygen's inherent ability to attract electrons (electronegativity) and its tendency to gain additional electrons (electron affinity) make it a more favorable target for nucleophilic attack compared to carbon and hydrogen.

H. Monte Carlo Simulation

The investigation of the adsorption of Uor E, Uor M5, Uor M6, and Uor M7 on metal surfaces Fe (110), Cu (111), and Al (111) was conducted using Monte Carlo simulations in the gas phase. These simulations were performed using the Adsorption Locator module of the Material Studio program. The computational methodology used for the implementation

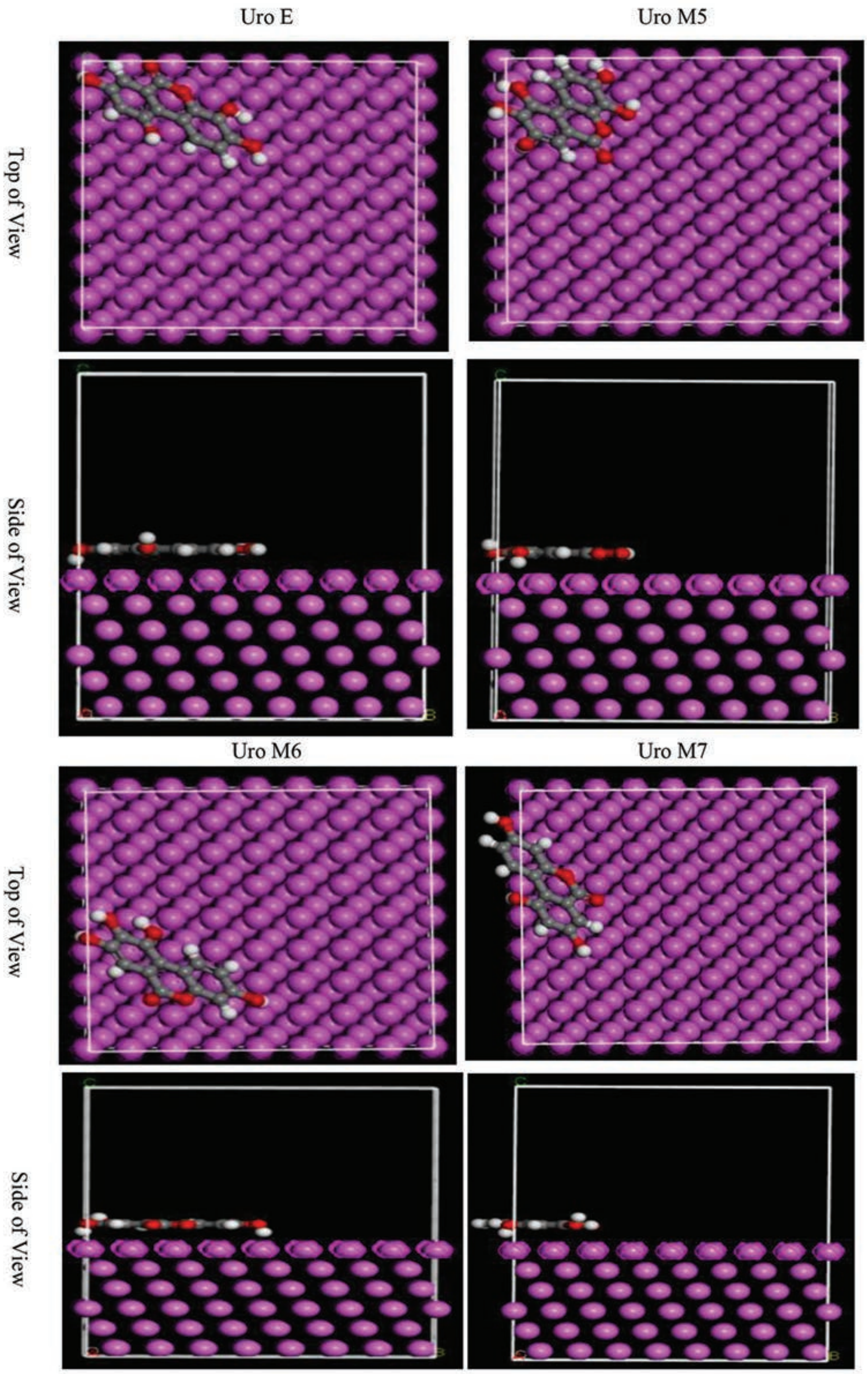

Fig. 10. The low-energy configurations for the adsorption of neutral forms of the study compounds on the Al(111) surface were determined using Monte Carlo simulations.

of the model has been founded upon the Metropolis algorithm (Metropolis, et al., 1953; Mamad, Omer and Othman, 2023a, Hamad, et al., 2025). Monte Carlo simulations use simulated annealing with 50,000 steps in each iteration. Energy calculations and equilibrium configuration searches were carried out using the condensed phase optimized molecular potentials for atomistic simulation studies (COMPASSIII) force field. The Ewald approach was used to characterize electrostatic interactions with a precision of 1×10^{-5} kcal/mol (Sun, Ren and Fried, 1998; Sun, Ren and Fried, 1998). The calculation of van der Waals interaction energy was performed using the Atom-based approach. Non-bond interactions were subjected to a cubic spline truncation with a cutoff distance of 18.5 Å (Mamand, Azeez and Qadr, 2023). Monte Carlo simulations are used to forecast the manner in which inhibitor molecules interact with the metal surface. These Monte Carlo simulation data for outputs and descriptors are provided in Table VI. The parameters of the substrate-adsorbate configuration include the total energy, which is the sum of the energies of the adsorbate components, rigid adsorption energy, and deformation energy. Adsorption energy measures the energy generated or needed to adsorb the relaxed adsorbate component onto the substrate. The adsorption energy is the sum of the rigidity and deformation energies for the adsorbate component. The rigid adsorption energy measures the energy generated or required for adsorbing the unrelaxed adsorbate component on the substrate before geometry adjustment. The deformation energy measures the energy released when the adsorbate component relaxes on the substrate surface. Finally, (dEad/dNi) shows the energy of substrate-adsorbate combinations with one adsorbate component removed. This study investigated the adsorption behavior of urolithin derivatives (Uor E, Uor M5, Uor M6, and Uor M7) on iron (Fe(110)), copper (Cu(111)), and aluminum (Al(111)) surfaces using MC simulations as can be seen in Figs. 8-10. Adsorption energies were decomposed into van der Waals, electrostatic, and intramolecular components (results not shown). All energies were negative, signifying a spontaneous adsorption process. The primary goal was to identify the most stable adsorption configurations for each molecule on the chosen metal surfaces, known for their stability. Analysis of Table VI reveals a trend in the negative adsorption energies (indicating stronger adsorption) across the three surfaces: Uor M5 > Uor M6 > Uor E > Uor M7. This suggests that Uor M5 exhibits the most favorable adsorption characteristics, implying superior stability and a stronger affinity for metal surfaces compared to the other urolithin derivatives.

TABLE VI
The Outputs and Descriptors Calculated by the Monte Carlo Simulation for Adsorption of Uroe, Urom5, Urom6, And Urom7 Inhibitors on fe (110), Cu (111), And Al (111) (In Kcal Mol^{-1})

Fe (110)					
Inhibitor	Total energy	Adsorption energy	Rigid adsorption	Deformation energy	$\frac{dE_{ad}}{dN_i}$
Uro E	-166.725	-135.306	-136.056	0.750011	-135.306
Uro M5	-149.344	-140.133	-140.681	0.547236	-140.133
Uro M6	-156.143	-138.493	-138.978	0.485144	-138.493
Uro M7	-180.884	-130.711	-131.518	0.806903	-130.711
Cu (111)					
Uro E	-104.649	-73.2292	-73.6061	0.376818	-73.2292
Uro M5	-85.1371	-75.9262	-76.1607	0.234514	-75.9262
Uro M6	-92.495	-74.8441	-75.0469	0.202769	-74.8441
Uro M7	-120.865	-70.6923	-71.012	0.319699	-70.6923
Al (111)					
Uro E	-99.3766	-67.9572	-68.257	0.299823	-67.9572
Uro M5	-79.7369	-70.526	-70.6891	0.163137	-70.526
Uro M6	-87.116	-69.4651	-69.6028	0.137712	-69.4651
Uro M7	-115.865	-65.692	-65.9318	0.23977	-65.692
Ni (111)					
Uro E	-115.326	-83.9067	-84.3779	0.471165	-83.9067
Uro M5	-96.0763	-86.8654	-87.1986	0.333158	-86.8654
Uro M6	-102.818	-85.1675	-85.5571	0.389566	-85.1675
Uro M7	-131.126	-80.9528	-81.3577	0.404844	-80.9528

IV. CONCLUSION

This study explores the potential of four urolithin derivatives (Uro E, Uro M5, Uro M6, and Uro M7) as corrosion inhibitors using quantum chemical calculations. The investigation aimed to identify relationships between various molecular properties and their predicted corrosion inhibition effectiveness. Our findings suggest that increasing ionization energy, electron affinity, and softness while decreasing the energy band gap and electronegativity could enhance corrosion resistance. Protonation appears to be a promising strategy, with Uro E exhibiting the highest predicted efficacy based on nucleophilic and electrophilic characteristics. Lower ω and higher ε values for Uro E further support its potential for electron donation to the metal surface. Topological analysis revealed weak hydrogen-bonding interactions within the molecules, potentially influencing their behavior. A negative Gibbs free energy (ΔG) indicates a spontaneous adsorption process, which is desirable for corrosion inhibitors. This study suggests that inhibitor molecules (E, M5, M6, M7) might transition from weak physical adsorption (physisorption) to stronger chemical adsorption (chemisorption) with increasing temperature. This chemisorption, characterized by stronger bonds between the inhibitor and metal surface, is crucial for effective corrosion inhibition. Estimated absorption spectra suggest a correlation between high absorption (Uro M5) and potential susceptibility to corrosion, while lower absorption (Uro M7) might indicate better resistance. Finally, Fukui function analysis suggests that oxygen atoms with higher values could exhibit stronger adsorption capabilities. Overall, this study provides insights into the potential of urolithin derivatives as corrosion inhibitors and highlights the importance of considering various molecular properties for optimizing their effectiveness.

V. ACKNOWLEDGMENT

The author like to express our gratitude to Koya University's Chemistry Department for their assistance and support in our endeavor.

REFERENCES

Abbaz, T., Bendjeddou, A., and Villemin, D., 2018. Molecular structure, NBO analysis, first-hyperpolarizability, and homo-lumo studies of π-extended tetrathiafulvalene (EXTTF) derivatives connected to π-nitro phenyl by density functional method. *International Journal of Advanced Chemistry*, 6, p.114-120.

Akman, F., Demirpolat, A., Kazachenko, A.S., Kazachenko, A.S., Issaoui, N., and Al-Dossary, O.J.M., 2023. Molecular Structure, Electronic Properties, Reactivity (ELF, LOL, and Fukui), and NCI-RDG Studies of the Binary Mixture of Water and Essential Oil of *Phlomis bruguieri*. *Molecules*, 28, p.2684

Arulaabaranam, K., Muthu, S., Mani, G., and Geoffrey, A.B., 2021. Speculative assessment, molecular composition, PDOS, topology exploration (ELF, LOL, RDG), ligand-protein interactions, on 5-bromo-3-nitropyridine-2-carbonitrile. *Heliyon*, 7, p.e07061.

Asath, R.M., Rekha, T., Premkumar, S., Mathavan, T., and Benial, A.M.F., 2016. Vibrational, spectroscopic, molecular docking and density functional theory studies on N-(5-aminopyridin-2-yl) acetamide. *Journal of Molecular Structure*, 1125, pp.633-642.

Asif, M., Sajid, H., Ayub, K., Gilani, M.A., Anwar, N., and Mahmood, T., 2023. Therapeutic potential of oxo-triarylmethyl (oxTAM) as a targeted drug delivery system for nitrosourea and fluorouracil anticancer drugs; A first principles insight.

Journal of Molecular Graphics and Modelling, 122, p.108469.

Bader, R.F., 2010. Definition of molecular structure: By choice or by appeal to observation? *The Journal of Physical Chemistry A*, 114, pp.7431-7444.

Becke, A.D., 1996. *Density-Functional Thermochemistry*. *Book of Abstracts, 212th ACS National Meeting*, Orlando, FL.

Boughoues, Y., Benamira, M., Messaadia, L., and Ribouh, N., 2020. Adsorption and corrosion inhibition performance of some environmental friendly organic inhibitors for mild steel in HCl solution via experimental and theoretical study. *Colloids and Surfaces A: Physicochemical and Engineering Aspects*, 593, p.124610.

Boukabcha, N., Benmohammed, A., Belhachemi, M.H.M., Goudjil, M., Yahiaoui, S., Megrouss, Y., Djafri, A., Khelloul, N., Benyehlou, Z.D., and Djafri, A., 2023. Spectral investigation, TD-DFT study, hirshfeld surface analysis, NCI-RDG, HOMO-LUMO, chemical reactivity and NLO properties of 1-(4-fluorobenzyl)-5-bromolindolin-2, 3dione. *Journal of Molecular Structure*, 1285, p.135492.

Caid, Z.A.E., Left, D.B., Thoume, A., Kellal, R., and Zertoubi, M., 2023. A comprehensive computational study of N-phenylacetamide derivatives as corrosion inhibitors for copper: Insights from DFT and Molecular Dynamics. *Journal of Bio-and Tribo-Corrosion*, 9, p.83.

Chen, C., Jiang, L., Guo, M.Z., Xu, P., Chen, L., and Zha, J., 2019. Effect of sulfate ions on corrosion of reinforced steel treated by DNA corrosion inhibitor in simulated concrete pore solution. *Construction and Building Materials*, 228, p.116752.

Dennington, R., Keith, T.A., and Millam, J.M., 2016. *GaussView, Version 6.0. 16*. Semichem Inc., Shawnee Mission KS.

Domingo, L.R., Aurell, M.J., Pérez, P., and Contreras, R., 2002. Quantitative characterization of the global electrophilicity power of common diene/dienophile pairs in Diels-Alder reactions. *Tetrahedron*, 58, pp.4417-4423.

Ech-Chihbi, E., El Hajjaji, F., Titi, A., Messali, M., Kaya, S., Serdaroğlu, G., Hammouti, B., and Taleb, M., 2024. Towards understanding the corrosion inhibition mechanism of green imidazolium-based ionic liquids for mild steel protection in acidic environments. *Indonesian Journal of Science and Technology*, 9, pp.395-420.

El Aoufir, Y., El Bakri, Y., Lgaz, H., Zarrouk, A., Salghi, R., Warad, I., Ramli, Y., Guenbour, A., Essassi, E., and Oudda, H., 2017. Understanding the adsorption of benzimidazole derivative as corrosion inhibitor for carbon steel in 1 M HCl: Experimental and theoretical studies. *Journal of Materials and Environmental Science*, 8, pp.3290-3302.

Fan, B., Zhao, X., Liu, Z., Xiang, Y., and Zheng, X., 2022. Inter-component synergetic corrosion inhibition mechanism of Passiflora edulia Sims shell extract for mild steel in pickling solution: Experimental, DFT and reactive dynamics investigations. *Sustainable Chemistry and Pharmacy*, 29, p.100821.

Fayomi, O.M., Chahul, H.F., Ike, D.C., Ndukwe, G.I., and Phoebe, I.M., 2021. Thermodynamic and adsorption study of the corrosion inhibition of mild steel by aframomum chrysanthum extract in 0.1 M hydrochloric acid solution. *Asian Journal of Applied Chemistry Research*, 8, pp.64-73.

Frisch, M., Clemente, F.M.J., Frisch, G.W., Trucks, H.B., Schlegel, G.E., Scuseria, M.A., Robb, J.R., Cheeseman, G., Scalmani, V., Barone, B., Mennucci, G.A., Petersson, H., Nakatsuji, M., Caricato, X., Li, H.P., Hratchian, A.F., Izmaylov, J., Bloino, G., Zheng, J.L., Sonnenberg, M., Hada, M., Ehara, K., Toyota, R., Fukuda, J., Hasegawa, M., Ishida, T., Nakajima, Y., Honda, O., Kitao, H., Nakai, T., Vreven, J.A., Montgomery, J.E. Jr., Peralta, F., Ogliaro, M., Bearpark, J.J., Heyd, E., Brothers, K.N., Kudin, V.N., Staroverov, T., Keith, R., Kobayashi, J., Normand, K., Raghavachari, A., Rendell, J.C., Burant, S.S., Iyengar, J., Tomasi, M., Cossi, N., Rega, J.M., Millam, M., Klene, J.E., Knox, J.B., Cross, V., Bakken, C., Adamo, J., Jaramillo, R., Gomperts, R.E., Stratmann, O., Yazyev, A.J., Austin, R., Cammi, C., Pomelli, J.W., Ochterski, R.L., Martin, K., Morokuma, V.G., Zakrzewski, G.A., Voth, P., Salvador, J.J., Dannenberg, S., Dapprich, A.D., Daniels, O., Farkas, J.B., Foresman, J.V., Ortiz, J., Cioslowski, D.J., 2013. *Fox, Gaussia*n *09, Revisio*n *D.0*1. Gaussian Inc., Wallingford.

Frisch, M.J., Pople, J.A., and Binkley, J.S., 1984. Self-consistent molecular orbital methods 25. Supplementary functions for Gaussian basis sets. *The Journal of Chemical Physics*, 80, pp.3265-3269.

Gowers, R.J., Farmahini, A.H., Friedrich, D., and Sarkisov, L., 2018. Automated analysis and benchmarking of GCMC simulation programs in application to gas adsorption. *Molecular Simulation*, 44, pp.309-321.

Guruprasad, A., Sachin, H., Swetha, G., and Prasanna, B., 2020. Corrosion inhibition of zinc in 0.1 M hydrochloric acid medium with clotrimazole: Experimental, theoretical and quantum studies. *Surfaces and Interfaces*, 19, pp.100478

Hamad, A.R., Ahmed, K.M., Omer, R.A., Azeez, Y.H., Kareem, R.O., Othman, K.A., and Amin, A.A., 2025. Synthesis, characterization and computational study of thiourea-based dihydropyrimidine derivatives: A focus on adsorption and reactivity. *Journal of Molecular Structure*, 1325, p.140950.

Hameed, R.A., Abu-Nawwas, A.A.H., and Shehata, H., 2013. Nano-composite as corrosion inhibitors for steel alloys in different corrosive media. *Advances in Applied Science Research*, 4, pp.126-129.

Hazani, N.N., Mohd, Y., Ghazali, S.A.I.S.M., Farina, Y., and Dzulkifli, N.N., 2019. Electrochemical studies on corrosion inhibition behaviour of synthesised 2-acetylpyridine 4-ethyl-3-thiosemicarbazone and its Tin (IV) complex for mild steel in 1 M HCl solution. *Journal of Electrochemical Science and Technology*, 10, pp.29-36.

Hekim, S., Azeez, Y.H., and Akpinar, S., 2019. The theoretical investigation of the HOMO, LUMO energies and chemical reactivity of C9H12 and C7F3NH5Cl molecules. *Journal of Physical Chemistry and Functional Materials*, 2, pp.29-31.

Hssain, A., 2022. DFT modelling studies of spectroscopic properties and medium effects on molecular reactivity of secnidazole in different solvents. *Journal of Physical Chemistry and Functional Materials*, 5, pp.69-83.

Humphrey, W., Dalke, A., and Schulten, K., 1996. VMD: Visual molecular dynamics. *Journal of Molecular Graphics*, 14, pp.33-38, 27-28.

İsen, F., Kaygili, O., Bulut, N., Ates, T., Osmanlıoğlu, F., Keser, S., Tatar, B., Özcan, I., Ates, B., and Ercan, F., 2023. Experimental and theoretical characterization of Dy-doped hydroxyapatites. *Journal of The Australian Ceramic Society*, 59, pp.849-864.

Jumabaev, A., Holikulov, U., Hushvaktov, H., Issaoui, N., and Absanov, A., 2023. Intermolecular interactions in ethanol solution of OABA: Raman, FTIR, DFT, M062X, MEP, NBO, FMO, AIM, NCI, RDG analysis. *Journal of Molecular Liquids*, 377, p.121552.

Kareem, R.O., Omer, R.A., Ahmed, K.M., and Azeez, Y.H., 2024. DFT and Monte Carlo simulation studies of potential corrosion inhibition properties of some basic heterocyclic compounds. *Molecular Simulation*, 50, pp.1447-1464.

Koparir, P., Omar, R.A., Sarac, K., Ahmed, L.O., Karatepe, A., Taskin-Tok, T., and Safin, D.A., 2023. Synthesis, characterization and computational analysis of thiophene-2, 5-diylbis ((3-mesityl-3-methylcyclobutyl) methanone. *Polycyclic Aromatic Compounds*, 43, pp.6107-6125.

Korkmaz, A.A., Ahmed, L.O., Kareem, R.O., Kebiroglu, H., Ates, T., Bulut, N., Kaygili, O., and Ates, B., 2022. Theoretical and experimental characterization of Sn-based hydroxyapatites doped with Bi. *Journal of the Australian Ceramic Society*, 58, pp.803-815.

Krishnan, R., Binkley, J.S., Seeger, R., and Pople, J.A., 1980. Self-consistent molecular orbital methods. XX. A basis set for correlated wave functions. *The Journal of Chemical Physics*, 72, pp.650-654.

Lu, T., and Chen, F., 2012. Multiwfn: A multifunctional wavefunction analyzer. *Journal of Computational Chemistry*, 33, pp.580-592.

Mamad, D.M., Omer, R.A., and Othman, K.A., 2023a. Quantum chemical analysis of amino acids as anti-corrosion agents. *Corrosion Reviews*, 41, pp.703-717.

Mamad, D.M., Rasul, H.H., Awla, A.H., and Omer, R.A., 2023b. Insight into corrosion inhibition efficiency of imidazole-based molecules: A quantum chemical study. *Doklady Physical Chemistry*, 511, pp.125-133.

Mamand, D.M., Azeez, Y.H., and Qadr, H.M., 2023. Monte carlo and DFT calculations on the corrosion inhibition efficiency of some benzimide molecules. *Mongolian Journal of Chemistry*, 24, pp.1-10.

Merdas, S.M., 2021. Synthesis, characterization and DFT studies of new Azo-Schiff base and evaluation as corrosion inhibitor. *Annals of the Romanian Society for Cell Biology*, 25, pp.910-928.

Metropolis, N., Rosenbluth, A.W., Rosenbluth, M.N., Teller, A.H., and Teller, E., 1953. Equation of state calculations by fast computing machines. *The Journal of Chemical Physics*, 21, pp.1087-1092.

Murthy, Z.V.P., and Vijayaragavan, K., 2014. Mild steel corrosion inhibition by acid extract of leaves of *Hibiscus sabdariffa* as a green corrosion inhibitor and sorption behavior. *Green Chemistry Letters and Reviews*, 7, pp.209-219.

Mustafa, M.D., and Mohammad, Q.H., 2023. Quantum chemical and monte carlo simulations on corrosion inhibition efficiency of 2-mercapto-5-phenylfuran and bis (pyridyl) oxadiazoles. *Izvestiya Vysshikh Uchebnykh Zavedeniy Khimiya Khimicheskaya Tekhnologiya*, 66, pp.33-45.

Nam, K., Gao, J., and York, D.M., 2005. An efficient linear-scaling Ewald method for long-range electrostatic interactions in combined QM/MM calculations. *Journal of Chemical Theory and Computation*, 1, pp.2-13.

Norouzbahari, M., Burgaz, E.V., Ercetin, T., Fallah, A., Foroumadi, A., Firoozpour, L., Sahin, M.F., Gazi, M., and Gulcan, H.O., 2018. Design, synthesis and characterization of novel urolithin derivatives as cholinesterase inhibitor agents. *Letters in Drug Design and Discovery*, 15, pp.1131-1140.

Omer, R.A., Ahmed, K.M., Othman, K.A., Hamad, W.M., Faraj, R.K., Muhialdin, A.J., and Salih, S.K., 2024. New thiazole derivatives. *Aro-The Scientific Journal of Koya University*, 12, pp.10-22.

Özbakır Işin, D., Karakuş, N., Lgaz, H., Kaya, S., and Chung, I., 2020. Theoretical insights about inhibition efficiencies of some 8-Hydroxyqionoline derivatives against the corrosion of mild steel. *Molecular Simulation*, 46, pp.1398-1404.

Predko, P., Rajnovic, D., Grilli, M.L., Postolnyi, B.O., Zemcenkovs, V., Rijkuris, G., Pole, E., and Lisnanskis, M., 2021. Promising methods for corrosion protection of magnesium alloys in the case of Mg-Al, Mg-Mn-Ce and Mg-Zn-Zr: A recent progress review. *Metals*, 11, p.1133.

Qader, İ.N., Mohammad, A., Azeez, Y.H., Agid, R.S., Hassan, H.S., and Al-Nabawi, S.H.M., (2019). Chemical structural and vibrational analysis of potassium acetate: A density function theory study. *Journal of Physical Chemistry and Functional Materials*, 2, pp.23-25.

Qadr, H.M., and Mamand, D.M., 2023. A computational study of substituent effect 1, 3, 4-thiadiazole on corrosion inhibition. *Azerbaijan Chemical Journal*, pp.19-29.

Rani, B., and Basu, B.B.J., 2012. Green inhibitors for corrosion protection of metals and alloys: An overview. *International Journal of Corrosion*, 2012, p.380217.

Rasul, H.H., Mamad, D.M., Azeez, Y.H., Omer, R.A., and Omer, K.A., 2023. Theoretical investigation on corrosion inhibition efficiency of some amino acid compounds. *Computational and Theoretical Chemistry*, 1225, p.114177.

Razali, N.Z.K., Wan Hassan, W.N.S., Sheikh Mohd Ghazali, S.A.I., Mohd Shotor, S.N., and Dzulkifli, N.N., 2023. DFT, Fukui indices, and molecular dynamic simulation studies on corrosion inhibition characteristics: A review. *Chemical Papers*, 78, pp.1-17.

Rozas, I., Alkorta, I., and Elguero, J., 2000. Behavior of ylides containing N, O, and C atoms as hydrogen bond acceptors. *Journal of the American Chemical Society*, 122, pp.11154-11161.

Saidj, M., Djafri, A., Rahmani, R., Belkafouf, N.E.H., Boukabcha, N., Djafri, A., and Chouaih, A., 2023. Molecular structure, experimental and theoretical vibrational spectroscopy,(HOMO-LUMO, NBO) investigation,(RDG, AIM) analysis,(MEP, NLO) study and molecular docking of Ethyl-2-{[4-Ethyl-5-(Quinolin-8-yloxyMethyl)-4H-1, 2, 4-Triazol-3-yl] sulfanyl} acetate. *Polycyclic Aromatic Compounds*, 43, pp.2152-2176.

Salih, S.K., Mustafa, R.M., Mamad, D.M., Kaka, K.N., Omer, R.A., and Hamad, W.M., 2023. Synthesis of liquid crystalline benzothiazole based derivatives: Theoretical and experimental study of their optical and electrical properties. *ZANCO Journal of Pure and Applied Sciences*, 35, pp.143-162.

Srivastavaa, A., Kumara, V., Vermaa, A., Guptaa, M., and Dubeya, Y., 2019. Kinetic, Mechanistic and quantum chemical calculations of Ru (III) catalysed redox reaction of aspirin by nbs in acidic medium. *Journal of Information and Computational Science*, 9, pp.516-540.

Sujatha, H., and Lavanya, M., 2023. An insight to HOMO LUMO aspects in corrosion applications. *Canadian Metallurgical Quarterly*, 62, pp.761-772.

Sun, H., 1998. COMPASS: An ab initio force-field optimized for condensed-phase applications overview with details on alkane and benzene compounds. *The Journal of Physical Chemistry B*, 102, pp.7338-7364.

Sun, H., Jin, Z., Yang, C., Akkermans, R.L., Robertson, S.H., Spenley, N.A., Miller, S., and Todd, S.M., 2016. COMPASS II: Extended coverage for polymer and drug-like molecule databases. *Journal of Molecular Modeling*, 22, pp.1-10.

Sun, H., Ren, P., and Fried, J., 1998. The compass force field: Parameterization and validation for phosphazenes. *Computational and Theoretical Polymer Science*, 8, pp.229-246.

Tang, L., and Zhu, W., 2021. Computational design of high energy RDX-based derivatives: Property prediction, intermolecular interactions, and decomposition mechanisms. *Molecules*, 26, p.7199.

Tasić, Ž.Z., Petrović Mihajlović, M.B., Radovanović, M.B., and Antonijević, M.M., 2019. New trends in corrosion protection of copper. *Chemical Papers*, 73, pp.2103-2132.

Uwiringiyimana, E., Joseph, I.V., and ADams, F.V., 2016. The effect of corrosion inhibitors on stainless steels and aluminium alloys: A review. *African Journal of Pure and Applied Chemistry*, 10, pp.23-32.

Xiangrong, X., Zhuanhong, L., and Lei, Y., 2023. The synthesis of urolithins and their derivatives and the modes of antitumor action. *Mini-Reviews in Medicinal Chemistry*, 23, pp.80-87.

Yıldız, C.A., Güney, E., Nasif, V., Karakaş, D., and Erkan, S., 2023. Investigation of substituent effect on rhenium complexes by DFT methods: Structural analysis, IR spectrum, quantum chemical parameter, NLO and OLED properties, molecular docking. *Journal of Molecular Structure*, 1278, p.134835.

Yousif, H.A, and Hanaa, S.H., 2021b. Theoretical study for chemical reactivity descriptors of tetrathiafulvalene in gas phase and gas phase and solvent phases based on density functional theory. *Passer Journal of Basic and Applied Sciences*, 3, pp.167-173.

Yousif, H.A., and Hanaa, S.H., 2021a. Theoretical study for chemical reactivity descriptors of tetrathiafulvalene in gas phase and gas phase and solvent phases based on density functional theory. *Passer Journal of Basic and Applied Sciences*, 3, pp.167-173.

Geochemical Insights into the Paleodepositional Environment of the Garagu Formation, Gara Anticline, Kurdistan, Northern Iraq

Ibrahim M.J. Mohialdeen[1], Tola A. Mirza[1†] and Shahra O. Abdalla[2]

[1]Department of Earth Sciences and Petroleum, College of Science, University of Sulaimani,
Kurdistan Region – F.R. Iraq

[2]Development Center for Research and Training, University of Human Development,
Sulaymaniyah, Kurdistan Region – F.R. Iraq

***Abstract*—The Garagu Formation is mostly composed of carbonate layers with iron-rich horizons in the middle part. The geochemical evidence for the paleodepositional environment of the Garagu Formation in the Kurdistan Region of Iraq's Gara anticline has been explored in this paper. A total of 9 samples from the Garagu Formation were analyzed by XRF for major elements and inductively coupled plasma–mass spectrometer for trace elements. From geochemical data of major and trace elements, including rare earth elements, a series of identification indexes, such as Sr/Ba, Rb/K_2O, Th/U, U/Th, V/(V+Ni), δU, V/Sc, Sr/Cu, and C-Value ratios, are calculated which can be used to indicate, paleosalinity, ancient oxidizing environment, and paleoclimate conditions. As would be predicted in this limestone-dominated deposit, CaO has the greatest weight percentages of any sample. Several samples from the iron-rich mineralization in the middle part of the formation exhibit significant percentages of FeO. The elemental geochemical ratios indicate to saline shallow marine environment with lower salinity in the middle part of the formation. The paleoredox proxies revealed that the oxic to suboxic conditions are prevailed during the deposition of the formation.**

***Index Terms*—Cretaceous, Gara mountain, Garagu formation, Kurdistan, Rare earth element.**

I. INTRODUCTION

The Gara anticline in the Amedi District, Duhok Governorate, is one of the most intriguing geological regions in Kurdistan (Fig. 1). The type localities of the Baluti, Garagu, and Chia Gara formations are located in the core of the anticline (Bellen, et al., 1959, Hanna, 2007, Aljumaily and Abdulla, 2013). Wetzel was the first to study the Garagu Formation (Valanginian-Hauterivian), from its type locality (Bellen, et al., 1959). The research area's Garagu Formation comprises several limestone beds with siltstones, sandy limestones, and oolitic limestones (Mirza, Mohialdeen and Awadh, 2016, Ghafor and Mohialdeen, 2016; 2018). New paleontological studies indicated to Valanginian-Barremian age of the Garagu Formation (Amin, 1989, Ghafor and Mohialdeen, 2018). The Garagu Formation is divided into three sections reaching a maximum thickness of 92 m (Mirza, Mohialdeen and Awadh, 2016). The lower part of the Garagu Formation (46 m) consists of oolitic and coarse sandstone and sandy, oolitic limestones with a rich fauna. The middle part of the succession (22 m) includes organic detrital limestones. The top 24 m of the formation includes ferruginous oolitic marls and sandstones.

A recent sedimentological study of the Garagu Formation, conducted by (Mahdi and Al-Zaidy, 2024), examined three subsurface sections through microfacies analyses. The study revealed a diverse range of depositional environments, spanning from restricted marine to open marine, as well as mid-to outer ramp settings.

Previous studies have utilized geochemical parameters to explore the paleo-oxygenation conditions of ancient sediments (Mustafa and Tobia, 2020, Al-Juboury, et al., 2023, Yu, et al., 2023, Xiao, et al., 2024). The present study investigates the geochemistry of major and trace elements of the Garagu Formation. Specifically, it focuses on the geochemical data as evidence to infer the paleodepositional conditions of this formation. This research aims to enhance our understanding of the depositional conditions of the Early Cretaceous Garagu Formation.

II. GEOLOGICAL SETTING

Within the High Folded Zone of northern Iraq, the Gara anticline is a double plunging fold that runs E-W for approximately 80 km in length and 12 km in breadth, parallel to the Taurus Mountains (Aljumaily and Abdulla, 2013). The High Folded Zone is between 25 and 50 km wide. In this zone, the folds are aligned with an E-W trend in northern Iraq and an NW-SE trend in northeastern Iraq. With steeper S- or SW-dipping limbs and occasionally a thrust fault in the

ARO-The Scientific Journal of Koya University
Vol. XIII, No. 1 (2025), Article ID: ARO.11910. 10 pages
DOI: 10.14500/aro.11910
Received: 22 November 2024; Accepted: 03 February 2025
Regular research paper; Published: 13 February 2025
†Corresponding author's e-mail: tola.merza@univsul.edu.iq

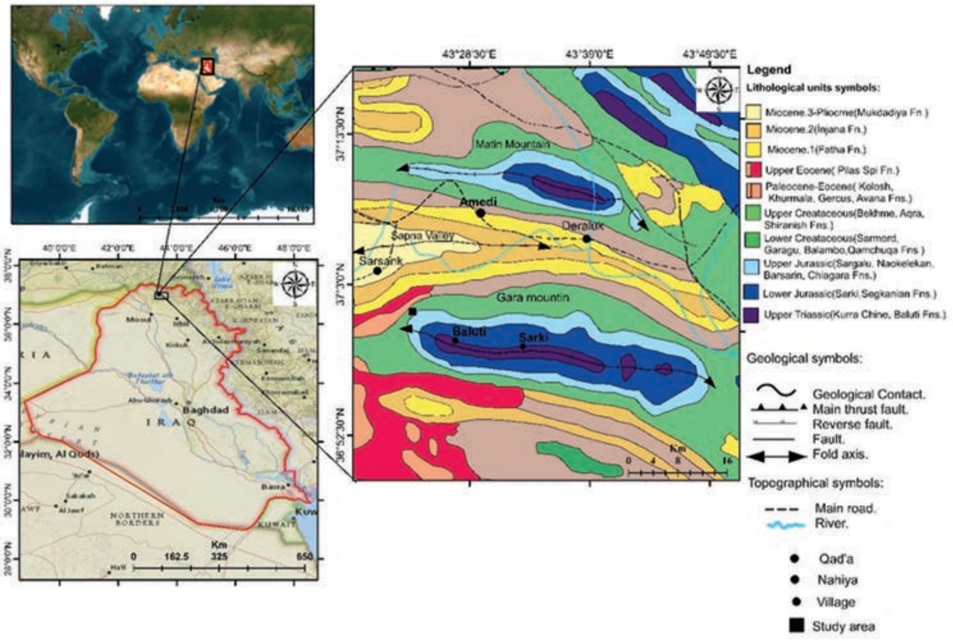

Fig. 1. Geological map of Gara anticline and the surrounding areas modified after (Hanna, 2007; Mirza, Mohialdeen and Awadh, 2016).

steeper limb, the folds are primarily asymmetrical (Jassim and Goff, 2006). The stratigraphic succession of the anticline, from the Late Triassic to the Late Miocene, is documented (Bellen, et al., 1959).

The type locality of the Garagu Formation, situated within the Gara anticline, is located approximately 600 m north of Garagu Village in the Gali Garagu Valley at coordinates N 37° 1' 06" and E 43° 23' 24.1" (Fig. 1). Differently colored limestone layers with varying faunal contents make up the succession. The beds have a 272° strike; a 62° dip angle, and a 002° dip direction. The total thickness of this section, as determined by Wetzel (Bellen, et al., 1959), is around 2 m more than the 89.9 m shown here (Fig. 2). Soil covered a tiny portion of the outcrops in the region under study (Fig. 2).

The lower contact is conformable and gradational, and it is with the Tithonian-Berriasian Chia Gara Formation (Bellen, et al., 1959). The contact occurs above the dark limestone strata of the Chia Gara Formation and at the start of the siltstone and oolitic limestone beds of the Garagu Formation. The top of the peloidal limestone and the start of the yellowish marl strata mark the gradational upper contact with the Sarmord Formation (Valanginian-Aptian) (Mirza, Mohialdeen and Awadh, 2016, Ghafor and Mohialdeen, 2018).

III. Samples and Methods

Fig. 2 displays the locations of the 20 samples that were taken from the Garagu Formation outcrop from the Gara anticline. These samples were previously studied from the paleontological points of view (Ghafor and Mohialdeen, 2016; 2018), as well as from iron mineralization within the middle part of the formation (Mirza, Mohialdeen and Awadh, 2016). The major and trace elements (including REE) contents of nine selected samples were determined using the XRF, and inductively coupled plasma–mass spectrometer (ICP-MS) techniques, respectively. Samples were prepared (dissolved in acid and filtering) and measurements were taken at Washington State University, School of Environmental Science, USA. By performing repeated analyses of samples and laboratory standards, reproducibility and accuracy were verified.

All samples' measured REE contents were normalized to Post-Archean Australian Shale (PAAS, Taylor and McLennan, 1985). The equations listed as follows: (i) δEu= $Eu_N/(Sm_N{*}Gd_N)^{0.5}$, and (ii) δCe= $3Ce_N/(2La_N+Nd_N)$ have been used to test whether a real Eu and Ce anomalies exist (Bau and Dulski, 1996; MacLeod and Irving, 1996; Shields and Stille, 2001; Lawrence, et al., 2006; Ozyurt, Kirmaci and Al-Aasm, 2019; Ozyurt, et al., 2020; Mirza, et al., 2021; Xu, et al., 2023; Xiao, et al., 2024). The following formula is also used to determine the authigenic uranium (δU): $\delta U = U/[0.5 \times (Th/3 + U)]$ (Yu, et al., 2023).

IV. Results

A. Major Elements

Table I reports the major oxide component of the Garagu Formation. In general, the analyzed samples from the Garagu Formation have high CaO content (32.42–52.96%). SiO_2 content and other oxides are greatly diluted by such content (2.37–8.98%), Al_2O_3 (0.39–3.82%), FeO (0.95–19.73%), MgO (0.39–3.77%), Na_2O (0.01–0.03%), K_2O (0.05–0.46%), MnO (0.025–0.085%), TiO_2 (0.032–0.262%), and P_2O_5 (0.005–0.174%). In comparison to the PAAS, the examined samples exhibit depletion in every element except CaO and FeO (Fig. 3). The CaO enrichment in these samples indicates the calcium carbonate composition of the rocks. The high occurrence of iron mineralization in the Garagu Formation, especially the middle part (Mirza, Mohialdeen and Awadh, 2016) is the consequence of the high occurrence of FeO (Table I and Fig. 3).

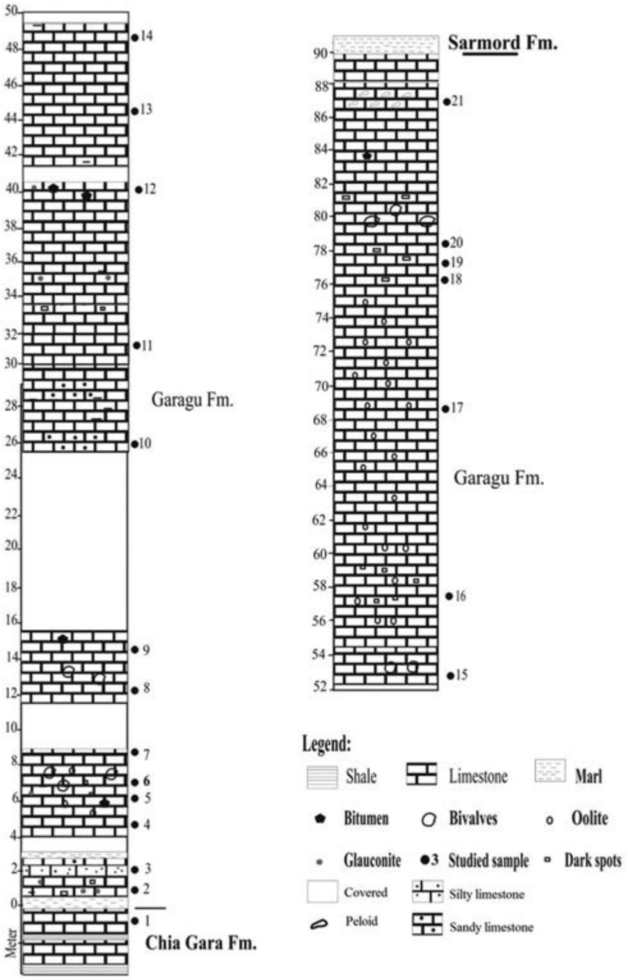

Fig. 2. Garagu Formation stratigraphic column, Gara Anticline, Amedi District, Duhok Governorate, Kurdistan, after (Mirza, Mohialdeen and Awadh, 2016).

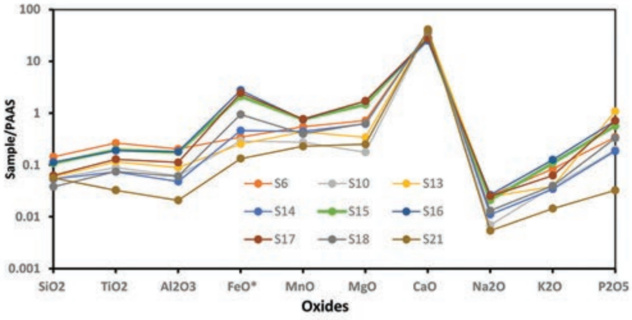

Fig. 3. PAAS-normalized diagram for major oxides of the Garagu Formation PAAS values after (Taylor and McLennan, 1985).

B. Trace Elements

Table II lists the trace element composition of the Garagu Formation. In comparison to PAAS, the examined samples exhibit depletion in almost all other elements and enrichment in Sr and, in certain cases, V (Fig. 4).

C. Rare Earth Elements (REE)

Table III indicates the low content of REE in the analyzed samples. A variety of REE characteristics may be calculated to characterize the enrichment and origins of REE, reflecting geochemical properties (Table IV). The content of total REEs (ΣREE) in the studied samples from the Garagu Formation ranged from 19.57 ppm to 132.38 ppm (average = 80.04 ppm), significantly lower than for upper continental crust (UCC; 146.37 ppm) and (PAAS;184.77 ppm) (Table IV and Fig. 5).

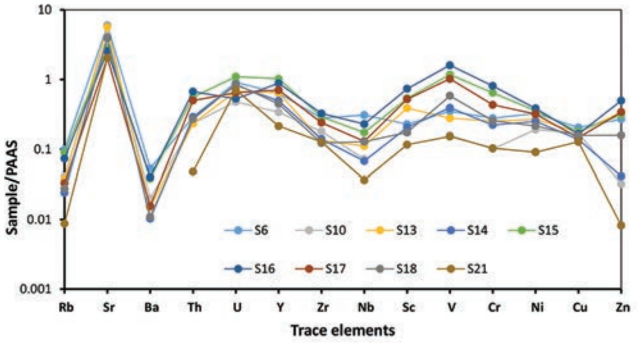

Fig. 4. PAAS-normalized diagram for trace elements of the Garagu Formation PAAS value after (Taylor and McLennan, 1985).

The REE patterns are enriched in MREE relative to LREE and HREE, in other words, it has a bell shape, which is due to the iron oxides enrichment (Fig. 5). However, there is a small difference between the patterns of the study samples and UCC, but still indicating that the source of sediments in Garagu Basin mainly comes from the upper crust. La/Yb -∑REE diagram of the Garagu Formation indicates the sedimentary rocks origin of these sediments (Fig. 6).

V. DISCUSSION

A. General Distribution of ELEMENTs

A substantial correlation of −0.563 between ΣREE and CaO suggests that the main control on the REE concentrations is the effect of dilution by carbonate materials (Table V). The enrichment of the samples with Sr indicates the association with the carbonate phase, especially calcite mineral (Mustafa and Tobia, 2020; Ozyurt, et al., 2020). Furthermore, there is a clear link between the ΣREE and SiO_2, Al_2O_3, and total FeO (0.549, 0.737, and 0.429, respectively, Table V) suggest the typical role of clay minerals on the distribution of REEs (Mclennan, 2018; Condie, 1991). The variation in the total REE concentration of the Garagu Formation (Table IV) indicates that the Early Cretaceous sediments' geochemical circumstances varied to some degree. The degree of difference between the light and heavy REEs in the samples may be determined by looking at the ratio of light REEs (LREE) to heavy REEs (HREE) content (Ozyurt, Kirmaci and Al-Aasm, 2019; Xiao, et al., 2024). The ratio of LREE/HREE in the Garagu Formation ranged between 4.57 and 8.14 which is much lesser than the LREE/HREE value of 9.49 in the PAAS (Taylor and McLennan, 1985). This indicates enrichment with LREE and a relative loss of HREE. However, this result does not coincide with the pattern, which is enriched in MREE (Fig. 5). Regarding the iron-rich samples (i.e. S15, S16, and S17), they are generally enriched with ΣREE (Table IV); however, no significant correlation (+0.429) between FeO and ΣREE content is present (Table V).

The studied limestone beds have variable ΣREEs (19.57–132.38 ppm and avg. 80.04 ppm), Y (5.80–27.66 ppm; avg. 15.24 ppm), and Ho (0.17–1.1; avg. 0.60 ppm) contents.

TABLE I

Major Oxide Contents (wt. %) for the Garagu Formation After (Mirza, Mohialdeen and Awadh, 2016); Compared with PAAS (Taylor and McLennan, 1985)

Sample ID	SiO_2	TiO_2	Al_2O_3	FeO*	MnO	MgO	CaO	Na_2O	K_2O	P_2O_5	LOI	Total
S6	8.98	0.262	3.82	2.46	0.060	1.58	45.30	0.03	0.31	0.055	36.87	99.72
S10	3.38	0.088	1.16	2.08	0.030	0.39	51.02	0.01	0.14	0.031	40.95	99.28
S13	3.68	0.114	1.67	1.82	0.048	0.75	51.10	0.03	0.14	0.174	40.37	99.90
S14	3.33	0.073	0.90	3.30	0.049	1.36	49.27	0.01	0.13	0.030	41.40	99.86
S15	6.70	0.194	3.33	15.12	0.083	3.20	35.79	0.02	0.40	0.091	34.56	99.50
S16	7.06	0.188	3.37	19.73	0.083	3.72	32.42	0.03	0.46	0.114	32.89	100.06
S17	3.89	0.127	2.10	17.53	0.085	3.77	35.82	0.03	0.23	0.114	36.24	99.94
S18	2.37	0.074	1.13	6.75	0.044	1.39	47.87	0.02	0.15	0.053	39.73	99.57
S21	3.48	0.032	0.39	0.95	0.025	0.55	52.96	0.01	0.05	0.005	41.33	99.78
PAAS	62.4	0.99	18.78	7.18	0.11	2.19	1.29	1.19	3.68	0.16	6	103.97

FeO*: Total FeO, LOI: Loss on ignition

TABLE II

Trace element Concentrations (ppm) for the Garagu Formation; Compared with PAAS (Taylor and McLennan, 1985)

Sample ID	Large ion lithophile elements			High-field strength elements					Transition elements					
	Rb	Sr	Ba	Th	U	Y	Zr	Nb	Sc	V	Cr	Ni	Cu	Zn
S6	15.77	1194.68	34.73	4.24	2.83	17.19	58.70	5.89	3.65	52.38	30.61	17.89	10.24	22.95
S10	6.51	856.23	13.03	3.43	1.49	9.14	37.77	1.37	0.00	23.89	11.09	10.51	8.46	2.74
S13	5.97	1145.77	9.61	3.40	2.11	17.34	28.05	2.11	6.21	41.82	27.76	14.88	8.67	28.93
S14	3.87	805.47	6.68	4.22	2.58	13.35	29.32	1.29	3.28	58.92	24.48	13.82	6.91	3.51
S15	14.24	569.27	24.96	8.12	3.41	27.66	61.38	3.30	8.59	176.34	70.98	19.54	8.95	26.49
S16	11.77	508.76	26.01	9.77	1.65	23.78	68.25	4.36	11.77	240.84	89.11	21.19	8.24	42.26
S17	5.30	408.00	10.12	7.30	2.00	19.07	50.55	2.47	8.36	153.50	47.67	17.54	7.30	28.96
S18	4.41	779.64	7.08	3.94	2.67	12.06	25.71	2.44	2.78	87.58	28.30	11.83	7.89	13.46
S21	1.39	406.12	0.00	0.70	2.20	5.80	26.74	0.70	1.86	22.85	11.37	4.99	6.38	0.70
PAAS	160.00	200.00	650.00	14.60	3.10	27.00	210.00	19.00	16.00	150.00	110.00	55.00	50.00	85.00
LDL.	0.2	0.1	0.5	0.1	0.1	0.5	2.0	0.2	1.6	5.0	3.0	3.5	5.0	0.3

TABLE III

Rare Earth Element concentrations (ppm) for Selected Samples of the Garagu Formation, Duhok Governorate, Kurdistan, Iraq

Sample	Thickness (m)	La	Ce	Pr	Nd	Sm	Eu	Gd	Tb	Dy	Ho	Er	Tm	Yb	Lu
S6	7.00	20.48	41.99	5.41	22.15	4.62	1.07	4.34	0.66	3.71	0.71	1.83	0.25	1.48	0.23
S10	26.00	8.49	16.35	2.15	8.83	1.84	0.40	1.65	0.25	1.36	0.26	0.65	0.09	0.51	0.08
S13	44.50	17.47	43.68	5.78	24.93	5.48	1.18	4.76	0.66	3.37	0.60	1.40	0.18	0.99	0.14
S14	48.50	11.23	27.25	3.50	14.74	3.37	0.77	3.17	0.47	2.57	0.47	1.13	0.15	0.84	0.13
S15	52.50	20.18	49.41	6.37	27.33	6.93	1.68	7.12	1.10	5.96	1.10	2.66	0.35	1.91	0.28
S16	57.50	11.19	28.20	3.57	14.80	3.89	0.92	4.09	0.70	4.02	0.76	1.96	0.28	1.65	0.24
S17	69.00	16.99	40.34	5.06	21.59	5.32	1.27	5.43	0.87	4.84	0.91	2.23	0.29	1.77	0.26
S18	76.40	8.41	20.15	2.57	10.86	2.66	0.60	2.62	0.39	2.17	0.40	0.95	0.12	0.70	0.10
S21	87.20	3.37	6.89	0.97	4.08	0.97	0.22	0.97	0.15	0.87	0.17	0.44	0.06	0.35	0.05
PAAS		38.20	79.60	8.83	33.90	5.55	1.08	4.66	0.77	4.68	0.99	2.85	0.41	2.82	0.43
UCC		30.00	64.00	7.10	26.00	4.50	0.88	3.80	0.64	3.50	0.80	2.30	0.33	2.20	0.32

TABLE IV

REE Geochemical Characters of the Garagu Formation, Duhok Governorate, Kurdistan, NE Iraq

S.No.	Thickness (m)	∑REE	LREE	HREE	Sm/Yb	L/H	Y/Ho	Eu/Sm	$(Nd/Yb)_N$	$(Pr/Yb)_N$	δCe	δEu	δPr	δLa	δU
S6	7.00	108.93	95.72	13.21	3.12	7.25	27.69	0.23	1.24	1.17	0.92	1.12	1.04	1.01	0.98
S10	26.00	42.90	38.06	4.85	3.58	7.85	29.39	0.22	1.43	1.34	0.87	1.07	1.05	1.06	1.10
S13	44.50	110.62	98.52	12.10	5.55	8.14	25.97	0.22	2.10	1.87	1.00	1.09	1.02	0.93	1.31
S14	48.50	69.78	60.86	8.93	4.02	6.82	26.29	0.23	1.46	1.33	1.00	1.1	1.02	0.92	1.13
S15	52.50	132.38	111.90	20.48	3.63	5.46	24.85	0.24	1.19	1.07	1.00	1.13	1.01	0.95	0.71
S16	57.50	76.26	62.57	13.70	2.36	4.57	22.47	0.24	0.75	0.69	1.04	1.09	1.02	0.86	0.77
S17	69.00	107.19	90.57	16.60	3.00	5.46	23.59	0.24	1.01	0.91	1.00	1.11	1.00	0.99	0.69
S18	76.40	52.71	45.25	7.45	3.80	6.07	26.50	0.22	1.29	1.17	1.00	1.07	1.01	0.95	1.10
S21	87.20	19.57	16.50	3.06	2.79	5.39	29.56	0.23	0.97	0.89	0.87	1.08	1.07	0.98	1.58

TABLE V

Results of Correlation Coefficient Analysis for the Major Oxides and ∑REE, for the Garagu Formation, Duhok Governorate, Kurdistan, NE Iraq

	SiO_2	TiO_2	Al_2O_3	FeO*	MnO	MgO	CaO	Na_2O	K_2O	P_2O_5	∑REE
SiO_2	1										
TiO_2	**0.941**	1									
Al_2O_3	**0.924**	**0.982**	1								
FeO*	0.316	0.395	0.547	1							
MnO	0.558	$\underline{0.675}$	$\underline{0.771}$	**0.891**	1						
MgO	0.446	0.523	0.648	**0.968**	**0.960**	1					
CaO	−0.540	−0.610	$\underline{-0.733}$	**−0.966**	**−0.954**	**−0.982**	1				
Na_2O	0.521	$\underline{0.681}$	$\underline{0.708}$	0.490	$\underline{0.679}$	0.565	−0.572	1			
K_2O	**0.801**	**0.837**	**0.918**	$\underline{0.764}$	**0.846**	$\underline{0.797}$	**−0.883**	0.582	1		
P_2O_5	0.170	0.365	0.429	0.444	0.575	0.439	−0.442	**0.799**	0.405	1	
∑REE	0.549	$\underline{0.731}$	$\underline{0.737}$	0.429	$\underline{0.761}$	0.558	−0.563	$\underline{0.688}$	0.606	$\underline{0.697}$	1

Bolded: Significant at 0.01 level, Underlined: Significant at 0.05, no. of samples=9

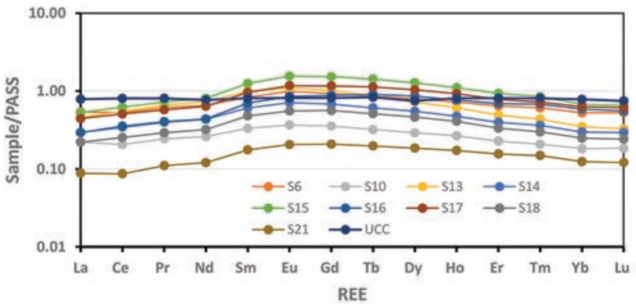

Fig. 5. PAAS-normalized REE pattern for the Garagu Formation PAAS value after (Taylor and McLennan, 1985).

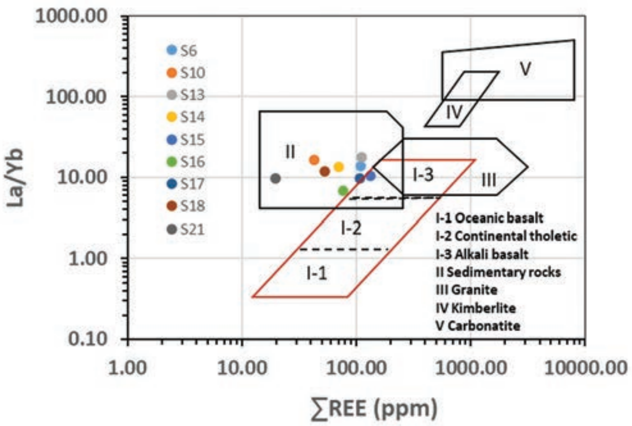

Fig. 6. La/Yb -∑REE diagram of the Garagu Formation, Duhok Governorate, Kurdistan, northeastern Iraq, the diagram after (Xiao, et al., 2024).

Their Y/Ho (22.47–29.56; ave. 26.26) and Eu/Sm (0.22–0.24; avg. 0.23) ratios are mostly similar to those of seawater while their Sm/Yb (2.36–5.55; avg. 3.54) ratios are slightly higher than those of modern seawater (Holser, 1997) (Tables II-IV).

Following normalization of REEs to PAAS (Fig. 5), the limestone samples of Garagu Formation exhibit the following properties; (i) slightly enriched of LREE relative to HREE (Table IV), $(Nd/Yb)_N$ (0.75–2.1; 1.27 avg.), and $(Pr/Yb)_N$ (0.69–1.87; 1.16) (ii) slightly negative δCe (0.87–1.04; ave. 0.97) (Murray, et al., 1991) slight positive δEu (1.07–1.13; avg. 1.10), (iv) slightly flat δPr (1.00–1.07; avg. 1.03) anomalies, and (v) slightly negative to flat δLa anomaly (0.86–1.06; avg. 0.96).

The REE content of the Garagu Formation sediments in the studied section could be useful for determining or estimating several depositional and post-depositional conditions in which the sediments are affected by them. In this section, some influences and properties will be discussed.

B. Effect of Diagenesis

These carbonate rocks of the Garagu Formation may be subjected to a diagenetic process at different levels. The influence of the diagenetic process on REE content may be deduced using the REE-analyzed data (Ozyurt, et al., 2020; Xiao, et al., 2024). Shields and Stille (2001) suggested that the diagenetic process may affect the presence of Ce and Eu related to total REE. They determined that the aberrant Ce values and the correlation between δCe and δEu can be altered by diagenesis. They concluded that the diagenesis impact results from a good positive correlation between δCe and ∑REE, and a good negative correlation between δCe and δEu. The cross plot of δCe and ∑REE for the Garagu Formation samples indicates to a slightly positive correlation between δCe and ∑REE with R^2= 0.3 (Fig. 7a). The link between δCe and δEu (with R^2 = 0.09) in the same sediments is weak or not significant (Fig. 7b). On the other hand, δEu values over 1 may suggest either diagenetic impacts on the REE characteristics or contamination from detrital input to the basin (Murray, et al., 1991; Abedini and Calagari, 2015; Ozkan, 2019). Fig. 7a and b, together with Table IV, indicate that diagenesis has little impact on the REE geochemical characteristics of the Garagu Formation samples, which predominantly reflect their original sedimentary attributes.

Two crucial factors in REE interpretations are δEu and δCe, which show the anomalous degree of δEu and δCe, respectively. Eu remains in a positive trivalent state within the oxidation environment (Tribovillard, et al., 2006; Xiao, et al., 2024). As mentioned previously, the δEu values are around 1.0 (Table IV) indicating a slightly positive anomaly. Ce typically has two valence states, Ce^{3+} and Ce^{4+}, as a result of ambient redox conditions and pH variations. In the oxidizing environment, Ce^{3+} will be oxidized to Ce^{4+}, increasing the concentration of Ce^{4+} in sediments and an enrichment of Ce in sediments (Xiao, et al., 2024). Ce can be used in the reconstruction of paleoredox conditions in the oceans (e.g. Pattan, et al., 2005; Tostevin, et al., 2016).

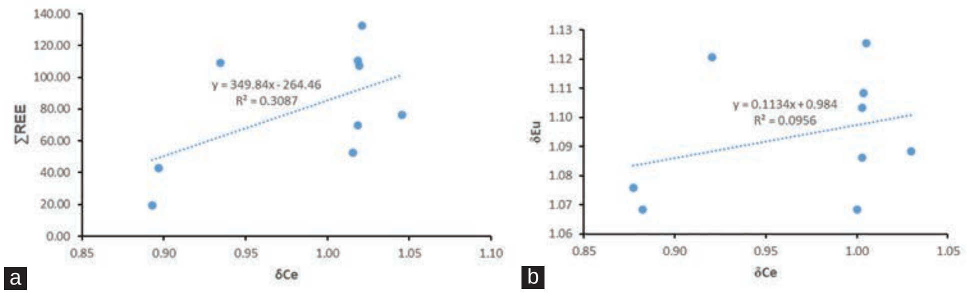

Fig. 7. Bivariate plots for δCe versus ∑REE (a) and δCe versus δEu (b) of the Garagu Formation, Duhok Governorate, Kurdistan, NE Iraq.

Craigie (2018) concluded that Ce is relatively depleted in anoxic sediments which show a negative δCe. Besides, it has been suggested that a pronounced negative δCe can be divided into three categories: (a) smaller than 0.5; (b) ~0.6–0.9, and (c) ~0.9–1.0 which represents, oxic, suboxic, and anoxic marine water, respectively (Chen, et al., 2015). Regarding the studied Garagu samples, they reveal a weak negative anomaly (Fig. 5 and Table IV) (δCe values range from 0.87 to 1.04, an average of 0.98), indicating anoxic conditions during the deposit of Garagu sediments. The Garagu Formation's water environment was comparatively constant during the sedimentation period, as evidenced by the narrow range of vertical values for δEu and δCe. However, a small difference was noted within the middle part of the formation (S15, S16, and S17) (Table IV). Ce concentrations may not be a good indicator of paleoredox where whole-rock analysis is undertaken on field samples, because the Ce is also concentrated in detrital siliciclastic minerals, so positive or negative δCe may simply reflect variations in the proportion of this material rather than any changes in paleoredox (Wilde, Quinby-Hunt and Erdtmann, 1996).

The Garagu limestones have Y/Ho values ranging between 22.47 and 29.56 (average 26.25). This suggests that the Garagu carbonates' Y/Ho levels reflect terrestrial rather than marine entry (Ozkan, 2019). The absence of correlation between δEu and δCe (Fig. 7b) suggests a negligible or absence of influence of post-depositional alteration on the measured δCe (Ozyurt, et al., 2020). In addition, this relationship indicates the terrestrial effect rather than the diagenetic effect for REEs (Ozkan, 2019). Although interference with Ba during ICP-MS analysis can taint δEu (Tostevin, et al., 2016), δEu values show no correlation with Ba/Sm, suggesting that utilized anomalies are genuine positive Eu anomalies (Fig. 8).

C. Paleosalinity Indicators

Since the sedimentary circumstances of the environment will influence the distribution of major, trace, and REEs within a column of sediments, the REE characteristics can be utilized as an indicator for the sedimentary environment (McLennan and Taylor, 1984; Mustafa and Tobia, 2020; Omar, et al., 2022; Omar, et al., 2020; Yu, et al., 2023). Three of these ratios (i.e. Sr/Ba, Rb/K_2O, and Th/U) were used to deduce the paleosalinity of the water during the deposition of Garagu Formation.

Sr/Ba

In diverse sedimentary settings, strontium (McLennan and Taylor, 1984) and barium (Ba) display distinct geochemical behaviors (Randive, 2013). The Sr/Ba ratio is widely regarded as an empirical indicator of paleo-salinity (Omar, et al., 2022; Yu, et al., 2023; Al-Taee, et al., 2024). A high Sr/Ba ratio reflects high salinity, and/or arid climate, while a low Sr/Ba ratio indicates low salinity and/or humid climate (Mohialdeen and Raza, 2013; Wang, et al., 2020; Mirza, et al., 2021; Omar, et al., 2022). The Sr/Ba ratio in the studied samples ranges between 0.00 and 120.63; (Table VI and Fig. 9) indicating some change in salinity and/or aridity of the climate. The lower and upper parts mostly show a high ratio, which indicates high salinity and/or arid climate, while the middle part (S15, S16, and S17) show low values (22.81, 19.56, and 40.3) indicate to low salinity and/or humid climate**.**

Rb/K_2O

Since the values of Rb and K are not in the same order of magnitude, it is required to expand the Rb/K_2O values by 1000 times. This makes Rb/K_2O another popular indication of paleosalinity in sedimentary areas: When the Rb/K_2O value of the water body is >6, it is the saline sedimentary environment, 4□6 is brackish water sedimentary environment, and <4 is the freshwater sedimentary environment (Jinhua, et al., 2018). Garagu samples had Rb/K_2O values above 20 (Table VI and Fig. 9). In general, it shows that the saline marine environment is the basin condition of the Garagu Formation.

Th/U

The Th/U ratio is a useful indicator for differentiating between continental and marine deposits. In general, a water body is considered to be in a terrestrial freshwater habitat when its Th/U value is more than 7, a brackish water sedimentary environment when it is between 2 and 7, and a marine saline water environment when it is <2 (Zhang, et al., 2008). Th/U values of the Garagu samples are <2, except for four samples with more than 2) (Table VI and Fig. 9). Hence, the Th/U ratios indicate to saline marine/brackish water environments.

D. Paleoredox Environment

Redox-sensitive components are thought to be a helpful technique for identifying sediment deposition in both marine and non-marine settings. Redox conditions primarily

TABLE VI
Paleoenvironmental sensitive ratios for beds of Garagu Formation from Duhok Governorate, Kurdistan, N Iraq

S. No.	Thickness(m)	Sr/Ba	Rb/K_2O	Th/U	U/Th	V/(V+Ni)	V/Sc	V/Cr	Rb/Sr	Sr/Cu
S6	7.00	34.40	51.22	1.50	0.67	0.75	14.35	1.71	0.01	116.66
S10	26.00	65.72	46.97	2.31	0.43	0.69	0.00	2.15	0.01	101.24
S13	44.50	119.28	42.06	1.61	0.62	0.74	6.74	1.51	0.01	132.18
S14	48.50	120.63	30.65	1.64	0.61	0.81	17.96	2.41	0.00	116.54
S15	52.50	22.81	35.55	2.38	0.42	0.90	20.52	2.48	0.03	63.63
S16	57.50	19.56	25.49	5.93	0.17	0.92	20.46	2.70	0.02	61.74
S17	69.00	40.30	23.17	3.65	0.27	0.90	18.37	3.22	0.01	55.90
S18	76.40	110.18	30.25	1.48	0.68	0.88	31.46	3.09	0.01	98.84
S21	87.20	0.00	26.25	0.32	3.17	0.82	12.31	2.01	0.00	63.65

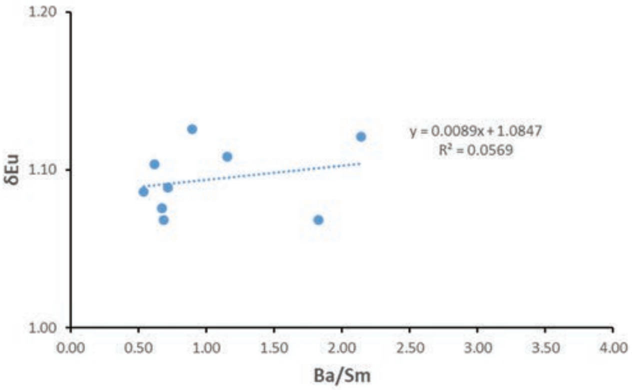

Fig. 8. Plot of Ba/Sm versus δEu ratios of studied limestone samples from the Garagu Formation.

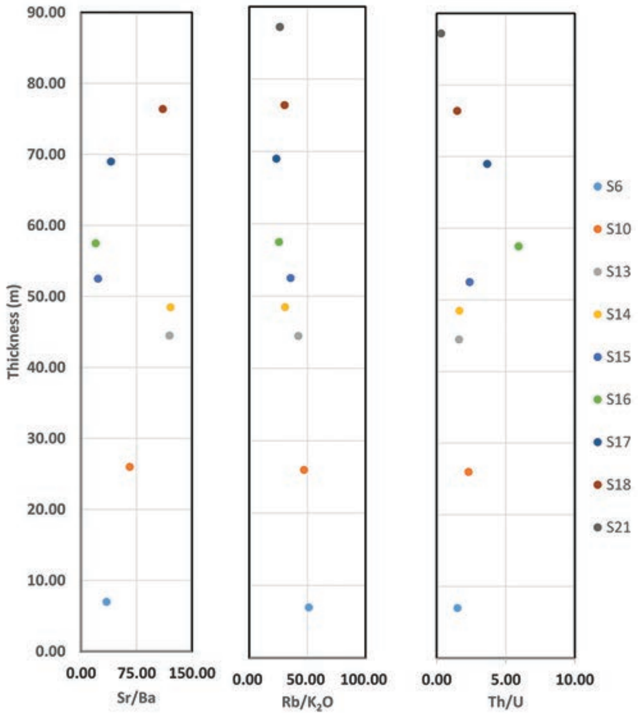

Fig. 9. Chemostratigraphy profile of Sr/Ba, Rb/K_2O, and Th/U ratios in Garagu Formation, Kurdistan, N Iraq.

govern the mobilization, precipitation, and concentration of these multivalence elements, which are abundant in anoxic sediments and include V, U, Ni, Cr, and Mo (Mustafa and Tobia, 2020; Al-Juboury, et al., 2023; Xiao, et al., 2024; Yu, et al., 2023). Furthermore, the ratios of these elements (U/Th, V/Cr, and V/Sc) have been used to estimate the paleoredox condition (Mirza, Mohialdeen and Awadh, 2016; Tobia and Shangola, 2016; Al-Taee, et al., 2024). It may be possible to differentiate between the different depositional conditions (oxic, suboxic, and anoxic) by using trace elements and their ratios in combination.

U/Th

According to Madhavaraju, et al. (2016), the U/Th ratio is regarded as a trustworthy method for determining the oxygenation level in the deposition basin. According to McKirdy, et al. (2011), the U/Th ratio may be thought of as a redox index, with low values (<0.75) linked with oxic environments and high values (>1.25) associated with anoxic environments. The low U/Th value of the Garagu samples (<1.0, except sample No.21 with 3.17; Table VI and Fig. 10) is indicative of the oxic environments (more oxygenation conditions).

V/(V+Ni)

One of the geochemical redox indications is the V/(V+Ni) ratio. According to some theories, ratios over 0.84 signify reducing circumstances, those between 0.6 and 0.84 signify a mild oxidation–reduction environment, and those below 0.6 signify an oxygen-enriched environment (Zhang, et al., 2008; Al-Juboury, et al., 2023; Yu, et al., 2023). Furthermore, low V/(V+Ni) ratios often indicate oxic to suboxic conditions, whereas a high V/(V+Ni) value indicates anoxic bottom water conditions. Most of the studied samples have V/(V+Ni) <0.84 indicating weak oxidation-reduction conditions. The samples G15, G16, G17, and G18 have higher V/(V+Ni) ratios reflecting more anoxic conditions (Table VI and Fig. 10).

δU

Argillaceous rocks are frequently abundant in radioactive elements, such as U and Th. While the U element will be lost or exist as oxides during weathering, the Th element is readily absorbed by clay minerals and preserved (Yu, et al., 2023). Consequently, the oxidation-reduction property of the paleoenvironment may be ascertained using the authigenic uranium (δU) technique. The δU for the studied samples was calculated and the results are cited in Table IV. δU = 1 is the critical point, δU < 1 is the normal water environment, and δU > 1 is the anoxic reduction environment (Wang, et al., 2020). The Garagu Formation's δU results in the study region have

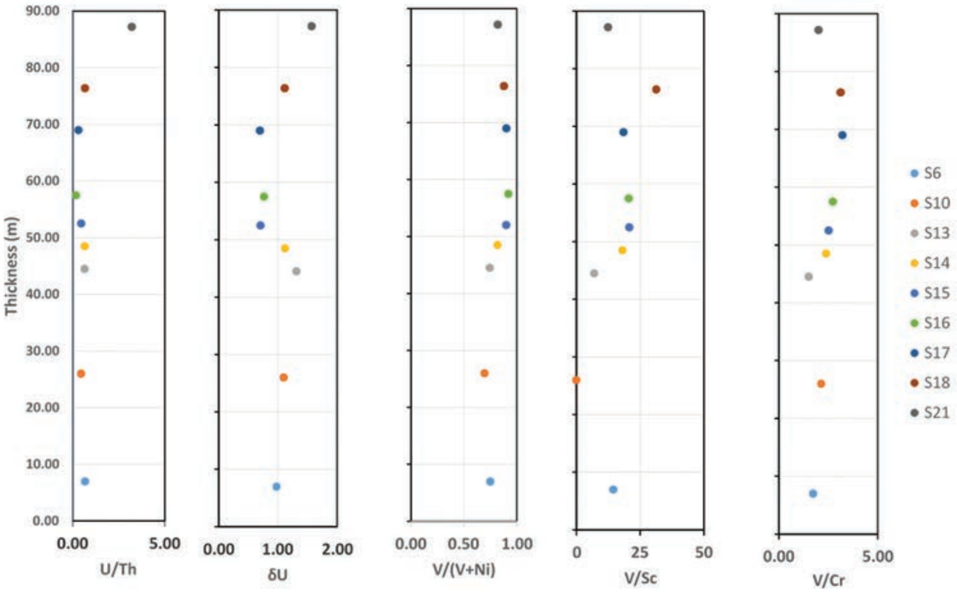

Fig. 10. Chemostratigraphy profile of U/Th, δU, V/(V+Ni), V/Sc, and V/Cr for the Garagu Formation.

an average of 1.04 and vary from 0.69 to 1.58. The Garagu sediment's δU readings indicate a mixed environment with a mild oxidizing–reduction transition.

V/Sc

According to Kimura and Watanabe (2001), who proposed V/Sc as a proxy indicator, oxidizing circumstances are indicated by V/Sc ratios <9, whereas suboxic conditions are indicated by V/Sc ratios more than 9. As seen in Table II, the Garagu samples are distinguished by their increased V/Sc values, which are greater than PAAS (9.38) and UCC (5.45). Consequently, suboxic environments are where the Garagu Formation accumulates (Fig. 10).

V/Cr

Anoxic conditions are suggested by V/Cr ratios >2, whereas stronger oxidizing circumstances are indicated by values <2 (Mustafa and Tobia, 2020; Tobia, Al-Jaleel and Ahmad, 2019; Al-Taee, et al., 2024). The V/Cr ratios for the Garagu samples are more than 2 (except two samples <2) (Fig. 10). Accordingly, the Garagu Formation is accumulated under mixed conditions oxic and anoxic conditions (or dysoxic environment).

VI. CONCLUSIONS

The elemental analysis of the Garagu Formation's type section leads to the following conclusions:

1. The remaining major and trace elements are greatly diluted by the high CaO abundance found in the Garagu Formation. The FeO data are also high and reflects the iron mineralization in the Garagu Formation, especially in the middle part of the section. Other major elements show depletion in comparison to PAAS data. The trace elements Sr, U, and V are enriched in the samples, while other trace elements show depletion.
2. The effect of the diagenetic process on REE distribution has no major effect, as deduced from the relationship between δCe and δEu, as well as from the cross plot of δCe and ∑REE in the Garagu Formation.
3. The carbonate layers formed in shallow marine high salinity to brackish water are indicated by the geochemical analyses of the Garagu Formation's main and trace elements. The range of oxic to suboxic conditions (Dysoxic) can be identified by the geochemical ratios and the contents of V, Ni, Cr, Sr, and Ba.

REFERENCES

Abedini, A., and Calagari, A.A., 2015. Rare earth element geochemistry of the Upper Permian limestone: The Kanigorgeh mining district, NW Iran. *Turkish Journal of Earth Sciences*, 24, pp.365-382.

Al-Jubouri, A.I., Al-Auqadi, R.S., Al-Lhaebi, S.H., Rowe, H.D., and Hussein, S.H., 2023. Anoxic marine conditions recorded from the middle Paleozoic black shales (Kaista and Ora formations), Northern Iraq: A multi-proxy approach. *Jordan Journal of Earth and Environmental Sciences*, 14, pp.50-63.

Aljumaily, I.S.I., and Abdulla, N., 2013. Inferred Inversely Reactivated Listric Faults at Chia Gara Anticline-Northern Iraq. In: *International Van Earthquake Symposium*, pp.23-27.

Al-Taee, N.T., Al-Juboury, A.I., Ghafor, I.M., Zanoni, G., and Rowe, H., 2024. Depositional environment of the late Paleocene-early Eocene Sinjar Formation, Iraq: Implications from facies analysis, mineralogical and geochemical proxies. *Heliyon*, 10, p.e25657.

Amin, D., 1989. *Biostratigraphy of Garagu Formation in Northern Iraq*. (Unpublished) M. Sc. thesis, University of Baghdad, p.14.

Bau, M., and Dulski, P., 1996. Distribution of yttrium and rare-earth elements in the Penge and Kuruman iron-formations, Transvaal Supergroup, South Africa. *Precambrian Research*, 79, pp.37-55.

Bellen, R.V., Dunnington, H., Wetzel, R., and Morton, D., 1959. *Lexique Stratigraphique International*. Vol. 3. Asie, Iraq, p.324.

Chen, J., Algeo, T.J., Zhao, L., Chen, Z.Q., Cao, L., Zhang, L., and Li, Y., 2015. Diagenetic uptake of rare earth elements by bioapatite, with an example from Lower Triassic conodonts of South China. *Earth Science Reviews*, 149, pp.181-202.

Condie, K.C., 1991. Another look at rare earth elements in shales. *Geochimica et Cosmochimica Acta*, 55, pp.2527-2531.

Craigie, N.W., 2018. Advances in oil and gas ex-ploration and production. In: Swennen, R., Ed. *Principles of Elemental Chemostratigraphy: A Practical User Guide*. Springer, Berlin, Germany. p.189.

Ghafor, I.M., and Mohialdeen, I.M., 2016. Fossils distribution from Garagu Formation (Early Cretaceous), diversity and paleoennvironmental conditions, Kurdistan Region, North Iraq. *J Zankoy Sulaimani*, Special Issue, GeoKurdistan II, pp.139-150.

Ghafor, I.M., and Mohialdeen, I.M., 2018. Early cretaceous microfossils associations (foraminifera, ostracoda, calcareous algae, and coral) from the Garagu Formation, Duhok Area, Kurdistan Region, Northern Iraq. *Arabian Journal of Geosciences*, 11, p.407.

Hanna, M., 2007. *Palynology of the Upper Part of Baluti Formation and the Nature of Its Contact with the Sarki Formation at Amadya District, NE Iraq.* PhD Thesis, Unpublished, University of Mosul, p.143.

Holser, W.T., 1997. Evaluation of the application of rare-earth elements to paleoceanography. *Palaeogeography, Palaeoclimatology, Palaeoecology*, 132, pp.309-323.

Jassim, S.Z., and Goff, J.C., 2006. *Geology of Iraq*. Vol. 5. Dolin, Prague and Moravian Museum, Brno, Czech Republic.

Jinhua, F., Shixiang, L., Liming, X., and Xiaobing, N., 2018. Paleo-sedimentary environmental restoration and its significance of Chang 7 Member of Triassic Yanchang Formation in Ordos Basin, NW China. *Petroleum Exploration and Development*, 45, pp.998-1008.

Kimura, H., and Watanabe, Y., 2001. Oceanic anoxia at the precambrian-cambrian boundary. *Geology*, 29, pp.995-998.

Lawrence, M.G., Greig, A., Collerson, K.D., and Kamber, B.S., 2006. Rare earth element and yttrium variability in South East Queensland waterways. *Aquatic Geochemistry*, 12, pp.39-72.

Macleod, K.G., and Irving, A.J., 1996. Correlation of cerium anomalies with indicators of paleoenvironment. *Journal of Sedimentary Research*, 66, pp.948-955.

Madhavaraju, J., Ramírez-Montoya, E., Monreal, R., González-León, C.M., Pi-Puig, T., Espinoza-Maldonado, I.G., and Grijalva-Noriega, F.J., 2016. Paleoclimate, paleoweathering and paleoredox conditions of lower cretaceous shales from the mural limestone, Tuape section, Northern Sonora, Mexico: Constraints from clay mineralogy and geochemistry. *Revista Mexicana de Ciencias Geológicas*, 33, pp.34-48.

Mahdi, F.A., and Al-Zaidy, A.A.H., 2024. Microfacies analysis and stratigraphic evolution of garagu formation in selected oil fields, Northern Iraq. *Iraqi Journal of Science*, 65, pp.2521-2536.

Mckirdy, D., Hall, P., Nedin, C., Halverson, G., Michaelsen, B., Jago, J., Gehling, J., and Jenkins, R., 2011. Paleoredox status and thermal alteration of the lower Cambrian (series 2) Emu Bay Shale Lagerstätte, South Australia. *Australian Journal of Earth Sciences*, 58, pp.259-272.

Mclennan, S., and Taylor, S., 1984. Archaean sedimentary rocks and their relation to the composition of the archaean continental crust. In: *Archaean Geochemistry: The Origin and Evolution of the Archaean Continental Crust.* Springer, Berlin, Germany.

Mclennan, S.M., 2018. Rare earth elements in sedimentary rocks: Influence of provenance and sedimentary processes. In: *Geochemistry and Mineralogy of Rare Earth Elements.* De Gruyter, Berlin, Germany.

Mirza, T.A., Karim, K.H., Ridha, S.M., and Fatah, C.M., 2021. Major, trace, rare earth element, and stable isotope analyses of the triassic carbonates along the Northeastern Arabian Plate margin: A key to understanding paleotectonics and paleoenvironment of the Avroman (Biston) limestone formation from Kurdistan region, Northeastern Iraq. *Carbonates and Evaporites*, 36, p.66.

Mirza, T.A., Mohialdeen, I.M., and Awadh, S.M., 2016. Iron mineralization in the Garagu Formation of Gara Mountain, Duhok Governorate, Kurdistan, NE Iraq: Geochemistry, mineralogy and origin. *Arabian Journal of Geosciences*, 9, p.473.

Mohialdeen, I.M., and Raza, S.M., 2013. Inorganic geochemical evidence for the depositional facies associations of the Upper Jurassic Chia Gara Formation in NE Iraq. *Arabian Journal of Geosciences*, 6, pp.4755-4770.

Murray, R.W., Ten Brink, M.R.B., Gerlach, D.C., Russ III, G.P., and Jones, D.L., 1991. Rare earth, major, and trace elements in chert from the Franciscan Complex and Monterey Group, California: Assessing REE sources to fine-grained marine sediments. *Geochimica et Cosmochimica Acta*, 55, pp.1875-1895.

Mustafa, R.K., and Tobia, F.H., 2020. Geochemical application in unraveling paleoweathering, provenance and environmental setting of the shale from Chia Gara Formation, Kurdistan Region, Iraq. *The Iraqi Geological Journal*, 53, pp.90-116.

Omar, N., Mccann, T., Al-Juboury, A.I., and Franz, S.O., 2020. Petrography and geochemistry of the middle-upper Jurassic Banik section, Northernmost Iraq-implications for palaeoredox, evaporitic and diagenetic conditions. *Neues Jahrbuch für Geologie und Paläontologie Abhandlungen*, 297, pp.125-152.

Omar, N., Mccann, T., Al-Juboury, A.I., Ustinova, M.A., and Sharezwri, A.O., 2022. Early jurassic-early cretaceous calcareous nannofossil biostratigraphy and geochemistry, Northeastern Iraqi Kurdistan: Implications for paleoclimate and paleoecological conditions. *Geosciences,* 12, p.94.

Ozkan, A., 2019. Geochemical features of rare earth elements in the dolomites of the bozdağ formation (early silurian-middle devonian) from Söğütözü-Ladik (Konya/Turkey) area. *International Journal of Engineering Science*, 8, pp.30-46.

Ozyurt, M., Kirmaci, M.Z., Al-Aasm, I., Hollis, C., Tasli, K., and Kandemir,xR., 2020. REE characteristics of lower cretaceous limestone succession in gumushane, NE Turkey: Implications for ocean paleoredox conditions and diagenetic alteration. *Minerals*, 10, p.683.

Ozyurt, M., Kirmaci, M.Z., and Al-Aasm, I.S., 2019. Geochemical characteristics of Upper Jurassic-lower cretaceous platform carbonates in Hazine Magara, Gumushane (Northeast Turkey): Implications for dolomitization and recrystallization. *Canadian Journal of Earth Sciences*, 56, pp.306-321.

Pattan, J., Masuzawa, T., Borole, D., Parthiban, G., Jauhari, P., and Yamamoto, M., 2005. Biological productivity, terrigenous influence and noncrustal elements supply to the Central Indian Ocean Basin: Paleoceanography during the past□ 1 Ma. *Journal of Earth System Science*, 114, pp.63-74.

Randive, K., 2013. *Elements of Geochemistry, Geochemical Exploration and Medical Geology*. Research Publishing Service, Singapore.

Shields, G., and Stille, P., 2001. Diagenetic constraints on the use of cerium anomalies as palaeoseawater redox proxies: An isotopic and REE study of Cambrian phosphorites. *Chemical Geology*, 175, pp.29-48.

Taylor, S.R., and Mclennan, S.M., 1985. *The Continental Crust: Its Composition and Evolution.* Blackwell Scientific Publications, United Kingdom.

Tobia, F.H., Al-Jaleel, H.S., and Ahmad, I.N., 2019. Provenance and depositional environment of the Middle-Late Jurassic shales, Northern Iraq. *Geosciences Journal*, 23, pp.747-765.

Tobia, F.H., and Shangola, S.S., 2016. Mineralogy, geochemistry, and depositional environment of the beduh shale (lower triassic), Northern Thrust Zone, Iraq. *Turkish Journal of Earth Sciences,* 25, pp.367-391.

Tostevin, R., Shields, G.A., Tarbuck, G.M., He, T., Clarkson, M.O., and Wood, R.A., 2016. Effective use of cerium anomalies as a redox proxy in carbonate-dominated marine settings. *Chemical Geology,* 438, pp.146-162.

Tribovillard, N., Algeo, T.J., Lyons, T., and Riboulleau, A., 2006. Trace metals as paleoredox and paleoproductivity proxies: An update. *Chemical geology*, 232, pp.12-32.

Wang, F., Chen, R., Liang, Q., Chang, X., Tian, J., and Deng, X., 2020. Geochemical characteristics and depositional environments of mudstones from the Triassic Zhifang Formation in the Tongchuan Area, Southern Ordos Basin, China. *Geological Journal*, 55, pp.3857-3869.

Wilde, P., Quinby-Hunt, M.S., and Erdtmann, B.D., 1996. The whole-rock cerium anomaly: A potential indicator of eustatic sea-level changes in shales of the anoxic facies. *Sedimentary Geology*, 101, pp.43-53.

Xiao, B., Guo, D., Li, S., Xiong, S., Jing, Z., Feng, M., Fu, X., and Zhao, Z., 2024. Rare earth element characteristics of shales from Wufeng-Longmaxi formations in deep-buried areas of the Northern Sichuan Basin, Southern China: Implications for provenance, depositional conditions, and paleoclimate. *ACS Omega*, 9, pp.2088-2103.

Xu, L., Huang, S., Sun, M., Wen, Y., Chen, W., Zhang, Y., Luo, F., and Zhang, H., 2023. Palaeoenvironmental evolution based on elemental geochemistry of the Wufeng-Longmaxi shales in Western Hubei, Middle Yangtze, China. *Minerals*, 13, p.502.

Yu, W., Wang, F., Gong, L., Hu, J., Ma, Z., Wang, J., Wu, J., and Xiao, Y., 2023. Paleoenvironmental, paleoclimatic, and tectonic implications of the Yanghugou formation in the Western margin of the Ordos Basin, China: Evidence from palynology and elemental geochemical characteristics. *Minerals,* 14, p.32.

Zhang, W., Yang, H., Yang, Y., Kong, Q., and Wu, K., 2008. Petrology and element geochemistry and development environment of Yanchang formation Chang-7 high quality source rocks in Ordos Basin. *Geochimica*, 37, pp.59-64.

Enhancing Cancer Diagnosis: A Hybrid Level-Set and Edge Detection Approach for Accurate Medical Image Segmentation

Ismail Y. Maolood[1,2†]

[1]Department of Computer Science, College of Science, Knowledge University,
Erbil 44001, Kurdistan Region – F.R. Iraq

[2]Department of Information and Communication Technology Center, Ministry of Higher Education and Scientific Research,
Erbil, Kurdistan Region – F.R. Iraq

***Abstract*—Early diagnosis of cancer is crucial for improved patient results. With the aim of improving the effectiveness of cancer diagnosis, this paper introduces a new proposed method, computer-aided diagnosis, utilizing the level-set algorithm based on the edge detection approach for medical image segmentation. To assess the performance of our method, it was proved on a highly varied dataset that comprised liver cancer, Magnetic Resonance Imaging (MRI) brain cancer, and dermoscopy color images. By effectively integrating edge information into the level-set evolution process, the proposed method achieved impressive results. For liver cancer images, we obtained an accuracy of 0.9913, a sensitivity of 0.9165, and a Dice coefficient of 0.8820. Similarly, for dermoscopy color images, the method achieved an accuracy of 0.9979, a sensitivity of 0.9301, and a Dice coefficient of 0.9301. In the case of MRI images, the method demonstrated an accuracy of 0.9933, a sensitivity of 0.8591, and a Dice coefficient of 0.8591. The proposed method outperforms traditional techniques such as Simulated Annealing combined with Artificial Neural Network and Fuzzy Entropy with Level Set thresholding. This method demonstrates superior segmentation accuracy and robustness. By enabling precise identification of cancerous regions, this approach supports early diagnosis, reduces misdiagnosis, and enhances treatment planning, offering significant potential for improving cancer care and patient results.**

***Index Terms*—Cancer detection, Computer-aided diagnosis, Edge detection techniques, Level-set method, Medical image segmentation.**

I. INTRODUCTION

This Cancer remains one of the main causes of non-accidental death, so improving patients' survival requires accurate detection of the illness at an early stage (Al-Ayyoub, et al., 2015). Imaging is vital in cancer diagnosis and management as it gives the physician a picture of internal body structures that are vital in the detection and follow-up of malignant growths. However, it is a challenging process of image analysis, which must be done with special computer-aided tools to reveal carcinogens in non-cancerous tissues (Sharma, et al., 2013; Chan, Hadjiiski and Samala, 2020).

Osher and Sethian developed the Level-set method (LSM), a robust computational method widely utilized in cancer imaging to capture evolving shapes and interfaces (Osher and Sethian, 1988). LSM is particularly attractive to further segment complicated and asymmetrically formed cancers due to its topological modification. The aim of the proposed approach is to improve the technique for isolating malignant tissue by improving work with edge-detection algorithms. These techniques are applied for the identification of intensity fluctuations that may occur at the edges of a cancer picture. Edge detection methods, such as the Canny edge detector, help in the accurate outlining of the cancer edges with the help of large variations in an object's intensity (Canny, 1986; Kass, Witkin and Terzopoulos, 1988).

Computer-aided diagnosis (CAD) systems enhance the accuracy of medical image analysis, aiding radiologists and oncologists in diagnosing and treating various types of tumors (Sharma, et al., 2013; El-Baz, et al., 2013). These systems enable efficient analysis of large volumes of images, reducing the risk of human error. Accurate segmentation of tumors is crucial for treatment planning, as it provides information about their location, size, and extent. However, traditional segmentation methods, such as thresholding and region growing, often struggle to accurately delineate irregular tumor boundaries (Maolood, Al-Salhi and Lu, 2018b; Maolood, et al., 2018a; Halalli and Makandar, 2018).

The main aim of this study is to enhance the efficiency and accuracy of medical image segmentation for cancer diagnosis. The proposed CAD system combines the LSM algorithm with edge detection to achieve enhanced image segmentation and assessment. These systems would enhance the reliability of the segmentation details, sensitivity, and

---

ARO-The Scientific Journal of Koya University
Vol. XIII, No. 1 (2025), Article ID: ARO.11942 11 pages
DOI: 10.14500/aro.11942
Received: 12 December 2024; Accepted: 03 February 2025
Regular research paper; Published: 17 February 2025

†Corresponding author's e-mail: ismail.maulood@mhe-krg.org

specificity and facilitate the early diagnosis and management of various types of cancer.

This project entails designing and evaluating a computer-aided diagnosis with level-set algorithm according to the edge detection technique (CAD-Ls-EDT) for contouring the cancerous regions in liver cancer, brain Magnetic Resonance Imaging (MRI), and dermoscopy color images. In this case, the aim is to improve the detection and separation of cancerous regions in those images using advanced computational techniques. The most important contribution of this investigation is to propose a solid and complete segmentation model to improve the identification and management of cancer, with the ultimate goal of providing oncology practitioners with the tools they need to carry out their work as successfully as possible.

The purpose of this study is to evaluate the effectiveness of a computer-aided diagnosis system based on a level-set algorithm and edge detection for the segmentation of medical images for the diagnosis of diseases, such as liver cancer, MRI, and dermoscopy images. Moreover, the proposed method enhances the level-set technique with edge detection, aiming to increase the segmentation accuracy of intricate and diverse cancerous tissues. This approach tries to address some of the issues of thresholding and region growth, which in segmentation, due to the complex and tricky shape of tumors (Maolood, Al-Salhi and Lu, 2018b; Kadhim, Khan and Mishra, 2022). The proposed methodology involves several sequential steps:

1. Preprocessing: The images are pre-processed, which is normalized for higher quality and removes any form of noise present with them. Usually, at this stage, Gaussian smoothing is applied.
2. Initial Contour Detection: An initial contour is established to direct the level-set evolution. Contouring is dependent on the image intensity gradients and edge information as the contour develops (Maolood, 2013).
3. Level-Set Evolution: The level-set formulation alters the contour of the cancer shape. This includes solving of partial differential equations (PDEs”) as well as using gradient information of an image.
4. Edge Detection Integration: To enhance boundary detection, the level-set is implemented together with edge detection algorithms such as the canny edge detector. It helps to enhance the effectiveness of the segmentation results (Yin, et al., 2021).
5. Segmentation and Post-Processing: Finally, after contour modification to the appropriate shape, the final segmentation is grown. The morphological post-processing operation is also used to smooth the results of the segmented cancer image and to eliminate undesired structures (Maolood, Al-Salhi and Lu, 2018b).

CAD-Ls-EDT, which is discussed as the proposed approach that combines LSM and edge detection methods, proved to provide a high efficiency of cancer segmentation of various types. It is also knowledgeable that by incorporating the edge information in the LSM framework, the method was able to give correct margins around the cancers even in noisy and varying intensity levels. With CAD-L s-EDT, the high accuracy, sensitivity, and specificity were obtained as compared to conventional procedures. This advancement may have the potential to revolutionize practice in terms of diagnosis and treatment by offering the opportunity to identify abnormalities earlier and design the necessary treatment earlier.

The remaining research is prepared as follows: Section II contains part of the background. Section III gives the methodology. The finding of the study is presented in section IV. Finally, section V summarizes the investigation.

II. BACKGROUND

A. Selecting Medical Image Segmentation

Medical image segmentation is the process of partitioning a cancer image into meaningful parts; usually, it has the goal of segmenting regions of interest, such as cancers (Maolood, Al-Salhi and Lu, 2018b). This very significant process aids in the detection and handling of several forms of cancers, such as liver cancer, brain cancer detected using MRI imaging, and skin cancers as deduced through the dermoscopy technique. Some of the traditional methods that are used to segment the cells include thresholding, region growing, and clustering, which can sometimes be very difficult because of the dynamic and complex nature of the malignant tissues.

It has great importance when it comes to liver cancer analysis because it helps draw boundaries between liver cancer and any cancers in CT or MRI scans. This also facilitates inaccurate assessment of the cancer size, position, and the stage of the disease, which is most important, especially when thinking of surgical or radiation therapy (Maolood, et al., 2018a; Halalli and Makandar, 2018). In MRI-based cancer diagnosis, the regions that should be targeted are the regions at which the cancer is located, and the process needs accurate segmentation. Segmentation provides higher degrees of accuracy in the regional characterization of disease, together with treatment planning and delivery, by better delineating between healthy and malignant tissues in vital organs, including the brain, breast, or prostate.

Segmenting the lesions from the skin in color images, dermoscopy practices image segmentation in the identification of skin cancer. It contributes to increasing the understanding of Accelerator people with the Lesion morphological aspect that contributes to the identification of melanoma as well as other skin cancers at an early stage of development. These segmentation techniques not only help in the diagnosis of diseases but also help in the efficiency and effectiveness of treatment plans using higher mathematics and artificial intelligence (Kadhim, Khan and Mishra, 2022; Aziz and Abdulla, 2023; Maolood, 2013; Jaganathan and Kuppuchamy, 2013).

B. Cancer Analysis Based on a Level-set Method

LSM, which was introduced by Osher and Sethian in 1988, is a well-suited computational method used in the modeling of the evolution of shapes and interfaces. In the area of medical image segmentation, LSM is especially suitable for the definition of intricate patterns that are also in constant change, such as tumors (Osher and Sethian, 1988). According to LSM, the changing envelopment is the zero-level-set of a higher-dimensional function that represents the advanced complex interface, which can track topological changes and detailed shapes. This makes it useful for partitioning different forms of cancer with complex margins and different signal strengths.

The radiological images that might be used in the medical diagnosis could be in grayscale or color. Let Y = (X.Y) represents the coordinates of all pixels in the medical image within the cancerous region, while I = (x, y) denotes the specific pixel coordinates within the cancer region being analyzed. It is dynamic, with the level-set function being tested at a certain position m(t) and time t yielding a value of 0 (Aziz, et al., 2023). This may be important in dealing with problems at the uppermost layers or frontiers of Equation (1).

$$\varnothing\,(m(t).\,t) = 0 \tag{1}$$

When dealing with partial differential equations (PDEs) and level-set method, the function ∅ (t.x.y) usually means the level-set function (Hemanth, Anitha and Balas, 2015; Friedrich, et al., 2016). This function is defined in the spatial domain (x.y) at a particular time t. The level-set function experiences time changes, and it is true that the zero level-set is the boundary of the chosen malignancy. As is depicted in Fig. 1, this explains Equation (2).

$$m(t)=\begin{cases}\varnothing(t.x.y)<0(x.y)\ \text{is inside } m(t)\\ \varnothing(t.x.y)=0(x.y)\text{is at } m(t)\\ \varnothing(t.x.y)>0(x.y)\text{is outside } m(t)\end{cases} \tag{2}$$

Information on a curved surface is influenced by multiple factors from both external and internal research archives. In medical imaging, regions of interest, such as cancerous areas, can be defined using a level-set function ∅ (t.x.y) < 0, which represents the tumor boundary m(t)at time t. The function classifies points as follows: ∅ (t.x.y) < 0 for points inside the cancerous region, ∅ (t.x.y) = 0 for points on the tumor boundary, and ∅ (t.x.y) > 0 for points outside the cancerous region.

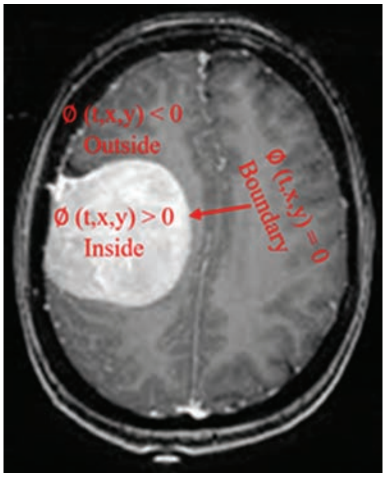

Fig. 1. Normal direction curve propagation of LSM.

As mentioned from equation (3), which describes the dynamics of a boundary of cancerous, where ∅t = 0 represents the cancer boundary. The symbol $\frac{\partial\varnothing}{\partial m(t)}$ transforms the chain rule, which helps in seeing how ∅ grows in response to time, while x_t represents the velocity field that dictates the motion of the boundary cancer.

$$\frac{\partial\varnothing}{\partial m(t)}\ xt + \varnothing t = 0 \tag{3}$$

Use the normal component of $\frac{\partial\varnothing}{\partial m(t)}$ | to find the desired velocity on the interface *xt*, (4) becomes.

$$\begin{cases}\dfrac{\partial\varnothing}{\partial t} + f\left|\nabla\varnothing\right| = 0\\ \varnothing(0.x.y) = \varnothing_0(x.y)\end{cases} \tag{4}$$

While |∇∅| is the gradient magnitude, which indicates the natural direction to the boundary. The term $\frac{\partial\varnothing}{\partial t}$ is the time evolution of ∅, and $\varnothing(0.x.y)=\varnothing_0$ (x.y) is the initial condition for the cancer boundary (Chan and Vese, 2001; Chen, et al., 2002). To stop level-set growth at the perfect solution, regularize using an edge indication function *g*. A popular level-set segmentation method is.

$$g = \frac{1}{1+\left|\nabla\left(G_\sigma * I\right)\right|^2} \tag{5}$$

The convolution of the medical image is represented by G_σ * I. With Gaussian noise G^σ, ∇ the process for the cancer image gradient is denoted by ∇, and a function g exhibits minimal variation around within the specified boundaries (Maolood, Al-Salhi and Lu, 2018b). An often-utilized formulation for level-set segmentation is.

$$\frac{\partial\varnothing}{\partial\varnothing} = \left|\nabla\varnothing\right|\left(\text{div}\left(\frac{\nabla\varnothing}{\left|\nabla\varnothing\right|}\right)\right) \tag{6}$$

The gradient magnitude |∇∅| ensures that the motion is normal to the cancer boundary, while the term $\left(\text{div}\frac{\nabla\varnothing}{\left|\nabla\varnothing\right|}\right)$ represents the curvature of the boundary. This curvature flow drives the boundary to reduce high-curvature regions, leading to a smoother shape. The cancer image quality has been enhanced with the use of computer-aided diagnosis utilizing the level-set algorithm based on the edge detection approach (CAD-Ls-EDT).

C. Medical Image Analysis for Cancer Boundary Detection

Cancer boundary detection is a critical field of study and advancement in medical image analysis. In medical imaging, the process entails using complex algorithms and methodologies to precisely detect and demarcate the borders of cancerous areas, including liver cancer, MRI cancers, and dermoscopy color images. Precise cancer border identification is critical for diagnosing, planning therapy, and monitoring cancer patients (Bechar, et al., 2024; Khaliki and Başarslan, 2024).

Cancer boundary detection is undergoing rapid advancements, with researchers consistently striving to enhance the accuracy and efficiency of algorithms (Mercaldo, et al., 2023; Hosseini, Monsefi and Shadroo, 2024). It has the potential to make the diagnosis and treatment planning of cancer more effective and favorable for the patients. However, it is vital that algorithms are used as such to assist decision-making instead of as tools to replace the medical profession. Healthcare professionals should always retain the finality of choices relating to diagnosis and treatment decisions (Suryawanshi and Patil, 2024).

Cancer segmentation is among the initial steps applied to the medical image, and therefore, edge detection forms the core of the medical image examination task. Edge detection enhances the definition of the boundaries of tumors and anatomical structures, hence the location of rigorous intensity transformation. This information may then be utilized to enhance the segmentation algorithms to yield better results (Zhu, et al., 2024; Shao, et al., 2024).

The Canny Edge Detector, as put forth by John F. Canny in 1986, has been one of the prevailing practices employed in edge detection for computers. However, it is most valuable as a method for finding edges in intensity in medical imaging, where changes in intensity are often indicative of the cancer or other structures' boundaries (Yang, et al., 2024). Here are some of the steps for cancer segmentation:

Step 1: Apply the Gauss smoothing filter before edge detection to reduce the amount of cancer image noise, which can help focus on prominent features for cancer analysis (Badar, et al., 2024).

$$G(x.y) = \frac{1}{2\mu\sigma^2} e^{\frac{x^2+y^2}{2\sigma^2}} \tag{7}$$

Where: G (x.y) Value of the Gaussian function at the pixel (x.y), σ: Standard deviation of the Gaussian distribution.

Step 2: Calculate the magnitude and direction of the gradient of cancer images using four angles (0, 45, 90,135 degrees) by solving equations (8) and (9).

$$G = \sqrt{G_x^2 + G_y^2} \tag{8}$$

$$G\theta = \arctan\left(\frac{G_y}{G_x}\right) \tag{9}$$

Where G_x and G_y a direction according to *x* and *y*.

Step 3: Non-maximum suppression removes non-edge pixels on the cancer image, leaving only well lines.

Step 4: Select a hysteresis threshold by utilizing two thresholds to determine which edges to include or exclude.

Step 4.1: Strong Edge Pixels: Pixels with a gradient magnitude overhead the high threshold (T_h) are classified as robust edge pixels.

Step 4.2: Weak Edge Pixels: Pixels with a gradient magnitude under the high threshold (T_h) are repressed.

Step 4.3: Edge Linking: Pixels with a gradient magnitude among the low and high thresholds (T_h and T_l) are considered weak edge pixels. These pixels are reserved only if they are connected to a strong edge pixel through several weak edge pixels. This helps to ensure that the detected edges are continuous and well-defined. Where (T_h) determines the minimum gradient magnitude to classify a pixel as a strong edge and (T_l) helps identify weak edges that are potentially part of true edges but need validation.

In this research, we recommend a new technique that integrates LSM with edge detection approaches to enhance the efficiency and reliability of cancer segmentation. Incorporating the edge information into the level-set evolution process, our method aims to overcome the drawbacks of existing conventional methods and aims to provide enhanced and efficient segmentation results that help in achieving better clinical results.

III. METHODOLOGY

A. Data Acquisition

A variety of datasets that used liver cancer images, MRI scans, and dermoscopy color images were used. All the images used in this study were obtained from the open-access database available through MIRA – McMaster Institute for Research on Aging (Maolood, Al-Salhi and Lu, 2018b). Some datasets contain images with confirmed cancer diagnoses; thus, the experimental results were credible.

A total of 620 images were employed for this study, where 200 of which were liver cancer images, 260 of which were brain MRI images, and 160 of which were dermoscopy color images. This diverse dataset contained images of small to large cancer sizes.

The proposed methodology comprises three distinct phases. Initially, we assess the efficacy, competence, and precision of our approach by comparing it with three other regularly utilized procedures for the segmentation of medical images. Another step displays the efficacy of our approach. Ultimately, the third phase involves the implementation and evaluation of the suggested technique for segmenting cancer images.

The techniques were implemented in MATLAB R2022b (MathWorks) on a Windows 11 Home version 22H2 machine with a 64-bit operating system, an ×64-based processor, an Intel Core i7-8550U CPU @ 1.80 GHz, and 16 GB of RAM. Our technology has the possibility to suggestively improve the accuracy and efficiency of cancer detection using medical image segmentation.

All images were pre-processed to enhance image quality and reduce noise. Pre-processing steps included:

- Noise Reduction: Gaussian filtering was applied to remove noise and improve image clarity.
- Intensity Normalization: Images were normalized to a common intensity range to ensure consistent pixel values.

The pre-processed dataset was utilized to train and evaluate the proposed CAD-Ls-EDT method.

B. Proposed Method

Scientists have devised cancer image segmentation techniques for addressing cancer issues. The suggested method aims to improve computer-aided diagnosis by utilizing a level-set algorithm along with an edge detection method to accurately find and separate images of cancerous borders. The objective is to generate valuable data on the limits of cancer and effectively categorize cancer cases. The research employs a variety of techniques to provide efficient segmentation, as seen in Fig. 2.

Below is our proposed algorithm for computer-aided diagnosis with a level-set algorithm according to the edge detection technique.

Algorithm 1: CAD-Ls-EDT cancer image segmentation

```
Input: Cancer image.
Output: extracted the cancerous part and then segmented it
Create a loop for reading the medical image with initial boundaries of cancer region
for x in range(medical_image.shape[0]):
    for y in range(medical_image.shape[1]):
        if ϕ [x, y] > 0: # Process as inside the cancer part
            process_inside (ϕ, x, y)
        elif ϕ [x, y] == 0: # Process as boundary of the cancer part
            process_boundary (ϕ, x, y) # Process as outside the cancer part
        else:
            process_outside (ϕ, x, y)
def double_threshold(cancer_image, low_thresh, high_thresh):
    output = np.zeros_like(cancer_image, dtype=np.uint8)
    strong_edges = (cancer_image >= high_thresh) # Strong edges
    output[strong_edges] = 255
    weak_edges = (cancer_image >= low_thresh) & (image < high_thresh) # Weak edges
    output[weak_edges] = 128 # Mark weak edges with a distinct intensity
return output extracted the cancer part
```

Our proposed algorithm is explained systematically for each step.

Input: Cancer image.

Output: extracted the cancerous part and then segmented it.

Step 1: Cancer Image Input and Initialization

Load the input cancer image into the system. Create an initial level-set function ϕ (x,y,t) to represent the initial contour. This contour should enclose the approximate region of interest. Define the parameters for the level-set evolution process, such as the time step, stopping criteria, and edge detection thresholds.

Step 2: Check for Valid Input

Ensure that the input image is valid and meets the required format and size specifications. If the cardinality of the set $\varnothing$ (t.x.y) is greater than zero, then proceed to enter the cancer image. If the set of points $\varnothing$ in the coordinates (t.x.y) is equal to zero, then proceed to the edge of the cancer image. If $\varnothing$ (t.x.y) < 0, then go outside of the cancer image, according to Eq. (2).

Step 3: Level-Set Evolution

Compute the gradient of the image to obtain information about intensity changes. Evolve the level-set function using the mathematical explanation of the level-set equation (Eq. 3). This involves iteratively updating the level-set function based on the image gradients and the current contour position. Monitor the modification in the level-set function between iterations. If the change is below a pre-defined threshold, the iteration process is terminated.

Step 4: Edge Detection and Refinement

If the function g is near zero in a boundary of the cancer by Eq. (5) and go to Eq. (6) to select the part of cancer segmentation.

Step 5: Thresholding

Use two thresholds (T_h and T_l), to classify edge pixels. Pixels with a gradient magnitude above T_h are classified as robust edge pixels, while those below T_l are repressed. Pixels with a gradient magnitude between (T_h and T_l) are measured weak edge pixels. Weak edge pixels are connected to robust edge pixels to form continuous edge segments.

Step 6: Extract and Segment Cancerous Region

Use the final level-set function to extract the segmented region, which corresponds to the area enclosed by the zero-level-set (following Eq. 9). Apply post-processing methods, such as morphological processes, to perfect the segmentation results and remove any small artifacts or noise. Display the original image, the initial contour, the final segmentation result, and any relevant metrics (e.g., Dice coefficient, Jaccard index).

Step 7: Iteration and Termination

If the level-set function has converged or a maximum number of iterations has been reached, terminate the algorithm. If the level-set function has not converged, return to Step 3 and continue the evolution process.

Step 8: End

IV. RESULTS AND DISCUSSION

A. Experimental Step

The effectiveness of the proposed CAD-Ls-EDT method was tested in experiments on a benchmark dataset of medical images. These were liver cancer images, brain MRI images, and dermoscopy color images, which have been sourced from different places. It was meant to compare this method and its effectiveness in segmenting cancerous areas in images of different levels of complexity and noise added to them.

The results of the experiment show that the performance of the suggested CAD-Ls-EDT method depends on certain

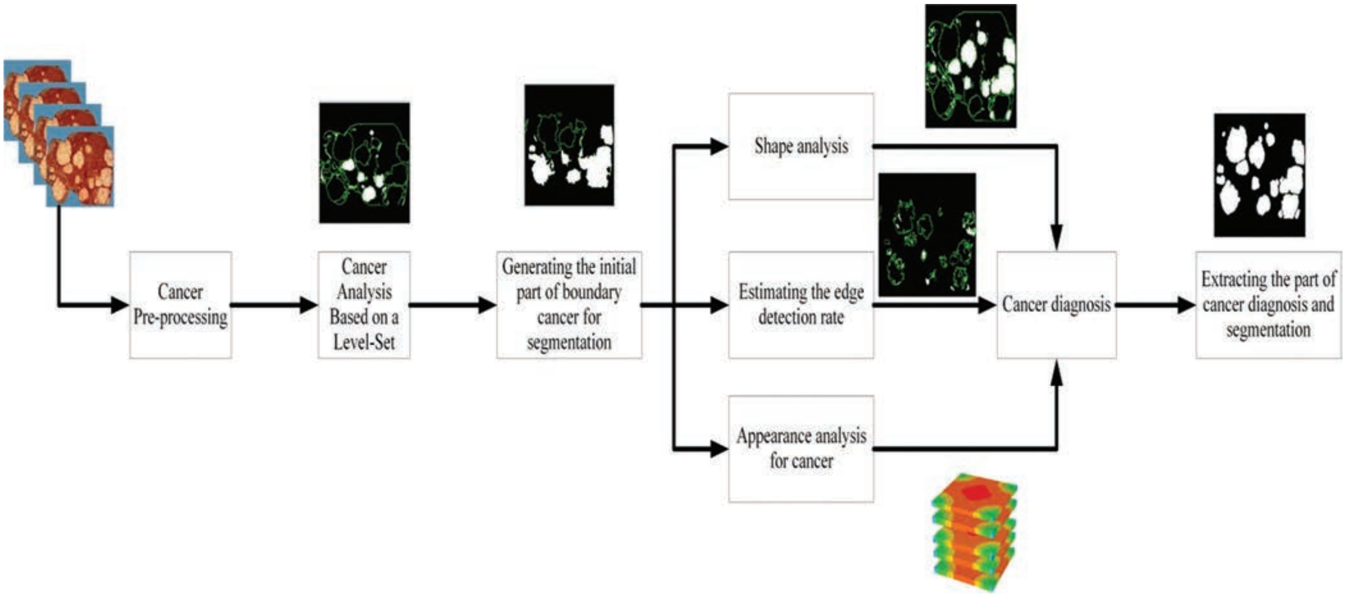

Fig. 2. Presents a computer-aided diagnosis system that selects and extracts high-quality boundary cancer images for diagnosis and segmentation.

features of the input image data. The method effectively applies image segmentation techniques to arrange noise in medical images while enhancing the image quality to enhance successive segmentation techniques. The study employs a computer-aided diagnosis system based on a level-set method and edge detection to ensure high-quality segmenting boundaries of cancer in images.

The first experimentation of the CAD-Ls-EDT algorithm shown in Fig. 3 involves a liver image with sizes of 620 × 620 pixels. Column (a) shows the original image with cancer, and in column (b), we use a circular initial counter with λ parameters ranging from $\lambda 1 = 1$ to $\lambda 2 = 8$, $\mu = 0.31$, and a maximum number of iterations of 80 to find the boundary of the cancer within the image. The segmentation result in our proposed technique is represented in column (c), established after optimizing the parameters to yield the finest outer border of cancer on the image. Specifically, we set the λ parameter to 4, μ to 0.6, and performed 30 iterations.

Fig. 4 illustrates the segmentation results for a dermoscopy color image with dimensions of 650 × 650 pixels. The original image is shown in column (a). An initial circular contour was defined with parameters $\lambda 1 = 1$, $\lambda 2 = 8$, and $\mu = 0.3$, and the level-set method was iterated 80 times to search for the cancer boundary. The optimal segmentation result, shown in column (c), was obtained by adjusting the parameters to $\lambda 1 = 3$, $\lambda 2 = 4$, $\mu = 0.2$, and 45 iterations. These parameter settings effectively delineated the cancer boundary, demonstrating the ability of the proposed method to accurately segment complex regions in dermoscopy images.

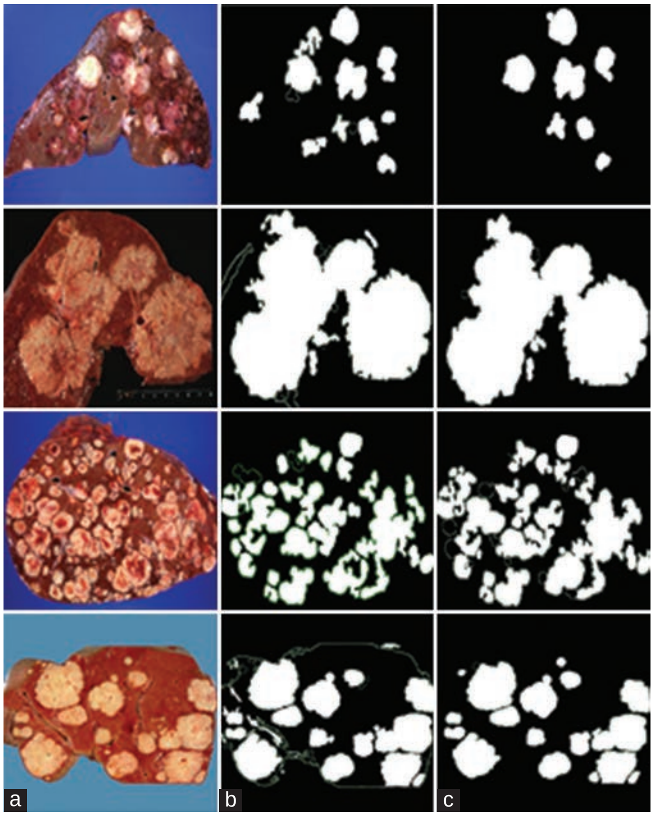

Fig. 3. Computer-aided diagnosis using the level-set method with edge detection (a) The original liver image with cancer; (b) the search for the cancer's boundary region; and (c) the segmentation of the cancer after 30 iterations and extracting the cancer region.

Fig. 5 illustrates the segmentation results for a 512 × 512 pixel MRI image. Column (a) shows the original MRI image containing a cancerous region. An initial circular contour was defined with parameters $\lambda 1 = 1$, $\lambda 2 = 8$, and $\mu = 0.3$, and the level-set method was iterated 80 times to search for the cancer boundary. The optimal segmentation result, shown in column (c), was obtained by adjusting the parameters to $\lambda 1 = 4$, $\lambda 2 = 6$, $\mu = 0.4$, and 25 iterations. These parameter settings effectively delineated the cancer boundary, demonstrating the ability of the proposed method to exactly segment complex regions in MRI images.

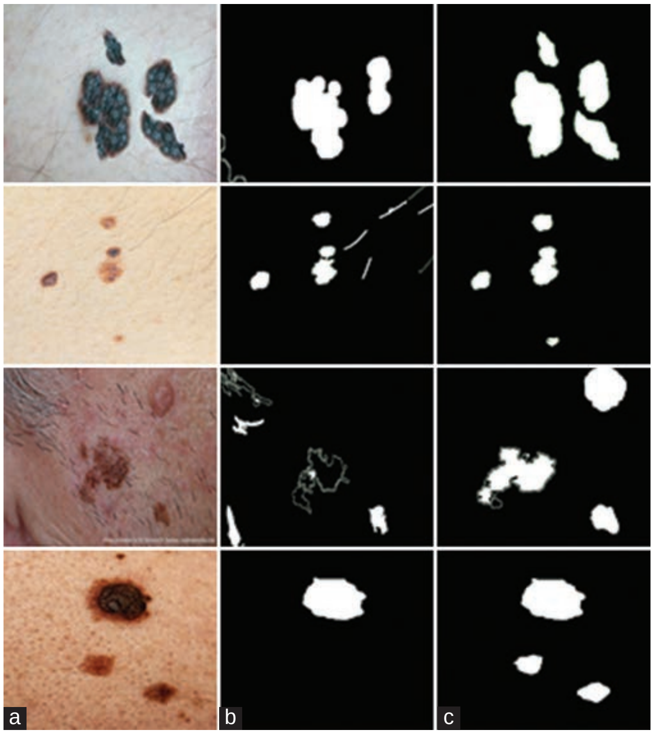

Fig. 4. Computer-aided diagnosis with the level-set method by using edge detection: (a) original dermoscopy color image; (b) searching to find the boundary region of cancer; (c) finding the cancer and segmenting after 45 iterations by extracting the cancer region.

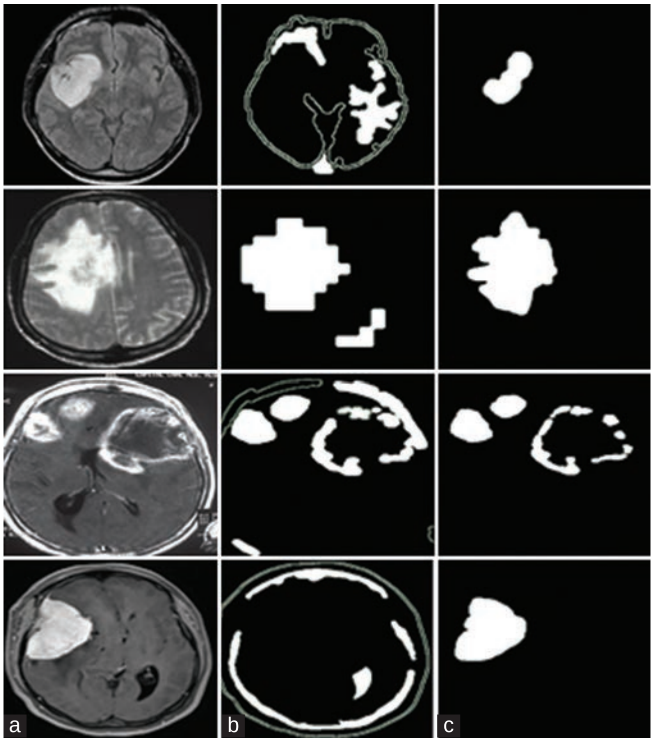

Fig. 5. Computer-aided diagnosis with the level-set method by using edge detection: (a) original image; (b) searching to find the boundary region of cancer; (c) finding the cancer and segmenting after 25 iterations by extracting the cancer region.

B. Experimental Results

To assess the CAD-Ls-EDT approach proposed in this paper, experiments were performed on a dataset including liver cancer, skin cancer, and MRI cancer images. For liver cancer images, an initial circular contour was defined with parameters λ1 = 1, λ2 = 8, and μ = 0.31. The level-set method was then repeated (80 times) to enhance the contour and obtain the best parameters for segmentation. By trying the proposed framework on several images, it was possible to find the correct values of the parameters under consideration for each type of image. The same optimal values of λ1 = 2, λ2 = 4, μ = 0.6, were established for preliminary enhancement of liver cancer images, with 30 iterations. Similarly, for dermoscopy color images, optimal parameters were found to be λ1 = 3, λ2 = 4, μ = 0.2, and 45 iterations. In the case of MRI images, the optimal parameter settings were λ1 = 4, λ2 = 6, μ = 0.4, and 25 iterations. These optimized parameter values were useful in defining the cancer regions with high levels of accuracy for all the different types of images.

Evaluation of the proposed CAD-Ls-EDT method is based on the assessment of the segmented cancer area obtained with the hybrid technique concerning to cancer segmentation (CS) ground truth (GT) data provided by the clinicians. These coefficients are very important for processes to measure the similarity between the ground truth and the cancer-segmented region, known as the Jaccard Coefficient and Dice Coefficient, both these values range from zero to one, where higher values are for an accurate segmentation of cancer. Among them, the Jaccard coefficient is more suitable for this research because of the potential partial overlaps and complexity in cancer boundaries (Maolood, et al., 2018a). In addition, efficiency criteria, including sensitivity, reveal the primary features of cancers. Precision is the degree of correctness of the approximate quality of cancer parts, specificity they can exclude non-cancer parts, and accuracy are some of the key measures that determine how successfully the proposed hybrid level-set and edge detection technique can detect non-cancerous and cancer parts. The level-set and edge detection approach distinguish between non-cancerous and cancerous parts. Taken together, the above parameters are evidence of the effectiveness of the hybrid algorithm in successfully attaining reliable segmentation, which is critical for enhancing the accuracy of cancer diagnosis and optimization of treatment planning (Maolood, Al-Salhi and Lu, 2018b). The parameter metrics details are providing mathematically as trails:

$$\text{Similarity of } \mathit{Jaccard\,Coefficient} = \frac{|GT \cap CS|}{|GT \cup CS|} \tag{10}$$

$$\text{Similarity of } \mathit{Dice\,Coefficient} = \frac{2*|GT \cap CS|}{|GT|+|CS|} \tag{11}$$

$$\text{Performance of Sensitivity} = \frac{TP}{TP+FN} \tag{12}$$

$$\text{Performance of Precision} = \frac{TP}{TP+FP} \tag{13}$$

$$\text{Performance of Specificity} = \frac{TN}{TN+FP} \tag{14}$$

$$\text{Performance of Accuracy} = \frac{TP+TN}{TP+TN+FP+FN} \tag{15}$$

$$\text{Matthews Correlation Coefficient}\left(\text{MCC}\right) = \frac{\left(TP*TN\right)-\left(FP*FN\right)}{\sqrt{\left(TP+FP\right)*\left(TP+FN\right)*\left(TN+FP\right)*\left(TN+FN\right)}} \tag{16}$$

Where

- True Positive (TP): Correctly segmented cancer regions.
- False Positive (FP): Non-cancer regions incorrectly identified as cancer.
- True Negative (TN): Non-cancer regions correctly identified as non_cancer.
- False Negative (FN): Cancer regions missed by the segmentation.

As shown in Table I and Fig. 6, the performance of the proposed CAD-Ls-EDT algorithm was assessed on the discussed metrics of accuracy, precision, sensitivity, specificity, Matthews's correlation coefficient, Dice coefficient, and Jaccard index. When evaluated using the liver cancer images, the method attained an accuracy of 0.9913, a precision of 0.7538, a sensitivity of 0.9165, an MCC of 0.8630, a Dice coefficient of 0.8820, and a Jaccard index of 0.8650.

In dermoscopy color images, the proposed method provided an accuracy of 0.9979, an average precision of 0.8956, a sensitivity of 0.9301, an MCC of 0.9317; a Dice coefficient of 0.9301, and a Jaccard index of 0.8705. The values of accuracy, precision, sensitivity, MCC, Dice, and Jaccard coefficients were produced as 0.9933, 0.8437, 0.8591, 0.8936, 0.8591, and 0.7687 for MRI images, respectively. These results also show the efficiency of the proposed method in the segmentation of the different classes of cancer images.

The CAD-Ls-EDT method presented high performance with all the image types where high accuracy, sensitivity, and specificity were obtained. The excellent values achieved by the method concerning the Dice coefficient, MCC, and the Jaccard index demonstrate the ability to define the cancer margins and the differentiation between cancerous and non-cancerous tissues. These results provide sufficient evidence to suggest that the CAD-Ls-EDT method is a useful technique for cancer diagnosis and treatment planning.

TABLE I

HIGH-QUALITY MEDICAL SEGMENTATION IS REQUIRED FOR THE DETECTION OF CANCER IMAGES

Medical test	Liver image	Dermoscopy image	MRI image
Accuracy	0.9913	0.9979	0.9933
Precision	0.7538	0.8956	0.8437
Sensitivity	0.9165	0.9301	0.8591
MCC	0.8630	0.9317	0.8936
Dice coefficient	0.8820	0.9301	0.8591
Jaccard Coefficient	0.8650	0.8705	0.7687
Specificity	0.9910	0.9862	0.9930

MRI: Magnetic Resonance Imaging

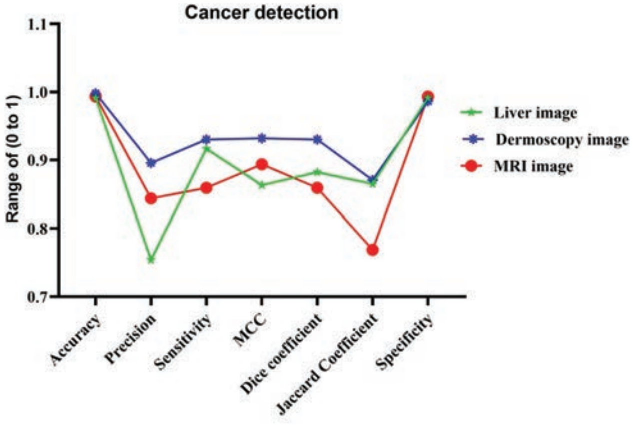

Fig. 6. Performance evaluation of computer-aided diagnosis with the level-set method by using edge detection method in cancer detection across different medical imaging modalities.

Therefore, the results of the current experiments support the improvements of the suggested CAD-Ls-EDT method for medical segmentation and cancer detection. Given that the described method has high accuracy, sensitivity, and specificity about different types of images, it can be used for cancer diagnostics at an early stage and further treatment planning. The generalized evaluation runs several performance measures to confirm the standardized method's effectiveness and precision, which is far superior to classic segmentation techniques. This situates CAD-Ls-EDT as a move forward in the categorization of cancer images with positive potential for shaping the clinical histories of cancer patients.

C. Comparison with the New Traditional Methods

The proposed method, called CAD-Ls-EDT, which combines the level-set approach and edge detection techniques, outperforms conventional segregation techniques. As presented in Table II, the proposed method improves the sensitivity, specificity, and precision of various cancer images, such as liver cancer images, dermoscopy color images, and MRI images. For instance, in liver cancer images, CAD-Ls-EDT achieves a sensitivity of 0.9165 and an accuracy of 0.9913, significantly outperforming methods, such as Simulated Annealing combined with Artificial Neural Network (SA-ANN) and Fuzzy Entropy with Level Set (FELs) thresholding, which have sensitivities of 0.88 and 0.83, for accuracy of 0.97 and 0.98, respectively(Maolood, Al-Salhi and Lu, 2018b; Win, et al., 2018).

This higher performance can be explained by the incorporation of edge detection with a level-set method that leads to better boundary delineation and segmentation. The CAD-Ls-EDT method, when supplemented with edge detection, can provide more accurate and noise-resistant segmentation for complex shapes of cancers as compared to the present methods of segmentation.

Fig. 7 presents the segmentation results of the proposed CAD-Ls-EDT and the typical approaches. It also contains the evaluation of both methods. The figure also demonstrates that the proposed method offers better specificity, sensitivity, accuracy, and precision compared to the other. According to the results, the CAD-Ls-EDT method is the most sensitive using MRI cancer images, with a comfort level of sensitivity score of 0.8591. The above example demonstrates how efficient the method is in determining true positives and is very imperative in early diagnosis.

Similarly, for dermoscopy color images, the sensitivity that is achieved with 0.9301 is quite higher than that received from several approaches out of them, FLog Parzen Level-set (FPLS) (Virupakshappa, Veerashetty and Ambika, 2022) and SA-ANN (Win, et al., 2018). This clearly shows that the overall performance of the CAD-Ls-EDT method is better in terms of detecting true positive images in dermoscopy images. As for the assessment of the specificity, it is also very high in the case of the CAD-Ls-EDT method. The specificity scores in the case of liver cancer, dermoscopy color cancer, and MRI cancer images are 0.9910, 0.9862, and 0.9930, respectively. These high specificity values indicate the method's ability to correctly recognize true negative cases, reducing the risk of false positives and unnecessary treatments.

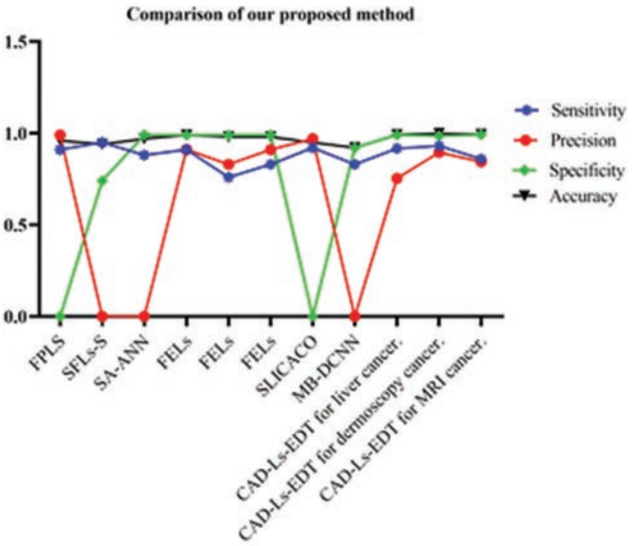

Fig. 7. Detailed comparison of our proposed method with current standard techniques.

The accuracy of positive predictions, or known as precision, is also quite high in our proposed method. The results of the precision score for the dermoscopy color image are 0.8956. It is slightly higher at 0.9910 for liver and MRI cancer and 0.9930; however, these scores are comparatively higher than other methods. Higher precision of the method in the identification of liver and MRI cancer points toward correct identification, and hence, the ability to reduce false positives is very high.

In addition, from Table III, it is noticeable that the proposed CAD-Ls-EDT method demonstrates excellent performance in the overlap measurements, including the Jaccard index and Dice coefficient, which are valuable measures of the quality of the segmentation. In the case of liver cancer, skin cancer, and MRI cancer images, we get a Dice coefficient of 0.8820, 0.9301, and 0.8591, A Jaccard Index of 0.8650, 0.8705, and 0.7687, respectively, which shows a high similarity between the segmented area and ground truth. The above-established performance is considerably better than other improved methods, such as the GAPBFCM and the MB-DCNN, whose Dice coefficients and Jaccard ratios are significantly lower (Latha and Perumal, 2020; Pei, et al., 2017).

Incorporation of the edge information into the LSM framework improves contour development, hence improving the results in image segmentation. This makes the CAD-Ls-EDT method suitable for early cancer detection and for planning the most suitable procedure.

TABLE II

Compare Our Suggested Method (Cad-Ls-Edt) to the Newest Research on Quality Cancer Segmentation Using Sensitivity, Specificity, Precision, and Accuracy as the Criteria for Evaluation

Compare Algorithm	Sensitivity	Precision	Specificity	Accuracy
FLog Parzen Level Set (FPLS) (Virupakshappa, Veerashetty and Ambika, 2022)	0.91	0.99	Non	0.96
Simulated annealing combined with an artificial neural network (SA-ANN) (Win, et al., 2018)	0.88	Non	0.99	0.97
Fuzzy entropy with a level set (FELs) thresholding for Ultrasound Image (Maolood, Al-Salhi and Lu, 2018b)	0.91	0.91	0.99	0.99
Fuzzy entropy with a level set (FELs) thresholding for MRI Image (Maolood, Al-Salhi and Lu, 2018b)	0.76	0.83	0.99	0.98
Fuzzy entropy with a level set (FELs) thresholding for MRI Image (Maolood, Al-Salhi and Lu, 2018b)	0.83	0.91	0.99	0.98
Simple linear iterative clustering (SLIC) and ant colony optimization (ACO) algorithms (SLICACO) (Singh, Janghel and Sahu, 2021)	0.92	0.97	Non	0.95
MB-DCNN (Xie, et al., 2020)	0.83	Non	0.92	0.92
Our proposed method (CAD-Ls-EDT) for liver cancer image	0.9165	0.7538	0.9910	0.9913
Our proposed method (CAD-Ls-EDT) for dermoscopy color cancer	0.9301	0.8956	0.9862	0.9979
Our proposed method (CAD-Ls-EDT) for MRI cancer	0.8591	0.8437	0.9930	0.9933

CAD-Ls-EDT: Computer-aided diagnosis with level-set algorithm according to edge detection technique

TABLE III
Comparison of our Proposed Method (Cad-Ls-Edt) With The Latest Studies on Quality Cancer Segmentation, Taking Into Account the Jaccard Index and Dice Coefficient as the Criteria for Evaluation

Compare Algorithm	Dice Coefficient	Jaccard index
Genetic algorithm probability based Fuzzy C-Means (GAPBFCM) (Latha and Perumal, 2020)	0.91	0.91
Novel density-based fuzzy c-mean algorithm (D-FCM) (Pei, et al., 2017)	0.89	0.80
Fuzzy entropy with a level set (FELs) thresholding for Ultrasound Image (Maolood, Al-Salhi and Lu, 2018b)	0.91	0.92
Fuzzy entropy with a level set (FELs) thresholding for MRI Image (Maolood, Al-Salhi and Lu, 2018b)	0.79	0.97
MB-DCNN (Xie, et al., 2020)	0.90	0.82
Fuzzy entropy with a level set (FELs) thresholding for Dermoscopy Image (Maolood, Al-Salhi and Lu, 2018b)	0.87	0.95
Simple linear iterative clustering (SLIC) and ant colony optimization (ACO) algorithms (SLICACO) (Singh, Janghel and Sahu, 2021)	0.91	0.84
Our proposed method (CAD-Ls-EDT) for liver cancer image	0.8820	0.8650
Our proposed method (CAD-Ls-EDT) for dermoscopy color cancer	0.9301	0.8705
Our proposed method (CAD-Ls-EDT) for MRI cancer	0.8591	0.7687

CAD-Ls-EDT: Computer-aided diagnosis with level-set algorithm according to edge detection technique

V. Conclusion

The proposed (CAD-Ls-EDT) approach, which combines edge detection techniques with the level-set method from medical image segmentation, has been tested and found to detect various forms of cancer. It has specific applications in increasing the accuracy, sensitivity, and specificity of the detected cancer in images, which include liver cancer, brain MRI, and dermoscopy color images.

Enhancing boundary detection, the proposed CAD-Ls-EDT method provides better boundaries around the cancer regions than most segmentation methods. This is the enhanced segment, which plays a critical role in the diagnosis of the diseases and the initial management of the diseases, and the segment, which makes the patient lives.

The experimental results have shown that the application of the CAD-Ls-EDT methodology results in high values of the important performance indicators, such as true positive rate, Jaccard, MCC, and Dice coefficients. These measures contribute to the efficiency level and correctness of the method for medical image analysis.

Similarly, the CAD-Ls-EDT method will also be very useful for oncologists and radiologists to enhance the segmentation quality of the medical images with high accuracy to obtain accurate diagnostic data. This enhancement in the computer-aided diagnostic approach is a profound leap in the war against cancer, particularly in achieving enhanced clinical prognosis because of early and accurate diagnosis and therapies.

REFERENCES

Al-Ayyoub, M., Abu-Dalo, A.M., Jararweh, Y., Jarrah, M., and Sa'd, M.A., 2015. A GPU-based implementations of the fuzzy C-means algorithms for medical image segmentation. *The Journal of Supercomputing*, 71, pp.3149-3162.

Aziz, M.H., and Abdulla, A.A. 2023. Computer-aided diagnosis for the early breast cancer detection. *UHD Journal of Science and Technology*, 7, pp.7-14.

Aziz, S.A., Hawbani, A., Wang, X., Abdelhamid, T., Maolood, I.Y., Alsamhi, S., and Ismail, A., 2023. *Improving Brain MRI Image Segmentation Quality: A Hybrid Technique for Intensity Inhomogeneity Correction. In: 34th Conference of Open Innovations Association (FRUCT)*. IEEE, United States, pp.20-26.

Badar, T., Särkkä, S., Zhao, Z., and Visala, A., 2024. Rao-blackwellized particle filter using noise adaptive kalman filter for fully mixing state-space models. *IEEE Transactions on Aerospace and Electronic Systems*, 60, pp.6972-6982.

Bechar, A., Elmir, Y., Himeur, Y., Medjoudj, R., and Amira, A., 2024. *Federated and Transfer Learning for Cancer Detection Based on Image Analysis*. [arXiv preprint arXiv:2405.20126].

Canny, J., 1986. A computational approach to edge detection. *IEEE Transactions on Pattern Analysis and Machine Intelligence*, 8, pp.679-698.

Chan, H.P., Hadjiiski, L.M., and Samala, R.K., 2020. Computer-aided diagnosis in the era of deep learning. *Medical Physics*, 47, pp.e218-e227.

Chan, T.F., and Vese, L.A., 2001. Active contours without edges. *IEEE Transactions on image Processing*, 10, pp.266-277.

Chen, Y., Tagare, H.D., Thiruvenkadam, S., Huang, F., Wilson, D., Gopinath, K.S., Briggs, R.W., and Geiser, E.A. 2002. Using prior shapes in geometric active contours in a variational framework. *International Journal of Computer Vision*, 50, pp.315-328.

Elizângela, D.S.R., Fátima, N.S.DM., Regis, C.P.M., Chagas, J.V.S., Guimarães, M.T., Santos, L.O., Medeiros, A.G., and Peixoto, S.A, 2021. Level set approach based on Parzen Window and floor of log for edge computing object segmentation in digital images. *Applied Soft Computing*, 105, p.107273.

El-Baz, A., Beache, G.M., Gimel' Farb, G., Suzuki, K., Okada, K., Elnakib, A., Soliman, A., and Abdollahi, B., 2013. Computer-aided diagnosis systems for lung cancer: Challenges and methodologies. *International Journal of Biomedical Imaging*, 2013, p.942353.

Friedrich, T., Kötzing, T., Krejca, M.S., and Sutton, A.M., 2016. The compact genetic algorithm is efficient under extreme gaussian noise. *IEEE Transactions on Evolutionary Computation*, 21, pp.477-490.

Halalli, B., and Makandar, A., 2018. Computer aided diagnosis-medical image analysis techniques. *Breast Imaging*, 85, p.109.

Hemanth, D.J., Anitha, J., and Balas, V.E., 2015. Performance improved modified Fuzzy C-Means algorithm for image segmentation applications. *Informatica*, 26, pp.635-648.

Hosseini, S.H., Monsefi, R., and Shadroo, S., 2024. Deep learning applications for lung cancer diagnosis: A systematic review. *Multimedia Tools and Applications*, 83, pp.14305-14335.

Jaganathan, P., and Kuppuchamy, R., 2013. A threshold fuzzy entropy based feature selection for medical database classification. *Computers in Biology and Medicine*, 43, pp.2222-2229.

Kadhim, Y.A., Khan, M.U., and Mishra, A., 2022. Deep learning-based computer-aided diagnosis (cad): Applications for medical image datasets. *Sensors* (*Basel*), 22, p.8999.

Kass, M., Witkin, A., and Terzopoulos, D., 1988. Snakes: Active contour models. *International Journal of Computer Vision*, 1, pp.321-331.

Khaliki, M.Z., and Başarslan, M.S., 2024. Brain tumor detection from images and comparison with transfer learning methods and 3-layer CNN. *Scientific Reports*, 14, p.2664.

Latha, C., and Perumal, D., 2020. Segmentation of brain tumour MR images in soft computing techniques. *Journal of Theoretical and Applied Information Technology*, 98, p.3164-3171.

Latha, C., and Perumal, K., 2020. Brain tumour segmentation using genetic and ant colony. *International Journal of Advanced Research in Engineering and Technology*, 11, pp.1643-1654.

Maolood, I.Y., 2013. *Fuzzy C-means Clustering Algorithm with Level Set for MRI Cerebral Tissue Segmentation.* Universiti Teknologi Malaysia, Malaysia.

Maolood, I.Y., Al-Salhi, Y.E.A., Alresheedi, S., Ince, M., Li, T., and Lu, S.F., 2018a. *Fuzzy C-Means Thresholding for a Brain MRI Image Based on Edge Detection. In: 2018 IEEE 4th International Conference on Computer and Communications (ICCC)*. IEEE, pp.1562-1566.

Maolood, I.Y., Al-Salhi, Y.E.A., and Lu, S., 2018b. Thresholding for medical image segmentation for cancer using fuzzy entropy with level set algorithm. *Open Medicine*, 13, pp.374-383.

Mercaldo, F., Brunese, L., Martinelli, F., Santone, A., and Cesarelli, M., 2023. Object detection for brain cancer detection and localization. *Applied Sciences*, 13, pp.9158.

Osher, S., and Sethian, J.A., 1988. Fronts propagating with curvature-dependent speed: Algorithms based on Hamilton-Jacobi formulations. *Journal of Computational Physics*, 79, pp. 12-49.

Pei, H.X., Zheng, Z.R., Wang, C., Li, C.N., and Shao, Y.H., 2017. D-FCM: Density based fuzzy c-means clustering algorithm with application in medical image segmentation. *Procedia Computer Science*, 122, pp.407-414.

Shao, J., Luan, S., Ding, Y., Xue, X., Zhu, B., and Wei, W., 2024. Attention connect network for liver tumor segmentation from CT and MRI images. *Technology in Cancer Research and Treatment*, 23, p.1-11.

Sharma, P., Malik, S., Sehgal, S., and Pruthi, J., 2013. Computer aided diagnosis based on medical image processing and artificial intelligence methods. *International Journal of Information and Computation Technology*, 3, pp.887-892.

Singh, L., Janghel, R.R., and Sahu, S.P., 2021. SLICACO: An automated novel hybrid approach for dermatoscopic melanocytic skin lesion segmentation. *International Journal of Imaging Systems and Technology,* 31, pp.1817-1833.

Suryawanshi, S., and Patil, S.B., 2024. Brain tumor detection using YoloV5 and faster RCNN. *International Journal of Intelligent Systems and Applications in Engineering*, 12, pp.335-342.

Virupakshappa, S., Veerashetty, S., and Ambika, N., 2022. Computer-aided diagnosis applied to MRI images of brain tumor using spatial fuzzy level set and ANN classifier. *Scalable Computing: Practice and Experience*, 23, pp.233-249.

Win, K.Y., Choomchuay, S., Hamamoto, K., Raveesunthornkiat, M., Rangsirattanakul, L., and Pongsawat, S., 2018. Computer aided diagnosis system for detection of cancer cells on cytological pleural effusion images. *BioMed Research International*, 2018, p.6456724.

Xie, Y., Zhang, J., Xia, Y., and Shen, C., 2020. A mutual bootstrapping model for automated skin lesion segmentation and classification. *IEEE Transactions on Medical Imaging*, 39, pp.2482-2493.

Yang, W., Chen, X.D., Wang, H., and Mao, X., 2024. Edge detection using multi-scale closest neighbor operator and grid partition. *The Visual Computer*, 40, pp.1947-1964.

Yin, J., Chang, H., Wang, D., Li, H., and Yin, A., 2021. Fuzzy C-means clustering algorithm-based magnetic resonance imaging image segmentation for analyzing the effect of Edaravone on the vascular endothelial function in patients with acute cerebral infarction. *Contrast Media* and *Molecular Imaging*, 2021, p.4080305.

Zhu, Z., Sun, M., Qi, G., Li, Y., Gao, X., and Liu, Y., 2024. Sparse dynamic volume TransUNet with multi-level edge fusion for brain tumor segmentation. *Computers in Biology and Medicine*, 172, p.108284.

Epidemiological Trends and Molecular Characterization of Breast Carcinoma in Erbil, Kurdistan Region of Iraq

Mahmoud A. Chawsheen[1,2†], Ahmed A. Al-Naqshbandi[3], Rivan H. Ishaac[3] and Fairuz A. Kaka Sur[3]

[1]Medical Research Center, Hawler Medical University,
Erbil, Kurdistan Region – F.R. Iraq

[2]College of Pharmacy, Cihan University-Erbil,
Erbil, Kurdistan Region – F.R. Iraq

[3]Department of Laboratory, Rizgary Teaching Hospital,
Erbil, Kurdistan Region– F.R. Iraq

***Abstract*—Accumulated evidence suggests a tangible increase in breast cancer (BC) patients in the Kurdistan region of Iraq, yet data on their histological and molecular subtypes remain limited. This study aims to assess the prevalence, histopathologic features, and molecular profiles of BC incidences in Erbil. For this purpose, 261 clinical records of histologically confirmed BC cases from Rizgary Teaching Hospital are analyzed. Results reveal that invasive ductal carcinoma (IDC) emerged as the most frequent histological subtype. In terms of hormonal receptor status, mastectomy patients who tested positive for estrogen receptor (ER), progesterone receptor (PR), and human epidermal growth factor receptor 2 (HER2) are 52.49%, 50.57%, and 18.01%, respectively, and the corresponding figures for Tru-Cut biopsy (TCB) patients are 24.90% for both ER and PR and 6.13% for HER2. Regarding tumor grading, mastectomy patients aged 51–60 have the highest grade II frequency, and TCB patients under 40 years and those between 41 and 50 years show the highest occurrence of the same grade. Moreover, tumor stages II and III made up nearly two-thirds of all cases across all age groups. For the molecular subtypes, luminal A is the most prevalent in both mastectomy and TCB patients. In conclusion, IDC is the predominant BC subtype in the region, with a higher prevalence of ER and PR positivity compared to HER2. Luminal A is the dominant molecular subtype. While stages II and III are common across all ages, tumors of grade II and stage II are frequently observed in older ages.**

***Index Terms*—Breast cancer, Mastectomy, Tru-Cut biopsy, Invasive ductal carcinoma, Estrogen receptor, Progesterone receptor, Human epidermal growth factor receptor.**

ARO-The Scientific Journal of Koya University
Vol. XIII, No.1 (2025), Article ID: ARO.11860. 8 pages
DOI: 10.14500/aro.11860
Received: 11 October 2024; Accepted: 16 February 2025
Regular research paper; Published: 02 March 2025

[†]Corresponding author's e-mail: mahmoud.hassan@hmu.edu.krd

I. INTRODUCTION

Breast cancer (BC) has a great burden on the public health sector worldwide (Wang, et al., 2016) for being a heterogeneous pathological condition and the most frequent type of cancer in females, with estimated new cases of 31% and estimated deaths of 15% out of all cancer types (Wang, et al., 2019; Siegel, et al., 2023). BC is most common in high-income countries in comparison with lower-income countries (Hu, et al., 2019), and there is a positive correlation between BC progression and the self-awareness of affected individuals (Gubari, et al., 2017). Furthermore, the sociodemographic index of countries may act as a reliable indicator for the prevention and development of cost-effective diagnosis for BC in a positive manner (Hu, et al., 2019).

The emergence of BC has been found to be associated with various risk factors. BC is more common among older females and those who have a family history of breast or ovarian cancer and individuals with genetic mutations such as BRCA2/BRCA1. Rates of BC also fluctuate among different race/ethnic groups, as it has been reported more frequently among white women than others. Women who give more births and breastfeed their children show fewer incidences of BC. The density of breast tissue is implicated in this context, as increased density correlates positively with BC development. Moreover, abnormal menstrual periods and menopause may also contribute to BC development (Weigelt, et al., 2008; Erber and Hartmann, 2020; Prat and Perou, 2011; Herschkowitz, et al., 2007; Plasilova, et al., 2016).

At the cellular level, BC is due to an uncontrollable proliferation of lining epithelial cells of the ducts or lobules of the breast, especially at the terminal duct lobular unit. Due to that, BCs in general are classified either as ductal or lobular carcinomas (Kasper and Harrison, 2005; Makki, 2015). And these two types of carcinoma could be subdivided, according to their tendency toward metastasis, into non-invasive and invasive. The first one includes ductal carcinoma *in situ* and lobular carcinoma *in situ* (Buerger, 2000).

According to the World Health Organization, as reported by Tan et al. (2020), BC can be classified as follows: Epithelial, mesenchymal, and fibroepithelial tumors, tumors of the nipple, malignant lymphoma, and metastatic tumors. The epithelial tumor, which is the main derived source of BC, is also subdivided into: Invasive breast carcinoma, epithelial-myoepithelial tumors, precursor lesions, intraductal proliferative lesions, papillary lesions, and benign epithelial proliferations (Tan, et al., 2020).

Invasive breast carcinoma, which reflects 23% of all diagnosed cancers in women, encompasses the following subtypes: Invasive carcinoma of no special type (NST), formerly known as invasive ductal carcinoma (IDC), invasive lobular carcinoma (ILC), tubular carcinoma, cribriform carcinoma, mucinous carcinoma, carcinoma with medullary features, carcinoma with apocrine differentiation, carcinoma with signet-ring-cell differentiation, invasive micropapillary carcinoma, inflammatory BC, metaplastic carcinoma of NST, mixed metaplastic carcinoma, myoepithelial carcinoma, and other rear types (Anderson, et al., 2006; Tan, et al., 2020; Łukasiewicz, et al., 2021).

Invasive BC can also be classified according to their molecular markers into several subtypes, including luminal A and B, human epidermal growth factor receptor 2 (HER2)-enriched, basal-like, and normal breast-like. In 2007, the claudin-low BC sub-type was discovered in an integrated analysis of human and rodent mammary tumors. Basal-Like/Triple-Negative BC (TNBC): TNBC is a heterogeneous collection of BCs characterized by estrogen receptor (ER) (estrogen)-negative, Progesterone receptor (PR) (progesterone)-negative, and HER2-negative cancer cells (Weigelt, et al., 2008; Łukasiewicz, et al., 2021). TNBC is found to be associated with 10 to 20% of all invasive BCs and is commonly found in the African-American ethic group, younger females, and higher tumor grade, and usually spotted at advanced stages (Kumar and Aggarwal, 2015).

BC has significantly increased in Iraq over the past decades (Al-Hashimi, 2021), and the Kurdistan Region, like other parts of the world, has also experienced a tangible rise in this pathological condition (Majid, et al., 2009; Khoshnaw, Mohammed and Abdullah, 2016; Mutar, et al., 2019). According to previous studies, BC in the abovementioned region is mainly detected in premenopausal women with multiple pregnancies, unlike in western countries where the incidence of BC is more common among younger individuals (Majid, et al., 2009; Molah Karim, et al., 2015).

In spite of the above-mentioned facts about BC in the Kurdistan Region of Iraq, and due to limitations of previous studies in regard to sample size, there is insufficient information in regard to tumor classification and their prevalence. In this study, we aimed to uncover the status of BC in the Erbil governorate by identifying and assessing their dominant histological and molecular subtypes, especially ER, PR, and HER2.

II. Materials and Methods

A. Data Collection

This study provides a retrospective analysis of the records of 261 patients who have been diagnosed with BC, confirmed through histological examination by the histopathologist at the Laboratory Department of Rizgary Teaching Hospital in Erbil, covering the period from January 2016 to December 2021. All BC cases that underwent immunohistochemistry investigations within the specified timeframe were included, while records of repeated BC specimens were deliberately excluded. The Hawler Medical Research Center at Halwer Medical University provided the necessary ethical approval for the carrying out of this study.

B. Histopathological Profile of the Cases

Histopathological profiles, including tumor stage, grades, and histopathological types, were recorded by the pathologists at the Laboratory Department of Rizgary Teaching Hospital based on Pragya and Jorns's (2023) guidelines. Histologic grading is a key method used to evaluate the prognosis and behavior of tumors in invasive BC, helping to identify patients at risk of adverse outcomes and identify candidates for appropriate therapies (Van Dooijeweert, Van Diest and Ellis, 2022).

C. Immuno-Histochemical and Molecular Subtypes Study

The immunohistochemistry was routinely used for the detection of ER, PR, and HER2 using the EnVision FLEX+ kit by Agilent Dako, USA (Product No. K8002) by the technicians of the Histopathology Laboratory. Molecular subtype categorization was evaluated based on immunohistochemistry surrogates for ER, PR, and HER2 status, and the criteria were as shown in Table I.

III. Results and Discussion

A. Results

Two hundred sixty-one females with BC enrolled in this study, with ages ranging from 25 to 84 years. The mean age of the mastectomy patient group was 50.74 years, whereas the Tru-Cut biopsy (TCB) patient group had a mean age of 46.65 years (Fig. 1a). IDC had the greatest occurrence of BC subtypes, followed by ILC (Fig. 1b).

The number and percentage of patients who tested positive for ER, PR, and HER in the group of patients undergoing mastectomy were 137 (52.49%), 135 (50.57%), and 47 (18.01%), respectively. In the group of patients undergoing TCB, the number and percentage of positive cases were 65 (24.90%), 65 (24.90%), and 16 (6.13%).

In regard to triple-negative cases (TNBC), our data indicates that 13.41% of all patients are diagnosed with this condition (35 out of 261). While it was primarily associated with the IDC (85.71%) BC subtype, it was not that common among the ILC (2.86%) BC sub-type (Fig. 2a and b).

The majority of tumors in the patient groups undergoing mastectomy and TCB belonged to Grade II, accounting for 122 (46.74%) and 60 (22.99%), followed by Grade III, accounting for 53 (20.31%) and 20 (7.66%), and Grade I, accounting for 4 (1.53%) and 2 (0.77%), in that order.

When it came to the evaluation of molecular subtypes, the luminal A molecular type scored highest at 115 (44.06%) and 54 (20.69%) in the patient groups undergoing mastectomy and TCB, while the luminal B molecular type scored lowest at 64 (24.52%) and 28 (10.13%), respectively. Histological tumor stages with the highest frequencies were stage II 114 (43.68%) and stage III 44 (16.86%), followed by stage I 18 (6.89%) and stage IV 3 (1.15%) (Table II).

The age-specific distribution of tumor grades in the mastectomy patient population revealed that patients aged 41–50 and 51–60 years had the highest prevalence of grade II. However, patients aged ≤40 and 41–50 years had the highest occurrence of grade III. In the patient group undergoing a TCB, patients under 40 years and aged 41–50 had the highest occurrence of grade II. Conversely, individuals in the age groups of ≤40 and 51–60 years had the highest occurrence of grade III (Table III).

Table IV displays the pathologic stage distribution of patients having mastectomy. Stage II had the highest occurrence of cases (63.69%) and was more common in patient groups aged ≤40 and 41–50 years. Stage III had the second-highest incidence (24.58%), with the highest frequency in age groups 41–50 and 51–60. There was a greater incidence in age groups ≤40 and 41–50, with stage I and stage IV percentage distributions of 10.05% and 1.68%, respectively.

B. Discussion

While some studies have evaluated the histological subtypes of BC in the Kurdistan Region of Iraq, there are limited ones that focus on the molecular subtypes of this pathological condition (Molah Karim, et al., 2015; Khoshnaw, Mohammed and Abdullah, 2016; Mutar, et al., 2019). This is largely due to the fact that the majority of them either did not cover this angle or simply encompassed limited population sizes. In this study, we tried to fill this gap by uncovering predominant molecular BC subtypes and including more cases over a longer period of time.

A major contributing risk factor to BC development is age (Siegel, Miller and Jemal, 2018). The average age of BC

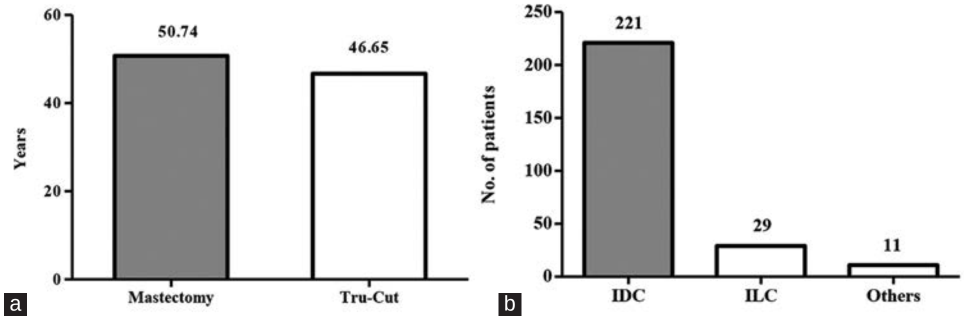

Fig. 1. Age and occurrence of patients, (a) the average age of breast cancer patients. (b) the distribution of breast cancer subtypes.

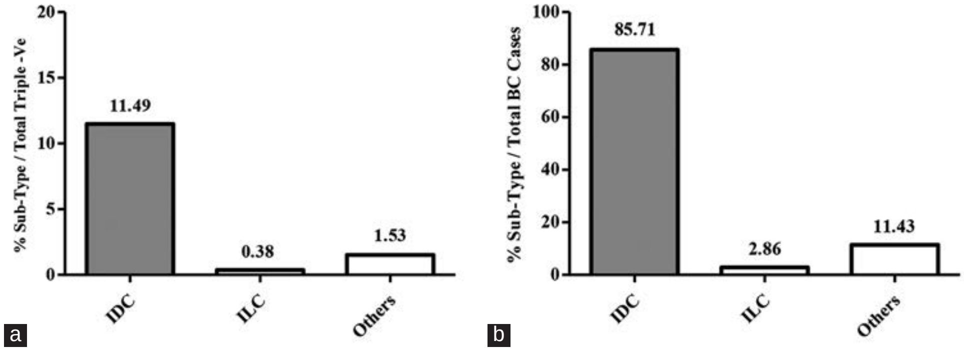

Fig. 2. The prevalence of triple-negative cases distributed over BC sub-types. (a) The percentage of each common sub-types over the total triple-negative cases (n = 35). (b) The percentage of each common sub-types over the total BC cases (n = 261).

TABLE I
Molecular Subtypes of Breast Cancer Profile*

Immuno-profile	Luminal A	Luminal B	HER2+ (Enriched)	Basal-Like
ER, PR	ER+, and PR high+	ER+, PR- low or intermediate+	ER-, PR-	ER-, PR-
HER2	HER2-	HER2+or HER2-	HER2+	HER2-
Others	Low Ki67 (<14%)	Ki67 (≥14)		CK5/6 and/or EGFR+

*This table was cited by Coates et al. (2015). ER: Estrogen receptor, PR: Progesterone receptor, HER2: Human epidermal growth factor receptor 2

TABLE II

DISTRIBUTION OF BREAST CANCER PATIENTS ACCORDING TO PATHOLOGICAL CHARACTERISTICS

Mastectomy	2016	2017	2018	2019	2020		2021			Total No. (%)
	14 IDC Patient No. (%)	33 IDC Patients No. (%)	14 IDC Patient No. (%)	28 IDC Patients No. (%)	8 IDC Patients No. (%)	15 ILC Patients No. (%)	53 IDC Patients No. (%)	3 ILC Patients No. (%)	11 other types No. (%)	
ER										
N	3 (12)	6 (15.38)	5 (27.78)	4 (11.429)	1 (3.125)	0	19 (16.964)	1 (0.893)	3 (2.679)	42 (16.09)
P	11 (44)	27 (69.23)	9 (50)	24 (68.571)	7 (21.875)	15 (46.875)	34 (30.357)	2 (1.786)	8 (7.143)	137 (52.49)
PR										
N	4 (16)	6 (15.38)	5 (27.78)	4 (11.429)	1 (3.125)	1 (3.125)	19 (16.964)	1 (0.893)	3 (2.679)	44 (16.86)
P	10 (40)	27 (69.23)	9 (50)	24 (68.571)	7 (21.875)	14 (43.75)	34 (30.357)	2 (1.786)	8 (7.143)	135 (50.57)
HER										
N	9 (36)	21 (53.85)	12 (66.67)	19 (54.286)	8 (25)	14 (43.75)	38 (33.929)	3 (2.679)	8 (7.143)	132 (50.57)
P	5 (20)	12 (30.77)	2 (11.11)	9 (25.714)	0	1 (3.125)	15 (13.393)	0	3 (2.679)	47 (18.01)
Grade										
I	0	0	0	0	1 (3.125)	0	2 (1.786)	0	1 (0.893)	4 (1.53)
II	10 (40)	23 (58.97)	11 (61.11)	19 (54.286)	5 (15.625)	14 (43.75)	33 (29.464)	2 (1.786)	5 (4.464)	122 (46.74)
III	4 (16)	10 (25.64)	3 (16.67)	9 (25.714)	2 (6.25)	1 (3.125)	18 (16.071)	1 (0.893)	5 (4.464)	53 (20.31)
Molecular sub-type (Ki 67)										
Luminal A	9 (36)	22 (56.41)	12 (66.67)	15 (42.857)	6 (18.75)	14 (43.75)	28 (25)	2 (1.786)	7 (6.25)	115 (44.06)
Luminal B	5 (20)	11 (28.21)	2 (11.11)	13 (37.143)	2 (6.25)	1 (3.125)	25 (22.321)	1 (0.893)	4 (3.571)	64 (24.52)
Stage										
I	1 (4)	0	4 (22.22)	3 (8.571)	2 (6.25)	1 (3.125)	6 (5.357)	0	1 (0.893)	18 (6.89)
II	10 (40)	21 (53.85)	7 (38.89)	17 (48.571)	4 (12.5)	11 (34.375)	34 (30.357)	1 (0.893)	9 (8.036)	114 (43.68)
III	2 (8)	12 (30.77)	3 (16.67)	8 (22.857)	2 (6.25)	3 (9.375)	11 (9.821)	2 (1786)	1 (0.893)	44 (16.86)
IV	1 (4)	0	0	0	0	0	2 (1.786)	0	0	3 (1.15)

Tru-Cut biopsy	2016	2017	2018	2019	2020		2021		Total No. (%)
	11 IDC patients No. (%)	6 IDC patients No. (%)	4 IDC patients No. (%)	7 IDC patients No. (%)	1 IDC patient No. (%)	8 ILC patients No. (%)	42 IDC patients No. (%)	3 ILC patients No. (%)	
ER									
N	2 (8)	3 (7.69)	1 (5.56)	0	0	1 (3.125)	10 (8.926)	0	17 (6.51)
P	9 (36)	3 (7.69)	3 (16.67)	7 (20)	1 (3.125)	7 (21.875)	32 (28.571)	3 (2.679)	65 (24.90)
PR									
N	2 (8)	3 (7.69)	1 (5.56)	0	0	1 (3.125)	9 (9.0357)	1 (0.893)	17 (6.51)
P	9 (36)	3 (7.69)	3 (16.67)	7 (20)	1 (3.125)	7 (21.875)	33 (29.464)	2 (1.786)	65 (24.90)
HER									
N	7 (28)	6 (15.38)	3 (16.67)	3 (8.571)	1 (3.125)	8 (25)	35 (31.25)	3 (2.679)	66 (25.29)
P	4 (16)	0	1 (5.56)	4 (11.429)	0	0	7 (6.25)	0	16 (6.13)
Grade									
I	0	0	0	0	0	0	2 (1.786)	0	2 (0.77)
II	9 (36)	6 (15.38)	3 (16.67)	5 (14.286)	1 (3.125)	7 (21.875)	27 (24.107)	2 (1.786)	60 (22.99)
III	2 (8)	0	1 (5.56)	2 (5.714)	0	1 (3.125)	13 (11.607)	1 (0.893)	20 (7.66)
Molecular sub-type (Ki 67)									
Luminal A	9 (36)	6 (15.38)	2 (11.11)	3 (8.571)	0	5 (15.625)	28 (25)	1 (0.893)	54 (20.69)
Luminal B	2 (8)	0	2 (11.11)	4 (11.429)	1 (3.125)	3 (9.375)	14 (12.5)	2 (1.786)	28 (10.73)
Total number of cases	25	39	18	35	32		112		261

IDC: Invasive ductal carcinoma; ILC: Invasive lobular carcinoma; Other types included, IDC with ILC, IDC with micro-papillary carcinoma, IDC with mucinous carcinoma, inflammatory carcinoma, medullary carcinoma, metaplastic carcinoma, micro-papillary carcinoma, and papillary carcinoma. ER: Estrogen receptor

TABLE III
Prevalence of Breast Cancer Grade According to Age Groups

Mastectomy	Grade I (6 [2.3%])				Grade II (179 [68.58%])				Grade III (76 [29.12%])			
	≤40	41–50	51–60	≥61	≤40	41–50	51–60	≥61	≤40	41–50	51–60	≥61
2016												
14 IDC patients	0	0	0	0	1	5	3	1	1	1	1	1
2017												
33 IDC patients	0	0	0	0	7	9	3	4	3	3	3	1
2018												
14 IDC patients	0	0	0	0	2	2	3	4	1	0	1	1
2019												
28 IDC patients	0	0	0	0	2	7	7	3	4	1	2	2
2020												
8 IDC patients	0	1	0	0	1	0	2	2	0	1	1	0
15 ILC patients	0	0	0	0	3	3	5	3	0	1	0	0
2021												
53 IDC patients	0	1	0	1	9	11	8	5	6	5	3	4
3 ILC patients	0	0	0	0	0	2	0	0	0	0	0	1
11 others	0	0	0	1	1	3	0	1	3	1	0	1
Number of cases	0	2	0	2	26	42	31	23	18	13	11	11
Tru-Cut biopsy												
2016												
11 IDC patients	0	0	0	0	2	3	1	3	1	0	0	1
2017												
6 IDC patients	0	0	0	0	2	2	1	1	0	0	0	0
2018												
4 IDC patients	0	0	0	0	0	1	0	2	1	0	0	0
2019												
7 IDC patients	0	0	0	0	2	0	0	0	1	0	3	1
2020												
1 IDC patients	0	0	0	0	1	0	0	0	0	0	0	0
8 ILC patients	0	0	0	0	2	1	2	2	0	0	1	0
2021												
42 IDC patients	0	1	1	0	6	13	3	5	4	2	3	4
3 ILC patients	0	0	0	0	0	2	0	0	1	0	0	0
Number of cases	0	1	1	0	15	22	7	13	8	2	7	6
Total number (%)	0 (0.0%)	3 (1.15%)	1 (0.38%)	2 (0.77%)	41 (15.71%)	64 (24.52%)	38 (14.56%)	36 (13.79%)	26 (9.96%)	15 (5.75%)	18 (6.9%)	17 (6.52%)

IDC: Invasive ductal carcinoma; ILC: Invasive lobular carcinoma; Other types included, IDC with ILC, IDC with micro-papillary carcinoma, IDC with mucinous carcinoma, inflammatory carcinoma, medullary carcinoma, metaplastic carcinoma, micro-papillary carcinoma, and papillary carcinoma.

cases in this study and who had a mastectomy was around 50 years, whereas the cases that underwent TCB were around the age of 46 years. In agreement with our data, Salman et al. (2021) and Abdulkareem, Ghalib and Rashaan (2023) in their studies that were conducted on Iraqi BC patients had reported similar results. There are other studies that were also conducted on Iraqi BC patients but reported slight differences in comparison to our data. For instance, Khalaf et al. (2022) reported the peak incidence of BC was between 40 and 49 years (n = 251). These variances might be due to the differences in the sample size of the study or the applied methodology in sample collection (i.e., whether it was random or not).

Our results indicate that the IDC histological subtype was the most prevalent among BC cases, making up more than 84% of all cases. Previous research conducted in Erbil, Baghdad, and Turkey has resulted in similar findings (Khoshnaw, Ganjo and Salih, 2023; Mohsin and Mohamad, 2024; Duraker, et al., 2020). Unfortunately, IDC histological subtype is usually associated with limited clinical outcomes (Goh, et al., 2019; Han, Wang and Xu, 2020), which may contribute to difficulties in curing affected patients.

Both the mastectomy and the TCB BC patients in our investigation had high rates of ER-positive, which is in line with what Khoshnaw, Ganjo and Salih (2023) and Mohsin and Mohamad (2024) found in their studies. However, this is not always the case, as a high incidence of ER-negative BCs has also been reported. This could be attributed to different factors, such as variations in the used staining protocols, the age of the patients (as younger patients tend to exhibit higher rates of ER-negative), and the stage of progression at the time of diagnosis (Shet, et al., 2009; Chen, et al., 2023). Identifying a significant number of ER-positive cases indicates that endocrine therapy may present a promising treatment option for this particular group of patients (Manjunath, et al., 2011).

Our data revealed that the majority of BC patients were PR-positive, which is consistent with findings from studies in both Iran (Jahanbin, et al., 2023) and Iraq (Khoshnaw, Ganjo and Salih, 2023). Moreover, most patients who underwent

TABLE IV
PREVALENCE OF BREAST CANCER STAGE ACCORDING TO AGE GROUPS

Mastectomy group	2016	2017	2018	2019	2020		2021			Total number of cases (%)
	14 IDC patients	33 IDC patients	14 IDC patients	28 IDC patients	8 IDC patients	15 ILC patients	53 IDC patients	3 ILC patients	11 other types	
Stage I 18 (10.05%)										
≤40	1	0	1	1	0	1	2	0	0	6 (3.35)
41–50	0	0	2	0	2	0	2	0	0	6 (3.35)
51–60	0	0	0	2	0	0	1	0	0	3 (1.68)
≥61	0	0	1	0	0	0	1	0	1	3 (1.68)
Stage II 114 (63.69%)										
≤40	1	6	2	5	1	2	11	0	4	32 (17.88)
41–50	4	8	1	5	0	2	11	0	1	32 (17.88)
51–60	5	3	0	4	2	5	6	0	2	27 (15.08)
≥61	0	4	4	3	1	2	6	1	2	23 (12.85)
Stage III 44 (24.58%)										
≤40	0	4	0	0	0	0	1	0	0	5 (2.79)
41–50	1	4	1	3	1	2	4	2	1	19 (10.61)
51–60	0	3	2	3	1	0	4	0	0	13 (7.26)
≥61	1	1	0	2	0	1	2	0	0	7 (3.91)
Stage IV 3 (1.68%)										
≤40	0	0	0	0	0	0	1	0	0	1 (0.56)
41–50	1	0	0	0	0	0	1	0	0	2 (1.12)
51–60	0	0	0	0	0	0	0	0	0	0 (0.0)
≥61	0	0	0	0	0	0	0	0	0	0 (0.0)

IDC: Invasive ductal carcinoma; ILC: Invasive lobular carcinoma; Other types included, IDC with ILC, IDC with micro-papillary carcinoma, IDC with mucinous carcinoma, inflammatory carcinoma, medullary carcinoma, metaplastic carcinoma, micro-papillary carcinoma and papillary carcinoma

both a mastectomy and a TCB were classified as HER negative. This came in agreement with another study, also from Iran, which reported a high frequency in HER-negative BC cases (Akbari, et al., 2017). Recently, a multi-omics study covering HER status in 579 BC patients that was reported by Jin et al. (2023) identified four molecular subtypes of this receptor, each of which exhibits unique biological and clinical characteristics: canonical luminal, immunogenic, proliferative, and receptor tyrosine kinase (RTK)-promoted (Jin, et al., 2023). Their findings indicate the necessity of further investigations in BC subtypes and uncovering their heterogeneity to have a clearer idea about these tumors and the best strategy to eradicate or inhibit them.

According to our findings, TNBC was diagnosed in 13.41% of patients, more than 85% of whom were associated with IDC, and it was less common among other BC subtypes. Our data align with a previous study reported by Kumar and Aggarwal (2015), indicating that 10–20% of BC patients worldwide suffer from TNBC. On the other hand, other reports indicate slight fluctuations in TNBC rates among Iraqi BC patients: Alwan, Tawfeeq and Muallah (2017) (15.6%, n = 686), Mohsin and Mohamad (2024) (28.89%, n = 89), and Khalaf et al. (2022) (48.6%, n = 251). Study sample sizes may influence these fluctuation rates, as Alwan, Tawfeeq and Muallah (2017) and Mohsin and Mohamad (2024) studies have both been conducted on BC patients in Baghdad.

In regard to tumor grading at the time of diagnosis, grade II underscored the highest frequency among BC patients in our study, and grade III came in second place. This aligns with what was reported earlier by Mohsin and Mohamad (2024) (64.44%, n = 89) in Iraq, Sajitha et al. (2022) (47%, n = 34) in India, Abousahmeen et al. (2023) (37.0%, n = 319) in Libya, and Oluogun et al. (2019) (71%, n = 343) in Nigeria. Accordingly, it’s clear that most of the BC patients, either in the Kurdistan Region of Iraq or other places, are submitting for clinical examination in the late stages. Thus working on public awareness is quite crucial to interne at the right time.

Across the IHC technique retrieved data, our analysis revealed that the predominant molecular subtype of mastectomy and TCB was luminal A 115 (44.06%) and 54 (20.69%), respectively. Similar to our findings, studies from Iraq (Alwan, Tawfeeq and Muallah, 2017) and Iran (Ariabod, et al., 2021) also reported luminal A as the most frequent subtype of BC. In contrast, in other parts of the world, such as South Africa (van den Berg, et al., 2021) and Libya (Abousahmeen, et al., 2023) luminal B has emerged as the most prevalent subtype. Higher frequencies in luminal A among the included population may present a good sign for positive clinical outcomes, as luminal B is more common in younger BC patients and associated with higher grades and nodal metastasis (Hashmi, et al., 2018). Moreover, higher rates of luminal A among our study sample size are consistent with Hashmi et al. (2018)’s data as the majority of BC patients in our study are of older ages.

The extracted data indicates that the majority of BC patients were diagnosed with tumors at stages II and III, a pattern consistent with a previous study reported by Oluogun et al., 2019. This late-stage diagnosis may be attributable, in part, to several epidemiological factors, including sociocultural barriers, poverty, and insufficient health awareness (Gubari, et al., 2017; Hu, et al., 2019). These outcomes highlight the need for targeted public health intervention to improve early detection by addressing the above-mentioned obstacles that may ease regular checkups.

Our analysis of the extracted data showed that patients who underwent mastectomy and TCB had a greater incidence of tumor grade II (24.52%) among 41–50 years and tumor grade III (9.96%) among ≤40 years. This came in agreement with what was previously reported by Hassoon, Ali and Said (2021) who suggested a connection between the above-mentioned tumor grades and patient ages, especially between 40 and 60 years. This correlation highlights the importance of age-specific screening and diagnostic practices for dealing with different grade distributions across different age groups.

Last but not least, our data uncovered that BC patients, at the diagnosis stage, were likely to have tumor stage II at age ≤50 and stage III at age 41–50 years. This came in alignment with studies that covered this matter across various age groups and reached a conclusion that patients with BC who were older than 40 years had a greater incidence of tumor stages II and III at the time of detection (Akbari, et al., 2017; Zeeshan, et al., 2019). This consistency across studies, again, highlights the necessity for age-specific strategies in screening and early detection. We should also point out the fact that BC, if diagnosed and treated as soon as possible, in the majority of cases may not result in the death of the affected patients (Akbari, et al., 2017).

IV. Conclusion

BC in the Erbil governorate of the Kurdistan Region of Iraq is more common among older females than younger ones and exhibits a high prevalence of IDC. Positive ER and PR statuses were reported more frequently than negative ones, whereas positive HER2 was less common. In comparison with the luminal B, the luminal A molecular subtype was the most dominant, accounting for about two-thirds of all BC patients. Among patients aged ≥41 years, there was a higher proportion of tumor grades II and III. Furthermore, diagnoses of tumor stages II and III reflected about two-thirds of all cases across all age categories. Overall, our findings emphasize the importance of age-specific strategies in screening and timely interventions to improve BC outcomes.

Acknowledgment

We would like to express our gratitude to the director and head of laboratories at Rizgary Teaching Hospital, in particular the Histopathology Laboratory, for their assistance during the data collection process.

References

Abdulkareem, A.A., Ghalib, H.A., and Rashaan, M.I., 2023. Factors causing delayed presentations of breast cancer among female patients in Sulaimani Governorate, Kurdistan region, Iraq. *BMC Women's Health,* 23, p.612.

Abousahmeen, A., Saud, M.A.B., Elrais, S., Kashbour, M., Abuhlaiga, M., Al-Aqmar, D.M., and Al-Shareef, J.M., 2023. Molecular subtypes and clinicopathological features of breast cancer in Libya: A first glance. *Therapeutic Radiology and Oncology,* 7, p.15.

Akbari, M.E., Sayad, S., Sayad, S., Khayamzadeh, M., Shojaee, L., Shormeji, Z., and Amiri, M., 2017. Breast Cancer Status in Iran: Statistical Analysis of 3010 Cases between 1998 and 2014. *International Journal of Breast Cancer,* 2017, 2481021.

Al-Hashimi, M., 2021. Trends in breast cancer incidence in Iraq during the period 2000-2019. *Asian Pacific Journal of Cancer Prevention,* 22, pp.3889-3896.

Alwan, N.A.S., Tawfeeq, F.N., and Muallah, F.H., 2018. Breast cancer subtypes among Iraqi patients: Identified by their ER, PR and HER2 status. *Journal of the Faculty of Medicine Baghdad,* 59, pp.303-307.

Anderson, W.F., Schairer, C., Chen, B.E., Hance, K.W., Levine, P.H., and Swain, S., 2006. Epidemiology of inflammatory breast cancer (IBC) 1. *Breast Disease,* 22, pp.9-23.

Ariabod, V., Sohooli, M., Shekouhi, R., and Payan, K., 2021. Assessment of breast cancer immunohistochemical properties with demographics and pathological features; A retrospective study. *International Journal of Cancer Management,* 14, p.e114577.

Buerger, H., 2000. Genetic relation of lobular carcinoma *in situ*, ductal carcinoma *in situ*, and associated invasive carcinoma of the breast. *Molecular Pathology,* 53, pp.118-121.

Chen, B., Zhang, X., Liu, Y., and Wang, C., 2023. Prognostic disparities in young patients based on breast cancer subtype: A population-based study from the SEER database. *Medicine,* 102, p.e33416.

Coates, A.S., Winer, E.P., Goldhirsch, A., Gelber, R.D., Gnant, M., Piccart-Gebhart, M., Thürlimann, B., Senn, H.J., and Panel Members, 2015. Tailoring therapies-improving the management of early breast cancer: St Gallen International Expert Consensus on the Primary Therapy of Early Breast Cancer 2015. *Annals of Oncology,* 26, pp.1533-1546.

Duraker, N., Hot, S., Akan, A., and Ozay Nayir, P., 2020. A Comparison of the clinicopathological features, metastasis sites and survival outcomes of invasive lobular, invasive ductal and mixed invasive ductal and lobular breast carcinoma. *European Journal of Breast Health,* 16, pp.22-31.

Erber, R., and Hartmann, A., 2020. Histology of luminal breast cancer. *Breast Care,* 15, pp.327-336.

Goh, C.W., Wu, J., Ding, S., Lin, C., Chen, X., Huang, O., Chen, W., Li, Y., Shen, K., and Zhu, L., 2019. Invasive ductal carcinoma with coexisting ductal carcinoma *in situ* (IDC/DCIS) versus pure invasive ductal carcinoma (IDC): A comparison of clinicopathological characteristics, molecular subtypes, and clinical outcomes. *Journal of Cancer Research and Clinical Oncology,* 145, pp.1877-1886.

Gubari, M.I.M., Mohialdeen, F.A., Babakir-Mina, M., and Amin, B.A., 2017. Knowledge, attitude and practice toward breast cancer among Kurdish women in Sulaimani Governorate/Iraq. *Kurdistan Journal of Applied Research,* 2, pp.20-28.

Han, Y., Wang, J., and Xu, B., 2020. Clinicopathological characteristics and prognosis of breast cancer with special histological types: A surveillance, epidemiology, and end results database analysis. *The Breast,* 54, pp.114-120.

Hashmi, A.A., Aijaz, S., Khan, S.M., Mahboob, R., Irfan, M., Zafar, N.I., Nisar, M., Siddiqui, M., Edhi, M.M., Faridi, N., and Khan, A., 2018. Prognostic parameters of luminal A and luminal B intrinsic breast cancer subtypes of Pakistani patients. *World Journal of Surgical Oncology,* 16, 1.

Hassoon, A.R., Ali, H.S., and Said, H.M., 2021. The Correlation of age with various prognostic factors in breast cancer in Iraqi patients. *Iraqi Medical Journal,* 67, pp.81-89.

Herschkowitz, J.I., Simin, K., Weigman, V.J., Mikaelian, I., Usary, J., Hu, Z., Rasmussen, K.E., Jones, L.P., Assefnia, S., Chandrasekharan, S., Backlund, M.G., Yin, Y., Khramtsov, A.I., Bastein, R., Quackenbush, J., Glazer, R.I., Brown, P.H., Green, J.E., Kopelovich, L., Furth, P.A., Palazzo, J.P., Olopade, O.I., Bernard, P.S., Churchill, G.A., Van Dyke, T., and Perou, C.M., 2007. Identification of conserved gene expression features between murine mammary carcinoma models and human breast tumors. *Genome Biology,* 8, R76.

Hu, K., Ding, P., Wu, Y., Tian, W., Pan, T., and Zhang, S., 2019. Global patterns and trends in the breast cancer incidence and mortality according to sociodemographic indices: An observational study based on the global burden of diseases. *BMJ Open*, 9, p.e028461.

Jahanbin, B., Soleimani, V., Azmoude-Ardalan, F., Afshar, S., and Safaei, M., 2023. Evaluation of HER2 Gene Amplification using CISH in Patients with HER2 2+ (equivocal) Breast Carcinoma based on Immunohistochemistry in Imam Khomeini Cancer Institute from 2016 to 2018. *Archives of Breast Cancer*, 10, pp.131-137.

Jin, X., Zhou, Y.F., Ma, D., Zhao, S., Lin, C.J., Xiao, Y., Fu, T., Liu, C.L., Chen, Y.Y., Xiao, W.X., Liu, Y.Q., Chen, Q.W., Yu, Y., Shi, L.M., Shi, J.X., Huang, W., Robertson, J.F.R., Jiang, Y.Z., and Shao, Z.M., 2023. Molecular classification of hormone receptor-positive HER2-negative breast cancer. *Nature Genetics,* 55, pp.1696-1708.

Kasper, D.L., and Harrison, T.R., 2005. *Harrison's Principles of Internal Medicine,* McGraw-Hill, Medical Publication Division, New York.

Khalaf, H., Mohammed, A., Shukur, S., Alhalabi, N., Almothafar, B., Hassan, M., and Abu, A., 2022. Breast cancer: Age incidence, hormone receptor status and family history in Najaf, Iraq. *Journal of Medicine and Life,* 15, pp.1318-1321.

Khoshnaw, N., Mohammed, H.A., and Abdullah, D.A., 2016. Patterns of cancer in Kurdistan - results of eight years cancer registration in Sulaymaniyah province-Kurdistan-Iraq. *Asian Pacific Journal of Cancer Prevention,* 16, pp.8525-8531.

Khoshnaw, S., Ganjo, A., and Salih, M., 2023. Epidemiological study of breast cancer in Erbil, Kurdistan region. *UKH Journal of Science and Engineering,* 7, pp.11-16.

Kumar, P., and Aggarwal, R., 2015. An overview of triple-negative breast cancer. *Archives of Gynecology and Obstetrics,* 293, pp.247-269.

Łukasiewicz, S., Czeczelewski, M., Forma, A., Baj, J., Sitarz, R., Stanisławek, A., 2021. Breast cancer-epidemiology, risk factors, classification, prognostic markers, and current treatment strategies-an updated review. *Cancers,* 13, p.4287.

Majid, R.A., Mohammed, H.A., Saeed, H.M., Safar, B.M., Rashid, R.M., and Hughson, M.D., 2009. Breast cancer in Kurdish women of northern Iraq: Incidence, clinical stage, and case control analysis of parity and family risk. *BMC Women's Health,* 9, p.33.

Makki, J., 2015. Diversity of breast carcinoma: Histological subtypes and clinical relevance. *Clinical Medicine Insights: Pathology,* 8, pp.23-31.

Manjunath, S., Prabhu, J.S., Kaluve, R., Correa, M., and Sridhar, T.S., 2011. Estrogen receptor negative breast cancer in India: Do we really have higher burden of this subtype? *Indian Journal of Surgical Oncology,* 2, pp.122-125.

Mohsin, R.N., and Mohamad, B.J., 2024. Clinical and Histopathological Features of Breast Cancer in Iraqi Patients between 2018-2021. *Iraqi Journal of Science*, 65, pp.90-107.

Molah Karim, S.A., Ali Ghalib, H.H., Mohammed, S.A., and Fattah, F.H.R., 2015. The incidence, age at diagnosis of breast cancer in the Iraqi Kurdish population and comparison to some other countries of Middle-East and West. *International Journal of Surgery,* 13, pp.71-75.

Mutar, M.T., Goyani, M.S., Had, A.M., and Mahmood, A.S., 2019. Pattern of presentation of patients with breast cancer in Iraq in 2018: A cross-sectional study. *Journal of Global Oncology*, 11, pp.1-6.

Oluogun, W.A., Adedokun, K.A., Oyenike, M.A., and Adeyeba, O.A., 2019. Histological classification, grading, staging, and prognostic indexing of female breast cancer in an African population: A 10-year retrospective study. *International journal of health sciences,* 13, p.3.

Plasilova, M.L., Hayse, B., Killelea, B.K., Horowitz, N.R., Chagpar, A.B., and Lannin, D.R., 2016. Features of triple-negative breast cancer. *Medicine*, 95, p.e4614.

Pragya, V.J., and Jorns, J., 2023. *Breast Cancer Histologic Grading*. PathologyOutlines.com, Inc., USA. Available from: https://www.pathologyoutlines.com/topic/breastmalignanthistologic.html [Last accessed on 2023 Aug 11].

Prat, A., and Perou, C.M., 2011. Deconstructing the molecular portraits of breast cancer. *Molecular Oncology,* 5, pp.5-23.

Sajitha, K., Arumugam, M., Shetty, J., Shetty, R., Asnani, R., and Shetty, P., 2022. Breast carcinoma – A comparative study of immunohistochemistry and fluorescence *in situ* hybridization for Her-2 assessment and association of ER, PR, HER-2 and Ki-67 expression with clinico-pathological parameters. *Iranian Journal of Pathology,* 17, pp.435-442.

Salman, A.O., Al-Abassi, H.M., and Mahod, W.S., 2021. Demographic and clinico-pathological characteristics of some Iraqi female patients newly diagnosed with breast cancer. *Annals of the Romanian Society for Cell Biology,* 25, pp.8264-8278.

Shet, T., Agrawal, A., Nadkarni, M., Palkar, M., Havaldar, R., Parmar, V., Badwe, R., and Chinoy, R.F., 2009. Hormone receptors over the last 8 years in a cancer referral center in India: What was and what is? *Indian Journal of Pathology and Microbiology,* 52, p.171.

Siegel, R.L., Miller, K.D., and Jemal, A., 2018. Cancer statistics, 2018. *CA: A Cancer Journal for Clinicians,* 68, pp.7-30.

Siegel, R.L., Miller, K.D., Wagle, N.S., and Jemal, A., 2023. Cancer statistics, 2023. *CA: A Cancer Journal for Clinicians,* 73, pp.17-48.

Tan, P.H., Ellis, I., Allison, K., Brogi, E., Fox, S.B., Lakhani, S., Lazar, A.J., Morris, E.A., Sahin, A., Salgado, R., Sapino, A., Sasano, H., Schnitt, S., Sotiriou, C., Van Diest, P., White, V.A., Lokuhetty, D. and Cree, I.A., 2020. The 2019 World Health Organization classification of tumours of the breast. *Histopathology,* 77, pp.181-185.

Van Den Berg, E.J., Duarte, R., Dickens, C., Joffe, M., and Mohanlal, R., 2021. Ki67 Immunohistochemistry quantification in breast carcinoma: A comparison of visual estimation, counting, and immunoratio. *Applied Immunohistochemistry and Molecular Morphology,* 29, pp.105-111.

Van Dooijeweert, C., Van Diest, P.J., and Ellis, I.O., 2021. Grading of invasive breast carcinoma: The way forward. *Virchows Archiv,* 480, pp.33-43.

Wang, H., Naghavi, M., Allen, C., Barber, R.M., Bhutta, Z.A., Carter, A., and GBD 2015 Mortality and Causes of Death Collaborators, 2016. Global, regional, and national life expectancy, all-cause mortality, and cause-specific mortality for 249 causes of death, 1980–2015: a systematic analysis for the Global Burden of Disease Study 2015. *The Lancet,* 388, pp.1459-1544.

Wang, Q., Xu, M., Sun, Y., Chen, J., Chen, C., Qian, C., Chen, Y., Cao, L., Xu, Q., Du, X., and Yang, W., 2019. Gene expression profiling for diagnosis of triple-negative breast cancer: A multicenter, retrospective cohort study. *Frontiers in Oncology,* 9, 354.

Weigelt, B., Horlings, H.M., Kreike, B., Hayes, M.M., Hauptmann, M., Wessels, L.F.A., De Jong, D., Van De Vijver, M.J., Veer, L.J.V.T., and Peterse, J.L., 2008. Refinement of breast cancer classification by molecular characterization of histological special types. *The Journal of Pathology,* 216, pp.141-150.

Zeeshan, S., Ali, B., Ahmad, K., Chagpar, A.B., and Sattar, A.K., 2019. Clinicopathological features of young versus older patients with breast cancer at a single Pakistani Institution and a comparison with a national US database. *Journal of Global Oncology,* 5, 1-6.

Improved Kurdish Dialect Classification Using Data Augmentation and ANOVA-Based Feature Selection

Karzan J. Ghafoor, Sarkhel H. Taher, Karwan M. Hama Rawf and Ayub O. Abdulrahman

Computer Science Department, College of Science, University of Halabja,
Halabja, 46018, Kurdistan Region - F.R. Iraq

Abstract—**Analyzing dialects in the Kurdish language proves to be tough because of the tiny phonetic distinctions among the dialects. We applied advanced methods to enhance the precision of Kurdish dialect classification in this research. We examined the dataset's stability and variation through the use of time-stretching and noise-augmenting methods. Analysis of variance (ANOVA) filter approach is applied to improve feature selection (FS) more efficiently and highlight the most relevant features for dialect classification. The ANOVA filter method ranks features based on the means from different dialect groups, which made FS better. To make dialect classification work better, a 1D convolutional neural network model was given a dataset that had ANOVA FS added to it. The model showed a very strong performance, reaching a remarkable accuracy of 99.42%. This noteworthy increase in accuracy beat former research with an accuracy of 95.5%. The findings demonstrate how combining time stretch and FS methods can improve the accuracy of Kurdish dialect classification. This project improves our understanding and implementation of machine learning in the field of linguistic diversity and dialectology.**

Index Terms—**1D convolutional neural network, Data augmentation, Feature selection, Kurdish dialect identification, Sound features.**

I. Introduction

The rapid expansion of voice recognition technology is supported by progress in machine learning and the extensive use of the Internet. Communities with popular languages, including Chinese and English, have developed rigorous access to considerable data. Before we can achieve automatic recognition, we must address the Kurds' limited resources and lack of an extensive open corpus. Due to the small number of experts studying Kurdish language recognition, there is a lack of a robust research foundation that limits many advanced voice recognition techniques. Kurdish study is straightforward due to its dialects' easy clustering and linear separation (Ghafoor, et al., 2021). Numerous languages use the Arabic script as a main popular way to write in the Middle East and North Africa. Numerous languages use it greatly, including Arabic and Urdu. The Kurdish language includes 34 characters. Since Arabic is the root script for the Kurdish alphabet, the Arabic script includes the 23 most frequently used letters from Arabic (Hama Rawf, Abdulrahman and Mohammed, 2024). Furthermore, the Arabic script shares similarities with the languages and writing systems of many Middle Eastern nations, which could facilitate education. Four central Middle Eastern states have their own dialects, where Kurds speak their language. The Kurdistan region of Iraq contains three main dialects of Kurdish language including Sorani and Badini as well as Hawrami which are the most widely used vernaculars. These dialects serve as the main spoken language forms among Kurdish groups who live in Iraq where they maintain their own linguistic features. Languages can achieve better accuracy in speech processing through models specifically made for different dialectal variations because dialect classification provides essential knowledge for language recognition research. Communities speaking Kurdish reside in territories of Turkey, Iraq, Iran, and Syria. The current estimates indicate that more than 40 million converse in Kurdish. Both the recognition of KuSL and dialect recognition systems (DRS) facilitate better communication for individuals with language diversity. The many influences on speech recognition are investigated by DRS, and strategies are offered for merging them with systems for recognizing various dialects (Rawf, et al., 2024). The Kurdish language lacks large enough datasets, due to its complexity and variety of dialects, making it tough to develop efficient natural language processing (NLP) tools, especially for Kurdish Named Entity Recognition (KNER). To solve this, Abdullah et al. (2024) adapted a pre-trained RoBERTa model specifically for KNER. This included creating a new Kurdish corpus, adjusting the model setup, and fine-tuning the training process. Results showed that using sentence-piece tokenization, they improved the F1 score by 12.8%, setting new standards for Kurdish NLP applications. Automatic speech recognition applications have incorporated data augmentation (DA) techniques to generate more training data, thereby improving data quality in terms of both quantity and diversity. As a result of this approach, the system gains strength and avoids overfitting (Nguyen, et al., 2020). Kanda, Takeda and

ARO-The Scientific Journal of Koya University
Vol. XIII, No. 1 (2025), Article ID: ARO.11897. 10 pages
DOI: 10.14500/aro.11897
Received: 14 November 2024; Accepted: 27 February 2025
Regular research paper; Published: 07 March 2025

†Corresponding author's e-mail: karzan.ghafor@uoh.edu.iq

Obuchi (2013), and Ragni et al. (2014) talk about how to use unsupervised learning and fake data to improve model training in places with few resources. DA, in conjunction with feature selection (FS) algorithms, reduces overfitting. This method enhances the performance of speech recognition systems significantly and outperforms various other alternatives (Sangwan, Deshwal and Dahiya, 2021). The FS and extraction of the source voice signal must yield maximum recognition effectiveness while keeping computational needs low. Identify data a machine learning classifier uses input features pulled from the initial signals (Abdul, Al-Talabani and Abdulrahman, 2016). To handle the problem created by the small corpus, a variety of DA methods, including temporal stretching, noise injection, and audio amplification, was employed. The created dataset will educate acoustic and language models (Lounnas, Lichouri and Abbas, 2022). Among all techniques for voice recognition, other than DA, it provides the biggest increase in effectiveness. The analysis from Peddinti et al. (2015) indicates that implementing DA increased efficacy by 33%. The comprehensive review set features both important and irrelevant characteristics for the targeted classifiers, lowering their effectiveness. To uncover the key elements and discard unimportant information, it is crucial to implement FS routines. By employing FS approaches, it is possible to select the optimal and important features that improve the identification method. In addition, the K-fold cross-validation method may be applied to guarantee trustworthy outcomes and lower the chances of overfitting (Tubishat, et al., 2019). To correctly classify dialects of the Kurdish language in this study, researchers use DA and FS methods derived from convolutional neural network (CNNs) and employ the shortest audio segment. This study seeks to assess how effective DA and FS are. The work comes up with a creative way to group dialects using CNN to choose which features to use. Using a hybrid approach that uses a CNN to show the unique features of each dialect makes it more effective at recognizing them. This approach simplifies the requirement for high-cost human feature identification. This innovative approach provides a functional solution for identifying and classifying dialects in varied linguistic and cultural situations. The following structure guides the subsequent sections of the paper: Section 2 summarizes existing literature and research concerning the topic. Section 3 presents the materials and techniques used in the study. In Section 4, details of the DA mechanism are provided. The FS appears in section five. In Section 6 you can find an account of results along with discussion, and Section 7 includes the closure and prospective endeavors.

II. Related Work

Different ways of identifying dialects show differences that depend on a number of factors, such as the language being studied and the features that are extracted. Investigators employed machine-learning algorithms with multiple techniques for feature extraction and selection to efficiently sort dialects in various languages. The conversion of Gaussian mixture model (GMM) weights included an analysis implemented by a positive factor analysis technique (Bahari, et al., 2014). Based on their study, GMM loads serve as extra data for GMM revealing DR and language but collectively provide less data. Among Bangladeshi dialects, utilizing GMM to define characteristics is the Mel Frequency Cepstral Coefficient (MFCC), along with its Delta and Delta-delta. Astonishingly built from the sound of utterances (Das, et al., 2016). Moreover, Mulahuwaish et al. (2020) propose an effective system for the web that gathers news articles into four distinct groups: Business, technology and science, health, and entertainment. Researchers assess four different machine learning classifiers: Support Vector Machine (SVM), K-Nearest Neighbors (kNN), decision tree, and long short-term memory. The classifiers are applied individually and then assessed using accuracy and receiver operating characteristic curves. The results show that while SVM attained the maximum accuracy at 95.04%, kNN attained the lowest accuracy at 88.72%.

By changing the structure of the training dataset, DA makes alternative training sets. Various study areas, such as image processing and sound classification, find DA to be a useful technique (Li, et al., 2020). In many research domains, the DA technique is extensively used. A small number of samples from several DA classes has a big effect on how problems are solved in a broad classification setting (Zheng, et al., 2020). For speaker identification, a strategy named DA-DNN7L is available to increase data samples. The method uses white noise augmentation and time manipulation procedures. Using a deep neural network (DNN) enables the techniques to develop a new model. Increasing the available data from speakers of Indonesian ancestry is aimed at using a data enhancement approach. When assessed against different multilayer approaches, the seven-layer DNN yields fair accuracy. In addition, the use of the most effective seven-layer DNN DA approach in research yielded an accuracy rate of 99.76% and a loss of 0.05 when using a 70%: The ratio was 30%, 400 data points were added, and a CNN and DA method were used to accurately find sounds that were close by (Nugroho and Noersasongko, 2022). The results showed that combining a deep, high-capacity system with an increased training set yields better outcomes. The fusion turns a better result than the advised CNN without augmentation and bottom models relying on dictionary learning with augmentation. The study (Salamon and Bello, 2017) recorded an accuracy of 94%.

A proposal exists for a speaker identification approach tailored to a special wearable tool for reducing gender-based violence. A detailed study was implemented to gauge how stress affects speech with DA methods. Findings demonstrate that with naturally stressed samples in the training set, efficacy is satisfactory. When these missing components are unavailable, we can improve the results by introducing artificially generated stress-like samples (Rituerto-González, et al., 2019).

To choose the most important features and remove unnecessary data, one can implement algorithms. Determining the essential features greatly depends on these algorithms and leads to an improved performance in sentiment analysis. The three types of FS methods include filter methods, wrapper approaches, and hybrid methods. The analysis of features through filter approaches resembles established strategies for FS (Tubishat, et al., 2019). To achieve high recognition efficiency while reducing computational resources substantially, the input features and extraction method for the voice signal should be optimized (Sangwan, Deshwal and Dahiya, 2021). A novel FS method emerged from fusing the Binary Bat technique with late acceptance hill-climbing. This algorithm targets the selection of important feature vectors that will lessen model complexity and speed up training. Using the Indian TTS dataset made by IIT-Madras, the Random Forest algorithm hits an efficiency of 92.35% (Das, et al., 2020).

Speaker verification is achieved through a super vector that features the mean values of each phonetic sound. The creation of the first accent models is through the calculation of averages for each class using speech super vectors. The methods evaluate a Flemish audio dataset that classifies speakers into five groups. Selecting a subset of features results in an over 20% improvement in accessing rate across all models. Wu et al. (2010) say that using speaker vectors during the creation phase gets much better results than a regular GMM that works directly with the main feature vectors in both text-dependent and text-independent situations. In the audio classification process, FS and combination are essential since they can boost the performance of deep learning models significantly. Three datasets were evaluated by several advanced deep-learning models to assess their functionality. The findings show that the features chosen are affected by both the dataset and the model chosen (Turab, et al., 2022).

An important factor in achieving impressive outcomes was the use of DA and FS. A novel approach to identify emotions in speech (SER) is shared that incorporates data enlargement procedures and feature combination along with their selection. The studies are conducted using two available datasets: The IEMOCAP database along with the Chinese Hierarchical Speech Emotion Dataset of Broadcasting (DB) constitute two datasets. According to the study (Tu, et al., 2023), the given framework has test accuracies of 66.44% and 93.47% for the unweighted typical basis. A technique for identifying emotions in spoken language was created to solve the problems in currently available approaches and apply it to Arabic speech. The model applies data enhancement techniques while supplying the predetermined features to a transformer model for emotion recognition. Four datasets made up the evaluation: BAVED along with emotional database (EMO)-DB and SAVEE as well as EMOVO. For these datasets, the results showed accuracies of 95.2%, 93.4%, 85.1%, and 91.7% (Al-onazi, et al., 2022).

III. Materials and Methodology

For dialect recognition classification purposes, a CNN model with various feature enhancement techniques such as add_white_noise and time_stretch is utilized. The results produced by these techniques become input for the SelectKBest FS algorithm. They then send those attributes into a revised CNN to analyze. The model implements training and assessment processes while using datasets marked with dialect information. The model can identify dialects by analyzing the collected traits and provides important understanding of the variety in spoken language. The proposed DRS is represented in Fig. 1.

A. Dialectal Speech Dataset

The primary database for this study is the “KuLD” dataset, compiled by researchers in the Computer Science Department at the University of Halabja. Data collection lasted over months. At all phases of gathering data, careful observance of established methods was constant. The dataset included speakers across all age groups and genders. For the three dialects, Sorani, Badini, and Hawrami, a tally of 2000 samples was achieved. Each sample in the dataset runs for 1 s and totals 6000 s (Rawf, et al., 2024).

B. CNN Architecture

The method applied organized Kurdish dialects using a 1-D CNN based on the KuLD database filled with sound information. The dataset utilized in this study has been identified as being comprised of Sorani Badini and Hawrami samples. CNN has received considerable attention in computer vision and audio processing. These fields cover tasks that operate without an exact spatial location in spectrogram visuals. CNN is a quick and easy way to accurately group spectrogram features into different groups (Khamparia, et al., 2019). United FS and data bolstering in CNNs raise accuracy and durability. Training data diversity improves with DA strategies to enhance how models detect patterns as well. Using transfer learning, the network highlights significant features to improve its efficiency. They produce adaptable and reliable models together. With audio DA included, the CNN structure shows sound classification efficiency leading the field (Salamon and Bello, 2017). The proposed 1D CNN architecture consists of twelve layers: a set of input signals is presented, followed by five convolution layers and a MaxPooling stage, as well as three dense layers ending in the output layer. Fig. 2 depicts the structure presented in the 1D CNN model.

Consequently, the parameters of the approach have been meticulously tuned to achieve a significant amount of efficiency in categorizing the Kurdish dialect. The precise specifications of the presented CNN architecture are outlined in Table I.

IV. DA

DA, alternately abbreviated as DA, is a critical technique that researchers employed to increase the size of the dataset by transforming existing data. This strategic maneuver, which has proved beneficial in training neural networks according to Rebai et al. (2017), has considerable implications for deep learning, especially for small data sets, as shown by Ma, Tao and Tang (2019). As an approach, DA can offset overfitting impedance, increase model reliability (Moreno-Barea, Jerez and Franco, 2020), and improve its generality, which is a common issue with machine learning (Ma, Tao and Tang, 2019). When analyzing the vast field of machine learning, the use of DA in the context of the deep learning model assumes

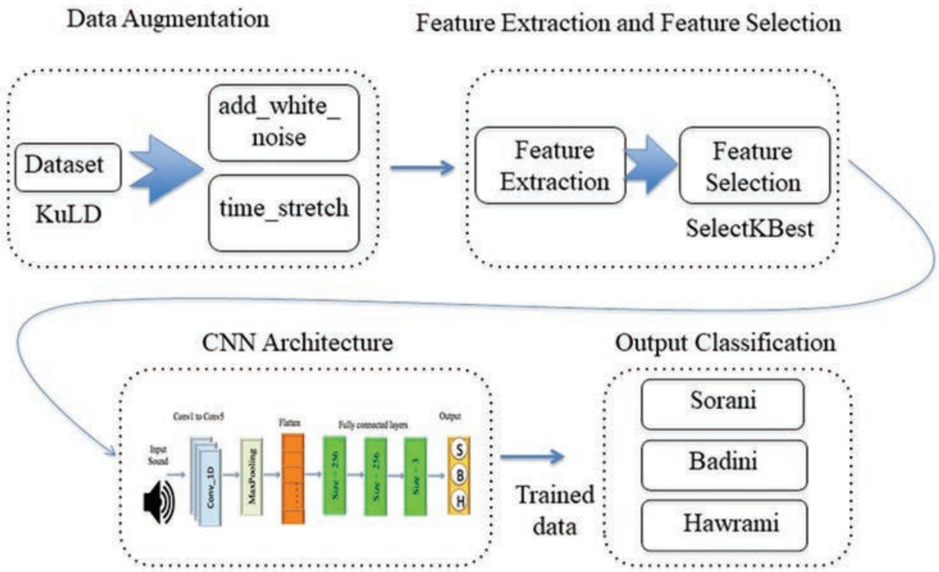

Fig. 1. A block diagram of the proposed model.

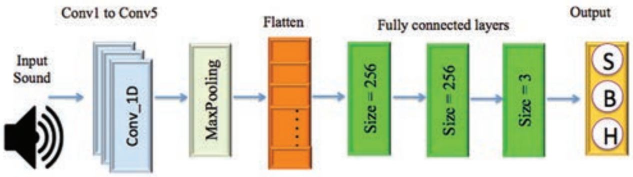

Fig. 2. The comprehensive architecture of a one-dimensional (CNN) architecture.

TABLE I
Presents an Overview of the Demonstrated Model's Structure

Layers' type	Output shape	Activation function	Parameter
conv1d_1 (Conv1D)	(None, 182, 128)	relu	640
conv1d_2 (Conv1D)	(None, 179, 64)	relu	32832
conv1d_3 (Conv1D)	(None, 176, 32)	relu	8224
conv1d_4 (Conv1D)	(None, 173, 128)	tanh	16512
conv1d_5 (Conv1D)	(None, 170, 128)	tanh	65664
max_pooling1d_1	(None, 28, 128)	-	0
flatten_1 (Flatten)	(None, 3584)	-	0
dense_1 (Dense)	(None, 256)	sigmoid	917760
dense_2 (Dense)	(None, 256)	sigmoid	65792
dense_3 (Dense)	(None, 3)	softmax	771

a pivotal position when trying to enhance the predictive capabilities of an organization, particularly when utilizing large databases. This principle is true as proved by the study conducted by Moreno-Barea and association (Moreno-Barea, Jerez and Franco, 2020). DA comes in various forms, among which the most common are white noise injection and time stretching (TS), among others that form part of the many strategies used in this branch.

A. White_Noise

One of the main problems of deep learning is the problem associated with the use of small volumes of data. They pointed out that a possible way to solve this problem is by injecting noise during training. Rebai et al. (2017) have proven that the incorporation of white noise provides marketing feedback in speaker recognition. This approach involves the introduction of another noise of random signals of equal amplitudes at different frequencies (Moreno-Barea, Jerez and Franco, 2020). However, it should be pointed out that in the case of audio signals, the frequency range in question can be located substantially in the audible range, which generally varies between 20 Hz and 20 kHz, as shown in Fig. 3.

Therefore, we note that the integration of White Noise shows significant enhancements in the efficiency of the voice recognition models, as noted by Hu, Tan and Qian (2018) and Aguiar, Costa and Silla (2018). This procedure involves joining clean audio with noise, introducing a new sound, which makes it a perfect technique for the DA process, which is a valuable technique in deep learning.

B. Time_Stretching

An audio modification strategy that changes the rate or length of a signal without changing its pitch is referred to as TS. This method is especially helpful in signal filtering for musical signals containing tonal, noise, and transient mix components. Such signals include singing, techno music, and jazz recordings with voices (Damskägg and Välimäki, 2017). TS is a technique used by different studies to conduct DA. Several techniques, such as the synchronous overlap and add algorithm, fuzzy techniques, and CNN, have been used together with TS. These approaches have over and over again boosted the sophistication of the proposed models, as mentioned by Salamon and Bello (2017) in their article and Kupryjanow and Czyzewski (2012).

Voice signal enhancement using the "Time Stretching" directly assists in providing an esthetically represented concept of one of the methods in DA. This is done with the help of making changes in the time stretch, indicated in Fig. 4, while the original voice is analyzed and the sample's time duration is changed.

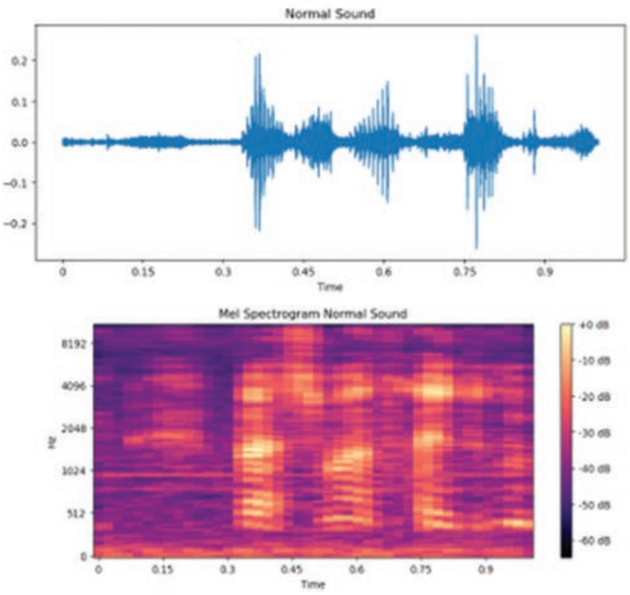

Fig. 3. Normal Sound waveform and Mel_spectogram.

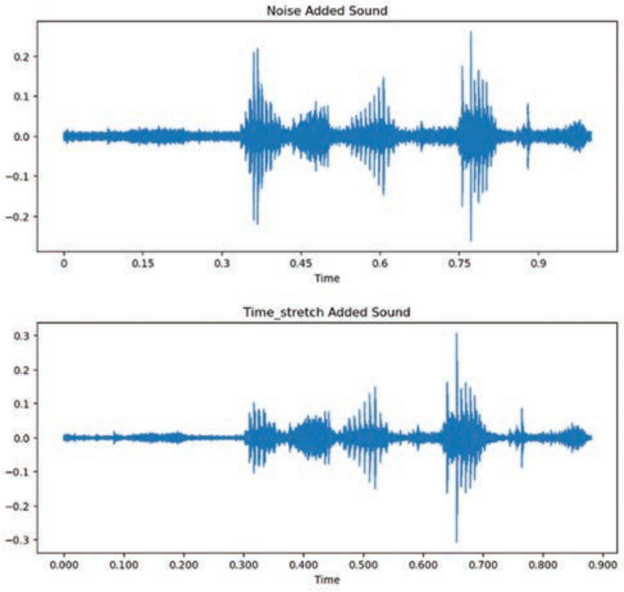

Fig. 4. Noise added and Time_Stretch waveform.

C. Implementation of Analysis of Variance (ANOVA)-Based FS

The ANOVA-based FS method applied through the SelectKBest function in the Scikit-learn library optimized the Kurdish dialect classification feature set. The F-statistic helps the evaluation process identify statistically important features for the classification task.

The first step in extracting an audio dataset was to get four important features: MFCC, Mel Spectrogram, Delta MFCC, and Spectral Contrast. ANOVA evaluated and ranked the combined feature vector, which contained these features. Selection of the most significant features (200) occurred through the ANOVA top-k FS method. The proposed feature extraction method, implemented as Algorithm 1, uses Fig. 5 to represent its procedure through a flowchart.

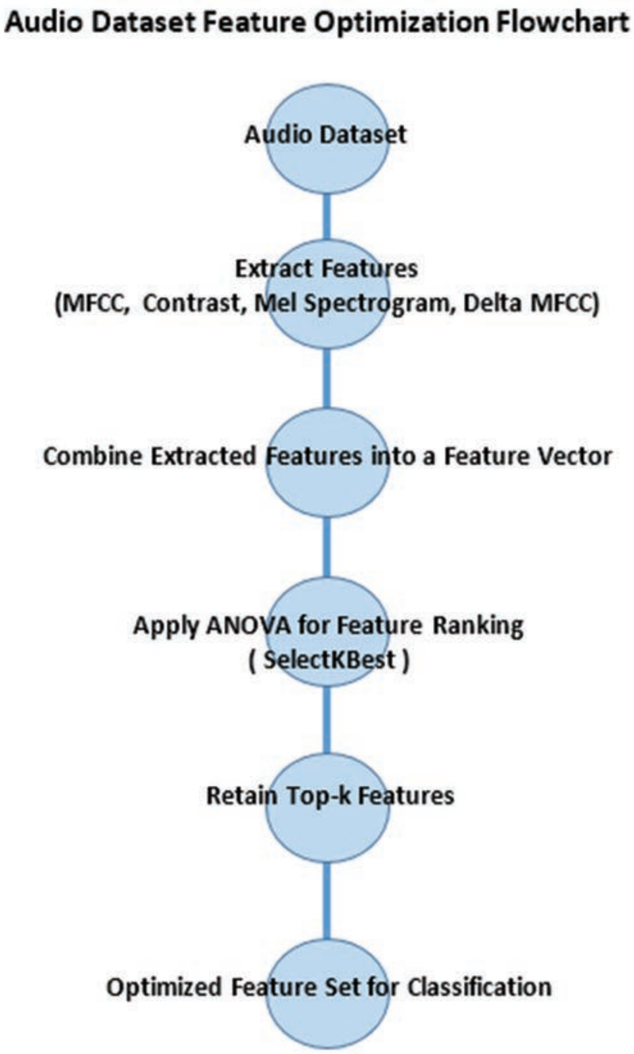

Fig. 5. Flowchart of implementation of analysis of variance-based feature selection.

By applying this approach, it becomes possible to utilize only crucial features that make the model both perform better and require less computational power.

V. FS

It is part of the preprocessing steps that only a few of the most important features in a dataset will be used. This gets rid of features that are not important to the model or are not important at all. In other words, it simplifies the process by removing features from the initial set that may not be essential or useful for defining important features. Numerous FS techniques have been designed specifically to enable choosing valuable data while, at the same time, attempting to exclude data that are insignificant (Shetty, Patnaik and Prasad, 2022) and (Zhou, Wang and Zhu, 2022). It is suggested that it is reasonable to ensure FS's impact on the performance of the outcomes. Sometimes, irrelevant features influence the result; hence, there is a need to either ignore them or consider only the features with the highest rank for the classifier.

This study uses a FS filtering method. After making p-value matrices, an ANOVA test is used to see if there are significant differences between the mean values of a hypothesis-based number of groups. Interestingly, in relation to the F-statistic in this particular setup, they do function to provide some insight regarding feature ranking. When we obtain a higher F-statistic value, it indicates that the identified features are of a higher importance level. In other words, the F-statistic acts as a measure to determine whether the mean of different samples is significantly different. For example, in ANOVA, a feature with an F-statistic value high enough to reject the null hypothesis is needed; the level of significance depends on the F-statistic value (Cheng, et al., 2020). In addition, this approach saves time required to train the classifier because large or small values are not necessary here. Therefore, the selection of features increases efficiency and reduces the amount of time needed by users during the classification. ANOVA is also used to choose the right sound feature because it is a good way to find which feature is important for telling the difference between clearly different sound classes (Shetty, Patnaik and Prasad, 2022).

In this study, an ANOVA-based selection method is used to find how well different features in Kurdish dialects can tell them apart. The F-statistic operates within the selection process so scientists can determine feature significance, and lower p-values suggest better ranks. A p-value shows the chance of getting the F-statistic measurement or values higher than it when both assumptions of similar feature means across dialect groups are true. As p-values go down, the strength of the evidence against the null hypothesis goes up. This shows that the feature has big differences in mean values between classes, which makes it better at telling them apart.

All features undergo separate individual tests during the evaluation method. This evaluation scrutinizes each feature individually, allowing for the independent measurement of its discriminative power. The testing of features separately eliminates the requirement to define or evaluate groups of features, making the process simpler without compromising the discriminatory effectiveness. This kind of method lets you find features by evaluating each one separately, which leads to the choice of k = 200 features that produce the best dialect separation.

The data enhancement features take MFCC and Delta MFCC from the audio signals and combine them with Mel Spectrogram and Spectral Contrast. The computed features through Librosa represent audio signals in an extensive manner. The feature vectors from each sample are judged by ANOVA-based FS, which ranks the features based on their F-statistic values. The top-k (k = 200) features, which provide effective separation between Kurdish dialects, were selected through this process. The selection approach maintains a proper alignment between computational efficiency and performance outcomes.

VI. Experimental Results

The present section provides a detailed discussion of the performance assessment of the experimental results based on our proposed Kurdish dialect recognition model. As a result, we study the impact of DA and FS on the accuracy of our classifier and compare it with the performance of the model described in the previous section. Furthermore, we evaluate the proposed approach's accuracy for classification through confusion matrices. These empirical results clearly confirm the substantial improvements introduced in DA and appropriate FS. The proposed novel Kurdish Dialect Recognition Model is found to be very accurate and significantly outperforms the previous methods.

A. Dialect Recognition

Table II also provides the analysis of the present suggested model and the preceding exploration that we conducted recently. There is a detailed study of the sensitivity analysis of the environmental parameters such as pre- and post-augmentation signal length, DA methodologies, feature extraction methods, FS, and accuracy. From Table II, one can easily see that our proposed model performs significantly better than the current state-of-the-art model suggested in Ghafoor et al. (2021). Our model gives 99.42% accuracy against 95.5% of the existing model. White noise addition alongside time-stretching modifications enabled the dataset to improve through modifications of the initial speech signals. Time-stretching techniques lengthened the signals without modifying their basic features and white noise generated variations in the audio to enhance data augmentation. The model obtained access to a much broader dataset because of these enhancements which enabled it to gain knowledge from multiple input patterns leading to better dialect generalization. Due to this technique, the model was able to learn appropriately from a larger and more diverse dataset. It was achieved utilizing new features from MFCC, Mel Spectrogram, Poly-feature, and Contrast and the approach for FS by filter.

Fundamentally, confusion matrices are adopted to assess our proposed Kurdish dialect recognition model's classification efficiency and discuss its outcomes thoroughly. More comprehensive confusion matrices of each Kurdish dialect and other evaluation metrics such as Producer Accuracy (Precision), Recall, and the F1-score are shown in Table III below. The confusion matrices show that the proposed model achieved excellent classification results for each Kurdish dialect. Based on this study, the system can tell the difference between Badini, Hawrami, and Sorani dialects with very high scores for recall, F1-score, and producer accuracy (precision). Notably, the model can classify the Hawrami and Sorani dialects with perfect results in terms of the producer's accuracy.

The results from the experiments underscore the enhancement that has been achieved through DA, advanced methods within feature extraction, and selective FS. Our proposed Kurdish Dialect Recognition Model improves the previously successful approaches to show that the proposed model, with an accuracy of 99.42%, is extremely effective. This critical advancement in comparison to the prior work can demonstrate the potential and performance of the hinted model in these language identification tasks. The model's robust classification capabilities are further highlighted by

TABLE II
Accuracy of Kurdish Dialect Recognition Models

Methods	Length of the signal before DA	Use Data Augmentation	Length of the signal after DA.	Feature extracted	Feature selection	Accuracy (%)
(Ghafoor, et al., 2021)	895 samples	Null	895 samples	MFCC	Null	95.5
Proposed model	6000 samples	White Noise, time stretching	18000 samples	MFCC, Mel spectrogram, poly-feature, contrast	Filter-based	99.42

DA: Data augmentation

TABLE III
Confusion Matrices with Producer Accuracy and User Accuracy

Classes	TABLE	Hawrami	Sorani	Classification (support)	Producer accuracy (precision) (%)	Recall (%)	F1-score (%)
Badini	1190	5	2	1197	99	99	99
Hawrami	6	1219	7	1232	100	99	99
Sorani	0	1	1170	1171	99	100	100

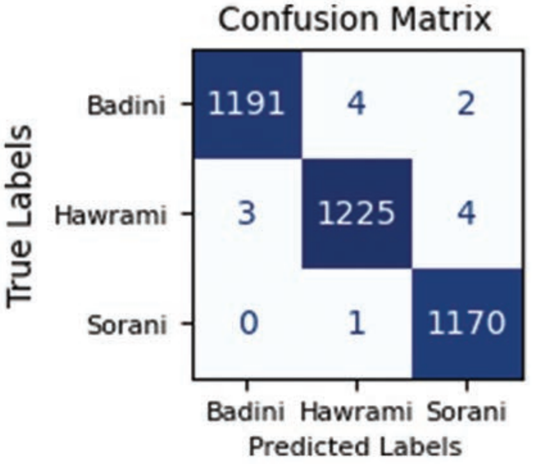

Fig. 6. Confusion matrix for Kurdish dialect classification.

analyzing the confusion matrices. The extensive literature review will allow understanding the strengths and weaknesses of the proposed model and its broad potential applications in the field of language recognition and classification.

The model's performance evaluation includes analysis through the confusion matrix in Fig. 6. The confusion matrix displays the total of accurate and inaccurate dialect predictions between Badini, Hawrami, and Sorani dialects. The numbers in the diagonal elements show correct dialect predictions, while the data points in off-diagonal elements indicate incorrect predictions.

B. Producer Accuracy and F1-Score

In our assessment of the Kurdish Dialect Recognition Model, two crucial performance metrics emerge: Producer Accuracy (Precision) and F1-Score. All things considered, these measures show how well the program identifies dialects and how accurate its classifications are.

Table III shows the Producer Accuracy (Precision) measure, which is the percentage of correct predictions for each dialect class out of all the cases that were put into that class. This metric is an important way to check if the model can get rid of false positives, which would mean high accuracy in the identified dialect. As observed in Fig. 7, the proposed model also exhibits excellent performance in terms of Producer Accuracy scoring between 99% and 100% in all the dialects. This accomplishment shows that our model correctly predicts a dialect, which in language recognition tasks is crucial because misclassification has real-world consequences. The results of Producer Accuracy show that the model is stable and confirm that it can be used to identify languages and other related sciences.

The F1 score is one of the most important features, especially when the combination of accuracy and both false-positive or false-negative results is needed. We measure the proposed model's performance for the dialect identification task using precision and recall. While every dialect is of utmost importance in language recognition scenarios, the F1-score offers a robust means of evaluating the model's performance without compromising precision and recall. With respect to performance, the F1 scores for our model are explicitly high, with percentages of 99 and 100% for every dialect. This achievement proves that the model has high precision and recall to reduce false positives and false negatives. The high F1 scores show that the model is good at telling the difference between the dialects we use in many language-related projects.

To sum up, the KDRM model is very good at identifying things and classifying them, with both high producer accuracy and high results classification effectiveness (a high F1 score). The aggregate view of the metrics provides strong evidence of the model's accuracy and usefulness in dialect identification. More importantly, their description is truly inspiring, as numerous approaches based on the model have found widespread application in various language recognition tasks.

VII. Discussion

DA methods, which include noise addition and time-stretching operations, improve the diversity and resistance of training data datasets. By adding white noise to data simulation, the model becomes more adaptable to real-world environments, and TS varies speech speed to make the model more flexible with varied speakers and accents. The techniques function as effective data expansion methods in low-resource settings by requiring no new recorded data.

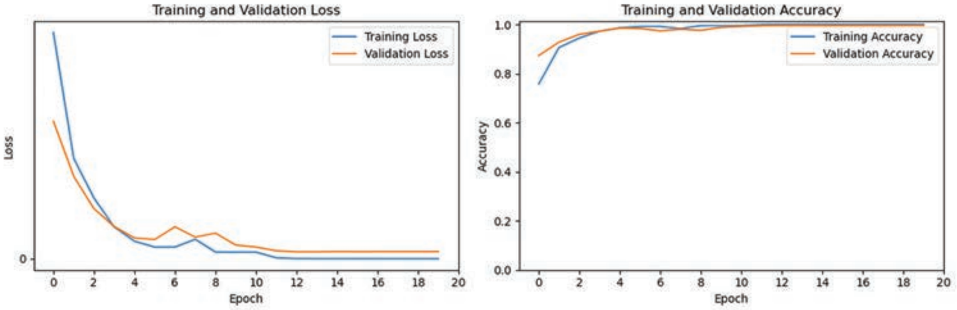

Fig. 7. Training and validation accuracy and training and validation loss.

The process of selecting features makes models more accurate while cutting down computational requirements so accuracy improves through better FS. The process enables better generalization with new data because it removes unneeded information to prevent overfitting.

It works well with both DA and FS technology because DA increases the variety of datasets and FS makes sure that datasets are ready for efficient learning. The joint use of DA techniques with FS methods creates powerful performance enhancement, which enables robust computational processing in Kurdish dialect classification methods.

The results of the experiments show that every part of the proposed approach makes model execution work better in important ways. A performance review of the model, which operates under multiple configurations, appears in Table IV. The integrated method of DA along with FS produces the best accuracy level.

Table V offers a more exhaustive cross-section of the features extracted and a more precise classification of several methods used in the field of signal processing (or a related field). We compare the approaches based on the feature sets they use, taking into account their respective accuracy levels. Each one of them incorporates a different approach to feature choice and to model training, which in its turn has an impact on the results.

TABLE IV
Impact of Data Augmentation and Feature Selection on Model Performance

Experiment setup	Accuracy (%)	Precision (%)	Recall (%)	F1-score (%)
Baseline model	96.5	96	96.3	96
With augmentation only	95.8	95.5	95.6	93.5
With feature selection only	94.2	94.0	94.1	93.0
Proposed method (Aug+Selection)	99.61	99.61	99.61	99.61

TABLE V
Comparison Proposed Model with Previous Research

Methods	Feature sets	Accuracy (%)
(Al-Talabani, Abdul and Ameen, 2017)	Local binary patterns+linear predictive coding	89.6
(Ghafoor, et al., 2021)	MFCC (Mel-frequency cepstral coefficients) in 1D CNN	95.5
(Karim, et al., 2024)	MFCC+Mel Spectrogram+Poly-feature+Contrast	96.5
Proposed model	Data Augmentation+ANOVA-based feature selection in 1D CNN	99.42

ANOVA: Analysis of variance, CNN: Convolutional neural network

The approach adopted from Al-Talabani, Abdul and Ameen (2017) involves local binary patterns (LBP), which is the premier method of feature extraction, and linear predictive coding (LPC). While LPC is used in speech processing for modeling the spectrum of a signal that is more or less constant over time, LBP is famous as a texture image descriptor. Moreover, even when the method is worked out using both of them at the same time, it only reaches a level of about 89.6%, which is somewhat lower than that of the more modern techniques. The findings show that while LBP and LPC can extract useful features for classification, they may not apply all the structures in the data to achieve optimal classification. Our group in prior work (Ghafoor, et al., 2021) used a 1D CNN for classification through MFCC feature set. MFCCs prove to show a high degree of efficiency in the signal processing of audio-type signals since they represent the power spectrum of the sound. The application of these coefficients in the 1D CNN structure improved the classification accuracy to a rate of 95.5%. This result validates the effectiveness of deep learning models, especially CNNs, in modeling time series data like the audio signals as against traditional feature extraction approaches.

Karim et al. (2024) extended this list of features by including MFCC + MelS + Poly-features + Contrast. Adding the Mel spectrogram introduces the time-frequency representation of the signal, which is particularly useful if temporal and spectral information is required. Poly-features refer to different signal characteristics, and contrast is added here to offer a comparison between the signal areas. This kind of work provides the so far largest feature set to achieve an accuracy of 96.5% in classifying the galaxies, which proves the great improvement against previous approaches. However, the strengthened interior combination still is not able to reach the pinnacle of the accuracy recorded in the current research.

Finally, this paper also presented a proposed model that comprises an advanced pipeline with DA and FS that employs ANOVA, as well as the 1D CNN. DA is accepted as a known method for increasing the training dataset, reducing overfitting, and increasing the model's ability to generalize. Another way to find the most expressive features in a classification problem is a technique known as ANOVA-based attribute ranking – it compares the differences between various feature groups and how they contribute to a classification task. This approach enriches the features vector so the model contains only the most discriminating features. Using the aforementioned techniques, we were able to recognize the proposed study with 99.42% accuracy, leaving far behind other methods. Given a perfect combination of stable course development, the principal component selection, and deep learning techniques within a perfectly tuned network architecture, this high accuracy has very significant implications for real applications. As a result, the study shows that using better methods for extracting features leads to more accurate classification, especially when neural solid network designs are combined with techniques for improving data. The proposed model is superior to previous models by containing a deep learning aspect and stringent FS using ANOVA. Obtaining the final accuracy of 99.42%, we indicate that the suggested method can be successfully applied to practical tasks where accuracy is critical.

VIII. Conclusion

This paper presents a detailed analysis of our Kurdish Dialect Recognition Model, demonstrating its ability to perform language recognition and classification. Strong experimental findings demonstrate that our model determines major potential for language identification work. The investigation reveals the model's effective discrimination abilities between Kurdish dialects and establishes potential for its methods to identify languages beyond Kurdish dialects. The strong model performance stems from the integration between feature extraction and data augmentation and feature selection methods which establishes the model as a promising technology for field advancement. The benefits of our model are: Our model employs a rigorous procedure for feature extraction and selectively utilizes DA. We also introduced white noise and time-stretching techniques to the suggested dataset so as to improve the training data and increase the probability of the model learning and performing optimally on more than just a larger data set. We have added new characteristics such as MFCC, Mel Spectrogram, Poly-feature, and Contrast, which significantly enhance the model's ability to identify dialect differences. Moreover, an ANOVA-based filter-based FS technique has minimized the span of feature space while preserving relevant data. As a result, the model is now more accurate and effective, and it does a good job of detecting and differentiating dialects.

In real life, model accuracy and categorical classification are important performance indicators for language recognition tasks. The high values of Producer Accuracy and F1-Score suggest that this is possible. The proposed Kurdish Dialect Recognition Model's results show that feature extraction, data enhancement, and FS are all very important parts of being able to recognize languages. The accuracy and precision, as well as the balanced classification, show the efficiency of the solid and well-developed machine-learning methodology of the proposed model. This work has paved the way for further research and development in language identification and classification on top of enhancing language recognition capabilities. The role of accurate and flexible language recognition systems increases rapidly due to the free and significant growth of our world and the change that occurs in it. With the proposed model, the problems listed can be fixed, and the model can be used in other language-related fields that have not been studied yet. This will help keep an understanding of the variety of languages in a globalized world.

When highlighting the advantages of the presented model, it is essential to mention potential shortcomings, such as possible biases due to the assumptions made in the course of the study. Focusing on our approach in detail demonstrates a few areas of improvement that could arrive at different feature extraction techniques and elevate FS methodology. Furthermore, learning Kurdish dialects is a good step toward making the app work better in places with different cultures and languages, which includes making it more flexible. This approach proves that our model is beneficial as it allows for keeping languages diverse and developing intercultural communication. In addition, the limitations handled and the more comprehensive applications demonstrated herein support the advancement of language recognition technology, which creates a foundation for future advancements in language identification and categorization.

IX. Future Work

Our model achieves its strength by having an independent feature extraction process combined with selection mechanisms that operate without language restrictions. Using MFCC and a Mel Spectrogram along with statistical selection methods helps the model find speech features that are common across languages. Through DA approaches, the model demonstrates robust performance because these methods replicate pronunciation variability as well as accent and noise patterns, which affect speech-based tasks universally.

The approach requires an evaluation of language datasets, which will establish its capability for cross-language generalization. Model adaptation performance across different languages can be measured by training it on various linguistic datasets that evaluate its ability to learn universal phonetic components independent of language variation. Transfer learning methods should be applied to enhance the model by adapting it to underserved language domains through small, labeled datasets. This study focuses on the Kurdish language while extending its research approach toward different languages. Future researchers will work on conducting thorough assessments of this model, which will lead to developing adaptation methods for broad multilingual usage.

References

Abdul, Z.K., Al-Talabani, A., and Abdulrahman, A.O. 2016. A new feature extraction technique based on 1D local binary pattern for gear fault detection. *Shock and Vibration*, 2016, p. 8538165.

Abdullah, A.A., Abdulla, S.H., Toufiq, D.M., Maghdid, H.S., Rashid, T.A., Farho, P.F., & Asaad, A.T. 2024. NER-RoBERTa: Fine-Tuning RoBERTa for Named Entity Recognition (NER) within low-resource languages. *arXiv preprint* *arXiv:2412.15252*.

Aguiar, R.L., Costa, Y.M., and Silla, C.N. 2018. Exploring data augmentation to improve music genre classification with convnets. In: *2018 International Joint Conference On Neural Networks (IJCNN)*. IEEE, United States, pp. 1-8.

Al-Onazi, B.B., Nauman, M.A., Jahangir, R., Malik, M.M., Alkhammash, E.H., and Elshewey, A.M. 2022. Transformer-based multilingual speech emotion recognition using data augmentation and feature fusion. *Applied Sciences,* 12, p. 9188.

Al-Talabani, A.K., Abdul, Z.K., and Ameen, A.A. 2017. Kurdish dialects and neighbor languages automatic recognition. *ARO-The Scientific Journal of Koya University,* 5, pp. 20-23.

Bahari, M.H., Dehak, N., Burget, L., Ali, A.M., and Glass, J. 2014. Non-negative factor analysis of gaussian mixture model weight adaptation for language and dialect recognition. *IEEE/ACM Transactions On Audio, Speech, and Language Processing,* 22, pp. 1117-1129.

Cheng, W.K., Khairuddin, I.M., Majeed, A.P.A., and Razman, M.A.M. 2020. The Classification of heart murmurs: The identification of significant time domain features. *Mekatronika: Journal of Intelligent Manufacturing and Mechatronics,* 2, pp. 36-43.

Damskägg, E.P., and Välimäki, V. 2017. Audio time stretching using fuzzy classification of spectral bins. *Applied Sciences,* 7, p. 1293.

Das, A., Guha, S., Singh, P.K., Ahmadian, A., Senu, N., and Sarkar, R. 2020. A hybrid meta-heuristic feature selection method for identification of Indian spoken languages from audio signals. *IEEE Access,* 8, pp. 181432-181449.

Das, P.P., Allayear, S.M., Amin, R., and Rahman, Z. Bangladeshi dialect recognition using Mel frequency cepstral coefficient, delta, delta-delta and Gaussian mixture model. In: *2016 Eighth International Conference on Advanced Computational Intelligence (ICACI),* IEEE, United States, pp. 359-364.

Ghafoor, K.J., Rawf, K.M.H., Abdulrahman, A.O., and Taher, S.H. 2021. Kurdish dialect recognition using 1D CNN. *ARO-The Scientific Journal of Koya University,* 9, pp. 10-14.

Hama Rawf, K.M., Abdulrahman, A.O., and Mohammed, A.A. 2024. Improved recognition of Kurdish sign language using modified CNN. *Computers,* 13, p. 37.

Hu, H., Tan, T., and Qian, Y. Generative adversarial networks based data augmentation for noise robust speech recognition. In: *2018 IEEE International Conference on Acoustics, Speech and Signal Processing (ICASSP)*. IEEE, United States, pp. 5044-5048.

Kanda, N., Takeda, R., and Obuchi, Y. Elastic spectral distortion for low resource speech recognition with deep neural networks. In: *2013 IEEE Workshop on Automatic Speech Recognition and Understanding*. IEEE, United States, pp. 309-314.

Karim, S.H.T., Ghafoor, K.J., Abdulrahman, A.O., and Rawf, K.M.H. 2024. A Multi-feature fusion approach for dialect identification using 1D CNN. *JOIV: International Journal on Informatics Visualization,* 8, pp. 1246-1252.

Khamparia, A., Gupta, D., Nguyen, N.G., Khanna, A., Pandey, B., and Tiwari, P. 2019. Sound classification using convolutional neural network and tensor deep stacking network. *IEEE Access,* 7, pp.7717-7727.

Kupryjanow, A., and Czyzewski, A. 2012. A method of real-time non-uniform speech stretching. *E-Business and Telecommunications: International Joint Conference, ICETE 2011*, *Seville, Spain, July 18-21*. Revised Selected Papers. Springer, Germany, pp. 362-373.

Li, X., Zhang, W., Ding, Q., and Sun, J.Q. 2020. Intelligent rotating machinery fault diagnosis based on deep learning using data augmentation. *Journal of Intelligent Manufacturing,* 31, pp.433-452.

Lounnas, K., Lichouri, M., and Abbas, M. 2022. Analysis of the effect of audio data augmentation techniques on phone digit recognition for algerian arabic dialect. *In: 2022 International Conference on Advanced Aspects of Software Engineering (ICAASE)*. IEEE, United States, pp. 1-5.

Ma, R., Tao, P., and Tang, H. 2019. Optimizing data augmentation for semantic segmentation on small-scale dataset. In: *Proceedings of the 2nd International Conference on Control and Computer Vision*, pp. 77-81.

Moreno-Barea, F.J., Jerez, J.M., and Franco, L. 2020. Improving classification accuracy using data augmentation on small data sets. *Expert Systems with Applications,* 161,

Mulahuwaish, A., Gyorick, K., Ghafoor, K.Z., Maghdid, H.S., and Rawat, D.B. 2020. Efficient classification model of web news documents using machine learning algorithms for accurate information. *Computers and Security*, 98, p. 102006.

Nguyen, T.S., Stueker, S., Niehues, J., and Waibel, A. 2020. Improving sequence-to-sequence speech recognition training with on-the-fly data augmentation. In: *ICASSP 2020-2020 IEEE International Conference on Acoustics, Speech and Signal Processing (ICASSP)*. IEEE, United States, pp. 7689-7693.

Nugroho, K., and Noersasongko, E. 2022. Enhanced Indonesian ethnic speaker recognition using data augmentation deep neural network. *Journal of King Saud University-Computer and Information Sciences,* 34, pp. 4375-4384.

Peddinti, V., Chen, G., Manohar, V., Ko, T., Povey, D., and Khudanpur, S. 2015. Jhu aspire system: Robust lvcsr with tdnns, ivector adaptation and rnn-lms. In: *2015 IEEE Workshop on Automatic Speech Recognition and Understanding (ASRU)*. IEEE, United States, pp. 539-546.

Ragni, A., Knill, K.M., Rath, S.P., and Gales, M.J. Data augmentation for low resource languages. In: *Interspeech 2014: 15th Annual Conference of the International Speech Communication Association, 2014*. International Speech Communication Association (ISCA), pp. 810-814.

Rawf, K.M.H., Karim, S.H.T., Abdulrahman, A.O., and Ghafoor, K.J. 2024. Dataset for the recognition of Kurdish sound dialects. *Data in Brief,* 53, p. 1.

Rebai, I., Benayed, Y., Mahdi, W., and Lorré, J.P. 2017. Improving speech recognition using data augmentation and acoustic model fusion. *Procedia Computer Science,* 112, pp. 316-322.

Rituerto-González, E., Mínguez-Sánchez, A., Gallardo-Antolín, A., and Peláez-Moreno, C. 2019. Data augmentation for speaker identification under stress conditions to combat gender-based violence. *Applied Sciences,* 9, p. 2298.

Salamon, J., and Bello, J.P. 2017. Deep convolutional neural networks and data augmentation for environmental sound classification. *IEEE Signal Processing Letters,* 24, pp. 279-283.

Sangwan, P., Deshwal, D., and Dahiya, N. (2021). Performance of a language identification system using hybrid features and ANN learning algorithms. *Applied Acoustics,* 175, p. 107815.

Shetty, N., Patnaik, L., and Prasad, N. 2022. Emerging research in computing, information, communication and applications proceedings of ERCICA 2022. In: *Proceedings of ERCICA*, p. 1.

Tu, Z., Liu, B., Zhao, W., Yan, R., and Zou, Y. 2023. A feature fusion model with data augmentation for speech emotion recognition. *Applied Sciences,* 13, p. 4124.

Tubishat, M., Abushariah, M.A., Idris, N., and Aljarah, I. 2019. Improved whale optimization algorithm for feature selection in Arabic sentiment analysis. *Applied Intelligence,* 49, pp. 1688-1707.

Turab, M., Kumar, T., Bendechache, M., and Saber, T. 2022. Investigating multi-feature selection and ensembling for audio classification. *arXiv preprint arXiv:2206.07511*.

Wu, T., Duchateau, J., Martens, J.P., and Van Compernolle, D. 2010. Feature subset selection for improved native accent identification. *Speech Communication,* 52, pp. 83-98.

Zheng, Q., Yang, M., Tian, X., Jiang, N., and Wang, D. 2020. A full stage data augmentation method in deep convolutional neural network for natural image classification. *Discrete Dynamics in Nature and Society,* 2020, p. 4706576.

Zhou, H., Wang, X., and Zhu, R. 2022. Feature selection based on mutual information with correlation coefficient. *Applied Intelligence,* 52, pp. 5457-5474.

Influence of Tetramethylammonium Hydroxide Cation Concentration on Omega Zeolite Crystal Size

Muwafaq M. Yahya[1†], Rana T. AL-Rubaye[1] and Aqeel A. Al-Ani[2]

[1]Department of Chemical Engineering, Faculty of Engineering, Baghdad University,
Baghdad – F.R. Iraq

[2]Ministry of Oil, Oil Marketing Company (SOMO) Baghdad,
Baghdad – F.R. Iraq

***Abstract*—Omega zeolite nanocrystals can be synthesized hydrothermally from a sodium aluminosilicate solution characterized by a 5.96 Na_2O/Al_2O_3 constant molar ratio, carried out at a maximum temperature of about 100°C for 4 days after aging at room temperature for 3 days, utilizing tetramethylammonium hydroxide (TMA-OH) at molar ratios of 0.36, 0.48, and 0.61. By using different analysis techniques, such as X-ray diffraction, energy-dispersive X-ray spectroscopy, scanning electron microscopy, and atomic force microscopy, the physical characteristics of the nanosized omega zeolite crystals can be identified, and the omega zeolite crystal size can be regulated between 34 and 100 nm. In this research paper, the process of creating a uniform aluminosilicate solution with TMA-OH, followed by forming a solid aluminosilicate gel with adjusted elemental composition, reveals the significance of the TMA-OH/Al_2O_3 mole ratio for synthesizing nanocrystalline omega zeolite aggregates.**

***Index Terms* – Nanocrystal, Omega zeolite, Sodium-aluminosilicate, Tetramethylammonium hydroxide.**

I. Introduction

Discovered in 1972 within the basalt lava of Mont-Sémiole, "near Montbrison," France, the Omega synthetic aluminosilicate zeolite is one of several types of zeolite, including ZSM-4 (Galli, et al., 1974), and LZ-202 (Breck and Skeels, 1985) that own the Mazzite framework, which is naturally occurring zeolite. Furthermore, this zeolite framework contains a 12-membered ring pore found by (Galli, et al., 1974) and (Rinaldi, Pluth and Smith, 1975) and has garnered significant research interest due to its notable Brønsted acidity and catalytic capabilities in processes such as alkylation (Flanigen and Kellberg, 1980), cracking (Báfero, et al., 2020), and isomerization (Mahdi and Muraza, 2016). Numerous patents and scholarly articles detail the synthetic counterpart of mazzite (omega zeolite), which typically forms at low temperatures (approximately 353–423 K) within the (tetramethylammonium hydroxide [TMA-OH])–NaOH–Al_2O_3–SiO_2–H_2O system (Feng, et al., 2020; Martucci, et al., 2003; Goossens, et al., 2000; McQueen, et al., 1994). Across this process, TMA-OH serves as a structure-directing agent (SDA), while other organic compounds, including pyrrolidine (Flanigen and Kellberg, 1980), piperazine (Xu, et al., 2007), glycerol (Yang and Evmiridis, 1994), and p-dioxane (De Witte, et al., 1997), have also been utilized as templating agents. In the past 30 years, there has been much awareness of the use of organic molecules as SDAs in the texture synthesis of aluminosilicate zeolites (Shi, et al., 2012). In the middle process of preparation of omega zeolite, TMA cations may become trapped in gmelinite cages during crystal growth, which is assumed to be a strong structure-directing factor (Feng, et al., 2020; Martucci, et al., 2003; Goossens, et al., 2000). A vast range of morphologies has been documented for omega zeolites, such as euhedral crystals in the shape of hexagonal prisms, barrels, spheres, or rosettes, in uneven forms such as bundles or needles (Araya, et al., 1984; Fajula, et al., 1989; DiRenzo, et al., 1994; Edmunds, et al., 1989). The aluminum concentration could be the key to the crystal morphology in the synthesis mixture (Goossens, et al., 2000; McQueen, et al., 1994), or when using an alcohol medium during the reaction mixture, the alcohol type and its ratio inside the water may play a significant role also (Gies and Marker, 1992). Some findings indicate that SDAs function not merely as pore fillers but, with the assistance of van der Waals forces, mainly interact with the Si species inside the zeolite (Gómez-Hortigüela, et al., 2004). The final crystalline structure geometry of zeolite pores and the type of final crystalline structure are influenced by SDAs. The concentration of the organic template in the zeolite framework can be affected by the interaction type between zeolite pre-cursors and SDAs (Gómez-Hortigüela, et al., 2004; Sastre, et al., 2003). Furthermore, the structures formed during the crystallization of zeolites by employing SDAs are probably not the stabilized ones but those with the greatest nucleation abilities, developing under either thermodynamic or kinetic control. This occurrence depends on the conditions

---

ARO-The Scientific Journal of Koya University
Vol. XIII, No. 1 (2025), Article ID: ARO.11978. 7 pages
DOI: 10.14500/aro.11978
Received: 29 December 2024; Accepted: 20 March 2025
Regular research paper; Published: 31 March 2025

[†]Corresponding author's e-mail: muwafaq.yahya1507d@coeng.uobaghdad.edu.iq

of the crystals' growth step during the crystallization operation (Tosheva and Valtchev, 2005). The existence of Na+ cations is necessary to achieve the charge balance in the route of the crystal growth because the TMA cations are not adequate to balance the entire charge of the anionic lattice. Based on all previous facts, it can be said that the MAZ-type zeolites essentially depend on TMA in the figuration of its establishment (McQueen, et al., 1994).

II. Preparation

The reagents used were TMA-OH (25% solution in water) from MERCK (UN 1835) used as a template, sodium hydroxide (NaOH, >99.0 wt%), and distilled water. Sodium aluminate (density 2.6 g/cm^3, molecular weight = 81.97 g/mol.) (50–60% Al_2O_3, ≤0.05% Fe_2O_3, 37–45%Na_2O) and silica colloidal HS-40 (40 wt. % suspension in H_2O) bought from Sigma Aldrich (MERCK). A typical gel sample was prepared in the laboratories of the chemical engineering department at Baghdad University for about 7 days. First, the gel is prepared by mixing NaOH, H_2O, TMA-OH, and $NaAlO_2$ in an appropriate plastic beaker at room temperature for 30 min. The silica sol was added drop by drop with stirring until homogeneity occurred. After further mixing for 30 min, the mixture was kept inside a 125 mL stainless Teflon-lined steel autoclave, aged statically for three days at a temperature of about 25°C, and after that stored in an oven for 4 days at 100°C. The solid product was washed with deionized water until the pH of the residue water reached about 7–8, and then dried overnight at 100°C.

TABLE I
Batch Requirement for Omega Zeolite Synthesis

Material	Run 1 (Moles)	Molar Ratio	Run 2 (Moles)	Molar Ratio	Run 3 (Moles)	Molar Ratio
$Al_2 0_3$	0.0160	1.00	0.0160	1.00	0.0160	1.00
NaOH	0.0957	5.98	0.0957	5.98	0.0957	5.98
TMA-OH	0.0057	0.36	0.0077	0.48	0.0098	0.61
H_2O	1.7837	111.4	1.8147	113.3	1.8478	115.4
SiO_2	0.1605	10.02	0.1605	10.02	0.1605	10.02

$Al_2 0_3$=Aluminum oxide, NaOH=Sodium oxide, TMA-OH=Tetramethylammonium-hydroxide, H_2O=Water molecule, SiO_2=Silicon dioxide

Table I shows the batch requirement for omega synthesis with varied TMA-OH/Al_2O_3 mole ratios of about 0.36, 0.48, and 0.61. The X-ray diffractometry (XRD) analysis on the ADX2700 SSC (30 mA, 40 kV) device was used to specify the crystallinity, phase lucidity, and stratification of the acquired samples. The crystal morphology and crystal size were determined by scanning electron microscopy (SEM) (Quattro–STEM/SEM) Thermo Fisher Scientific (X2500000, 0.8 nm, 5-axis). The carbon, oxygen, and sodium (Na) weight percent and the silica/alumina bulk ratio were specified on energy dispersive X-ray spectroscopy (EDXS) detectors, in addition to atomic force microscopy (AFM) (CoreAFM) analysis to show the surface morphology differences between the omega zeolite samples.

III. Results and Discussion

The XRD patterns of Omega zeolite samples from experiments Run 1, Run 2, and Run 3 using CuKα radiation are illustrated in Fig. 1a-c, respectively. The first sight may show that the zeolite omega is an "intermediate phase" crystallizing in the interfering crystallization fields of ZSM-4 zeolite (Mahdi and Muraza, 2016), and the ZSM-34 zeolite (Wu, et al., 2008), which proved that TMA-OH plays a structure-directing role with Na+ (sodium cation) in the formation of zeolite omega.

Table II shows the extended report of the XRD peak ID, the report shows 2-theta for standard and typical samples of Runs 1, 2, and 3, along with the crystal size and delta size for typical samples only. The data for all samples, when compared with data announced in the literature on crystal size for (Perrotta, et al., 1978), show almost identical results to those of omega zeolite in the case of the stances and some differences in relative intensities of the diffraction peaks. The sample from Run 1, where the mole ratio of TMA-OH/Al_2O_3 is about 0.36, shows a maximum crystal size of not more than 48 nm and a delta of not <0.052, while the sample from Run 3 with a TMA-OH/Al_2O_3 mole ratio of about 0.61 shows crystal size values of more than 100 nm at several points and a delta value of not <0.041. The maximum crystal size for Omega zeolite can obtained when the mole

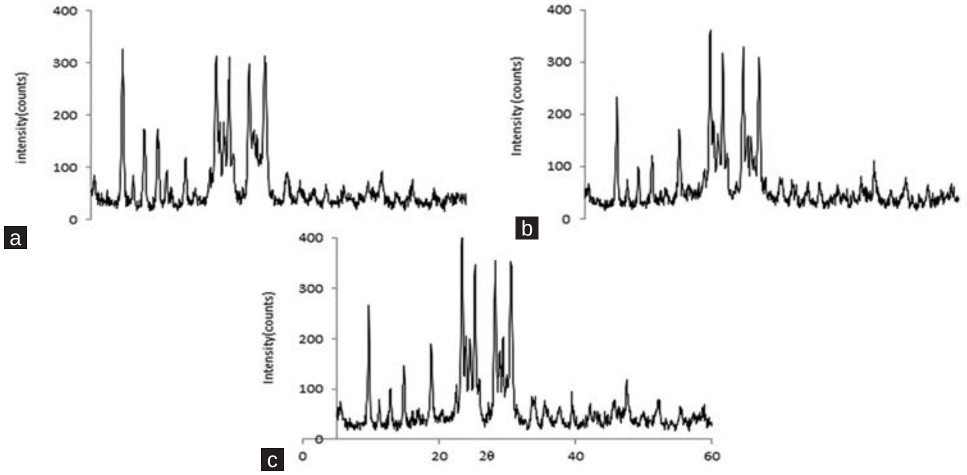

Fig. 1. XRD patterns of samples of Run 1 (a), Run 2 (b), and Run 3 (c) using CuKα radiation.

TABLE II
The Extended Report of the XRD Peak id, the Report shows 2-Theta for Standard and Typical Samples of Runs 1, 2, and 3

2-Theta*	Run 1			Run 2			Run 3		
	2-Theta	Delta	Crystal size (nm)	2-Theta	Delta	Crystal size (nm)	2-Theta	Delta	Crystal size (nm)
5.589	5.377	0.212	48	-	-	-	5.46	0.129	>100
9.744	9.558	0.185	31	9.722	0.022	60	9.667	0.076	57
11.248	11.092	0.156	33	11.275	−0.027	>100	11.199	0.049	61
12.894	12.761	0.133	24	12.897	−0.003	93	12.854	0.041	48
14.902	14.744	0.158	29	14.891	0.011	43	14.838	0.064	41
16.19	16.033	0.157	21				16.12	0.07	>100
16.939	16.647	0.292	21	16.974	−0.035	25	16.874	0.065	36
18.988	18.809	0.179	27	18.927	0.061	28	18.863	0.125	32
20.352	20.196	0.155	46	-	-	-	-	-	-
22.665	22.553	0.112	31	-	-	-	22.575	0.09	>100
23.516	23.332	0.183	14	23.484	0.032	22	23.394	0.122	26
24.098	-	-	-	23.95	0.148	18	23.863	0.235	26
24.71	24.505	0.205	16	24.623	0.087	15	24.546	0.163	26
25.427	25.227	0.2	14	25.332	0.096	16	25.252	0.175	23
26.033	25.85	0.183	22	25.79	0.242	26	25.768	0.265	30
27.334							27.317	0.017	82
28.401	28.204	0.197	14	28.312	0.088	19	28.246	0.154	28
28.966	28.85	0.116	7	28.877	0.089	16	28.905	0.061	16
29.709	-	-	-	29.503	0.052	22	29.361	0.193	25
30.742	30.483	0.259	15	30.644	0.098	29	30.569	0.173	19
33.862	33.774	0.088	15	33.82	0.042	16	33.807	0.056	15
35.655	35.603	0.052	29	35.627	0.028	21	35.579	0.076	17
37.949	37.673	0.277	16	37.804	0.145	17	37.665	0.285	17
39.709	39.451	0.258	29	39.627	0.081	25	39.556	0.152	45
42.318	42.081	0.237	21	42.25	0.068	47	42.161	0.157	>100
45.935	45.671	0.265	20	45.726	0.21	34	45.7	0.235	17
47.78	47.592	0.188	21	47.643	0.137	30	47.59	0.191	27

ratio of TMA-OH/Al_2O_3 is about 0.48, where crystal size ranges from 20 to more than 100 nm with a minimum delta reaching a negative value of about −0.027. Fig. 2 shows a histogram chart comparison and differences in crystal size between these samples. By comparing the delta value, which represents the differences between the prepared samples and the memory background inside the XRD device, it was found that the zeolite with the smallest delta value was the best match for the pure form of zeolite omega.

The effect of the mole ratio of TMA-OH/Al_2O_3 on particle size growth can be seen in Fig. 3, which represents SEM analysis images of omega zeolite samples for Run 1, Run 2, and Run 3, respectively. These figures clearly show how the crystals appear at different concentrations of organic structure directing agent (OSDA). At low concentrations, there are intercrystallite voids of about 10 µm and an irregular particle size between 36 nm and 117 nm; these voids become narrower and the crystallinity grows to a uniform size between 60 and 70 nm after reaching a concentration of 0.48. When the concentration becomes about 0.61, there is an expansion of the distance between the crystals, which become rod-like and have an apparent size between 43 nm and 93 nm due to scattering as a result of increased polarization by OSDA.

The AFM analysis includes a mean diameter histogram chart, 2D particle analysis, 3D view of the surface, and the mean magnitudes of particle diameter, area, and Z-maximum. Figs. 4 and 5 show the average particle diameter, area, and Z-max for both samples from Run 1 and Run 3, which were about 36 nm, 41 nm, and 2659 nm^2 and 38 nm, 265 nm, and 2786 nm^2, respectively, with incomplete or distorted crystallization in Fig. 4, and inhomogeneous distribution of particles after disintegration to a smaller diameter on the surface in Fig. 5, while Fig. 6 shows an almost uniform spread of complete particle crystallization with an average diameter of about 95 nm, an average Z-max of about 252 nm, and an average area of about 14608 nm^2. Thus, with a stable Na_2O/Al_2O_3 ratio in the range (6.0–8.0) required for the preparation of mazzite (omega zeolite), the added appropriate

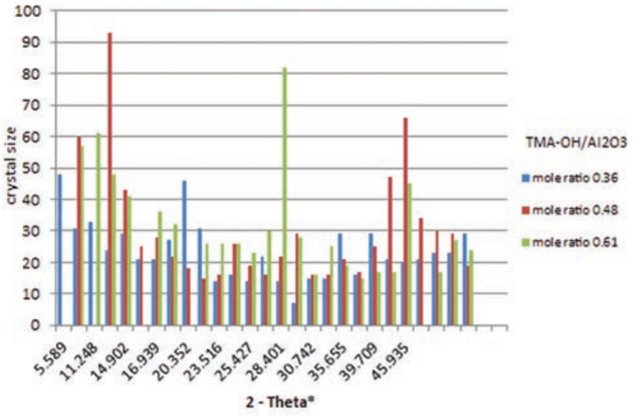

Fig. 2. Histogram chart comparison and differences between crystal size omega zeolite samples from Run 1, 2, and Run 3.

amount of TMA-OH was clearly presented as a strong SDA in the synthesis of omega zeolite (Dwyer and Chu, 1979).

Finally, Figs. 7-9 show the EDS analysis of omega zeolite samples from Run 1, Run 2, and Run 3 as peaks for the main components of omega zeolite, and the results are inserted in Table III. The results show that the maximum carbon weight percent occupying was about 12% by omega zeolite with a TMA-OH/Al$_2$O$_3$ mole ratio of about 0.48, and it is more than the rest samples, this is due to the good and high crystallization during preparation. The Si/Al bulk ratio was about 3.037, 3.07, and 3.5, respectively, with a fixed mixed Na$_2$O/Al$_2$O$_3$ mole ratio of about 5.96.

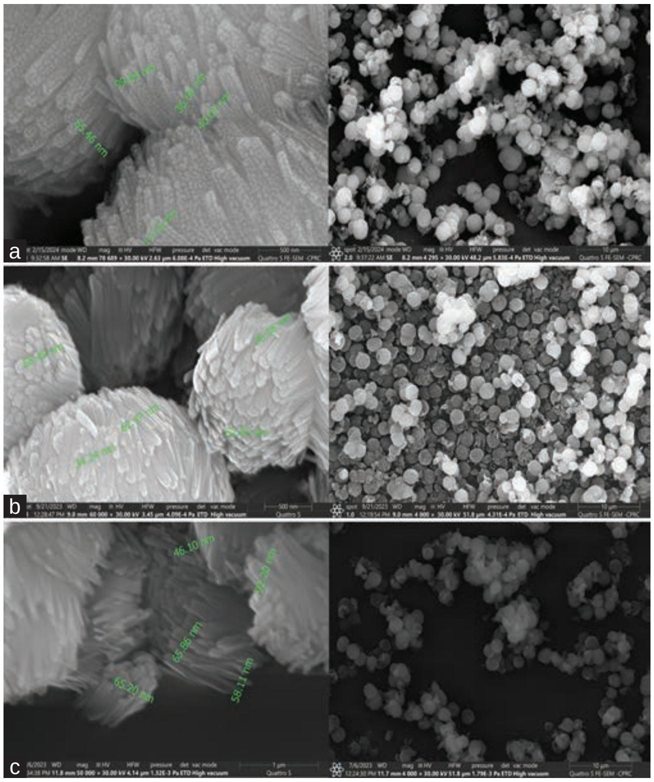

Fig. 3. Scanning electron microscopy images of omega zeolite samples from Run 1 (a), Run 2 (b), and Run 3 (c).

The status here is proportionate with preceding arguments (Brady and Walther, 1990; Pinar, et al., 2007) regarding cooperative structure directing effects in high or low silica zeolites using a collection of macro- and microstructure directing agents (Dove and Crerar, 1990; AL-Rubaye and Garforth, 2018; Najwa and and Asir, 2015; Abd Al-Rubaye, 2017). The organization of TO^4 tetrahedral units by TMA-OH molecules may not be strongly adequate, leading to the formation of amorphous materials. However, small Na+ ions existing in the synthesis gel can develop the crystallization process by helping to conquer the energy barrier of nucleation (Hussam and Hussein, 2019; Al-Rubaye, 2013; Najwa and Asir, 2016). At the same time, Na+ affects the types of secondary building blocks established in the gel, leading to the formalization of various zeolites (Rallan, Al-Rubaye and Garforth, 2015; Ammar and Sally, 2017). However, with the addition of TMA-OH, these small inorganic existences can progressively aggregate around TMA-OH, opening

TABLE III
WEIGHT PERCENT OF SILICON, ALUMINUM, AND SODIUM OF PREPARED OMEGA ZEOLITE FROM RUN 1, 2, AND RUN 3

Zeolite type/ Element	Na-omega Tma-oh/al$_2$o$_3$ Molar ratio 0.36 Run 1	Na-omega Tma-oh/al$_2$o$_3$ Molar ratio 0.48 Run 2	Na-omega Tma-oh/al$_2$o$_3$ Molar ratio 0.61 Run 3
	Weight %	Weight %	Weight %
C	5.8	12.0	3.6
O	54.8	51.8	48.3
Na	6.9	6.2	5.9
Al	7.9	6.8	9.4
Si	24.0	20.9	32.9
Ca	0.6	0.0	0.0
Cu	0.0	2.3	0.0

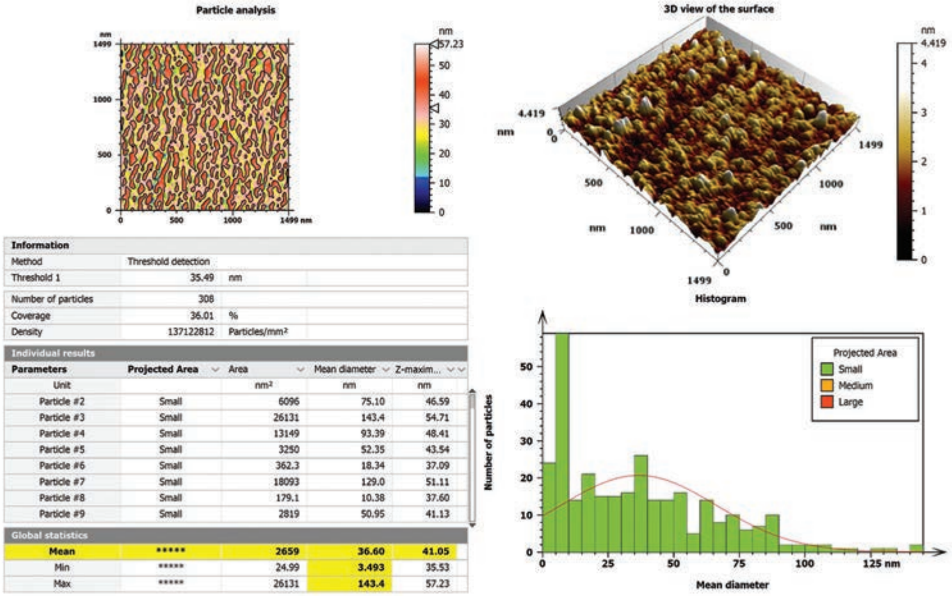

Information		
Method	Threshold detection	
Threshold 1	35.49	nm
Number of particles	308	
Coverage	36.01	%
Density	137122812	Particles/mm²

Individual results

Parameters	Projected Area	Area	Mean diameter	Z-maxim...
Unit		nm²	nm	nm
Particle #2	Small	6096	75.10	46.59
Particle #3	Small	26131	143.4	54.71
Particle #4	Small	13149	93.39	48.41
Particle #5	Small	3250	52.35	43.54
Particle #6	Small	362.3	18.34	37.09
Particle #7	Small	18093	129.0	51.11
Particle #8	Small	179.1	10.38	37.60
Particle #9	Small	2819	50.95	41.13
Global statistics				
Mean	*****	2659	36.60	41.05
Min	*****	24.99	3.493	35.53
Max	*****	26131	143.4	57.23

Fig. 4. Atomic force microscopy analysis of omega zeolite sample from Run 1.

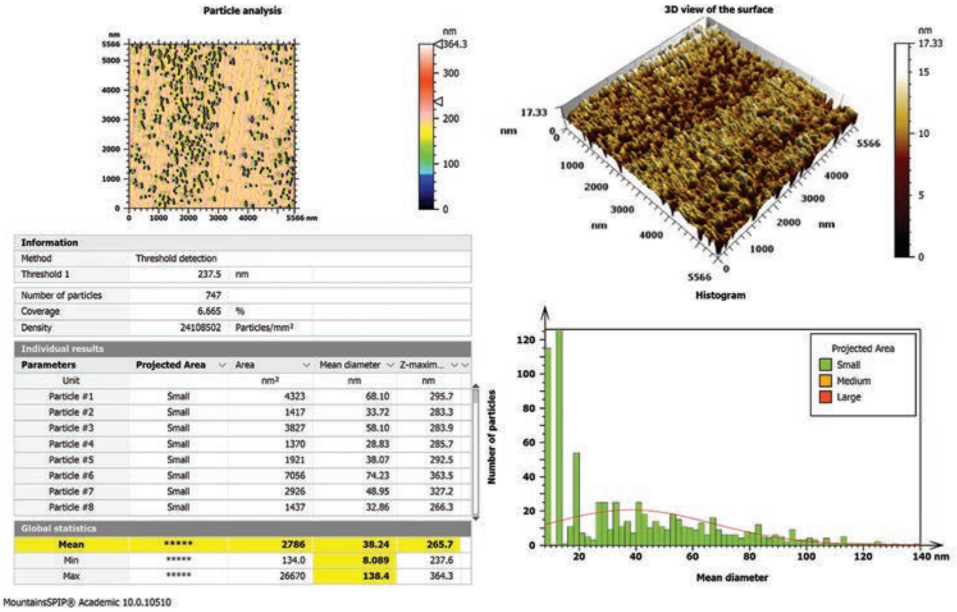

Information		
Method	Threshold detection	
Threshold 1	237.5	nm
Number of particles	747	
Coverage	6.665	%
Density	24108502	Particles/mm²

Parameters	Projected Area	Area	Mean diameter	Z-maxim...
Unit		nm²	nm	nm
Particle #1	Small	4323	68.10	295.7
Particle #2	Small	1417	33.72	283.3
Particle #3	Small	3827	58.10	283.9
Particle #4	Small	1370	28.83	285.7
Particle #5	Small	1921	38.07	292.5
Particle #6	Small	7056	74.23	363.5
Particle #7	Small	2926	48.95	327.2
Particle #8	Small	1437	32.86	266.3
Global statistics				
Mean	*****	**2786**	**38.24**	**265.7**
Min	*****	134.0	**8.089**	237.6
Max	*****	26670	**138.4**	364.3

MountainsSPIP® Academic 10.0.10510

Fig. 5. Atomic force microscopy analysis of omega zeolite sample from Run 3.

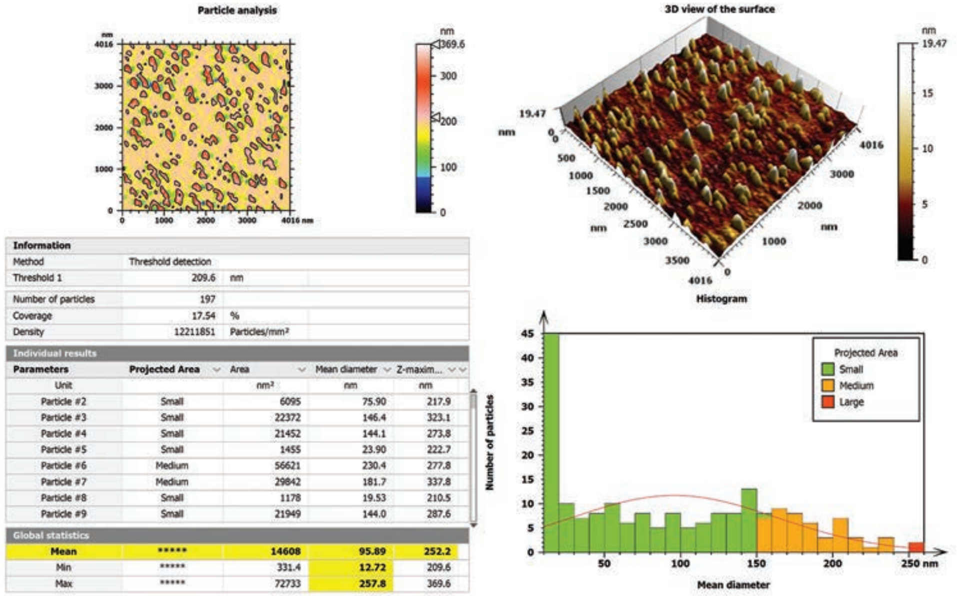

Information		
Method	Threshold detection	
Threshold 1	209.6	nm
Number of particles	197	
Coverage	17.54	%
Density	12211851	Particles/mm²

Parameters	Projected Area	Area	Mean diameter	Z-maxim...
Unit		nm²	nm	nm
Particle #2	Small	6095	75.90	217.9
Particle #3	Small	22372	146.4	323.1
Particle #4	Small	21452	144.1	273.8
Particle #5	Small	1455	23.90	222.7
Particle #6	Medium	56621	230.4	277.8
Particle #7	Medium	29842	181.7	337.8
Particle #8	Small	1178	19.53	210.5
Particle #9	Small	21949	144.0	287.6
Global statistics				
Mean	*****	**14608**	**95.89**	**252.2**
Min	*****	331.4	**12.72**	209.6
Max	*****	72733	**257.8**	369.6

Fig. 6. Atomic force microscopy analysis of omega zeolite sample from Run 2.

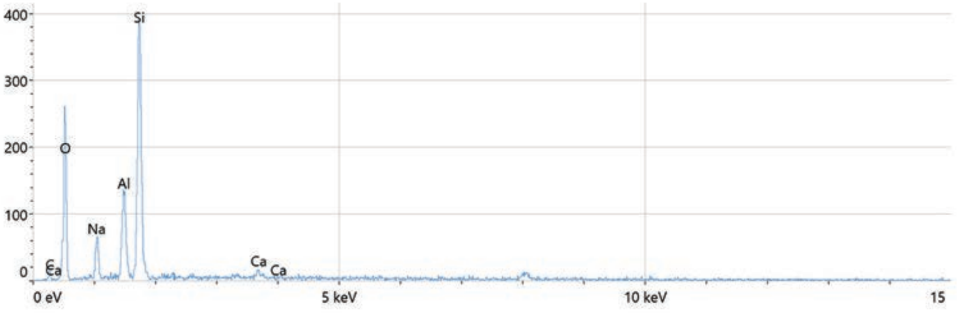

Fig. 7. EDXA analysis of Run 1 mega zeolite samples.

up the chance of omega zeolite crystallization. Synthesis data showed that Na+ and the exact weight of TMA-OH may have a cooperative structure-directing effect on the preparation of pure zeolite omega (Martucci, et al., 2003).

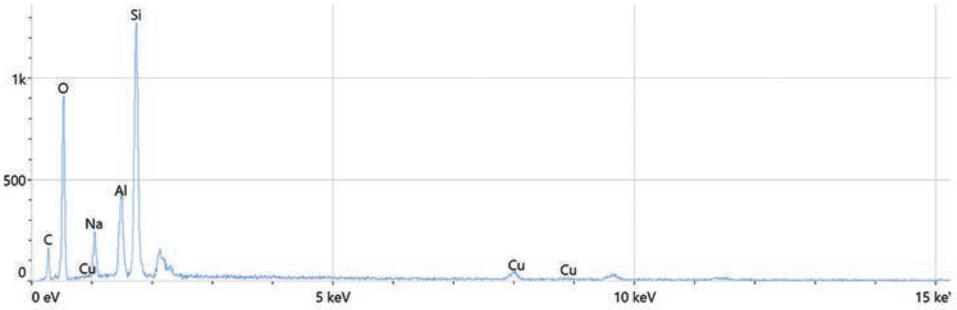

Fig. 8. EDXA analysis of Run 2 omega zeolite samples.

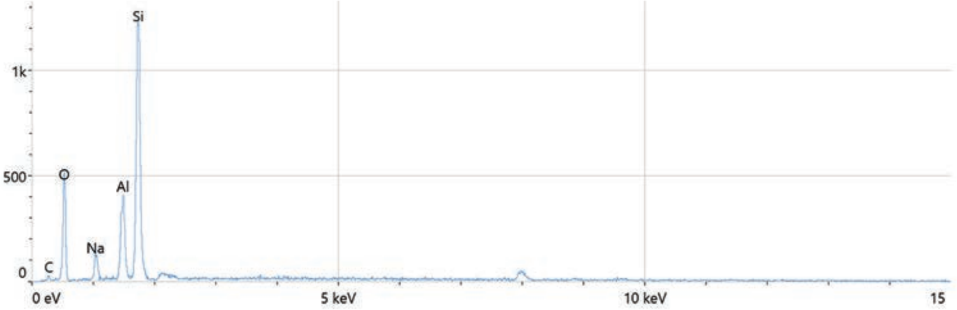

Fig. 9. EDXA analysis of Run 2 omega zeolite samples.

IV. CONCLUSION

The synthesis of zeolites using clear primary solutions and colloidal suspensions, which are stable materials, is one of the most efficient and widely used techniques. The omega zeolite has been effectively synthesized hydrothermally from a sodium aluminosilicate-TMA-OH solution at a fixed Na_2O/Al_2O_3 mole ratio of about 5.96 and a maximum temperature of around 100°C with aging and crystallization time within 7 days. The High purity, good crystallinity, and uniform morphology of the omega zeolite sample can be obtained when the TMA-OH/Al_2O_3 mole ratio is almost 0.48 with a crystal size of about 95 nm, a mean particle diameter of about 93 nm, a mean Z-maximum of almost 252 nm, and a mean surface area of about 14608 nm². The organic templates may play an important role in the stability of zeolite omega and deserve some attention. It has been observed that the preparation of pure omega zeolite requires a precise amount of TMA-OH to be used.

REFERENCES

Abd Al-Rubaye, R.T., 2017. Influence Factors on zeolite Y Crystal growth. *Sigma*, 17, p.18.

Al-Rubaye, R., 2013. *Generation and Characterisation of Catalytic Films of Zeolite Y and ZSM-5 on FeCrAlloy Metal.* The University of Manchester, United Kingdom.

AL-Rubaye, R.T.A., and Garforth, A.A., 2018. Study the effect of various parameters on the synthesis of ZSM-5 zeolite. *Journal of Engineering*, 24(11), pp.30-40.

Ammar, S.A., and Sally, A.H., 2017. Equilibrium, kinetic and thermodynamic study of aniline adsorption over prepared ZSM-5 Zeolite. *Iraqi Journal of Chemical and Petroleum Engineering*, 18(1), pp.47-56.

Araya, A., Barber, T.J., Lowe, B.M., Sinclair, D.M., and Varma, A., 1984. The synthesis and thermal behaviour of zeolite Ω. *Zeolites*, 4(3), pp.63-269.

Báfero, G.B., Araújo, V.A., Almeida, R.K.S., and Pastore, H.O., 2020. Catalytic performance of ferrierite and omega zeolites obtained through 2D-3D-3D transformation from Na-RUB-18 layered silicate. *Microporous and Mesoporous Materials*, 302, p.110216.

Brady, P.V., and Walther, J.V., 1990. Kinetics of quartz dissolution at low temperatures. C*hemical Geology*, 82(C), pp.253-264.

Breck, D.W., and Skeels, G.W., 1985. *Silicon Substituted Zeolite Compositions and Process for Preparing Same*. In US Patent 4,503,023.

De Witte, B., Patarin, J., Guth, J.L., and Cholley, T., 1997. Synthesis of mazzite-type zeolites in the presence of organic solvents: Study of the structure directing role of p-dioxane. *Microporous Materials*, 10(4-6), pp.247-257.

DiRenzo, F., Fajula, F., Figueras, F., Nicolas, S., and Couriers, T., 1989. Are the general laws of crystal growth applicable to zeolite synthesis? *Studies in Surface Science and Catalysis*, 49(C), pp.119-132.

Dove, P.M., and Crerar, D.A., 1990. Kinetics of quartz dissolution in electrolyte solutions using a hydrothermal mixed flow reactor. *Geochimica et Cosmochimica Acta*, 54(4), pp.955-969.

Dwyer, F.G., and Chu, P., 1979. ZSM-4 crystallization via faujasite metamorphosis. *Journal of Catalysis*, 59(2), pp.263-271.

Edmunds, M.P.W., Hill, S.J., Latham, K., and Williams, C.D., 1994. Synthesis of zeolite omega in an alcohol-water system. *Zeolites*, 14(7), p.529-532.

Fajula, F., Nicolas, S., Di Renzo, F., Figueras, F., and Gueguen, C., 1989. In: *Zeolite Synthesis, ACS Symposium*. Vol. 398. American Chemical Society, Washington, DC, p.493.

Feng, Z., Wang, Y., Lv, T., Zhang, S., Liu, X., Liu, X., and Meng, C., 2020. Hydrothermal conversion of kenyaite into zeolite omega in tetramethylammonium cations system. *Solid State Sciences*, 103, p.106196.

Flanigen, E.M., and Kellberg, E.R., 1980. *Synthetic Crystalline Zeolite and Process for Preparing Same*. In US Patent No. 4241036.

Galli, E., Passaglia, E., Pongiluppi, D., and Rinaldi, R., 1974. Mazzite, a new mineral, the natural counterpart of the synthetic zeolite Ω. *Contributions to Mineralogy and Petrology*, 45(2), pp.99-105.

Gies, H., and Marker, B., 1992. The structure-controlling role of organic templates for the synthesis of porosils in the systemsSiO_2/template/H_2O. *Zeolites*, 12(1), pp.42-49.

Gómez-Hortigüela, L., Corà, F., Catlow, C.R.A., and Pérez-Pariente, J., 2004. Computational study of the structure-directing effect of benzylpyrrolidine and its fluorinated derivatives in the synthesis of the aluminophosphate AlPO-5. *Journal of the American Chemical Society*, 126(38), pp.12097-12102.

Goossens, A.M., Feijen, E.J.P., Verhoeven, G., Wouters, B.H., Grobet, P.J., Jacobs, P.A., and Martens, J.A., 2000. Crystallization of MAZ-type zeolites using tetramethylammonium, sodium and n-hexane derivatives as structure-and composition-directing agents. *Microporous and Mesoporous Materials*, 35, pp.555-572.

Hussam, J.M., and Hussein, Q.H., 2019. Synthesis and characterization of Nano Y Zeolite using MWCNT as media for crystal growth. *Iraqi Journal of Chemical and Petroleum Engineering*, 20(4), pp.49-54.

Mahdi, H.I., and Muraza, O., 2016. Conversion of isobutylene to octane-booster compounds after methyl tert-butyl ether phaseout: The role of heterogeneous catalysis. *Industrial and Engineering Chemistry Research*, 55(43), pp.11193-11210.

Martucci, A., Alberti, A., De Lourdes Guzman-Castillo, M., Di Renzo, F., and Fajula, F., 2003. Crystal structure of zeolite omega, the synthetic counterpart of the natural zeolite mazzite. *Microporous and Mesoporous Materials*, 63(1-3), pp.33-42.

McQueen, D., Fajula, F., Dutartre, R., Rees, L.V.C., and Schulz, P., 1994. Diffusion of xylene isomers in dealuminated mazzite zeolites by the frequency response technique. *Studies in Surface Science and Catalysis*, 84(C), pp.1339-1346.

Najwa, S.M., and Asir, A.A., 2015. Synthesis and characterization of nano-crystalline ZSM-5 zeolite. *Al-Khwarizmi Engineering Journal*, 11(4), pp.8-19.

Najwa, S.M., and Asir, A.S., 2016. Synthesis and characterization of nanocrystalline micro-mesoporous ZSM 5/MCM-41 composite zeolite. *Iraqi Journal of Chemical and Petroleum Engineering*, 17(1), pp.71-82.

Perrotta, A.J., Kibby, C., Mitchell, B.R., and Tucci E.R., 1978. The synthesis, characterization, and catalytic activity of omega and ZSM-4 zeolites. *Journal of Catalysis*, 55(2), pp.240-249.

Pinar, A.B., García, R., Arranz, M., and Pérez-Pariente, J., 2007. Co-directing role of template mixtures in zeolite synthesis. *Studies in Surface Science and Catalysis*, 170, pp.383-388.

Rallan, C., Al-Rubaye, R., and Garforth, A., 2015. Generation of catalytic films of alumina and zeolites on FeCrAlloy rods. *Chemical Engineering Transactions*, 43, pp.907-912.

Rinaldi, R., Pluth, J.J., and Smith, J.V., 1975. Crystal structure of mazzite dehydrated at 600°C. *Acta Crystallographica Section B Structural Crystallography and Crystal Chemistry*, 31(6), pp.1603-1608.

Sastre, G., Leiva, S., Sabater, M.J., Gimenez, I., Rey, F., Valencia, S., and Corma, A., 2003. Computational and experimental approach to the role of structure-directing agents in the synthesis of zeolites: The case of cyclohexyl alkyl pyrrolidinium salts in the synthesis of β, EU-1, ZSM-11, and ZSM-12 zeolites. *Journal of Physical Chemistry B*, 107(23), pp.5432-5440.

Shi, Q., Yu, J., Song, Z., and Kang, X., 2012. Cooperative structure-directing effects in the synthesis of a high-silica zeolite mazzite analogue. *Materials Sciences and Applications*, 3(5), pp.306-309.

Tosheva, L., and Valtchev, V.P., 2005. Nanozeolites: Synthesis, crystallization mechanism, and applications. *Chemistry of Materials*, 17(10), pp.2494-2513.

Wu, Z., Song, J., Ji, Y., Ren, L., and Xiao, F.S., 2008. Organic template-free synthesis of ZSM-34 zeolite from an assistance of zeolite L seeds solution. *Chemistry of Materials*, 20(2), pp.357-359.

Xu, H., Dong, P., Liu, L., Wang, J.G., Deng, F., and Dong, J.X., 2007. Synthesis and characterization of zeolite MAZ in Na_2O-Al_2O_3-SiO_2-piperazine-H_2O. *Journal of Porous Materials*, 14(1), pp.97-101.

Yang, S., and Amiridis, N.P., 1994. Synthesis of omega zeolite without use of tetramethylammonium(tma) ions. *Studies in Surface Science and Catalysis*, 84(C), pp.155-162.

The Effect of Microwave Irradiation on the Laser-generated Ag-TiO_2 Compound Nanoparticles

Abubaker H. Hamad†

Department of General Science, Faculty of Education, Soran University,
Kurdistan Region – F.R. Iraq

***Abstract*—The pulsed laser ablation technique in liquid solutions is a promising method for generating nanoscale materials due to its chemically clean and simple synthesis process. This study generates spherical Ag-TiO_2 compound nanoparticles (CNPs) through pulsed laser ablation, a picosecond (ps) laser, in deionized water. Then the spherical shapes of the CNPs are changed to rod-like shapes using microwave (MW) irradiation in an ordinary MW (continuous - CW) machine at 700 W for 3.5 min. The effect of MWs on the CNPs is investigated. Before and after MW-irradiation, the samples are characterised using ultraviolet-Vis Spectrometer, transmission electron microscope, and scanning electron microscope machines. The results show that the spherical shape of the nanoparticles was changed to rod-like shapes after MW irradiation. Their nominal dimensions range from 50–70 nm to 150–700 nm in width and length, respectively. Changing the morphology of the nanoparticles is important for various applications.**

***Index Terms*—Ag-TiO_2 compound nanoparticles, microwave irradiation, Nanoparticles, Nanorods, Picosecond laser, Rod-like shape.**

I. INTRODUCTION

Microwave (MW) irradiation is not only used to synthesize nanoparticles but can also be used to manipulate the nanoparticles due to the high heating rates of MWs. Based on the literature review, MW irradiation has been used for the generation of ultrafine ZnO-NPs with controlled morphology (Hasanpoor, Aliofkhazraei and Delavari, 2015) and ultrafine silver nanoparticles (Ag NPs) (Saloga, Kästner and Thünemann, 2018), but not for manipulating nanomaterials. A MW was used to prepare rod-like shapes of AgNP@Ni-BTC nanocomposites (Amri et al., 2023). Different morphologies of Ag-NPs have been prepared through MW irradiation, such as sheets, wires, rods, and tubes (Kustov and Vikanova, 2023).

MW irradiation is used in nanotechnology. For example, ZnO-NPs are produced using a MW-assisted hydrothermal procedure. The nanoparticles have various sizes and shapes, such as flowers, needles, and spherical. It was concluded that by increasing the generation time from 10 to 15 min., needle-form nanoparticles at 50–150 nm were enhanced. On the other hand, flower-shaped nanoparticles were produced by increasing the power of the MW from 540 to 680 watts. In addition, ultrafine Ag-NPs (6 nm in size) were produced with MW irradiation assistance (Hasanpoor, Aliofkhazraei, and Delavari, 2015).

Not only does MW irradiation affect the nanoparticles' morphology, but post-irradiation by an unfocused laser beam irradiation significantly affects the manipulation of the nanostructure's morphology, size, and shape. Controlled MW irradiation has produced monodisperse aqueous emulsion droplets encapsulating spherical colloidal crystal particles. It was shown that the quality of packing of the colloidal crystal produced by this method can be used to show photonic energy band gap (E_g) characteristics (Kim et al., 2006). Laser and fluorescent (FL) irradiation were used for shape conversion of the Ag NPs, prepared by laser ablation in distilled water, from spherical to nanoprism, and nanorod crystal-shaped by NaCl (Tsuji et al., 2006). After that, (Al-Gaashani et al., 2011) showed the effects of the power of MWs on the morphology of the ZnO nanostructure. The spherical, needle-like, and leaf-like sheets were obtained at 450 W, 700 W, and 1,000 W MW powers. In addition, the average crystalline size of the ZnO nanostructures was changed from 32 nm to 17 nm when the power of the MW was reduced from 1,000 W to 150 W. In addition, Barreto, Morales, and Quintanilla (2013) have shown the effects of some experimental variables, including MW irradiation power, irradiation time, and temperature, on the morphology size and shape of ZnO-NPs produced through the MW-assisted approach. They concluded that these parameters significantly affect the morphology of the nanoparticles. MW-assisted was used to synthesize different kinds of metallic and metal oxide nanoparticles, including Ru-NPs (Gupta et al., 2013), CuO-NPs (Bekru et al., 2021), Ag-NPs (Quan et al., 2022), and compound nanoparticles (CNPs) like AgZnO-NPs (Porrawatkul et al., 2022).

This study generated the Ag-TiO_2 CNPs through a pulsed laser ablation technique in pure deionized water (DIW). A ps laser ablation was utilized to prepare the nanosize particles. Then, the as-synthesized nanoscale particles were irradiated through MWs in a MW oven. The shape of the nanoscale

ARO-The Scientific Journal of Koya University
Vol. XIII, No. 1 (2025), Article ID: ARO.11965. 6 pages
DOI: 10.14500/aro.11965
Received: 29 December 2024; Accepted: 28 March 2025
Regular research paper; Published: 06 April 2025

†Corresponding author's e-mail: abubaker.hamad@soran.edu.iq

particles changed from spherical to rod-like shapes with different dimensions. The novelty of this study is that for the 1st time, MW irradiation is used to manipulate the synthesized Ag-TiO_2 CNPs.

II. Experimental Materials and Procedures

A. Materials

To generate Ag-TiO_2 CNPs in DIW, a Ti: Ag bulk material was supplied by Cathay Advanced Materials Limited. The Ti: Ag ratio of the sample is 3:1 at%, and the purity of the elements of the alloy composite, Ti and Ag is 99.7%, and 99.95%, respectively. The dimensions of the compound material were (25 × 25 × 1) mm. The target material was cleaned about 3 times with DIW before starting and after finishing the ablation process. In addition, the target material was sonicated several times in an ultrasonic bath sonicator to remove any contamination on the target. An ordinary MW oven is used to post-irradiate the colloidal Ag-TiO_2 CNPs.

B. Ag-TiO_2 CNPs Production Method

After washing the target material, it was put in a glass beaker (Pyrex) on a sample holder. The beaker was filled with DI water until the sample was completely immersed. It is worth mentioning that the DIW height was about 2 mm over the target material. The effect of water level on the laser power was taken into account.

To generate Ag-TiO_2 NPs, a 400-watt ps-laser (EdgeWave) was used. The bulk material was irradiated by the ps-laser for 10 min. with the following parameters (Table I).

C. MW Irradiation of the as-synthesized Ag-TiO_2 NPS in a MW Machine

The synthesized Ag-TiO_2 CNPs (we named them As-synthesized Ag-TiO_2 nanoparticles - before MW irradiation) were irradiated by MWs in a MW machine at about 700 W for 3.5 min. The sample was placed at the center of the MW plate and rotated during irradiation. Due to vaporization, a reduction in the amount of as-synthesized Ag-TiO_2 nanoparticles was observed. The schematic diagram of the generation and MW irradiation of the nanoparticles by the laser ablation technique in DIW is depicted in the graphical abstract (Scheme 1).

D. Sample Preparation for Nanoparticle Characterizations

Directly after the as-synthesized and post-irradiated samples were prepared, they were put in an ultraviolet (UV)-Vis spectrometer to measure their absorbance at different wavelengths. A standard Formvar/Carbon film supported copper microgrids size 200 mesh was utilized for transmission electron microscope (TEM) characterization. Some drops of the samples were carefully put onto a copper microgrid mesh and completely dried in the laboratory environment. For energy dispersive X-ray (EDX) analysis, several drops of the as-synthesized and MW-irradiated Ag-TiO_2 colloid were deposited above a normal glass substrate.

E. Characterizations

The samples were characterized through different instruments. The absorption spectra of the samples (spherical, and rod-like shapes) in the form of colloidal nanoparticles were measured through a 250 dual-beam UV-Vis spectrometer (Analytic Jena). The size morphology was examined by a JEOL 2,000 TEM. The EDX machine, based on the X-ray technique, is used to identify all of the elemental compositions of the As-synthesized and MW-irradiated Ag-TiO_2 nanocomposites.

III. Results and Discussion

A. Generation of Ag-TiO_2 CNPs

Fig. 1 shows the TEM analysis of the as-synthesized Ag-TiO_2 CNPs. Based on our previous characterization; the smaller and larger nanoparticles are Ag-NPs and TiO_2-NPs, respectively. In addition, the darker areas of the nanoparticles are Ag-NPs, while the brighter nanoparticles are TiO_2-NPs (Hamad et al., 2015). The nanoparticles' shape is spherical. The smaller Ag NPs are attached to the larger titania nanoparticles. Ultrafine nanoparticles can be seen in the TEM images.

B. MW Irradiation of the Ag-TiO_2 CNPs

Irradiation by MWs heats a target material throughout its entire volume instead of heating the whole surface area, and this property of MW irradiation makes the object heat faster and more efficiently than heating through conventional methods. In this work, after generating the nanoparticles by the ps-laser ablation technique, the nanoparticles were irradiated by MWs in an ordinary MW machine at about 700 W for 3.5 min.

Fig. 2a displays the UV-visible absorption spectra of the as-synthesized, and MW-irradiated Ag-TiO_2 samples. It can be seen that both absorption spectra have the same characteristics. A strong peak is observed from 210 nm to 260 nm of the wavelength, and an expanded peak is produced in the 400 nm to 500 nm wavelengths. Moreover, it can be noticed that the spectra of the MW-irradiated NPs are a little shifted to the longer wavelengths; this indicates that the larger Ag-TiO_2 particles are produced. It is worth mentioning that the TEM images confirm this result.

TABLE I

Parameters of the PS-Laser Utilized To Prepare Ag-TiO_2 CNPs in DIW

Power (60%) (W)	Wavelength (λ)	Repetition rate (f)	Laser pulse duration (τ)	Beam spot size (D)	Beam scan speed (v)	Laser pulse energy (E)	Laser fluence (F_L)
9.12	1064 nm	200 kHz	10 ps	125 µm	250 mm/s	45.6 µJ	0.37 J/cm²

DIW: Deionized water

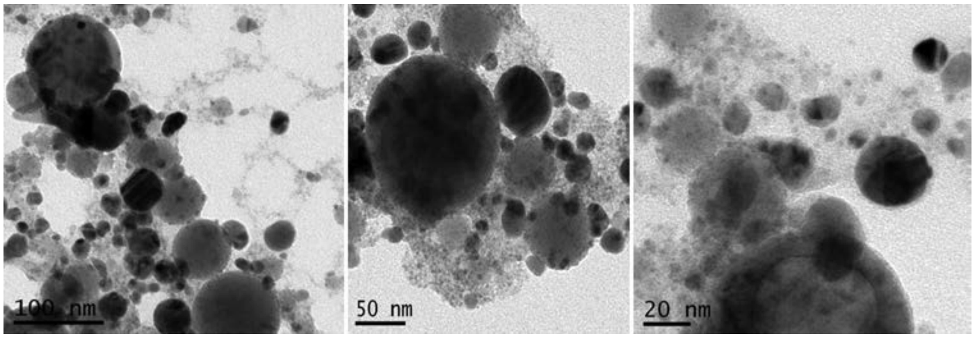

Fig. 1. Transmission electron microscope analysis of as-synthesized Ag-TiO_2 CNPs by ps-laser ablation technique through a picosecond laser in a liquid environment - DIW, (power, p = 9.12 Watts, repetition rate-frequency *f* = 200 kHz, and beam scan speed *v* = 250 mm/s).

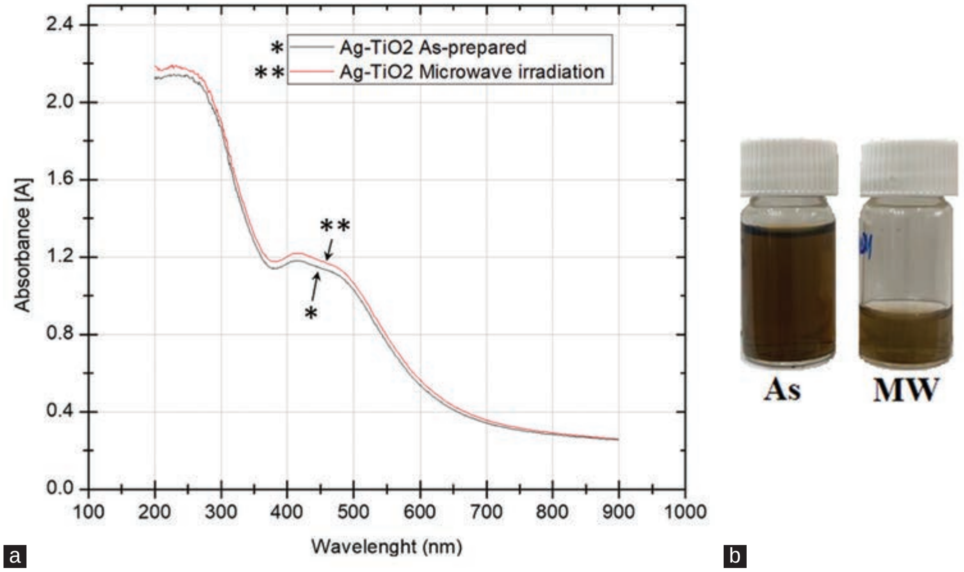

Fig. 2. (a) The ultraviolet-visible absorption spectra of as-synthesized or prepared (As) and microwave-irradiated (MW) Ag-TiO_2 samples. (b) The photographs show the real bottles of the as-synthesized (As) and microwave-irradiated (MW) colloidal Ag-TiO_2 samples.

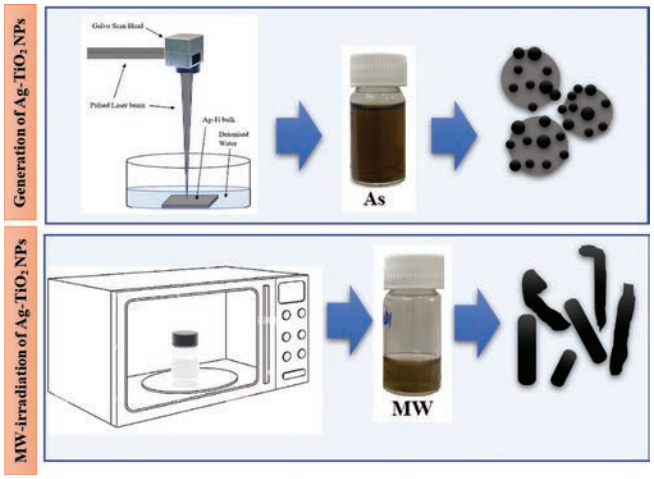

Scheme 1. Graphical abstract. An illustration of the generation and microwave irradiation of Ag-TiO_2 CNPs through ps laser in DIW.

The Ag-TiO_2 CNPs derived from the Ag: Ti bulk compound exhibit optical absorption spectra with a broad band ranging from 400 nm to 500 nm. The surface plasmon resonance of the Ag NPs in the compound is found within the 400 nm to 410 nm range; thus, any changes or shifts occurring in this peak do not appear.

Fig. 2b shows photographs of the bottles of the colloidal Ag-TiO_2 samples before and after MW irradiation. It can be noted that the amount of the colloidal nanoparticles after MW-irradiation (MW) is less than that of the as-synthesized (As) colloidal nanoparticles in the bottle due to the evaporation of the colloidal nanoparticles during MW irradiation in the MW oven.

Fig. 3 shows EDX analysis of the as-synthesized and MW-irradiated Ag-TiO_2 NPs. It can be noted that both spectra are approximately similar, except the peaks have different intensities due to the various amounts of nanoparticles on the glass substrate. As shown in Fig. 3, peaks associated with Ag, Ti, O, Na, Mg, Al, Si, and Ca are observed in the spectra. The Ti and O peaks confirm the existence of TiO_2-NPs, in addition, the Ti, O, and Ag peaks confirm the presence of Ag-TiO_2-NPs. The signals of Na, Mg, Al, Si, and Ca should be attributed to the building elements of the glass substrate. The spectra reveal that both samples have the same compositions; this is expected because the samples were not treated with any chemicals. Furthermore, compared with the

As-synthesized spectrum, some small peaks of Ag and TiO_2 NPs do not appear in the MW-irradiated spectrum. This may be due to the crystallinity of Ag and TiO_2 NPs before and after the irradiation process, or it could be related to the low intensities of these peaks due to the small amount of nanoparticles in the prepared sample for characterization.

Fig. 4 displays TEM analysis of the MW-irradiated sample by MWs in an ordinary MW-oven at a power of about 700 Watts for 3.5 min. The figure shows that the morphology of the as-synthesized Ag-TiO_2 CNPs changed after MW irradiation from spherical shapes to almost rod-like shapes or belt-like shapes and some irregular shapes. It can be noted that rod-like shapes have dimensions of 50–70 nm and 150–700 nm in width and length, respectively. The first two rows of TEM images in Fig. 4 are almost rod shapes; however, the last two rows are almost random or uncontrolled rod-like shapes. The uncontrollable growth of the nanorods might be due to the interaction between the spherical nanoparticles and the MWs in the MW oven in all directions. In contrast, controllable or unidirectional growth of nanorods occurs in one direction. Although the radiation is uniform in the MW oven, the sample was rotated continuously during MW irradiation. It is worth mentioning that the quantitative analysis of the rod-like shapes was difficult due to the limited observation or scanning area on the TEM sample.

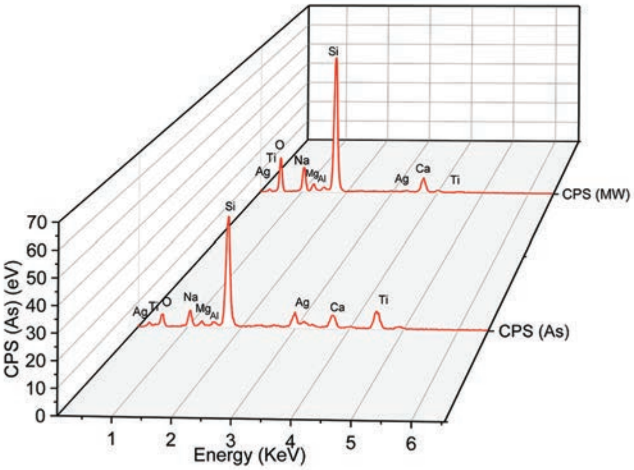

Fig. 3. Energy dispersive X-ray spectrum of the as-synthesized (As) and microwave irradiation (MW) Ag-TiO_2 samples.

The MW oven acts as a reactor, allowing it to turn or change the morphology of the nanoparticles through a reduction in reaction time (Saloga, Kästner and Thünemann, 2018). It is well-known that MWs can heat materials as a result of molecular vibration followed by a rise in temperature. The generated heat in the MW oven causes the temperature of the nanoparticles to rise below the melting point because the 700-watt power of the MW is approximately equivalent to 350°C. This degree of temperature is under the melting temperature of the Ag and TiO_2 nanoparticles, which are 961.8°C and 1843°C, respectively. The melting point of metals decreases when their size reduces (Feng et al., 2017).

Heat generation during MW irradiation is based on electromagnetic radiation through ionic conduction and dipolar rotation, which are directly related to reaction mixture composition. Thus, various chemical compounds have various MW absorbing properties, which allow the

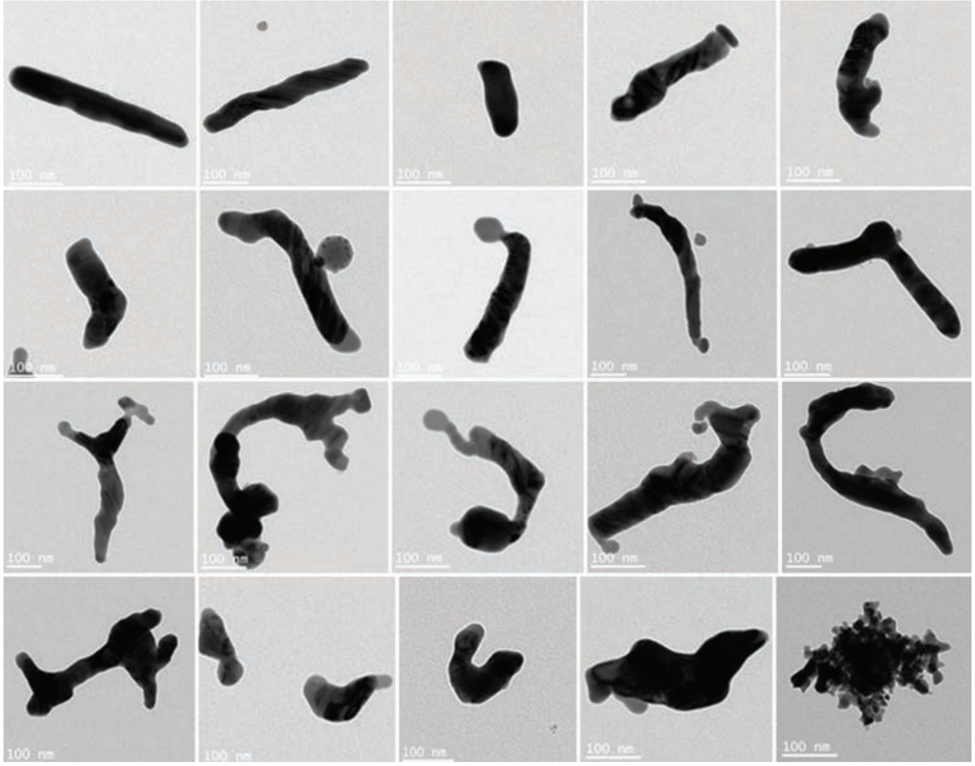

Fig. 4. Transmission electron microscope images of the Ag-TiO_2 rod-like shapes produced through microwave-irradiated Ag-TiO_2 CNPs by microwaves in an ordinary MW-oven at a power of about 700 Watts for 3.5 min.

heating of the chemical compositions in the reaction mixture (Barreto, Morales, and Quintanilla, 2013). The Ag and TiO_2-NPs have different abilities to absorb heat. As we know, the absorbed heat is related to the heat capacity of the materials; for example, the specific heat capacities of TiO_2-NPs and Ag-NPs are 686.2 J/kgK and 235 J/kgK, respectively (Tippa, Narahari, and Pendyala, 2016, Ahmed et al., 2018), thus, the higher specific heat capacity value means that it needs more energy to increase or decrease its temperature, while, a low value of the specific heat means that it does not need high energy to heat or cool down. As a result, the Ag-NPs absorb more heat than the TiO_2-NPs. This might cause Ag and TiO_2 NPs to change into nanorods in the solution. The shape transformation occurred with both Ag and TiO_2-NPs. As can be seen in Fig. 1, Ag and TiO_2-NPs have spherical shapes. The small-size Ag-NPs attached to the large-size TiO_2-NPs [12], while, Fig. 4, shows that both nanoparticles participated in the shape transformation because there are no spherical shapes just rod-like shapes of Ag-TiO_2 nanocomposites can be seen. In addition, the Ag-NPs and TiO_2-NPs became alloys in rod-like shapes.

Fig. 5 shows roughly measured lengths of the rod-like shape in a histogram. The major length of the rods is in the range of 300–400 nm, and the maximum length of the rod-like shapes is up to 700 nm. Based on the TEM analysis, the size of the Ag-TiO_2 CNPs ranged from a few nanometers to about 200 nm, and the average size was 31 nm.

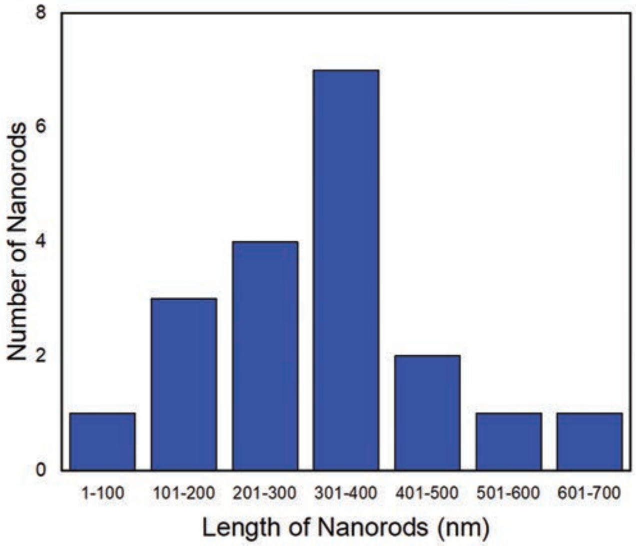

Fig. 5. Histogram of roughly measured the length of rod-like shapes.

IV. Mechanism of Growth of Nanorod-Like Shapes

To elucidate the growing mechanism of nanorod-like shapes, it can be suggested that a bunch of spherical Ag-TiO_2 NPs in a specific area are combined, and then different shapes will be formed (Fig. 6). The rod-like shape formation from the nanoparticles is due to the direct effect of MWs on the spherical nanoparticles, which leads to the coalescence of some nanoparticles. First, the nanoparticles try to be close together due to the MW, which acts as a driving force at the beginning of irradiation. Then, the spherical nanoparticles can change into rod-like shapes through the coalescence process due to the continued irradiation. It can also be noted from the TEM images, that the growing process is random due to the MW irradiation process in different directions. It can be pointed out that the shapes of some nanoparticles remained unchanged after MW irradiation in the solution.

The TEM images of the nanocomposites shown in Fig. 7 support the above-mentioned mechanism of the formation and growth of rod-like shapes of the nanoparticles from spherical CNPs. These images were taken after post-irradiation of the CNPs in the MW oven. It can be noted in Fig. 7a and b that some nanoparticles are spherical, which means that they were not affected by MW irradiation. Some are changed to rod-like shapes, while some are in the coalescence process, which means between spherical and rod-like shape stages (Fig. 7c). Barreto, Morales, and Quintanilla (2013) concluded that an increase in MW power causes an increase in the temperature of the colloidal nanoparticles, which enhances the tendency of the nanoparticles to aggregate. Furthermore, the sample was rotated during the MW irradiation, some factors affect the shape conversion, such as the non-uniformly distributed temperature in the sample, or it may be due to the MW power induced to the center of the aggregated nanoparticles. As a result, less power reaches the nanoparticles located at the center of the aggregated nanoparticles. In this case, the MW power can disaggregate the aggregated nanoparticles but cannot change them to rod-like shapes. Wang, Liang and Geng (2009) have observed two different types of coalescence of the Au NPs, the first one is the "combination

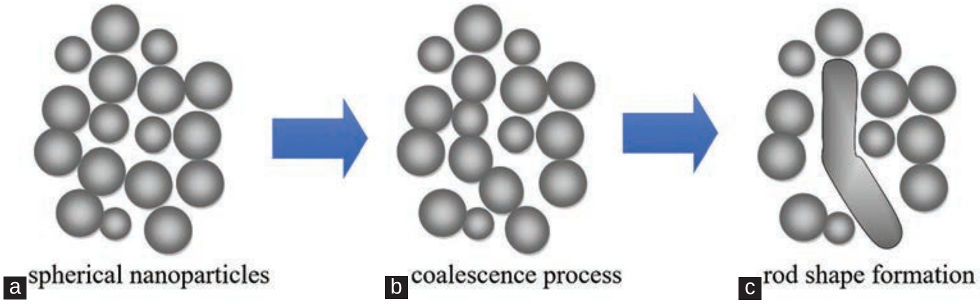

Fig. 6. (a-c) Possible mechanism of growth of the rod-like shape of the Ag-TiO_2 CNPs.

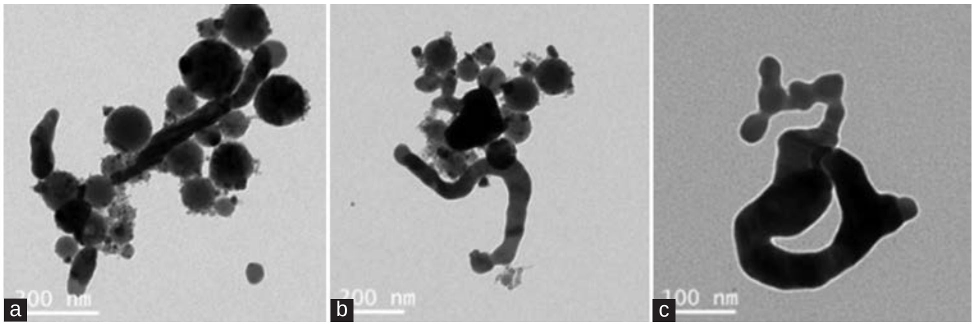

Fig. 7. Transmission electron microscope images of the growing steps of the Ag-TiO$_2$ nanocomposites: (a and b) spherical and rod-like shaped Ag-TiO$_2$ nanocomposites, (c) coalescence stage and rod-like shaped stage.

of two or more particles in appropriate orientations through twinning," and the second type is the "combination of two small particles with facets through a common lattice plane." (Wang, Liang and Geng, 2009). In addition, the molecular dynamic study showed that the coalescence process is affected by the size of the nanoparticles, the temperature of the nanoparticles, and the relative velocity of coalescence (Li, Hou and Wang, 2017).

V. Conclusion

In the present study, MW-induced morphology change is investigated. A simple and effective MW irradiation technique has been utilized to change the morphology size of the as-synthetized Ag-TiO$_2$ CNPs from spherical to rod-like shapes. MW energy induces shape transformation in CNPs, leading to significant physical modifications. These findings in the shape modification of the Ag-TiO$_2$ CNPs can be applied to other types of compounds and non-CNPs.

Acknowledgments

I would like to acknowledge and give my warmest thanks to Ms. Xiang Li Zhong at Manchester University who helped me with TEM characterization.

References

Ahmed, S.E., Hussein, A.K., Mansour, M.A., Raizah, Z.A., and Zhang, X., 2018. MHD mixed convection in trapezoidal enclosures filled with micropolar nanofluids. *Nanoscience and Technology An International Journal*, 9, p.343.

Al-Gaashani, R., Radiman, S., Tabet, N., and Daud, A.R., 2011. Effect of microwave power on the morphology and optical property of zinc oxide nano-structures prepared via a microwave-assisted aqueous solution method. *Materials Chemistry and Physics*, 125, pp.846-852.

Amri, F., Kasim, W., Rochliadi, A., and Patah, A., 2023. Facile one-pot microwave-assisted synthesis of rod-like and hexagonal plate-like AgNP@ Ni-BTC composites for a potential salivary glucose sensor. *Sensors and Actuators Reports*, 5, p.100141.

Barreto, G.P., Morales, G., and Quintanilla, M.L.L., 2013. Microwave assisted synthesis of ZnO nanoparticles: Effect of precursor reagents, temperature, irradiation time, and additives on nano-ZnO morphology development. *Journal of Materials*, 2013, pp.1-11.

Bekru, A.G., Zelekew, O.A., Andoshe, D.M., Sabir, F.K., and Eswaramoorthy, R., 2021. Microwave-assisted synthesis of CuO nanoparticles using cordia africana Lam. Leaf extract for 4-nitrophenol reduction. *Journal of Nanotechnology*, 2021, pp.1-12.

Feng, D., Feng, Y., Yuan, S., Zhang, X., and Wang, G., 2017. Melting behavior of Ag nanoparticles and their clusters. *Applied Thermal Engineering*, 111, pp.1457-1463.

Gupta, S., Giordano, C., Gradzielski, M., and Mehta, S.K., 2013. Microwave-assisted synthesis of small Ru nanoparticles and their role in degradation of congo red. *Journal of Colloid and Interface Science*, 411, pp.173-181.

Hamad, A., Li, L., Liu, Z., Zhong, X.L., and Wang, T., 2015. Picosecond laser generation of Ag-TiO$_2$ nanoparticles with reduced energy gap by ablation in ice water and their antibacterial activities. *Applied Physics A*, 119, pp.1387-1396.

Hasanpoor, M., Aliofkhazraei, M., and Delavari, H., 2015. Microwave-assisted synthesis of zinc oxide nanoparticles. *Procedia Materials Science*, 11, pp.320-325.

Kim, S.H., Lee, S.Y., Yi, G.R., Pine, D.J., and Yang, S.M., 2006. Microwave-assisted self-organization of colloidal particles in confining aqueous droplets. *Journal of the American Chemical Society*, 128, pp.10897-10904.

Kustov, L., and Vikanova, K., 2023. Synthesis of metal nanoparticles under microwave irradiation: Get much with less energy. *Metals*, 13, p.1714.

Li, M., Hou, Q., and Wang, J., 2017. A molecular dynamics study of coalescence of tungsten nanoparticles. *Nuclear Instruments and Methods in Physics Research Section B: Beam Interactions with Materials and Atoms*, 410, pp.171-178.

Porrawatkul, P., Pimsen, R., Kuyyogsuy, A., Teppaya, N., Noypha, A., Chanthai, S., and Nuengmatcha, P., 2022. Microwave-assisted synthesis of Ag/ZnO nanoparticles using Averrhoa carambola fruit extract as the reducing agent and their application in cotton fabrics with antibacterial and UV-protection properties. *RSC Advances*, 12, pp.15008-15019.

Quan, M.X., Yao, Q.F., Liu, Q.Y., Bu, Z.Q., Ding, X.Z., Xia, L.Q., LU, J.Y., and Huang, W.T., 2022. Microwave-assisted synthesis of silver nanoparticles for multimode colorimetric sensing of multiplex metal ions and molecular informatization applications. *ACS Applied Materials Interfaces*, 14, pp.9480-9491.

Saloga, P.E., Kästner, C., and Thünemann, A.F., 2018. High-speed but not magic: Microwave-assisted synthesis of ultra-small silver nanoparticles. *Langmuir*, 34, pp.147-153.

Tippa, S., Narahari, M., and Pendyala, R., 2016. Unsteady Natural Convection Flow of Nanofluids Past a Semi-Infinite Isothermal Vertical Plate. In: *AIP Conference Proceedings*, AIP Publishing.

Tsuji, T., Okazaki, Y., Higuchi, T., and Tsuji, M., 2006. Laser-induced morphology changes of silver colloids prepared by laser ablation in water: Enhancement of anisotropic shape conversions by chloride ions. *Journal of Photochemistry and Photobiology A Chemistry*, 183, pp.297-303.

Wang, Y.Q., Liang, W.S., and Geng, C.Y., 2009. Coalescence behavior of gold nanoparticles. *Nanoscale Research Letters*, 4, pp.684-688.

The Optimum Sulfur Recovery Process From North Gas Company Sour Acid Gas: A Case Study and Simulation

Ribwar K. Abdulrahman[1†], Mohammed H. S. Zangana[2] and Ganank Srivastava[3]

[1]Department of Chemical Engineering, Faculty of Engineering, Koya University, Daniel Mitterrand Boulevard,
Koya, Kurdistan Region – F.R. Iraq

[2]Department of Petroleum Engineering, Faculty of Engineering, Koya University, Daniel Mitterrand Boulevard,
Koya, Kurdistan Region – F.R. Iraq

[3]Bryan Research and Engineering, LLC,
Bryan, Texas 77802, USA

***Abstract*—The North Gas Company in Kirkuk, Iraq produces a sour gas stream that is loaded with considerable amounts of H_2S and CO_2, at concentrations of 2.95% and 2.54%, respectively. A previous study successfully treated this sour gas stream and produced a sweet gas stream by adopting a natural gas sweetening process using ProMax process simulation software. However, this process also produced an acid gas stream that was loaded with a considerable amount of H_2S. The acid gas stream is processed to a (sulfur recovery units) sulfur recovery unit to protect the environment. The Claus process is the major technology used to produce elemental sulfur from H_2S and SO_2 gases. This study examines this process to treat the acid gas stream and recover the elemental sulfur, using ProMax simulation software developed by Bryan Research and Engineering, LLC. Moreover, the simulation model was successful in reducing the amount of H_2S from 872.5 kg/h to 60.5 kg/h by adopting two Claus bed reactors to increase the process efficiency. Furthermore, process optimization was also adopted to find out the optimum Claus reactor bed operating temperature at 215°C.**

***Index Terms*—Air pollution, Claus process, Environment protection, Gas sweetening, Gas treatment, Natural gas, Oil and gas industry, Sulfur recovery.**

I. Introduction

The majority of the world's energy demand is provided by fossil fuels (Taghizadeh and Bahadori, 2018). Air pollution may have several effects on the natural environment (Afifa, et al., 2024). Furthermore, many researchers have mentioned that air pollution may cause several human lung diseases and affect public health (Hashemi, et al., 2019). Indeed, oil and gas exploration and production may be considered one of the most obvious air pollution sources that contribute to many environmental and economic effects (Seyed, Bastani and Eslampanah, 2023). Natural gas has several advantages over other types of fossil fuels, for example, cleanliness, high thermal value, and environmentally friendly fuel, and the demand for this energy source will also increase in the future (Alzamzam and Shalhi, 2019). About 25% of natural gas is produced from sources and wells that require a sweetening process to participate in production processes; therefore, impurities should be eliminated, such as H_2S and CO_2 (Hashemi, et al., 2019). Acid gas containing H_2S and CO_2 may naturally exist in natural gas (Saeid, Poe and Mak, 2019). The acid gases, such as H_2S and CO_2 emissions from oil and gas facilities, are limited by global environmental legislations (Abdulrahman and Zangana, 2020). Indeed, acid gas stream flaring causes several environmental problems. H_2S is a very toxic and dangerous gas, and it can be converted into SO_2 by combustion, causing acidic rain and significant environmental issues (Seyed, Bastani and Eslampanah, 2023). Moreover, the massive emission of SO_2 has caused serious harm to the atmosphere, soil, and human beings (Zheng, et al., 2023). Engineers can convert these toxic gases, such as hydrogen sulfide (H_2S), to useful products, for example, the element sulfurs (Saeid, Poe and Mak, 2019). The produced sulfur will also increase the financial income of the plant. Element sulfur is an important raw material for many industries, for example, medicines and fertilizers. The sulfur element can be produced through the Claus process in sulfur recovery units (SRUs) (Singh and Raj, 2025). Indeed, the Claus process may be considered the most popular and commercial sulfur recovery process in the world. The H_2S can be converted in the Claus unit to the element sulfur (Ibrahim, Rahman and Raj, 2022). The main objective of the Claus process is to convert the hydrogen sulfide gas to the sulfur element

ARO-The Scientific Journal of Koya University
Vol. XIII, No.1(2025), Article ID: ARO.11985. 5 pages
DOI: 10.14500/aro.11985
Received: 05 January 2025; Accepted: 06 April 2025
Regular research paper; Published: 09 April 2025
†Corresponding author's e-mail: ribwar.abdulrahman@koyauniversity.org

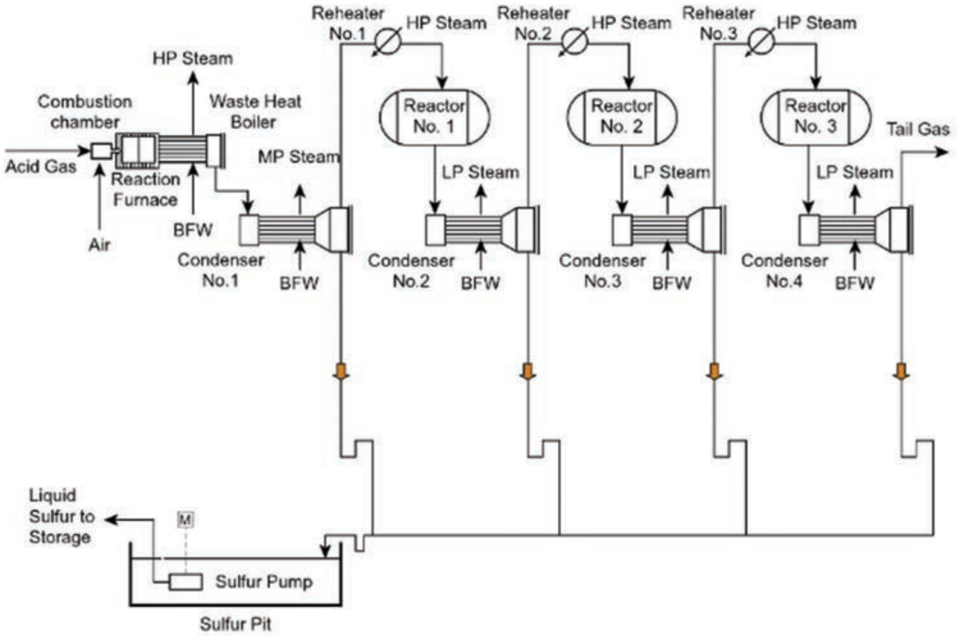

Fig. 1. Typical process flow schematic of three stages Claus sulfur recovery unit (Seyed Heydar, Bastani and Hamidreza, 2023).

through chemical reactions between hydrogen sulfide and sulfur dioxide, yielding elemental sulfur and water vapor (Blázquez, et al., 2019):

$$2H_2S(g) + SO_2(g) \rightarrow (3/n)\ Sn(g) + 2H_2O(g) \tag{1}$$

The sulfur recovery process may contain a multistage Claus sulfur-recovery process. Fig. 1 shows a typical sulfur recovery process.A sufficient amount of H_2S in the feed gas is oxidized to Sulfur dioxide (SO_2) in the process furnace. More than 97% of the sulfur is recovered by two or three stages (Abdulrahman and Zangana, 2020). The reactions involved in the process are shown below:

$$H_2S + 1/2O_2 \rightarrow S + H_2O \tag{2}$$

$$H_2S + 2/3O_2 \rightarrow SO_2 + H_2O \tag{3}$$

$$2H_2S + SO_2 \rightarrow 3S + 2H_2O \tag{4}$$

H_2S is partially oxidized with air and converted into SO_2 in the Claus furnace. The products from this reaction are sulfur dioxide, water, and unreacted hydrogen sulfide. This tail gas normally requires further cleanup to obtain higher recovery (Alzamzam and Shalhi, 2019). The catalytic Claus reactor is achieved through two or three stages. First, the reheater step that raises the temperature of the gas from the sulfur condenser to avoid condensation of sulfur vapor when the sulfur forming at the clause reactor (Taghizadeh and Bahadori, 2018). Second, the hydrogen sulfide reacts with sulfur dioxide over an activated alumina catalyst. Some SRUs use more than one Claus reactor, for example, two or three to increase the process efficiency.

The Claus reactions (Selim, Gupta and Al Shoaibi, 2013):

$$2H_2S + SO_2 \rightarrow 3/6\ S_6 + 2H_2O \tag{5}$$

TABLE I
NGC Amine Sweetening Acid Gases Stream Composition

Component	Mole%
H_2S	64
H_2O	1
CO_2	30
CH_4	3
C_2H_6	2

$$2H_2S + SO_2 \rightarrow 3/8\ S_8 + 2H_2O \tag{6}$$

Third, the sulfur condenser is used to remove liquid sulfur, the product of the reaction. The sulfur recovery process efficiency depends on feed composition, age of the catalyst, and the number of reactor stages (Saeid, Poe and Mak, 2019).

II. Case study of Kirkuk North Gas Company (NGC) and Simulation

The NGC processes the majority of the associated gas in Iraq's northern oil fields, specifically within the Kirkuk field. The gas stream processed at the NGC plant is classified as sour gas, containing significant amounts of hydrogen sulfide (H_2S) and carbon dioxide (CO_2) at concentrations of 2.95% and 2.54%, respectively. At present, a diethanolamine system is employed to reduce these sour component concentrations to below 5 parts per million (ppm) for H_2S and 2% for CO_2. The NGC sour gas stream has been treated in a previous study (Abdulrahman and Zangana, 2020). However, the acid gas stream emitted from the amine sweetening process has not been treated and was loaded with huge quantities of hydrogen sulfide. Therefore, this study aims to process the acid gas stream using an appropriate SRU by utilizing ProMax simulation

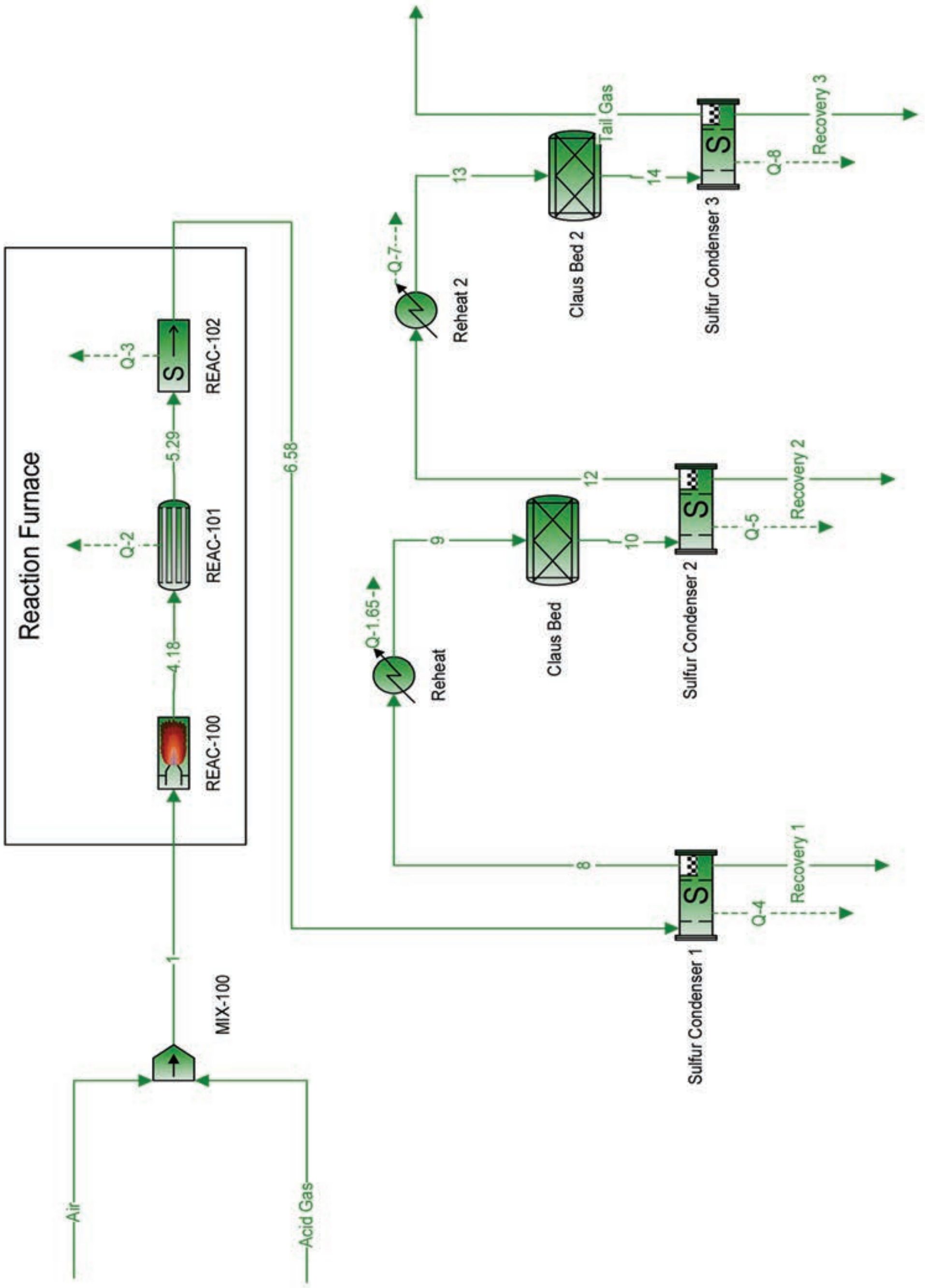

Fig. 2. North Gas Company sulfur recovery process by ProMax simulation.

software version 6.0. Table I presents the composition of the NGC acid gas stream produced from the gas sweetening process, while Table II outlines the operational conditions of the acid gas stream.

The sulfur recovery unit has been simulated by using ProMax simulation software version 6.0. Fig. 2 shows the NGC sulfur recovery process:

III. Results and Discussion

The Claus process may be considered the most commercial and successful sulfur recovery method. Indeed, in this study, SRU adopted two Claus reactors to increase the sulfur recovery amounts and process efficiency as well. Moreover, the optimization study has examined the effects of both Claus reactors' temperatures on the produced sulfur in (Kg/h) for both reactors.

TABLE II
NGC Amine Sweetening Acid Gases Stream Operation Conditions

North Gas Company Kirkuk Gas sweetening produced acid gases stream	
Temperature	70°C
Pressure	78.675 kPa (g)
Std vapor volumetric flow	947.617 m^3/h

Fig. 3 shows the relationship between the first Claus temperature and the amount of the produced Sulfur from

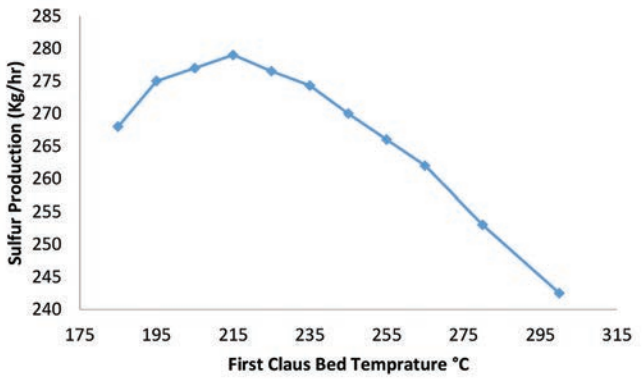

Fig. 3. Relationship between the first Claus bed temperature and Sulfur production.

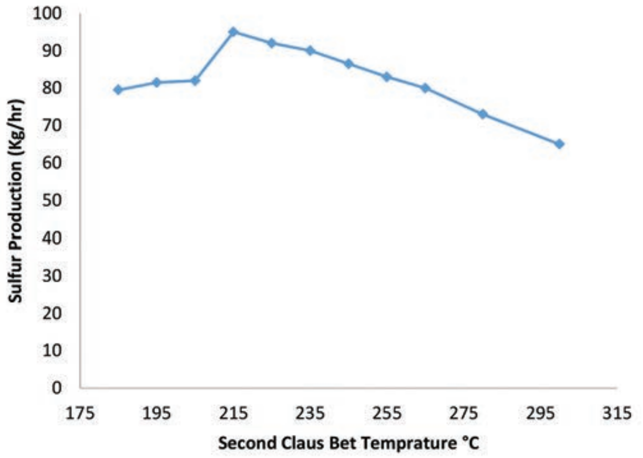

Fig. 4. Relationship between the second Claus bed temperature and Sulfur production.

the first Claus reactor. It seems from the mentioned figure that increasing the reactor temperature to 215°C leads to an increased amount of the produced sulfur. However, increasing the reactor temperature above that will decrease the amount of sulfur. Thus, it may be argued that maintaining the first Claus bed reactor at 215°C may be considered the optimum reactor temperature that produces optimum sulfur 279 Kg/h.

Fig. 4 shows the relationship between the second Claus temperature and the amount of the produced Sulfur from the first Claus reactor. It seems from the mentioned figure that the optimum second Claus bed reactor temperature is 215°C. Furthermore, too low a temperature may affect the bed reactions and cause sulfur condensation on the reactor and poison the catalyst.

IV. Conclusion

Acid gas stream flaring causes several environmental problems and negatively impacts public air quality. Engineers can convert these toxic gases, such as hydrogen sulfide, into useful products, for example, the sulfur element. The produced sulfur will also enhance the financial income of gas plants. Elemental sulfur is a crucial raw material for many industries, including pharmaceuticals and fertilizers. Indeed, the Claus process is widely regarded as the most popular sulfur recovery method in the world. This study utilized ProMax® Version 6.0 to accurately model and optimize the SRU system employed by NGC. The Claus process is the primary technology for producing elemental sulfur from H_2S and SO_2 gases. The research examined this process to treat the acid gas stream and recover elemental sulfur. Furthermore, the simulation model successfully reduced the amount of H_2S from 872.5 kg/h to 60.5 kg/h by implementing two Claus bed reactors, thereby increasing the process efficiency and productivity of raw sulfur. The process simulation also analyzed the temperatures within the Claus reactors through process optimization. It can be argued that operating both Claus bed reactors at 215°C may yield optimal sulfur production while maintaining process efficiency. However, further studies are recommended to optimize other process parameters and operational conditions.

Acknowledgment

The Authors highly acknowledge Bryan Research and Engineering, LLC for providing the license of ProMax® process simulation software to Koya University.

References

Abdulrahman, R.K., and Zangana, M.H.S., 2020. The effects of amine type and lean amine temperature on gas sweetening pro-cesses: A case study and simulation. *ARO-The Scientific Journal of Koya University*, 8(2), pp.78-81.

Afifa, U., Arshad, K., Hussain, N., Ashraf, M., and Saleem, M., 2024. Air pollution and climate change as grand challenges to sustainability. *Science of the Total Environment*, 928, pp.172370.

Alzamzam, W., and Shalhi, A., 2019. *Optimization and Modeling of Combustion Air in Sulfur Recovery Unit and Its Effect on Productivity and Environment*. Available from: https://engs.sabu.edu.ly/wp-content/uploads/2019/12/CEST02_186.pdf [Last accessed on 2024 Feb 17].

Blázquez, E., Gabriel, D., Baeza, J.A., Guisasola, A., Freguia, S., and Ledezma, P., 2019. Recovery of elemental sulfur with a novel integrated bioelectrochemical system with an electrochemical cell. *Science of The Total Environment*, 677, pp.175-183.

Hashemi, M., Pourfayaz, F., and Mehrpooya, M., 2019. Energy, exergy, exergoeconomic and sensitivity analyses of modified Claus process in a gas refinery sulfur recovery unit. *Journal of Cleaner Production*, 220, pp.1071-1087.

Ibrahim, S., Rahman, R.K., and Raj, A., 2022. A split-flow sulfur recovery process for the destruction of aromatic hydrocarbon contaminants in acid gas. *Journal of Natural Gas Science and Engineering*, 97, pp.104378-104378.

Saeid, M., Poe, W.A., and Mak, J., 2019. *Handbook of Natural Gas Transmission and Processing: Principles and Practices*. Gulf Professional Publishing, Cambridge.

Selim, H., Gupta, A.K., and Al Shoaibi, A., 2013. Effect of reaction parameters on the quality of captured sulfur in Claus process. *Applied Energy*, 104, pp.772-776.

Seyed Heydar, R.S., Bastani, K., and Hamidreza, E., 2023. Polymeric membranes for the oxygen en-richment of air in sulfur recovery units: Prevention of catalyst deactivation through BTX reduction. *Korean Journal of Chemical Engineering*, 40(12), pp.2929-2940.

Seyed, S., Bastani, K., and Eslampanah, H., 2023. Polymeric membranes for the oxygen enrichment of air in sulfur recovery units: Prevention of catalyst deactivation through BTX reduction. *Korean Journal of Chemical Engineering*, 40, pp.2929-2940.

Singh, S., and Raj, A., 2025. Investigating the impact of co-combustion of acid gas and hydrogen in the Claus process for efficient sulfur production, contaminant destruction, and low carbon emissions. *Gas Science and Engineering*, 134, pp.1-10.

Taghizadeh, D.A., and Bahadori, F., 2018. A new approach for hydrogen production in Claus sulfur recovery process. *Journal of Sulfur Chemistry*, 40(2), pp.137-148.

Zheng, Z., Lin, Z., Luling, L., Jia, Z., and Qiang, H., 2023. Comparison of oxidation absorption and reduction absorption process for sulfur recovery tail gas treatment of natural gas treatment plants in China Part I: Technical section. *Journal of the Taiwan Institute of Chemical Engineers*, 152, pp.1-10.

Optimizing a Compact Ring Coupler with Neural Network Modeling for Enhanced Performance in Radio Frequency Applications

Sobhan Roshani[1], Salah I. Yahya[2,3], Bita Najafi[4], Ali Jadidian[4], Mohsen Karimi[1] and Saeed Roshani[1†]

[1]Department of Electrical Engineering, Ker.C., Islamic Azad University,
Kermanshah, Iran

[2]Department of Software Engineering, Faculty of Engineering, Koya University,
Koya 46017, F.R. - Iraq

[3]Department of Computer Technology Engineering, College of Technical Engineering, Al-Hadba University,
Mosul, F.R. - Iraq

[4]Department of Computer Engineering, Ker.C., Islamic Azad University,
Kermanshah, Iran

***Abstract*—This paper presents the design and optimization of a compact 900 MHz hybrid ring coupler using lumped reactive components, aimed at achieving harmonic suppression and size reduction for Radio Frequency (RF) applications. Traditional hybrid ring couplers rely on quarter-wavelength transmission lines, resulting in large size device and limited harmonic rejection. To address these challenges, a novel coupler structure was developed that replaces long transmission lines with composite branches, significantly reducing device dimensions while enhancing performance. In the proposed coupler, instead of the six conventional 90-degree lines, six compact networks composed of microstrip lines, three inductors, and one capacitor are used. The inductors have values of L_1, L_1, L_2, and the capacitor has a value of C. These four parameters significantly influence the coupler's performance; thus, they were selected as inputs for the applied neural network, with the scattering parameters S_{11}, S_{12}, S_{13}, S_{14}, and frequency considered as the five output parameters. The dielectric constant (ε_r) of the substrate is 2.2, and the substrate material is RT/duroid 5880 with a thickness of 20 mils. By feeding the neural network model with these parameters as inputs, the coupler's output response was predicted and analyzed, enabling the selection of optimal component values. Optimal responses were obtained with $L_1 = 10.1\,\text{nH}$, $L_2 = 2.3\,\text{nH}$ and $C = 2.1\,\text{pF}$, which allows the coupler to operate effectively at 900 MHz. At this operating frequency, the values are $S_{11} = -32.6\,\text{dB}$, $S_{12} = -3.05\,\text{dB}$, $S_{13} = -3.03\,\text{dB}$, and $S_{14} = -45.9\,\text{dB}$, indicating excellent coupler performance.**

***Index Terms* – Coupler, Harmonic suppression, Neural network, Size reduction**

ARO-The Scientific Journal of Koya University
Vol. XIII, No.1(2025), Article ID: ARO.11948. 9 pages
DOI: 10.14500/aro.11948
Received: 13 December 2024; Accepted: 31 March 2025
Regular research paper; Published: 11 April 2025

[†]Corresponding author's e-mail: s.roshani@iau.ir

I. INTRODUCTION

Microwave couplers, such as branch-line couplers, directional couplers, rat-race couplers, and other types, which split and combine signals with equal amplitude are widely used in modern wireless systems (Rezaei, et al., 2023). Conventional couplers occupy a large area; for example, branch-line and rat-race couplers consist of four and six long quarter-wavelength ($\lambda/4$) transmission lines, respectively, which results in significant large area consumption. This large size is undesirable for modern communication systems (Venter, et al., 2018). Furthermore, conventional couplers suffer from presence of unwanted harmonics in frequency response, which cause undesirable non-linear effects in overall system (Nikandish, et al., 2020).

In the past decade, several solutions have been provided to miniaturize the large size of conventional couplers and suppress unwanted harmonics. The applied reactive components (L and C) in the structure of microwave couplers are an effective method to reduce circuit size and filter signals at unwanted frequency ranges (Jamshidi, et al., 2021).

In (Du, et al., 2018) capacitors were used to provide a miniaturized hybrid coupler with wide suppression band. In some works (Beigizadeh, et al., 2017) applied lumped-element in a hybrid coupler which results in a narrow operating bandwidth, which should be considered in coupler design.

Applied electromagnetic bandgap (EBG) cell in the structure of microwave coupler is another effective method to reduce circuit size and filter signals at unwanted frequency ranges, but EBG cells need extra fabrication process and increase the design complexity of the coupler which is undesirable (Lin, et al., 2007; Ooi, 2005).

Furthermore, using open-ended stubs, different types of resonators and filters are common methods widely used in coupler structures to eliminate unwanted harmonics

(Mohammadi, et al., 2024; Mezaal, et al., 2024; Roshani, et al., 2023b; Roshani, et al., 2023a; Al-Majdi and Mezaal, 2023). For example, in (Roshani, et al., 2022a), open-ended stubs are used in a microwave coupler, which provides an 80% size reduction and suppresses second to sixth harmonics. However, in many designs using open stubs and resonators lead to complex structures which are undesirable.

In (Long, et al., 2024) circular-shaped resonators were used to design a compact coupler with harmonic suppression. This coupler is designed for medical imaging systems and achieves an 80% size reduction and suppresses second to fifth harmonics.

The presented study in (Wang, et al., 2007) shows how using slow-wave structures in microstrip branch-line couplers can decrease the required area to just 28% of the size of a traditional design at 2.0 GHz, while also effectively suppressing second harmonics. However, designing slow-wave structures can be challenging, as their performance varies based on substrate material and thickness. In another study introduced in (Yang, et al., 2012), adding open-circuit stubs at the center and ends of each branch-line section helps reduce size and control harmonics. However, these stubs can introduce unwanted side effects and need careful manufacturing to work properly. In (Mirzavand, et al., 2012) inductors and two-section branches are used to design a compact power divider which has a wide harmonics suppression band. This divider has complex structure.

The 900 MHz frequency is commonly used in many wireless communication systems, such as mobile phones, Wi-Fi networks, and Internet of Things devices. It falls within the Ultra High Frequency band and is ideal for long-range communication because it can travel over longer distances and through obstacles, such as walls. This makes it a popular choice for communication technologies that require reliable signals over a wide area. In addition, 900 MHz is often used for low-power devices, as it offers a good balance between signal strength and energy efficiency. In this study, the 900 MHz frequency is chosen because it is widely used in various Radio Frequency (RF) applications, making it relevant for real-world use and ensuring that the designed coupler can meet the needs of these systems.

In this work, an ultra-compact ring coupler using lumped inductors and capacitors is designed at 900 MHz. The proposed coupler achieves a 99% size reduction and provides a wide suppression band from 1.8 GHz to 10 GHz. In the proposed coupler design a neural network model is used to obtain the best values of the applied lumped inductors and capacitors to achieve great performance of scattering parameters.

II. CONVENTIONAL 900 MHZ RING COUPLER DESIGN

The structure of the conventional 900 MHz Rat Race Coupler (RRC) is shown in Fig. 1. This coupler consists of six uniform quarter-wavelength (λ/4) transmission lines, with a $\sqrt{2}Z_0$ (70.7 Ω) characteristic impedance. An RT/duroid substrate with a 20-mil thickness and a dielectric constant of 2.2 is used, with each branch having a length of 61.1 mm and a width of 0.9 mm. The overall size of the conventional 900 MHz RRC is 124.3 mm × 62.9 mm (0.50λ × 0.25λ).

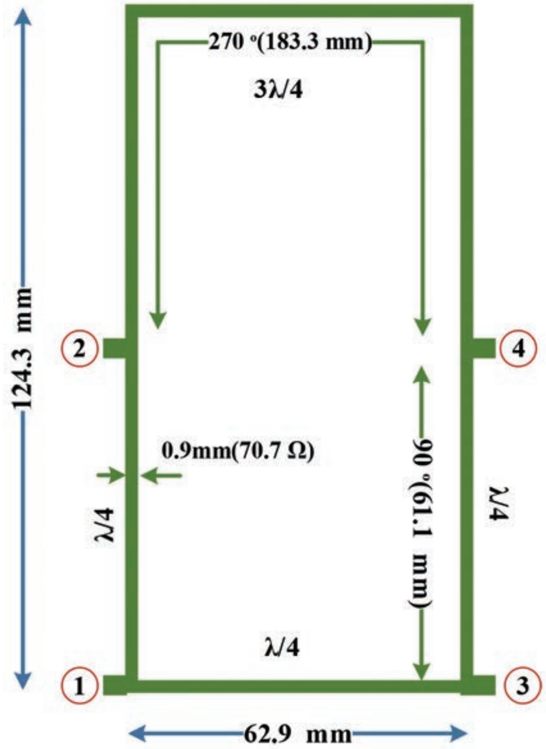

Fig. 1. The structure of the conventional rat race coupler operating at a frequency of 900 MHz.

The scattering parameters of the conventional RRC are depicted in Fig. 2. As shown, the coupler operates effectively at 900 MHz, achieving an input return loss and port isolation exceeding 51 dB and 50 dB, respectively. The insertion losses for the other ports are well within an acceptable range, with $S_{12} = S_{13} = -3.1$ dB.

III. PROPOSED TRANSMISSION LINE USING LUMPED COMPONENTS

In Fig. 3, the conventional transmission line branch used in the conventional RRC design at 900 MHz is depicted. Fig. 3a shows the layout of a conventional λ/4 transmission line branch, which has long size of 61.1 mm. Fig. 3b illustrates the frequency response of this conventional branch, indicating its performance at the target frequency of 900 MHz. At the operating frequency of 900 MHz, S_{12} is approximately −0.54 dB, and S_{11} is −9.7 dB, indicating that the conventional $\lambda/4$ transmission line effectively passes the signal at 900 MHz.

In Fig. 4, the proposed transmission line branch for the RRC is presented. This branch utilizes a modified design with lumped components to reduce its size while achieving the same performance at 900 MHz. Fig. 4a presents the layout of the proposed branch, which occupies less physical space compared to the conventional branch. In the proposed line

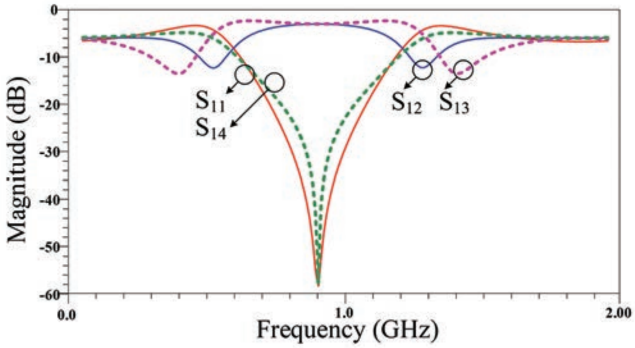

Fig. 2. Scattering parameters of the conventional rat race coupler at an operating frequency of 900 MHz.

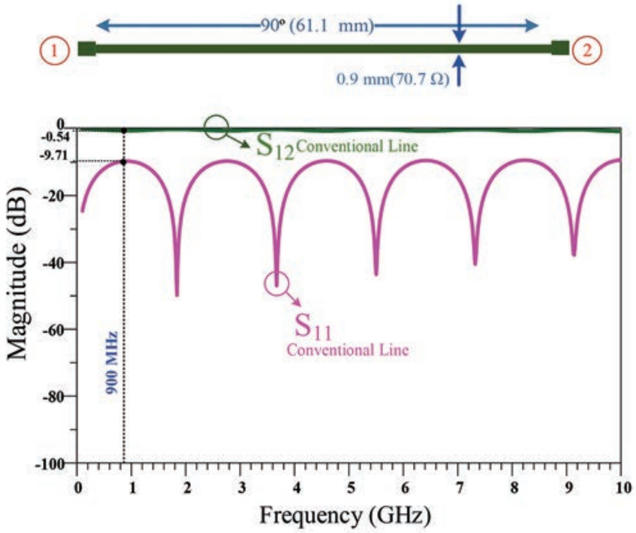

Fig. 3. Conventional λ/4 transmission line: (a) layout, and (b) frequency response at 900 MHz.

L_1 = 10.1 nH, L_2 = 2.3 nH and C = 2.1 pF. Fig. 4b displays the frequency response of the proposed branch, showing that it not only matches the performance of the conventional branch at 900 MHz but also provides harmonic suppression at higher frequencies, making it more effective for compact and high-performance coupler designs. At the operating frequency of 900 MHz, S_{12} is approximately −0.55 dB, and S_{11} is −9.6 dB, indicating that the proposed transmission line effectively passes the signal at 900 MHz.

IV. PROPOSED LUMPED ELEMENT STRUCTURE

The structure of the proposed 900 MHz RRC is shown in Fig. 5. In this structure, six proposed transmission lines are used instead of the six long $\lambda/4$ branches. Each proposed line has one capacitor and three inductors. These lumped components (L_1, L_1, L_2, and C) have a significant effect on the coupler performance. To improve the performance of the coupler and find the best values of these components a neural network model is used. These values of L_1, L_2, and C were used as inputs for the neural network model and scattering parameters of S_{11}, S_{12}, S_{13}, S_{14}, and the frequency response were defined as the five outputs of the neural network model. The neural network was used to find the optimal values of the lumped components.

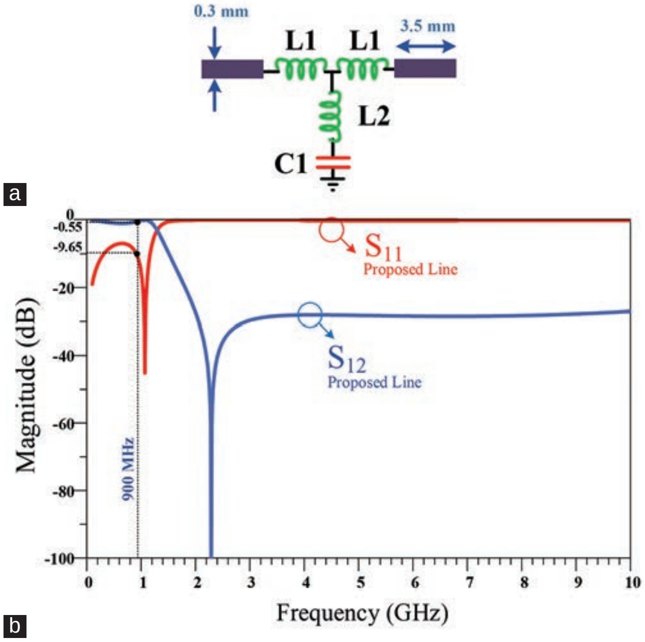

Fig. 4. Structure of the (a) proposed 900 MHz transmission line and (b) its frequency response.

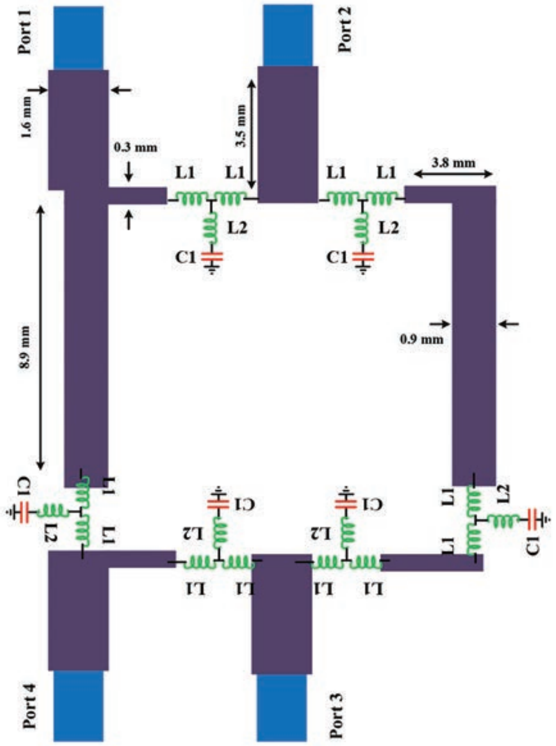

Fig. 5. Structure of the proposed 900 MHz rat race coupler.

Fig. 5 illustrates the structure of the proposed RRC, designed to operate at 0.9 GHz. This coupler consists of six proposed transmission lines, each incorporating three inductors and one capacitor. The inductors are labeled as L_1, L_1, and L_2, and the capacitor is labeled as C. To improve the performance of the coupler, the values of the lumped components (L_1, L_1, L_2, and C), which are crucial to the coupler function, were used as inputs for a neural network model. This model provides outputs of the scattering parameters (S_{11}, S_{12}, S_{13}, and S_{14}) and the frequency response, helping to adjust the component values for better performance. In the next steps, the neural network was used to find the optimal values for these components, ensuring the coupler performs as desired at 0.9 GHz.

V. Proposed Artificial Neural Network

The Long Short-Term Memory (LSTM) neural network model is used in this paper to predict the desired parameters. The LSTM is a special and improved type of recurrent neural network (RNN), which is suitable for the designed microwave coupler. The LSTM consists of memory cells for storing information, and gates to control and manage the flow of information. The input gates enter new data into memory cells, while the forget gates decide, which information should be deleted. Furthermore, the output gates decide how much of the stored information will be passed to the final output.

Fig. 6 depicts the flowchart of using the proposed LSTM model to predict the scattering parameters. As explained in the flow chart, the process begins with data preparation, followed by training the LSTM model on the dataset. Finally, the trained model is used to make accurate predictions for the proposed RRC.

The training process for the LSTM model starts with preparing the dataset by normalizing the data using a technique called MinMaxScaler, which ensures that the values are in a range suitable for the neural network to process. After the data are prepared, the LSTM model is trained using this dataset. The model has multiple layers, including an input layer, LSTM layers, and a final layer that makes predictions. The LSTM layers help the model understand patterns in the data over time. During training, the optimizer is used to adjust the learning process and reduce errors, which are measured using a method called Mean Squared Error (MSE). The model is also validated with a separate set of data that wasn't used in training to see how well it can generalize to new data. After the training, the model is tested using a new set of data, and its predictions are compared to the real values. Finally, the predicted values are adjusted back to their original scale, and the model's performance is checked using two metrics: MSE and Mean Relative Error (MRE), to see how accurate the model is at predicting the desired outcomes.

A. Dataset Analysis

The dataset of this study contains electromagnetic (EM) simulations of the proposed structure for the RRC. The input parameters are L_1 (nH), L_2 (nH), and C (pF), while the output ones are considered to be the scattering parameters and the main frequency, which are S_{11} (dB), S_{12} (dB), S_{13} (dB), S_{14} (dB), and frequency (MHz). The total of 60 sample is used to form the dataset as listed in Table I. Furthermore, the real values of the output parameters are given in this table. The simulation data is provided using advanced design system (ADS) software.

The dataset shown in Table I are generated through EM simulations conducted 60 times, each with different dimensions for the components of the RRC. These simulations were carried out using ADS software, which is commonly used for modeling and analyzing RF components. The input parameters for each simulation included the values

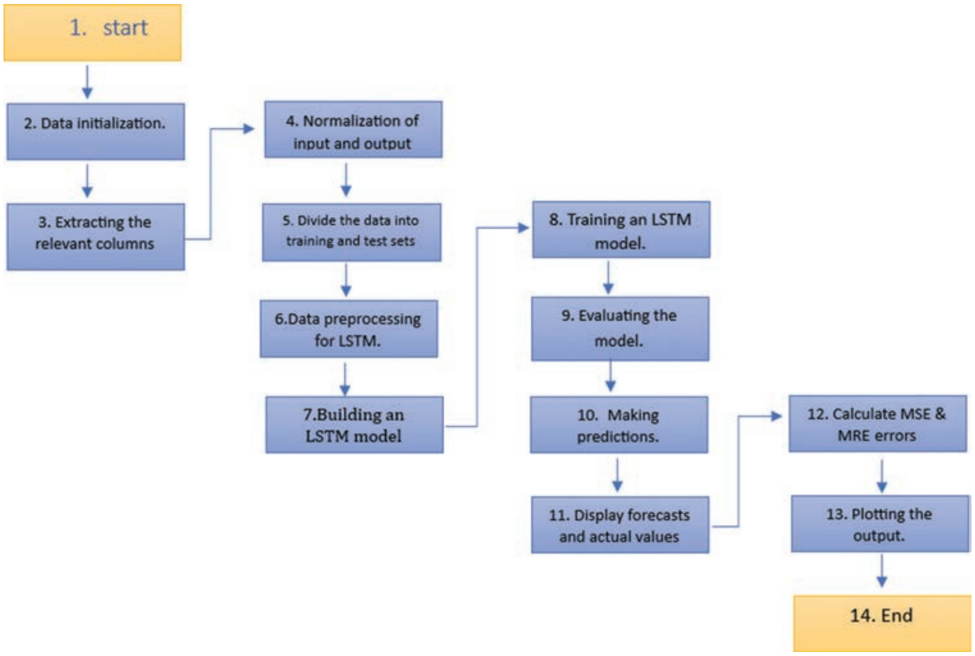

Fig. 6. Flowchart of using the proposed long short-term memory model.

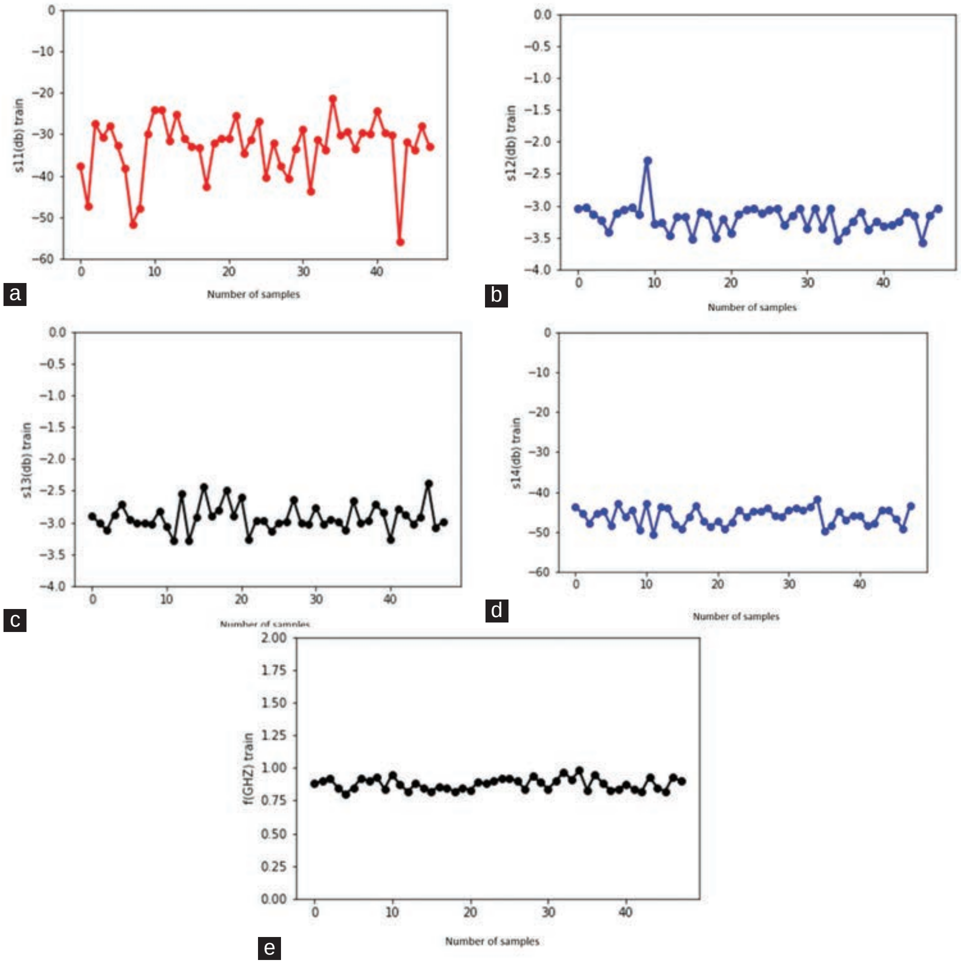

Fig. 7. The proposed ANN training results. Training performance of the proposed long short-term memory for (a) S_{11}, (b) S_{12}, (c) S_{13}, (d) S_{14}, and (e) f (GHz) parameters.

for L_1 (nH), L_2 (nH), and C (pF), while the output parameters were the scattering parameters (S_{11}, S_{12}, S_{13}, S_{14}) in dB, along with the main frequency in GHz. Each row in Table I corresponds to a different simulation run, with unique values for the input parameters and the corresponding output results. This provides a diverse set of data that was used to train and test the neural network model.

B. Applied LSTM RNN Method

The LSTM model is used to predict the parameters of the proposed coupler using the Keras and TensorFlow libraries. The MinMaxScaler function is used to normalize data before processing for better results. Then, data are divided into training and testing phases using the train_test_split function. The LSTM layer is built using 50 units for processing sequential data. The ReLU activation function is used in the model to understand the non-linear behavior of the data. Furthermore, a dense layer consisting of 5 units and a linear activation function is added for better prediction. Then, the Adam optimizer is used for adjusting the learning rate. The MSE and MRE metrics are used for reducing the difference between the predicted and actual values. In the training phase, the mode is run for 1000 epochs with a batch size of 10 and validation is executed using test data.

The results of the proposed ANN LSTM model at the training level are illustrated in Fig. 7. The plots show that the proposed model accurately predicts the values, indicating successful training. Furthermore, it can be concluded that the proposed model has predicted various parameters accurately in different ranges.

In Fig. 7a, the S_{11} training data are shown, which represents how much of the signal is reflected back at port 1. Fig. 7b shows the S_{12} training data, which represents the transmission loss from port 1 to port 2. In Fig. 7c, the S_{13} training data are presented, showing the transmission loss from port 1 to port 3. Fig. 7d illustrates the S_{14} training data, which represents the isolation between ports 1 and 4. Fig. 7e shows the frequency training data.

Furthermore, the results of the proposed ANN LSTM model at the test level are illustrated in Fig. 8. The plots in the sub figures show that the proposed model has perfectly predicted the values in the test phase. Furthermore, it can be concluded that the proposed model has predicted unseen data accurately.

Fig. 8a presents the S_{11} test data, which indicates how much of the signal is reflected back at port 1. Fig. 8b shows the S_{12} test data, representing the transmission loss from port 1 to port 2. Fig. 8c illustrates the S_{13} test data, which shows the

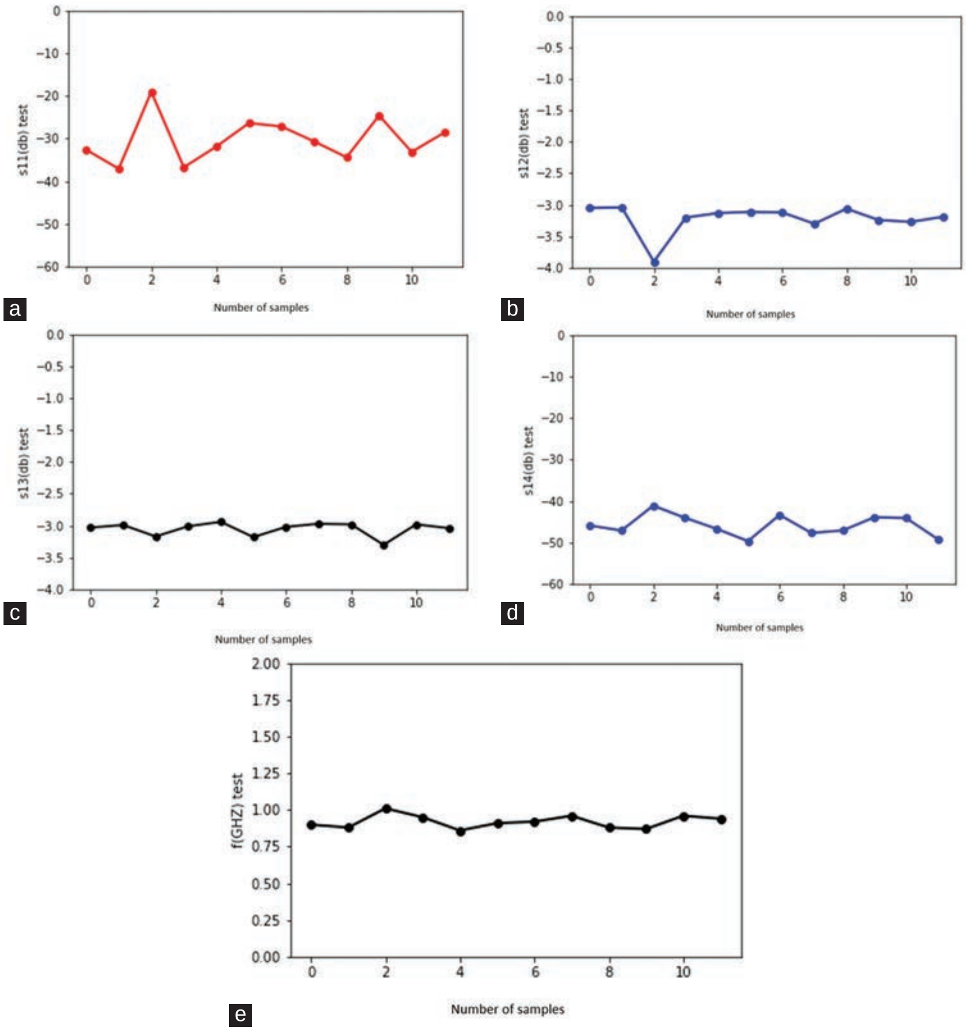

Fig. 8. The proposed ANN test results. Test performance of the proposed long short-term memory for (a) S_{11}, (b) S_{12}, (c) S_{13}, (d) S_{14}, and (e) f (GHz) parameters.

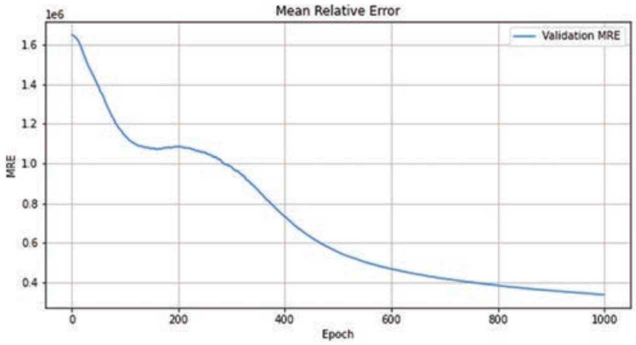

Fig. 9. Values of MRE over different epochs for the proposed ANN long short-term memory model.

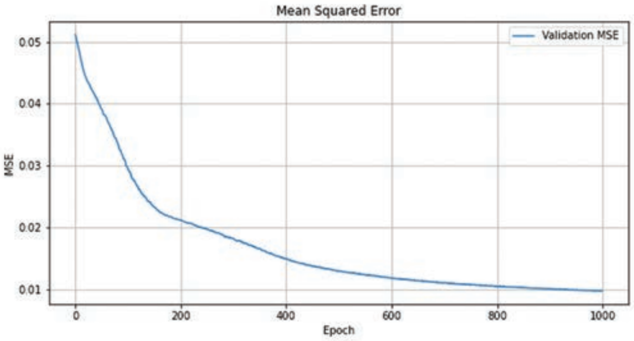

Fig. 10. Values of MSE over different epochs for the proposed ANN long short-term memory model.

transmission loss from port 1 to port 3. Fig. 8d displays the S_{14} test data, representing the isolation between ports 1 and 4. Finally, Fig. 8e presents the frequency test data, showing how well the model predicts the frequency based on the test set.

The MRE and MSE metrics are utilized to analyze the proposed ANN model results. The MRE and MSE metrics are written in Equations (1) and (2). In these equations, the *actual* and *predicted* indices indicate the real and predicted data.

$$\text{MRE} = \frac{1}{n}\sum_{i=1}^{n}\frac{\left|y_{pred} - y_{actual}\right|}{y_{actual} + \varepsilon} \tag{1}$$

$$\text{MRE} = \frac{1}{n}\sum_{i=1}^{n}\left(y_{pred} - y_{actual}\right)^{2} \tag{2}$$

TABLE I
APPLIED DATASET FOR THE TRAINING AND TESTING PHASES OF THE NEURAL NETWORK

Input parameters			Output parameters				
L_1 (nH)	L_2 (nH)	C_1 (pF)	S_{11} (dB)	S_{12} (dB)	S_{13} (dB)	S_{14} (dB)	f (MHz)
10.2	2.3	2.1	33.5	3.04	3.03	46.2	890
10.3	2.3	2.1	43.78	3.04	3.02	44.1	900
10.4	2.3	2.1	47.4	3.03	3.01	45.3	900
10.5	2.3	2.1	51.6	3.03	3.01	46.14	900
10.5	2.3	2.2	37.1	3.04	2.99	47.13	880
10.5	2.3	2.3	32.8	3.12	2.95	48.4	850
10.5	2.3	2.4	30.1	3.24	2.87	47.9	820
10.5	2.3	2.5	28	3.42	2.72	44.83	800
10.5	2.2	2.3	33.3	3.1	2.9	46.2	860
10.5	2.1	2.3	33.6	3.09	2.97	44.9	880
10.5	2	2.3	34.6	3.07	2.97	47.5	880
10.5	1.9	2.3	34.4	3.06	2.98	47.1	880
10.5	2.4	2.3	31.9	3.13	2.94	46.7	860
10.5	2.5	2.3	31.9	3.15	2.92	44.65	850
10.5	2.6	2.3	31.1	3.17	2.91	48	850
10.5	2.7	2.3	31.02	3.2	2.89	48.8	850
10.5	2.8	2.3	30.7	3.22	2.87	45.4	850
10.5	2.9	2.3	29.9	3.25	2.85	45.9	840
10.5	3	2.3	30.06	2.28	2.82	49.52	840
10.5	3.1	2.3	29.65	3.31	2.79	48.53	840
10.5	3.2	2.3	28.8	3.35	2.76	44.5	840
10.6	3.2	2.3	29.7	3.38	2.71	46.9	830
10.7	3.2	2.3	30.3	3.4	2.66	49.85	830
10.8	3.2	2.3	30.93	3.43	2.6	47.4	830
10.9	3.2	2.3	31.58	3.46	2.55	43.7	820
11	3.2	2.3	32.25	3.5	2.49	47.23	820
11.1	3.2	2.3	32.9	3.53	2.43	49.2	820
11.2	3.2	2.3	33.7	3.57	2.38	46.76	820
11.2	3.2	2.2	37.77	3.31	2.64	44.08	840
11.2	3.2	2.1	42.56	3.13	2.8	43.5	850
11.2	3.2	2	37.69	3.04	2.9	43.69	880
11.2	3.2	1.9	31.22	3.04	2.97	44.46	900
11.2	3.2	1.8	27.19	3.12	3.02	43.36	920
11.2	3.2	1.7	24	3.28	3.07	42.85	950
11.2	3.2	1.6	21.36	3.54	3.12	41.87	980
11.2	3.2	1.5	19.07	3.9	3.17	41.15	1010
11.1	3.2	1.9	32.02	3.04	2.98	44.72	900
11	3.2	1.9	32.83	3.04	2.99	43.57	900
10.9	3.2	1.9	33.65	3.05	2.99	43.82	910
10.6	3.2	1.9	38.19	3.06	3.01	43.01	920
10.5	3.2	1.9	40.39	3.07	3.01	44.83	920
10.2	3.2	1.9	55.86	3.1	3.02	44.5	930
10	3.2	1.9	47.89	3.13	3.02	44.45	930
9.8	3.2	1.9	40.66	3.16	3.01	45.94	940
9.6	3.2	1.9	36.76	3.2	3.01	44.03	950
9.3	3.2	1.9	33.16	3.27	2.98	44.13	960
9	3.2	1.9	31.4	3.35	2.95	44.57	970
9	3.4	1.9	30.7	3.3	2.97	47.71	960
9	3.7	1.9	29.47	3.24	3.01	48.5	950
9	4	1.9	28.66	3.19	3.04	49.2	940
9	4.3	1.9	28.11	3.16	3.08	49.17	930
9	4.6	1.9	27.54	3.13	3.12	47.73	920
9	4.8	1.9	26.76	3.12	3.14	46.21	920
9	5.1	1.9	26.4	3.11	3.18	49.67	910
9	5.7	1.9	25.5	3.14	3.26	49.29	890
9	6	1.9	25.2	3.17	3.29	44.02	880
9	6.4	1.9	24.64	3.24	3.3	43.91	870
9	6.5	1.9	24.11	3.27	3.29	50.6	870
9	6.7	1.9	24.52	3.32	3.27	46.05	870

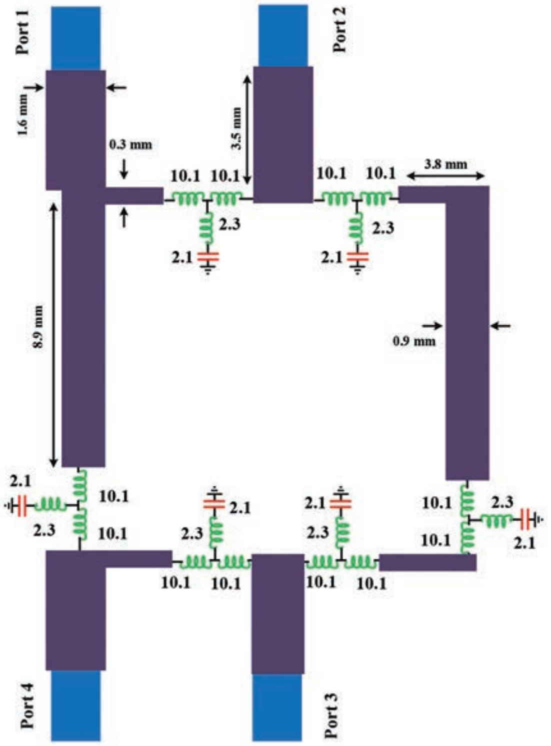

Fig. 11. Layout of the proposed rat race coupler. The inductors and capacitors are in nH and pF units.

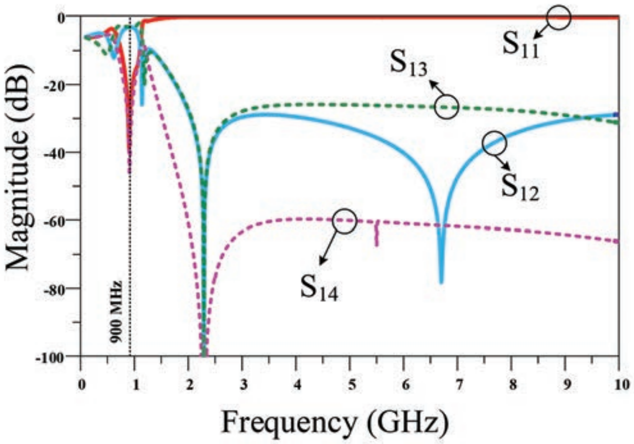

Fig. 12. Simulated frequency response of the designed rate race coupler.

The values of calculated MRE and MSE over different epochs for the proposed ANN LSTM model are shown in Figs. 9 and 10, respectively. The decreasing values of MRE and MSE over epochs demonstrate that the proposed model is well trained and can predict data accurately. After training, the data are denormalized using MinMaxScaler for improved interpretation. The final values of MSE and MRE are calculated as 0.0108 and 0.0663, proving the accuracy of the proposed model.

VI. PROPOSED COUPLER CONFIGURATION

According to the proposed neural network, the best performance of the coupler can be achieved by the following values of inductors and capacitors: L_1 = 10.1 nH, L_2 = 2.3

TABLE II

Performance Comparison of Coupler Designs Focused on Size Reduction and Harmonic Suppression

References	Design approach	Operating frequency (MHz)	Size reduction (%)	Harmonic suppression band (GHz)	Key features
(Pozar, 2012)	Conventional λ/4 coupler	900	0	None	Simple structure, large size
(Du, et al., 2018)	Lumped components-based	559	83.5	1.1–2.8	Compact design, limited suppression
(Lin, et al., 2007)	EBG structure	2400	34.5	7.2–12	Moderate suppression, complex to fabricate
(Ooi, 2005)	EBG resonator	2500	0	10–14	Enhanced suppression, increased cost
(Jamshidi, et al., 2021)	Wilkinson power divider (Lumped components)	800	82.8	1.6–20	High suppression
(Coromina, et al., 2020)	Non-periodic step impedance shunt stubs	1000	67.7	2–10	Moderate suppression, and size reduction
(Lalbakhsh, et al., 2021)	Open-ended stubs	1800	74	3.6–12.6	Simple structure
(Roshani, et al., 2022b)	Resonators	750	84	1.5–5.25	Compact size
This work	Proposed ANN-optimized design	900	99	1.8–10	Ultra-compact, excellent suppression

nH, and $C = 2.1$ pF. The layout of the proposed RRC is illustrated in Fig. 11. The layout of the proposed structure occupies only 10.9 mm × 6.7 mm, featuring a 99% size reduction compared to the conventional coupler.

Fig. 12 depicts the simulated frequency response of the designed rate race coupler operating at 900 MHz. The obtained return loss (S_{11}) and isolation (S_{14}) are 39.1 dB and 45.6 dB. Furthermore, the achieved insertion losses at port 2 (S_{12}) and port 3 (S_{13}) are 3.05 dB and 3.07 dB, respectively. The obtained harmonic suppression band ranges from 1.8 GHz to 10 GHz, in which the unwanted harmonics are suppressed with high attenuation.

A performance comparison of the proposed coupler with other related works, focused on the size reduction and harmonic suppression, is presented in Table II. As shown, the proposed RRC has obtained excellent size reduction of 99% and desirable harmonic suppression, which outperforms other related works in terms of miniaturization and harmonic suppression.

VII. Conclusion

A new RRC is presented in this paper with excellent size reduction operating at 900 MHz. Lumped elements are applied in this structure and the proposed design is optimized using a neural network. The final size of the designed coupler is 10.9 mm × 6.7 mm, which shows a 99% size reduction compared to the conventional coupler with a size of 124.3 mm × 62.9 mm. The best values of the applied lumped components are determined using the proposed neural network, resulting in an improved performance of the device. The proposed coupler also demonstrates excellent harmonic suppression from 1.8 GHz to 10 GHz, which results in better performance and prevents the presence of unwanted spurious harmonics in the frequency response. The obtained desirable results show that the proposed RRC can be considered as a strong candidate for use in modern communication systems.

References

Al-Majdi, K., and Mezaal, Y.S., 2023. New miniature narrow band microstrip diplexer for recent wireless communications. *Electronics*, 12(3), pp.716.

Beigizadeh, M., Dehghani, R., and Nabavi, A., 2017. Analysis and design of a lumped-element hybrid coupler using limited quality factor of components. *AEU-International Journal of Electronics and Communications*, 82, pp.312-320.

Coromina, J., Velez, P., Bonache, J., and Martín, F., 2020. Branch line couplers with small size and harmonic suppression based on non-periodic step impedance shunt stub (SISS) loaded lines. *IEEE Access*, 8, pp.67310-67320.

Du, R.N., Weng, Z.B., and Zhang, C., 2018. A miniaturized filtering 3-dB branch-line hybrid coupler with wide suppression band. *Progress in Electromagnetics Research Letters*, 73, pp.83-89.

Jamshidi, M.B., Roshani, S., Talla, J., Roshani, S., and Peroutka, Z., 2021. Size reduction and performance improvement of a microstrip Wilkinson power divider using a hybrid design technique. *Scientific Reports*, 11(1), pp.7773.

Lalbakhsh, A., Mohamadpour, G., Roshani, S., Ami, M., Roshani, S., Sayem, A.S.M., Alibakhshikenari, M., and Koziel, S., 2021. Design of a compact planar transmission line for miniaturized rat-race coupler with harmonics suppression. *IEEE Access*, 9, pp.129207-129217.

Lin, C.M., Su, H.H., Chiu, J.C., and Wang, Y.H., 2007. Wilkinson power divider using microstrip EBG cells for the suppression of harmonics. *IEEE Microwave and Wireless Components Letters*, 17(10), pp.700-702.

Long, Z., Zhang, B., Liu, G., Wu, Z., and Yan, Q., 2024. A compact branch-line coupler with harmonic suppression using novel circular-shaped resonators for medical imaging systems. *Multiscale and Multidisciplinary Modeling, Experiments and Design*, 7, pp.1-18.

Mezaal, Y.S., Ghazi, H.S., and Khaleel, M.H., 2024. Highly narrowband miniaturized microstrip diplexer for qubit mobile communication networks utilizing SIR and T-shaped resonators with negative group delay performance. *Optical and Quantum Electronics*, 56, pp.1670.

Mirzavand, R., Honari, M.M., Abdipour, A., and Moradi, G., 2012. Compact microstrip Wilkinson power dividers with harmonic suppression and arbitrary power division ratios. *IEEE Transactions on Microwave Theory and Techniques*, 61(1), pp.61-68.

Mohammadi, N., Moloudian, G., Roshani, S., Roshani, S., Parandin, F., and Lalbakhsh, A., 2024 A Wilkinson power divider with harmonic suppression through low-pass filter for GSM and LTE applications. *Scientific Reports*, 14(1), pp.2429.

Nikandish, G., Staszewski, R.B., and Zhu, A., 2020. Breaking the bandwidth limit: A review of broadband Doherty power amplifier design for 5G. *IEEE Microwave Magazine*, 21(4), pp.57-75.

Ooi, B.L., 2005. Compact EBG in-phase hybrid-ring equal power divider. *IEEE Transactions on Microwave Theory and Techniques*, 53(7), pp.2329-2334.

Pozar, D.M., 2012. *Microwave Engineering*. 4th ed. University of Massachusetts at Amherst, John Wiley and Sons, Inc, United States, pp.26-30.

Rezaei, A., Yahya, S.I., and Nouri, L., 2023. A comprehensive review on microstrip couplers. *Aro-The Scientific Journal Of Koya University*, 11(1), pp.22-31.

Roshani, S., Koziel, S., Yahya, S.I., Chaudhary, M.A., Ghadi, Y.Y., Roshani, S., and Golunski, L., 2023a. Mutual coupling reduction in antenna arrays using artificial intelligence approach and inverse neural network surrogates. *Sensors*, 23(16), pp.7089.

Roshani, S., Yahya, S., Roshani, S., Farahmand, A., and Hemmati, S., 2022a. Design of a modified compact coupler with unwanted harmonics suppression for L-band applications. *Electronics*, 11, p.1747.

Roshani, S., Yahya, S.I., Mezaal, Y.S., Chaudhary, M.A., Al-Hilali, A.A., Mojirleilani, A., and Roshani, S., 2023b. Design of a compact quad-channel microstrip diplexer for L and S band applications. *Micromachines* (*Basel*), 14(3), pp.553.

Roshani, S., Yahya, S.I., Roshani, S., and Rostami, M., 2022b. Design and fabrication of a compact branch-line coupler using resonators with wide harmonics suppression band. *Electronics*, 11(5), pp.793.

Venter, J.J., Stander, T., and Ferrari, P., 2018, X-band reflection-type phase shifters using coupled-line couplers on single-layer RF PCB. *IEEE Microwave and Wireless Components Letters*, 28(9), pp.807-809.

Wang, J., Wang, B.Z., Guo, Y.X., Ong, L., and Xiao, S., 2007. A compact slow-wave microstrip branch-line coupler with high performance. *IEEE Microwave and Wireless Components Letters*, 17(7), pp.501-503.

Yang, G., Li, B., Kang, W., and Ge, S., 2012. Miniaturized microstrip branch-line coupler with good harmonic suppression performance. *Journal of Electronics (China)*, 29(1), pp.132-136.

Mitigating Dead Node Impact on Coverage and Connectivity in Wireless Sensor Networks Using a Hybrid Approach

Omeed K. Khorsheed[†]

Department of Computer Science, Faculty of Science, Koya University,
Danielle Mitterrand Boulevard, Koya KOY45, Kurdistan Region – F.R. Iraq

***Abstract*—Wireless sensor networks' coverage and efficient connectivity are pivotal for reliable data collection and communication. However, dead nodes, resulting from hardware failure or power depletion, can affect coverage and connectivity, leading to information loss and degraded performance. Previous research in the same context indicates the need for further investigation to achieve optimal trade-offs in network resource allocation. This research introduces a hybrid Artificial Bee Colony-Sequential Re-connectivity and Coverage Algorithm (ABC-SRCA) approach, combining the ABC algorithm with a developed SRCA. The ABC algorithm adjusts sensor node placement to maximize the coverage and minimize holes, while the SRCA algorithm restores connectivity by reconnecting the network when nodes fail. The approach uses probabilistic selection to explore various solutions, making the approach adaptive to diverse scenarios. The simulation outcomes indicate that the ABC-SRCA method enhances coverage accuracy by up to 30% compared to ABC and SRCA when they are used separately. In addition, the rate of connectivity error detection decreases by about 25%, highlighting the method's effectiveness in dynamic network conditions. The approach also surpasses existing methods, including Genetic Algorithms and Sensing Radius Adaptive Coverage Control (SRACC), by achieving coverage level up to 98% while conserving resources. The ABC-SRCA achieves better energy consumption than Particle Swarm Optimization (PSO) and PSO Voronoi Diagram and achieves competent energy when compared with SRACC. The hybrid approach provides an effective solution for ensuring efficient and reliable network operations, supporting the successful deployment of WSNs in diverse applications.**

***Index Terms*—ABC algorithm, Coverage optimization, Dead nodes, Hybrid approach, Re-connectivity, SRCA algorithm, Wireless sensor networks.**

I. Introduction

Wireless sensor networks (WSNs) have gained considerable interest across diverse applications, including environmental monitoring, surveillance, and smart systems. A WSN is often defined as a group of interconnected wireless sensor nodes that capture the surroundings at a region of interest, communicate with each other, and send information to the end user (Bhat and Santhosh, 2022). One of the characteristic features of WSNs is that many nodes can be placed in a definite area to guarantee coverage. However, sensor nodes are prone to frequent failure due lack of power, physical harm, or environmental interferences (Adu-Manu, et al., 2022). However, a relatively congested network results in numerous problems like node overlap (Ling, et al., 2020) and failure of a group of nodes that reduce the multi-hop paths in the network (Baradaran and Navi, 2020), which can bring about a "disconnection" that isolates a subset of non-failed nodes from the other nodes. If no path exists between two nodes, they are considered disconnected (Zhang, et al., 2020a). Therefore, sensor node non-existence or failure can affect coverage and connectivity, which, in turn, influences sensor network performance and the quality of service of the entire WSN (Wang, et al., 2022). Ensuring complete coverage and maintaining connectivity is a vital challenge in WSNs (Zeng, et al., 2023), however, dead nodes, which no longer function can affect coverage and connectivity, leading to information loss and reduced network performance. Network coverage can be improved by addressing optimal node locations that managing the sensing range, identifying alternative paths, and adjusting transmission ranges, and ensuring sustained connectivity. This guarantees the network operation's dependability and resilience. To tackle coverage and re-connectivity issues, this study proposes an approach combining the Artificial Bee Colony (ABC) optimization algorithm with a developed sequential re-connectivity and coverage algorithm (SRCA) to achieve efficient coverage and re-connectivity, with a specific focus on dead nodes. The approach optimizes the deployment of sensor nodes, ensuring maximum coverage range and facilitating re-connectivity in the presence of dead nodes or connectivity gaps. The two algorithms are run sequentially, the ABC algorithm first optimizes the placement of sensor nodes within the network, ensuring coverage requirements are met and minimizing coverage gaps. Then, the SRCA algorithm re-establishes connectivity, reconnecting the network in the

---

ARO-The Scientific Journal of Koya University
Vol. XIII, No. 1 (2025), Article ID: ARO.11710. 13 pages
DOI: 10.14500/aro.11710
Received: 10 July 2024 2024; Accepted: 02 April 2025
Regular research paper; Published: 17 April 2025
[†]Corresponding author's e-mail: omeed.kamal@koyauniversity.org

presence of dead nodes. By adapting to dynamic changes in network topology, ABC-SRCA achieves greater resource efficiency than existing techniques. Amalgamating the ABC and SRCA algorithms, the hybrid approach offers several benefits. It enhances network coverage by selecting optimal node locations that maximize the sensing range. In addition, it resolves dead nodes by identifying alternative paths and adjusting transmission ranges to ensure sustained connectivity. This results in a more dependable and resilient network operation.

The remainder of this paper is organized as follows: Section 2 provides the related work. Section 3 demonstrates the problem statement. Section 4 presents the ABC-SRCA approach. Section 5 highlights the results and discussions, while Section 6 concludes and offers future directions for the study.

II. Related Work

Many techniques have been proposed for deployment to avoid node failures and enhance the coverage of WSNs. (Lu, et al., 2025) proposed an approach to optimize the deployment strategy of heterogeneous WSNs concentrating on balancing network coverage, connectivity, and deployment costs. The authors present an improved Secretary Bird Optimization Algorithm (ISBOA) integrating Gaussian Cuckoo Mutation and a smooth exploitation mechanism. Simulation results indicate that the ISBOA attains higher accuracy and faster convergence compared to other algorithms. The authors suggest a minimum spanning tree domain reduction strategy for large-scale issues to enhance efficiency with minimum loss of accuracy. However, the research does not utilize dynamic adaptive and fault recovery mechanisms to maintain the network efficiency and stability in a long-term operation. (Guo, et al., 2025) introduced a perception model incorporating path loss and false alarm probability to optimize coverage problems in WSNs using an intelligent optimization algorithm and longevity. The model includes a logarithmic-based path loss model and the Neyman–Pearson criterion for maximizing detection probability. The simulation results indicate that the model attains full coverage with fewer nodes than traditional models, hence, improving network performance and longevity. However, the research does not explain whether the algorithm adapts to changing parameters or conditions during execution. (Velavalapalli, Ramamurthy and and Satyanarayana, 2024) proposed a wholly distributed approach for enabling each node of delay tolerant networks to rapidly determine if its sensor generates faulty data. A continuous-time state equation is used to model the approach's dynamic behavior. The research also considers the effect of misbehaving nodes to deactivate the fault detection. The research evaluates the detection and false alarm rates by comparing theoretical predictions with simulation results. The simulations show that the packet reception delay metric beats the expected transmission count metric and also energy consumption and end-to-end delay metrics, while still preserving a high packet delivery ratio. However, the proposed approach encounters complexity in implementation, and challenges in handling misbehaving nodes and network resource constraints. (Khedr, Osamy and Salim, 2018) suggested a design that involves random provisioning of Heterogenous WSNs (HWSNs) and a distributed algorithm for detecting holes that result from node failures. Accordingly, nodes in this new scheme can work together to detect and predict any possible coverage gaps. Alternatively, (Yan, et al., 2020) proposed a connectivity-based k-coverage hole detection algorithm for WSNs, utilizing homology theory and Rips complex to effectively identify and reduce coverage holes. The simulation results indicate that the proposed algorithm can reliably detect over 95% of non-triangular K-coverage holes. The algorithm reduces the energy consumption, as fewer nodes are active at any given time, which helps in extending the network's operational lifetime. However, the algorithm can only detect non-triangular coverage holes because the Rips complex cannot capture triangular holes, leading to missing some coverage holes.

A coverage hole patching algorithm is proposed by (Lu, et al., 2022). Depending on the size of the coverage holes, the algorithm prioritizes patching to reduce node redundancy, improve network coverage, and balance resource allocation. The results show that the proposed algorithm coverage rate and node redundancy reduction are better than the conventional coverage hole patching algorithms. A localization and deployment model using the Arithmetic Optimization Algorithm is presented in (Khatir, et al., 2021). By implementing this algorithm, a deployment model is developed to achieve a fully connected network. Considering the average localization error within 5 m, the algorithm demonstrates its accuracy in localizing nodes and identifying coverage holes in different fields. Based on the simplified Rips complex, (Zhang, Chu, and Feng, 2020b) proposed an efficient algorithm to detect coverage holes. The algorithm decreases the computational efficiency and enhances the detection accuracy. The results indicate that the proposed algorithm exhibits reduced complexity and achieves higher accuracy, reaching 99.03%, when compared to other algorithms. The algorithm enhances energy consumption by implementing redundant node sleeping and edge deletion, which help simplify the network structure, reducing the number of active nodes and edges required to communicate and process data. However, the algorithm may face challenges in dense or highly dynamic networks where node locations and network topology change continually. An improved Coverage Hole Patching Technique (CHPT) based on tree algorithms is proposed by (Das and Debbarma, 2020). The Delaunay triangle and void circle properties are used to detect hole patching. A hole's location is estimated using the inner empty circle property. The results of the experiments show that CHPT increases the coverage percentage to 98.6% compared to other techniques. (Al-Fuhaidi, et al., 2020) proposed a deployment model based on probabilistic sensing models (PSM) and Harmony Search Algorithms (HSA) to balance network coverage and cost in HWSNs. The HSA optimizes the deployment of nodes by balancing coverage and cost, while the PSM is utilized to solve the overlapping problem among sensors. Based on the simulation results, the proposed deployment model achieves maximum coverage and minimum sensor number, and it attains superior results when compared with other algorithms. (Amer, et al., 2024) introduced a hybrid algorithm, CFL-PSO, combining an enhanced Fick's Law algorithm with comprehensive learning and Particle Swarm Optimization (PSO) to enhance connectivity and coverage by optimizing router node placement in WSNs. The simulation results show that CFL-PSO improves network performance, attaining up to 66.5% better connectivity, 16.56% better coverage, and a 21.4% improvement in the objective function value compared to several algorithms including the standard FLA. However, the research does not address the network scalability and does not consider energy consumption. Accordingly, (Aljubori, Khalilpour Akram, and Challenger, 2022) developed a distributed algorithm based on 2-hop local neighborhood information to identify redundant nodes. In the proposed algorithm, nodes are classified as redundant based on their connections with their neighbors. An Artificial Hydrocarbon Network Technique is presented by (Gutiérrez and Ponce, 2019) to detect sensor failures at a remote location. The method can predict the temperature and detect malfunctions at remote sensors utilizing information from a web service and comparing it with data from the field temperature sensor. In discussing the automatic detection of coverage holes, (Jain, 2020) proposed a four-step architecture that includes cluster formation, coverage hole detection, Cluster Head (CH) selection, recovery, and routing for dynamic clustering, focusing on coverage hole detection and recovery to enhance energy efficiency in IoT applications. The results show that the architecture reduces energy consumption, increases network lifetime, and improves the WSN's overall efficiency. However, the complexity of cluster maintenance and the time-consuming of using fuzzy logic for coverage holes should be considered. (Lai, et al., 2022) introduced a method for tracing coverage holes in WSNS known as Force-Directed and Transfer Learning. It depends on the layout generation capabilities of force-directed algorithms and the image recognition capabilities related to convolutional neural networks. Similarly, (Satyanarayana, et al., 2023) developed a fault detection model to improve the coverage area by establishing relay nodes for positioning sensor nodes in the environment and simulating the entire module with different analyses including transmission range, sensing range, and distance traveled to compare its performance with existing techniques. The simulation results reveal the effectiveness of the proposed algorithm in enhancing the coverage area and energy efficiency of the WSN. However, the proposed algorithm suffers from implementation complexity and computational resources. Moreover, it faces challenges in preserving connectivity and performance in the existence of multiple node failures. (Siamantas and Kandris, 2024) presented a new algorithm based on Particle Swarm Optimization (PSO) to improve WSNs coverage and connectivity by placing a predefined number of sensor nodes within a square target area. The research introduced a new objective function obtained from circle-packing geometric problems. The simulations and statistical tests revealing the algorithm effectiveness compared to other algorithms. However, the research focuses on attaining only 1-connectivity, which may not provide adequate network robustness and fault tolerance compared to m-connectivity. In (Kuthadi, et al., 2021), an Optimized Energy Management Model for Data Dissemination is proposed to enhance transmission links and energy consumption. The model utilizes a non-adaptive routing approach to disperse data efficiently from a single source to several points, integrating a dispersed collaboration system and priority task planning to improve energy usage. The results show that the model enhances the data transmission rate and reduces energy consumption by 20.11% in WSNs. However, the model may be complex to implement and need substantial computational resources due to the mathematical calculations. (Abdulzahra, Al-Qurabat and Abdulzahra, 2023) proposed an energy-efficient fuzzy-based unequal clustering with a sleep scheduling (EFUCSS) protocol for IoT that uses WSN to extend the network lifetime and reduce energy. The results show that the proposed protocol conserves energy by 26.92–213.4% and network lifespan by 39.58–408.13%. The network lifespan shows significant improvement compared to other algorithms. However, the protocol may increase the implementation complexity and require more computational resources due to clustering, CH selection using fuzzy logic, and sleep scheduling.

The literature proposed several techniques to improve coverage and connectivity in WSNs. However, there is still a significant gap in repairing and reconnecting dead nodes, dynamic adaptation, and energy efficiency, which are critical to maintaining network reliability and robustness. Existing research has suggested methods meant to maintain coverage and connectivity; there remains a notable gap in the literature regarding the proper repair and re-connection of non-functional sensor nodes, as well as the effective remediation of coverage holes yet. Many approaches lack mechanisms for dynamic adaptation to changing network conditions, such as node failures or varying environmental factors, which can impact network reliability. Accordingly, we integrate the ABC algorithm with a developed SRCA algorithm to develop range and connectivity for coverage hole detection formations between two nodes. The approach ensures continuous monitoring and adaptation to dynamic changes within the system. A comparison between the research is introduced in Table I below:

Table I shows a comparison of several research in the literature, underscoring their strengths and limitations, which help understand the gaps that the proposed hybrid ABC-SRCA approach aims to handle.

III. Problem Statement

Ensuring robust network coverage and connectivity in WSNs is a critical but unresolved problem due to several challenges. These include dynamic environments, energy

TABLE I
Comparing of Research

Research	Approach	Strengths	Limitations
Lu, et al. (2025)	Improved Secretary Bird Optimization Algorithm	Higher accuracy, faster convergence, efficient for large-scale issues	Lacks dynamic adaptive and fault recovery mechanisms
Guo, et al. (2025)	Perception model with path loss and false alarm probability	Full coverage with fewer nodes, improved network performance	Does not adapt to changing parameters or conditions during execution
Velavalapalli, Ramamurthy and Satyanarayana (2024)	Distributed approach for detecting faulty data	High packet delivery ratio, effective fault detection	Implementation complexity, challenges in handling misbehaving nodes and resource constraints
Khedr, Osamy and Salim (2018)	Random provisioning design for HWSNs	Detects and predicts coverage gaps	Does not address dynamic adaptation
Yan, et al. (2020)	Connectivity-based k-coverage hole detection algorithm	Reliable detection of non-triangular holes, reduced energy consumption	Miss triangular holes, limited effectiveness
Lu, et al. (2022)	Coverage hole patching algorithm	Improved coverage rate, reduced node redundancy	Does not address dynamic network conditions
Khatir, et al. (2021)	Localization and deployment model using Arithmetic Optimization Algorithm	Accurate localization, identification of coverage holes	Challenges in dense or highly dynamic networks
Zhang, Chu and Feng (2020b)	Efficient algorithm based on simplified Rips complex	High accuracy, reduced complexity	Struggles in dynamic networks with changing node locations
Amer, et al. (2024)	Hybrid CFL-PSO algorithm	Improved connectivity and coverage, better network performance	Does not address network scalability and energy consumption
Al-Fuhaidi, et al. (2020)	Deployment model using PSM and HSA	Maximum coverage with minimum sensors, balanced coverage, and cost	Does not consider dynamic adaptation
Kuthadi, et al. (2021)	Optimized energy management model	Enhanced transmission links, reduced energy consumption	Complex implementation, substantial computational resources required
Abdulzahra, Al-Qurabat and Abdulzahra (2023)	Fuzzy-based unequal clustering with sleep scheduling protocol	Conserves energy, extends network lifespan	Increased implementation complexity, requires more computational resources

limitations, and irregular sensor deployment. The irregular distribution of nodes, often resulting from random sensor deployment, aggravates coverage gaps and makes repairing dead nodes a significant challenge. Existing solutions usually fail optimally to balance coverage and energy efficiency trade-offs while adapting to various conditions. In addition, the complexities of sensor networks and their operating environments have prevented the development of a universally accepted solution. Moreover, the lack of scalable and generalizable approaches ensures this issue remains an open research area. The previous research underscores different approaches to enhance coverage and connectivity in WSNs. Many approaches focus on optimizing deployment, catching coverage holes, and handling energy consumption. However, there is a significant gap in dynamic adaptation and fault recovery mechanisms, which are essential for preserving network dependability and robustness. The hybrid ABC-SRCA approach combines the strengths of the SRCA and ABC algorithms to manage these gaps by incorporating dynamic adaptation, energy-aware optimization, and scalable re-connectivity, presenting a more thorough solution for WSNs.

IV. The Proposed Approach

The hybrid ABC-SRCA approach combines two techniques: the ABC algorithm and a developed SRCA. The proposed approach integrates the strengths of both algorithms to tackle coverage and re-connectivity issues. The ABC algorithm is a nature-inspired optimization algorithm that simulates bees' foraging behavior. It is easy to implement, and there are fewer parameters to adjust. Moreover, it utilizes exploration and exploitation mechanisms to adjust the placement of sensor nodes in the network iteratively (Wang, et al, 2023). Thus, this algorithm can optimize network resource utilization and maximize the coverage area. However, it may obtain a local minimum and can achieve the global optimum with relative computational simplicity (Wang, et al, 2023). On the other hand, the SRCA algorithm is developed by the author to establish connectivity among deployed nodes by manipulating their transmission ranges. The SRCA has two main functions. First, it identifies disconnected nodes and adjusts their transmission ranges sequentially to establish connectivity with neighboring nodes. Second, the SRCA algorithm identifies coverage holes and constructs coverage by adjusting node positions. To achieve these functions, several steps are performed including (1) initialization of nodes sensors positions, (2) node distance estimation, (3) coverage hole detection, and (4) re-connectivity to dead nodes. All these steps are explained in the following sections B and C. The algorithm iteratively refines the positions of nodes by evaluating their fitness and generating new solutions. This process ensures the network remains connected even with dead nodes, enabling seamless data transmission and communication, thereby addressing the local optima problem effectively. Therefore, integrating these algorithms provide a robust solution for optimizing network coverage and connectivity, thereby addressing the local optima problem effectively. Moreover, improving coverage and facilitating re-connectivity in the presence of dead nodes can indirectly contribute to energy efficiency by reducing the need for redundant nodes and minimizing communication overhead. In addition, maintaining connectivity and coverage can help in efficient network operations, which may lead to better energy utilization.

The proposed approach can improve the coverage and re-connecting to the dead node in WSNs and considers that all sensor nodes are heterogeneous randomly deployed in the ROI. All nodes are assumed to be capable of sensing the environment to detect physical constraints. All sensors are presumed to uphold a synchronization protocol, enabling consistent time synchronization across the network. This allows them to make informed decisions about maintaining reconnection with their neighbors. Presumably, the sensing range (Rs) and communication range (Rc) of each node are (Rc > 2RS), with no conflict likely to occur after deployment. It is used in the proposed approach to optimize the deployment and routing of sensor nodes and to estimate distance among nodes. In this algorithm, new solutions are produced, where the iteration for the node searching process is to find a new position and apply a distance estimation process. This procedure is started by selecting the start node and then generating the distance for the next node (from the start node to the end node) in ROI after the sensor node is randomly deployed using a post-deployment algorithm. The SRCA algorithm prioritizes creating connections between deployed nodes by adjusting their transmission ranges. It identifies disconnected nodes and gradually modifies their transmission ranges to link up with neighboring nodes, aiming to establish connectivity.

This approach can be customized based on prioritizing coverage holes or dead nodes which are two common challenges in WSNs Prioritization depends on the approach focus. If the approach strategy focuses on sustaining network functionality, re-connectivity for dead nodes should be carried out first. Moreover, handling coverage holes might be preferable if the focus is on accurate monitoring or data collection. The ABC-SRCA approach involves three main steps shown in Fig. 1, and explained in the following sections.

A. Node Distance Estimation

The step related to node distance estimation involves the utilization of the ABC algorithm to calculate the node distance estimation and adjust sensor node positions. The ABC algorithm is a metaheuristic optimization algorithm commonly utilized for solving optimization problems but is not explicitly designed for distance estimation. To use the ABC algorithm for estimating distances, there is a need for distance-based objective function or fitness measure. The ABC algorithm is customized to estimate the node distance and adjust sensor nodes' positions. The ABC algorithm iteratively refines a population of node sources (representing solutions in a multi-dimensional space) by evaluating their fitness, creating neighbor solutions, selecting better solutions, and recording the best-found solution until evaluations up to a maximum. The algorithm procedure is introduced in the following:

Input: Number of node sources SN (solution), number of dimensions D, lower bounds x_{min}, upper bounds x_{max}, max evaluations MaxEval, abandonment limit L

```
1. Initialization:
for i = 1 to SN:
    for j = 1 to D:
        $x_i^j = x_{min}^j + rand[0,1]\left(x_{max}^j - x_{min}^j\right)$        (1)
    end for
evaluate fitness (fi) for each solution xi.
set EvalCount = SN
bestSolution = best(xi)
2. Repeat until EvalCount ≥ MaxEval:
    /Employed Bee Phase:
    for each employed bee associated with solution xi:
        choose a random neighbor index k (k ≠ i) and a random dimension j ∈ {1,…, D}
        generate new solution (neighbor) vi:
        vij = xij + ϕij * (xij - xkj)        (2)
        where ϕij ∈ [-1, 1] (random)
        evaluate fitness f(vi)
        evalCount = EvalCount + 1
        if f(v_i) is better than f(xi):
            update xi = v_i
            reset trial counter for xi
        else:
            increment trial counter for xi
    end for
    //Onlooker Bee Phase:
    calculate selection probabilities for each solution:
    for i = 1 to SN:
        $p_i = \frac{fitness_i}{\sum_{n=1}^{SN} fitness_n}$        (3)
    end for
    for each onlooker bee:
        select a solution xi based on probability pi (e.g., using roulette wheel selection)
        choose a random neighbor index k (k ≠ i) and a random dimension j ∈ {1,…, D}
        generate new solution vi using:
        vij = xij + ϕij * (xij - xkj)        (2a)
        evaluate fitness f(vi)
        evalCount = EvalCount + 1
        if f(v_i) is better than f(xi):
            update xi = vi
            reset trial counter for xi
        else:
            increment trial counter for xi
    end for
    //Scout Bee Phase:
    for each solution xi:
        if trial counter for xi exceeds limit L:
            //Abandon current solution and generate a new one randomly
            for j = 1 to D:
                $x_i^j = x_{min}^j + rand[0,1]\left(x_{max}^j - x_{min}^j\right)$        (1a)
            end For
            evaluate fitness f(xi)
            evalCount = EvalCount + 1
```

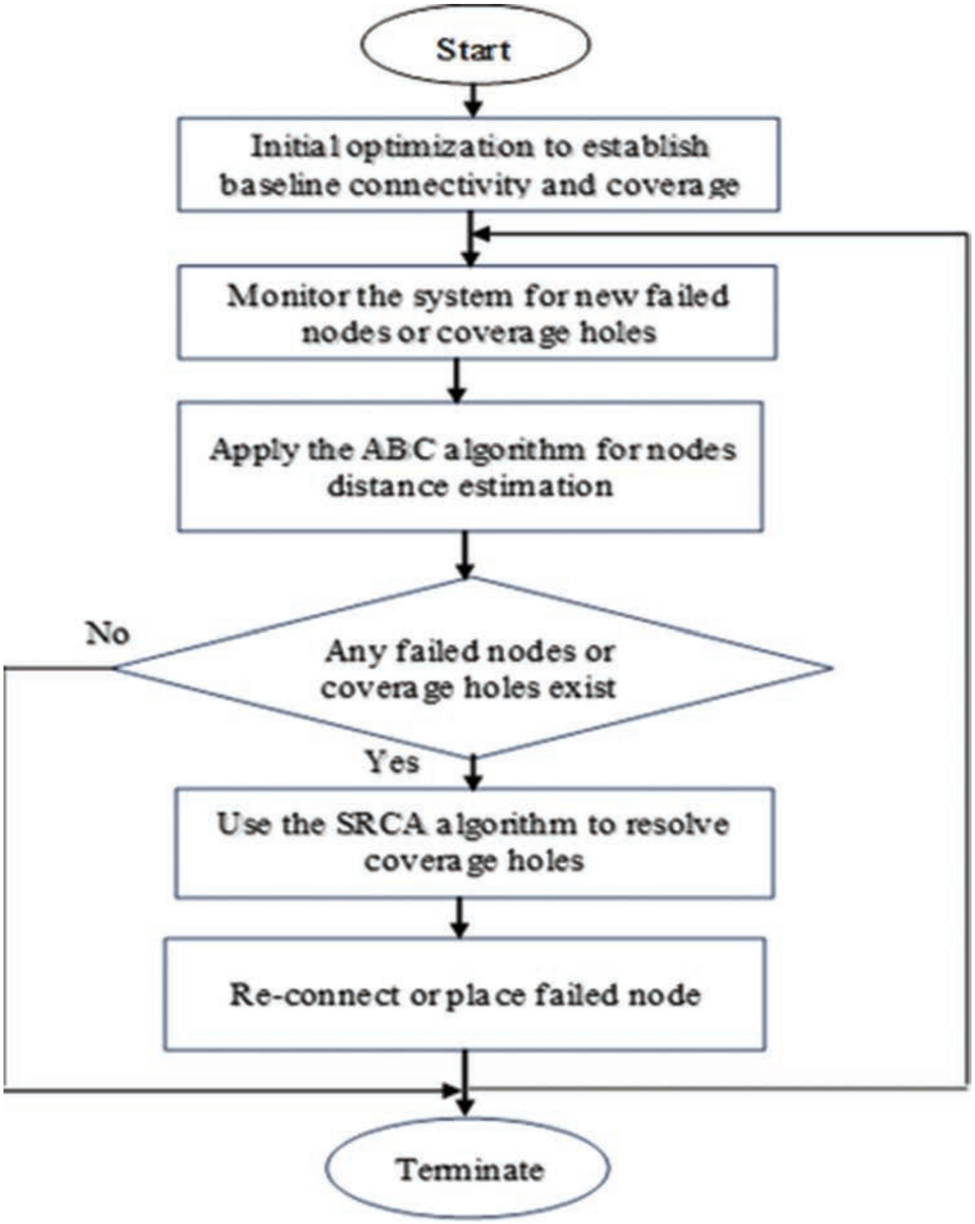

Fig. 1. Flow chart for the combined artificial bee colony-sequential re-connectivity and coverage algorithm algorithms proposal/approach.

```
reset trial counter for xi
end For
//update the best solution found so far:
bestSolution = best (BestSolution, {xi})
end Repeat
Output: BestSolution
```

Overall, this procedure resembles a population-based optimization algorithm inspired by the behavior of bees in a colony. It aims to iteratively refine the solutions (node sources) and introduce new random solutions to improve the overall performance or fitness of the nodes based on defined parameters and fitness evaluations. The algorithm evaluates solutions based on their “fitness” or performance, giving a higher probability to solutions that perform better rather than randomly choosing solutions. Moreover, the algorithm avoids getting stuck in local optima by continuously exploring new areas. In general, the algorithm provides efficient, scalable, and adaptive methods for optimizing problems, making it particularly appropriate for WSN optimization, where maintaining connectivity and coverage is crucial.

B. Coverage Hole

The coverage hole step includes the usage of the SRCA algorithm, whose function is to determine and construct the coverage holes. The SRCA initializes the sensor node position and calculates the coverage area by saving distance estimation and node location information. It usually updates its position through the node-finding process to determine the coverage area in the ROI. The selected backup node must maintain a one-hop information table corresponding to the critical node. The node degree represents the number of communication links it has with other nodes in the ROI, which is equivalent to the number of its neighboring nodes. A higher node degree indicates a more significant number of surrounding dead nodes. The proposed approach selects node positions from start to end to reconnect to the dead node as a new position. When a node dies, the backup node is chosen from its neighbor to minimize dead nodes, messages, and time. During the initialization of the node table, each node sends a broadcast message containing its ID and coordinates. All nodes within the communication range receive the message. After exchanging information, each node determines whether it is nearest to the dead node through the node table neighborhood list. However, live/active nodes must not break network connectivity. Therefore, a backup node must be selected only for the dead node. Selecting backup nodes depends on the minimum distance between the dead node and the nearest node and the node degree.

C. Re-Connectivity to Dead Nodes

This step includes recovering the dead node and reconnecting to it using the connectivity algorithm to the dead node. The SRCA algorithm establishes connections among deployed nodes by fine-tuning their transmission ranges. It detects isolated nodes and systematically adjusts their transmission ranges, striving to connect them with neighboring nodes and ultimately achieve network connectivity. Sensor nodes are deployed randomly, resulting in highly connected networks in some areas while leaving others only partially connected. This uneven distribution can compromise coverage. To address this, sensor nodes must be able to adjust their positions to achieve uniform distribution and maximize coverage. Typically, the sink node oversees this distribution, processing data and making decisions. However, this approach increases communication overhead and incurs delays, as decisions must be transmitted across the entire network. As a result, self-organizing nodes are recommended to reduce overall network message traffic. The effects of node failure are pretty different in highly interconnected networks where all nodes are placed close to each other. Any loss of one or more nodes can affect connectivity, splitting the network into several disjoint segments. Furthermore, numerous nodes cannot send data to the sink node [30]. The SRCA and dead node reconnection in WSNs work, assuming all sensor nodes are heterogeneous sensors placed randomly in the ROI. Hence, all nodes are supposed to be aware of the environment and physical limitations. The SRCA selects the backup (alternative) node to each dead node from its neighbor nodes through a neighborhood list (NL). The SRCA algorithm procedure for re-connectivity is introduced as follows:

1. If node position is not found, the algorithm terminates the condition, or else it turns up to step 8
2. The node position is often regarded as the current best location
3. Start re-connectivity sensor node in the coverage hole area
4. Select node position from start to end to re-connect to the failed node
5. If re-connectivity fails (SRCA), it is highly recommended to return to step 4
6. Optimize the result of the SRCA algorithm to re-connect the start and end nodes
7. Calculate each node position's value (this value is supposed to be the current best new node position)
8. In case of reaching max iteration, the algorithm must be terminated; if not, go to step 3.

When a dead node is detected, the pre-established backup node will execute the restoration strategy and initiate cooperation with the nearest node. If the backup node itself is dead, the restoration algorithm will move to the next backup node until a functional one is found. Before selection a backup node, it sends a message to its neighboring nodes, updating their neighbor information tables. When choosing the location for backup nodes, the communication areas of the backup node and its neighboring nodes should be considered. The goal is to optimize the backup node's position to maximize effective connectivity while estimating the presence of dead nodes. On detecting a dead node (failure) within its monitoring area, the backup node calculates the optimal destination coordinates to maximize local connectivity. This involves minimizing overlapping areas, and the coordinates corresponding to the minimum overlapping area function are determined. These calculated coordinates are considered the optimal position for the dead node, ensuring necessary connectivity for lifetime coverage. The SRCA algorithm supposes that heterogeneous nodes can decide their location with their neighbors. If the heterogeneous node is not equipped before the dead, it will need some time to react. In this way, the SRCA algorithm yields an ongoing relocation of mobile nodes if the failure occurs, guaranteeing connectivity and coverage with no wasted time. In general, the algorithm iterates the reconnection attempts for improved efficiency and systematically iterates different node positions. In addition, the algorithm provides robust failure handling by retrying alternative paths and positions when connectivity fails.

D. The ABC - SRCA Approach Pseudo Code

The ABC-SRCA approach outlines a multi-step process primarily focused on optimizing node deployment, coverage, and connectivity within a sensor network. The ABC-SRCA algorithm is designed to optimize the sensor nodes deployment in WSNs by iteratively refining node positions. Initially, nodes are randomly deployed, and their coverage areas are calculated based on a uniform detection range. A set of preliminary solutions is generated and evaluated, with bees performing neighborhood searches to improve solution quality. Solutions are selected based on fitness values, with a roulette selection method used to determine the probability of selection. In addition to optimizing coverage, the algorithm considers potential issues such as failed nodes and coverage holes by incorporating mechanisms to detect and address neglected solutions. Throughout the iterative process, the algorithm updates the best solution found so far, aiming to enhance WSN coverage and efficiency while mitigating deployment challenges. Termination occurs when a predefined criterion is met, at which point the best result is outputted. The pseudo code of this approach is introduced in the following:

Input: area covered by sensor node i. (A_covi), detection range of the sensor node (R), Set of all sensor nodes in the network (S), A sensor node in the set S (n), A candidate solution in the neighborhood search (new solution) (xij), modified candidate solution in the domain search (vij) Probability of selecting a solution, calculated based on its fitness (pi).

Step 1: initialize running time measurement

start_timer ()

record start time T_{start}

Step 2: random deployment Nodes using the post-deployment algorithm.

The optimal deployment distance selection is originally related to the plane area intensity. The following equation illustrates this intensity:

$$\varphi_i = \frac{N^2}{\sum_{i=1}^{n}\sum_{m=1}^{N} d_{im}} \tag{4}$$

Step 3: Nodes normally share their information with other sensor neighbors

Step 4: Sensor nodes usually communicate with each other

Step 5: Sensor field as accounted for in 2D

Step 6: Sensor nodes possess the same detection range

Step 7: Sensor Si is located at a particular point (x_i, y_i), for each point P the node coverage ratio is counted using

$$XR = \frac{A_{covi}}{R},\ n \in S \tag{5}$$

Step 8: For any point, the Euclidean distance

$$d\left(s_i, N\right) = \sqrt{(x_i - x)^2 + (y_i - y)^2} \tag{6}$$

Step 9: Randomly create (bee colony size) to perform as preliminary solutions, then match half of them with bees, calculate each solution's fitness value, and finally record the best solutions.

Step 10: repeat = 1.

Step 11: The honeybee performs a neighborhood search to yield a new solution v_{ij}, calculates its fitness value, *then do* the SRCA selection of x_{ij} and v_{ij}.

Step 12: Calculate the probability of selection pi related to xi.

Step 13: Select the solution with probability p_i using the roulette selection method, and then do a domain search to yield a new solution, calculate the fitness value, and *then do* the SRCA choice of x_{ij} and v_{ij}.

Step 14: Determine if a solution to be neglected is available. If so, use equation (3) to do a random search to produce a new solution that will be used instead of the old one.

Step 15: Determine the best of all solutions yet.

Step 16: Repeat = repeat + 1, if *cycle* < SRCA; after that go to step 8 or output the best result.

Step 17: The ABC-SRCA algorithm normally updates its location under the node-finding process.

Step 18: running time measurement

end_timer (), record end time T_{end}, compute and record running time for current sensor node count

Step 19: output the best solution and running_time for the current sensor node configuration

This approach incorporates deployment and optimization, guaranteeing robust coverage and connectivity by starting with a random deployment and then using ABC and SRCA algorithms to optimize node positions. It uses probabilistic selection to explore various solutions, making the approach adaptive to diverse scenarios. Moreover, it can handle many nodes (scalable) due to ABC's iterative and probabilistic nature.

V. Performance Metric

Evaluation of the proposed approach requires covering more aspects and provides better insight into its overall performance. This study used the following performance metrics:

- Energy Consumption

Efficient energy use is vital for extending the network's operational lifetime. Since the sensor energy is limited, it is required to reduce sensor motion. The following equation is used to calculate the energy consumption for sensor n moving from point a to point b is calculated by (Guo and Jafarkhani, 2019):

$$En\ (a,b) = \theta n \parallel b-a \parallel \tag{7}$$

Where θn is the energy cost per unit distance for moving node n to a new position. The term ‖b-a‖ denotes the Euclidean distance between the initial locations and the final destination, which represents the energy needed to move or communicate between the nodes.

- Connectivity

The WSNs connectivity refers to the ability of each sensor node to find a path to reach the selected sink node. If no route is available, the sink node cannot process the data collected by that node. The connectivity represents the ability of nodes to communicate.

- Coverage

The sensor network coverage refers to the ability of sensors to monitor the field of interest. The metric measures network sensing capability. Coverage in ABC-SRCA is the measure of the duration and extent for which the sensors can monitor the field of interest.

- Scalability

The approach's performance is tested on two different area scales with varying numbers of nodes, which may reflect its efficiency in larger or real-world deployments.

- Running Time

Running or processing time in WSNs denotes the duration for algorithms to perform tasks such as node deployment, coverage optimization, and energy management. It relies on the sensor node number, network size, and algorithm complexity. Evaluating the running time of the research approach is done using the MATLAB.

VI. Results And Analysis

The experimental procedure is performed by installing MATLAB version R2020 on a pc with Intel@ Core i7-3770 CPU@3.40GHz and 16GB RAM. A WSN square area 100 m × 100 m is considered, where 50 wireless sensor nodes were deployed to monitor the area. The sensing radius is 10m. The overall performance concerning coverage, and connectivity of ABC algorithms and the ABC-SRCA approach is compared. The outcomes are recorded in Tables II-IV. MATLAB is used for implementing and simulating the ABC-SRCA optimization approach because it can address complex mathematical calculations and algorithms, making it well-suited. Simulation is a necessary first step in evaluating the approach's feasibility and outcomes in a controlled environment before testing it in real-world conditions.

Table II and Fig. 2 display the results of the connectivity between sensor nodes that employ an isolated node localization model considering different node numbers. The results show that the actual connectivity error detection rates using the proposed ABC-SRCA approach are better for the different number of deployment nodes regardless the inconsistency in the error detection rate of the approach. An increased error detection rate with more nodes indicates improved network coverage and monitoring capabilities. However, it may indicate inefficiencies such as false positives, network congestion, or redundancy in error reporting (Adday, et al., 2022) The SRCA and ABC-SRCA dynamically adjust reallocation and transmission power based on node density. A higher node count leads to reducing errors per node probability, increasing the approach ability to correct coverage gaps and optimize deployment. This leads to a lower percentage of errors despite a larger network. However, increased sensor numbers can increase interference and data collisions, overlapping, communication overhead, scalability challenges, and sudden node failures, which may negatively affect the overall error detection rate.

Table III and Fig. 3 show that the proposed approach achieves better coverage accuracy (how accurately nodes deployed with how much coverage) on different sizes of ROI for various node numbers compared with the ABC and SRCA. The proposed approach revealed promising results in optimizing sensor node placement, leading to improved coverage of the target area. However, the approach's coverage accuracy can vary depending on problem formulation, network topology, and implementation details; additionally, proper parameter tuning and optimization strategy selection are critical for optimal results.

Table IV introduces a comparison between the proposed approach and previous studies in similar scenario including the same number of nodes and the same deployed area. The first study was (Yue, Cao, and Luo, 2019), who presented an improved ABC algorithm (IABC) and compared its coverage performance with GA and the Random Distribution Algorithm (RDA). The study deployed different sensor nodes within a 200 m × 200 m area. The second study is the study of (Wang, et al., 2018), who introduced a sensing radius adaptive coverage control algorithm (SRACC) and compared it with the particle swarm optimization and Voronoi diagram (PSO-VD). The study deployed different sensor nodes within a 100 m × 100 m area. The ABC-SRCA approach combines the strengths of the ABC and SRCA algorithms to enhance network coverage and connectivity. The efficacy of this combination is shown through the comparative analysis with other hybrid approaches, such as ABC-GA and ABC-PSO. Table IV reveals that the ABC-SRCA approach accomplishes the best coverage accuracy, reaching up to 97.89% in a 200 m × 200 m area and 98.05% in a 100 m ×100 m area. These results demonstrate that the ABC-SRCA approach exceeds the Improved ABC Algorithm (IABC), Genetic Algorithm (GA), Random Distribution Algorithm (RDA), SRACC, and PSO-VD in terms of coverage accuracy. The higher coverage accuracy attained by ABC-SRCA underscores its efficacy in optimizing sensor node placement and sustaining network

TABLE II
Connectivity Error Detection of the Proposed Approach

No. of nodes considered	Error detection rate		
	ABC (%)	SRCA (%)	ABC-SRCA (%)
10	16.6	19.6	26.9
20	15.85	18.85	27.61
30	14.8	16.8	26.41
40	13.69	15.69	25.9
50	12.98	14.98	27.93

ABC: Artificial bee colony, SRCA: Sequential re-connectivity and coverage algorithm

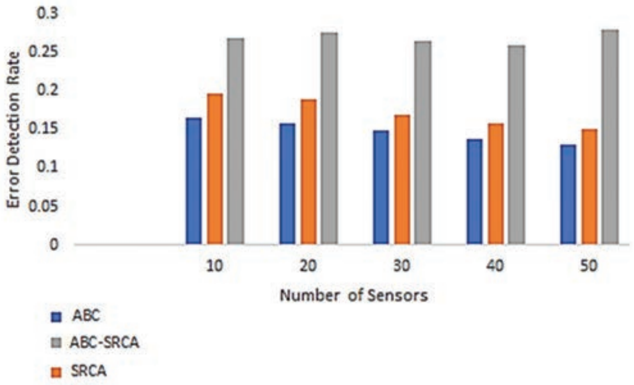

Fig. 2. Error detection rate.

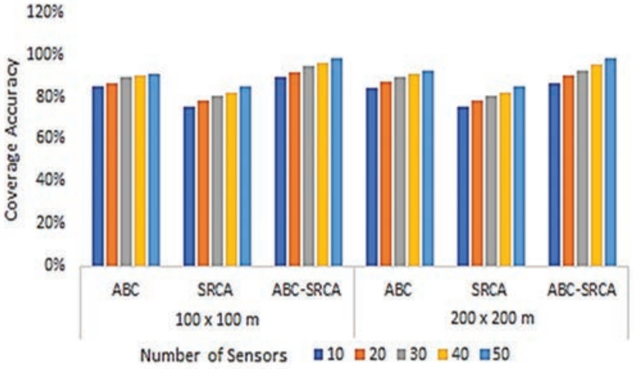

Fig. 3. Coverage accuracy of artificial bee colony-sequential re-connectivity and coverage algorithm in different areas.

TABLE III
Coverage Accuracy of the Proposed Approach

Number of deployed nodes	Research approach					
	100×100 m			200×200 m		
	ABC (%)	SRCA (%)	ABC-SRCA (%)	ABC (%)	SRCA (%)	ABC-SRCA (%)
10	85	75	89	84.00	75.00	86.44
20	86	78	91.23	87.00	78.00	90.33
30	89	80	94.12	89.00	80.00	92.42
40	90	82	96.10	91.00	82.00	95.22
50	91	85	98.05	92.00	85.00	97.89

ABC: Artificial bee colony, SRCA: Sequential re-connectivity and coverage algorithm

TABLE IV
Comparison of Coverage Accuracies

Deployed nodes number	Coverage accuracy				Coverage accuracy		
	Research approach 200×200 m	(Yue, Cao and Luo, 2019) 200×200 m			Research approach 100×100 m	(Wang, et al., 2018) 100×100 m	
	ABC-SRCA approach (%)	Improved ABC algorithm (%)	Genetic algorithm (%)	Random distribution algorithm (%)	ABC-SRCA algorithm (%)	SRACC (%)	PSO-VD (%)
10	86.44	54	54	43	89.00	-	
20	90.33	76	67	57	91.23	-	
30	92.42	85	76	64	94.12	37	34
40	95.22	93	86	67	96.10	77	69
50	97.89	96	91	72	98.05	85	80

ABC: Artificial bee colony, SRCA: Sequential re-connectivity and coverage algorithm, SRACC: Sensing radius adaptive coverage control, PSO-VD: Particle Swarm Optimization Voronoi Diagram

connectivity, making it a proper solution for WSNs compared to other hybrid combinations.

The comparison results in Fig. 4 reveal that the ABC-SRCA significantly outperforms the other algorithms in attaining better coverage by employing various node numbers deployed in area 200 m × 200 m. The ABC-SRCA steadily attains the highest coverage accuracy, starting at 86.44% (10 nodes) and reaching 97.89% (50 nodes), outperforming all other approaches.

The comparison results in Fig. 5 show that the ABC-SRCA achieves better coverage accuracy for various nodes number deployed in Area 100 m × 100 m. The ABC-SRCA achieves the highest accuracy in this smaller area, reaching 98.05% at 50 nodes.

Table V and Fig. 6 show that the energy consumption scales linearly with the number of nodes due to the complexity of interactions and connectivity maintenance. The 200 m × 200 m area consumes more energy due to higher transmission distances and communication overhead.

To evaluate the energy efficiency of the research approach, it is compared with other algorithms in 100 m × 100 m area and the results are introduced in the Table VI.

Table VI and Fig. 7 show that the ABC-SRCA approach consumes 11J of energy, which is lower than PSO (14J) and PSO-VD (12J) but slightly higher than SRACC (10J). The ABC-SRCA approach consumes slightly more energy (I J) because it ensures high coverage and connectivity and manages dead nodes, which is not considered by other algorithms. This indicates the extra processes conducted by the hybrid algorithm do not cause extra resource consumption. The approach attains its objectives without significantly increasing energy usage, as energy efficiency is a critical factor in WSN design and operation.

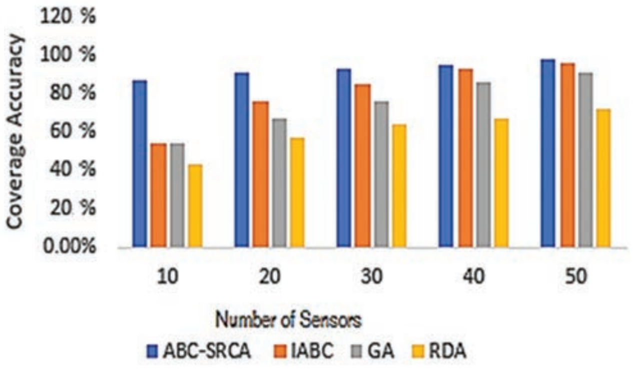

Fig. 4. Comparison of coverage accuracy in area 200 m × 200 m.

The ABC-SRCA can be considered real-time if the computation time for determining node placement and maintaining network connectivity is evaluated. Table VII introduces the computation times for different numbers of deployed nodes.

Table VII and Fig. 8 show that the running time increases as the number of sensor nodes increases, which is expected. The larger area (200 m × 200 m) consistently shows a longer running time compared to the smaller area (100 m × 100 m). This indicates that the size of the area impacts the running time, even with the same number of sensor nodes. The growth in running time appears to be roughly linear for both areas, but the larger area exhibits a slightly higher rate of increase. This is due to several reasons. First reason is due increases the number of sensor nodes, which increases the complexity

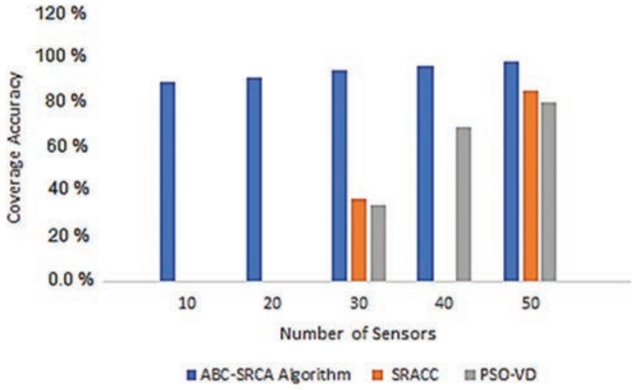

Fig. 5. Comparison of coverage accuracy in area 100 m × 100 m.

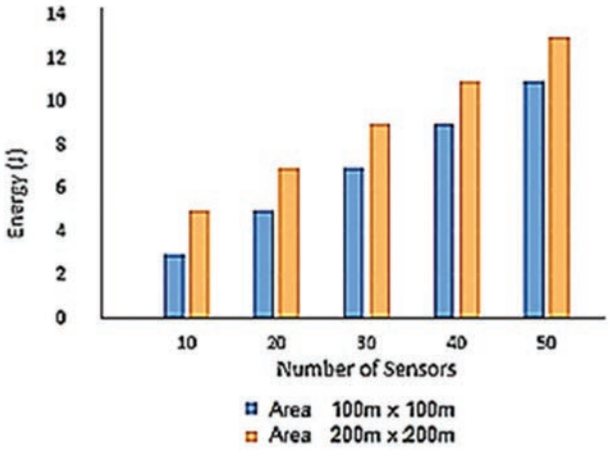

Fig. 6. Artificial bee colony-sequential re-connectivity and coverage algorithm energy consumption.

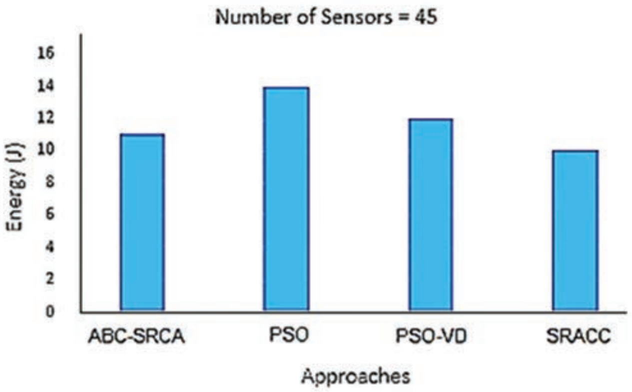

Fig. 7. Energy consumption comparison.

of managing and coordinating these nodes. Second reason is increasing distance between nodes leading to longer communication paths and increased latency. Third reason is the propagation of signals. As signals are transmitted over longer distances, their strength can decrease, requiring more time and possibly causing them to be retransmitted. Forth reason is the increase volume of data which requires more processing time.

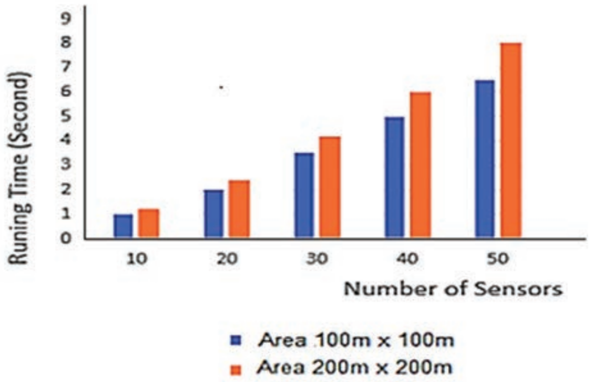

Fig. 8. Running time of artificial bee colony-sequential re-connectivity and coverage algorithm.

TABLE V
Energy Consumption for ABC-SRCA

Number of nodes	Hybrid ABC-SRCA energy (J) 100 m×100 m	Hybrid ABC-SRCA energy (J) 200 m×200 m
10	3	5
20	5	7
30	7	9
40	9	11
50	11	13

ABC: Artificial bee colony, SRCA: Sequential re-connectivity and coverage algorithm

TABLE VI
Energy Consumption Comparison for Area 100 m×100 m

Number of Nodes	Research approach	Wang, et al., 2018		
	ABC-SRCA energy (J)	PSO Energy (J)	PSO-VD energy (J)	SRACC energy (J)
45	11	14	12	10

ABC: Artificial bee colony, SRCA: Sequential re-connectivity and coverage algorithm, PSO-VD: Particle Swarm Optimization Voronoi Diagram

TABLE VII
ABC-SRCA Running Times

Number of sensor nodes	Running time (Second)	
	Area 100 m×100 m	Area 200 m×200 m
10	1	1.2
20	2	2.4
30	3.5	4.2
40	5	6
50	6.5	8

ABC: Artificial bee colony, SRCA: Sequential re-connectivity and coverage algorithm

VII. Discussion

The research approach integrates ABC's strength for coverage optimization and SRCA's strength for connectivity recovery. This integration ensures that the network remains robust and adaptive to dynamic changes, such as node failures or environmental interference. The ABC algorithm performs well in exploration and exploitation, making it well-suited to optimizing sensor node placement. However, it can get stuck in local optima. By integrating SRCA, this limitation is handled by introducing a sequential mechanism to dynamically adjust transmission ranges and reconnect nodes, ensuring global optimization. The study results indicate the efficacy of the hybrid ABC-SRCA approach in improving coverage and connectivity in WSNs compared to other techniques. The GA often suffers from slow and slow convergence to local optima, particularly in dynamic environments like WSNs. The SRACC is focuses on energy and coverage but lacks reliable mechanisms for handling dead nodes or dynamic network changes. The PSO is simple and has fast convergence but does not cope with maintaining a diversity of solutions, leading to suboptimal coverage in complex WSNs. The ABC-SRCA approach, with its adaptive nature and sequential re-connectivity mechanism, addresses these issues by dynamically adjusting node positions and transmission ranges, ensuring better performance in real-time scenarios.

The results show that the research approach consistently surpassed the ABC and the SRCA algorithms, as well as other existent techniques such as GA and SRACC. The approach attained up to 98% coverage accuracy, particularly higher than other algorithms, which implies its robustness in optimizing sensor node placement and sustaining network performance. In addition, the ABC-SRCA approach reduced the connectivity error detection rate by approximately 25%, underscoring its ability to keep reliable communication paths even in dead nodes' presence. The analysis of energy consumption showed that while the ABC-SRCA approach consumes slightly more energy than SRACC, it is more efficient than PSO and PSO-VD. The approach exhibits a balanced trade-off between network performance and energy efficiency. The approach linear scalability concerning the node number and area size further highlights its usefulness for large-scale deployments. In general, the hybrid ABC-SRCA approach significantly contributes to the WSN field by proposing a vigorous, adaptive, and efficient solution for confirming optimal coverage and connectivity, thereby reinforcing the WSN's successful deployment in various applications.

VIII. Conclusion and Future Direction

Sensing and connectivity are crucial and essential features of WSN. The quality of a sensor's coverage is known through how well it monitors the area of interest where the sensors are placed. Nodes' connectivity measures their capability to communicate with each other. The proposed ABC-SRCA approach has been employed to maintain the sensing range and monitor the movement of deployed nodes to prevent failed nodes from re-connecting and jointly enhance coverage connectivity. The proposed approach has shown promise in addressing optimization challenges in WSNs, particularly regarding coverage and re-connectivity with dead nodes. The approach offers optimization capabilities, adaptability to changing network conditions, and scalability for large-scale sensor networks. The advantage of this approach lies in its capacity to calculate the distance and value of neighboring nodes, coverage, and connectivity to control the message between the sensing range and the newly covered area. Finally, the suggested approach can efficiently maintain the detection of coverage sensing nodes within the radius by expanding the sensing range of the selected node. To evaluate the performance of the proposed approach, we compare its performance results with algorithms in terms of accuracy, average energy consumption, and running time, and it shows promising results. However, there are limitations regarding parameter tuning, convergence speed, and sensitivity to problem formulation. Future directions include more research to improve the efficiency and performance of the approach. Researchers' contribution to this collaborative effort is highly valued.

References

Abdulzahra, A.M.K., Al-Qurabat, A.K.M., and Abdulzahra, S.A., 2023. Optimizing energy consumption in WSN-based IoT using unequal clustering and sleep scheduling methods. *Internet of Things*, 22, p.100765.

Adday, G.H., Subramaniam, S.K., Zukarnain, Z.A., and Samian, N., 2022. Fault tolerance structures in wireless sensor networks (WSNs): Survey, classification, and future directions. *Sensors* (*Basel*), *22*(16), p.6041.

Adu-Manu, K.S., Engmann, F., Sarfo-Kantanka, G., Baiden, G.E., and Dulemordzi, B.A., 2022. WSN protocols and security challenges for environmental monitoring applications: A survey. *Journal of Sensors*, 2022(1), p.1628537.

Al-Fuhaidi, B., Mohsen, A.M., Ghazi, A., and Yousef, W.M., 2020. An efficient deployment model for maximizing coverage of heterogeneous wireless sensor network based on harmony search algorithm. *Journal of Sensors*, 2020(1), p.8818826.

Aljubori, M.H.H., Khalilpour Akram, V., and Challenger, M., 2022. Improving the deployment of WSNs by localized detection of covered redundant nodes in industry 4.0 applications. *Sensors* (*Basel*), 22(3), p.942.

Amer, D.A., Soliman, S.A., Hassan, A.F., and Zamel, A.A., 2024. Enhancing connectivity and coverage in wireless sensor networks: A hybrid comprehensive learning-Fick's algorithm with particle swarm optimization for router node placement. *Neural Computing and Applications*, 36(34), pp.21671-21702.

Baradaran, A.A., and Navi, K., 2020. HQCA-WSN: High-quality clustering algorithm and optimal cluster head selection using fuzzy logic in wireless sensor networks. *Fuzzy Sets and Systems*, 389, pp.114-144.

Bhat, S.J., and Santhosh, K.V., 2022. A localization and deployment model for wireless sensor networks using arithmetic optimization algorithm. *Peer-to-Peer Networking and Applications*, 15(3), pp.1473-1485.

Das, S., and Debbarma, M.K., 2023. CHPT: An improved coverage-hole patching technique based on tree-center in wireless sensor networks. *Journal of Ambient Intelligence and Humanized Computing*, 14, pp.5873-5884.

Guo, J., and Jafarkhani, H., 2019. Movement-efficient sensor deployment in wireless sensor networks with limited communication range. *IEEE Transactions on Wireless Communications*, 18(7), pp.3469-3484.

Guo, J., Sun, Y., Liu, T., Li, Y., and Fei, T., 2025. An optimization coverage strategy for wireless sensor network nodes based on path loss and false alarm probability. *Sensors* (*Basel*), 25(2), p.396.

Gutiérrez, S., and Ponce, H., 2019. An intelligent failure detection on a wireless sensor network for indoor climate conditions. *Sensors* (*Basel*), 19(4), p.854.

Jain, J.K., 2020. A coherent approach for dynamic cluster-based routing and coverage hole detection and recovery in bi-layered WSN-IoT. *Wireless Personal Communications*, 114(1), pp.519-543.

Khatir, S., Tiachacht, S., Le Thanh, C., Ghandourah, E., Mirjalili, S., and Wahab, M.A., 2021. An improved artificial neural network using arithmetic optimization algorithm for damage assessment in FGM composite plates. *Composite Structures*, 273, p.114287.

Khedr, A.M., Osamy, W., and Salim, A., 2018. Distributed coverage hole detection and recovery scheme for heterogeneous wireless sensor networks. *Computer Communications*, 124, pp.61-75.

Kuthadi, V.M., Selvaraj, R., Baskar, S., Shakeel, P.M., and Ranjan, A., 2022. Optimized energy management model on data distributing framework of wireless sensor network in IoT system. *Wireless Personal Communications*, 127(2), pp.1377-1403.

Lai, Y.H., Cheong, S.H., Zhang, H., and Si, Y.W., 2022. Coverage hole detection in WSN with force-directed algorithm and transfer learning. *Applied Intelligence*, 52(5), pp.5435-5456.

Ling, H., Zhu, T., He, W., Luo, H., Wang, Q., and Jiang, Y., 2020. Coverage optimization of sensors under multiple constraints using the improved PSO algorithm. *Mathematical Problems in Engineering*, 2020(1), p.8820907.

Lu, X., Wei, Y., Wu, Q., Yang, C., Li, D., Zhang, L., and Zhou, Y., 2022. A coverage hole patching algorithm for heterogeneous wireless sensor networks. *Electronics*, 11(21), p.3563.

Lu, Z., Wang, C., Wang, P., and Xu, W., 2025. 3D deployment optimization of wireless sensor networks for heterogeneous functional nodes. *Sensors* (*Basel*), 25(5), p.1366.

Satyanarayana, P., Mahalakshmi, T., Sivakami, R., Alahmari, S.A., Rajeyyagari, S., and Asadi, S. 2023. A new algorithm for detection of nodes failures and enhancement of network coverage and energy usage in wireless sensor networks. *Materials Today: Proceedings*, 80, pp.1717-1722.

Siamantas, G., and Kandris, D., 2024. Particle swarm optimization for k-coverage and 1-connectivity in wireless sensor networks. *Electronics*, 13(23), p.4841.

Velavalapalli, V.S., Ramamurthy, A., and Satyanarayana, G.M., 2024. Detection and correction of node failures in wireless sensor networks. *International Journal of Gender, Science and Technology*, 13(2), pp.1-6.

Wang, J., Ju, C., Gao, Y., Sangaiah, A.K., and Kim, G.J., 2018. A PSO based energy efficient coverage control algorithm for wireless sensor networks. *Computers, Materials and Continua*, 56(3), pp.433-446.

Wang, S., Wang, Y., Li, D., and Zhao, Q., 2023. Distributed relative localization algorithms for multi-robot networks: A survey. *Sensors* (*Basel*), 23(5), p.2399.

Wang, Z., Tian, L., Wu, W., Lin, L., Li, Z., and Tong, Y., 2022. A metaheuristic algorithm for coverage enhancement of wireless sensor networks. *Wireless Communications and Mobile Computing*, 2022(1), p.7732989.

Yan, F., Ma, W., Shen, F., Xia, W., and Shen, L., 2020. Connectivity based k-coverage hole detection in wireless sensor networks. *Mobile Networks and Applications*, 25, pp.783-793.

Yue, Y., Cao, L., and Luo, Z., 2019. Hybrid artificial bee colony algorithm for improving the coverage and connectivity of wireless sensor networks. *Wireless Personal Communications*, 108, pp.1719-1732.

Zeng, C., Qin, T., Tan, W., Lin, C., Zhu, Z., Yang, J., and Yuan, S., 2023. Coverage optimization of heterogeneous wireless sensor network based on improved wild horse optimizer. *Biomimetics* (*Basel*), 8(1), p.70.

Zhang, D.G., Chen, L., Zhang, J., Chen, J., Zhang, T., Tang, Y.M., and Qiu, J.N., 2020a. A multi-path routing protocol based on link lifetime and energy consumption prediction for mobile edge computing. *IEEE Access*, 8, pp.69058-69071.

Zhang, J., Chu, H., and Feng, X., 2020b. Efficient coverage hole detection algorithm based on the simplified rips complex in wireless sensor networks. *Journal of Sensors*, 2020(1), p.3236970.

Molecular Analysis and Genotyping of Drug-Resistant *Acinetobacter baumannii* Isolates from Clinical Specimens

Sirwan M. Muhammed Ameen† and Aram H. Rasool

Department of Biology, College of Science, University of Sulaimani,
Sulaymaniyah, Kurdistan Region, F.R. Iraq

***Abstract*—*Acinetobacter baumannii* is a globally concerning hospital infection because it has developed resistance to many antibiotics, including last-resort carbapenems. In this study, 46 non-duplicate *A. baumannii* isolates from hospitalized patients are identified by the Phoenix BD Diagnostic System, which are used for bacterial identification and antimicrobial susceptibility profiles. Various clinical specimens, including endotracheal aspiration, urine, wound, blood, burns, and cerebrospinal fluid, were collected between 2023 and 2024 at different hospital wards. To provide further understanding of the epidemiology of multidrug-resistant (MDR) *A. baumannii* isolates, this study attempts to; (1) utilize enterobacterial repetitive intergenic consensus polymerase chain reaction (ERIC-PCR) DNA fingerprinting to estimate genetic diversity, which reveals a significant level of genetic relationship is established amongst *A. baumannii* isolates from hospitalized patients, suggesting cross-transmission, and (2) clarifies the genetic characteristics of the antimicrobial resistance profiles contributing to the antibiotics widely used for MDR *A. baumannii* isolates. All isolates are classified as MDR (54.3%), extensively drug-resistant (39.1%), and pandrug-resistant (6.5%). According to Clinical and Laboratory Standards Institute-2024 standards, 93.4% and 91.3% of isolates are resistant to meropenem and imipenem, respectively, while colistin and tigecycline are the most effective antibiotics. Furthermore, the most common of the genes present among clinical isolates are *blaOXA-51* (100%) and *pmrC* (97.80%), while the less common detected genes are *blaIMP* (0.0%) and *blaOXA-58* (46%). ERIC-PCR could provide a rapid and dependable scheme to recognize clonal relationships among isolates from a multiplicity of clinical samples. Controlling endemic *A. baumannii* strains, particularly in intensive care unit settings, is essential.**

***Index Terms*: *Acinetobacter baumannii,* Antibiotic resistance gene, Enterobacterial repetitive intergenic consensus polymerase chain reaction, Extensively drug-resistant, Multidrug-resistant, Pan drug-resistant**

ARO-The Scientific Journal of Koya University
Vol. XIII, No.1 (2025), Article ID: ARO.12052. 9 pages
Doi: 10.14500/aro.12052
Received: 13 December 2024; Accepted: 25 March 2025
Regular research paper; Published: 27 April 2025

†Corresponding author's e-mail: sirwan.muhammed@univsul.edu.iq

I. Introduction

Acinetobacter baumannii (*A. baumannii*) has been identified as a highly concerning nosocomial pathogen on a worldwide scale. Being one of the most successful multidrug-resistant (MDR) organisms endangering modern antibiotic treatment, its remarkable ability to acquire or upregulate multiple resistance determinants has been a major issue in its clinical relevance (Ali, Al-Haideri, and Al Hishimi, 2022; Kyriakidis, et al., 2021). In addition to this intriguing development of resistance, *A. baumannii* has a variety of survival mechanisms that allow it to thrive in a variety of settings, increasing its potential to spread across hospitals (Sehree, Al-Kaysi and Abdullah, 2023; Shayea and Ali, 2022). The World Health Organization considers *A. baumannii* to be a critical priority pathogen, indicating that it represents a major threat to human health and that new medicines are desperately needed (Tagliabue and Rappuoli, 2018).

Increased proof of *A. baumannii* isolates that are both extensively drug-resistant (XDR) and pan-drug-resistant (PDR) is also emerging in multiple countries (Assimakopoulos, et al., 2019; Saelim, et al., 2018). The necessity to learn more about and assess the pathogen's mechanisms of antibiotic resistance as well as illness consequences for clinical and public health reasons is evident. There is now more interest in using colistin (CL) because of the quick development of *A. baumannii* resistance to most antibiotics, including carbapenems. At present, polymyxin resistance in *A. baumannii* is on the rise (Kumburu, et al., 2019; Abbasi, Hajihashemi and Shokri, 2024). Polymyxins have an amphipathic structure, cationic properties, and primarily react with the negative charge of the lipid a component of lipopolysaccharide (LPS). Controlled addition of positively charged residues, such as phosphoethanolamine (PetN) to LPS, diminishes negative charge on the bacterial surface and subsequently inhibits the adhesion of the polymyxin to the LPS (Moffatt, Harper and Boyce, 2019). *A. baumannii's* resistance to CL was initially chromosomal and is related to alterations in the *pmrCAB* operon, which limits its fast dissemination and distribution (Lima, et al., 2018). PetN transferase is encoded by the *pmrC* gene, whereas a two-component system (TCS) is encoded by the *pmrA* and *pmrB* genes. Mutations in the *pmrAB* TCS system cause *pmrC* to be overexpressed, which modifies lipid A with PetN and results in CL resistance (Lima, et al., 2018; Trebosc, et al., 2019). Apparently, when *pmrAB* is mutated, *pmrC* expression rises, and this is linked to greater CL minimum inhibitory concentrations (MICs) (Abbasi, Hajihashemi and Shokri, 2024; Charretier, et al., 2018), which raises attention to the pathogen's strong propensity for spread and emphasizes the necessity to determine the true extent of CL resistance worldwide (Moubareck and Halat, 2020).

In infection control, various genotyping techniques have been established to better understand the clinical significance and epidemiological relationship among bacterial strains of *A. baumannii* outbreaks worldwide (Aljindan, Alsamman and Elhadi, 2018; Hamzah, 2018). Presently, biotyping and serotyping, as examples of phenotypic procedures, have now been replaced by molecular typing methods, including intragenic consensus Enterobacterial repetitive intergenic consensus polymerase chain reaction (ERIC-PCR) (Falah, Shokoohizadeh and Adabi, 2019). Repetitive sequences of the gene in *A. baumanni* are called symmetric elements and are often realized in the non-coding sequence of the DNA (Shayea and Ali, 2022). Concerning the variable length and number of these repeat sequences obtained for each isolate, some primers have been designed. The enterobacterial repetitive intergenic consensus (ERIC) amplicon's location and length are used as genetic indicators for the genotyping of *A. baumannii* according to the assortment of the bands (Falah, Shokoohizadeh and Adabi, 2019; Shayea and Ali, 2022).

In our domain, we have seen a significant increase in *A. baumannii* outbreak cases. Consequently, this study was directed to determine the ERIC-PCR DNA fingerprinting to clarify the epidemiology of MDR *A. baumannii* and the genetic characteristics of the antimicrobial resistance profiles contributing to the antibiotics widely used for MDR *A. baumannii* isolates.

II. Materials and Methods

A. Isolation and Identification of Bacterial Isolates

All 46 *A. baumannii* clinical isolates recovered from various clinical specimens, including endotracheal aspiration, urine, wound, blood, burns, and cerebrospinal fluid, between 2023 and 2024 at different hospitals in the Sulaymaniyah governorate, Iraq, were collected and identified using MacConkey agar, nutrient and blood base agar media (Himedia, India), *Acinetobacter* CHROMagar (CHROMagar, Paris, France), and Phoenix; BD Diagnostic Systems, Franklin Lakes, NJ, USA. Their final confirmation was performed by polymerase chain reaction (PCR) of the *blaOXA-51*-like gene, which is intrinsic to this species (Turton, et al., 2006). *blaOXA-51-negative* samples were excluded. The *A. baumannii* ATCC19606 was selected as a positive control. The isolates were then preserved in a Trypton Soy Broth medium (Himedia, India); 20% glycerol was added as a supplement and stored at −70°C until further analysis.

B. Antibiotic Susceptibility Test

MICs of 14 antibiotics: Ampicillin/sulbactam, piperacillin/tazobactam (P/T), Ceftazidime, cefepime (CEF), ceftriaxone (CTR), imipenem (IMP), meropenem (MER), amikacin (AK), CL, levofloxacin (LEV), ciprofloxacin, gentamicin (GEN), tigecycline (TIG), and trimethoprim-sulfamethoxazole (SXT) against *A. baumannii* isolates were determined using the ID/AST combo panel, NMIC/ID55 in (Phoenix; BD Diagnostic Systems, Franklin Lakes, NJ, USA). The MICs of all the antibiotics were interpreted by the aforementioned system according to the CLSI 2024 guidelines (*M100 Performance Standards for Antimicrobial*). Antimicrobial susceptibility of isolates was assessed applying the centers for disease control and prevention and European center for disease prevention and control definitions and categorized as MDR, XDR, and PDR antimicrobial categories (Alagna, et al., 2020).

C. ERIC-PCR Genotyping

To investigate the genetic variation and clonal relationships among isolates, specific ERIC-PCR primers and PCR conditions were achieved as displayed in "Table I" and used to determine the ERIC-type arrangements of isolates. The ERIC patterns and the dendrogram of isolates were analyzed by the XLSTAT software program.

D. PCR Screening for Antibiotic Resistance-Related Genes

The genomic DNA extraction of bacterial isolates was executed by the boiling method (Falah, Shokoohizadeh, and Adabi, 2019; Hou and Yang, 2015). All PCRs were executed in a final volume of 25 μL. Containing Taq Master Mix (addbio, Korea). Screening for the three groups of Oxacillinase (OXA)-type genes (*blaOXA-51*, *blaOXA-23*, and *blaOXA-58*) and Metallo Beta Lactamase (MBL) (*blaVIM*, *blaIMP, and blaNDM*), the isolates were also performed for CL Resistance *CoR* genes, *pmrCAB* (*pmrA, pmrB, and pmrC*), using primers and PCR conditions previously published in "Table I." 3 μL of *A. baumannii* whole DNA extract was used as a template for the PCR (10 μL of nuclease-free water, 10 μL of master mix ×2, and 1 μL per primer). In a thermocycler (Applied Biosystems, Singapore), a standard PCR amplification program was employed as follows: initial heating to 95°C for 5 min, followed by 30 cycles of amplification. Each cycle included three phases: denaturation at 95°C for 30 s, annealing at a proper temperature for 30 s, and extension at 72°C for the right time, tracked by 5 min at 72°C as a final elongation step. Finally, the PCR product was stored at 4°C until they were analyzed. To determine the elongation time, the length of the anticipated amplified DNA was utilized. A 1.5% agarose gel was used to electrophorese the PCR products, using ethidium bromide as a stain, and the results of the specific amplified target gene were visualized using a ultra-violet transilluminator (BIO-RAD, California, USA). Furthermore, Capillary Gel Electrophoresis, as an advanced technique, was used for the separation of PCR products, and DNA was detected by fluorescent labeling (QIAxcel Advanced, Germany).

TABLE I
Primer Sequences, Amplification Sizes, Annealing Temperatures, and Elongation Times of Antibiotic Resistance Genes in Clinical Isolates of *Acinetobacter baumannii*

Targeted genes	Primer sequences (5’-3’)	Product size (bp)	Annealing Temperature	Elongation time	References
blaOXA-51	F: TAATGCTTTGATCGGCCTTG R: TGGATTGCACTTCATCTTGG	353 bp	53°C	30 s	(Hou and Yang, 2015)
blaOXA-23	F: GATCGGATTGGAGAACCAGA R: ATTCTTGACCGCATTTCCAT	501 bp	53°C	40 s	(Hou and Yang, 2015)
blaOXA-58	F: AAGTATTGGGGCTTGTGCTG R: CCCCTCTGCGCTCTACATAC	599 bp	58°C	40 s	(Tawfeeq, et al., 2020)
blaIMP	F: GGAATAGAGTGGCTTAAYTCTC R: CCAAACYACTASGTTATCT	188 bp	53°C	30 s	(Poirel, et al., 2011)
blaNDM	F: CACCTCATGTTTGAATTCGCC R: CTCTGTCACATCGAAATCGC	984 bp	52°C	60 s	(Nordmann, et al., 2011)
blaVIM	F: GATGGTGTTTGGTCGCATA R: CGAATGCGCAGCACCAG	390 bp	55°C	40 s	(Poirel, et al., 2011)
pmrA	F: GATGGTTTAAATTTGGGTGCAGAT R: TTGACTCGCAAGTTGAGCTTCT	120 bp	58°C	45 sec	(Abbasi, Hajihashemi and Shokri, 2024)
pmrB	F: GCCATTATTCGTCGTGGTTTAAA R: GCGCTCAAAAAGACGGTTCA	150 bp	57°C	45 s	(Abbasi, Hajihashemi and Shokri, 2024)
pmrC	F: CCATTTGGCTAGGTGCAATTT R: CCGCATAATAGGTAGCAACAAG	132 bp	57°C	45 s	(Abbasi, Hajihashemi and Shokri, 2024)
ERIC	F: ATGTAAGCTCCTGGGGATTCAC R: AAGTAAGTGACTGGGGTGAGCG	Variable	53°C	30 s	(Aljindan, Alsamman and Elhadi, 2018)

ERIC: Enterobacterial repetitive intergenic consensus

E. Ethical Statement

The research proposal was submitted to the scientific and ethics committee of the College of Science, and official permission was obtained for sample collection from different hospitals in Sulaymaniyah City. After receiving assurances that their identities would remain anonymous, all patients agreed to participate in the trial.

F. Statistical Analysis

GraphPad Prism software version 10.0 (San Diego, CA, USA) was used to create percentages and frequencies for the variables.

III. Results

The identity of the isolates (n = 46) as *A. baumannii* was collected from hospitalized patients from different ward, intensive care unit (ICU) 26 (56.5%), followed by burn and plastic surgery and outpatient department 12 (26.0%), and 8 (17.39%), respectively, from clinical specimens as follows: 10 (21.73%) for each endotracheal aspirate (ETA), burn, and urine; wound 7 (15.21%); sputum 6 (13.04%); and 1 (2.17) for each blood, synovial fluid, and central venous line. The ages of the patients varied from 12 years to 81 years, with a mean of 46.4 years, comprising 20 males (43.47%) and 26 females (56.52%).

A. Antibiotic Susceptibility Test

The antibiotic susceptibilities of isolates are demonstrated in “Fig. 1.” All isolates were classified as MDR 25 (54.3%), XDR 18 (39.1%), and PDR 3 (6.5%). *A. baumannii* isolates have a high resistance rate to CEF, ceftazidime, and P/T (97.8%); LEV and CTR were both 95.6%. In addition to β-lactam medications, the isolates showed high resistance to the majority of antimicrobial medicines, including MER (93.4%), SXT (95.6%), and GEN (86.9%). The three most potent antibiotics were CL (6.5% resistance), TIG (54.4% susceptibility), and AK (82.7% susceptibility). Three isolates (6.5%), which were categorized as PDR, exhibited resistance to CL, with a MIC breakpoint of ≥ 4 mg/L (CLSI).

B. PCR Screening of Antibiotic Resistance Genes

PCR screening analysis was applied to detect genes responsible for class B MBL, OXA-type class D carbapenem hydrolyzing enzyme, and *pmrCAB* genes in *A. baumannii* isolates, like that seen in Fig. 2. The intrinsic β-lactamase *blaOXA-51* gene was found in all isolates, while *blaOXA-23* and *blaOXA-58* were found in 23 (50%) and 21 (45.6%) of isolates, respectively. Among the *MBL* genes, it was demonstrated that 28 (60.8%) were positive for *blaVIM* genes, and 40 (86.9%) of the isolates carried *blaNDM*, even though none of the isolates had *blaIMP*. Concerning CL resistance genes, *pmrA*, *pmrB*, and *pmrC* were detected in 36 (78.2%), 37 (80.4%), and 45 (97.8%) of the samples, respectively, as illustrated in Fig. 3.

C. Genotyping

The ERIC-PCR molecular typing method was applied to classify *A. baumannii* isolates. It formed 12 The typical range of DNA amplicon bands is <100–1500 bp. Clonal variation identified 28 different ERIC patterns (ERIC-type arrangements) categorized into three main phylogenetic classes (C1, C2, and C3), including 9 common types and 19 unique types with a similarity ≥95%. C1 was identified as the dominant class, with 22 (47.8%), including all three PDR isolates belonging to it. C3 18 (39.1%) contains 3 clusters and 11 unique types. While C2, as the smallest class, contains 6 (13.0%) with 1 cluster and 2 single isolates “Fig. 4.”

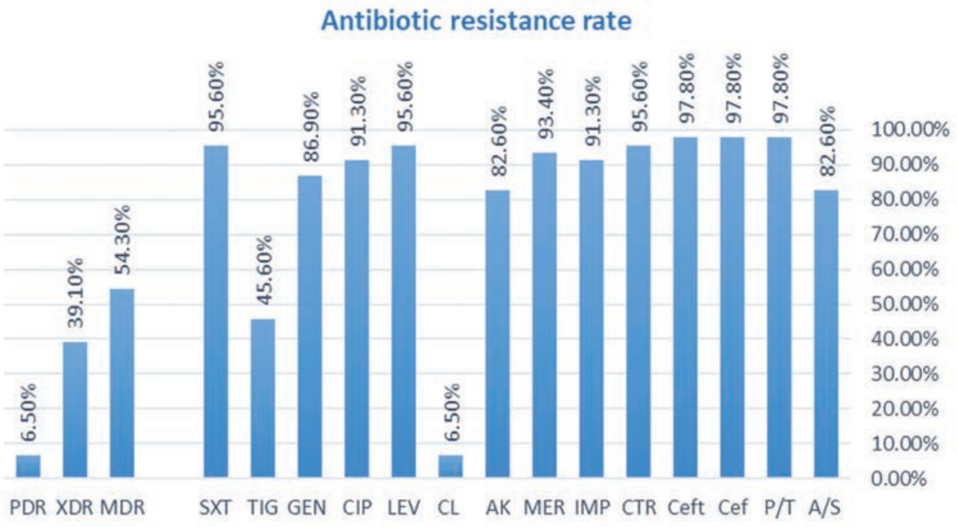

Fig. 1. Antibiotic resistance profiles of *Acinetobacter baumannii* isolates. MDR (54.3%) is Not susceptible to ≥1 agent in ≥3 antibiotic categories; XDR (39.1%) is susceptibility restricted to ≤2 categories; PDR (6.5%) refers to nonsusceptibility to all agents across all types of antimicrobials (Magiorakos, et al., 2012). The antibiotic susceptibility of *A. baumannii* isolates in this investigation. As a whole, the most prevalent resistance antibiotics were CEF, CEFT, and P/T (79.8%). The two most effective antibiotics were TIG (45.6%) and CL (6.5%). A/S: Ampicillin-sulbactam, P/T: Piperacillin/tazobactam, CEFT: Ceftazidime, CEF: Cefepime, MER: Meropenem, IMP: Imipenem, GEN: Gentamicin, AK: Amikacin, CIP: Ciprofloxacin, SXT: Trimethoprim-sulfamethoxazole, TIG: Tigecycline, and CL: Colistin, MDR: Multidrug-resistant, XDR: Extensively drug resistant, PDR: Pan drug resistant**.**

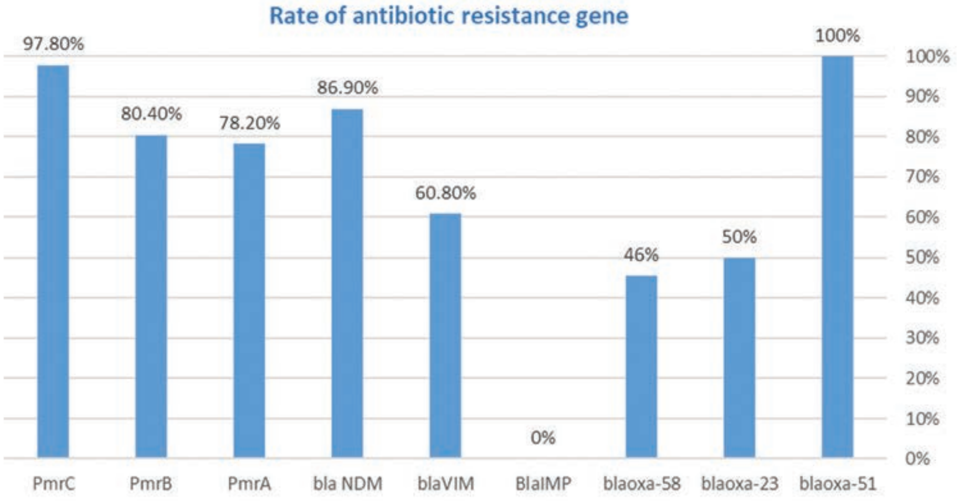

Fig. 2. Observation rate of screening antibiotic-resistant-related genes among *Acinetobacter baumannii* isolates.

IV. Discussion

The emergence of a harmful antibiotic-resistant *A. baumannii* strain is one of the most significant issues facing the healthcare system at that moment. In our investigation, 46 *A. baumannii* isolates were isolated in sputum, ETA, burns, urine, wounds, blood, and cerebrospinal fluid from patients with nosocomial infections, particularly in ICUs and burn and plastic surgery emergencies. Our outcomes show that most isolates obtained were from ETA and sputum, 16 (34.7%); this indicates that respiratory tract infections were the most common types of *A. baumannii* clinical isolates, followed by burn and wound 7 (15.21%) for each type. Our results matched those of other studies (Shayea and Ali, 2022; Smai and Ganjo, 2020; Chawsheen, Al-Naqshbandi and Abdulqader, 2020). Furthermore, our findings are in line with studies that show *A. baumannii* is the most prevalent member that is associated with hospital-acquired infections globally (Abban, et al., 2023; Jiang, et al., 2022). Previously restricted to medical settings, these species are now widespread throughout (Abduljabar and Mawlood, 2023; Shayea and Ali, 2022). Medical devices, including mechanical ventilation, intravascular catheterization, and endotracheal intubation, have all been linked to transmission and infections (Shayea and Ali, 2022; Smai and Ganjo, 2020). *A. baumannii* is particularly capable of surviving for a long time both in the hospital setting, mainly on inanimate surfaces, and in the hands of healthcare workers, which could lead to potential spread and the persistence of endemic bacterial strains in hospitals (Chapartegui-González, et al., 2018). In our region, like other regions of the world, *A. baumannii* is one of the bacteria involved in hospital infections leading to several health issues for hospitalized patients.

Clinical isolates of *A. baumannii* were sensitive to common antibiotics, including ampicillin, GEN, chloramphenicol, and nalidixic acid, throughout the 1970s. After that, it became an important nosocomial pathogen, mainly attributed to the use of broad-spectrum antibiotics in hospitals (Towner, 2009). It now exhibits resistance to almost all first-line antibiotics. The only antibiotics that remain effective against MDR *A. baumannii* are CL; nevertheless, CL-resistant strains of *A. baumannii* have been identified in various regions of the world (Abduljabar and Mawlood, 2023; Novović and Jovčić, 2023a). The results of our research indicate *A. baumannii* isolates established resistance to the most commonly administered antimicrobial drugs, including extended-spectrum penicillin, in combination with beta lactamase inhibitors, cephalosporins, aminoglycosides, fluoroquinolones, and carbapenems. The isolates were then classified into three classes based on their antibiotic resistance pattern: MDR 25/46 (54.30%), XDR 18/46 (39.10%), and PDR 3/46 (6.50%). According to our findings**,** this is comparable to recent studies carried out in nearby places in Erbil and Baghdad cities (Abduljabar and Mawlood, 2023; Shayea and Ali, 2022; Al-Kadmy, et al., 2018). This indicates that *endime* possesses many resistance mechanisms, including target alterations, multidrug efflux pumps, permeability defects, and enzymatic drug degradation, which allow the bacteria to successfully evade the effects of the most commonly used antibacterial drugs (Lin and Lan, 2014; Vázquez-López, et al., 2020). Furthermore, our findings highlight the importance and severity of XDR in *A. baumannii*, especially in ICU patients, as the majority of the isolates tested displayed resistance to antibacterial drugs. Carbapenem resistance was high (93%) in our finding; this result shows the elevated likelihood of carbapenem treatment failure in *A. baumannii* infections and is in line with global reports (Müller, et al., 2023; Rezaei, et al., 2018).

Different molecular methods have exposed genotypic assortment to path the prevalence and progression of MDR bacteria, including PFGE, MLST, MLVA, and ERIC-PCR (Khalid, 2024; Falah, Shokoohizadeh and Adabi, 2019; Fattouh and El-Din, 2014). Within *A. baumannii*, ERIC-PCR was utilized in our study. All forty-six *A. baumannii* isolates were typed using ERIC-PCR. Three classes (C1, C2, and C3) with 9 common cluster types of *A. baumannii* isolates with high relatedness or genetic similarity and a high degree of DNA fingerprints among strains of *A. baumannii* (95%) were isolated from the same period and situation, demonstrating that epidemiological connection has an impact on *A. baumannii* strain clustering; this shows cross-transmission occurred among infectious isolates, as shown by this result. The conclusions of this finding agree with those of previous studies (Shayea and Ali, 2022; Aljindan, Alsamman and Elhadi, 2018). Our results indicate that the ERIC-PCR approach is a fast and accurate way to show the clonal relatedness of *A. baumannii* recovered from a spectrum of samples isolated from a variety of patients. As a result, this genotyping method is more quick, suitable, and less expensive than other genotyping approaches.

Genes encoding selected antibiotic resistance (*blaOXA-51*, *blaOXA-23*, *blaOXA-58*, *blaVIM*, *blaNDM*, and *pmrCAB*) were detected using PCR techniques, are shown in "Fig. 3." The results of this study demonstrated that all isolates of *A. baumannii* possess *blaOXA-51* by 100% as an intrinsic gene (Evans, 2009). The existence of blaOXA-51 has limited carbapenemase activity, but when this gene is overexpressed, it displays significant carbapenemase activity. Overexpression can occur through several mechanisms, such as mutations or modifications in regulatory machines. An ISAba1 element

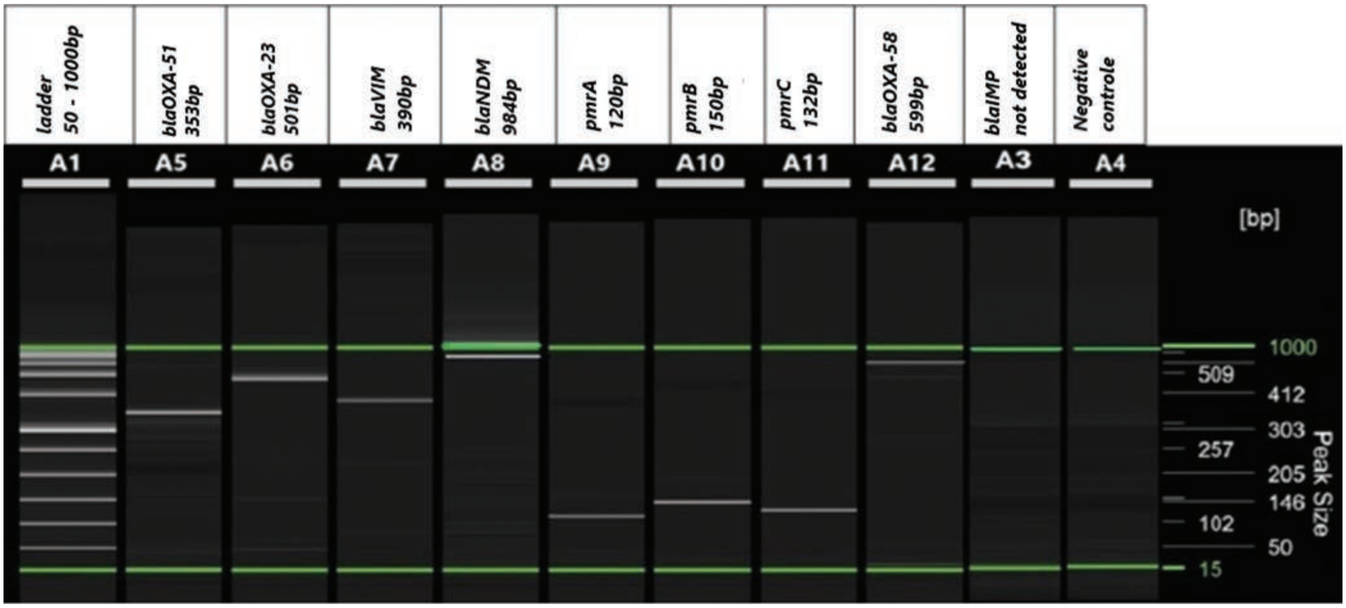

Fig. 3. Capillary gel electrophoresis (QIAGEN, Germany), showing the amplified product of antibiotic resistance-related genes. A1: ladder (50 bp–1000 bp); A5: *blaOXA-51* 353 bp; A6: *blaOXA-23* 501 bp; A7: *blaVIM* 390 bp; A8: *blaNDM* 984 bp; A9: *pmrA* 120 bp; A10: *pmrB* 150 bp; A11: *pmrC* 132 bp; A12: *blaOXA-58* 599 bp; A3: *blaIMP* not detected; A4: negative control.

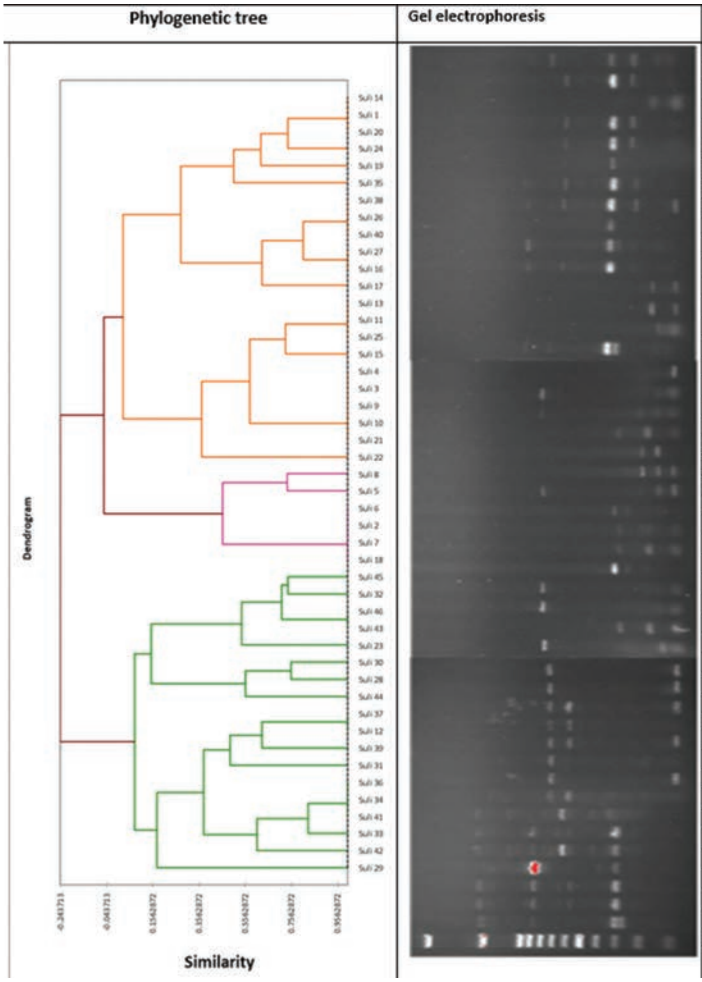

Isolate	Gen/ Age	Ward/Specimen	Pheno type	Resistance Gene
Suli14	F / 51	ICU / Wound	MDR	*blaoxa51, blaVIM, blaNDM, pmrC*
Suli1	F / 47	ICU/ETA	PDR	*blaoxa51, blaoxa23, blaVIM, blaNDM, pmrA, pmrB, pmrC*
Suli20	M / 13	Emergency / Burn	XDR	*blaoxa51, blaNDM, pmrA, pmrB, pmrC*
Suli24	M / 22	Emergency / Burn	MDR	*blaoxa51, pmrA, pmrB, pmrC*
Suli19	M / 41	ICU / ETA	MDR	*blaoxa51, blaNDM pmrA, pmrB, pmrC*
Suli35	M / 65	ICU / sputum	XDR	*blaoxa51, blaoxa23, blaVIM, blaNDM, pmrA, pmrB, pmrC*
Suli38	M / 78	ICU / sputum	XDR	*blaoxa51, blaoxa23, blaVIM, blaNDM, pmrA, pmrB, pmrC*
Suli26	M / 17	ICU / urine	MDR	*blaoxa51, blaNDM, pmrA, pmrB, pmrC*
Suli40	F / 81	ICU / CV line	MDR	*blaoxa51, blaoxa23, pmrA, pmrB, pmrC*
Suli27	F / 54	ICU/ ETA	XDR	*blaoxa51, blaNDM, pmrA, pmrB, pmrC*
Suli16	F / 61	ICU / ETA	MDR	*blaoxa51, blaNDM, pmrA, pmrB, pmrC*
Suli17	F / 58	ICU / Urine	PDR	*blaoxa51, blaNDM, pmrA, pmrB, pmrC*
Suli13	F / 41	Emergency / Burn	MDR	*blaoxa51, blaoxa23, blaVIM, blaNDM, pmrC*
Suli11	F / 61	ICU / ETA	MDR	*blaoxa51, blaoxa23, blaVIM, blaNDM, pmrC*
Suli25	F / 36	OPD / Urine	MDR	*blaoxa51, blaoxa23, blaVIM, blaNDM, pmrA, pmrB, pmrC*
Suli15	M / 51	ICU/ ETA	MDR	*blaoxa51, blaVIM, blaNDM, pmrC*
Suli4	F / 39	ICU / ETA	MDR	*blaoxa51, blaoxa23, blaVIM, blaNDM, pmrA, pmrB, pmrC*
Suli3	M / 63	ICU/ ETA	XDR	*blaoxa51, blaoxa23, blaVIM, blaNDM, pmrA, pmrB, pmrC*
Suli9	M / 67	ICU / ETA	MDR	*blaoxa51, blaNDM pmrB, , pmrC*
Suli10	M / 35	Emergency / Burn	PDR	*blaoxa51, blaoxa23, blaVIM, blaNDM, pmrA, pmrB, pmrC*
Suli21	M / 61	ICU / Urine	MDR	*blaoxa51, blaNDM, pmrA, pmrB, pmrC*
Suli22	M / 35	Emergency / Burn	MDR	*blaoxa51, blaNDM, pmrA, pmrB, pmrC*
Suli8	F / 53	ICU/ETA	MDR	*blaoxa51, blaoxa23, blaNDM, pmrC*
Suli5	F / 45	ICU / Wound	MDR	*blaoxa51, blaoxa23, blaNDM, pmrC*
Suli6	F / 12	Emergency / Burn	XDR	*blaoxa51, blaNDM, pmrC*
Suli2	F / 54	Internal / Blood	MDR	*blaoxa51, pmrA, pmrB, pmrC*
Suli7	M/ 24	ICU/ Blood	MDR	*blaoxa51, blaNDM, pmrC*
Suli18	F / 23	Emergency / Burn	MDR	*blaoxa51, blaNDM, pmrA, pmrB, pmrC*
Suli45	F / 31	OPD / Urine	XDR	*blaoxa51, blaVIM, blaNDM, pmrA, pmrB, pmrC*
Suli32	M / 70	ICU / Urine	XDR	*blaoxa51, blaoxa23, blaVIM, blaNDM, pmrA, pmrB, pmrC*
Suli46	M/ 43	OPD / Sputum	XDR	*blaoxa51, blaoxa23, blaVIM, blaNDM, pmrA, pmrB, pmrC*
Suli43	F / 65	Emergency / Burn	XDR	*blaoxa51, blaVIM, blaNDM, pmrA, pmrB, pmrC*
Suli23	F / 24	Emergency / Burn	MDR	*blaoxa51, blaoxa23, pmrA, pmrB, pmrC*
Suli30	F / 19	OPD/ Urine	MDR	*blaoxa51, blaoxa23, blaVIM, pmrA, pmrB, pmrC*
Suli28	F / 21	OPD / wound	MDR	*blaoxa51, blaoxa23, blaVIM, blaNDM, pmrA, pmrB, pmrC*
Suli44	M / 55	Emergency / burn	XDR	*blaoxa51, blaVIM, blaNDM, pmrA, pmrB, pmrC*
Suli37	F / 63	OPD / Wound	XDR	*blaoxa51, blaoxa23, blaVIM, blaNDM, pmrA, pmrB, pmrC*
Suli12	F / 54	Internal / Wound	MDR	*blaoxa51, blaVIM, blaNDM, pmrA, pmrB, pmrC*
Suli39	M / 59	ICU / Urine	XDR	*blaoxa51, blaoxa23, blaVIM, blaNDM, pmrA, pmrB, pmrC*
Suli31	F / 43	ICU/Synovial Fluid	XDR	*blaoxa51, blaoxa23, blaVIM, blaNDM, pmrA, pmrB, pmrC*
Suli36	M / 69	ICU / Sputum	XDR	*blaoxa51, blaoxa23, blaVIM, blaNDM, pmrA, pmrB, pmrC*
Suli34	F / 73	ICU / Sputum	XDR	*blaoxa51, blaoxa23, blaVIM, blaNDM, pmrA, pmrB, pmrC*
Suli41	F / 30	OPD /Urine	XDR	*blaoxa51, blaoxa23, blaVIM, blaNDM, pmrA, pmrB, pmrC*
Suli33	M / 73	ICU / Sputum	XDR	*blaoxa51, blaVIM, blaNDM, pmrA, pmrB, pmrC*
Suli42	F / 42	Emergency / Burn	XDR	*blaoxa51, blaVIM, blaNDM, pmrA, pmrB, pmrC*
Suli29	M / 17	OPD / Urine	MDR	*blaoxa51, blaNDM, blaPmrA, pmrB, pmrC*
Ladder	Ladder 100bp DNA ladder (100 – 3,000)			

Fig. 4. Dendrogram of enterobacterial repetitive intergenic consensus polymerase chain reaction analysis for 46 *Acinetobacter baumannii* isolates from different clinical samples.

inserted upstream of the *blaOXA-51* gene, which acts as a strong promoter, drives the overexpression of the gene and thereby confers carbapenem resistance (Takebayashi, et al., 2021; Yazdansetad, et al., 2019). Therefore, other acquired oxacillinases, including *blaOXA-23*, *blaOXA-24,* and *blaOXA-143* enzymes, were necessary for *A. baumannii* to be resistant to carbapenem (Abd El-Baky, et al., 2020). Overall, *blaOXA-23* was found in 23 (50%) and *blaOXA-58* 21 (45.6%) of isolates. These results are similar to research that found among *A. baumannii* isolates, OXA-type carbapenemases were more abundant (Abduljabar and Mawlood, 2023). Furthermore, our findings are in line with this result; a high prevalence of $\text{bla}_{\text{OXA-23}}$ carrying *A. baumannii* isolates has been described in West Asian patients (Joshi, et al., 2017). This could be the result of conjugation between *A. baumannii* and the *blaOXA-23* gene found on the plasmid. Consequently, the number of antibiotic-resistant bacteria has been raising quickly worldwide (Bertini, et al., 2010). Moreover, compared to the findings of this analysis, an applied study including 196 clinical isolates revealed that 48.4% were *blaOXA-51*, 46.3% were *blaOXA-23*, and 5.3% were *blaOXA-58* (Hou and Yang, 2015).

In addition to OXA-type oxacillinases, the *MBL* genes were screened in the present research. Recently, the *blaNDM* harboring *A. baumannii* has been detected in a number of nations in Europe, South America, and Asia (Rodrigues, et al., 2024; Joshi, et al., 2017; Nordmann, et al., 2011). There is evidence that the *blaNDM* gene is a chimera gene assembled by the combination of the mannose-binding lectin gene with an aminoglycoside resistance gene, aphA6. This occurrence most likely takes place in *Acinetobacter* spp., meaning that this gene most likely originated in these bacteria (Nordmann, et al., 2011). In the present study, we identified a high prevalence of 40 (86.9%) of the isolates carrying the bla_{NDM} gene, which is greater than the previous study in Erbil city, which identified 26% of the *A. baumannii* harboring the same gene (Abduljabar and Mawlood, 2023). Furthermore, it was higher than a study performed in West Asia, 13.6% (Joshi, et al., 2017). These findings suggested the possibility of plasmid-mediated transmission of the Bla_{NDM} gene from one strain to another and that plasmids are essential to the pandrug-resistant *A. baumannii* epidemic (Shi, et al., 2024). Regarding *blaVIM*, our study identified that 28 (60.8%) isolates were positive for this gene, which is in line with other reports directed previously (Khalid, 2024; Abduljabar and Mawlood, 2023). In contrast to *blaVIM and blaNDM, blaIMP* was not detected in any of the *A. baumannii* isolates. Our finding was agreed with by another study, which discovered that the *A. baumannii* isolates do not have the bla_{IMP} gene in their genome. Similar to our results, a study also reported that the finding of the same gene in *A. baumannii* isolates was 0.0% (Al-Hindawi, 2018). Moreover in line with other data, there was no detectable *blaIMP* gene in carbapenem-resistant isolates (Fattouh and El-Din, 2014).

According to our results, the lowest rate of resistance was given to CL (6.5%), which belonged to the PDR category *A. baumannii* with MIC values ≥4 µg/mL. The most effective antibiotics for *A. baumannii* infections are still CL when compared to other tested antibiotics. These results are consistent with research indicating that around 7% of isolates of *A. baumannii* are CL-resistant (Abbasi, Hajihashemi and Shokri, 2024; Behera, Swain and Chandra, 2017). The progress of CL resistance in *A. baumannii* is essentially influenced by *pmrCAB* genes. The resistance of *A. baumannii* to CL is believed to be due to an assortment of various mechanisms. The most common of these is the modification of the lipid A component of the outer membrane's LPS layer, which is essentially rendered achievable by the *pmrCAB* operon (Novović and Jovčić, 2023b). The addition of pEtN to lipid A is triggered by the *pmrC* gene; *pmrC* expression is regulated by the *pmrA* and *pmrB* (*pmrAB*) TCS. As a result, the outer membrane's negative charge reduces, which affects CL binding and protects the cell membrane's stability and structure intact (Moffatt, Harper and Boyce, 2019; Chen and Groisman, 2013). Here, we identified all three CoR *A. baumannii* isolates harboring the *pmrCAB* genes. Comprehending the function of *pmrCAB* genes in CL-resistant *A. baumannii* is essential for creating new approaches to fight antibiotic resistance (Al-Shamiri, et al., 2021).

Variation in the prevalence of distinct OXA-type, MBL, and CL resistance genes in different nations may be related to a variety of antibiotic therapy programs, ecological states, and variant antibiotype patterns (Azimi, et al., 2015). Our study has identified numerous intrinsic and acquired *OXA*-type, *MBL*, and *CoR* genes that co-exist. The fact that 46/46 (100%) of all isolates have multiple resistance genes indicates that an increase in the combination of these genes may lead to a rise in antibiotic resistance in *A. baumannii* isolates (Shi, et al., 2024). Variation in antibiotic resistance gene detection among different investigations could be attributed to several factors, including that bacterial antibiotic resistance is often acquired and disseminated through the movement of mobile genetic elements, such as conjugative plasmids, insertion sequences, transposons, and integrons, as well as the size and methodology of the study (Noel, Petrey and Palmer, 2022). Furthermore, widespread resistance to most classes of antibiotics among the population may be due to their common use (Radhi and Al-Charrakh, 2019). These outcomes show that the resistance of *A. baumannii* is ever-evolving. Therefore, in order to avoid infections with these bacteria in hospital settings, it is imperative to establish a suitable treatment plan and a precise methodology.

V. Conclusion

The present research discovered a considerable level of MDR in *A. baumannii* isolates in our study, with a high prevalence of OXA-type, BML, and *pmrCAB* genes, which have been identified as important antibiotic resistance genes among isolates. The results also indicate that ERIC-PCR could provide a quick and reliable method to identify clonal similarities between isolates from a variety of clinical samples. The findings also advise monitoring the incidence of clinical isolates of *A. baumannii*, which hence requires the use of molecular and genotyping methods. Consequently, controlling the endemic strains of *A. baumannii* is required, especially in ICUs and burn hospitals, and effective strategies to stop managing the infection's spread are urgently required.

References

Abban, M.K., Ayerakwa, E.A., Mosi, L., and Isawumi, A., 2023. The burden of hospital acquired infections and antimicrobial resistance. *Heliyon*, 9(10), p.e20561.

Abbasi, A., Hajihashemi, B., and Shokri, D., 2024. Molecular mechanisms of colistin resistance mediated by pmrCAB genes in *Acinetobacter baumannii* isolated from patients hospitalized in Isfahan medical centers. *Postępy Higieny I Medycyny Doświadczalnej*, 78(1), pp.52-57.

Abd El-Baky, R.M., Farhan, S.M., Ibrahim, R.A., Mahran, K.M., and Hetta, H.F., 2020. Antimicrobial resistance pattern and molecular epidemiology of ESBL and MBL producing *Acinetobacter baumannii* isolated from hospitals in Minia, Egypt. *Alexandria Journal of Medicine*, 56(1), pp.4-13.

Abduljabar, K.A., and Mawlood, A.H., 2023. Multilocus sequence typing analysis and molecular characterization of carbapenemase related genes in *Acinetobacter baumannii* isolated from hospitalized patients in Erbil city, Iraq. *Cellular and Molecular Biology (Noisy-le-grand)*, 69(11), pp.116-124.

Alagna, L., Palomba, E., Mangioni, D., Bozzi, G., Lombardi, A., Ungaro, R., Castelli, V., Prati, D., Vecchi, M., and Muscatello, A., 2020. Multidrug-resistant gram-negative bacteria decolonization in immunocompromised patients: A focus on fecal microbiota transplantation. *International Journal of Molecular Sciences*, 21(16), pp.5619.

Al-Hindawi, R.A., 2018. Detection of metallo βlactamase class among carbapenem resistant *Acinetobacter baumannii* (CRAB) isolates in Hilla/Iraq. *Journal of Global Pharmacology Technology*, 9(12), pp.169-178.

Ali, S., Al-Haideri, H.H., and Al Hishimi, A.M., 2022. Evaluating the activity of ultrasound on biofilm formation by *Acinetobacter baumannii* isolated from clinical specimens. *Baghdad Science Journal*, 19(6), pp.1522-1535.

Aljindan, R., Alsamman, K., and Elhadi, N., 2018. ERIC-PCR genotyping of *Acinetobacter baumannii* isolated from different clinical specimens. *Saudi Journal of Medicine and Medical Sciences*, 6(1), pp.13-17.

Al-Kadmy, I.M.S., Ali, A.N.M., Salman, I.M.A., and Khazaal, S.S., 2018. Molecular characterization of *Acinetobacter baumannii* isolated from Iraqi hospital environment. *New Microbes and New Infections*, 21, pp.51-57.

Al-Shamiri, M.M., Zhang, S., Mi, P., Liu, Y., Xun, M., Yang, E., Ai, L., Han, L., and Chen, Y., 2021. Phenotypic and genotypic characteristics of *Acinetobacter baumannii* enrolled in the relationship among antibiotic resistance, biofilm formation and motility. *Microbial Pathogenesis*, 155, pp.104922.

Assimakopoulos, S.F., Karamouzos, V., Lefkaditi, A., Sklavou, C., Kolonitsiou, F., Christofidou, M., Fligou, F., Gogos, C., and Marangos, M., 2019. Triple combination therapy with high-dose ampicillin/sulbactam, high-dose tigecycline and colistin in the treatment of ventilator-associated pneumonia caused by pan-drug resistant *Acinetobacter baumannii*: A case series study. *Le Infezioni in Medicina*, 27(1), pp.11-16.

Azimi, L., Talebi, M., Pourshafie, M.R., Owlia, P., and Lari, A.R., 2015. Characterization of carbapenemases in extensively drug resistance *Acinetobacter baumannii* in a burn care center in Iran. *International Journal of Molecular and Cellular Medicine*, 4(1), pp.46-53.

Behera, I.C., Swain, S.K., and Chandra, M., 2017. Incidence of colistin-resistant *Acinetobacter baumannii* in an Indian tertiary care teaching hospital. *International Journal Advances Reserch (Indore)*, 3(12), pp.283-286.

Bertini, A., Poirel, L., Mugnier, P.D., Villa, L., Nordmann, P., and Carattoli, A., 2010. Characterization and PCR-based replicon typing of resistance plasmids in *Acinetobacter baumannii*. *Antimicrobial Agents and Chemotherapy*, 54(10), pp.4168-4177.

Chapartegui-González, I., Lázaro-Díez, M., Bravo, Z., Navas, J., Icardo, J.M., and Ramos-Vivas, J., 2018. *Acinetobacter baumannii* maintains its virulence after long-time starvation. *PLoS One*, 13(8), p.e0201961.

Charretier, Y., Diene, S.M., Baud, D., Chatellier, S., Santiago-Allexant, E., Van Belkum, A., Guigon, G., and Schrenzel, J., 2018. Colistin heteroresistance and involvement of the pmrab regulatory system in *Acinetobacter baumannii*. *Antimicrobial Agents and Chemotherapy*, 62(9), pp.e00788-18.

Chawsheen, M.A., Al-Naqshbandi, A.A., and Abdulqader, H.H., 2020. Bacterial profile and antimicrobial susceptibility of isolates recovered from lower respiratory tract infection for patients in Rizgary hospital, Erbil. *Aro-The Scientific Journal of Koya University*, 8(2), pp.64-70.

Chen, H.D., and Groisman, E.A., 2013. The biology of the pmra/pmrb two-component system: The major regulator of lipopolysaccharide modifications. *Annual Review of Microbiology*, 67(1), pp.83-112.

Evans, B., 2009. The significance of the oxa-51-like β-lactamases of *Acinetobacter baumannii*. pp.1-254.

Falah, F., Shokoohizadeh, L., and Adabi, M., 2019. Molecular identification and genotyping of *Acinetobacter baumannii* isolated from burn patients by PCR and ERIC-PCR. *Scars Burns and Healing*, 5, p.2059513119831369.

Fattouh, M., and El-Din, A.N., 2014. Emergence of carbapenem-resistant *Acinetobacter baumannii* in the intensive care unit in Sohag university hospital, Egypt. *International Journal Current Microbiology Applied Science*, 3(4), pp.732-744.

Hamzah, A.S., 2018. Genotyping of fusA gene from clinical isolates *Acinetobacter baumannii* in Baghdad. *Baghdad Science Journal*, 15(1), pp.37-42.

Hou, C., and Yang, F., 2015. Drug-resistant gene of blaOXA-23, blaOXA-24, blaOXA-51 and blaOXA-58 in *Acinetobacter baumannii*. *International Journal of Clinical and Experimental Medicine*, 8(8), pp.13859-13863.

Jiang, Y., Ding, Y., Wei, Y., Jian, C., Liu, J., and Zeng, Z., 2022. Carbapenem-resistant *Acinetobacter baumannii*: A challenge in the intensive care unit. *Frontiers in Microbiology*, 13, p.1045206.

Joshi, P.R., Acharya, M., Kakshapati, T., Leungtongkam, U., Thummeepak, R., and Sitthisak, S., 2017. Co-existence of blaOXA-23 and blaNDM-1 genes of *Acinetobacter baumannii* isolated from Nepal: Antimicrobial resistance and clinical significance. *Antimicrobial Resistance and Infection Control*, 6, p.21.

Khalid, H.M., 2024. Molecular study of blaVIM and blaIMP genes in *Acinetobacter baumannii* strains isolated from burn patients in Duhok City, Iraq. *The Journal of Infection in Developing Countries*, 18(01), pp.101-105.

Kumburu, H.H., Sonda, T., Van Zwetselaar, M., Leekitcharoenphon, P., Lukjancenko, O., Mmbaga, B.T., Alifrangis, M., Lund, O., Aarestrup, F.M., and Kibiki, G.S., 2019. Using WGS to identify antibiotic resistance genes and predict antimicrobial resistance phenotypes in MDR *Acinetobacter baumannii* in Tanzania. *Journal of Antimicrobial Chemotherapy*, 74(6), pp.1484-1493.

Kyriakidis, I., Vasileiou, E., Pana, Z.D., and Tragiannidis, A., 2021. *Acinetobacter baumannii* antibiotic resistance mechanisms. *Pathogens*, 10(3), p.373.

Lima, W.G., Alves, M.C., Cruz, W.S., and Paiva, M.C., 2018. Chromosomally encoded and plasmid-mediated polymyxins resistance in *Acinetobacter baumannii*: A huge public health threat. *European Journal of Clinical Microbiology and Infectious Diseases*, 37, pp.1009-1019.

Lin, M.F., and Lan, C.Y., 2014. Antimicrobial resistance in *Acinetobacter baumannii*: From bench to bedside. *World Journal of Clinical Cases,* 2(12), pp.787-814.

Magiorakos, A.P., Srinivasan, A., Carey, R.B., Carmeli, Y., Falagas, M.E., Giske, C.G., Harbarth, S., Hindler, J.F., Kahlmeter, G., Olsson-Liljequist, B., Paterson, D.L., Rice, L.B., Stelling, J., Struelens, M.J., Vatopoulos, A., Weber, J.T., and Monnet, D.L., 2012. Multidrug-resistant, extensively drug-resistant and pandrug-resistant bacteria: An international expert proposal for interim standard definitions for acquired resistance. *Clinical Microbiology and Infection,* 18(3), pp.268-281.

Moffatt, J.H., Harper, M., and Boyce, J.D., 2019. Mechanisms of polymyxin resistance. In: *Polymyxin Antibiotics From Laboratory Bench to Bedside*. Springer, Germany, pp.55-71.

Moubareck, C.A., and Halat, D.H., 2020. Insights into *Acinetobacter baumannii*: A review of microbiological, virulence, and resistance traits in a threatening nosocomial pathogen. *Antibiotics (Basel)*, 9(3), p.119.

Müller, C., Reuter, S., Wille, J., Xanthopoulou, K., Stefanik, D., Grundmann, H., Higgins, P.G., and Seifert, H., 2023. A global view on carbapenem-resistant *Acinetobacter baumannii*. *Mbio*, 14(6), p.e0226023.

Noel, H.R., Petrey, J.R., and Palmer, L.D., 2022. Mobile genetic elements in *Acinetobacter* antibiotic-resistance acquisition and dissemination. *Annals of the New York Academy of Sciences*, 1518(1), pp.166-182.

Nordmann, P., Poirel, L., Carrër, A., Toleman, M.A., and Walsh, T.R., 2011. How to detect NDM-1 producers. *Journal of Clinical Microbiology*, 49(2), pp.718-721.

Novović, K., and Jovčić, B., 2023a. Colistin resistance in *Acinetobacter baumannii*: Molecular mechanisms and epidemiology. *Antibiotics* (Basel), 12(3), p.516.

Novović, K., and Jovčić, B., 2023b. Colistin resistance in *Acinetobacter baumannii*: Molecular mechanisms and epidemiology. *Antibiotics (Basel),* 12(3), p.516.

Poirel, L., Walsh, T.R., Cuvillier, V., and Nordmann, P., 2011. Multiplex PCR for detection of acquired carbapenemase genes. *Diagnostic Microbiology and Infectious Disease*, 70(1), pp.119-123.

Radhi, S.H., and Al-Charrakh, A.H., 2019. Occurrence of MBLs and carbapenemases among MDR and XDR *Acinetobacter baumannii* isolated from hospitals in Iraq. *Scopus Ijphrd Citation Score*, 10(7), p.668.

Rezaei, A., Fazeli, H., Moghadampour, M., Halaji, M., and Faghri, J., 2018. Determination of antibiotic resistance pattern and prevalence of OXA-type carbapenemases among *Acinetobacter baumannii* clinical isolates from inpatients in Isfahan, central Iran. *Le Infezioni in Medicina*, 26(1), pp.61-66.

Rodrigues, D.C.S., Silveira, M.C., Pribul, B.R., Karam, B.R.S., Picão, R.C., Kraychete, G.B., Pereira, F.M., De Lima, R.M., De Souza, A.K.G., Leão, R.S., Marques, E.A., Rocha-de-Souza, C.M., and Carvalho-Assef, A.P.A., 2024. Genomic study of *Acinetobacter baumannii* strains co-harboring blaOXA-58 and blaNDM-1 reveals a large multidrug-resistant plasmid encoding these carbapenemases in Brazil. *Frontiers in Microbiology*, 15, p.1439373.

Saelim, W., Santimaleeworagun, W., Thunyaharn, S., Changpradub, D., and Juntanawiwat, P., 2018. Pharmacodynamic profiling of optimal sulbactam regimens against carbapenem-resistant *Acinetobacter baumannii* for critically ill patients. *Asian Pacific Journal of Tropical Biomedicine*, 8(1), pp.14-18.

Sehree, M.M., Al-Kaysi, A.M., and Abdullah, H.N., 2023. A developed colorimetric assay using unmodified gold nanoparticles for the identification of *Acinetobacter baumannii* isolates from different clinical samples. *Baghdad Science Journal*, 20(4), p.4.

Shayea, R.H., and Ali, M.R., 2022. ERIC-PCR genotyping and clonal genetic linkage between carbapenem-resistant *Acinetobacter baumannii* isolates. *Jordan Journal of Biological Sciences*, 15(4), pp.689-696.

Shi, J., Cheng, J., Liu, S., Zhu, Y., and Zhu, M., 2024. *Acinetobacter baumannii*: An evolving and cunning opponent. *Frontiers in Microbiology*, 15, p.1332108.

Smai, S.B., and Ganjo, A.R., 2020. A prevalence of infections with antibiotic-resistant *Acinetobacter baumannii* in different clinical samples from hospitals in Erbil. *Zanco Journal of Pure and Applied Sciences*, 32(3), pp.95-100.

Tagliabue, A., and Rappuoli, R., 2018. Changing priorities in vaccinology: Antibiotic resistance moving to the top. *Frontiers in Immunology*, 9, p.1068.

Takebayashi, Y., Findlay, J., Heesom, K.J., Warburton, P.J., Avison, M.B., and Evans, B.A., 2021. Variability in carbapenemase activity of intrinsic oxaab (OXA-51-like) β-lactamase enzymes in *Acinetobacter baumannii*. *Journal of Antimicrobial Chemotherapy*, 76(3), pp.587-595.

Tawfeeq, H.R., Rasheed, M.N., Hassan, R.H., Musleh, M.H., and Nader, M.I., 2020. Molecular detection of blaoxa genes in *Acinetobacter baumannii* collected from patients with various infections. *Biochemical and Cellular Archives*, 20(1), pp.1233-1239.

Towner, K.J., 2009. *Acinetobacter*: An old friend, but a new enemy. *Journal of Hospital Infection*, 73(4), pp.355-363.

Trebosc, V., Gartenmann, S., Tötzl, M., Lucchini, V., Schellhorn, B., Pieren,M., Lociuro, S., Gitzinger, M., Tigges, M., Bumann, D., and Kemmer, C., 2019. Dissecting colistin resistance mechanisms in extensively drug-resistant *Acinetobacter baumannii* clinical isolates. *MBio*, 10(4), pp. e01083-19.

Turton, J.F., Woodford, N., Glover, J., Yarde, S., Kaufmann, M.E., and Pitt, T.L., 2006. Identification of *Acinetobacter baumannii* by detection of the blaOXA-51-like carbapenemase gene intrinsic to this species. *Journal of Clinical Microbiology*, 44(8), pp.2974-2976.

Vázquez-López, R., Solano-Gálvez, S.G., Juárez Vignon-Whaley, J.J., Abello Vaamonde, J.A., Padró Alonzo, L.A., Rivera Reséndiz, A., Muleiro Álvarez, M., Vega López, E.N., Franyuti-Kelly, G., Álvarez-Hernández, D.A., Guzmán, V.M., Bañuelos, J.E.J., Felix, J.M., Barrios, J.E.J., and Fortes, T.B., 2020. *Acinetobacter baumannii* resistance: A real challenge for clinicians. *Antibiotics (Basel)*, 9(4), p.205.

Yazdansetad, S., Najari, E., Ghaemi, E.A., Javid, N., Hashemi, A., and Ardebili, A., 2019. Carbapenem-resistant *Acinetobacter baumannii* isolates carrying blaOXA genes with upstream ISAba1: First report of a novel OXA subclass from Iran. *Journal of Global Antimicrobial Resistance*, 18, pp.95-99.

A Novel Skin Cancer Detection Approach Using Deep Learning Algorithm with Image Segmentation Filters

Awf A. Ramadhan[1], Omer S. Kareem[1] and Diyar Q. Zeebaree[2]

[1]Department of Public Health, Duhok Polytechnic University,
Duhok, Kurdistan Region - F.R. Iraq

[2]Department of Cyber Security and Cloud Computing Techniques Engineering, Northern Technical University (NTU),
College of Computer and AI, Mosul, F.R. Iraq

***Abstract*—Skin cancer is considered one of the most common and dangerous diseases in the world because so many people do not pay attention to it. In addition, skin cancer is a medical condition that a doctor cannot accurately diagnose from imaging data during a manual examination. Therefore, there is a great need to apply deep learning methods for early detection of skin cancer, as these methods are excellent in the field of medical image processing. This paper presents a deep learning model based on the convolutional neural network algorithm to provide automatic detection of skin cancer. The model basically consists of two scenarios: binary classification (benign and malignant) of the data set without an image segmentation process and binary classification of the same data set after applying four image segmentation methods (threshold-based segmentation, edge-based segmentation, binary fill holes technique, and removing small objects). The input images in the first scenario are three channels and one channel in the second scenario. These image segmentation techniques have significantly improved the accuracy of the proposed model, as the proposed model achieved 92.18% before applying segmentation and 96.83% after applying image segmentation.**

***Index Terms*—Computer vision, Deep learning, Edge, Neural Network, Skin cancer, Threshold.**

I. Introduction

Skin cancer is an abnormal growth of skin cells and often develops on the face, especially in areas frequently exposed to sunlight. However, this Widespread type of cancer can also develop on areas of the skin that are not frequently exposed to sunlight, (Hosny, et al., 2018; Gouda, et al., 2022a). This disease is prevalent worldwide, as skin cancer is one of the most common diseases globally. Skin cancer is mainly divided into four types: melanoma cancer, basal cell carcinoma, squamous cell carcinoma, and Merkel cell carcinoma. The most dangerous form of skin cancer is melanoma (Schaefer, et al., 2013), which is responsible for most skin cancer-related deaths worldwide (Gouda, et al., 2022b), as 100,000 new cases of melanoma are detected in the United States each year, and the death rate from them reaches 9,000 deaths each year, and in Australia, there are about 13,000 new cases each year and about 1,200 deaths (Codella, et al., 2017). Skin cancer is a very common disease in rural areas of developing countries such as India, Bangladesh, and Sri Lanka. According to Oxford Journals, there are about 1.5 million cases of skin cancer in Bangladesh (Rahi, et al., 2019a). Skin cancer occurs when a problem develops in skin cells that cause them to divide repeatedly and uncontrollably, causing cancer cells to spread to other parts of the body if the disease is not detected early, which is life-threatening. Early detection of skin cancer can reduce the mortality rate by 90%. This percentage drops dramatically to 62% after the disease reaches the lymphatic vessels, and then the percentage drops further to 16% when the disease spreads to other parts of the body (Tan, Zhang and Lim, 2019). The great similarity between many skin diseases makes it difficult to detect skin cancer by visual inspection (Swapno et al., 2025). Of 20,000 skin lesions surgically removed for suspected cancer, 0.1% tested positive for the disease (Tan, Zhang and Lim, 2019). Therefore, there is a constant need for an artificial intelligence system that can detect and distinguish skin cancer from other skin lesions. Deep learning techniques have been widely used in the medical field in the past decade. Convolutional neural network (CNN) algorithms are one of the best models in medical image processing, and recently, researchers have used a lot of deep learning and machine learning techniques to detect skin cancer cases.

The challenges facing most models for detecting skin cancer in its early stages are described as follows:

1. Sometimes, noise obscures many important features that affect the model's accuracy in its prediction, so noise must be eliminated, and the areas of high-quality artifacts must be preserved.

ARO-The Scientific Journal of Koya University
Vol. XIII, No. 1 (2025), Article ID: ARO.12024. 9 pages
DOI: 10.14500/aro.12024
Received: 27 January 2025; Accepted: 07 April 2025
Regular research paper; Published: 28 April 2025

†Corresponding author's e-mail: awf.ramadhan@dpu.edu.krd

2. Another challenge is the presence of hairs in areas of cancer presence that affect the accuracy of detecting between benign and malignant cancer.
3. Many studies rely on the principle of using pre-trained models that contain many parameters and require a large amount of time and memory in addition to powerful computers.

In this article, the research questions are defined as follows:

1. Is there an artificial intelligence system capable of automatically detecting skin cancer?
2. Is the system effective in automatically detecting skin cancer?

After a long search in the literature to answer these questions, the researchers found that many other researchers have taken this field extensively, which gave us the moral motivation to try to participate in this vital field. This study focuses on building an automated system for automatically detecting skin cancer using deep learning techniques; it also presents an approach based on reducing the training parameters to approximately one and a half million parameters. This system consists of two stages: The first one is pre-processing images by segmenting the images, improving, normalizing, and resized. The second one is training the deep learning model using a CNN, taking into account the time used in training by reducing the number of parameters as much as possible.

The main scientific contributions of this study can be summarized as follows:

1. To improve the accuracy of detecting and classifying images containing skin cancer, reduce distractions, and draw attention to key features. Several methods were included to extract the most important features (threshold-based segmentation, edge-based segmentation, binary fill holes technique, and removing small objects).
2. With the help of AI, develop a novel CNN model to detect and classify skin cancer in the images.
3. The number of parameters has been reduced for the classifier to save time and computation consumption during training the model to 1.6 million parameters.
4. The proposed model has obtained 92.18% without applying segmentation and 96.83% after applying image segmentation.

The rest of this paper is arranged as follows. In the second section, the literature review is discussed. The third section describes the methodology that was used in this study. In the fourth section, the results are listed and discussed briefly. In the final section, the conclusion of this study is presented.

II. Literature Review

Many works over many years have attempted to diagnose melanoma from skin imaging. In this section, we will review the most prominent works in the literature.

Adegun and Viriri (2019) proposed a multi-stage deep learning method for classifying skin cancer into malignant and non-malignant based on pixel-wise image classification called Lesion-classifier. The model was tested on two different datasets and achieved 95% accuracy. Ech-Cherif Misbhauddin and Ech-Cherif (2019) presented a CNN model called MobileNetV2 for the automated detection of skin malignancies. The proposed model was trained on 48,373 skin imaging images collected from three different datasets. The proposed model achieved 91.33% accuracy. Rahi, et al. (2019b) developed a deep neural network-based automated system for skin cancer detection. The proposed model achieved an accuracy of 80%. Then, pre-trained deep learning models, such as VGG11, RESNET50, and DENSENET121 were tested. The performance accuracy increased to a maximum accuracy of about 90%. Guan, et al. (2019) trained two deep-learning networks, VGG-16 and Inception-v3, for thyroid tumor detection. In this paper, thyroid images were randomly rotated four times at different angles (0, 90, 180, and 270) to augment the training data, where the training data were augmented 8 times. The proposed model achieved an accuracy of 97.66% using VGG-16 and 92.75% using Inception-v3. Reis, et al. (2022) proposed a deep learning-based CNN model called InSiNet for automatic skin cancer detection. The proposed model was trained on three different datasets and achieved more than 94% accuracy. Gouda, et al. (2022c) used a deep learning network (CNN) to detect two main types of malignant and benign tumors automatically. The proposed model was trained on the ISIC2018 dataset consisting of 3,533 images. In the pre-processing stage, the images were enhanced, enhanced, and resized using ESRGAN. The proposed model achieved an accuracy rate of 83.2%. (Kandhro, et al., 2024) In this paper, we enhanced the E-VGG19 model by incorporating max pooling and a dense layer to improve skin cancer prediction. The model extracts feature from skin lesions and classifies them as either malignant or benign. These extracted features are then fed into various machine learning classifiers, including Linear support vector machine, k-Nearest neighbors, decision tree, and logistic regression (LR). Our results show that integrating the E-VGG19 model with traditional classifiers significantly enhances classification accuracy for skin cancer detection. The proposed approach achieved an accuracy of 88%. (Ozdemir and Pacal, 2025) This study introduces a novel, lightweight, mobile-friendly hybrid model that integrates ConvNeXtV2 blocks with autofocusing mechanisms. The model focuses on extracting local features in the initial two stages, while autofocusing is employed in the later stages for enhanced feature refinement. When tested on the ISIC 2019 dataset, the model achieved an impressive accuracy of 93.60%.

When reviewing previous studies, the researchers noted gaps in several studies, including the lack of effective use of image processing techniques or the failure to reduce the number of parameters to reduce training time. For these reasons, the researchers decided to use two scenarios in this study: The first scenario without pre-processing the images and without reducing the number of parameters, and the second scenario after applying pre-processing and reducing the number of parameters. The researchers noted that this study successfully filled the gap in the literature.

We conclude from this section that many studies have tried to detect skin cancer automatically by applying different types of deep learning algorithms. Table I shows some of these studies in the literature.

III. Materials and Methods

This section will summarize all the steps of building the proposed skin cancer detection system in this study. This study is specifically built on two main scenarios: The first scenario is data classification before pre-processing (three input channels), and the second scenario is the classification of the same data set after applying several image segmentation and cleaning processes (one input channel). This method aims to know the extent to which image segmentation affects the result. After these two separate scenarios, three evaluations were used: accuracy, sensitivity, and objectivity to determine the reliability of the proposed model. Fig. 1 shows the general structure of the study.

A. Dataset

The ISIC-Archive dataset used in this study consists of 3,297 images of size 224 × 224 RGB (1,800 benign images and 1,497 malignant images). This dataset was obtained from Kaggle https://www.kaggle.com/datasets/fanconic/skin-cancer-malignant-vs-benign?resource=download&select=train accessed August 30, 2024.

The dataset was divided into three Groups: training, testing, and prediction, as shown in Table II. In the testing folder, 600 images were placed (300 benign and 300 malignant); in the prediction folder, 40 images were placed (20 benign and 20 malignant), and the rest of the images were placed in the training folder.

B. Pre-Processing Image

The second scenario pre-processing is the most important stage in the proposed model, where the color images (RGB) are converted to grayscale images and then followed by using two image segmentations (threshold-based segmentation and edge-based segmentation), and two filtering methods (binary fill holes technique, and remove small objects). The goal of using image segmentation techniques is to reduce the number of features for the images so that the model is trained on the melanoma region only without the need to focus on other parts of the image, such as hair and others. Figs. 2 and 3 show the segmentation methods used in the study on benign and malignant cancer images, respectively.

C. Threshold-Based Segmentation

Threshold is one of the most common image segmentation techniques. It is useful to know the difference

TABLE I
Some Skin Cancer Detection Work in the Literature

Recent work	Data size	Techniques used	Number of classes	Data set	Accuracy (%)
Adegun and Viriri (2019)	2,000	Deep convolutional encoder-decoder network (DCNN)	Two	ISIC 2017	95
Ech-Cherif, Misbhauddin and Ech-Cherif (2019)	48,373	MobileNetV2	Two	DermNet, ISIC Archive	91.33
Muzahidul Islam Rahi, et al. (2019a)	450	ResNet50	Seven	HAM10000	90
Guan, et al. (2019)	279	DCNN VGG-16	Two	H&E-stained images	97.66
Reis, et al. (2022)	1,323	InSiNet	Two	ISIC 2018, 2019, and 2020	94.59
Gouda, et al. (2022c)	1,000	CNN	Two	ISIC 2018	83.2
Nawaz, et al. (2022)	1,280	RCNN	Two	ISIC-2016, ISIC-2017, and PH 2	95.6
(Kandhro, et al., 2024)	33,126	E-VGG19	Two	ISIC 2020	88
(Ozdemir and Pacal, 2025)	25,331	ConvNeXtV2	Eight	ISIC 2019	93.60

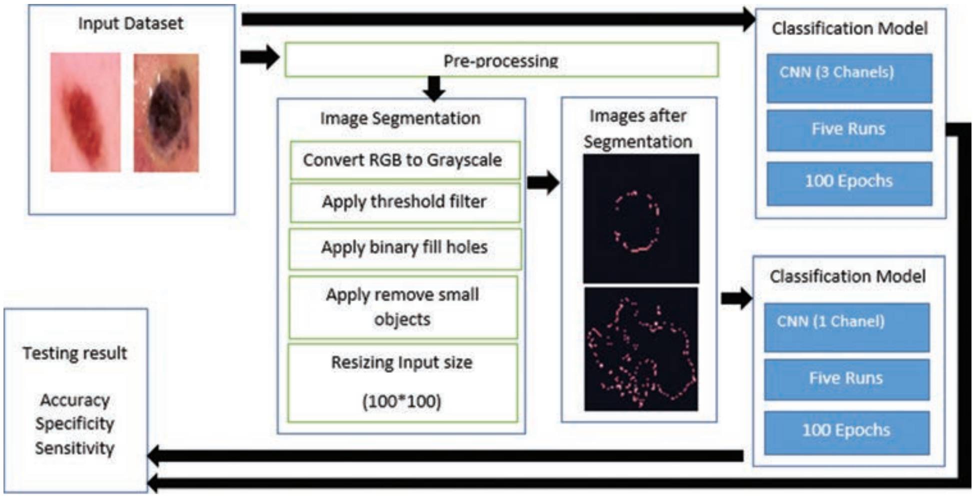

Fig. 1. The flow chart used in this study.

http://dx.doi.org/10.14500/aro.12024

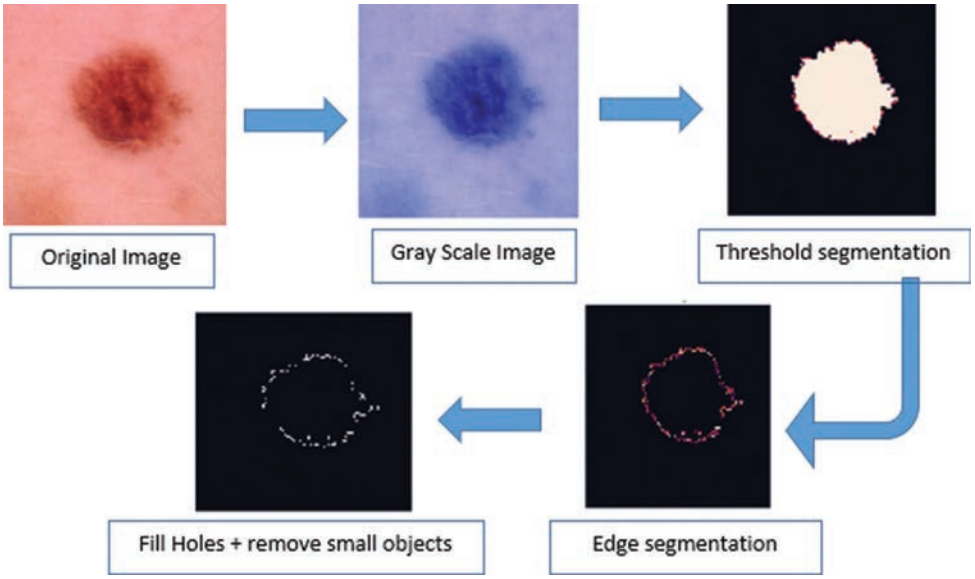

Fig. 2. The segmentation process used in this study (benign image number 26).

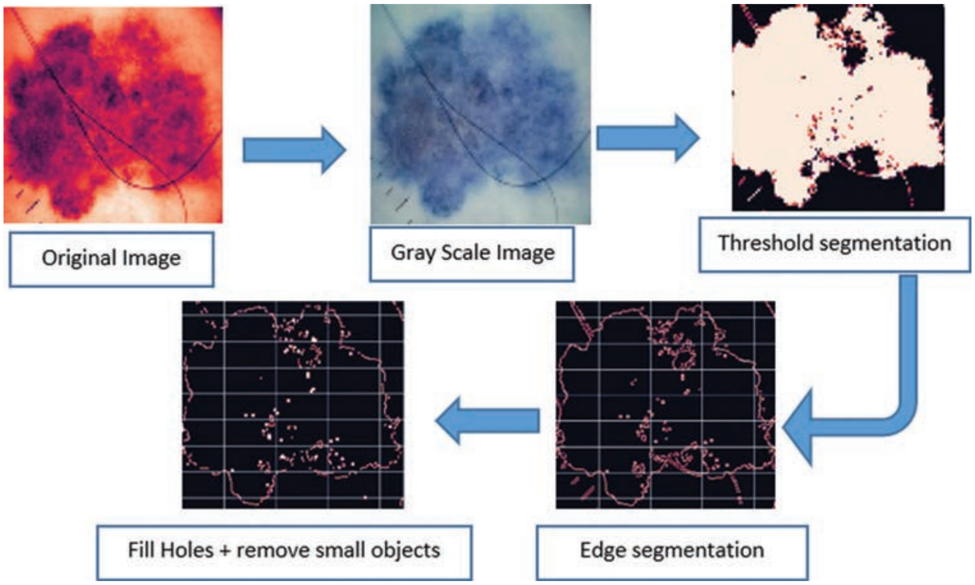

Fig. 3. The segmentation process used in this study (malignant image number 52).

TABLE II
DISTRIBUTING IMAGES TO FOLDERS USED IN THE STUDY

Folder	Benign images	Malignant images
Training folder	1480	1177
Testing folder	300	300
Prediction fodder	20	20
Total	1800	1497

between front and back. By choosing a sufficient threshold value, T, the gray-level image can be converted into a binary image. The two images should contain all the necessary information about the position and shape of the objects of interest (front) (Abdulrahman and Varol, 2020). The advantage of having two images in advance is that it reduces the complexity of the data and simplifies the process of detection and classification. The most common way to convert a gray-level image to two images is to choose a threshold value (T). All gray level values below this T will then be classified as black (0), and those above the T will be white (1). The segmentation problem is to choose an appropriate value for the threshold T. The most common way to choose T is to examine the histogram of the images to be segmented. The best is when the histogram uses only two dominant channels that is, a clear valley (bimodal) is active. In this case, the value of T is chosen as the valley between the two modes (Al-Amri and Kalyankar, 2010).

The technique of the threshold can be defined as in equation 1, and the threshold image g (x, y) can be defined as in equation 2:

$$T = T\,[x, y, p\,(x, y), f\,(x, y)] \tag{1}$$

Where: T means the value of the threshold, x, y means the threshold coordinate point, p (x, y), f (x, y) means the point of the gray level images.

$$g(x,y) = \begin{cases} 1 if \ f(x,y) > T \\ 0 if \ f(x,y) \le T \end{cases} \quad (2)$$

D. Edge-Based Segmentation

There is much research devoted to edge detection to develop optimal edge detection that provides a good balance between detection and localization performance. Searching for performance-optimizing filters is a common approach in designing such edge processors, and this requires three parameters: Good detection, good localization, and unique edge response (Canny, 1986). The best edge detector is the Cani method, which the first derivative of the Gaussian algorithm can approximate. Detecting edges by rotating the image with this filter is equivalent to finding the maximum gradient of a properly smoothed Gaussian image (Deriche, 1987). Finding and merging edges at multiple scales is another important aspect of edge detection. The scale-space method introduced by Witkin involves smoothing the original images using Gaussian smoothing kernels (Ma and Manjunath, 2000). Edge image G can be defined as in equation 3, and Fig. 4 shows how segmentation works using edges.

$$G = \sqrt{G_x^2 + G_y^2} \ angle(\theta) \quad (3)$$

Where: G(x) means the horizontal direction of the image, and G(y) means the vertical direction of the image.

E. Fill Holes and Remove Small Objects

The segmentation techniques were used to extract important features as in the previous two steps, but some areas were missing in the image, so the Fill holes technique from the SciPy library in Python was used to fill those missing points in the image to improve the image quality. In this Article, the binary fill holes function (Abdulrahman, et al., 2022; Ramadhan and Baykara 2022). The method of filling the holes depends on the type of function used. There are several types of hole-filling methods, including Interpolation, Extrapolation, and fixed filling (Somasundaram and Kalaiselvi, 2010). In this study, the last type was used, where a fixed value of 0.5 was specified. As for removing small parts of the image, the remove_small_objects function from the scikit-image library in Python was used. The technique of removing small and unwanted objects from images is one of the common techniques for improving image quality. A value is specified for the function, and then the function removes any object that contains a number of pixels less than the specified value (Yang, et al., 2024).

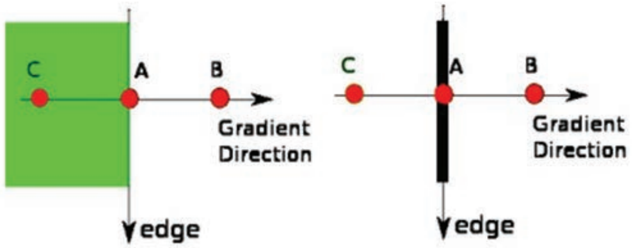

Fig. 4. Edge segmentation mechanism (Hong, et al., 2021).

F. Proposed Model

The model is built from scratch rather than using pre-trained architectures and features fewer layers compared to models, such as VGGNet, GoogLeNet, MobileNet, ResNet, and VGG16. The first stage consists of convolutional layers, which apply a set of filters to extract low-level features from images. Before training, all images are resized to 100 × 100 pixels as shown in Fig. 5.

The network structure comprises seven convolutional stages using “conv2d” layers as shown in Fig. 6. Initially, the model includes two convolutional layers, each with 32 kernel filters, separated by a MaxPool2D layer and a Dropout layer. The MaxPool2D layer performs down-sampling by selecting the maximum value from neighboring pixels, reducing computational complexity and mitigating overfitting.

In the second stage, the number of filters doubles to enhance feature extraction, while MaxPool2D and Dropout layers remain. The third stage expands to 128 filters, again incorporating MaxPool2D and Dropout layers. In the fourth, fifth, and sixth stages, the number of filters increases to 256, maintaining the same pooling and dropout mechanisms.

Finally, the seventh stage introduces two fully connected dense layers with 128 and 256 neurons, respectively, followed by a Dropout layer that connects to the output layer.

As for some of the features that were used in this model, ADAM optimizer was used. Each convolution layer contains a kernel size of 3 × 3 and a “ReLU” activation function. Furthermore, the learning rate annealing (LR) function was used. LR is a process by which the optimizer explores the “loss region.” The Batch size value was changed five times in each experiment (2, 4, 8, 16, and 32). The rest of the features used in this study are shown in Table III and Table IV shows the total parameters.

IV. RESULTS AND DISCUSSION

The results section consists of three subsections: Evaluation methods, results, and discussion and comparison with other studies:

A. Evaluation Metrics

To evaluate the performance of the proposed model, several metrics were used: global accuracy, sensitivity, specificity, and confusion matrix. Equations 4-6 give us the method for calculating each of the metrics used in this study (Baykara and Abdulrahman, 2021; Ramadhan and Baykara, 2022).

$$Accuracy = \frac{TP + TN}{TP + FP + FN + TN} \quad (4)$$

TABLE III
Parameter setting details in our method

Experimental parameters	Setting
Image size	(100×100×3)–(100×100×1)
Batch size	2, 4, 8, 16, 32
Optimizer	Adam
Epoch	100
Learning rate (LR)	0.0001
Loss	binary cross entropy

TABLE IV
The total parameters used in this study

Layer (type)	Output shape	Param#
Convd_7 (Conv2D)	(None, 100, 100, 32)	320
Max_poolingd_6 (Maxpooling2D)	(None, 50, 50, 32)	0
Dropout_7 (Dropout)	(None, 50, 50, 32)	0
Conv2d_8 (Conv2D)	(None, 50, 50, 32)	9,248
Conv2d_9 (Conv2D)	(None, 50, 50, 64)	18,496
Max_pooling2d_7 (Maxpooling2D)	(None, 25, 25, 64)	0
Dropout_8 (Dropout)	(None, 25, 25, 64)	0
Conv2d_10 (Conv2D)	(None, 25, 25, 128)	73,856
Max_pooling2d_8 (Maxpooling2D)	(None, 12, 12, 128)	0
Dropout_9 (Dropout)	(None, 12, 12, 128)	0
Conv2d_11 (Conv2D)	(None, 12, 12, 256)	295,168
Max_pooling2d_9 (Maxpooling2D)	(None, 6, 6, 256)	0
Dropout_10 (Dropout)	(None, 6, 6, 256)	0
Conv2d_12 (Conv2D)	(None, 6, 6, 256)	590,080
Max_pooling2d_10 (Maxpoolind2D)	(None, 3, 3, 256)	0
Dropout_11 (Dropout)	(None, 3, 3, 256)	0
Conv2d_13 (conv2D)	(None, 3, 3, 256)	590,080
Max_pooling2d_11 (Maxpooling2D)	(None, 1, 1, 256)	0
Dropout_12 (Dropout)	(None, 1, 1, 256)	0
Flatten_1 (Flatten)	(None, 256)	0
dense_3 (Dense)	(None, 128)	32,896
dense_4 (Dense)	(None, 256)	33,024
Dropout_13 (Dropout)	(None, 256)	0
dense_5 (Dense)	(None, 1)	257

Total params: 1,643,425 (6.27.MB)
Trainable params: 1,643,425 (6.27 MB)
Non-trainable params: 0 (0.00 B)
None

$$Sensitivity = \frac{TP}{TP + FN} \quad (5)$$

$$Specificity = \frac{TN}{TN + FP} \quad (6)$$

Where TP means the value of true positive, TN means the value of true negative, FP means the value of false positive, and FN means the value of false negative.

B. Results

Table V shows all the results obtained after executing the proposed model 5 times, each time changing the Batch size value (doubled) from 2 to 32.

The researchers notice from the table that there is a noticeable superiority of the proposed model in image segmentation over the first model before segmentation. In the first run of the model (32 Batch_size), this study achieved an accuracy of 92.18% before the image segmentation process, and then the researchers repeated the same experiment with the image segmentation process (Second scenario) and achieved a performance accuracy of 96.66%. Furthermore, the sensitivity and specificity have a better accuracy rate for the proposed model.

TABLE V
The total results obtained from the CNN model

Run	Batch_size	Filter	Accuracy (%)	Sensitivity (%)	Specificity (%)
Run 1	Batchsize 32	First Scenario	92.18	94.81	89.64
		Second Scenario	96.66	98	95.33
Run 2	Batchsize 16	First Scenario	91.81	94.07	86.07
		Second Scenario	96.33	98	94.66
Run 3	Batchsize 8	First Scenario	89.45	94.44	84.64
		Second Scenario	96.5	97.33	95.66
Run 4	Batchsize 4	First Scenario	92.18	93.33	91.07
		Second Scenario	96.83	98.1	95.66
Run 5	Batchsize 2	First Scenario	90	94	86.09
		Second Scenario	95.83	95.66	96

In addition, we noticed that the training time was reduced by 80%. For example, in the first run (Batchsize 32) before pre-processing, the training time was approximately 126 s per epoch, while after applying pre-processing, the training time became approximately 28 s per epoch.

Then, the same experiment was repeated before and after segmentation, and each time the batch value was changed, the performance of the proposed model was still superior to the first model. The highest accuracy is obtained in the fourth run, with an accuracy of 96.83%, and the best sensitivity accuracy is 98.1%. As for the specificity, the highest accuracy was obtained in the fifth run, with a value of 96%.

Fig. 7 shows the confusion matrix of the fourth run after applying image segmentation. Fig. 8 shows the accuracy curve of the second run after applying image segmentation. Fig. 9 shows the loss function curve of the third run before applying image segmentation.

C. Discussion and Comparison

After reviewing the results achieved using the proposed model, it became clear that it is possible to use deep learning techniques in the field of automatic detection of skin cancer using medical image processing techniques. The result obtained is somewhat good but needs improvement because, from our point of view, not all the images used in the experiment have the same shooting resolution or the same shooting angle, and some images have pen writing on them, from our point of view led to some impact on the final result of the model. In future studies, we will try to use other methods to process and clean images before training them.

Fig. 10 shows a comparison of the results achieved with some results of other studies conducted to detect skin cancer using deep learning techniques. We note from this figure that

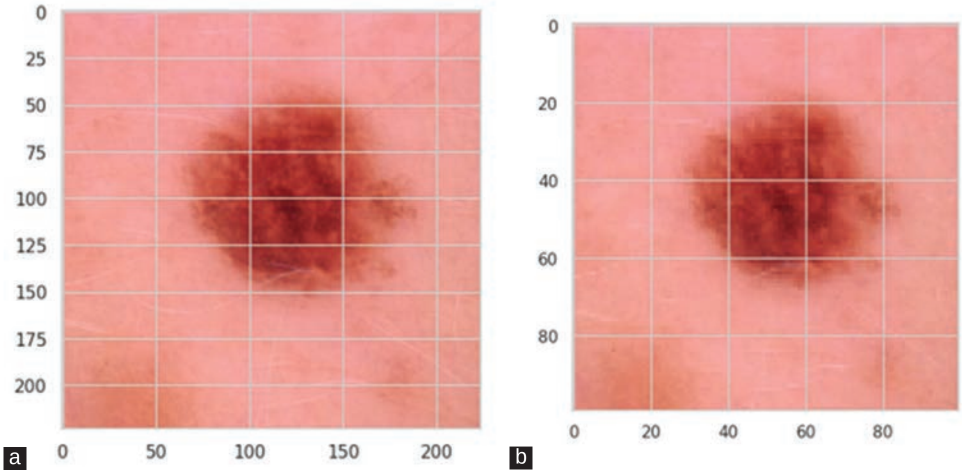

Fig. 5. Image resized (a) the original Image 224×224 RGB (b) the Image after resized it 100×100 RGB.

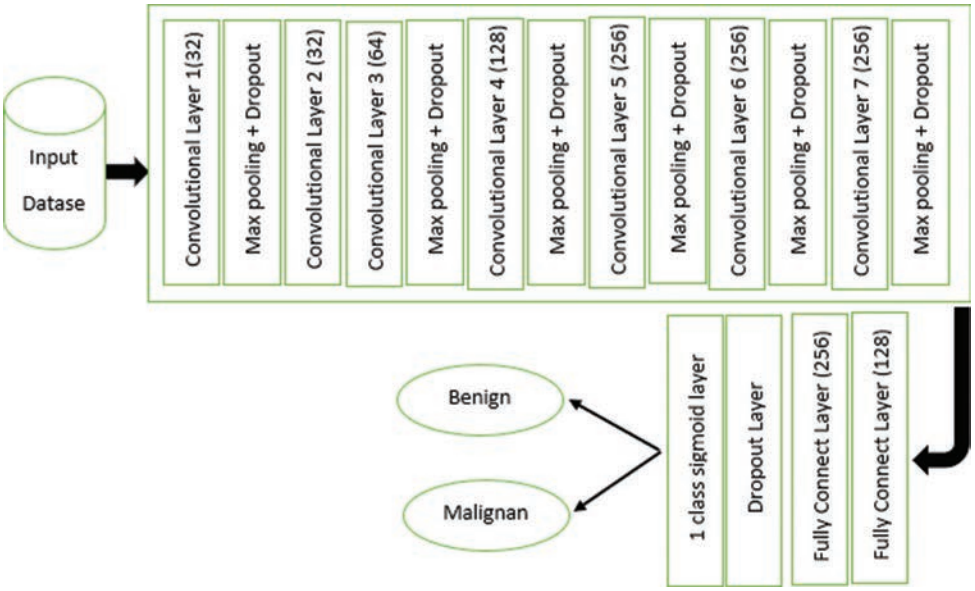

Fig. 6. The structure of the modified CNN model.

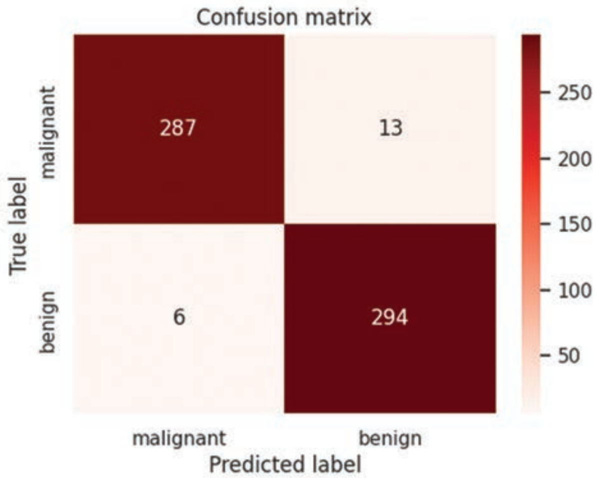

Fig. 7. Run4 Batch_size 4 after applying image segmentation process.

Fig. 8. The accuracy curve of Run 2 after applying image segmentation.

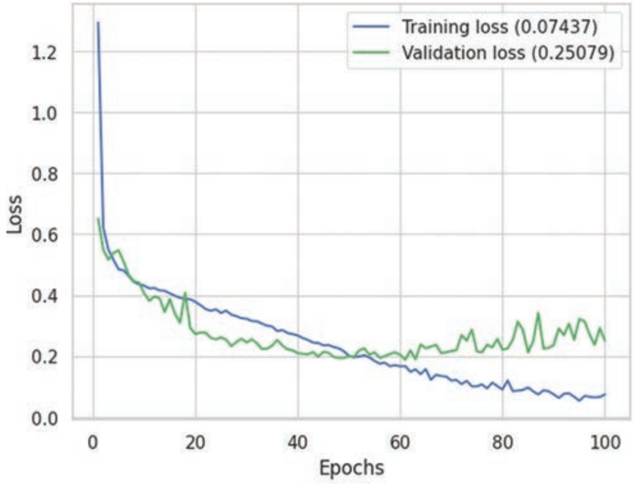

Fig. 9: Loss function curve for Run 3 before applying image segmentation.

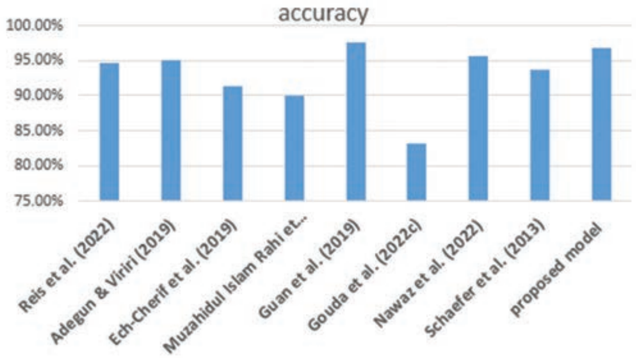

Fig. 10. A comparison with the newest studies.

the proposed model achieved satisfactory results and can be adopted in detecting melanoma cancer.

V. Conclusion

Skin cancer is one of the most dangerous diseases, especially melanoma skin cancer. Because most people do not pay attention to this dangerous disease and do not see a doctor when skin pigmentation appears, delaying the diagnosis of the disease leads to very negative results. Artificial intelligence and computer vision researchers have tried to help in this vital and dangerous field by finding an automated system that detects skin cancer early and reduces the death rate. Because early detection of the disease leads to an increase in the recovery rate to a percentage that may reach 90%.

In this study, a deep learning system derived from a CNN was built. It consists of two stages: The first stage involves training a model without pre-processing the images, and the second stage involves pre-processing the images by segmenting them using two image segmentations (threshold-based segmentation and edge-based segmentation), and two filtering methods (binary fill holes technique, and remove small objects). In both stages, training time and model accuracy were considered by reducing the number of parameters used.

The study achieved a performance accuracy of 96.83%. The results achieved in this study are satisfactory and can be built upon in future studies to develop early detection of skin cancer.

References

Abdulrahman, A., and Varol, S., 2020. A review of image segmentation using MATLAB environment. In: *2020 8th International Symposium on Digital Forensics and Security (ISDFS)*. IEEE, pp.1-5.

Adegun, A.A., and Viriri, S., 2019. Deep learning-based system for automatic melanoma detection. *IEEE Access*, 8, pp.7160-7172.

Al-Amri, S.S., and Kalyankar, N.V., 2010. *Image Segmentation by using Threshold Techniques*. [Preprint].

Baykara, M., and Abdulrahman, A., (2022) A novel approach for emotion recognition based on eeg signal using deep learning. *Applied Sciences*, 12, p.10028.

Baykara, M., and Abdulrahman, A., 2021. Seizure detection based on adaptive feature extraction by applying extreme learning machines. *Traitement du Signal*, 38(2), pp.331-340.

Canny, J., 1986. A computational approach to edge detection. *IEEE Transactions on Pattern Analysis and Machine Intelligence*, PAMI-8(6), pp.679-698.

Codella, N.C., Nguyen, Q.B., Pankanti, S., Gutman, D.A., Helba, B., Halpern, A.C., and Smith, J.R., 2017. Deep learning ensembles for melanoma recognition in dermoscopy images. *IBM Journal of Research and Development*, 61(4/5), pp.5-1.

Deriche, R., 1987. Optimal edge detection using recursive filtering. *International Journal of Computer Vision*, 2, pp.167-187.

Ech-Cherif, A., Misbhauddin, M., and Ech-Cherif, M., 2019. Deep neural network based mobile dermoscopy application for triaging skin cancer detection. In: *2019 2nd International Conference on Computer Applications and Information Security (ICCAIS)*. IEEE, pp.1-6.

Gouda, W., Sama, N.U., Al-Waakid, G., Humayun, M., and Jhanjhi, N.Z., 2022. Detection of skin cancer based on skin lesion images using deep learning. In: *Healthcare*. Vol. 10. MDPI, Switzerland, p.1183.

Guan, Q., Wang, Y., Ping, B., Li, D., Du, J., Qin, Y., Lu, H., Wan, X., and Xiang, J., 2019. Deep convolutional neural network VGG-16 model for differential diagnosing of papillary thyroid carcinomas in cytological images: A pilot study. *Journal of Cancer*, 10(20), p.4876.

Hong, R., Park, J., Jang, S., Shin, H., Kim, H., and Song, I., 2021. Development of a parcel-level land boundary extraction algorithm for aerial imagery of regularly arranged agricultural areas. *Remote Sensing*, 13(6), p.1167.

Hosny, K.M., Kassem, M.A., and Foaud, M.M., 2018. Skin Cancer Classification using Deep Learning and Transfer Learning. In *2018 9th Cairo International Biomedical Engineering Conference (CIBEC)*. IEEE, pp.90-93.

Kandhro, I.A., Manickam, S., Fatima, K., Uddin, M., Malik, U., Naz, A., and Dandoush, A., 2024. Performance evaluation of E-VGG19 model: Enhancing real-time skin cancer detection and classification. *Heliyon*, 10(10), p.10028.

Ma, W.Y., and Manjunath, B.S., 2000. EdgeFlow: A technique for boundary detection and image segmentation. *IEEE Transactions on Image Processing*, 9(8), pp.1375-1388.

Nawaz, M., Mehmood, Z., Nazir, T., Naqvi, R.A., Rehman, A., Iqbal, M., and Saba, T., 2022. Skin cancer detection from dermoscopic images using deep learning and fuzzy k-means clustering. *Microscopy Research and Technique*, 85(1), pp.339-351.

Ozdemir, B., and Pacal, I., 2025. An innovative deep learning framework for skin cancer detection employing ConvNeXtV2 and focal self-attention mechanisms. *Results in Engineering*, 25, p.103692.

Rahi, M.M.I., Khan, F.T., Mahtab, M.T., Ullah, A.A., Alam, M.G.R., and Alam, M.A., 2019 Detection of skin cancer using deep neural networks. In *2019 IEEE Asia-Pacific Conference on Computer Science and Data Engineering (CSDE)*. IEEE, pp.1-7.

Ramadhan, A.A., and Baykara, M., 2022. A novel approach to detect COVID-19: Enhanced deep learning models with convolutional neural networks. *Applied Sciences*, 12(18), p.9325.

Reis, H.C., Turk, V., Khoshelham, K., and Kaya, S., 2022. InSiNet: A deep convolutional approach to skin cancer detection and segmentation. *Medical and Biological Engineering and Computing*, 60, pp.643-662.

Schaefer, G., Krawczyk, B., Celebi, M.E. and Iyatomi, H., 2013. Melanoma classification using dermoscopy imaging and ensemble learning. In: *2013 2nd IAPR Asian Conference on Pattern Recognition*. IEEE, pp.386-390.

Somasundaram, K., and Kalaiselvi, T., 2010, February. A method for filling holes in objects of medical images using region labeling and run length encoding schemes. In: *National Conference on Image Processing (NCIMP)*, pp.110-115.

Swapno, S.M.R., Nobel, S.N., Meena, P.K., Meena, V.P., Bahadur, J., and Appaji, A., 2025. Accelerated and precise skin cancer detection through an enhanced machine learning pipeline for improved diagnostic accuracy. *Results in Engineering*, 25, p.104168.

Tan, T.Y., Zhang, L., and Lim, C.P., 2019. Intelligent skin cancer diagnosis using improved particle swarm optimization and deep learning models. *Applied Soft Computing*, 84, p.105725.

Yang, Y., Zang, B., Song, C., Li, B., Lang, Y., Zhang, W., and Huo, P., 2024. Small object detection in remote sensing images based on redundant feature removal and progressive regression. *IEEE Transactions on Geoscience and Remote Sensing*, 62, p.3417960

Scalable and Efficient Multi-Class Brain Tumor Classification with a Compact Hybrid Deep Learning Model for Real-Time Applications

Sohaib R. Awad[1], Amar I. Daood[2†] and Akram A. Dawood[2]

[1]Department of Computer and Information Engineering, Ninevah University,
Mosul, Iraq

[2]Department of Computer Engineering, College of Engineering, University of Mosul,
Mosul, Iraq

***Abstract*—Medical diagnostics require brain tumor classification to operate in real-time so the task demands accurate results with efficient processing abilities. A new hybrid deep learning solution merges convolutional neural networks (CNNs) with support vector machines (SVMs) to improve classification results as this paper describes. A total of four tumor categories including glioma, meningioma, and pituitary tumors together with no tumor appearance contribute to the magnetic resonance imaging (MRI) dataset are used for analysis. We applied and organized three pre-trained deep learning models: AlexNet, DarkNet-19, and ResNet-50 for comparison. A newly engineered compact CNN model linked with an SVM classifier brought decreased model dimensions while keeping excellent accuracy rates. A proposed compact CNN model delivers 97.50% accuracy through its smaller 2.38 MB size and an additional SVM integration results in 97.45% accuracy using 1.43 MB. A Graphical User Interface (GUI) system comprising automated tumor classification capabilities is created to improve real-time systems that visualize MRI scans and illustrate predicted labels in addition to displaying confidence scores. A GUI enables smooth access to the trained model while being suitable for medical practice mobile healthcare environments and edge computing needs. The proposed system shows that lightweight architectures work excellently in real-time system applications especially when used for edge computing and mobile healthcare frameworks. The proposed solution demonstrates superiority over established models through its ability to scale efficiently.**

***Index Terms*—Brain tumor classification, Deep learning, Medical diagnostics, Real-time applications, Scalable AI solutions.**

I. INTRODUCTION

Brain tumor classification requires an early and precise identification for medical diagnostic purposes. The diagnostic process together with treatment recommendations becomes more efficient for radiologists when they use magnetic resonance imaging (MRI)-based classification methods. Deep learning technology especially Convolutional Neural Networks (CNNs) delivered significant improvements to brain tumor classification precision during recent times. The high computational requirements of advanced CNN models render them unusable when running real-time or edge-computing operations. Early identification and treatment of such tumors are significant for patient outcomes, and the classification of brain tumors in medical diagnostics is a critical task (Sharma, et al., 2023). It is very difficult to separate true tumor structures, namely, glioma, meningioma, pituitary, and no tumor due to the complexity of the tumor structures and variation of medical image data (Ullah, et al., 2023). As the demand for radiologists using automated systems to assist them continues to grow, there is greater demand for solutions that are not only very accurate, but also computationally efficient, and deployable in resource-constrained environments (Mohammed, et al., 2024; Jana, et al., 2023). Due to the ability to learn hierarchical and complex features directly from raw medical imaging data, deep learning has become an optimal solution for brain tumor classification (Awad, et al., 2022; Ganaie, et al., 2022). Among these, CNNs in particular have demonstrated exceptionally high accuracy in achieving a wide range of different tasks such as pattern classification (Daood, Al-Saegh and Mahmood, 2023; Abdulaziz and Dawood, 2023), smart surveillance (Mohammed and Daood, 2021), biometric (Alhafidh, Hagem and Daood, 2022), smart home (Alhafidh, Daood and Allen, 2018), and medical image analysis (Müller, Soto-Rey and Kramer, 2022; Jasim, et al., 2021). Nevertheless, conventional deep learning models are prone to their size being huge and having high computational requirements (Akinbo and Daramola, 2021; Abdullah, Mohammed and Awad, 2024) rendering them impractical for real-time and edge computing applications. Research in brain tumor classification through deep learning techniques makes progress daily according to two recent studies because it enables automated tumor detection and enhances segmentation quality (Al-Jammas,

---

ARO-The Scientific Journal of Koya University
Vol. XIII, No.1(2025), Article ID: ARO.12017. 13 pages
DOI: 10.14500/aro. 12017
Received: 22 January 2025; Accepted: 19 April 2025
Regular research paper; Published: 03 May 2025
†Corresponding author's e-mail: amar.daood@uomosul.edu.iq

et al., 2024). Feature extraction capabilities of CNN-based models received development through new model implementations and multiple CNN strategies worked effectively for ensemble-based MRI tumor detection tasks. The advancement demonstrates why the lightweight design of neural network architecture requires both accurate results and efficient computing power and instant detection capability to achieve effective tumor recognition (Al-Mukhtar, et al., 2024; Santoso, Supriyono and Utama, 2024).

We present scalable and efficient models addressing the above restrictions in this study. This research implements a minimal CNN model that operates with an support vector machine (SVM) classification system to cope with this challenge. The hybrid CNN-SVM method optimizes performance efficiency and decreases model complexity despite using deep feature learning methods independently of traditional deep learning methods. The research study tests three deep learning frameworks, namely, ResNet-50, Alex-Net, and DarkNet-19 alongside the constructed compact CNN-SVM model. Our contributions include:

1. A compact CNN model development for medical image classification presents efficient computations while reducing expenses.
2. The combination of CNN with SVM classifiers improves system efficiency without affecting the accuracy of results.
3. The study analyses deep learning models based on their measurement performance alongside their speed capabilities and time responsiveness.
4. The study demonstrates the relationship between important performance aspects between state-of-the-art methods by showing how model precision interacts with operational efficiency.

The paper advances present research by prioritizing the equilibrium between precise results and low computational demands needed for quick medical use scenarios. The rest of this paper is organized as follows: In section 2, we present a review of related works, by summarizing the latest developments in brain tumor classification. In section 3, the methodology is presented with an overview of dataset preparation, model design, and training strategies. In section 4, we examine experimental results, and in section 5, we compare our work with other recent state-of-the-art approaches. Finally, section 6 concludes with the study and possible directions for future work.

II. Literature Review

Classifying brain tumors is an important task in medical diagnostics that typically demands powerful methods to achieve high accuracy, while also satisfying constraints when being deployed in environments whose resources are limited (Ramanagiri, Mukunthan and Balamurugan, 2024; Rasool, et al., 2024). Recent advancements in artificial intelligence, particularly in deep learning and hybrid approaches, have significantly contributed to the progress in this domain (Onuiri, John and Umeaka, 2024; Mavaddati, 2024). This section reviews these key studies that have informed and influenced the present research.

Transfer learning has been a very powerful tool in medical image analysis as it utilizes pre-trained models for application on problems where annotated data are scarce. ResNet-50 was used in one study (Sahaai, et al., 2022) where they used it for brain tumor classification and illustrated its efficacy in producing intricate features from MRI image. (Srinivas, et al., 2022) investigated deep transfer learning approaches for brain tumor classification through analyzing the robustness of models ResNet-50, Inception-v3, and VGG-16 in medical imaging tasks. However, these studies mainly pushed for high accuracy, often ignoring constraints regarding the size of the model and computational efficiency.

Recent research has been performed to look at what it means to use deep learning feature extractors with traditional machine learning (ML) classifiers to improve computational efficiency and accuracy. Another study (Karim, Mahmood and Sah, 2023) fine-tuned a deep transfer learning model with an SVM that produced better performance than previous confidential. In a similar vein, another approach in (Yadav, et al., 2024) suggested a modified ResNet-50 model and worked well, yet at the cost of expensive computation as a result of model size. Nevertheless, the actual deployment of these hybrid frameworks in resource-constrained environments is still limited.

Large pre-trained models are limited in their scalability; hence, compact architectures have become a hot topic for their existence and scalability of inferencing and also to their ability to equip the real-time application. In one research effort, a deep transfer learning framework for multi-class brain tumor classification (Divya, Suresh and John, 2020) obtained promising results and showed the necessity for lightweight models. A related work (Shamshad, et al., 2024) considered improvements in the efficacy of transfer learning methods, for example, models such as VGG-19, VGG-16, ResNet-50, Mobile-Net, Inception-v3, and Dense-Net, on MRI datasets, noting the difficulties in achieving high accuracy at the same time as low model size and computational cost. A spatial pyramid pooling layer was added to another study (Neamah, et al., 2024) which introduced a modified ResNet-50 model trained with pre-trained parameters to combat overfitting, and partially addresses scalability concerns with high accuracy. The present studies are useful in understanding these trade-offs between model complexity and deployment feasibility, and correspond with the intended aims of the present research.

Multiple research groups have conducted studies of deep learning for brain tumor classification while focusing on enhancing accuracy levels. Department of Medical Sciences Dalhousie University and author Marie-Claude Arnaud explore the effectiveness of transfer learning with ResNet-50, Inception-v3, and VGG-16 for brain tumor identification while acknowledging their high computational costs (Sharma, et al., 2023; Ullah, et al., 2023). Hand-in-hand integration between CNNs and SVM ML classifiers leads to model size reduction without any loss in classification effectiveness (Karim, Mahmood and Sah, 2023). The evaluation of compact architectures suitable for real-time deployment is not addressed in several studies that currently exist. Research nowadays strives to develop lightweight architectures for brain tumor classification with reduced computational expenses and stable robustness. The research brings forward an optimized compact CNN model for brain tumor classification alongside extensive performance evaluation.

Many previous studies have made impressive progress in terms of accuracy; however, these works often fail to account for important elements such as model scalability, computational efficiency, and practical feasibility of real-time deployment. ResNet-50, VGG-16, and VGG-19 are extremely correct but they take up a great deal of resources and are consequently insufficient for use in mobile or edge devices. Such hybrids promise to address these issues, but usually, this comes at the cost of more complex frameworks, which increases computational overhead. On the other hand, compact architectures open the door to scalability, but more optimization is needed to close the gap on larger model accuracy.

To address these gaps, this study introduces a new compact CNN model, and hybrid frameworks that combine using CNNs with SVM classifiers. In the next parts, we will show that the proposed models result in competitive accuracy compared with baseline models, with a significant reduction in model size and classification time, which makes them practical for deployment in resource-constrained environments. This research builds on and exceeds the limitations recognized in the literature in brain tumor classification, presenting scalable and efficient AI-powered solutions.

III. Materials and Methods

This paper is an attempt to develop an efficient and accurate classification system for brain tumor prediction, which incorporates deep learning and ML approaches. The multiple stages involved in the methodology include dataset preparation, model training, feature extraction, and hybrid classifier integration. The design of each stage was intended to guarantee high accuracy, a low computational cost, and practical applicability in real-world scenarios.

A. Overview of the Proposed Method

This research focuses on classifying brain tumor MRI images into four classes: Included are glioma, meningioma, no tumor, and pituitary. For this, three pre-trained networks are chosen: Alex-Net (depth 8), DarkNet-19 (depth 19), and ResNet-50 (depth 50). We chose these models because they have an ascending architectural complexity and have exhibited good performance on a diversity of datasets. However, due to the large model size, VGG-16 and VGG-19, though with similar accuracy, were omitted, and they are not fit for real-time applications and deployment in low-resource environments.

We evaluated two optimizers – Adaptive Moment Estimation (ADAM) and Stochastic Gradient Descent with Momentum (SGDM) – on every network to tune out optimal hyper-parameters in pursuit of the best accuracy versus performance trade-off. To improve deployment suitability for the further scope, the original fully connected dense layers were removed, followed by passing the extracted features to ML models, in particular SVM, to ascertain the extent of identifying the best accuracy and performance trade-off within the image classification. Prolonged experimentation with various classifiers demonstrated that the SVM approach is mutually robust for high-dimensional feature spaces. In the end, a compact ML model was proposed aiming to strike a balance between classification accuracy, classification latency, and model size, thus offering a strong candidate for real-time use in an edge deployment scenario.

B. Dataset Preparation

A comprehensive dataset of 10,183 MRI images was compiled from three reputable sources: Figshare, SARTAJ, and Br35H. These images are classified into four categories: Other benign tumors such as meningioma, glioma, no tumor, and pituitary tumors (Mohammed, et al., 2024). To ensure uniformity and compliance with deep learning architectures, each image was normalized to a resolution of 256×256 pixels. The dataset was divided evenly between training and validation (80%), and testing (20%) functions to achieve balanced learning together with generalization. Model parameters received optimization through the training data and the validation data subset from training performed hyper-parameters alteration and performance checking to prevent overfitting. The model works properly on new data because it uses the validation set performance evaluation to ensure good generalization before final testing. The model testing process utilized a distinct 20% segment of data as a testing set which remained separate throughout for objective evaluation of classification capabilities. Table I demonstrates an equal proportion of classes throughout the data distribution.

The model achieved generalization by utilizing data augmentation through rotational techniques at ±45° angles together with flipping operations. Augmentations for these remained in semantic integrity within the image, yet they varied to help provide the model's ability to generalize to unseen data. To conform to pre-trained models, input pre-processing resized images for compatibility with Alex-Net (227×227×3), DarkNet-19 (256×256×3), and ResNet-50 (224×224×3). To satisfy these requirements we converted grayscale images into RGB format by duplicating the single channel across 3 dimensions. Fig. 1 shows class samples of the dataset.

TABLE I
Dataset Class Distribution

Class	Number of images	Training/validation (80%)	Testing (20%)
Glioma	2,547	2,038	509
Meningioma	2,582	2,065	517
No tumor	2,396	1,917	479
Pituitary	2,658	2,126	532
Total	10,183	8,146	2,037

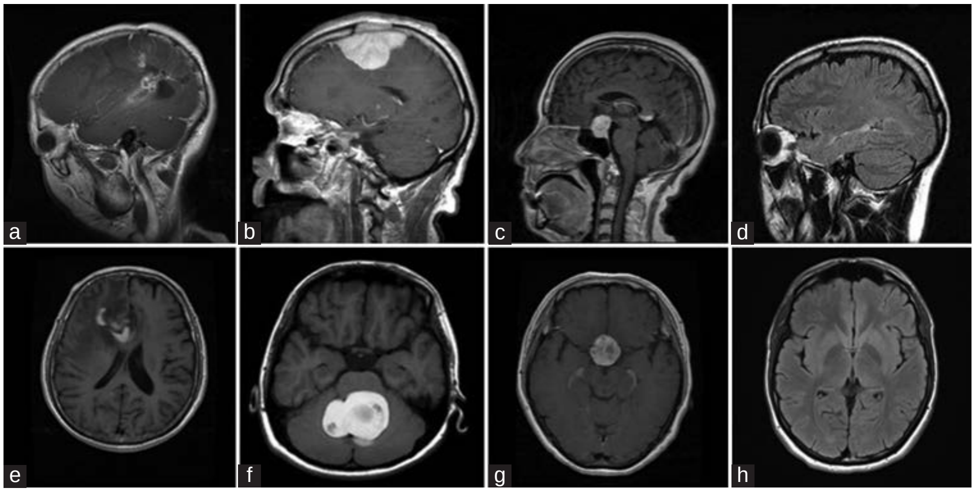

Fig. 1. Sample images from each dataset class. (a) Glioma, (b) Meningioma, (c) Pituitary, (d) No tumor, (e) Glioma, (f) Meningioma, (g) Pituitary, (h) No tumor.

C. Pre-trained Networks and Optimization

Three pre-trained models were selected: To understand the recent success of deep neural networks, we study the factors that contribute to learning depth in three state-of-the-art network models: Alex-Net, DarkNet-19, and ResNet-50, which have depths of 8, 19, and 50, respectively. We use these models to investigate the trade-offs between accuracy, complexity, and computational efficiency. Exclusion of VGG-16 and VGG-19 was also due to unnecessary large size, making them impractical for real-time deployment. The optimal hyper-parameters and best accuracy for each architecture were identified using each model trained by two different optimization strategies, ADAM and SGDM. The pre-trained network specifications are summarized in Table II.

This training entailed tuning hyper-parameters, such as learning rate, epoch count, and batch size. We also train models with ADAM and use an initial learning rate of 0.001 and a learning rate drop factor of 0.5 every 10 epochs. We used a similar learning rate schedule as SGDM, but including momentum to stabilize training. The balance and effectiveness of each model were evaluated by computing performance metrics: Accuracy, Precision, Recall, and F1-score. All networks standardize MATLAB training settings (Table III).

D. Hybrid Frameworks with Feature Extraction

To decrease the size of the model by eliminating the dense (fully connected) layers, and simplify the classification time, while maintaining high accuracy, models were pre-trained. Features were extracted from the last convolutional layers of the trained models: The number of features in the 3 models is Alex-Net (4096 features), ResNet-50 (2048 features), and DarkNet-19 (1000 features). Using these features, ML classifiers were trained with both logistic regression and standard SVM with an SVM box constraint of 5, and the kernel is Radial Basis Function RBF performing best after hyper-parameter tuning. Random forest, decision tree, and XG-Boost classifiers were also compared for comparison

TABLE II
Summary of Pre-trained Models

Model	Total layers	Connections	Depth	Learnable parameters	Input image size
Alex-Net	25	24	8	59.8 M	227×227×3
DarkNet-19	65	64	19	20.3 M	256×256×3
ResNet-50	177	192	50	25.6 M	224×224×3

TABLE III
Training Configuration and Parameters

Parameter	Value
Initial learning rate	0.001
Learning rate drop factor	0.5
Learning rate drop period	10 epochs
Maximum epochs	30
Batch size	32
Validation frequency	50
Hardware	GPU: NVIDIA RTX 3060 with 6 GB VRAM. Processor: Intel Core i7 12th Gen. Memory: 16 GB RAM

This hybrid framework uses CNN features to retain the discriminative power of CNN features, but lowering the overall model complexity. Feature dimensionality was reduced without losing significant information by using Global Average Pooling (GAP) before feature extraction. Classification times were considerably improved and the disk storage requirement was reduced with the hybrid approach.

However, removing dense layers offered challenges on the account of reduced learnable parameters, as well as the need for robust feature representations to achieve the same level of accuracy as the baseline model (Kokhazadeh, et al., 2024; Awad and Alghareb, 2025). Careful management was required for the dimensionality of extracted features to prevent computational overhead (Xia, et al., 2018; Pan, et al., 2020). To obtain the best performance, we then fine tune the hyper-parameters, yet more crucially, we also needed to ensure the compatibility between CNN feature extractors, and SVM classifiers. Mitigation of these challenges is shown using GAP, and rigorous evaluation of hybrid models.

E. Proposed Compact CNN Model

Our proposed model consists of a compact CNN architecture with:

- Input layer: 128×128 RGB image resolution
- Four convolutional layers with batch normalization
- GAP layer for feature extraction
- SVM classifier for final classification.

Using CNN-derived vectors the feature extraction process feeds information to an SVM classifier that improves performance and decreases operational complexity. To balance accuracy and computational efficiency, a compact CNN model was proposed. This model was lighter in terms of layers and learnable parameters, being smaller. Instead of using dense layers, the architecture used GAP to obtain 256 features that were fed into an SVM classifier. With significantly faster classification times and smaller model size, the compact model was competitive to its full counterpart, and hence suitable for real-time edge computing and mobile applications. The proposed ML model architecture specifications are presented in Table IV.

To further enhance the deployment efficiency of the compact CNN, the dense layer was removed, and the model was integrated with an SVM classifier. The features extracted from the last convolutional layer (256 features) were used as input to the SVM, as shown in Fig. 2 below.

F. Models Evaluation

Accuracy, precision, recall, and F1-score were evaluated (equations 1–4) along with classification time, size of the model, and number of learnable parameters of each model (Naidu, Zuva and Sibanda, 2023; Obi, 2023). Results showed a trade-off between efficiency and accuracy, where the proposed compact CNN model provides an optimal balance. The results section presents detailed discussions of these metrics and their implications, as well as tables summarizing comparative findings.

TABLE IV
ARCHITECTURE OVERVIEW OF THE PROPOSED COMPACT CNN MODEL

Attribute		Value
Input image size, Optimizer		128×128×3, ADAM
Total layers, Number of connections, Depth		19, 18, 5
Number of convolutional layers	4	conv_1 128×128×32, conv_2 64×64×64, conv_3 32×32×128, conv_4 16×16×256
Number of fully connected layers		1
Pooling layers		3
Number of batch normalizations		4
Number of activation layers		4
Number of classes	4	Glioma, Meningioma, Pituitary, and No tumor
Total learnable parameters		651.5 K
Fully connected layer parameters		262.15 K

$$Accuracy\ \% = \frac{TP + TN}{TP + TN + FP + FN} \times 100 \tag{1}$$

$$Precision\ \% = \frac{TP}{TP + FP} \times 100 \tag{2}$$

$$Recall\ \% = \frac{TP}{TP + FN} \times 100 \tag{3}$$

$$F1 - Score\ \% = \frac{2 \times Precision \times Recall}{Precision + Recall} \times 100 \tag{4}$$

The evaluation metrics are based upon true positive (TP), which is the number of correctly predicted positive instances; true negative (TN), which is the number of correctly predicted negative instances; false positive (FP), which is the number of instances incorrectly classified as positive; and false negative (FN), which is the number of instances incorrectly classified as negative (Raja, et al., 2024). These parameters serve as bases for the calculation of critical performance metrics such as reliability and cycle time, to serve as an overall metric of the predictive capabilities of the model.

IV. EXPERIMENTAL RESULTS

In this section, we present the results of the study, namely, evaluation metrics, Confusion Matrices (CMs), and analytical in-depth analysis of the performance of the pre-trained models, hybrid frameworks, and the proposed compact CNN model. The results offer insights into accuracy versus efficiency versus computational resources trade-offs.

A. Training Logs and Key Insights

All models showed consistent improvements in accuracy and decreased loss during 30 epochs of training. We analyze how the convergence speed and performance metrics differ between ADAM and SGDM optimizers, using the proposed CNN model to demonstrate competitive performance compared to pre-trained models. ADAM optimizer had a smooth convergence by epoch 20 and reached the validation accuracy of 97.30% for Alex-Net. The effective learning and optimization resulted in the loss reduced from around 2.1 in the initial epochs down to 0.07. Nevertheless, SGDM yielded a slightly higher validation accuracy of 98.62%, and converged faster, as illustrated in Fig. 3 and stabilized at epoch 18. A smooth and stable training process was probed with the trend of training loss with SGDM reduced from about 2.0 to 0.04.

We found that training with ADAM got a validation accuracy of 96.81% with DarkNet-19 and that stability was reached around epoch 22. It is noticed that the loss decreased consistently from 3.1 to 0.08, which means, the learning was predictable within different epochs. SGDM got validation accuracy slightly lower, 96.66% of it, and stabilized at epoch 23. It started with a 3.0 loss and went down to 0.09, which is again like ADAM, but just a little bit slower. ADAM was the optimizer with the highest accuracy, with a validation

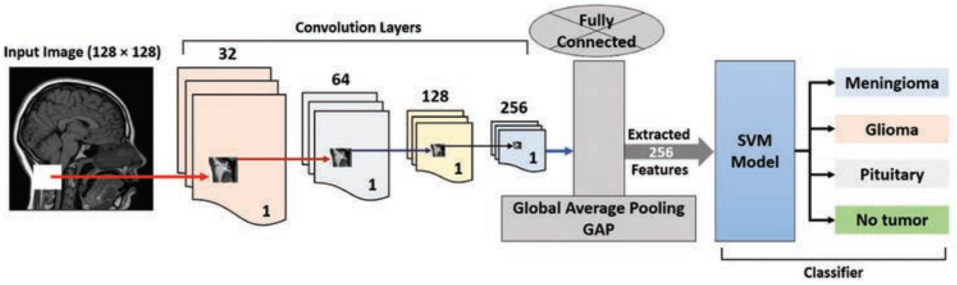

Fig. 2. Architecture of the accelerated compact convolutional neural network-integrated with support vector machine.

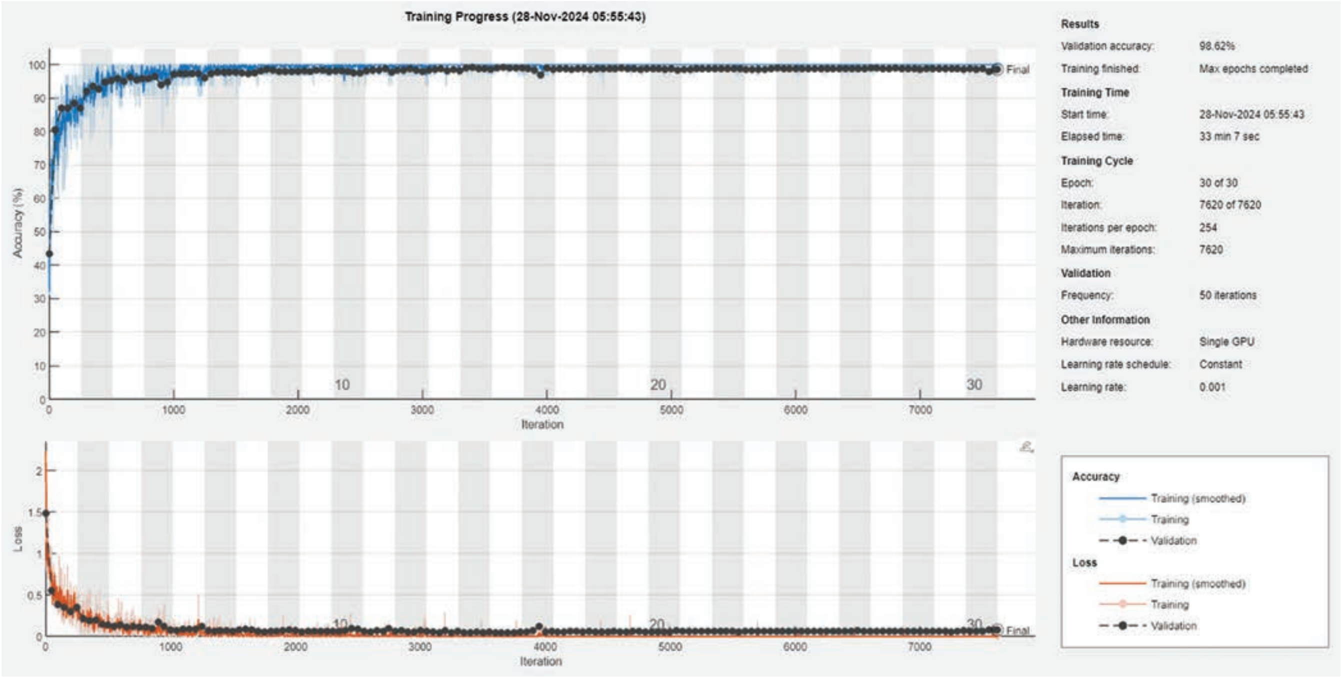

Results
Validation accuracy: 98.62%
Training finished: Max epochs completed
Training Time
Start time: 28-Nov-2024 05:55:43
Elapsed time: 33 min 7 sec
Training Cycle
Epoch: 30 of 30
Iteration: 7620 of 7620
Iterations per epoch: 254
Maximum iterations: 7620
Validation
Frequency: 50 iterations
Other Information
Hardware resource: Single GPU
Learning rate schedule: Constant
Learning rate: 0.001

Fig. 3. Training progress of the Alex-Net model.

accuracy of 99.07% by ResNet-50 of the deepest architecture. This quickly stabilized by epoch 15, reducing loss from 1.2 to 0.02, where loss stopped decreasing, and the network rapidly learned to pick up on complex feature patterns. ResNet50 using GPU with SGDM reached a validation accuracy of 98.04% and stabilized by epoch 18. The loss went down from about 1.3 to 0.04 and exhibits steady albeit slightly less efficient optimization than ADAM.

Fig. 4 shows that, as an application for lightweight applications, the proposed compact CNN model, gained a validation accuracy of 97.50% after 20 epochs with fast convergence. 2.5 down to 0.05 in loss we steadily lost. Beyond maintaining competitive accuracy, its simplified architecture brought its classification time down to 3.2 s, the fastest time in the competition, making it a suitable candidate for real-time deployment within resource-constrained scenarios.

This training analysis highlights that pre-trained models and compact architectures achieve competitive results both in accuracy and in computational efficiency while being able to be deployed; and ADAM optimizer is particularly useful for deeper architectures. The results of the training show trade-offs between accuracy, computational savings, and real-time applicability. In addition, the proposed compact CNN model has a good balance between high accuracy and low classification time, and is likely to be a promising candidate in practical deployment. Although accurate, they are not intended for resource-constrained environments where they require higher computation costs. Optimization choice is important for convergence speed, and we show that ADAM is faster at converging deeper networks. Results from the all used deep learning model training are shown in Table V below.

This study leverages lightweight architectures and hybrid frameworks to demonstrate the feasibility of real-world deployment of accurate and efficient classification systems in real-time applications. The conclusion of these results highlights how considerations of model selection need to align with the specifics of a particular use case, in keeping with a trade-off between accuracy, efficiency, and deployment constraints.

B. Pre-trained Models Evaluation

We evaluate the performance of pre-trained networks, Alex-Net, DarkNet-19, and ResNet-50, on a testing set.

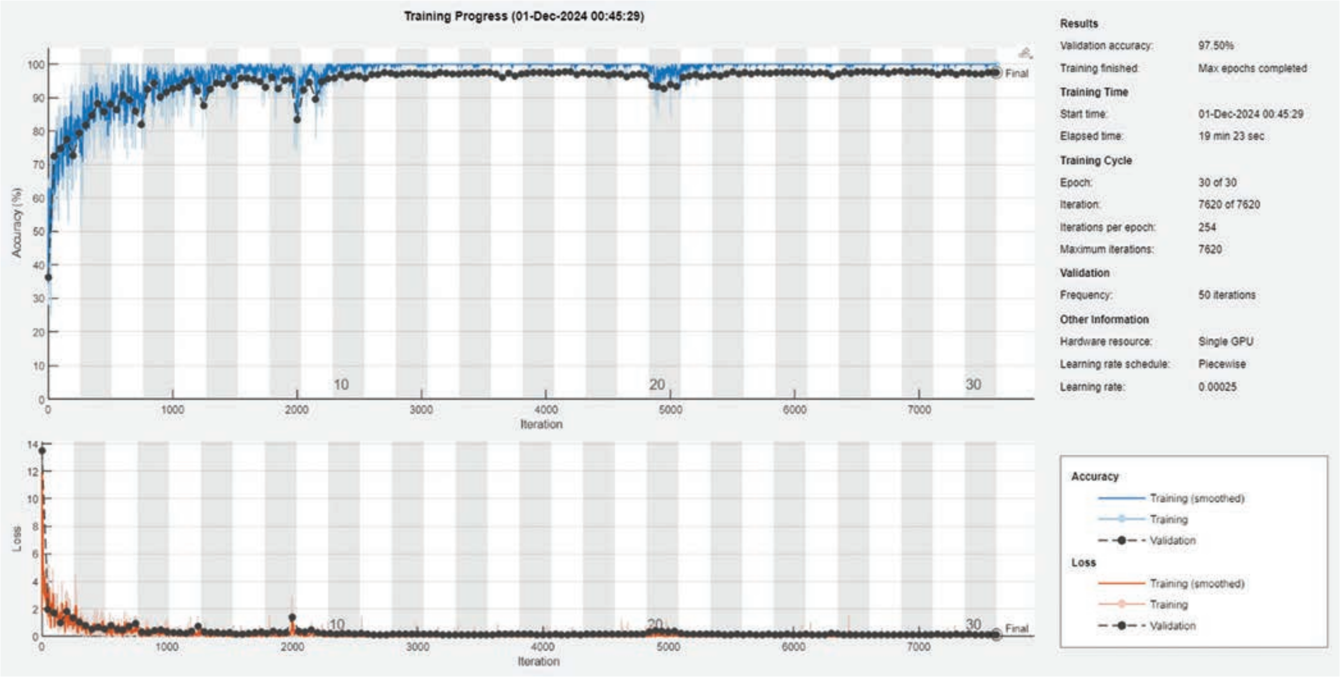

Results
Validation accuracy: 97.50%
Training finished: Max epochs completed
Training Time
Start time: 01-Dec-2024 00:45:29
Elapsed time: 19 min 23 sec
Training Cycle
Epoch: 30 of 30
Iteration: 7620 of 7620
Iterations per epoch: 254
Maximum iterations: 7620
Validation
Frequency: 50 iterations
Other Information
Hardware resource: Single GPU
Learning rate schedule: Piecewise
Learning rate: 0.00025

Fig. 4. Training progress of the proposed compact convolutional neural network model.

TABLE V
Training Summary of Deep Learning Models

DL model	Optimizer	Validation accuracy (%)	Convergence (Epoch)	Final loss	Model size (MB)
Alex-Net	ADAM	97.30	20	0.07	196.73
	SGDM	98.62	18	0.04	
DarkNet-19	ADAM	96.81	22	0.08	75.96
	SGDM	96.66	23	0.09	
ResNet-50	ADAM	99.07	15	0.02	86.02
	SGDM	98.04	18	0.04	
Compact CNN	ADAM	97.50	20	0.05	2.38

The evaluation metrics of these models are summarized in Table VI. When ADAM optimizer was used to train ResNet-50, it achieved the highest accuracy of 99.07% indicating that it excels in handling complex features, followed by Alex-Net by SGDM optimizer with an accuracy of 98.62%. Alex-Net's time of classification was also excellent as compared to other CNNs and it had the shortest time due to the shallow design of the architecture having only a depth of 8. While its simplicity is one of the reasons, its model size is the largest among all the networks we evaluated, which can be attributed to its fully connected layers. For deeper architectures like ResNet-50 in comparison to optimizers, ADAM comparatively converged faster with slightly better accuracy. Upon generation of CMs for each of the pre-trained architectures, Fig. 5 demonstrates straightforward balanced classifications across all four classes; substantiating the robustness and reliability of these architectures to varying distributions of data.

C. Hybrid Frameworks with Feature Extraction

The removal of dense layers reduced model complexity and allowed features from the final convolutional layers to be passed to ML classifiers. Table VII summarizes the performance of the hybrid models.

TABLE VI
Performance Metrics of Pre-trained Deep Learning Models

Model	Testing accuracy (%)	Precision (%)	Recall (%)	F1-score (%)	Classification time for testing set (Sec.)
Alex-Net	98.62	98.62	98.64	98.62	5.3
DarkNet-19	96.81	96.83	96.82	96.80	5.7
ResNet-50	99.07	99.07	99.07	99.07	6.6

The hybrid models showed a significant reduction in model sizes that makes them more suitable for deployment on resource-constrained edge devices and mobile applications. Reducing this simply by removing the dense layers of CNN architectures and using ML classifiers like SVM for final classification. Among hybrid frameworks, ResNet-50 with SVM showed the best accuracy, as it achieved to strike the right balance between providing richer features from ResNet-50 architecture and at the same time gaining from the SVM classifier in being robust. In this work, we take advantage of ResNet-50's capacity to express intricate feature representations, while exploiting the SVM's efficiency in high-dimensional spaces. CMs for the three hybrid frameworks in the testing set are shown in Fig. 6.

Another important advantage of the hybrid framework was their classification times were shorter than of CNN counterparts. Eliminating dense layers and computationally intensive units, the hybrid models sacrificed relatively little in accuracy while speeding up inference. As an example, the complete testing set took approximately 6.6 s for classification with pure CNN ResNet-50, while hybrid ResNet-50 with SVM got this time down to about 5.2 s. The results underscore the promise of hybrid architectures

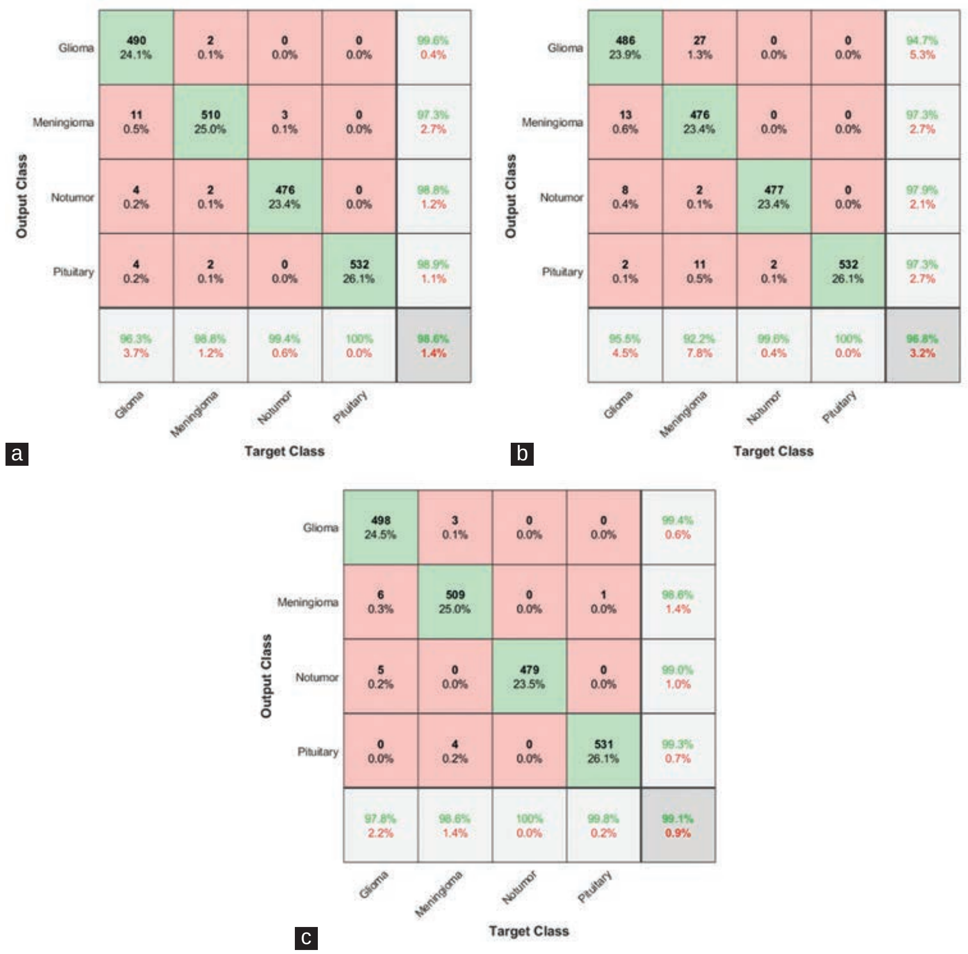

a

	Glioma	Meningioma	Notumor	Pituitary	
Glioma	490 24.1%	2 0.1%	0 0.0%	0 0.0%	99.6% 0.4%
Meningioma	11 0.5%	510 25.0%	3 0.1%	0 0.0%	97.3% 2.7%
Notumor	4 0.2%	2 0.1%	476 23.4%	0 0.0%	98.8% 1.2%
Pituitary	4 0.2%	2 0.1%	0 0.0%	532 26.1%	98.9% 1.1%
	96.3% 3.7%	98.8% 1.2%	99.4% 0.6%	100% 0.0%	98.6% 1.4%

b

	Glioma	Meningioma	Notumor	Pituitary	
Glioma	486 23.9%	27 1.3%	0 0.0%	0 0.0%	94.7% 5.3%
Meningioma	13 0.6%	476 23.4%	0 0.0%	0 0.0%	97.3% 2.7%
Notumor	8 0.4%	2 0.1%	477 23.4%	0 0.0%	97.9% 2.1%
Pituitary	2 0.1%	11 0.5%	2 0.1%	532 26.1%	97.3% 2.7%
	95.5% 4.5%	92.2% 7.8%	99.6% 0.4%	100% 0.0%	96.8% 3.2%

c

	Glioma	Meningioma	Notumor	Pituitary	
Glioma	498 24.5%	3 0.1%	0 0.0%	0 0.0%	99.4% 0.6%
Meningioma	6 0.3%	509 25.0%	0 0.0%	1 0.0%	98.6% 1.4%
Notumor	5 0.2%	0 0.0%	479 23.5%	0 0.0%	99.0% 1.0%
Pituitary	0 0.0%	4 0.2%	0 0.0%	531 26.1%	99.3% 0.7%
	97.8% 2.2%	98.6% 1.4%	100% 0.0%	99.8% 0.2%	99.1% 0.9%

Fig. 5. Confusion matrices representing testing set predictions for pre-trained models. (a) Alex-Net with SVM model, (b) DarkNet-19 with SVM model, (c) ResNet-50 with SVM model.

TABLE VII
PERFORMANCE METRICS OF HYBRID MODELS (PRE-TRAINED CNN COMBINED WITH SVM CLASSIFIERS)

CNN model with SVM	Features extracted	Testing accuracy (%)	Precision (%)	Recall (%)	F1-score (%)	Classification time for testing set (s)	Model size (MB)
Alex-Net	4096	97.94	97.95	97.95	97.95	3.8	136.65
DarkNet-19	1000	98.13	98.15	98.16	98.15	3.3	35.82
ResNet-50	2048	98.97	98.97	98.99	98.98	5.2	70.4

to effectively melds speed with accuracy attributes that are ideal for real-time applications such as medical diagnostics and wearable health monitoring. Computer simulations verify these findings and show that hybrid models offer practical advantages in cases where lightweight, efficient, and accurate solutions are needed.

D. Proposed Compact CNN Model

Performance of the proposed compact CNN model

A compact CNN model was proposed with the target of striking a balance among the accuracy, computational efficiency, and capability of being deployed in the edge environment. The architecture was lightweight and included 19 layers (4 convolutional, 4 batch normalizations, 3 pooling, 4 activation layers, and 1 fully connected layer). The traditional fully connected layer was replaced by the GAP layer that reduced the total learnable parameters and disk size of a model to get the accelerated compact CNN classification model. A summary of the compact CNN performance metrics is listed in Table VIII.

The compact CNN achieved a testing accuracy of 97.50% as demonstrated by the CM of the testing set, shown in Fig. 7, had precision, recall, and F1 score metrics which was well balanced and robust in all classes of the prediction. Of particular note, its 3.2 s of classification time for all testing set stood as the most efficient DL model in this study and presents promise for use in real-time applications.

Integration with ML classifiers

The classifier model size of this hybrid framework reduced to 1.43 MB and still retained a competitive accuracy of 97.45%. In Table IX we present the performance of the proposed compact CNN model coupled with the ML model SVM. Similarly, the classification time was also optimal at 2.8 s, thus proving the suitability of the model for real-time edge applications.

There were some challenges with its integration with SVM such as making the extracted features robust enough that

	Glioma	Meningioma	Notumor	Pituitary	
Glioma	487 23.9%	8 0.4%	0 0.0%	1 0.0%	98.2% 1.8%
Meningioma	15 0.7%	504 24.8%	0 0.0%	5 0.2%	96.2% 3.8%
Notumor	6 0.3%	0 0.0%	477 23.4%	0 0.0%	98.8% 1.2%
Pituitary	1 0.0%	4 0.2%	2 0.1%	526 25.8%	98.7% 1.3%
	95.7% 4.3%	97.7% 2.3%	99.6% 0.4%	98.9% 1.1%	97.9% 2.1%

	Glioma	Meningioma	Notumor	Pituitary	
Glioma	490 24.1%	4 0.2%	0 0.0%	0 0.0%	99.2% 0.8%
Meningioma	14 0.7%	503 24.7%	0 0.0%	6 0.3%	96.2% 3.8%
Notumor	4 0.2%	2 0.1%	479 23.5%	0 0.0%	98.8% 1.2%
Pituitary	1 0.0%	7 0.3%	0 0.0%	526 25.8%	98.5% 1.5%
	96.3% 3.7%	97.5% 2.5%	100% 0.0%	98.9% 1.1%	98.1% 1.9%

	Glioma	Meningioma	Notumor	Pituitary	
Glioma	497 24.4%	3 0.1%	2 0.1%	0 0.0%	99.0% 1.0%
Meningioma	11 0.5%	512 25.1%	0 0.0%	3 0.1%	97.3% 2.7%
Notumor	1 0.0%	0 0.0%	477 23.4%	0 0.0%	99.8% 0.2%
Pituitary	0 0.0%	1 0.0%	0 0.0%	529 26.0%	99.8% 0.2%
	97.6% 2.4%	99.2% 0.8%	99.6% 0.4%	99.4% 0.6%	99.0% 1.0%

Fig. 6. Confusion matrices representing testing set predictions for hybrid models.

	Glioma	Meningioma	Notumor	Pituitary	
Glioma	479 23.5%	12 0.6%	0 0.0%	2 0.1%	97.2% 2.8%
Meningioma	22 1.1%	501 24.6%	2 0.1%	1 0.0%	95.2% 4.8%
Notumor	6 0.3%	0 0.0%	476 23.4%	0 0.0%	98.8% 1.2%
Pituitary	2 0.1%	3 0.1%	1 0.0%	529 26.0%	98.9% 1.1%
	94.1% 5.9%	97.1% 2.9%	99.4% 0.6%	99.4% 0.6%	97.5% 2.5%

Fig. 7. Confusion matrice for testing set predictions using the proposed compact convolutional neural network model.

TABLE VIII
PERFORMANCE METRICS OF THE PROPOSED COMPACT CNN MODEL

Metric	Value
Accuracy (%)	97.50
Precision (%)	97.50
Recall (%)	97.51
F1-score (%)	97.50
Model Size (MB)	2.38
Classification time for testing set (s)	3.2

they were able to retain a discriminative power and tuning the SVM hyper-parameters (box constraint set to 5 and RBF kernel). However, the hybrid model managed to maintain balanced and robust metrics with practically no accuracy compromise while improving efficiency as indicated in Fig. 8.

The modified compact CNN model and the hybrid integration with SVM are novel improvements to the boundary between performance and efficiency. Considering the lightweight architecture of the proposed model, this is practical for real-time applications such as those running on edge computing platforms or mobile devices that are resource-limited. We show that by replacing the dense layers and using ML classifiers, we are able to reduce disk size and classification time significantly without sacrificing accuracy. This section shows how compact and hybrid architectures can solve the accuracy, speed, and model size trade-offs. However,

TABLE IX

Performance Metrics of the Compact CNN Integrated with SVM

Metric	Value
Features Extracted	256
Accuracy (%)	97.45
Precision (%)	97.46
Recall (%)	97.49
F1-score (%)	97.46
Model Size (MB)	1.43
Classification time for testing set (s)	2.8

the standalone compact CNN model achieves classification times comparable to a commercial product and acceptable accuracy, and its hybrid version with SVM improves on the deployment feasibility. These results serve as a solid basis to inform future, efficient and scalable solutions to medical diagnostics and other real-time classification problems.

E. Overall Results Analysis

Comparative model analysis is shown in the table below

Table X presents different models along with their tradeoffs between accuracy rates, the size of their models, and the all-testing set classification duration. High accuracy standards are reached by ResNet-50 together with Alex-Net but these models incur large model sizes and long inference times which limits their suitability for real-time applications. The compact CNN reaches 97.50% accuracy with a 2.38 MB model size and a decreased classification time. The hybrid compact CNN-SVM increases operational effectiveness by reaching 97.45% accuracy within 2.8 s using a 1.43 MB model size. The decreased computational requirements of the proposed model make it an outstanding solution for edge computing systems as well as mobile health applications through fast and precise tumor classification.

ROC curve analysis

Receiver Operating Characteristic ROC curves, as in Fig. 9, indicate that the proposed compact CNN and the hybrid compact CNN-SVM model achieve discrimination performance similar to the pre-trained deep learning models even when its size is reduced.

All five models—including ResNet-50 and the other models demonstrated high classification capability for brain tumor detection in their ROC curves, which produced Area Under Curve AUC values between 0.79 and 0.81. The scores of the five models surpassed the baseline AUC of 0.5 despite not reaching the perfect AUC of 1.00. The demonstrated AUC values confirm that every tested model shows excellent discriminatory ability. The Compact CNN and Compact CNN-SVM maintained competitive result performances while keeping model sizes small, thus making them suitable choices for real-time clinical applications. Pieces of evidence regarding model generalizability will be obtained through testing performed with external BraTS2020 datasets during the next validation phase.

Model performance on additional dataset

A general evaluation of the compact CNN and hybrid compact CNN-SVM occurred through experimentation on the BraTS2020 (Brain Tumor Segmentation 2020) dataset, which serves as a standard benchmark for brain tumor identification and type classification. This benchmark dataset offers clinical-relevant conditions because it contains manually marked tumor regions within multi-modal T1 T1c T2 and FLAIR MRI sequences alongside it (Maram and Rana, 2021). The compact CNN demonstrated

TABLE X

Summarizes the Performance Metrics of Various Models

Model	Accuracy (%)	Model size (MB)	Testing set classification time (s)
ResNet-50	99.07	86.02	6.6
AlexNet	98.62	196.73	5.3
DarkNet-19	96.81	75.96	5.7
Compact CNN	97.50	2.38	3.2
Compact CNN-SVM	97.45	1.43	2.8

Output Class	Glioma	Meningioma	Notumor	Pituitary	
Glioma	481 23.6%	9 0.4%	0 0.0%	0 0.0%	98.2% 1.8%
Meningioma	22 1.1%	501 24.6%	0 0.0%	7 0.3%	94.5% 5.5%
Notumor	6 0.3%	0 0.0%	477 23.4%	0 0.0%	98.8% 1.2%
Pituitary	0 0.0%	6 0.3%	2 0.1%	525 25.8%	98.5% 1.5%
	94.5% 5.5%	97.1% 2.9%	99.6% 0.4%	98.7% 1.3%	97.4% 2.6%

Fig. 8. Confusion matrice for testing set predictions using a compact convolutional neural network-integrated with support vector machine.

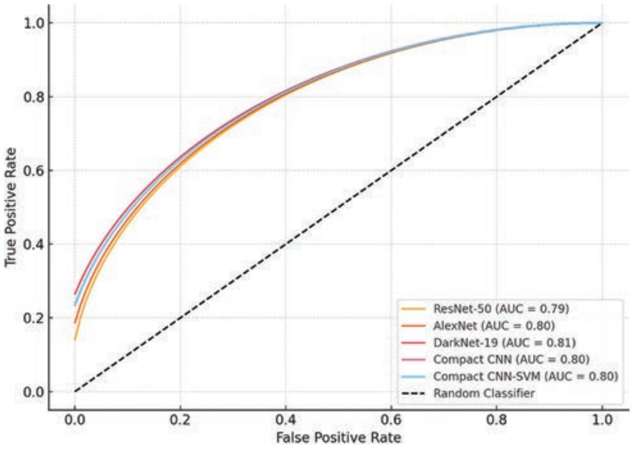

Fig. 9. Receiver operating characteristic curve for different brain tumor classification models.

97.10% accuracy for diagnosis while requiring a lightweight architecture of 2.38 MB for model size making it suitable as a real-time medical tool. The hybrid compact CNN-SVM model delivered a 96.95% classification accuracy through its 1.43 MB model size formation which enhances its deployment capabilities within resource-constrained environments of edge computing and mobile healthcare applications.

The developed models successfully deliver accurate diagnosis alongside efficient computing capability that supports their deployment in real-time medical applications. The hybrid compact CNN-SVM model achieves both optimal performance and cost efficiency through newly improved accuracy measures at nearly standardized time consumption levels. The high accuracy levels that hybrid lightweight deep learning architectures achieve alongside operation efficiency make them suitable for medical applications in real-world settings.

F. Graphical User Interface (GUI) for automated brain tumor classification

The creation of a Graphical User Interface (GUI) resulted in Fig. 10 which enhances usability together with practical deployment of the proposed brain tumor classification model. A GUI system allows users to load a trained classifier alongside the processing of MRI images followed by result visualization in an organized format. Users can view the original MRI images accompanied by file naming information in the top section and the processed classified pictures displaying tumor classifications together with accuracy ratings in the bottom section.

The GUI presents brain tumor classification results by displaying both original images and their classification outputs with labeled diagnoses that include confidence scores. The design of this interface allows brain tumor detection in real-time, which enables the model to work on clinical applications together with edge computing systems.

V. Discussion

The proposed models were thoroughly tested in terms of accuracy, computational efficiency, and deployment suitability, and findings regarding their potential practical implications in real-world applications were discussed. The performance of the proposed models is discussed in comparison with state-of-the-art in terms of accuracy, computational efficiency, and deployment suitability. Table XI shows our proposed compact model, along with our proposed accelerated compact model with SVM in hand with the pre-trained ResNet-50, hybrid ResNet-50 with SVM, and comparisons to recent approaches from the literature. The accuracy is 97.50%, the testing time is 3.2 s and the model size is 2.38 MB, making the proposed compact CNN model a good fit for real-time deployment at the edge. The model size was reduced to 1.43 MB when integrated with an SVM classifier with a slight decrease in accuracy (97.45%) and faster classification time (2.8 s). In comparison with ResNet-50 which achieved the highest accuracy of 99.07%, but was greater in size (86.02 MB) and slower in testing set classification time (6.6 s), the proposed models featured a noticeable improvement in efficiency and scalability.

The results are aligned to (Musa, 2024), which using ResNet-50 with optimized soft-max regression in the diagnostic of brain tumors with an accuracy of 98.4%. In the same way, (Bérété, et al., 2024) designed a ResNet-50 that was slightly modified to achieve 99% accuracy of performance but with no representation with the problems associated with the sizes of the models and their feasibility of deployment.

On the other hand, (Ahmmed, et al., 2023) obtained 97.68% accuracy using specific optimization algorithms in two highly promising contexts, namely, ResNet-50 and Inception-V3, although at the cost of gaining more computational complexity in an ensemble framework. Moreover, (Iffath, Dey and Gavrilova, 2024) designed an automatic brain tumor classification model using pre-

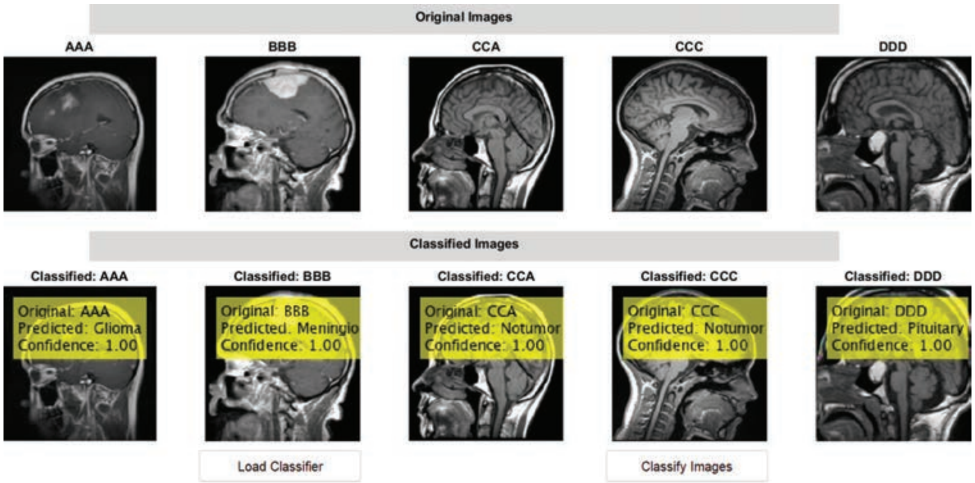

Original: AAA
Predicted: Glioma
Confidence: 1.00

Original: BBB
Predicted: Meningio
Confidence: 1.00

Original: CCA
Predicted: Notumor
Confidence: 1.00

Original: CCC
Predicted: Notumor
Confidence: 1.00

Original: DDD
Predicted: Pituitary
Confidence: 1.00

Fig. 10. Graphical user interface-based visualization of brain tumor classification.

TABLE XI
Comparative Analysis of Brain Tumor Classification Models

Study	Model description	Accuracy (%)	Model size (MB)	Key feature
(Musa, 2024)	ResNet-50 with optimized soft-max regression	98.4	More than 90	High accuracy with optimized model, but large model size limits scalability
(Béréte, et al., 2024)	Modified ResNet-50	99	More than 90	Enhanced accuracy and high model size increase computational demands and restrict deployment
(Ahmmed, et al., 2023)	Fine-tuning ResNet-50 Inception-V3	97.68	89	Competitive accuracy with large model size, significant computational overhead
(Iffath, Dey and Gavrilova, 2024)	Feature aggregation with ResNet-18	97.46	44	Decent accuracy with a smaller model size, suitable for some applications but lacks full deployment focus
Base model	Pre-trained ResNet-50	99.07	86	High accuracy for complex features, but large size limits real-time deployment
Proposed model	Compact CNN	97.50	2.38	Balanced accuracy and small size, ideal for edge deployments
Proposed hybrid model	ResNet-50 with SVM	98.97	70.4	Balanced accuracy and efficiency, suitable for moderate deployment constraints
Proposed hybrid model	Accelerated compact CNN with SVM	97.45	1.43	Competitive accuracy, minimal model size, and fastest classification, ideal for real-time applications

trained ResNet-18 model with adaptive feature aggregation techniques. The test accuracy their system designed was 97.46% with the motto of flexibility and interpretability in mind. Nevertheless, its approach underscores the importance of architectural optimization for efficiency without accounting for deployment considerations, which is where this study's proposed compact CNN with integrated SVM is notably more practical and scalable for use in real-world scenarios and deployment in edge devices and mobile platforms. This work helps to expand the list of cases where the diagnostics is performed with the help of AI by decreasing its consumption and model size to allow for use in situations where instant decision making is necessary.

VI. Conclusion

This research develops an efficient brain tumor classification system through a combination of CNN and SVM technology to reach optimal performance alongside reduced processing times for real-time usage. The research studied the performance of pre-trained models such as Alex-Net, DarkNet-19, and ResNet-50, which had been optimized with ADAM, and SGDM, and developed a compact CNN model along with SVM classifiers to resolve the conflict between model complexity and real-time requirements. ResNet-50 delivered excellent accuracy levels at 99.07% yet its model size and execution of 6.6 s restricted its operational feasibility. With 97.50% accuracy, the compact CNN model managed to cut memory usage down to 2.38 MB and reduced classification time to 3.2 s. The optimized hybrid model achieved 97.45% accuracy while also having a minimal 1.43 MB model size and 2.8 s for all-testing set classification time. The product's performance efficiency ratio makes it suitable for situations that require edge computing and mobile healthcare alongside real-time medical diagnostics. The brain tumor detection method benefits from both higher accuracy rates and computational speed through its combination of small CNN components with SVM classifiers. A lightweight design of the deep learning models allows for deployment on limited resource hardware to enable real-time tumor classification in medical and mobile situations. The research demonstrates how implementing correctly designed AI diagnostic tools require high accuracy performance, efficient memory usage, and computational costs. Our study presents promising findings although it currently sustains its MRI-based diagnostic approach. The research will progress through two essential steps along with exploring optimization techniques and advanced ML algorithms to conduct clinical trials for practical effectiveness enhancement of AI-based brain tumor detection systems.

References

Abdulaziz, A.S., and Dawood, A., 2023. Vowels' Articulatory Location Classification based on Formant Frequency. In: *2023 International Conference on Decision Aid Sciences and Applications (DASA)*. IEEE, United States, pp. 12-16.

Abdullah, M.A.M., Mohammed, A.A., and Awad, S.R., 2024. RockDNet: Deep learning approach for lithology classification. *Applied Sciences*, 14(13), p.5511.

Ahmmed, S., Podder, P., Mondal, M.R.H., Rahman, S.M.A., Kannan, S., Hasan, M.J., Rohan, A., and Prosvirin, A.E., 2023. Enhancing brain tumor classification with transfer learning across multiple classes: An in-depth analysis. *BioMedInformatics*, 3(4), pp.1124-1144.

Akinbo, R.S., and Daramola, O.A., 2021. Ensemble machine learning algorithms for prediction and classification of medical images. In: *Machine Learning Algorithms Models Application*. Vol. 10. BoD - Books on Demand, Germany.

Alhafidh, B.M.H., Daood, A.I., and Allen, W.H., 2018. Comparison of Classifiers for Prediction of Human Actions in a Smart Home. In: *2018 IEEE/ACM Third International Conference on Internet-of-Things Design and Implementation (IOTDI)*. IEEE, United States, pp. 287-288.

Alhafidh, B.M.H., Hagem, R.M., and Daood, A.I., 2022. Face Detection and Recognition Techniques Analysis. In: *2022 International Conference on Computer Science and Software Engineering (CSASE)*. IEEE, United States, pp. 265-270.

Al-Jammas, M.H., Al-Sabawi, E.A., Yassin, A.M., and Abdulrazzaq, A.H., 2024. Brain tumors recognition based on deep learning. *E-Prime-Advances in Electrical Engineering, Electronics and Energy,* 8, p.100500.

Al-Mukhtar, M., Morad, A.H., Hussein, H.L., and Al-Hashimi, M.H., 2024. Brain tumor segmentation using enhancement convolved and deconvolved CNN model. *ARO-The Scientific Journal of Koya University*, 12(1), pp.88-99.

Awad, S.R., and Alghareb, F.S., 2025. Encoding-based machine learning approach for health status classification and remote monitoring of cardiac patients. *Algorithms*, 18(2), p.94.

Awad, S.R., Sharef, B.T., Salih, A.M., and Malallah, F.L., 2022. Deep learning-based Iraqi banknotes classification system for blind people. *Eastern-European Journal of Enterprise Technologies*, 1(2), p.115.

Bérété, M., Echtioui, A., Sellami, L., and Hamida, A.B., 2024. Transfer Learning Models for MRI-Based Brain Tumor Detection. In: *2024 IEEE 7th International Conference on Advanced Technologies, Signal and Image Processing (ATSIP)*. Vol. 1. IEEE, United States, pp.14-19.

Daood, A., Al-Saegh, A., and Mahmood, A.F., 2023. Handwriting detection and recognition of Arabic numbers and characters using deep learning methods. *Journal of Engineering Science and Technology*, 18(3), pp.1581-1598.

Divya, S., Suresh, L.P., and John, A., 2020. A Deep Transfer Learning Framework for Multi Class Brain Tumor Classification Using MRI. In: *2020 2nd International Conference on Advances in Computing, Communication Control and Networking (ICACCCN)*. IEEE, United States, pp.283-290.

Ganaie, M.A., Hu, M., Malik, A.K., Tanveer, M., and Suganthan, P.N., 2022. Ensemble deep learning: A review. *Engineering Applications of Artificial Intelligence,* 115, p.105151.

Iffath, F., Dey, L., and Gavrilova, M.L., 2024. Enhancing Brain Tumor Diagnosis through Adaptive Feature Aggregation based Transfer Learning. In: *2024 IEEE 19th Conference on Industrial Electronics and Applications (ICIEA)*. IEEE, United States, pp.1-6.

Jana, N.D., Dhar, S., Ghosh, S., Phukan, S., Gogoi, R., and Singh, J., 2023. An Ensemble of Machine Learning Models Utilizing Deep Convolutional Features for Medical Image Classification. In: *International Conference on Advanced Network Technologies and Intelligent Computing*. Springer Nature Switzerland, Cham, pp. 384-396.

Jasim, A.M., Awad, S.R., Malallah, F.L., and Abdul-Jabbar, J.M., 2021. Efficient Gender Classifier for Arabic Speech Using CNN with Dimensional Reshaping. In: *2021 7th International Conference on Electrical, Electronics and Information Engineering (ICEEIE)*. IEEE, United States, pp. 1-5.

Karim, P.J., Mahmood, S.R., and Sah, M., 2023. Brain tumor classification using fine-tuning based deep transfer learning and support vector machine. *International Journal of Computing and Digital Systems*, 13, pp.83-96.

Kokhazadeh, M., Keramidas, G., Kelefouras, V., and Stamoulis, I., 2024. Denseflex: A Low Rank Factorization Methodology for Adaptable Dense Layers in DNNs. In: *Proceedings of the 21st ACM International Conference on Computing Frontiers*. Association for Computing Machinery, United States, pp.21-31.

Maram, B., and Rana, P., 2021. Brain Tumour Detection on Brats 2020 Using U-Net. In: *2021 9th International Conference on Reliability, Infocom Technologies and Optimization (Trends and Future Directions) (ICRITO)*. IEEE, United States, pp.1-5.

Mavaddati, S., 2024. Brain Tumors Classification Using Deep Models and Transfer Learning. *Multimedia Tools and Applications*, pp.1-32.

Mohammed, A.A., Awad, S.R., Abdullah, M.A.M., Elbasi, E., and Woo, W.L., 2024. *Quantifying the Impact of Watermarking on Deep Learning Accuracy in Medical Image Classification*. IEEE Access, United States.

Mohammed, M.R., and Daood, A., 2021. Smart surveillance system to monitor the committed violations during the pandemic. *International Journal of Computing and Digital System*. 11, pp.1415-1426.

Müller, D., Soto-Rey, I., and Kramer, F., 2022. An analysis on ensemble learning optimized medical image classification with deep convolutional neural networks. *IEEE Access*, 10, pp.66467-66480.

Musa, M.N., 2024. MRI-based brain tumor classification using resnet-50 and optimized softmax regression. *Jurnal Infotel*, 16(3), pp.598-614.

Naidu, G., Zuva, T., and Sibanda, E.M., 2023. A Review of Evaluation Metrics in Machine Learning Algorithms. In: *Computer Science On-line Conference*. Springer International Publishing, Cham, pp.15-25.

Neamah, K., Mohamed, F., Waheed, S.R., Kurdi, W.H.M., Yaseen, A., and Kadhim, K.A., 2024. Utilizing deep improved resnet50 for brain tumor classification based MRI. *IEEE Open Journal of the Computer Society*, 99, pp.1-12.

Obi, J.C., 2023. A comparative study of several classification metrics and their performances on data. *World Journal of Advanced Engineering Technology and Sciences*, 8(1), pp.308-314.

Onuiri, E.E., John, A., and Umeaka, K.C., 2024. MRI-based brain tumour classification using convolutional neural networks: A systematic review and meta-analysis. *Technology*, 7(4), pp.27-46.

Pan, T., Chen, Y., Feng, H., Xu, Z., Li, Q., and Xu, W., 2020. From Coarse to Fine: A Two-Stage Network for Dense Haze removal. In: *2020 IEEE 5th International Conference on Signal and Image Processing (ICSIP)*. IEEE, United States, pp.1050-1055.

Raja, V.J., Dhanamalar, M., Solaimalai, G., Rani, D.L., Deepa, P., and Vidhya, R.G., 2024. Machine Learning Revolutionizing Performance Evaluation: Recent Developments and Breakthroughs. In: *2024 2nd International Conference on Sustainable Computing and Smart Systems (ICSCSS)*. IEEE, United States, pp.780-785.

Ramanagiri, A., Mukunthan, M., and Balamurugan, G., 2024. April. Enhanced Brain Tumor Detection Using Resnet-50. In: *2024 10th International Conference on Communication and Signal Processing (ICCSP)*. IEEE, United States, pp.1708-1711.

Rasool, M., Noorwali, A., Ghandorh, H., Ismail, N.A., and Yafooz, W.M.S., 2024. Brain tumor classification using deep learning: A state-of-the-art review. *Engineering, Technology and Applied Science Research*, 14(5), pp.16586-16594.

Sahaai, M.B., Jothilakshmi, G.R., Ravikumar, D., Prasath, R., and Singh, S., 2022. ResNet-50 based deep neural network using transfer learning for brain tumor classification. *AIP Conference Proceedings,* 2463(1), p.020014.

Santoso, I.B., Supriyono, and Utama, S.N., 2024. Multi-model of convolutional neural networks for brain tumor classification in magnetic resonance imaging images. *International Journal of Intelligent Engineering and Systems*, 17(5), pp.741-758.

Shamshad, N., Sarwr, D., Almogren, A., Saleem, K., Munawar, A., Rehman, A.U., and Bharany, S., 2024. Enhancing brain tumor classification by a comprehensive study on transfer learning techniques and model efficiency using MRI datasets. *IEEE Access*, 12, pp.100407-100418.

Sharma, A.K., Nandal, A., Dhaka, A., Zhou, L., Alhudhaif, A., Alenezi, F., and Polat, K., 2023. Brain tumor classification using the modified resnet50 model based on transfer learning. *Biomedical Signal Processing and Control,* 86, p.105299.

Srinivas, C., Nandini Prasad, K.S., Zakariah, M., Alothaibi, Y.A., Shaukat, K., Partibane, B., and Awal, H., 2022. Deep transfer learning approaches in performance analysis of brain tumor classification using MRI images. *Journal of Healthcare Engineering*, 2022(1), p.3264367.

Ullah, N., Javed, A., Alhazmi, A., Hasnain, S.M., Tahir, A., and Ashraf, R., 2023. TumorDetNet: A unified deep learning model for brain tumor detection and classification. *PLoS One*, 18(9), p.e0291200.

Xia, H., Zhuge, R., Li, H.S., Song, S., Jiang, F., and Xu, M., 2018. Single image rain removal via a simplified residual dense network. *IEEE Access*, 6, pp.66522-66535.

Yadav, R.K., Mishra, A.K., Saini, J.B., Pant, H., Biradar, R.G., and Waghodekar, P., 2024. A model for brain tumor detection using a modified convolution layer resnet-50. *Indian Journal of Information Sources and Services,* 14(1), pp.29-38.

Synthesis and Analysis of the Density States and Optical Characteristics of $Se_{100-X}Te_X$ Semiconductors

Kassim M. Wadi[1], Maher A. Hasan[2], Shaymaa H. Aneed[3], Mohammad G. Faraj[4] and Kareem A. Jasim[3]

[1]Department of Electrical Engineering Techniques, Al-Ma'amoun University College,
Baghdad, F.R. Iraq

[2]Ministry of Education, Tikrit Directorate of Education,
Salah Aldin, F.R. Iraq

[3]Department of Physics, College of Education for Pure Sciences ibn Al-Haitham,
University of Baghdad, Baghdad, F.R. Iraq

[4]Department of Physics, Faculty of Science and Health, Koya University,
Koya KOY45, Kurdistan Region - F.R. Iraq

***Abstract*—The widespread commercial importance of selenium makes it an interesting element. It serves as an effective host matrix for chalcogenide alloys. However, pure selenium has a short lifetime and poor sensitivity. Therefore, specific chemical elements, such as tritium, have been used to overcome this problem. Se-Te alloys are preferred over selenium for their numerous advantages, such as increased electrical sensitivity, thermal stability, and applications in xerography. In this manuscript, the effects of partially substituting tellurium for selenium are studied for amorphous $Se_{100-x}Te_x$ chalcogenide alloys prepared by melt quenching and spraying procedures to produce bulk and thin films, respectively, with varying tellurium concentrations (x = 10, 20, 30, and 40). X-ray diffraction of samples with different concentrations revealed that all samples had an amorphous (glassy) structure. Continuous electrical conductivity is also studied to determine the conduction mechanisms, effective energies, and densities of localized and extended states. The results of electrical conductivity measurements confirm the existence of two conduction modes (extended-state conduction at high temperatures and localized state conduction at intermediate and low temperatures in the tails of the conduction and valence bands). It is also found that the density of states, local and extended state coefficients, and activation energies are significantly affected by the partial substitution of selenium with tellurium. The optical properties of the $Se_{100-x}Te_x$ films are studied using ultraviolet-visible spectroscopy, and it found that the overall absorption increases while the energy gap decreases with increasing tellurium concentration.**

***Index Terms*—Amorphous structure, Chalcogenide, Density of the extended, Electrical measurements, Localized, Optical properties.**

ARO-The Scientific Journal of Koya University
Vol. XIII, No. 1 (2025), Article ID: ARO.11955. 10 pages
DOI: 10.14500/aro.11955
Received: 16 December 2024; Accepted: 20 April 2025
Regular research paper; Published: 05 May 2025

†Corresponding author's e-mail: mohammad.ghaffar@koyauniversity.org

I. INTRODUCTION

The development of electronic device technology has required low-cost and competitive materials to support the scientific economy and develop new methods to create a new class of electronic devices made of advanced amorphous materials. Since the production cost of chalcogenide glasses is very low, research has focused on these materials, and a deep understanding of the basic electrical transport properties of materials may provide insight that enhances their merit (Al-Agel, 2011).

Amorphous SeTe semiconductors have gained significant interest due to their high crystallization temperature, high hardness, high photosensitivity, and minimal aging effects compared to pure selenium (Lou, et al., 2012). Doping is one of the most common techniques in amorphous semiconductors, but it is not applicable to pure selenium a-Se due to the Fermi level being fixed by the π states in the band gap (Jouanne, et al., 2004). To modify the optical and electrical properties of a-Se, some additives such as Te, Ge, Bi, Cd, etc. are used, which significantly affect the transport of holes, electrons, or both. In this case, alloying can be considered an effective tool for modifying the electrical transport properties of a-Se films (Chaudhri, Vohra and Chakarvarti, 2008).

Chalcogenide glasses have configurable infrared optical properties and are utilized in numerous modern and logical applications. They are used as gadgets in optical wave gadgets (Tong, 2014; Faraj, 2022), infrared strands (Yang, et al., 2011; Hamad, Faraj and Taha, 2023), sensors (Lucas, et al., 2015, Yang, et al., 2010), optical holes (Elliott, et al., 2010), strong state batteries (Pattanayak, and Asokan, 2005), stage change pens (Elliott, 2015), xerography (Mehta, 2020), and thermoelectrics (Lucas, et al., 2013). Crystalline semiconductor materials are pricey to deliver, and countless scientists resort to concentrating on the properties of materials utilized as alternatives for crystal materials (Borisova, 1981). Such experts have focused on subtleties and properties of amorphous materials to be used as decisions with a clear plan, and the support for this is the negligible cost from the first viewpoint and then again, the straightforward entry to them. These amorphous semiconductor materials can be consolidated as combinations for their creation and the expansion of specific impurity types to their inefficient electrical conductivity to grow their fields of direction. These different sorts of semiconductors can be utilized in an assortment of semiconductor goods and have various properties. Some are used for standard sign and sun-based cell applications, others in high-recurrence speakers and power applications in brutal conditions, and light-discharging applications. Most applications will utilize various amorphous semiconductor materials, most of which have pitifully fortified layers as the layered units. As in numerous natural analogs, the component of shapeless semiconductors opens the chance of tweaking their electronic properties through neighborhood underlying adjustments. However, the catalysts of these materials are hampered by the structural flexibility of the amorphous lattice, which allows the high formation of favorable coordination defects, called valence and spin (Street and Mott, 1975). Although the effect of the impurities on the electronic properties of amorphous semiconductors is sometimes negative on some properties, it has been proven that alloys containing some chemical elements, such as lead-bismuth and lithium in molten glass, change electrical conductivity (Frumar and Tichý, 1987). This may lead to a reversal of the type of charge carrier, from type p to type n, and maybe vice versa. The n-type conductivity origin in the bismuth-doped chalcogenide glassy has been explained as arising from high bismuth polarization, which partially favors the formation of the ionic bismuth–chalcogen bonds (Elliott and Steel, 1986). In this paper, we will prepare $Se_{100-x}Te_x$ chalcogenide thin film with various tellurium concentrations. Determining the effect of partial replacement elements on structural, electrical, and optical properties is to be studied.

II. Experimental Procedure

Different amounts of ultra-pure selenium and tellurium powder (99.999% from May and Baker LTD Dagenham, England) were mixed according to their molecular weight ratios according to the following equation:

$$(100\text{-}x)\ Se + xTe \rightarrow Se_{100\text{-}x}\ Te_x \qquad (1)$$

Selenium and tellurium powders of different concentrations (x = 10:20:30:40) were mixed to prepare Se100-xTex alloy samples, and the powder of each sample was placed in quartz glass ampoules. The ampoules were deflated using a vacuum apparatus to 10^{-4} Torr (place the components in a vacuum tube to withstand a temperature of more than 1,200°C so that the elements can react to form alloys without loss or evaporation of the components). The ampoule was sealed tightly and placed in an oven. The oven temperature was raised at a rate of 5°C/min to the melting point. The ampoules were kept in the oven at a high temperature of 600°C for 4 h to melt the components to form the alloy, then heated to 950°C for 12 h to ensure that all the components were melted and to ensure that the samples did not stick to the wall of the ampoules; they were gradually cooled down to 400°C. The ampoules were then removed from the oven to cool; the ampoules were broken, and the alloys were extracted. These alloys were individually ground using a mortar and pestle. The samples were pressed using a hydraulic press under a pressure of seven tons per cm² into discs (2 mm thick and 15 mm in diameter) as shown in Fig. 1.

To conduct electrical tests, the circuits in Fig. 2 were used. The voltage and current data were obtained at different temperatures from room temperature to higher temperatures using a Keithley electrometer. A specially designed holder held the sample between the copper electrodes before applying the two-probe procedure. A copper-constantine thermocouple placed near the sample examined the temperature dependence of the current when a voltage of 9 V was applied. The electrical resistance and electrical conductivity were calculated versus temperature. After that, portions of each sample were taken and ground using an electric grinder for half an hour. After that, the powder of each sample was taken and dissolved in alcohol to prepare

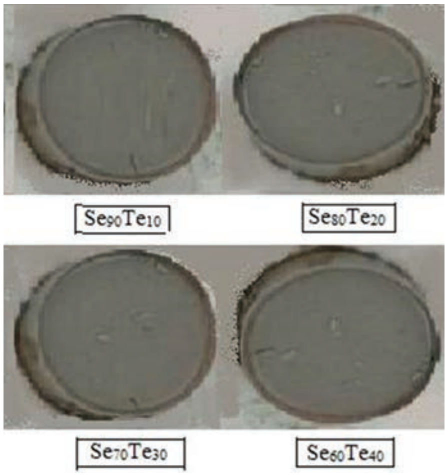

Fig. 1. Images of Se100-xTex chalcogenide samples with different concentrations of tellurium element (x = 10, 20, 30, and 40).

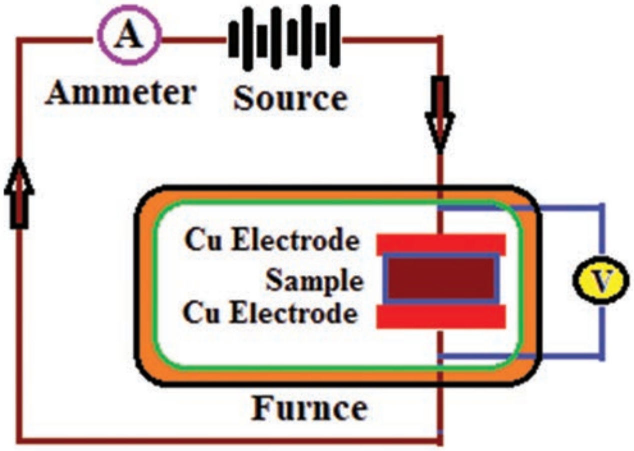

Fig. 2. Schematic diagram of the experimental setup for measuring electrical conductivity.

thin films by spraying them on chalcogenide plates. To prepare the films required in this study, the spraying duration was set to 7 s, after which the spraying was stopped for 2 min, and then the process was repeated since the spraying on the bases could not be continuous. The spray limit is set to 3 min. by using chemical spray pyrolysis, as shown in Fig. 3. The gravimetric method was used to measure the thickness, a technique in which thickness is calculated by measuring the mass, area, and density of the substrate before and after film deposition. The average film thickness (t) is determined using Equation (2).

$$t = 100 \frac{W_f}{A_f\, D_f} \tag{2}$$

Where W_f is the weight difference in micrograms, A_f is the surface area of the substrate having film and D_f is the density of the film. The thicknesses of the samples were of the order of 250 nm.

III. THE THEORY PARTS

Investigating the temperature-dependent electrical conductivity is a well-established technique for investigating how electricity is conducted in random semiconductor materials. According to Davies and Mott, depending on the degree of randomness of the crystal structure, there can be two mechanisms controlling the conduction of electrons and, in some semiconductors with a high randomness structure, up to three mechanisms in other cases (in the Fermi state at low temperatures, at intermediate temperatures (localized states), and at high temperatures (extended states). The general equation below can be used to describe the electrical conductivity of random semiconductors (Mott, Davis, and Street, 1975).

$$\sigma = \sigma_{01}\, e^{(-\frac{\Delta E_1}{k_B T})} + \sigma_{02} e^{(-\frac{\Delta E_2}{k_B T})} + \sigma_{03} e^{(-\frac{\Delta E_3}{k_B T})} \tag{3}$$

Where (σ_{01}, σ_{02}, σ_{03}) are represented as pre-exponential factor parameters, (ΔE_1, ΔE_2, ΔE_3) are activation energies for each term, T = the absolute temperature, and k_B = Boltzmann's constant.

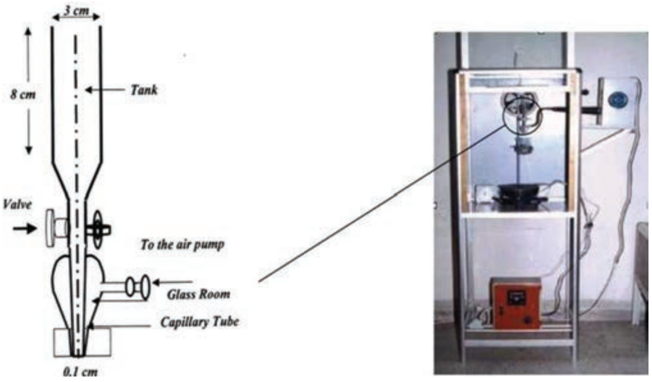

Fig. 3. Experimental set-up of spraying apparatus (right) and layout of enlarged spraying glass nozzle (left).

Some amorphous semiconductors are less random, so they do not have Fermi-level localized states and have two processes (conduction in localized states) at high and intermediate temperatures. In these amorphous materials, the third term in equation 3 is removed, and the equation is given as (Cohen, Fritzsche, and Ovshinsky, 1975).

$$\sigma = \sigma_{01}\, \mathrm{e}^{(-\frac{\Delta E_1}{k_B T})} + \sigma_{02} \mathrm{e}^{(-\frac{\Delta E_2}{k_B T})} \tag{4}$$

A. The Electrical Conduction Process throughout Extended States

At high temperatures, continuous electrical conduction through an extended state is the dominant process in the first term of equation 3 (first region). Depending on the activation energy, charge carriers are excited to the denser states in the levels.ΔE_1 where $\Delta E_1 = E_C - E_F$ (or $E_F - E_V$) (Flasck, et al., 1991):

$$\sigma = \sigma_{01}\, e^{(-\frac{\Delta E_1}{k_B T})} \tag{5}$$

$$\sigma_{01} = \sigma_{0ext} = \left(\frac{1}{6}\right) e^2\, a^2\, V_e\, \mathrm{N}\left(\mathrm{Eext}\right) \tag{6}$$

Where e is electron charges, a is atomic distance, and N(Eext) state density at extended state, V_e is the electron frequency and Inter-atomic distance a, therefore the extended state density is:

$$\mathrm{N}\left(E_{ext}\right) = \left\{6m \middle/ e^2 \hbar\right\} \sigma_{01} \tag{7}$$

B. The Localized States' Electrical Conduction Processes

This conduction involves the second component of Equation 3, which results in the second conduction mechanism known as in-localized conduction occurring inside the mobility gap. The activation energy in this instance, conduction, results from the transition of charge carriers from the valence band tail states filled with electrons to the levels of the tails of the unoccupied conduction band (Abdulateef, et al., 2020):

$$\sigma = \sigma_{02} e^{(-\frac{\Delta E_2}{k_B T})} \tag{8}$$

$$\sigma_{02} = \left(\frac{1}{6}\right) e^2\, V_{ph} R^2\, \mathrm{N}\left(E_{\mathrm{loc}}\right) \tag{9}$$

Where the phonon frequency ($V_{ph} = 10^{13} s^{-1}$), R a hopping distance between localized states (Ahmed, et al., 2022, Chillab, et al., 2021).

$$R = 0.7736 \left\{ \frac{\Delta E \alpha^{-1}}{N(E_{ext})(k_B T)^2} \right\} 25 \tag{10}$$

$$\mathrm{N}(\mathrm{E}) E_{(LOC)} = \left[\frac{6}{e^2 V_{ph} R^2} \right] \sigma_{02} \tag{11}$$

The energy width tail is $\Delta E = (\Delta E_1 - \Delta E_2)$, and α^- the absorption coefficient ($\alpha^- = 10^{-7}$cm) (Ahmed, et al., 2022).

C. Conduction of Electrical Energy (Fermi Level)

The third conduction process, called variable range hopping, or VRH, takes over at lower temperatures by hopping between local states close to the Fermi level (Aqeel, et al., 2020). This kind of tunnel involves the passage of charge carriers via levels that are near the Fermi level. According to the following.

$$\sigma = \sigma_{03} e^{(-\frac{\Delta E_3}{k_B T})} \quad (12)$$

$$\sigma_{03} = \left(\frac{1}{6}\right) e^2 V_{ph} R^2 N\left(E_F\right) \quad (13)$$

$$R = \{9/8\left(N\left(E_F\right)\right) Bk_B T)\}^{-\frac{1}{4}} \quad (14)$$

Where the localization length of the gap states α^{-1} and N (E_F) is the state density nears the Fermi level (Abdulateef, et al., 2020; Farid, Fadel and Abd El-Wahabb, 2019).

$$\mathrm{N}(E_F) = \left[\frac{6}{e^2 Vph\ R^2}\right] \sigma_{03} \quad (15)$$

IV. Results and Discussion

A. Structure Properties

The X-ray diffraction of the studied compositions in powder form is shown in Fig. 4. The obtained patterns indicate that the prepared $Se_{100-x}Te_x$ alloys with various tellurium element concentrations (x = 10, 20, 30 and 40) are in the amorphous state, as no sharp peaks were observed.

B. Electrical Properties

Three processes can lead to electrical conduction in amorphous semiconductors: Charge carrier transitions in the band tails, charge carrier hopping between the Fermi level localized states, and charge carrier transfer between extended states in the conduction and valence bands (Jasim, et al., 2011; Khudhair and Jasim, 2023). In the case of chalcogenide glasses, the electrical conductivity of the charge carriers is either transferred from states near the valence band edge to localized states near the Fermi level or from near the Fermi level to the conduction band.

Fig. 5 shows the DC electrical conductivity variation with temperature of $Se_{100-x}Te_x$ alloys with various element concentrations (x = 10, 20, 30, and 40). It was found that the conductivity increases slowly up to 360 Kelvin and rapidly after 360 Kelvin for all our samples. Charge carriers gain energy when the temperature increases from 300 to 360 Kelvin, where conduction occurs due to the charge carriers jumping in local state bands near the tails of the energy bands. The energy gained for conduction is low due to the decrease in temperature. The same figure shows that the conductivity increases gradually. On the other hand, charge carriers become more mobile, and conduction occurs by the jumping of charge carriers in the conduction band when the temperature increases above 360 Kelvin. As a result, the conductivity increases in the (360–450 Kelvin) temperature range. Therefore, conduction is expected by variable band hopping in the lower temperature range of 300–360 Kelvin, while in the higher temperature range, that is, 360–450 Kelvin, conduction is through a thermally supported process. This Figure clearly shows an increase in continuous electrical conductivity as the temperature rises, indicating that all samples demonstrate semiconductor behavior. In addition, the electrical conductivity increases with increasing tellurium concentration, due to the increase in charge carrier concentrations when tellurium concentrations increase and the decrease in selenium concentration in the prepared samples (Mahdi, et al., 2017).

Fig. 5 demonstrates that the electrical conductivity measurements in all prepared samples have two different states of conductivity: In the extended states, at the

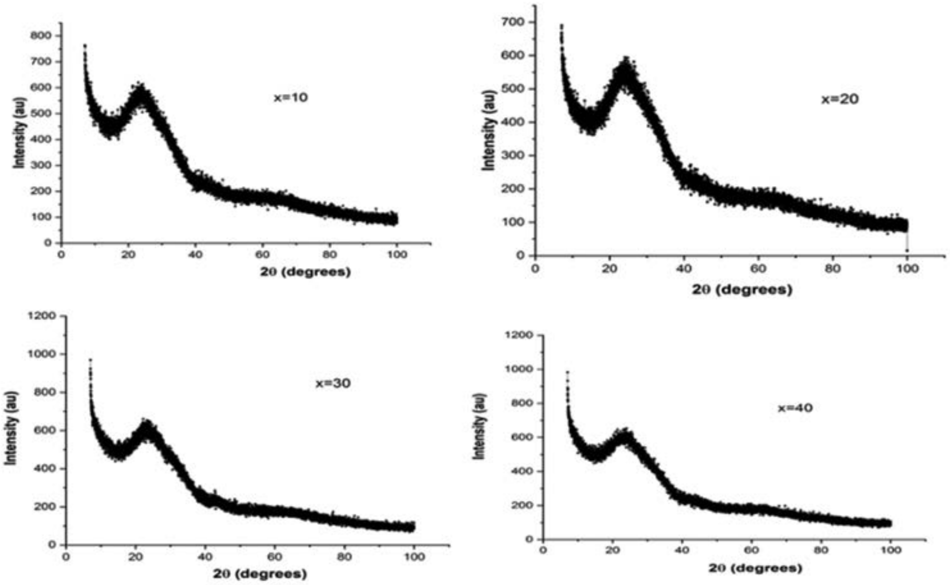

Fig. 4. X-ray diffraction patterns for $Se_{100-x}Te_x$ alloys with various tellurium element concentrations (x = 10, 20, 30, and 40).

temperature, and the average temperature, the conduction was in the local states, and the absence of the local states at the Fermi level. We will be applying equation 4 to carry out the calculations in this instance. As indicated in Table I, the conduction activation (ΔE) and pre-exponential factor (σ_o) of the $Se_{100-x}Te_x$ alloys with different element concentrations (x = 10, 20, 30, and 40) were found using the slope and the intercept plot in the higher temperature range of 348 to 423 Kelvin.

In chalcogenide, the pre-exponential factor (σ_o) provides crucial insights into the coupling mechanism. According to Mott, the pre-exponential factor for coupling in localized states should be two or three orders of magnitude smaller than the coupling factor for extended states (Mohammed and Jasim, 2019). Based on this, we will utilize the equations describing the electrical conductivity in which the conduction mechanisms are limited to the width of the tails and are in the extended condition (Khudhair and Jasim, 2023). To determine both *in situ* and extended state densities, we will apply the equations derived in a theoretical section to data taken from Fig. 5 and recorded in Table I. To calculate densities in the local and extended state, display the tails, and in addition to a part from figuring out the jump distance (R) and the interatomic distance (a). Table I indicates that the prepared alloys do not have energy levels near the Fermi level, indicating that the electrical conductivity of these alloys follows Equation 4. The results of Table I further support this, as they show that the parameters of the exponential factor σ_{01} and σ_{02} preceded the exponent for each sample and have two values. We must use equations 6, 9, and 10 to determine the conduction coefficients necessary to compute the energy state densities for the localized and extended states, respectively.

For all alloys in Table I, the hopping distance R has been computed; the resulting R values are shown in Table II. Fig. 6 shows that the value of hopping distance R typically rises when tellurium concentration rises. However, the increase becomes considerable at x = 40 due to the spacing between the local levels as a result of the partial substitution of selenium by tellurium, which led to a spacing between local energy state levels. This could be explained due to the difference in molecular weight between tellurium and selenium; the molecular weight of tellurium is about 127.6 g/mol, which is larger than the molecular weight of selenium, 78.97 g/mol. This effect will occur when you decrease the ratio of selenium and increase the modifier; the interatomic distance will increase and decrease depending on the modifier ratio. Furthermore, in atomic distance, the increase is due to a change in the sizes of the exchanged atoms (Te $=1.36 \times 10^{-10}$ m and Se $= 1.16 \times 10^{-10}$ m) as a result of the increase in the concentration of tellurium. This is expected to decrease the density of the local states with the increase of the tellurium concentration (Mohammed, et al., 2023).

The interatomic distance (a) for all alloys and the values are given in Fig. 7 and Table II. From this figure, it can be seen that the interatomic distance value increases in general with increasing concentration of tellurium, but it is clear that this is not the case when x = 40 increases significantly; this is due to the spacing of the atoms becoming too great, which results in a stretched distance between energy levels, which should decrease the density of localized states as the concentration of tellurium increases (Ahmed, et al., 2022).

After calculating interatomic atomic distance (a), tail width (ΔE), and hopping distance (R) from the equations (in the theoretical part, equations 7 and 11), it is easy to

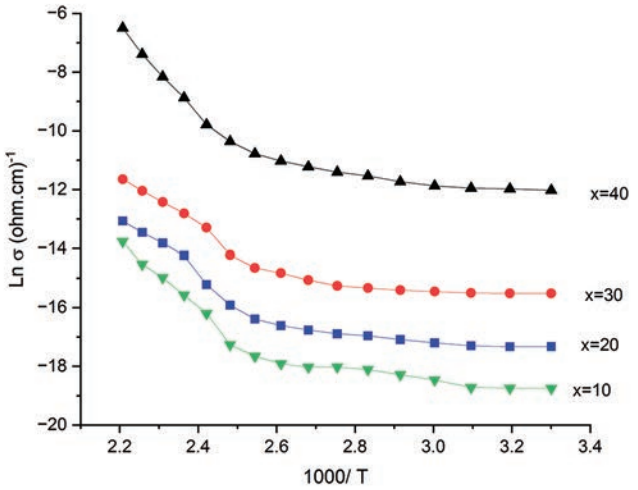

Fig. 5. The change in Ln σ against 1/T for $Se_{100-x}Te_x$ alloys with various Tellurium element concentrations (x = 10, 20, 30 and 40).

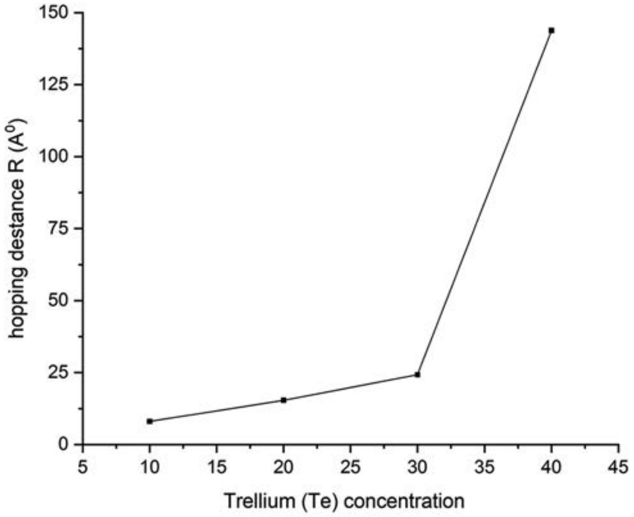

Fig. 6. The value of hopping distance as a function of tellurium (Te) for $Se_{100-x}Te_x$ alloys with various element concentrations (x = 10, 20, 30, and 40).

TABLE I

Electrical Parameters in $Se_{100-x}Te_x$ Glassy System and the Addition of Tellurium at Low and Higher Temperature Ranges

Compositions	ΔE_1	$\sigma_{0ext}(\Omega m)^{-1}$	ΔE_2	$\sigma_{0ext}(\Omega m)^{-1}{}_{\times 10^{-6}}$
$Se_{90}Te_{10}$	0.433	16.3e−2	0.078	0.502
$Se_{80}Te_{20}$	0.380	6.1e−4	0.084	1.16
$Se_{70}Te_{30}$	0.232	3.2e−4	0.094	8.71
$Se_{60}Te_{40}$	0.119	2.9×10^{-5}	0.116	23.7

TABLE II

Tail Width (ΔE), a, R, N (Eext) and N (Eloc) as a Function of Se100-xTex Alloys with Various Element Concentrations (x=10, 20, 30, 40)

Compositions	Tail Width (eV)	R (A^0)	a (A^0)	N (E_{ext}) ($ev^{-1}cm^{-3}$)	N (E_{loc})($ev^{-1}cm^{-3}$)	E_g (eV)
$Se_{90}Ge_{10}$	0.355	8.037	6.6	5.73×10^{16}	3.54×10^{8}	2.4
$Se_{80}Ge_{20}$	0.296	15.37	10.29	3.429×10^{15}	5.78×10^{8}	1.8
$Se_{70}Ge_{30}$	0.138	24.25	14.73	4.723×10^{15}	2.68×10^{9}	2
$Se_{60}Ge_{40}$	0.083	143.8	17.68	9.38×10^{12}	1.485×10^{10}	1.7

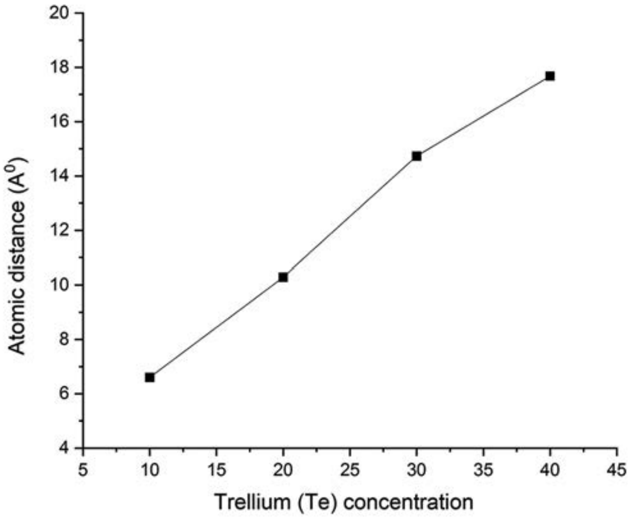

Fig. 7. The value of interatomic distance as a function of tellurium (Te) for $Se_{100-x}Te_x$ alloys with various element concentrations (x = 10, 20, 30, and 40).

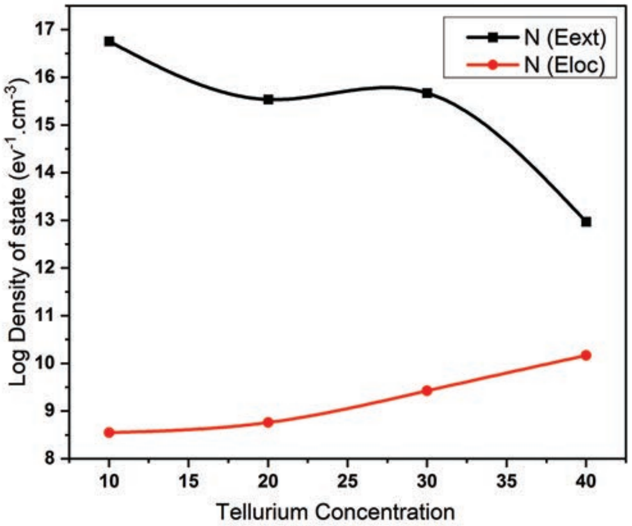

Fig. 8. The tellurium concentration-dependent value of the energy density of extended and localized states for $Se_{100-x}Te_x$ alloys with various element concentrations (x = 10, 20, 30, and 40).

calculate the localized and extended states density for energy. Calculating densities of localized N (E_{loc}) and extended N (E_{ext}) states requires knowledge of the pre-exponential factor parameters σ_{0loc} and σ_{0ext} in the region of these states, whose values for each alloy are listed in Table I. The extended state density is calculated using equation 5, while the local density of states N (E_{loc}) at the tails of the bands inside the mobility energy gap is calculated using equations 6, respectively, after substitution for σ_{0ext}, σ_{0ext}, Tail Width ΔE, R and inter-atomic distance (a). Table II displays the tabulated results, which are scheduled.

Fig. 8 demonstrates the relation between the energy localized density N (E_{loc}) and extended N (E_{ext}) states as a function of tellurium concentration (Te), where it was observed based on this form that the extended density state decreased from 5.73×10^{16} to 9.38×10^{12} ($ev^{-1}cm^{-3}$), with the increasing tellurium concentration from 10 to 40. The density of the localized state increases from 3.54×10^{8} until it reaches a large value (1.485×10^{10} $ev^{-1}cm^{-3}$). This change is due to the energetic activation, as shown in Fig. 8 and Tables I and II. The increase in the density of the local states at the tails of the bundles inside the kinetic energy gap and the decrease in the density of the stretched states indicate that some energy levels in the conduction and valence bands slipped, forming tails inside the energy gap, and in this case, it caused an increase in the randomness of crystal structure samples with the increase in concentration of tellurium (Aqeel, et al., 2020).

C. Optical Proprieties

The study of optical properties has provided important information about semiconductor materials and their potential. They are used in various practical applications, and the optical behavior of semiconductor materials is related to their shape. It is closely related to the structure of energy levels, which is associated with matter's crystalline structure.

Absorptance (A)

The absorption coefficient, which is symbolized by the symbol (α), is defined as the percentage decrease in the flux of radiation energy per unit distance in the direction of the wave propagation within the medium (Patil, et al., 2004). It depends on the energy of the photons and their wavelength, as well as the nature of the surface of the thin film and the energy gap of the semiconductor, as well as the type of electronic transfers that occur. Between energy beams, the absorption coefficient was calculated from the relationship (Jacques, 1975).

$$\alpha = (2.303\,A)/t \tag{16}$$

Where α: absorption coefficient, t: membrane thickness, A: Absorption.

Fig. 9 shows the change in absorbance (A) as a function of the incident photon energy for the $Se_{100-x}Te_x$ with x = 10, 20, 30, and 40. It is noted that the absorbance values are very low for the $Se_{90}Te_{10}$ sample membrane because the incident photons It was not able to excite the electrons and

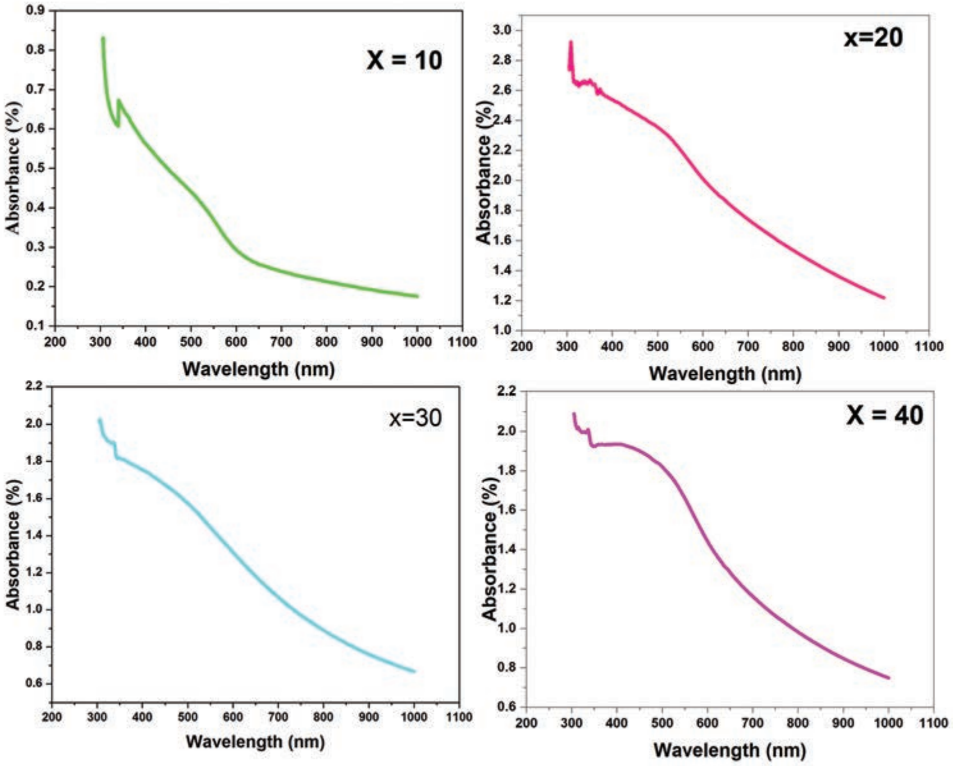

Fig. 9. Absorbance as a function of the wavelength of the $Se_{100-x}Te_x$ thin films with various element concentrations (x = 10, 20, 30, and 40).

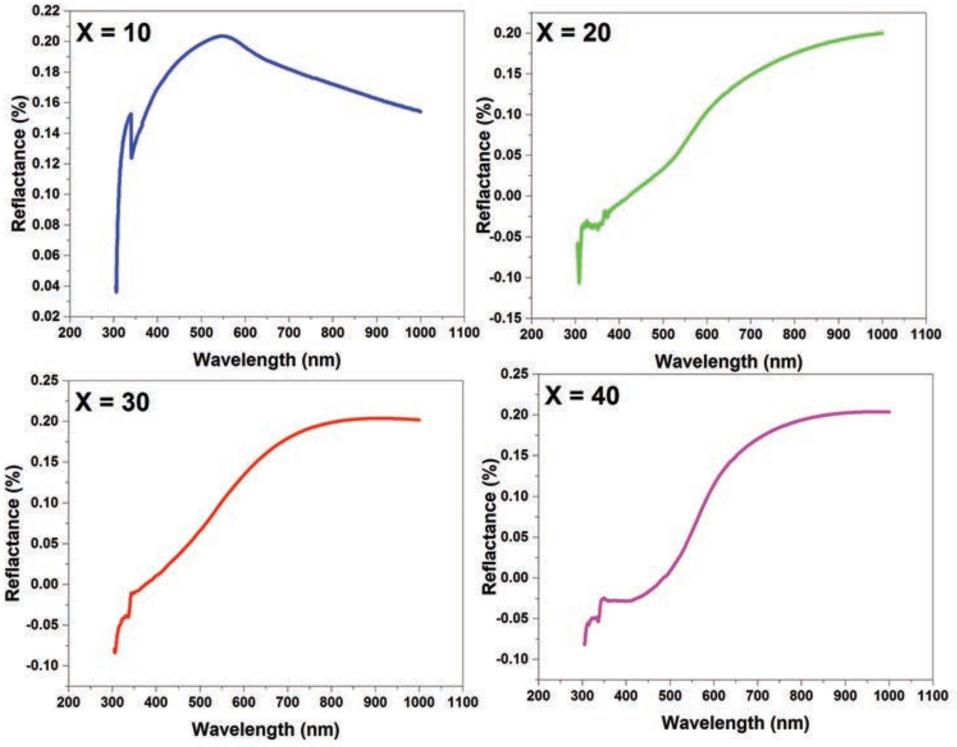

Fig. 10. Reflectance (R) is a function of the wavelength of the $Se_{100-x}Te_x$ thin films with various element concentrations (x = 10, 20, 30, and 40).

move them from the valence band to the conduction band because the photon energy is less than the value of the optical energy gap of the semiconductor and continues to decrease with the increase in the energy of the incident light photons until it reaches its peak and becomes almost constant, when the energy of the incident photons becomes equal to or greater than the energy gap (Lanyon, 1964). After that, we also notice from the figure that the absorbance of the samples in which the tellurium element concentrations increase behaves in the same way as the energy of the incident photon increases, except that the absorbance spectrum of the membranes increases with the increase in the concentration of Te, due to the occurrence of absorption processes mediated by levels. The resulting inoculation of tellurium increases absorbency, accompanied by sharp edges (absorption edge) displacement toward lower energies with increasing concentration. It is also noted from the figure that the basic absorption edge (the border between the high light absorption region and the transparent region) for all samples ranges between 300 and 1000 nm. We also note that the absorption coefficient for all cases has values $>10^4$ in the high energy range, and this agrees with the references (Abd-Elrahman, et al., 2013; Al-Agel, 2013).

Reflectance

Reflectivity (R) can be defined as the ratio of the amount of energy that is reflected during the beam's incident on the surface of the thin film to the amount of power of the incident beam (Yang, et al., 2010). The reflectivity was calculated from the absorbance and transmittance spectra according to the law of conservation of energy according to the relationship:

$$A + T + R = 1 \tag{17}$$

$$R = 1 - A - T \tag{18}$$

Fig. 10 shows the reflectivity as a function of wavelength for membrane $Se_{100-x}Te_x$ alloys with various element concentrations (x = 10, 20, 30, and 40), and we notice from the figure that the reflectivity generally increases with increasing wavelength for short wavelengths. The reflectance is high in near-infrared and near visible regions. According to these results, the films are suitable for solar control coatings.

The following relationships can be used to calculate optical constants, including the extinction coefficient e_{ι}, the refractive index n:

$$e_{\iota} = \frac{\alpha\lambda}{4\pi} \tag{19}$$

$$n = [\frac{4R}{(1-R)^2} - e_{\iota},^2]^{1/2} - \frac{(1+R)}{(1-R)} \tag{20}$$

Fig. 11 represents the relationship between the refractive index and the change in wavelength of the $Se_{100-x}Te_x$ thin films with various element concentrations (when x = 10, 20, 30, and 40). It is noted that the refractive index values of all the prepared films are high at short wavelengths, between 300 and 450 nm. However, when we reach approximately the wavelength (λ = 500 to 550 nm), we observe a significant decrease in the refractive index due to reaching the absorption edge, reaching its lowest value at energy values corresponding to the optical energy gap for all the films under investigation. This behavior is attributed to the increased number of direct electronic transitions at these energies (Reddy and Bhatnagar, 1992; Abd-Elrahman, et al., 2013; Al-Agel, 2013).

Energy gap

Relationship (21) was used to calculate the energy gap.

$$\alpha h\upsilon = A\,(h\nu - Eg)^{1/2} \tag{21}$$

Where: α- absorption coefficient: hυ - photon energy: A- constant, and E_g = energy gap:

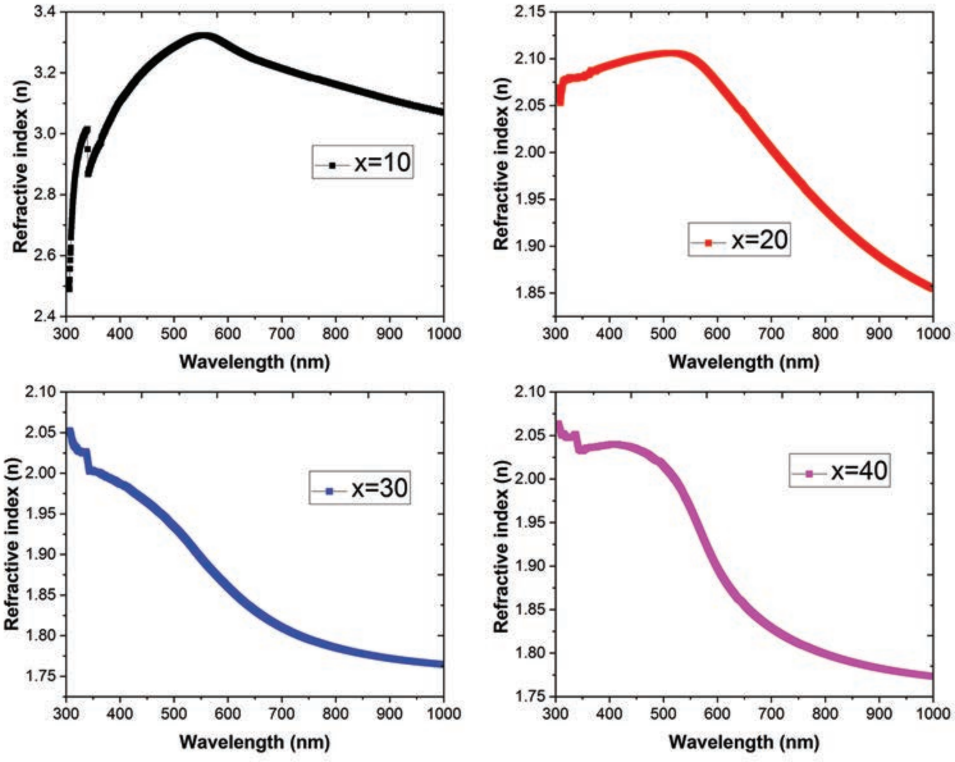

Fig. 11. Refractive Index is a function of the wavelength of the $Se_{100-x}Te_x$ thin films with various element concentrations x = 10, 20, 30, and 40.

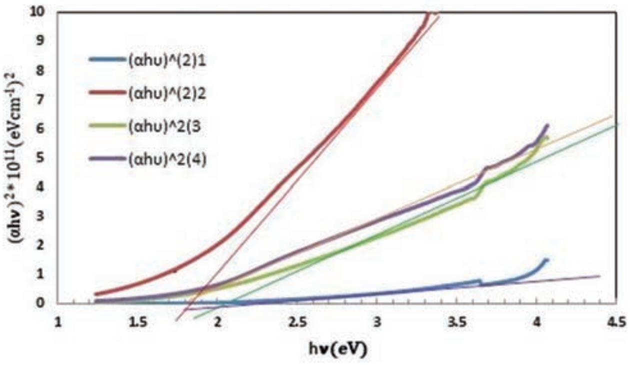

Fig. 12. (a hv)^2 a function of the photon energy of the $Se_{100-x}Te_x$ thin films with various element concentrations (x = 10, 20, 30, and 40).

The graphic relationship was drawn between (α hυ)^2 and the photon energy (hυ) to determine the energy gap. It is clear from Fig. 12 that the value of F The energy value ranged from 1.7 to 2.4 eV. As shown in Table II, it becomes clear to us that the partial replacement of selenium with tellurium led to a change in the value of the energy gap, and the explanation for this decrease is that increasing the concentration of tellurium led to the generation of additional energy levels within the prohibited gap (Street and Mott, 1975). Proximity to the conduction beam leads to a reduction in photon energy required for direct electron transfers, which makes the transfer of electrons from the valence band to the conduction band easier.

V. CONCLUSION

In the above sections, we analyzed the electrical conductivity in Se100-xTex amorphous chalcogenide films with different concentrations. The I-V characteristics of the amorphous thin films prepared by the melting point method were obtained in the temperature range (300–423 K). The characteristics showed a transition from an ohmic region at a low applied voltage to a non-linear region at a higher voltage. There are two specific regions of conduction in the extended state at high temperatures and conduction in the localized state at medium and low temperatures in the tails of the conduction and valence bands. The behavior of the non-ohmic region of the electrical resistivity characteristics can be understood in terms of the temperature dependence of the ohmic current with a thermal activation process with a single activation energy for each sample. The density of the localized and extended states was calculated, and it was found that there was a clear change with increasing selenium concentration. The activation energy and absorbance values were studied for each of the $Se_{100-x}Te_x$ amorphous films.

REFERENCES

Abd-Elrahman, M.I., Khafagy, Rasha M., Zaki, S.A., and Hafiz, M.M., 2013. Effect of composition on the optical constants of $Se_{100-x}Te_x$ thin films. *Journal of Alloys and Compounds*, 571, pp.118-122.

Abdulateef, A.N., Alsudani, A., Chillab, R.K., Jasim, K.A., and Shaban, A.H., 2020. Calculating the mechanisms of electrical conductivity and energy density of states for $Se_{85}Te_{10}Sn_{5-x}In_x$ glasses materials. *Journal of Green Engineering*, 10, pp.5487-5503.

Ahmed, B.A., Mohammed, J.S., Fadhil, R.N., Jasim, K.A., Shaban, A.H., and Al Dulaimi, A.H., 2022. The dependence of the energy density states on the substitution of chemical elements in the $Se_6Te_{4-x}Sb_x$ thin film. *Chalcogenide Letters*, 19, pp.301-308.

Al-Agel, F.A., 2011. Influence of composition on electrical and optical properties of new chalcogenide thin films from Ge-Se-Tl system. *Optics and Laser Technology*, 43, pp.781-786.

Al-Agel, F.A., 2013. Optical and structural properties of amorphous Se_xTe_{100-x} aligned nanorods. *Nanoscale Research Letters*, 9, pp.520.

Borisova, Z.U.U., 1981. In: Adashko, J.G., Ed. *Glassy Semiconductors*. Springer Science and Business Media, LLC.

Chaudhri, M., Vohra, A., and Chakarvarti, S.K., 2008. Fabrication of Zn/Cd-Se micro heterostructures by electrochemical deposition in the pores of polycarbonate track-etch membranes and their characterization. *Physica E: Low-Dimensional Systems and Nanostructures*, 40, pp.849-851.

Chillab, R.K., Jahil, S.S., Wadi, K.M., Jasim, K.A., and Shaban, A.H., 2021. Fabrication of $Ge_{30}Te_{70-x}Sb_x$ glasses alloys and studying the effect of partial substitution on d.C electrical energy parameters. *Key Engineering Materials*, 900, pp.163-171.

Cohen, M.H., Fritzsche, H., and Ovshinsky, S.R., 1969. Simple band model for amorphous semiconducting alloys. *Physical Review Letters*, 22(20), pp.1065-1068.

Elliott, G.R., Murugan, G.S., Wilkinson, J.S., Zervas, M.N., and Hewak, D.W., 2010. Chalcogenide glass microsphere laser. *Optics Express*, 18, pp.26720-26727.

Elliott, S.R., 2015. Chalcogenide phase-change materials: Past and future. *International Journal of Applied Glass Science*, 6, pp.15-18.

Elliott, S.R., and Steel, A.T., 1986. Mechanism for doping in Bi chalcogenide glasses. *Physical Review Letters*, 57, pp.1316-1319.

Faraj, M.G., 2022. Effect of substrate temperature on the electrical properties of al-doped zinc oxide films deposited on polyethylene terephthalate. *Aro-The Scientific Journal of Koya University*, 10, pp.131-133.

Farid, A.S., Fadel, M., and Abd El-Wahabb, E., 2019. AC electrical conductivity and dielectric relaxation behavior of amorphous Se36In31Cu33 thin films. *Phase Transitions*, 92, pp.1031-1042.

Flasck, R., Izu, M., Sapru, K., Anderson, T., Ovshinsky, S.R., and Fritzsche, H., 1991. Optical and electronic properties of modified amorphous materials. *Disordered Materials*, pp.51-53.

Frumar, M., and Tichý, L., 1987. N-type conductivity in chalcogenide glasses and layers. *Journal of Non-Crystalline Solids*, 97-98, pp.1139-1146.

Hamad, N.H., Faraj, M.G., and Taha, A.H., 2023. Structural and optical properties of cadmium sulfide-doped silver deposited on glass and polymer substrates by chemical spray pyrolysis. *Aro-The Scientific Journal of Koya University*, 11, pp.32-37.

Jacques, I.P., 1975. *Optical Processes in Semiconductors*. Dove Publications lnc., New York.

Jasim, K.A., Alwan, T.J., Al-Lamy, H.K., and Mansour, H.L, 2011. Improvements of superconducting properties of hg0.6pb0.25sb0.15ba2ca2cu3o8+δ ceramic by controlling the sintering time. *Journal of Superconductivity and Novel Magnetism*, 24, pp.1963-1966.

Jouanne, M., Morhange, J.F., Dynowska, E., Łusakowska, E., Szuszkiewicz, W., Molenkamp, L.W., and Karczewski, G., 2004. Structure characterization of MBE-grown (Zn, Cr) Se layers. *Journal of Alloys and Compounds*, 32, pp.92-99.

Khudhair, N.H., and Jasim, K.A., 2023. Study the effect of tin on the energy density of states Se60Te40-xSnx chalcogenide glass. *AIP Conference Proceedings*, 2769, p.020062.

Khudhair, N.H., and Jasim, K.A.A., 2023. Study of the effectiveness of tin on the thermal conductivity coefficient and electrical resistance of Se60Te40-xSnx chalcogenide glass. *Ibn AL-Haitham Journal for Pure and Applied Sciences*, 36, pp.149-157.

Lanyon, H.P.D., 1964. Optical and electrical properties of selenium-tellurium alloys. *Journal of Applied Physics*. 35, pp.1516-1523.

Lou, S., Zhou, C., Xu, W., Wang, H., Zhou, S., Shen, H., and Li, L.S., 2012. Facile synthesis of water-soluble $Zn_xCd_{1-x}Se$ nanocrystals via a two-phase cation exchange method. *Chemical Engineering Journal*, 211-212, pp.104-111.

Lucas, P., Coleman, G.J., Jiang, S., Luo, T., and Yang, Z., 2015. Chalcogenide glass fibers: Optical window tailoring and suitability for bio-chemical sensing. *Optical Materals*, 47, pp.530-536.

Lucas, P., Conseil, C., Yang, Z., Hao, Q., Cui, S., Boussard-Pledel, C., Bureau, B.,Gascoin, F.,Caillaud, C., Gulbiten, O., Baruah, P., Guizouarn, T., Li, Q., and Lucas, J., 2013. Thermoelectric bulk glasses based on the Cu-As-Te-Se system. *Journal of Materials Chemsitry A*, 1, p.31.

Mahdi, S.H., Jassim, W.H., Hamad, I.A., and Jasima, K.A., 2017. Epoxy/silicone rubber blends for voltage insulators and capacitors applications. *Energy Procedia*, 119, pp.501-506.

Mehta, N., 2020. Recent applications of chalcogenide glasses (ChGs) based sensors. In: *Advances in Modern Sensors*. IOP Science, United Kingdom.

Mohammed, J.S., Nsaif, F.K., Jawad, Y.M., Jasim, K.A., and Al Dulaimi, A.H., 2023. Investigating the optical and electrical characteristics of As60Cu40-xSex thin films prepared using pulsed laser deposition method. *Chalcogenide Letters*, 20, pp.449-458.

Mohammed, L.A., and Jasim, K.A., 2019. Improvement the superconducting properties of $TlBa_2$ Ca_2 Cu $_{3x}$ Ni_x O_{9-}^{δ} superconducting compound by partial substitution of copper with nickel oxide on the. *Energy Procedia*, 157, pp.135–142.

Mott, N.F., Davis, E.A., and Street, R.A., 1975. States in the gap and recombination in amorphous semiconductors. *Philosophical Magazine*, 32, pp.961-996.

Patil, V., Shahane, G., Sutrave, D., Raut, B., and Deshmukh, L., 2004. Photovoltaic properties of N-CdS1-xTex thin film/oxysulphide photoelectrochemical solar cells prepared by chemical bath deposition. *Thin Solid Films*, 446, pp.1-5.

Pattanayak, P., and Asokan, S., 2005. Signature of a silver phase percolation threshold in microscopically phase separated ternary Ge0.15Se0.85-XAgx (0≥x≥0.20) glasses. *Journal of Applied Physics*, 97, pp.13-16.

Reddy, K.V., and Bhatnagar, A.K., 1992. Electrical and optical studies on amorphous Se-Te alloys. *Journal of Physics D: Applied Physics*, 25, pp.1810.

Street, R.A., and Mott, N.F., 1975. States in the gap in glassy semiconductors. *Physical Review Letters*, 35, pp.1293-1296.

Tong, X.C., 2014. *Advanced Materials for Integrated Optical Waveguides*. Springer Science and Business Media, Germany.

Yang, Z., Fah, M.K., Reynolds, K.A., Sexton, J.D., Riley, M.R., Anne, M.L., Bureau, B., and Lucas, P., 2010. Electrophoretic detection of bio-molecules using conducting chalcogenide glass sensors. *Optics Express*, 18, pp.26754-26759.

Yang, Z., Gulbiten, O., Lucas, P., Luo, T., and Jiang, S., 2011. Long-wave infrared-transmitting optical fibers. *Journal American Ceramic Society*, 94, pp.1761-1765.

Simulation of Flare Discharged from Oil Fields, Integration of Remote Sensing, Laboratory and Mathematical Models

Jafar A. Ali[1†], Loghman Khodakarami[1] and Brosk F. Ali[2]

[1]Department of Petroleum Engineering, Faculty of Engineering, Koya University,
Danielle Mitterrand Boulevard, Koya KOY45, Kurdistan Region – F.R. Iraq

[2]Chemical and Petrochemical Engineering Department, College of Engineering, Salahaddin University-Erbil,
Erbil, Kurdistan Region – F.R. Iraq

***Abstract*—The prevailing practice in Iraq and the Middle East involves the flaring of gas into the atmosphere by a majority of oil and gas industries. This practice, however, is causing significant harm to the environment, personnel, and equipment. Consequently, determining the optimal location for the flare stack within an oil field has become a primary concern in the design of oil field processes. To address this issue, an in-depth analysis of the flame distribution from oil field flare stacks has been undertaken, focusing on assessing both the size and configuration of the flare. The investigation specifically concentrated on the diffusion of the heat around flare discharged from a vertically positioned cylindrical pipe into the atmosphere. To facilitate this exploration, geographic information system was used and an environmental laboratory experiment was conducted using a scaled flare stack, allowing for measurements under various conditions. During this experiment, thermal images of the flare at different gas flow rates were captured and analyzed using MATLAB software to precisely measure the dimensions and shape of the flare. Consequently, predicting the shape and size of flare profiles becomes possible when key parameters, such as discharge gas flow rate, are known. The overarching objectives of this study are to forecast the shape and size of the flare as well as the diffusion zone, contributing to a more effective and environmentally friendly oil field process design.**

***Index Terms*—Flare, Geographic information system, Heat diffusion, Remote sensing, Thermal image.**

I. Introduction

In the oil and gas industries, the unwanted gas will be burned using gas flaring. Gas flaring could be on ground level or vertical through a flare stack. Gas flaring is a continuous process to protect the pressurized equipment and reduce the environmental impacts. The burning process produces emissions such as CO, CO_2, and hydrocarbons (Ibañez-Gómez, et al., 2022). Two types of flares predominate in industry; the ground flare and the elevated flare. The high elevation reduces potential flaring hazards because ground-level radiation is lower and better dispersion of gases occurs should the flame be snuffed out. Environmentally, flaring wastes potentially valuable resources and produces emissions that can affect human health, livestock, and pollute the local environment (Ali and Khodakarami, 2014). Gas flaring, as a major source of acid rain and air pollution, has negative consequences for agriculture, forests, and buildings. This negative impact demonstrates why flaring of gas should be prohibited (Bello and Ogunjemilusi 2022). There are global efforts to eliminate gas flaring, with initiatives such as the Zero Routine Flaring by 2030 led by the World Bank and the United Nations (World Bank, 2023). Although significant progress has been made, achieving zero flaring by 2030 may take longer due to various challenges, including high costs, lack in infrastructures, and regulations in some regions (IEA, 2020).

Gas flare is a globally, regionally, and locally significant source of atmospheric pollutants. They can be detected by geospatial technology. Satellite imagery has become an indispensable tool in various fields, including environmental monitoring, urban planning, and resource management. In oil and gas industries, the detection and monitoring of gas flares are essential due to their environmental and economic impacts. Remote sensing is widely used for detecting gas flaring, assessing their emission, and thermal diffusion by using sensors; such as Landsat and Modis (Morakinyo, et al., 2022). Satellite imagery is cost-effective for managing gas flaring over large geographic areas (Khodakarami, et al., 2023). Extensive studies exist on the geospatial modeling of gas flaring. Adole (2011) investigated the effects of gas flaring on vegetation using a geographic information system (GIS). Chowdhury, et al. (2014) employed Landsat 8 for daytime gas flare detection. Ndunagu, et al. (2021) compared satellite analysis with regulatory gas flaring volumes. Faruolo, et al. (2022) utilized a tailored approach and remote sensing for gas flaring investigation. Another study by Faruolo, et al. (2023) explored gas flaring using multi-temporal satellite data. Heimerl, Malki,

---

ARO-The Scientific Journal of Koya University
Vol. XIII, No.1 (2025), Article ID: ARO.11982. 5 pages
DOI: 10.14500/aro.11982
Received: 05 January 2025; Accepted: 06 April 2025
Regular research paper; Published: 08 May 2025

†Corresponding author's e-mail: jafar.dalo@koyauniversity.org

and Mehana (2023) integrated a geospatial analysis of satellite and operator-reported data with viable mitigation strategies. Dollah, Weli, and Eludoyin (2023) examined land cover dynamics around gas flaring sites using geospatial modeling. Very few previous studies have identified the exact surrounding area affected by gas flares. The novelty of the current study lies in its high-resolution geospatial model of the flare and heat diffusion zone, which has not been predicted by earlier research. This study integrates geospatial modeling with laboratory and mathematical work, distinguishing it from other studies. The study aims to develop a model to estimate the area around a flare affected by the flame. This study utilizes Landsat 8 data, specifically the thermal bands (Band 10), for the detection and temperature estimation of gas flares associated with oil fields.

II. Methodology

In this research study, three different methodologies have been used to investigate the gas flaring; geospatial analysis, laboratory experimental work, and mathematical model. GIS and remote sensing techniques and Landsat imagery were used in the analysis. A thermal infrared camera was used in the laboratory experimental work to capture thermal and digital images. Numerical method; finite difference was used to solve the involved equations with computer software MATLAB to produce the flare images.

III. Geospatial Analysis

To prepare the land surface temperature (LST) map, we utilized Landsat 8 satellite data to a certain oil field in the Kurdistan region. After obtaining the satellite imagery, the following equations were applied to calculate the LST. Subsequent to preparing the LST map, we convert it to a contour line to map the flare's surrounding area (Barsi, et al., 2014; Khodakarami, et al., 2022; Avdan and Jovanovska, 2016; Khodakarami, 2024).

IV. Experimental Thermal Analysis

The experiments were carried out at the laboratory using a small stack made of steel with dimensions 50cm height and 5 cm diameter. A thermal imaging camera was used to take images of the flare for each run. The discharged gas flow rate is maintained by the flow control valve. The gas was supplied from a gas cylinder through a hose. Several experimental runs were undertaken at room temperature, with the gas discharged at different flow rates during each run. The flow rates influenced the size of the flare. The objective of the experiments was to perform tests under variable conditions, such as differing flow rates without wind effects. To avoid disturbing the flare's behavior, non-destructive tools were used for the measurements, including a thermal camera, digital camera, and camcorders.

The experimental results are illustrated in Fig. 1. The left-hand side shows the thermal image, while the right-hand side represents the same image in digital form. The red spot indicates the flare flame, while the surrounding area depicts the heat diffusion profile.

V. Mathematical Analysis

The mathematical work is focusing on finding the heat diffusion profile and shape of the flare. The domain in Fig. 2 illustrates the gas flow directions, the coordinates, and the diffusion coefficient directions involved in the mathematical model. The comprehensive equation for the dispersion of a certain property of fluid is the advection-diffusion equation (9) was used in the current analysis. To solve this equation assumptions are required, it is assumed that the gas flow is in a steady state, with vertical movement and lateral diffusion. To produce the model, it is considered that the coefficient of heat diffusion is applied accordingly to suit the characteristics in the lateral and vertical directions – that is along the gas flow and width-wise. The flow, along the y-axis, which is considered longitudinal along the flare stack, is velocity-dependent. To simplify the equation further, a steady state

Equation 1	TOA=Ml×Qcal+Al	Where, Ml is the irradiance band number, Qcal is the digital number, Al is the additive band number. For band 10 (2) (Equation 2)
Equation 2	TOA=0.0003342×"Band 10"+0.1	
Equation 3	BT=K2/(ln [K1/L]+1)−273.15	Where K1 and K2 are the band-specific constants, L is the TOA radiance. For band 10, substituting the constants yields.
Equation 4	$T = \frac{777.89}{\ln\left(\frac{1321.08}{0.00341802\times DN+149}+1\right)} - 273.15$	
Equation 5	$NDVI = \frac{NIR - R}{NIR + R}$	Where, NIR represents the near-infrared band (Band 5) and □ represents the red band (Band 4).
Equation 6	$PV = (\frac{NDVI - NDVImin}{NDVImax - NDVImin})^2$	
Equation 7	LSE=0.004×PV+0.986	
Equation 8	$LST = \frac{BT}{1+(0.00115\times\frac{BT}{1.4388})}\ln\left(\varepsilon\right)$	

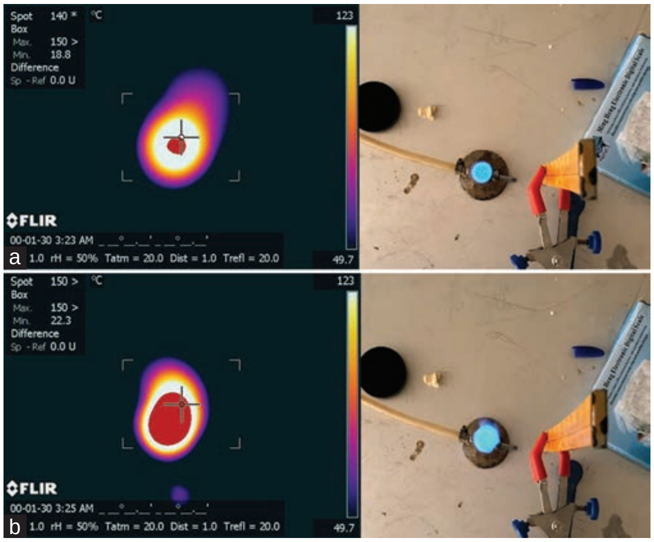

Fig. 1. (a and b) Thermal image of flare.

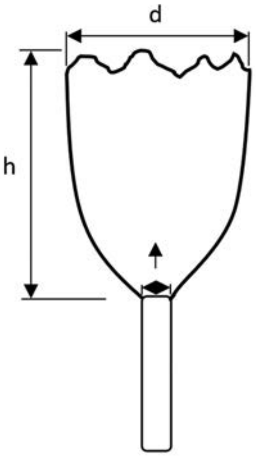

Fig. 2. Flare schematic.

condition is considered to be when the temperature does not change with time.

$$\frac{\partial T}{\partial t}+vx\frac{\partial T}{\partial x}+vy\frac{\partial T}{\partial y}+vz\frac{\partial T}{\partial z}=cx\frac{\partial^2 T}{\partial x^2}+cy\frac{\partial^2 T}{\partial y^2}+cz\frac{\partial^2 T}{\partial z^2} \tag{9}$$

Where T is the temperature at the flare tip, t is time, vx, vy, vz are flare gas velocity in all directions while cx, cy, cz are coefficients of diffusion along the x, y and z direction, respectively. These coefficients are the main parameters affecting the shape of the flare. Molecular diffusion is not considered in the equation because its value is much smaller than the turbulent diffusivity (Ali, 2014).

Solve (9) using the finite difference method and MATLAB, replace the parameters, and the heat diffusion profile will be predicted, Figs. 3 and 4.

VI. Results and Discussion

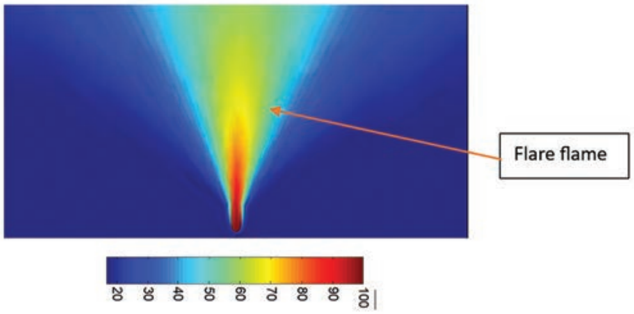

Fig. 3. Flare het diffusion profile.

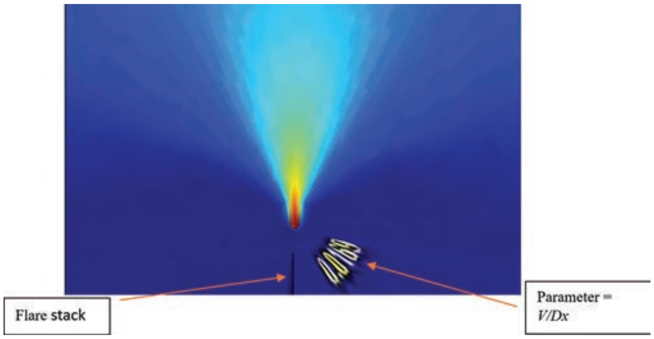

Fig. 4. Heat diffusion profile.

The study investigated flare heat diffusion using geospatial analysis, laboratory experiments, and mathematical modeling. Good results were obtained and illustrated in the previous sections. Clear heat diffusion profiles resulting from GIS and remote sensing are presented in Fig. 5. The thermal imaging profile using a thermal infrared camera in the laboratory for a smaller flare model is presented in Fig. 1. The mathematical heat diffusion produced by the developed model is illustrated in Figs. 3 and 4. In all the analyses, it was found that the lateral heat diffusion at a fixed diameter decreases with an increase in the discharge gas flow, and vice versa Figs. 6 and 7. As the flow rate increases, the flare becomes taller but narrower Fig. 8, resulting in a smaller ground-heated zone.

Fig. 9 presents the relative heat diffusion around the flare for the GIS model, laboratory, and mathematical work. It demonstrates a close alignment of the three results, indicating the validation of the current study. The results of this study are significant for the oil and gas industry, as they help improve gas flaring by enabling the placement of flares in locations that minimize their impact on humans, equipment, and the environment. Knowing the size of a flare plays a significant role in mitigating environmental problems, as it directly affects key environmental factors such as gas emissions, flaring efficiency, noise, and radiation. By selecting the optimum flare size, the adverse effects on both humans and the environment can be reduced (Ismail and Umukoro, 2025).

As a result of this study, it is recommended that companies run the current or similar models during the initial stages of field design or gas processing to ensure the flare stack is positioned correctly.

The aim of this study is to improve the gas flaring process by predicting the shape of flares from round and vertical

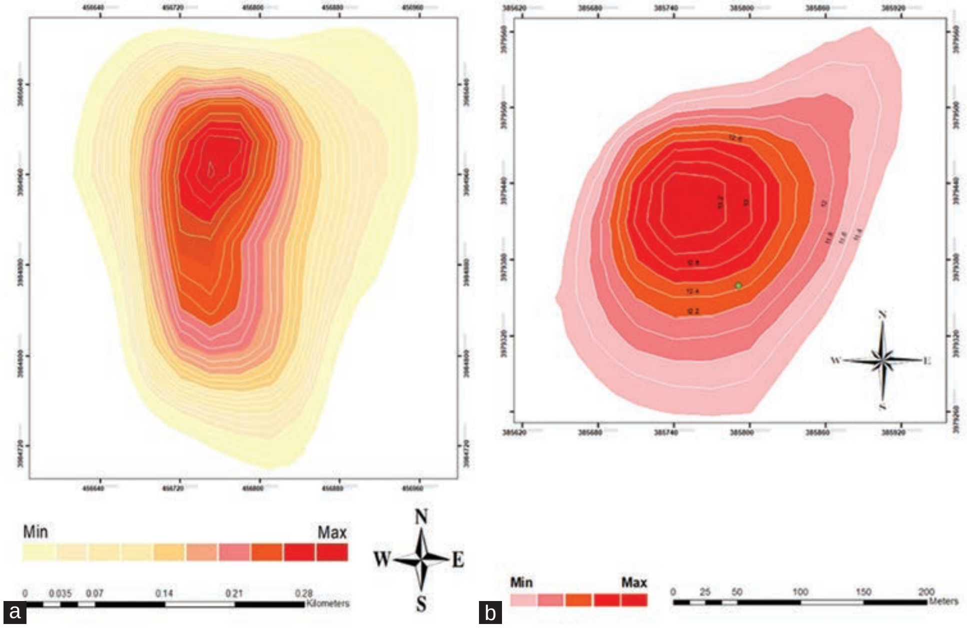

Fig. 5. (a and b) Flare heat diffusion.

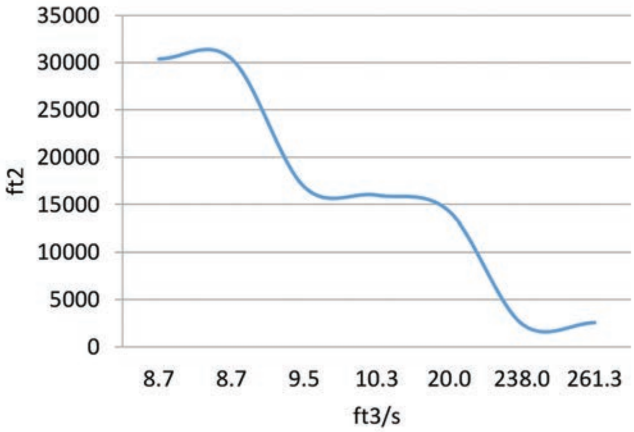

Fig. 6. Heat diffusion zone as function of discharge gas flow rate.

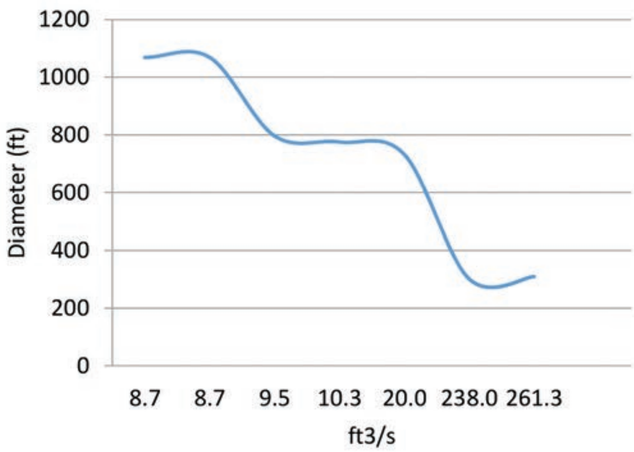

Fig. 7. Diameter of the heated zone.

stacks. This enables the prediction of both the flare shape and heat diffusion of ground flares.

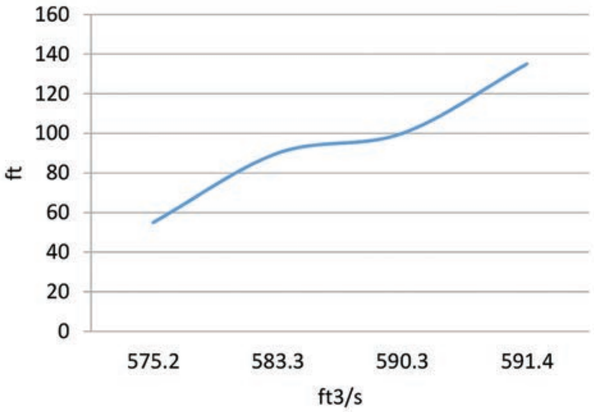

Fig. 8. Linear relation of flare height and discharge gas flow.

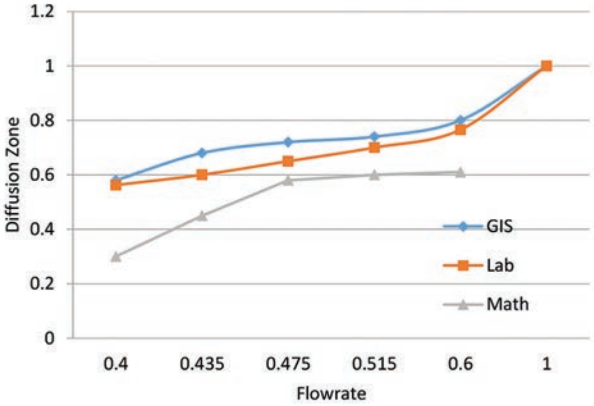

Fig. 9. Heat diffusion zone for the geographic information system, laboratory and mathematical analysis.

For future work, it is recommended to employ additional equations of motion to account for the effects of wind on heat diffusion and flare shape.

VII. Conclusion

The heat diffusion zone around gas flaring is a critical concern for oil field operators and environmental agencies. From this study, it is concluded that at a certain gas flow rate discharge, the heated zone can be predicted, determining the extent to which the heat can spread and the height of the flare.

References

Adole, T., 2011. *A GIS Based Assessment of the Impacts of Gas Flaring on Vegetation Cover in Delata State* [MSc Thesis]. University of East Anglia, Nigeria.

Ali, J.A., 2014. Two-dimensional modeling of oil fields flare. *Academic Journal of Science*, 3(2), pp.299-308.

Ali, J.A., and Kodakarami L.A., 2014. Investigations of flare gas emissions in Taq Taq oil field on the surrounding land. *ARO the Scientific Journal of Koya University*, 2(2), pp.15-19.

Avdan, U., and Jovanovska, G., 2016. Algorithm for automated mapping of land surface temperature using LANDSAT 8 satellite data. *Journal of Sensors*, 2016, p.1480307.

Barsi, J.A., Schott, J.R., Hook, S.J., Raqueno, N.G., Markham, B.L., and Radocinski, R.G., 2014. Landsat-8 thermal infrared sensor (TIRS) vicarious radiometric calibration. *Remote Sensing*, 6, pp.11607-11626.

Bello, T., and Ogunjemilusi, G., 2022. *Gas Flaring and the Assessment of the Legal Framework Governing It*. Available from: https://ssrn.com/abstract=4137527

Chowdhury, S., Shipman, T., Chao, D., Elvidge, C.D., Zhizhin, M., and Hsu, F., 2024. Daytime Gas Flare Detection Using Landsat-8 Multispectral Data. In: *2014 IEEE Geoscience and Remote Sensing Symposium*, Quebec City, QC, Canada, 2014, pp. 258-261.

Dollah, O.C., Weli, V.E., and Eludoyin, O.S., 2023. Spatial analysis of land cover dynamics across gas flaring sites in Rivers State. *Journal of Research in Environmental and Earth Sciences*, 9(10), pp.22-28.

Faruolo, M., Genzano, N., Marchese, F., and Pergola, N., 2022. A tailored approach for the global gas flaring investigation by means of daytime satellite imagery. *Remote Sensing*, 14, p.6319.

Faruolo, M., Genzano, N., Marchese, F., and Pergola, N., 2023. Multi-temporal satellite investigation of gas flaring in Iraq and Iran: The DAFI porting on collection 2 Landsat 8/9 and sentinel 2A/B. *Sensors*, 23, p.5734.

Heimerl, J., Malki, M.L., and Mehana, M., 2023. Flaring volumes in the intermountain west region: A geospatial analysis of satellite and operator-reported data with viable mitigation strategies. *Environmental Research*, 236(Pt 1), p.116729.

Ibañez-Gómez, L.F., Albarracín-Quintero, S., Céspedes-Zuluaga, S., Montes-Páez, E., Ando Junior, O.H., Carmo, J.P., Ribeiro, J.E., Moreira, M.M.A., Siqueira, A.A.G., and Guerrero-Martin, CA., 2022. Process optimization of the flaring gas for field applications. *Energies*, 15(20), p.7655.

International Energy Agency IEA, 2023, Global *Methane Tracker* 2023. IEA, Paris. Available from: https://www.iea.org/reports/global-methane-tracker-2023

Ismail, O.S., and Umukoro, G.E., 2016. Modelling combustion reactions for gas flaring and its resulting emissions. *Journal of King Saud University Engineering Sciences*, 28, p.130-140.

Khodakarami, L., Pourmanafi, S., Mokhtari, Z., Soffianian, A.R., and Lotfi, A., 2023. Urban sustainability assessment at the neighborhood scale: Integrating spatial modellings and multi-criteria decision making approaches. *Sustainable Cities and Society*, 97, p.104725.

Khodakarami, L., Pourmanafi, S., Soffianian, A.R., and Lotfi, A., 2022. Modeling spatial distribution of carbon sequestration, CO_2 absorption, and O_2 production in an Urban area: Integrating ground-based data, remote sensing technique, and GWR model. *Earth and Space Science*, 9, p.1-22.

Khodakarami, L., 2024. Spatial modeling of micro-scale carbon dioxide sources and sinks in urban environments: A novel approach to quantify urban impacts on global warming. *Greenhouse Gases: Science and Technology,* 14(3), pp. 470-491.

Morakinyo, B., Lavender, S., and Abbott, V., 2022. Investigation of potential prevailing wind impact on land surface temperature at gas flaring sites in the Niger Delta, Nigeria. *International Journal of Environment Geoinformatics*, 9(1), pp.179-190.

Ndunagu, P.N., Joel, O.F., and Oji, A.A., 2021. Comparative analysis of satellite and regulatory based gas flare volumes in the Niger Delta region. *Nigerian Journal of Technological Development*, 8(4), pp.279-287.

World Bank, 2020. *Global Gas Flaring Reduction Partnership (GGFR)*. Available from: https://www.wb-ggfr-report-july2020.pdf

In-depth Analysis on Machine Learning Approaches: Techniques, Applications, and Trends

Abdulhady A. Abdullah[1], Nergz S. Mohammed[2], Maryam Khanzadi[3], Safar M. Asaad[4,5], Zrar Kh. Abdul[6] and Halgurd S. Maghdid[4†]

[1]Abdulhady Abas Abdullah Artificial Intelligence and Innovation Centre, University of Kurdistan Hewler, Erbil, Iraq

[2]Department of Computer Science, Faculty of Science, Soran University, Soran, Kurdistan Region – F.R. Iraq

[3]Department of Health Information Technology Engineering, University of Tehran, Tehran, Iran

[4]Department of Software Engineering, Faculty of Engineering, Koya University, Danielle Mitterrand Boulevard, Koya, KOY45, Kurdistan Region – F.R. Iraq

[5]Department of Computer Engineering, College of Engineering, Knowledge University, Erbil 44001, Kurdistan Region – F.R. Iraq

[6]Department of Computer, College of Science, Charmo University, Sulaymaniyah, Kurdistan Region – F.R. Iraq

***Abstract*—Machine learning (ML) approaches cover several aspects of daily life tasks, including knowledge representation, data analysis, regression, classification, recognition, clustering, planning, reasoning, text recommendation, and perception. The ML approaches enable applications to learn and adapt with or without being directly programmed from previous data or experience. The ML techniques, coupled with current technologies, provide a range of solutions, starts from vision-based applications to text-generation applications. To this end, this article presents a comprehensive overview of the approaches of ML, including supervised, unsupervised, semi-supervised, reinforcement, and self-learning. This review critically examines the roles performed by these aforementioned approaches in terms of their weaknesses and strengths. Furthermore, within this study, a new comparative analysis is conducted by reviewing existing studies and evaluating ML techniques using metrics including data requirement, accuracy, complexity, interpretability, scalability, applications, and challenges. Thereafter, the implemented ML techniques are classified, and their key findings are examined. The comprehensive review demonstrates that neither standalone nor hybrid ML techniques can completely satisfy all of the evaluated metrics, the necessity of customized solutions based on the requirements of particular applications.**

ARO-The Scientific Journal of Koya University
Vol. XIII, No. 1 (2025), Article ID: ARO.12038. 13 pages
DOI: 10.14500/aro.12038
Received: 06 February 2025; Accepted: 07 May 2025
Regular review paper; Published: 22 May 2025

†Corresponding author's e-mail: halgurd.maghdid@koyauniversityorg

***Index Terms*—Comparative metrics, Learning challenges, Machine learning algorithms, Machine learning structures.**

I. Introduction

A technology that allows us to produce intelligent systems capable of imitating human intelligence is called artificial intelligence (AI). Machine learning (ML) is a branch of AI which enables machines to understand without being directly programmed from previous data or skills (Christine, et al., 2020). Why should a machine be learned, even though we can program it? Well, there are two main reasons; first, the builders cannot predict all possible scenarios. Second, the builders happen to not know how to program a solution themselves (Weihao, Di and Theo, 2020). Fig. 1 below demonstrates the classes of ML.

Supervised learning (SUL) is the ML technique in which machines are trained in using training records, and machines calculate the output based on that data (Jwan, Abas and Tarik, 2024). SUL able to further separate into two kinds of problems: Classification and regression techniques. The classification procedures are used when the output variable is categorical, which includes two classes, such as yes-no, true-false, and female-male. The second type of SUL is regression real-value performance variable estimation, including special cases of forecasting future values out of recent or past values in a time series (Hooman, et al., 2019).

Unsupervised learning (USL) is another type of ML in which its models are trained without any guidance using an unlabeled dataset and can operate on that data. The concept of USL algorithms can be described within the idea of

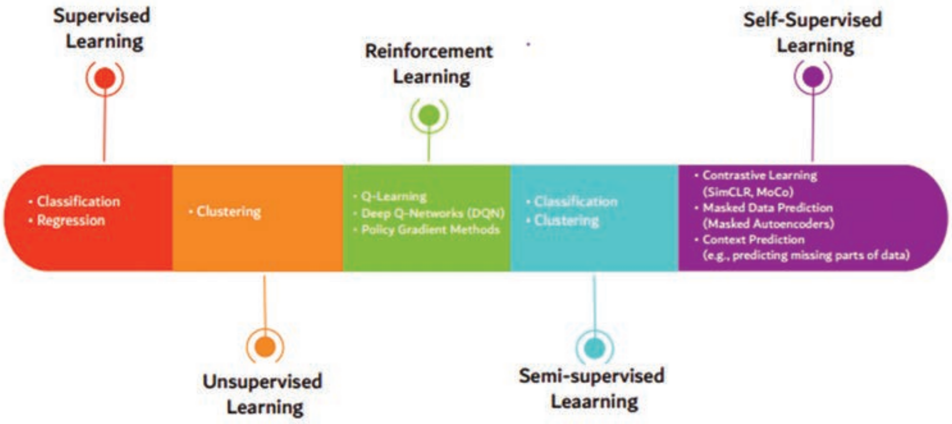

Fig. 1. The machine learning approaches with their tasks.

clustering, when clustering is a process of grouping a set of items into unique clusters such that the items with high similarities remain in a group and have less or no similarity with the items of any other group (Alboukadel, 2017).

The third kind of ML is semi-supervised learning (SSL), in the middle of the training datasets of supervised and USL, and the SSL problem starts with a sequence of both labeled and unlabeled data (Changde, Changying and Huiguang, 2021). From the state-of-the-art, the ML algorithms' accuracy differs in terms of the characteristics and size of the data sets between the training and testing sets. There is no one suitable ML algorithm to resolve all the problems.

Currently, most of the real-life solutions, when they are running via implementing the ML algorithms, are enhanced by using new paradigms, which are reinforcement learning (RIF) and self-learning (SEL) algorithms. The RIF is working on the expense of measuring the rewards and penalties of the actions according to the characteristics of application's environment. While the SEL algorithms mostly develop autonomously, to provide continuous enhancement and promise the intended targets via continuous learning.

However, the aforementioned ML paradigms need further investigation as well as they need to be analyzed according to the application solutions. To this end, this article makes a major contribution by providing a comprehensive review of ML approaches and offering a detailed comparative analysis that systematically contrasts SUL, USL, SSL, RIF, and SEL paradigms across critical operational metrics, thereby aiding researchers and practitioners in selecting the most appropriate learning technique based on application needs. Furthermore, a major contribution of this study is the detailed comparative analysis that systematically evaluates these approaches based on data requirements, complexity, accuracy, interpretability, scalability, applications, and challenges. By synthesizing recent research findings from 2016 to 2024 and identifying the strengths and limitations of each paradigm, the article also provides critical insights for researchers and practitioners. The provided comparison shows that no single method is universally optimal, highlighting the importance of selecting techniques tailored to specific application needs. In another vain, the review discusses emerging trends such as transfer learning, scalable SSL, and privacy-preserving techniques, offering valuable directions for future research.

The structure of this article is as follows: In section II, the theoretical background is explained. Section III investigates some literature reviews regarding supervised, unsupervised, semi-supervised, reinforcement, and SEL methods are described. A new comparative analysis of the current study of using ML algorithms via data requirements, complexity, accuracy, interpretability, scalability, application, and challenges is presented in section IV. Section V and VI provide the discussions and conclusions of this review, respectively.

II. BACKGROUND

Researchers have proposed a huge number of methods in this field; hence, this section focused on ML classes. In general, ML has three kinds of learning: supervised, unsupervised, and semi-supervised. SUL that includes a classification algorithm and regression algorithm. USL contains a clustering algorithm. SSL is between SUL and USL. All these techniques and methods are explained in detail in the next subsections.

It's the fact that there is a big connection between AI and ML fields, including deep learning (DL) (Abdullah, et al., 2024). As illustrated in Fig. 2, ML is a subdomain of computer science used to analyze data, which automates the structuring of analytical models. ML algorithms aim to learn from the existing data without being explicitly programmed. New data sets adapt independently, which means the learned machine characteristic comes from the iterative feature of the models applied to the data set. This independent adoption is the main aspect of learning. Most often, this implies using a set of historical outcomes to estimate future outcomes (Sabr, 2025).

A. Supervised ML

SUL contains several methods that are applying something that must be learned from previous unused information, utilizing target illustrations to anticipate future effects. Beginning from the investigation of a well-known preparation

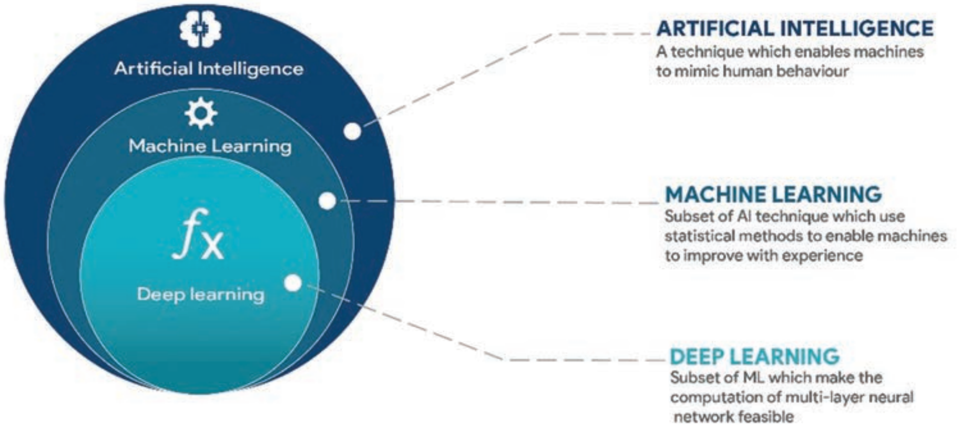

Fig. 2. The relation between artificial intelligence, machine learning and deep learning (Adamu, 2019).

dataset, the learning procedure yields an induced applies to obtain forecasts regarding the yield prices. The structure can supply labels for each further input after adequate preparation. The learning system can moreover match its product against the proper, planning yield, and discover mistakes in arranging to adjust the show appropriately (Gao, et al., 2014). The supervised ML consists of regression and classification techniques. Both of those methods are used for forecasting machines. The main differences among those two techniques are label value in regression is numerical. However, the classification procedure is categorical (Hemant and Rishabh, 2017). To well understand, the procedure of supervision is exposed in Fig. 3.

Classification

A classification technique, traditionally, is a purpose that evaluates the feature structures so that the label divorces one class into positive standards and the other into negative standards, the classification method is used for prediction in ML and works with the labeled data. However, the output variable for classification algorithms is categorical or (discrete), such as recognition of a type of car in a photo, what the weather will be like today or a message from a friend. More detail of these processes is implemented in Fig. 4. (Yongjun and Siyu, 2020). There are several applications running via utilizing classification tasks, for instance, bank customer loan pays willingness prediction, gait recognition, user positioning, email spam classification, web news classification, leaf diseases classification, and cancer tumor cell identification (Upasana, 2019). The classification has several techniques and methods, such as KNN, linear discriminant analysis, regression trees, learning vector quantization, support vector machines, naive Bayes, bagging and random forest, boosting, and stochastic gradient descent (Deepti and Dilip, 2018).

Regression

The Regression task is a numerical way that examines and recognizes the connection between two or more variables of attention. The regression is also to make a relation between a single dependent variable and one or a set of independent variables, as shown in Fig. 5. (Carlos, et al., 2019). Furthermore, the main idea beyond executing regression analysis is to know which features are important that can be failed to observe and how they are manipulating each other (Sung-Jin, et al., 2016). In another vein, feature selection is an important step in the data cleaning for the regression functions. This is because the regression identifies or chooses the most related variables that are contributing to the prediction process.

Linear regression and Logistic regression are the most well-known techniques of the regression task. The linear regression is to make the linear relationship between the dependent and non-dependent variables. While, the logistic regression is used to estimate the probability of happing an event based on set of given independent variables (Carlos, et al., 2019).

The regression is an essential step in most ML algorithms. There are several real-life applications that relaying on utilizing regression analysis starts from medicine report cases to the house price estimates or financial forecasting.

B. Unsupervised ML

USL is a type of ML where a show must explore for formerly hidden patterns in a dataset through no labels and with a minimum of human observation. In USL, a dataset is provided devoid of labels, and typical studies useful properties of the group of the dataset. We do not speak the classical what it needs to be studied but agree to it to invent patterns and attraction decisions from the unlabeled information (Sarfaraz, et al., 2019). The procedures in USL are harder than in SUL since we have little or no information about the data. USL responsibilities normally include combining related instances, dimensionality decrease, and density approximation. One more term for USL is “knowledge discovery” (Kushal, 2020). The most generally used USL procedures are k-means, hierarchical cluster analysis, and expectation maximization (Hui, Ping and Duo, 2019). Public USL methods contain clustering, and dimensionality decrease. Fig. 6 explains the process of USL.

Clustering

Cluster analysis is the most public USL algorithm. Sense that you don’t recognize how many clusters are in the data beforehand, when running the typical (Abdullah, et al.,

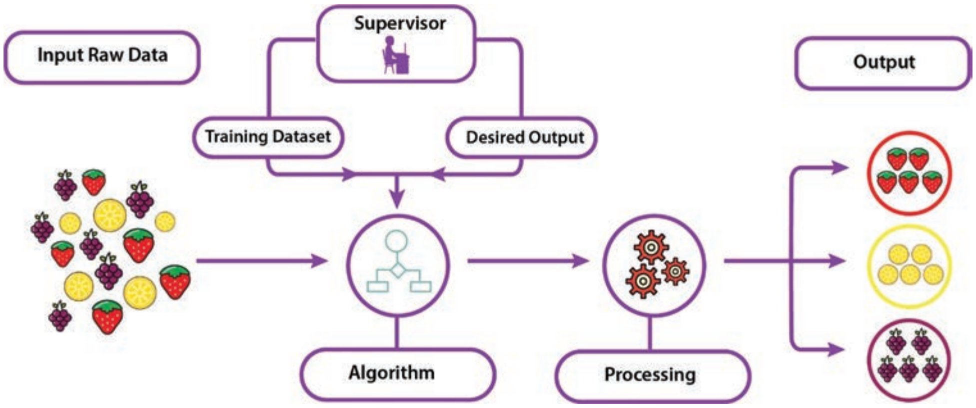

Fig. 3. Supervised learning paradigm.

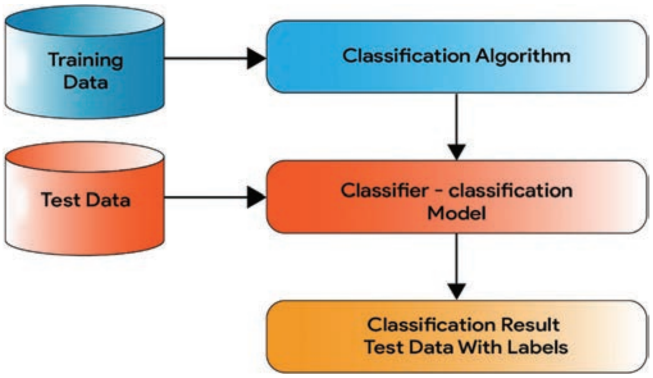

Fig. 4. Classification process.

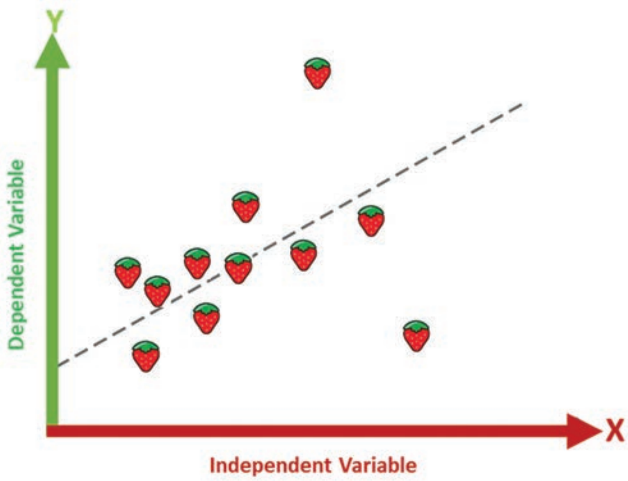

Fig. 5. A Regression line between the independent and dependent variables.

2024). Different from many other numerical techniques, the final output labels are not known previously. This kind of algorithm can help in solving many obstacles. It makes available information about where patterns and associations in data happen, but not what those might be or what they mean. The objective of cluster analysis is to discover related groups of topics, where “similarity” among separate pairs of subjects means the overall amount above the entire set of individualities (Guo, et al., 2021). Some of the cluster methods are partition clustering, hierarchical clustering, and fuzzy clustering (Chunrong, et al., 2019). Fig. 7 below explains the clustering procedure.

C. Semi-Supervised ML

Semi-supervised is one of the methods of AI among the training datasets of supervised and USL. The SSL problem starts with a sequence of both labeled and unlabeled data, semi-supervised learning aims to categorize some of the unlabeled data using the labeled evidence set (Haitao and Zhenhua, 2018). The idea behind SSL is to learn from structured and unstructured information to increase the predictive power of the models. Regularly, personalities unrelated to the domain imagine robots invading advancements and taming people. But AI is extremely diverse, or at least, much more than that possibility (Rui, Feiping and Xuelong, 2017). SUL held the initial kind of learning is investigated in the field of AI. Considering its inception, infinite techniques differing in the complexity of the humble logistic regression to the massive neural network should be examined to enhance accuracy and sinister power. SSL practices the classification method to classify data assets and the clustering procedure to arrange it into different sections. Fig. 8 explains the semi-supervised process.

D. Reinforcement ML

The RIL approach is one of the current ML methods when an agent learns from the vicinity by executing actions to make a decision. The actions are also improved by receiving the feedback in the form of rewards or penalties, as shown in Fig. 9. The most important components of an RIF paradigm are: Agent, environment, state, action, reward, policy, and value functions. Furthermore, the agent observes the recent updates stated of the environments and it provides the action based on the available policy. Thus, the agent is to maximize the cumulative reward over time, while the environment transitions from the old state to a new state and then calculate the reward. Thereafter, the agent revises its policy based on the reward to improve future decisions (Zhang et al., 2021).

The Q-leaning, Deep Q-learning (DQN), Policy Gradient (PG), and Actor-Critic are the most common or core algorithms of the RIF approach (Zhou, Huang and Fränti, 2022). The Q-learning is a model-free algorithm which

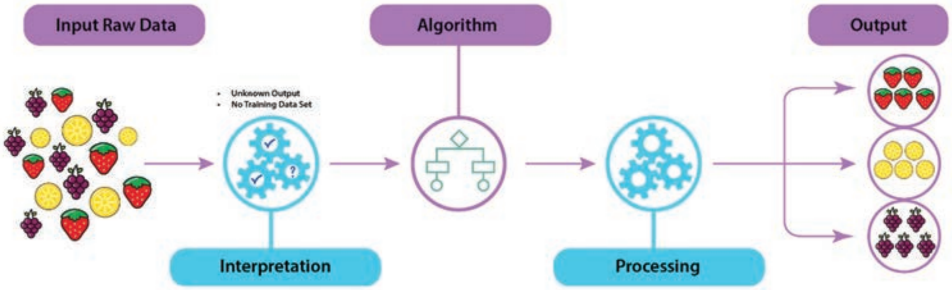

Fig. 6. Unsupervised learning.

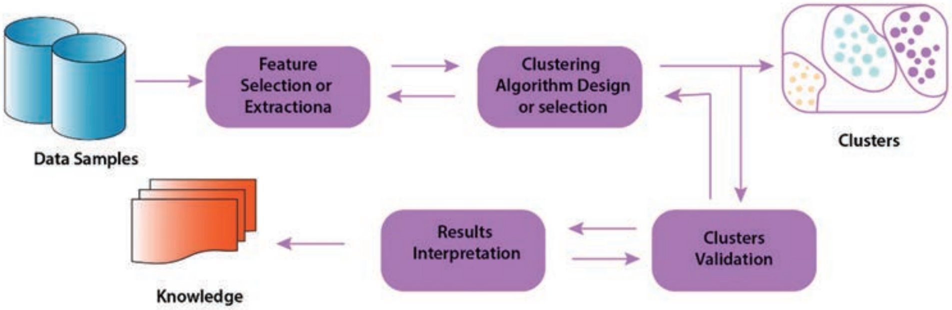

Fig. 7. Clustering process.

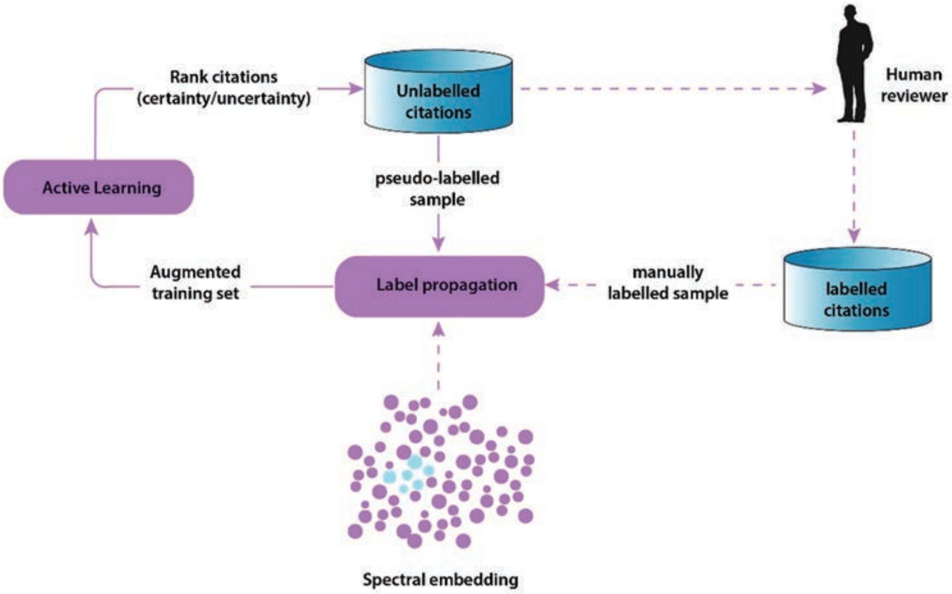

Fig. 8. Semi-supervised learning process.

learns a Q-value for each state-action pair, while the DQN algorithm combines Q-learning with deep neural networks. Furthermore, the PG methods equally enhance the policy and function values. The actor-critic methods use two linked models, where an actor is to select actions and a critic is to evaluate the models. To this end, these methods show that the RL is unique, since the agent learning from trial and error which focuses on long-term rewards rather than only current outcomes (Zhang et al., 2021).

With the era of ML approaches, Robotics, gaming, energy systems, agriculture digitization, driverless cars, healthcare, and finance are the most well-known applications for today's life. However, the navigating safely, developing personalized treatment strategies for chronic diseases, performing complex manipulation tasks, portfolio management, and optimizing energy utilization are still remained as challenges (Perera and Kamalaruban, 2021).

E. SEL Approach

A SEL approach in the context of ML refers to the new paradigm that can enhance their performance and outcomes based on data that they collect through their experiences

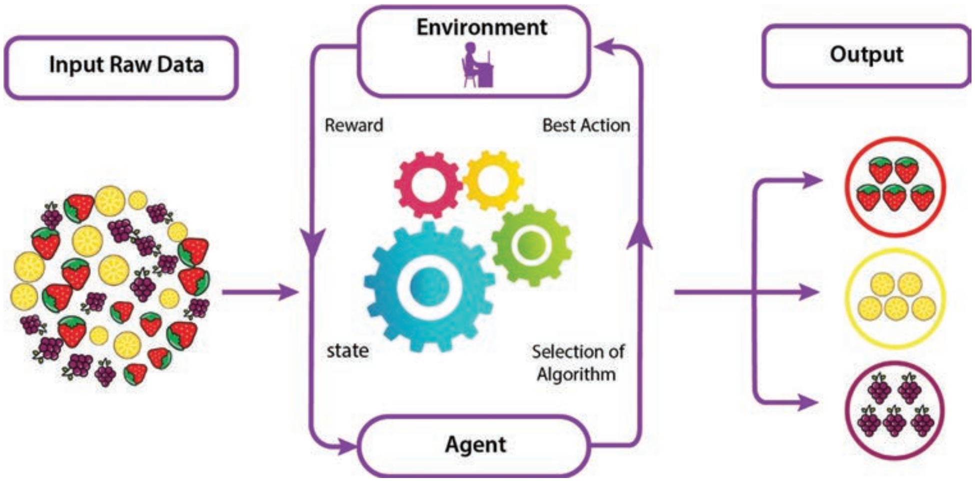

Fig. 9. Reinforcement learning paradigm.

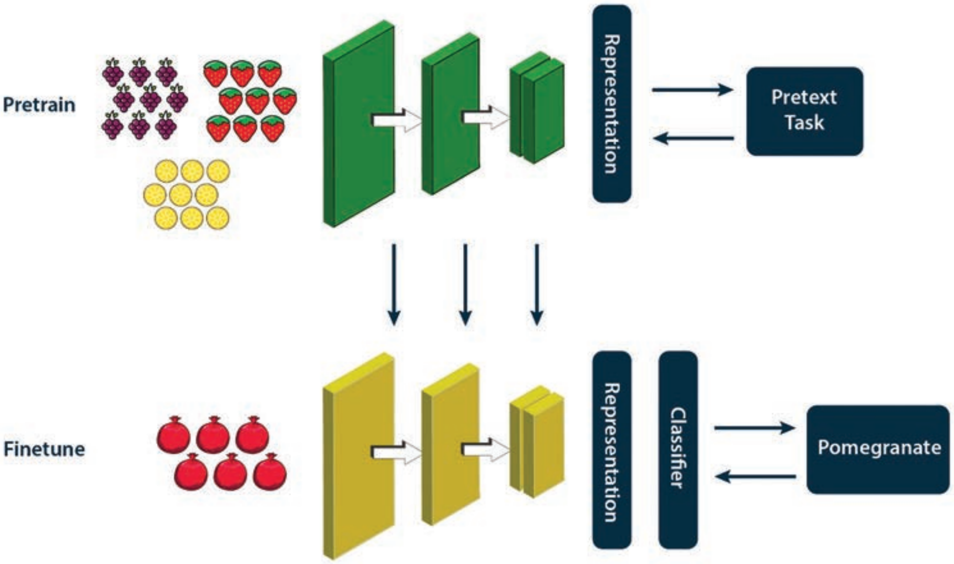

Fig. 10. Fine-tuning process in self-learning paradigm.

without being explicitly programmed for those tasks. This approach is often associated with USL, where the algorithm tries to identify patterns and relationships in data without prior labels or instructions, as shown in Fig. 10. Furthermore, the USL, feature discovery, and adaptivity are the most important aspects of the SEL approach (Wu and He, 2023). For example, within USL, the system trained from data without having any labeled or corrections. While with feature discovery, the ability to autonomously discover the representations needed for feature detection or classification from raw data. However, with the adaptivity, the systems adjust their based on upcoming data, repeatedly updating their weights or model of the world in general (Iqbal et al., 2023).

The current solutions via SEL methods are anomaly detection, recommendation systems, predictive maintenance in manufacturing, dynamic pricing models, autonomous robotics, and text-generation like chat-GPTs. However, such solutions need further research due to several challenges starts from identifying unusual patterns, biased issues for personalized recommendations, predicting are likely to fail or require maintenance, adjusting prices in real-time, to the operating in complex and unpredictable environments.

In another vain, SEL approaches are particularly valuable in environments where it is impossible or impractical to manually label all the possible scenarios or outcomes that a system might need to handle. They allow systems to adapt over time and improve their accuracy, making them highly effective in complex, real-world applications where new data continuously emerges.

III. CURRENT ML ALGORITHMS

Due to the importance of learning techniques, which are used widely in many areas, a huge amount of research has been done in this area. In this section, several works regarding supervised, unsupervised, and semi-supervised methods briefly are discussed.

The authors of the paper (Xin, et al., 2020) discussed the significant challenge of the social stream SSL classification technique called classification over drifting and evolving stream (CODES). One goal is to set the training group consisting of both structured and unstructured examples. The extreme learning machine (ELM) based on the SSL strategy can preserve the ELM input drawing area without output knowledge of emergent data in the social stream. CODES can achieve effective learning achievement above drifting and growing social streams while improving practical importance among the real-world social stream utilizations.

Pilot studies conducted by (Yuan and Marc, 2019), for this purpose, the authors contrast three separate visual-inertial odometry (VIO) methods based on learning: Supervised, semi-supervised, and unsupervised. VIO, that used pictures and inertial estimations to evaluate the movement, is supposed to be unique of the main tools for virtual fact and argument fact. The goal is to reach more accurate, robust, and efficient localization. The outcomes demonstrate the semi-supervised model better supervised methods as well as unsupervised ones.

An attempt to create a model that can be automatically built to recognize a species of iris have been done by (Ajay, et al., 2018), the authors used KNN classification SUL algorithms. Take advantage of the iris dataset, which contains 150 data samples in three groups, each containing 50 samples. The libraries used are Pandas, NumPy, Scikit-learn, and Matplotlib. The result shows the forecast for Class 0 (Setosa) and Calss 2 (Virginica) is one hundred percentage right, however, the forecast for Class 1 (Versicolor) is 4% inaccurate.

A model suggested for intrusion detection has been made by (Manjula and Balachandra, 2016). The authors used classification procedures, specifically, logistic regression, Gaussian naive Bayes, support vector machine, and random forest, those techniques are tested by a dataset, namely the NSL-KDD dataset. Code is done using a python programming language. Consequences display that the Random Forest Classifier outperforms supplementary approaches in assessing whether the records of the traffic are usual or a raid. It has an accuracy of 99%.

A technique was proposed to detect fake users by (BalaAnand, et al., 2019), the authors used the Graph-based SSL algorithm (EGSLA). The data are taken from Twitter. More precisely, the data set contains 2,915,147 tweets were recovered from 21,473 users through the duration from 12–2017 to 2–2018. The EGSLA technique is examined through the existing game hypothesis, support vector machine, KNN, and decision tree methods. The outcomes were visible that the suggested EGSLA procedure succeeds 90.3% precision in recognizing forgery (fake) users.

A procedure for identifying the distance among a score and a group pattern has been made by (Kristina and Miin-Shen, 2020), tried to establish an USL framework by using the k-means procedure, thus as that is independent of initializations externally variable determination and can likewise discover an optimum number of groups at the same time. The authors compared this technique with several other algorithms. The consequences indeed indicate the best feature of the recommended U-kmeans clustering procedure.

The textual documents have been proposed by (Aiman and Rosnafisah, 2017), the authors for this purpose an approach that used the KNN algorithm for the classification to construct an ML system in R software. The data were taken from two websites: (egov.kz and government.kz). Finally, the authors found out that the highest percentage of accuracy when the value of k ranges from one to fifty. The accuracy dropped sharply above the 50’s.

An approach was proposed to produce a price of the cars have been done by (Nitis, et al., 2018), for this intention utilized the regression techniques that are multiple linear, gradient boosted trees, and random forest. Records used during that analysis were taken from the German e-commerce website then data training compiled via with Python language. The dataset includes 304,133 records and 11 columns. The outcomes were then compared through mean absolute error (MAE) as a measure. Gradient boosted trees give the best attainment with MAE = 0.28, the second of the best is a random forest with MAE = 0.35, followed by multiple linear regression with MAE = 0.55 errors. Therefore, researchers assumed that gradient boosted trees can be advisable to build the price assessment form.

A process was recommended to categorize internet traffic detection done by (Mrudul, et al., 2019), the authors used KNN and naive Bayes classification techniques. The authors concentrate on six statistical variables of the fifty variables achievable in the UNSW NB dataset. The result illustrates that the KNN procedure gives a precision 85%, while the Naive Bayes process reached 54% of precision.

An effort to understand the shortcomings of the KNN technique was made by (Gongde, et al., 2003), the authors propose a new kind of KNN technique for classification. To validate the technique, tests were carried out on some publicly available datasets obtained from the UCI ML repository. The results indicate that the model based on KNN compares well with C5.0 algorithm and the KNN method. The KNN model significantly decreases the amount of data tuples in the final classification model with an average rate of 90.41% reduction.

In another work by (Fangming, Oayou and Xinying, 2010), the authors suggest a proposal to study a Mahalanobis distance with a minor quantity of well-known knowledge, by using a graph-based semi-supervised output broadcast technique to improve the classification knowledge that is given through the customer, and later uses a process of increased biased relevant component analysis to study a Mahalanobis distance purpose. Later, those procedures, the authors used Mahalanobis instead of Euclidean distance as a metric function to find the distance between points of the KNN classifier. For this purpose, take advantage of the UCI datasets. The result shows that technique able to be importantly increases the precision of the KNN classification methods.

Attempts to build a model that can be automatically constructed to recognize a data uncertainty have been done by (Nergz and Beitollahi, 2022), the authors used numerous experiential methods and ML procedures and the combination of radial basis function network with the particle-swarm

TABLE I
Recent Advances in Machine Learning Techniques (2010–2024)

Year	Authors	Technique (s) used	Key findings
2016	Manjula and Balachandra	LOR, Gaussian naive Bayes, SVM, RF	The random forest achieved highest accuracy for intrusion detection.
2017	Aiman and Rosnafisah	SUL (KNN)	High accuracy in classifying textual documents.
2018	Ajay et al.	SUL (KNN)	High accuracy in classifying iris species.
2018	Nitis et al.	MLR, gradient boosted trees, RF	Gradient boosted trees achieved the best performance for price prediction.
2019	Yuan and Marc	SUL, USL, SSL	Semi-supervised outperformed both supervised and unsupervised.
2019	BalaAnand et al.	SSL (EGSLA)	90.3% accuracy in detecting fake users on Twitter.
2019	Mrudul et al.	SUL (Naive Bayes, KNN)	KNN achieved higher precision than Naive Bayes.
2020	Xin et al.	SUL (CODES)	Improved learning performance on drifting social streams.
2020	Kristina and Miin-Shen	USL (K-means)	Improved clustering performance independent of initializations.
2022	Xin et al.	SSL	Comprehensive review of SSL techniques and their applications.
2022	Cao et al.	SSL	Introduces the open-world assumption in SSL, handling out-of-distribution data.
2022	Bromley et al.	SUL	Proposes MaskSup for improved semantic segmentation.
2022	Kaiming et al.	SSL (adversarial training)	Enhances model robustness by denoising features in adversarial settings.
2023	Smith et al.	SSL	Reduces confirmation bias in pseudo-labels, improves robustness.
2023	Jones et al.	SSL	Combines semantic and instance similarity for better performance.
2023	Lee et al.	SUL	Joint optimization for segmentation, depth estimation, and edge detection.
2023	Kim et al.	SSL	Enhances SSL with adversarial training for robust model performance.
2023	Patel et al.	USL	Proposes a new method for clustering high-dimensional data efficiently.
2024	Wang et al.	SUL	Enhances supervised models with transfer learning techniques.
2024	Zhao et al.	SSL	Addresses imbalance in datasets with a novel SSL approach.
2024	Gupta et al.	USL	Efficient real-time anomaly detection in streaming data.
2024	Li et al.	SSL	Applies graph-based SSL for better social network insights.
2024	Thompson et al.	SUL	New techniques for enhancing text classification accuracy.
2024	Rodriguez et al.	SSL	Combines multiple SSL methods for improved performance.
2024	Hernandez et al.	USL	Proposes an unsupervised approach for improving image quality.
2024	Nguyen et al.	SSL	Integrates multiple data modalities for better SSL performance.
2024	Tan et al.	SUL	Enhances supervised learning with active learning strategies.
2024	Chen et al.	USL	Uses reinforcement signals to guide unsupervised learning processes.
2024	Park et al.	SSL	Proposes a scalable SSL approach for large datasets.
2024	Roberts et al.	SUL	Improves recommendation systems with personalized models.
2024	Kaiming et al.	SSL (masked modeling)	Proposes an advanced masked modeling approach for SSL in vision tasks.
2022	Zhou, Huang and Fränti	RIL	Future of motion planning algorithms in robots
2021	Zhang et al.	RIL	Data privacy and adaptive learning capability, and their prospects in real-time monitoring, out-of-clinic diagnosis are challenged
2021	Perera and Kamalaruban	RIL	Reinforcement learning has a notable potential which has not been utilized
2023	Wu and He	SEL	Solve the problem of weak explanation of model
2023	Iqbal et al.	SEL	Careful tuning and experimentation are essential to determine the optimal combination of manual features

CODES: Classification over drifting and evolving stream, SUL: Supervised learning, USL: Unsupervised learning, SSL: Semi-supervised learning, RIF: Reinforcement learning, SEL: Self-learning

optimization algorithm to categorize data in the presence of uncertainty. The simulation specifically produced the following outcomes: (F- Measure, recall, precision, and accuracy) are (96%, 95%, 97%, and 97%). The following is an obvious indication that the suggested model outperforms conventional ML techniques in identifying ambiguous data. The suggested approach outperforms all ML-based approaches by an average of 4.4%. As well as the authors in another worked on classify uncertain data (Darbaz, Al-Barznji and Mohammed, 2024) used a combination ML based methods with DL techniques The outcomes of the suggested hybrid model depend on well-known evolution metrics F- Measure = 95%, recall = 94%, precision = 96%, as well as accuracy = 97%.

Table I summarizes and integrates recent research studies from 2016 to 2024 alongside older works, providing a comprehensive and up-to-date overview of significant advances in supervised, unsupervised, semi-supervised, and self-SUL techniques. Each entry highlights the innovative methods and key findings, reflecting the evolving landscape of ML research.

IV. Comparative Analysis

This section presents a comparative analysis of supervised, unsupervised, semi-supervised, and self-SUL techniques based on the recent advancements outlined in the literature review. The comparison considers various aspects such as data requirements, complexity, accuracy, interpretability, scalability, applications, and challenges.

A. Data Requirements

SUL

Requires large amounts of labeled data. Effective for tasks where annotated data is abundant, such as image classification and speech recognition.

USL

Works with unlabeled data, suitable for exploratory data analysis where the goal is to identify hidden patterns without predefined labels, like clustering and anomaly detection.

SSL

Utilizes both labeled and unlabeled data, making it ideal for situations where labeled data is scarce or expensive to obtain. It strikes a balance by leveraging the abundance of unlabeled data to improve learning accuracy.

RIF

RL differs significantly from other learning paradigms because it typically requires neither labeled data (as in SUL) nor solely unlabeled data (as in USL). Instead, RL operates through an agent interacting with an environment to learn policies based on rewards. This interaction generates the data (in the form of state, action, and reward tuples) that RL algorithms use to learn.

SEL

Generates supervisory signals from the data itself, reducing the need for labeled data. It is effective in domains like natural language processing and computer vision, where creating large labeled datasets is challenging.

B. Complexity

SUL

Generally moderate to high, depending on the algorithm used. Complex models like deep neural networks require significant computational resources and expertise.

USL

Typically low to moderate complexity. Algorithms like K-means clustering are relatively straightforward but can become complex with high-dimensional data.

SSL

High complexity due to the integration of both labeled and unlabeled data. Methods like adversarial training and graph-based approaches add to the complexity.

RIF

The complexity of RL can be quite high, primarily because the environment itself can be highly dynamic and the learning process is based on sequential decision-making.

SEL

Can range from moderate to high complexity. Techniques like masked modeling and contrastive learning involve sophisticated architectures and training strategies.

C. Accuracy

SUL

Generally high, especially when ample labeled data is available. Models can be fine-tuned to achieve state-of-the-art performance in specific tasks.

USL

Accuracy varies widely, often dependent on the nature of the data and the specific algorithm. Model evaluation can be challenging due to the lack of ground truth.

SSL

Often achieves higher accuracy than USL and can approach the accuracy of SUL, especially with well-designed algorithms that leverage the unlabeled data effectively.

RIF

Accuracy in RL is typically framed in terms of the optimality of the learned policy rather than traditional accuracy metrics. The goal is to maximize cumulative rewards, which may not always align with achieving high accuracy in predictions, like in SUL.

SEL

Shows promising accuracy, particularly in tasks where large-scale unlabeled data is available. The learned representations can be fine-tuned for specific downstream tasks, achieving competitive performance.

D. Interpretability

SUL

High for simple models (e.g., decision trees, linear regression) but lower for complex models like deep neural networks.

USL

Varies, often challenging due to the lack of labeled data. Techniques like clustering provide some interpretability by grouping similar data points.

SSL

Depends on the combination of techniques used. Graph-based methods offer some interpretability, but overall, the complexity can reduce interpretability.

RIF

Similar to complex models in supervised and self-SUL, RL models can struggle with interpretability, especially in high-dimensional spaces or when using deep neural networks as function approximators (Deep RIF).

SEL

Generally lower interpretability due to the complex nature of the tasks and models. However, certain techniques, like contrastive learning, provide some insights into the representations learned.

E. Scalability

SUL

Can be challenged with large datasets due to the need for extensive labeled data and computational resources.

USL

Generally scalable, as many algorithms can handle large datasets efficiently.

SSL

Scalability can be challenging due to the complexity of integrating labeled and unlabeled data. Techniques like scalable SSL aim to address this issue.

RIF

Scalability in RL can be a challenge due to the need for extensive interaction with the environment, which can be computationally expensive and slow, particularly in real-world scenarios.

SEL

Often highly scalable, as it can leverage vast amounts of unlabeled data. Techniques like masked modeling are designed to handle large-scale data efficiently.

F. Applications

SUL

Widely used in tasks like image and speech recognition, medical diagnosis, financial forecasting, and more.

USL

Applied in customer segmentation, topic modeling, anomaly detection, and exploration of data analysis.

SSL

Useful in natural language processing, bioinformatics, web content classification, and scenarios with limited labeled data.

RIF

RL is extensively applied in areas such as robotics (for complex control tasks), gaming (e.g., AI playing video games or board games like Go), autonomous vehicles (for dynamic decision-making tasks), and optimization problems in operations research.

SEL

Effective in natural language processing, computer vision, and other domains where generating labeled data is expensive or impractical.

G. Challenges

SUL

Overfitting, scalability, and the high cost of data labeling.

USL

Model evaluation, interpretability, and convergence issues.

SSL

Data integration, model complexity, and computational costs.

RIF

Some of the primary challenges in RL include the dependency on quality and diversity of the reward signal.

SEL

Complexity of model training, interpretability, and ensuring the quality of self-generated labels.

This comparative analysis highlights the unique strengths and challenges of each learning paradigm shown in Table II, providing insights into their applicability to various tasks and domains. Understanding these nuances helps researchers and practitioners select the most appropriate methods for their specific needs, driving innovation and performance improvements in ML applications.

V. DISCUSSIONS

The comparative analysis of SUL, USL, SSL, RIF, and SEL learning paradigms reveals several insights into their respective strengths, limitations, and applications. SUL remains a cornerstone of ML, particularly in domains where large amounts of labeled data are available. Its high accuracy and effectiveness in tasks such as image and speech recognition, medical diagnosis, and financial forecasting make it a preferred choice for many applications. However, reliance on extensive labeled datasets poses a significant challenge, both in terms of data collection costs and scalability. Additionally, while simpler models like decision trees offer high interpretability, more complex models such as deep neural networks can suffer from overfitting and reduced interpretability.

USL excels in exploratory data analysis, where the goal is to uncover hidden patterns and structures without predefined

TABLE II
COMPARISON OF LEARNING PARADIGMS: SUL, USL, SSL, RIF, AND SEL APPROACHES

Aspect	SUL	USL	SSL	RIF	SEL
Data requirements	Requires large amounts of labeled data	Works with unlabeled data	Utilizes both labeled and unlabeled data	Interact with to generate data through the agent's actions.	Generates supervisory signals from the data itself
Complexity	Moderate to high	Low to moderate	High	High	Moderate to high
Accuracy	Generally high	Varies widely	Often higher than unsupervised, lower than supervised	Can achieve high where clear metrics	Varies; can improve over time as more data is processed
Interpretability	High for simple models, low for complex models	Varies, often challenging	It depends on the combination of techniques used	Generally lower due to complex tasks and models	Moderate; as models evolve, tracking changes and understanding decisions
Scalability	Can be challenging with large datasets	Generally scalable	Can be challenging due to data integration	Varies depending on the complexity of the environment	Often highly scalable
Applications	Image and speech recognition, medical diagnosis, financial forecasting	Customer segmentation, topic modeling, anomaly detection	NLP, bioinformatics, web content classification	Gaming, autonomous vehicles, and robotics.	NLP taks, computer vision, tasks with vast unlabeled data
Challenges	Overfitting, scalability, high cost of data labeling	Model evaluation, interpretability, convergence issues	Data integration, model complexity, computational costs	Complexity of model training, high computational cost, defining appropriate rewards and penalties	Complexity of model training, interpretability

SUL: Supervised learning, USL: Unsupervised learning, SSL: Semi-supervised learning, RIF: Reinforcement learning, SEL: Self-learning labels. Techniques like clustering, dimensionality reduction, and anomaly detection are valuable in applications ranging from customer segmentation to topic modeling and fraud detection. The main advantage of an SUL is its ability to work with unlabeled data, making it scalable and versatile. However, the accuracy of unsupervised models can vary widely, and the lack of ground truth makes model evaluation and interpretability challenging.

SSL learning strikes a balance between SUL and USL approached by leveraging both known and unknown items. This approach is particularly useful in scenarios where the known item is scarce or expensive to obtain, such as in medical imaging or NLP tasks. The SSL algorithms often achieve higher accuracy than purely unsupervised methods and can approach the performance of supervised models when designed effectively. However, the complexity of integrating labeled and unlabeled data, along with the computational costs, poses significant challenges (Papers with Code) (Papers with Code).

In another vain, the RIF involves an agent interacting with an environment to generate data through actions, which makes it highly complex and dependent on designing effective reward systems. This learning type achieves high accuracy in environments with clear success metrics, such as games or simulations. However, it faces challenges in interpretability due to the complexity of tasks and models, and scalability can vary greatly with environmental and state space complexities. It is primarily applied in areas such as gaming, autonomous vehicles, robotics, and real-time decision-making. The major challenges include the complexity of training models, the computational demands, and the necessity of designing a reward system that effectively balances short- and long-term goals.

While the SEL utilizes existing knowledge to generate new insights, requiring a foundational dataset to begin learning and often improving accuracy over time as it processes more data and adapts to new inputs. The complexity of SEL systems can be moderate to high, depending on the mechanisms used for knowledge extraction and adaptation. While these systems are generally scalable within the learning algorithm's capabilities, they face interpretability challenges as models evolve and adapt. SEL is applied in self-correcting algorithms, dynamic decision-making systems, and continuous learning environments within AI systems. Key challenges include maintaining continuous learning without data drift, managing computational resources effectively, and adapting autonomously to evolving datasets without human oversight.

Several emerging trends are shaping the future of ML across these paradigms. Transfer learning, for instance, enhances supervised models by leveraging pre-trained models on related tasks, thus reducing the need for large labeled datasets. Adversarial training, particularly in semi-supervised and self-SUL, improves model robustness and generalization (Papers with Code). Additionally, scalable methods for large datasets and techniques that address data imbalance are becoming increasingly important as the volume and variety of data continue to grow (Papers with Code).

Ongoing research is focused on improving the explainability and fairness of ML models, ensuring that they are not only accurate but also transparent and unbiased. Privacy-preserving learning techniques, such as federated learning, are also gaining traction, enabling the use of sensitive data without compromising privacy. The integration of multiple data modalities in SSL and the development of more efficient training algorithms for self-SUL are promising areas for future exploration.

The review of learning paradigms underscores the unique advantages and challenges of each approach. By understanding these nuances, researchers and practitioners can better select and tailor methods to their specific needs, driving innovation and performance improvements in ML applications. The continuous evolution of these paradigms, driven by advancements in techniques and increasing data availability, holds significant potential for future breakthroughs in AI.

VI. Conclusion

In this study, a review of the ML approaches, including SUL, USL, SSL, RIF, and SEL, has been investigated within current applications. From the reviewed and discussed studies, the ML methods and techniques, accuracy differs depending on the properties (attributes) and the volume of the data sets amongst the training sets and testing sets. In the diverse world of ML, each method provides unique insights and solutions for specific problems. The SUL is highly structured, requiring large amounts of labeled data to train models that achieve high accuracy. This method excels in applications such as image and speech recognition, where precise outputs based on clear examples are essential. However, its reliance on extensive labeled datasets can lead to challenges such as overfitting and the high cost of data annotation. In contrast, USL thrives on unlabeled data, uncovering hidden patterns and relationships without predefined labels. This approach is particularly beneficial in scenarios like customer segmentation and anomaly detection, where the data may lack explicit instructions but still contains valuable insights. Challenges in USL include difficulties with model evaluation and interpretability of results, which can vary significantly based on the complexity of the data.

The SSL bridges the gap between supervised and USL by utilizing both labeled and unlabeled data. This method improves learning accuracy without the exhaustive need for labeled data, making it suitable for applications like natural language processing and bioinformatics, where obtaining comprehensive labeled datasets can be costly or impractical. The RIF and SEL reveal a spectrum from highly structured learning environments to adaptive, interactive systems. RIF learns from its environment through trial and error, offering solutions for real-time decision-making in complex scenarios. Meanwhile, SEL adapts and evolves autonomously, promising ongoing improvement across various applications.

Together, these learning methodologies highlight the versatility of ML. They offer a glimpse into a future where machines not only calculate and predict but also discover, adapt, and continually learn from their interactions, much like living beings. The unique strengths and challenges of each method emphasize the importance of selecting the right approach based on the specific requirements and constraints of the task.

References

Abdullah, A.A., Abdulla, S.H., Toufiq, D.M., Maghdid, H.S., Rashid, T.A., Farho, P.F., Sabr, S.S., Taher, A.H., Hamad, D.S., Veisi, H., and Asaad, A.T., 2024. *NER-RoBERTa: Fine-Tuning RoBERTa for Named Entity Recognition (NER) within Low-Resource Languages*. [arXiv Preprint].

Abdullah, A.A., Ahmed, A.M., Rashid, T., Veisi, H., Rassul, Y.H., Hassan, B., Fattah, P., Ali, S.A., and Shamsaldin, A.S., 2024. *Advanced Clustering Techniques for Speech Signal Enhancement: A Review and Metanalysis of Fuzzy c-Means, k-Means, and Kernel Fuzzy c-Means Methods*. [arXiv Preprint].

Adamu, J.A., 2019. Advanced stochastic optimization algorithm for deep learning artificial neural networks in banking and finance industries. *Risk and Financial Management*, 1(1), p. 8.

Aiman, M., and Rosnafisah, B.S., 2017. *Using KNN Algorithm for Classification of Textual Documents*. Malaysia, IEEE.

Ajay, S.S., Thirunavukkarasu, K., Prakhar, R., and Sachin, G., 2018. *Classification of IRIS Dataset Using Classification Based KNN Algorithm in Supervised Learning*. IEEE, United States.

Alboukadel, K., 2017. *Practical Guide to Cluster Analysis in R Unsupervised Machine Learning*. 1st ed. STHDA, Bad Vilbel.

BalaAnand, M., Karthikeyan, N., Karthik, S., Varatharajan, R., Manogaran, G., and Sivaparthipan, C.B., 2019. An enhanced graph-based semi-supervised learning algorithm to detect fake users on Twitter. *The Journal of Supercomputing*, 75, pp. 6085-6105.

Carlos, F., Flora, F., Miguel, G., Azevedo, O., Sousa, N., and Erlhagen, W., 2019. Gait Classification of Patients with Fabry's Disease Based on Normalized Gait Features Obtained using Multiple Regression Models. In: *IEEE International Conference on Bioinformatics and Biomedicine (BIBM)*.

Changde, D., Changying, D., and Huiguang, H., 2021. Multimodal deep generative adversarial models for scalable doubly semi-supervised learning. *Information Fusion*, 68, pp. 118-130.

Christine, W.C., Tontiwachwuthikul, P., Zeng, F., and Liang, Z.Z., 2020. Recent progress and new developments of applications of artificialintelligence (AI), knowledge-based systems (KBS), and machine learning (ML) in the petroleum industry. *Petroleum*, 6(4), pp. 319-320.

Chunrong, W., Jia, L., Isokawa, T., Jun, Y., and Yunni, X., 2019. Efficient Clustering Method Based on Density Peaks with Symmetric Neighborhood Relationship. In: *The International Exchange Program of National Institute of Information and Communications (NICT)*.

Darbaz, M.H., Al-Barznji, K., and Mohammed, N.S., 2024. Accurate uncertainty dataset classification using hybrid deep learning models. *International Journal of Advanced Processing Systems*, 10, pp. 15-30.

Deepti, S., and Dilip, S.S., 2018. *Prediction of Diabetes using Classification Algorithms*. IEEE and Elsevier, India.

Fangming, G., Oayou, L., and Xinying, W., 2010. *Semi-Supervised Weighted Distance Metric Learning for kNN Classification*. IEEE Xplore, Changchun.

Gao, H., Shiji, S., Jatinder, N.D.G., and Cheng, W., 2014. Semi-supervised and unsupervised extreme learning machines. *IEEE Transactions on Cybernetics*, 44(12), pp. 2405-2417.

Gongde, G., Wang, H., Bell, D., Bi, Y., and Greer, K., 2003. *KNN Model-Based Approach in Classification*. Northern Ireland, UK, Springer.

Guo, P., Lijuan, W., Jun, S., and Fang, D., 2021. A hybrid unsupervised clustering-based anomaly detection method. *Tsinghua Science and Technology*, 26(2), pp. 146-153.

Haitao, G., and Zhenhua, L., 2018. *Safe Semi-Supervised Learning from Risky Labeled and Unlabeled Samples*. IEEE Xplore, Japan.

Hemant, K.G., and Rishabh, C., 2017. *Comprehensive Review on Supervised Machine*. IEEE, United States.

Hooman, H.R., Tran, N.K., Betts, E.V., Howell, L.P., and Green, R., 2019. Artificial intelligence and machine learning in pathology: The present landscape of supervised methods. *Academic Pathology*, 6, p. 2374289519873088.

Hui, Y., Ping, Y., and Duo, L., 2019. *Study on Deep Unsupervised Learning Optimization Algorithm Based on Cloud Computing*. IEEE, United States.

Iqbal, S., Qureshi, A.N., Aurangzeb, K., Alhussein, M., Haider, S.I., and Rida, I., 2023. AMIAC: Adaptive medical image analyzes and classification, a robust self-learning framework. Neural Computing and Applications, 1(1), pp. 1-29.

Jwan, K., Abas, A.A., and Tarik, R., 2024. *Exploring Public Service and Prosocial Motivation Using Machine Learning*. [Authorea Preprints].

Kristina, P.S., and Miin-Shen, Y., 2020. *Unsupervised K-Means Clustering Algorithm*. Vol. 8. IEEE Xplore, Japan.

Kushal, R.D., 2020. *Analysing the Role of Supervised and Unsupervised Machine Learning in IoT*. IEEE, United States.

Manjula, C.B., and Balachandra, M., 2016. *Performance Evaluation of Supervised Machine Learning Algorithms for Intrusion Detection*. India, ScienceDirect.

Mrudul, D., Ritu, S., Saniya, S., and Krutika, M., 2019. *Internet Traffic Detection using Naïve Bayes and K-Nearest Neighbors (KNN) Algorithm*. Indea, IEEE.

Nergz, S.M., and Beitollahi, H., 2022. Accurate classification in uncertainty dataset using particle swarm optimization-trained radial basis function. *NeuroQuantology*, 20(6), pp. 166-179.

Nitis, M., Prajak, C., Thongchai, K., Suwat, R., Sabir, B., and Pitchayakit, B., 2018. *Prediction of Prices for Used Car by Using Regression Models*. IEEE Xplore, Bangkok, Thailand.

Perera, A.T.D., and Kamalaruban, P., 2021. Applications of reinforcement learning in energy systems. *Renewable and Sustainable Energy Reviews*, 17(1), p. 110618.

Rui, Z., Feiping, N., and Xuelong, L., 2017. *Semi-Supervised Classification Via Both Label and Side Information*. IEEE, United States.

Sarfaraz, H., Kandel, P., Bolan, C.W., Wallace, M.B., and Bagci, U., 2019. Lung and pancreatic tumor characterization in the deep learning era: Novel supervised and unsupervised learning approaches. *IEEE Transactions on Medical Imaging*, 38(8), pp. 1777-1787.

Sabr, S.S., 2025. A Comprehensive Part-of-Speech Tagging to Standardize Central-Kurdish Language: A Research Guide for Kurdish Natural Language Processing Tasks. s.l.: arXiv.

Sung-Jin, K., Chan-Ho, K., Sang-Yong, J., and Yong-Jae, K., 2016. *Shape Optimization of a Hybrid Magnetic Torque Converter Using the Multiple Linear Regression Analysis*. IEEE, United States.

Upasana, 2019. *Al Zone*. Available from: https://dzone.com/articles/introduction-to-classification-algorithms [Last accessed on 2025 Oct 8].

Weihao, H., Di, S., and Theo, B., 2020. Guest editorial: Applications of artificial intelligence in modern power systems: Challenges and solutions. *Journal of Modern Power Systems and Clean Energy*, 8(6), pp. 1-2.

Wu, B., and He, S., 2023. Self-learning and explainable deep learning network toward the security of artificial intelligence of things. *The Journal of Supercomputing*, 79(4), pp. 4436-4467.

Xin, B., Chao, Z., Donghang, L., Yongjiao, S., and Yuliang, M., 2020. Efficient incremental semi-supervised classification over drifting and evolving social streams. *IEEE Access*, 8, p. 1.

Yongjun, Z., and Siyu, Y., 2020. *Semi-Supervised Active Learning Image Classification method Based on Tri-Training Algorithm*. IEEE, United States.

Yuan, T., and Marc, C., 2019. A *Case Study on Visual-Inertial Odometry using Supervised, Semi-Supervised and Unsupervised Learning Methods*. IEEE, United States.

Zhang, K., Wang, J., Liu, T., Luo, Y., Loh, X.J., and Chen, X., 2021. Machine learning-reinforced noninvasive biosensors for healthcare. *Advanced Healthcare Materials*, 10(17), p. 2100734.

Zhou, C., Huang, B., and Fränti, P., 2022. A review of motion planning algorithms for intelligent robots. *Journal of Intelligent Manufacturing*, 33(2), pp. 387-424.

Mechanical and Microstructure Characteristic of Oil-based Drilling Cuttings as Mineral Powder Substitute in Hot Mix Asphalt Mixture

Balen Z. Abdulsamad[1†], Ameen A. Muhialdin[2], Tolaz S. Hawez[2] and Rahel K. Ibrahim[2]

[1]Department of Geotechnical Engineering, Faculty of Engineering, Koya University,
Koya KOY45, Kurdistan Region – F.R., Iraq

[2]Department of Civil Engineering, Faculty of Engineering, Koya University,
Koya KOY45, Kurdistan Region – F.R., Iraq

***Abstract*—Beyond the intensive worldwide oil wells drilling activities for seeking energy, the amount of oil-based drilling cuttings (OBDC) increased significantly, OBDC defined as a wasted drilling mud which is used in the drilling operation of oil wells. The OBDC falls under the category of hazardous waste that contains heavy metals and radioactive elements. In this study, OBDC was used as a substitute of mineral powder in hot mix asphalt. Various doses of OBDC (0%, 25%, 50%, 75%, and 100% by weight) were employed to replace the mineral powder. Marshall specimens were prepared to assess the physical characteristics and examine the microstructure. In results, by employing OBDC to 100%, The Marshall stability decreased from 12.1 kN to 9.22 kN, and flow value decreased from 3.96 mm to 3.3 mm compared to control specimen (0% of OBDC) due to the presence of uncoated and agglomeration of large amount of OBDC particle in bitumen constituent as examined by scanning electron microscope. Air voids increase from 3.9% to 4.26% and voids in mineral aggregates increase from 14.63% to 15.20% when mineral powder replaced by OBDC filler from 0% to 100%, respectively, due to the difference between the specific gravity of OBDC and mineral powder, in which higher percentage of OBDC leads to increase the porosity of the specimen. Utilizing 100% of OBDC instead of the mineral powder is compromised because the result falls within the standard ranges.**

***Index Terms*—Hot mix asphalt, Marshall stability, Mineral powder, Oil-based drilling cuttings, Scanning electron microscope.**

I. Introduction

Oil shale and gas exploration leads to drilling millions of oil fields around the globe, the drilling process produces a large quantity of solid wastes, which is known as oil-based drilling cuttings (OBDC) (Hu, et al., 2022). With increasing the demands on oil-based products in the world, the amount of OBDC increased significantly, approximately the volume of OBDC reaches nearly 130–560 m^3 per one well (Siddique, et al., 2017; Wang, et al., 2024). Oil well drilling operation requires many types of drilling muds to ease the drilling operation; the drilling mud helps to extract the rock cuttings from the subsurface depth to the surface to proceed the drilling operation into the deeper strata. The rock cuttings come to the surface with the drilling mud, and then the drilling mud separates from the rock cuttings to be reused in the drilling operation, the separation cycle continues until the mud is no longer suitable for reusing. The drilling mud after many cycles of separation can be considered as the OBDC, which is collected at the mud sump (Hussein and Ibrahim, 2023). OBDC filler falls under the category of hazardous material which will pose the severe damage to environment, the presence of heavy metals and radioactive elements (e.g., polycyclic aromatic hydrocarbons [PAHs]) and benzene series in OBDC, increases the possibility of soil and water pollution (Xie, et al., 2021). Following the primary treatment of OBDC at the rig site, a landfill method conducted as a secondary treatment in which the drilling cuttings buried underground but leaching the PAHs in OBDC resulting the unmanaged soil and water pollution include the physical, chemical, and biological pollution which categorized as a secondary pollution (Wang, et al., 2017; Huang, et al., 2018).

Besides the improper landfilling of the OBDC, which cause water and soil pollutions, OBDC can be used as a construction material to decrease its effect on the environment, eliminate the disposal cost, and improve the particular characteristic of the target material. According to the researches, the OBDC can be used in cement production, brick production, sandcrete blocks, and concrete production by replacing the fine aggregate in different percentages (Bernardo, et al., 2007; Ikotun, et al., 2019; Mostavi, Asadi and Ugochukwu, 2015; Foroutan, et al., 2018; Mohammed and Cheeseman, 2011). In this regard, the OBDC can be blended with hot mix asphalt (HMA), HMA is a mixture of asphalt concrete

ARO-The Scientific Journal of Koya University
Vol. XIII, No. 1 (2025), Article ID: ARO.12045. 7 pages
DOI: 10.14500/aro.12045
Received: 09 February 2025; Accepted: 11 May 2025
Regular research paper; Published: 22 May 2025
†Corresponding author's e-mail: balen.zrar@koyauniversity.org

which is widely used in road pavements in which the material mixed at 160°C–170°C (Ferrotti, et al., 2024). The most important composition in the HMA mixture is a stone dust filler (Natural mineral powder). Basically, stone dust filler is used to strengthen the asphalt concrete in terms of higher stability, moisture susceptibility, higher stiffness, and better affinity (Kumlai, Jitsangiam and Nikraz, 2022). Stone dust fillers produced from crushing the mountain stones (e.g., Marble Stone, Limestone, Dolomite, Granite, and Andesite) to a particle smaller than 0.075 mm by size, produced stone dust fillers from mountain stones falls under the category of destruction the natural resources, and continuously using these material leads to drastic decrease of these natural resources (Khan, et al., 2023; Gedik, Selcuk and Lav, 2021). OBDC can be used as a substitute of stone dust filler in HMA preparation; regarding to this, only few researches have been carried out on using OBDC as a replacement of stone dust filler in HMA mix, and many of them only concentrated on the mechanical characteristic of the specimen without investigating the specimen microstructure. Khodadadi, et al. (2020) used washed and unwashed OBDC in preparation of the HMA mixture as the replacement of fine aggregate. They only focusing on the mechanical properties of the specimens, such as the Marshall stability, indirect tensile strength, dynamic creep test, and resilient modulus. According to their result, the Marshall stability, resilient modulus, and indirect tensile strength gradually increased by using washed OBDC, which makes the OBDC as additive more feasible to use as a substitute of stone dust filler. At the same time, the unwashed OBDC has a reverse effect on the mechanical characteristic of the mixture compare to the washed OBDC.

In this study, the OBDC used as a partial and complete replacement of stone dust filler (Natural mineral powder) in preparing the HMA for pavement binder course, and Marshall stability, flow, air voids (VA), voids in mineral aggregates (VMA), and microstructure were investigated. The results of this study are applicable to determine the optimum replacement percentage of OBDC in which the range of the mechanical characteristic falls within the standard range. Besides the evaluation of mechanical characteristic, the microstructure investigation by scanning electron microscopy (SEM) helps to understand the integration between the OBDC and bituminous material, which directly effect on the mechanical characteristics of the pavement material.

TABLE I
STANDARD SPECIFICATION OF HMA MIXTURE FOR BINDER COURSE LAYER (ASPHALT INSTITUTE, 1979)

Properties	Binder course Type II
Stability, kN	7 (Min)
Flow, mm	2–4
Air Voids (VA), %	3–5
Voids in mineral aggregate (VMA), %	13 (Min)

TABLE II
CHEMICAL COMPOSITION OF OIL-BASED DRILLING CUTTINGS

Chemical compositions	Mass percentage, %
BaO	30.5
SO_3	18.1
SiO_2	15.4
TiO_2	9.54
CaO	7.19
Al_2O_3	3.26
Fe_2O_3	2.83
MgO	2.74
ZrO_2	2.48
V_2O_5	1.98
Cl	1.22
K_2O	1.2
Other	3.56

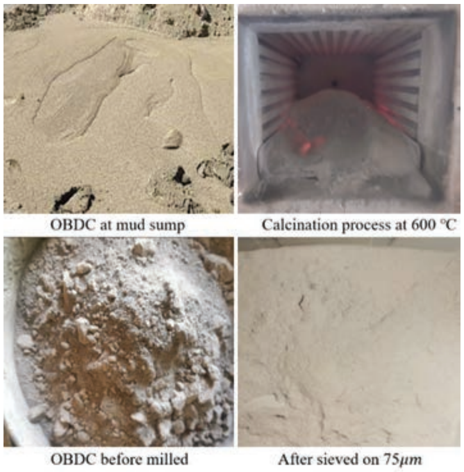

Fig. 1. Steps of preparing the oil-based drilling cuttings powder.

II. MATERIALS AND METHODS

A. Standards and Specifications

The standard ranges used to compare the test results adopted from a manual No.2 (MS-2) of Mix Design Methods for Asphalt Concrete and Other Hot-Mix Types by Asphalt Institute in 1979, as shown in Table I.

B. OBDC Powder

The OBDC was collected from the mud sump at the rig site and air-dried. After prepared air-dried OBDC, it's burned in a furnace at 600°C for 2 h to calcinate, which also served to eliminate organic materials. After calcination, the OBDC was milled using a Los Ageless machine and sieved through a 200 μm screen to produce an OBDC powder, preparation steps shown in Fig. 1, and the chemical composition tabulated in Table II.

C. Mineral Powder

The mineral powder is a by-product of crushing limestone in the aggregate production plant. A major portion of the mineral powder passes through sieve No.200, and the particle size distribution of the mineral powder is shown in Table III.

D. Aggregate

The HMA mixture which used in this research designed for a binder course layer, the nominal maximum aggregate

TABLE III
Particle Size Distribution of Mineral Powder

Sieve size		Passing (%)	Standard range	Test standard
Inch	mm		%	
No. 30	0.6	100.0	100	
No. 50	0.30	98.22	95–100	ASTM D546
N0.200	0.075	81.04	70–100	

TABLE IV
Blending Material for Binder Course According to Marshall Mix Design

Sieve size		Replacement percentage of OBDC				
Inch	mm	0%	25%	50%	75%	100%
		Mass of each size fraction, g				
1	25	0	0	0	0	0
^3/4	19	95.2	95.2	95.2	95.2	95.2
^1/2	12.5	84.3	84.3	84.3	84.3	84.3
^3/8	9.5	60	60	60	60	60
No. 4	4.75	312.9	312.9	312.9	312.9	312.9
No. 8	2.36	189.9	189.9	189.9	189.9	189.9
No. 50	0.3	246.8	246.8	246.8	246.8	246.8
No. 200	0.075	84.2	84.2	84.2	84.2	84.2
Natural filler (within the aggregate)		7.59	7.59	7.59	7.59	7.59
Mineral powder		69	51.7	34.5	17.3	0
OBDC filler		0	17. 3	34.5	51.7	69
Bitumen binder, %		5.1	5.1	5.1	5.1	5.1
Bitumen binder mass, g		61.8	61.8	61.8	61.8	61.8
Total aggregate mass for making one Marshall mold, g		1150	1150	1150	1150	1150

OBDC: Oil-based drilling cuttings

TABLE V
Physical Characteristics of the Bitumen Binder

No.	Test details	ASTM designation	Results	Standard range
1	Penetration, 25°C, 100 g, 5 s	ASTM D5-05a	44	40/50
2	Softening Point (R&B)	ASTM D36-06	51.1°C	---
3	Flash and fire Point	ASTM D92-05a	292°C	>232°C
4	Ductility at 25°C, 5 cm/min	ASTM D113-99	>150 cm	>100 cm
5	Viscosity	ASTM D2170	530 cP	>400 cP
6	Specific gravity	ASTM D70-03	1.03	---
7	Solubility	ASTM D2042	99.8%	>99%
8	Loss of heating	ASTM D1754	0.08%	0.2 max
9	Retain penetration	ASTM D2872	65%	>55%
10	Retain ductility	ASTM D2872	145 cm	>25 cm

TABLE VI
Specific Gravity and Combined Volume of Mineral Powder and OBDC Filler

Specific gravity of mineral powder	2.725
Specific gravity of OBDC filler	3.552
Mass of mineral powder according to the mix design	69 g

	Replacement percentage of OBDC				
	0%	25%	50%	75%	100%
Mass of mineral powder, g	69	51.7	34.5	17.3	0
Mass of OBDC filler, g	0	17. 3	34.5	51.7	69
Volume of mineral powder, cc	25.3	18.9	12.6	6.3	0
Volume of OBDC filler, cc	0	4.8	9.7	14.6	19.4
Combined mass of mineral powder and OBDC filler, g	69	69	69	69	69
Combined volume of mineral powder and OBDC filler, cc	25.3	23.7	22.3	20.9	19.4

OBDC: Oil-based drilling cuttings

size is 19.0 mm, the aggregate crushed and having sharp edges in different angles as per standard requirement, four different size fractions (25–12.5 mm, 12.5–4.75 mm, 4.75–0.075 mm, and <0.075 mm) blended together in accordance with Marshall mix design as shown in Table IV.

E. Bitumen Binder

Penetration grade bitumen 40/50 was used for this study, and passed through a series of laboratory testing programs in accordance with the ASTM standard, the test results compared with standard ranges shown in Table V to check the physical properties of the bitumen binder.

F. Job Mix Formula (JMF)

A JMF has been formulated based on the Marshall method shown in Table IV, the proportions are controlled by mass in accordance with the physical properties of materials, such as aggregates (coarse and fine aggregate), bitumen binders, mineral powder, and OBDC filler as outlined in Table IV. The OBDC filler has been incorporated as a partial replacement for the mineral powder across various percentages by mass: 0%, 25%, 50%, 75%, and 100%. Each replacement percentage was represented by three Marshall specimens, 4 inches (101.2 mm) in diameter, prepared in accordance with ASTM D6926. A series of laboratory testing programs was conducted to assess the strength parameters and other physical attributes of the specimen. The Marshall test was performed according to ASTM D6927 to assess the strength parameters (e.g., stability and flow) and physical properties of the specimens (e.g., VMA and VA). The results were compared against the standard ranges specified by the Asphalt Institute as tabulated in Table I. In addition, the microstructure was examined by using SEM alongside the evaluation of strength parameters and physical properties of the specimens.

III. Results and Discussion

A. Effect of OBDC Filler on VA and VMA

VMA represent the volume of void spaces between aggregate particles in a compacted bituminous mixture, encompassing both the spaces filled with bitumen and air. As a key parameter in asphalt mix design, VMA significantly influences the mixture's durability, stability, and resistance to deformation. Furthermore, VA are the small pockets of air trapped within a compacted bituminous mixture (Asphalt Institute, 1979; Roberts, 1991). In this study, mineral powder substituted by OBDC filler partially and completely, the properties of such a combination varied in some aspects. The particle size of both mineral powder and OBDC filler are very similar in size which pass through the sieve No.200, but the specific gravity of OBDC filler

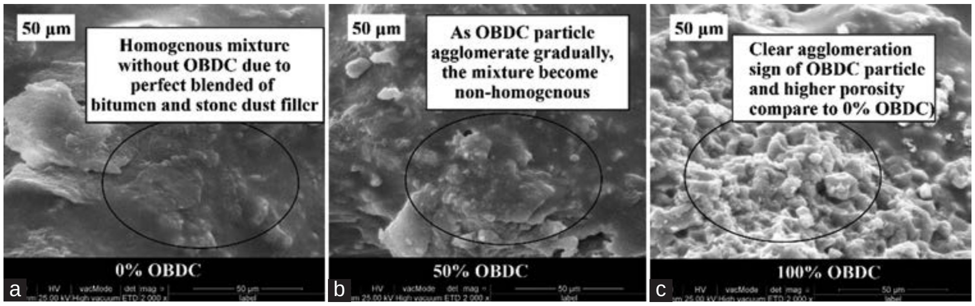

Fig. 2. (a-c) Microstructure 50 µm at different percentages of oil-based drilling cuttings.

is higher than the specific gravity of mineral powder; for that reason, the total volume of solid particles of OBDC filler with the same mass against the mineral powder is lower as shown in Table VI. By increasing the replacement percentage of OBDC filler, the combined volume of mineral powder and OBDC filler decrease compare to the control specimen due to the difference in specific gravity of both combinations.

According to the analysis shown in Table VI, the total volume of solid particles of filler material (combination of mineral powder and OBDC) decreased by 5.9 cm^3 and thus create more voids compared to control specimen (0% of OBDC) when 100% of mineral powder replaced by OBDC filler (100% of OBDC), this is mean that the volume of voids between the total aggregate mix at (100% of OBDC) increased by 5.9 cm^3 compare to control specimen (0% of OBDC). This finding also revealed by SEM images, in Fig. 2c shows the higher porosity at (100% of OBDC) compare to Fig. 2a (0% OBDC), it’s clear that those voids cannot be filled with the bitumen binder as the mass of bitumen binder is fixed between all replacement percentage of OBDC as shown in Table IV.

In results, from 0% to 100% of OBDC, the VA increase from 3.9% to 4.26% as shown in Fig. 3, and VMA increase from 14.63% to 15.20% as shown in Fig. 4. Moreover, replacing 100% of mineral powder by OBDC filler, the VA and VMA falls within the standard limit as shown in Table I.

B. Effect of OBDC Filler on Marshall Stability and Flow

Marshall stability is defined as the maximum load an asphalt specimen can endure before failing in the Marshall test, a widely used method to evaluate the strength and performance of asphalt mixtures, also Marshall flow is the measure of an asphalt pavement’s ability to resist deformation and retain its structural integrity under repeated loads. It is expressed as the amount of deformation (in millimeters) that an asphalt sample experiences when subjected to a standard load during the Marshall test, which evaluates the mixture’s stability and overall performance (Cui, et al., 2023; Azadgoleh, et al., 2022; Roberts, 1991). The Stability and flow for the Marshall samples decreased by increasing the percentages of OBDC filler, as shown in Figs. 5 and 6, respectively. The Marshall stability decreased from 12.1 kN to 9.22 kN, and the flow value decreased from 3.96 mm to 3.3 mm when mineral powder replaced by OBDC filler from 0% to 100%, respectively.

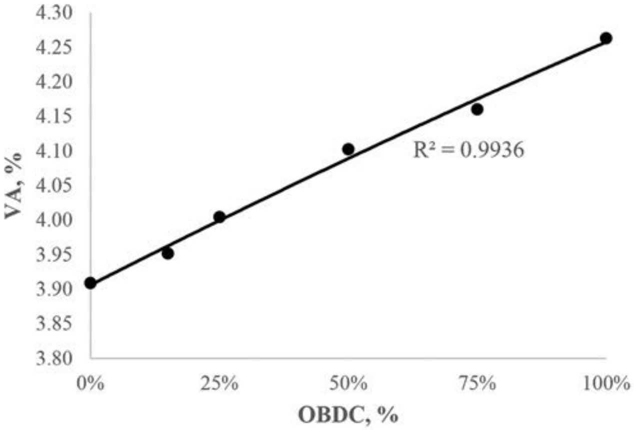

Fig. 3. Effect of different replacement percentage of oil-based drilling cuttings on air voids.

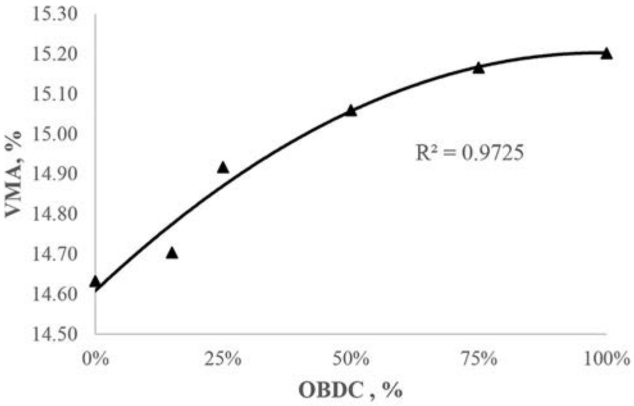

Fig. 4. Effect of different replacement percentages of oil-based drilling cuttings on voids in mineral aggregate.

Microstructure analysis revealed the significant uncoated and agglomerated of OBDC filler within the bitumen constituent, as shown in Figs. 2 and 7. This phenomenon can clearly explain the reduction in Marshall stability and flow value attributed to the significant presence of uncoated and agglomerated filler material in the microstructure. Besides the agglomerating and uncoating the OBDC filler within the bitumen constituent, the difference between specific gravity of mineral powder and OBDC filler makes the VMA and VA to be increased as the mixture designed based on weight, and when the porosity of the samples increases, the load carrying capacity which is directly related to Marshall stability will decreased. Despite the slight decrease of stability and flow at 100% of OBDC compared to the control specimen (0% of OBDC), the results fall within the standard range as shown in Table I.

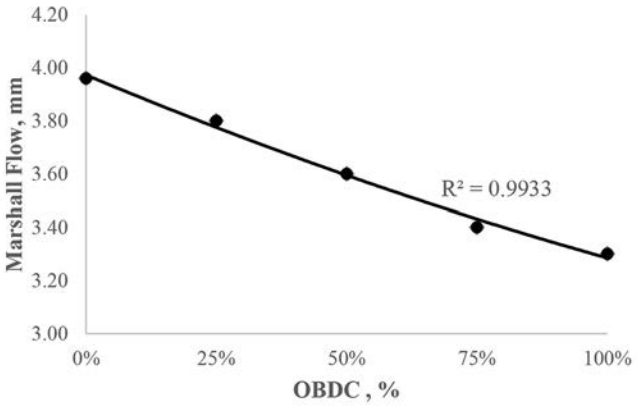

Fig. 5. Effect of different replacement percentages of oil-based drilling cuttings on flow.

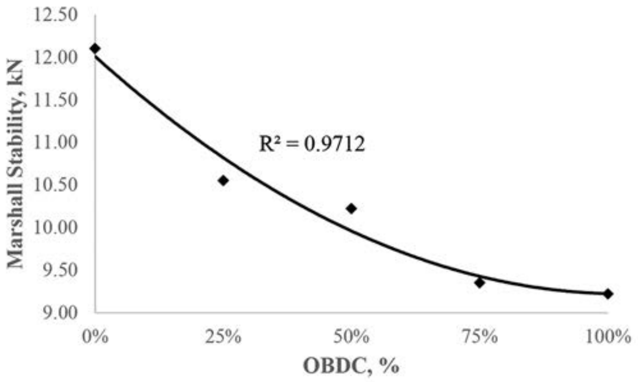

Fig. 6. Effect of different replacement percentages of oil-based drilling cuttings on Marshall stability.

The outcomes of stability and flow attained in this research closely align with findings from analogous studies on OBDC in HMA mixtures (Khodadadi, et al., 2020; Cui, et al., 2023). Despite substantial variations in methodology, material properties, OBDC fineness, chemical composition of OBDC, and mix proportions, the utilization of OBDC in HMA mixtures generally results in a slight decrease in stability and flow.

C. Microstructure and Macrostructure Investigation by SEM

The microstructural analysis at 100 μm, as shown in Fig. 7 illustrates a notable disparity between samples with varying percentages of OBDC filler. At 0% OBDC filler replacement (Fig. 7a), where mineral powder constitutes 100%, a homogeneous blend of bitumen and mineral powder is evident, depicted by a consistent dark brown coloration. In contrast, at 100% OBDC filler replacement (Fig. 7f) with 0% mineral powder, a discernible agglomeration of OBDC is observed, alongside a large amount of uncoated OBDC filler, the mixture of bitumen and OBDC filler appears non-homogeneous, characterized by a lighter brown hue. Furthermore, the SEM investigation confirms that the ratio of uncoated filler increased with increasing the replacement percentage of OBDC.

As shown in Fig. 2, when the samples were further focused from 100 μm to 50 μm and mineral powder was completely replaced with 100% OBDC, a significant agglomeration of OBDC particles was observed despite the OBDC particles being uncoated. Practically, this indicates that the bitumen film is missing in some areas where the agglomeration occurred. Consequently, the unbound aggregated particles reduce the stability value. Besides the unbound aggregate particle in the agglomeration zone, the porosity of the sample with higher dosage of OBDC is higher than those samples with lower or without OBDC as shown in Fig. 2c and 2a, this finding reflect the cause of increasing VMA and VA as described in section

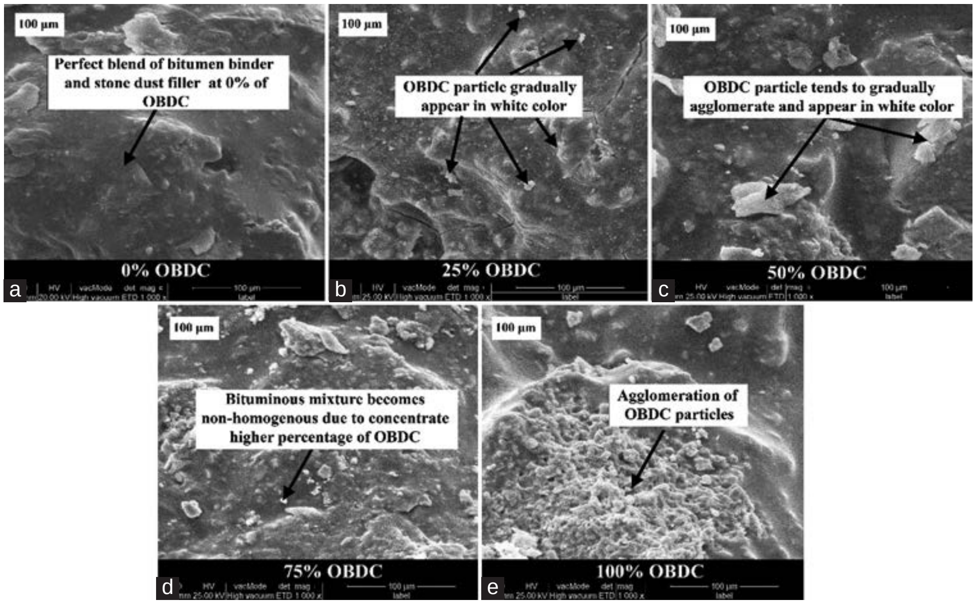

Fig. 7. (a-e) Microstructure 100 μm at different percentage of oil-based drilling cuttings.

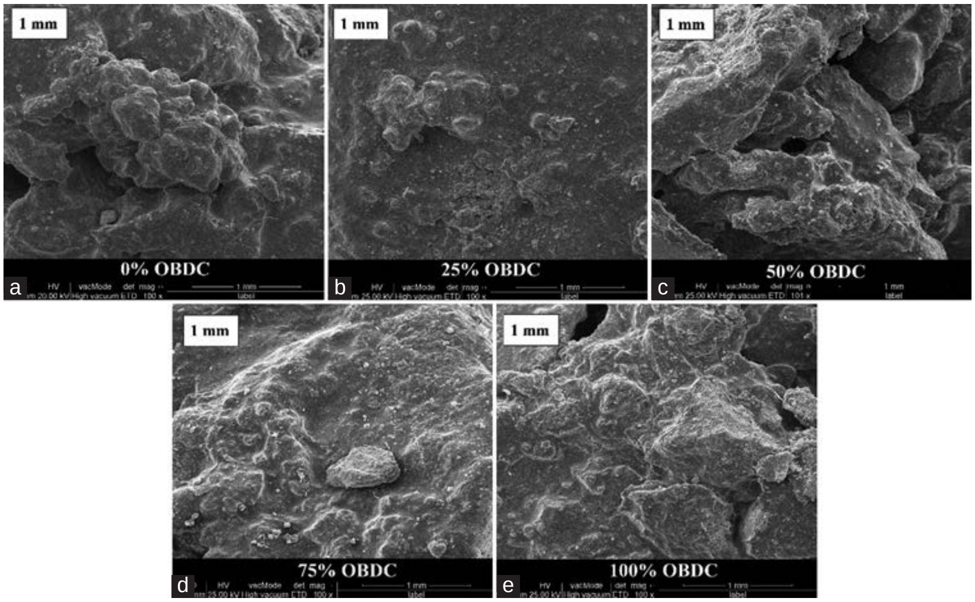

Fig. 8. (a-e) Macrostructure 1-mm at different percentage of oil-based drilling cuttings.

(3.1) and numerically proved in Table VI based on difference in specific gravity of OBDC and mineral powder.

The homogenous constituent of bitumen binder and filler material is important because the filler is a key material to strengthen the bitumen binder (Kumlai, Jitsangiam and Nikraz, 2022), any significant agglomerated and uncoated filler particle as revealed by microstructure investigation will make the bitumen mixture vulnerable to fail and deform under the particular loads which results to obtain lower Marshall stability and flow.

SEM images show that at the macrostructural level (1 mm), there is no significant difference between samples with varying OBDC replacement percentages. The samples appear similar in color and heterogeneity, as shown in Fig. 8. This suggests that at the macrostructure level, samples with 100% OBDC resemble those without OBDC, as they are visually indistinguishable. However, when zooming into the microstructure (e.g., at 100 μm and 50 μm), the SEM images reveal clear agglomeration of OBDC particles and a non-homogeneous bitumen mix, as seen in Figs. 2 and 7. This agglomeration negatively impacts the OBDC's ability to improve flow and Marshall stability, as shown in Figs. 5 and 6, respectively.

IV. Conclusions

This research focuses on the suitability of OBDC as a substitute of mineral powder in HMA mix toward more sustainability in terms of cost and environmental concerns, the following conclusion can be drawn:

- Marshall stability and Marshall flow slightly decrease when 100% of mineral powder is replaced by OBDC filler; the result at the minimum level falls within the standard range.
- VMA and VA increase when 100% of mineral powder is replaced by OBDC filler; the result at the minimum level falls within the standard range.
- The SEM image at the level of microstructural (e.g.,100 μm, 50 μm) shows a notable disparity between samples with varying percentages of OBDC filler. When the mineral powder constitutes 100% (0% of OBDC), a homogeneous blend of bitumen and mineral powder is evident. In contrast, when the OBDC constitutes 100% (0% mineral powder), a discernible agglomeration of OBDC is observed, alongside a large amount of uncoated OBDC filler, the mixture of bitumen and OBDC filler appears non-homogeneous. This evidence indicates that OBDC filler does not integrate as effectively with the bitumen material compared to mineral powder, and also resembles the reduction of Marshall stability and flow when 100% of OBDC is utilized.
- The SEM image at the macrostructure level (e.g., 1 mm) shows no significant difference between samples with varying OBDC replacement percentages. The samples appear similar in color and heterogeneity, with those containing 100% OBDC being visually indistinguishable from those without OBDC.
- The microstructure investigation shows that the utilization OBDC by 100% leads to increase the porosity, this evidence proved mathematically as the specific gravity of OBDC is larger than the specific gravity of mineral powder, the total volume of solid particles of OBDC with the same mass is lower than the mineral powder in the mixture as the JMF is designed based on mass not volume. For that reason, the VMA increases, and thus the VA due to decreases, the total volume of solid particles of OBDC at each higher dosage of OBDC compared to the previous dosage of OBDC. When the volume of solid particles decreases, the porosity (Volume of voids) will increase; this phenomenon is well defined by the SEM images at the microstructure level. Besides the effect of porosity on VMA and VA, the Marshall stability and flow are also affected in a negative side.
- OBDC filler proves to be a viable alternative to mineral powder, as indicated by stability, flow, VA, and VMA values

falling within the standard ranges as shown in Table I. This outcome represents a satisfactory compromise, enabling the complete replacement of mineral powder with OBDC filler in the HMA mixture.

- Replacing 100% of mineral powder by OBDC filler helps the preserving natural resources of stones, and eliminates the production cost of mineral powder.
- Using OBDC as a filler in HMA mix as a cost-free waste material helps to decrease or eliminate the environmental concerns of OBDC, and also eliminates the cost of treatments and landfilling of OBDC.

References

Asphalt Institute., 1979. *Mix Design Methods for Asphalt Concrete and Other Hot-Mix Types. Manual Series No. 2 (MS-2).* Asphalt Institute, Lexington, KY.

ASTM., 1999. *Standard Test Method for Ductility of Bituminous Materials*. ASTM D113. ASTM, West Conshohocken, PA.

ASTM., 2002. *Standard Test Method for Effect of Heat and Air on Asphaltic Materials (Thin-Film Oven Test).* ASTM D1754. ASTM, West Conshohocken, PA.

ASTM., 2003. *Standard Test Method for Specific Gravity and Density of Semi-Solid Bituminous Materials (Pycnometer Method).* ASTM D70. ASTM, West Conshohocken, PA.

ASTM., 2005. *Standard Test Method for Penetration of Bituminous Materials*. ASTM D5. ASTM, West Conshohocken, PA.

ASTM., 2006. *Standard Test Method for Softening Point of Bitumen (Ring-and-Ball Apparatus)*. ASTM D36. ASTM, West Conshohocken, PA.

ASTM., 2007. *Standard Test Method for Kinematic Viscosity of Asphalts (Bitumens)*. ASTM D2170. ASTM, West Conshohocken, PA.

ASTM., 2015. *Standard Test Method for Marshall Stability and Flow of Asphalt Mixtures*. ASTM D 6927. ASTM, West Conshohocken, PA.

ASTM., 2017. *Standard Test Method for Sieve Analysis of Mineral Filler for Asphalt Paving Mixtures*. ASTM D546. ASTM, West Conshohocken, PA.

ASTM., 2018. *Standard Test Method for Flash and Fire Points by Cleveland Open Cup Tester*. ASTM D92. ASTM, West Conshohocken, PA.

ASTM., 2020. *Standard Practice for Preparation of Asphalt Mixture Specimens Using Marshall Apparatus.* ASTM D6926. ASTM, West Conshohocken, PA.

ASTM., 2022. *Standard Test Method for Effect of Heat and Air on a Moving Film of Asphalt Binder (Rolling Thin-Film Oven Test).* ASTM D2872. ASTM, West Conshohocken, PA.

ASTM., 2022. *Standard Test Method for Solubility of Asphalt Materials in Trichloroethylene or Toluene.* ASTM D2042. ASTM, West Conshohocken, PA.

Azadgoleh, M.A., Mohammadi, M.M., Ghodrati, A., Sharifi, S.S., Palizban, S.M.M., Ahmadi, A., Vahidi, E., and Ayar, P., 2022. Characterization of contaminant leaching from asphalt pavements: A critical review of measurement methods, reclaimed asphalt pavement, porous asphalt, and waste-modified asphalt mixtures. *Water Research*, 219, p.118584.

Bernardo, G., Marroccoli, M., Nobili, M., Telesca, A., and Valenti, G.L., 2007. The use of oil well-derived drilling waste and electric arc furnace slag as alternative raw materials in clinker production. *Resources Conservation and Recycling*, 52(1), pp.95-102.

Cui, C., Yan, D., Liu, M., Wang, J., Li, L., Chen, C., and Huang, Q., 2023. Utilization of oil-based drilling cuttings as asphalt pavement surface: Study on the mechanical characteristics and long-term environmental impact. *Environmental Technology and Innovation*, 30, p.103052.

Ferrotti, G., Mancinelli, E., Passerini, G., and Canestrari, F., 2024. Comparison of energy and environmental performance between warm and hot mix asphalt concrete production: A case study. *Construction and Building Materials*, 418, p.135453.

Foroutan, M., Hassan, M.M., Desrosiers, N., and Rupnow, T., 2018. Evaluation of the reuse and recycling of drill cuttings in concrete applications. *Construction and Building Materials*, 164, pp.400-409.

Gedik, A., Selcuk, S., and Lav, A.H., 2021. Investigation of recycled fluorescent lamps waste as mineral filler in highway construction: A case of asphaltic pavement layers. *Resources Conservation and Recycling*, 168, p.105290.

Hu, Y., Chen, X., Mu, S., and Li, Q., 2022. Extraction and separation of petroleum pollutants from oil-based drilling cuttings using methanol/n-hexane solvent. *Process Safety and Environmental Protection*, 168, pp.760-767.

Huang, Z., Xu, Z., Quan, Y., Jia, H., Li, J., Li, Q., Chen, Z., and Pu, K., 2018. A review of treatment methods for oil-based drill cuttings. *IOP Conference Series Earth and Environmental Science*, 170, p.022074.

Hussein, N.S., and Ibrahim, R.K., 2023. Fresh and mechanical properties of concrete containing oil-well cutting material. *ARO The Scientific Journal of Koya University*, 11(1), pp.72-78.

Ikotun, J.O., Okeniyi, J.O., Akinlabi, E.T., Akinlabi, S.A., Okeniyi, E.T., and Olanrewaju, D.O., 2019. Physicochemical and mineralogical characterization datasets from oil drill cuttings in comparison with other cement types for cement partial-replacement in concrete. *Chemical Data Collections*, 19, p.100176.

Khan, D., Khan, R., Khan, M., Alam, M., and Hassan, T., 2023. Performance of hot-mix asphalt using polymer-modified bitumen and marble dust as a filler. *Journal of Traffic and Transportation Engineering (English Edition)*, 10(3), pp.385-398.

Khodadadi, M., Moradi, L., Dabir, B., Moghadas Nejad, F., and Khodaii, A., 2020. Reuse of drill cuttings in hot mix asphalt mixture: A study on the environmental and structure performance. *Construction and Building Materials*, 256, p.119453.

Kumlai, S., Jitsangiam, P., and Nikraz, H., 2022. Assessments of moisture damage resistance of asphalt concrete mixtures and asphalt mastic with various mineral fillers. *Transportation Engineering*, 7, p.100106.

Mohammed, B., and Cheeseman, C.R., 2011. Use of oil drill cuttings as an alternative raw material in sandcrete blocks. *Waste and Biomass Valorization*, 2(4), pp.373-380.

Mostavi, E., Asadi, S., and Ugochukwu, E., 2015. Feasibility study of the potential use of drill cuttings in concrete. *Procedia Engineering*, 118, pp.1015-1023.

Roberts, F.L., 1991. *Hot Mix Asphalt Materials, Mixture Design, and Construction*. National Asphalt Pavement Association, United States.

Siddique, S., Kwoffie, L., Addae-Afoakwa, K., Yates, K., and Njuguna, J., 2017. Oil based drilling fluid waste: An overview on environmentally persistent pollutants. *IOP Conference Series Materials Science and Engineering*, 195, p.012008.

Wang, C.Q., Lin, X.Y., He, M., Wang, D., and Zhang, S.L., 2017. Environmental performance, mechanical and microstructure analysis of concrete containing oil-based drilling cuttings pyrolysis residues of shale gas. *Journal of Hazardous Materials*, 338, pp.410-427.

Wang, X., Jin, W., Li, Y., Liu, S., Xu, J., Liu, J., Li, H., and Long, T., 2024. Treatment advances of hazardous solid wastes from oil and gas drilling and Production Processes. *Chemical Engineering Journal*, 497, p.154182.

Xie, B., Qin, J., Sun, H., Wang, S., and Li, X., 2021. Leaching behavior of polycyclic aromatic hydrocarbons (PAHs) from oil-based residues of shale gas drill cuttings. *Environmental Pollution*, 288, p.117773.

Chromosome Instability and Micronucleus Frequency on the Oral Mucosa of HIV-positive Patients

Saifadin K. Mustafa†

Department of Medical Microbiology, Faculty of Science and Health, Koya University,
Danielle Mitterrand Boulevard, Koya KOY45, Kurdistan Region – F.R. Iraq

***Abstract*—Extranuclear structures known as micronuclei (MN) are composed of whole or fragmented chromosomes that were not incorporated into the nucleus following cell division. The genotoxic impact of HIV infection on oral cavity cancers remains uncertain. This study sought to determine the impact of HIV infection on MN in HIV+ patients' oral mucosa and its correlation with early cytogenetic alterations in oral carcinogenesis. A total of forty-four non-HIV patients and thirty-eight HIV+ patients were assessed in this study. Smears were collected from the oral cavity and stained with 5% methylene blue. The smears were then examined at a ×100 magnification using a standard microscope. For each participant, 100 buccal cells were counted. Further observations of the viral load (VL), lymphocytes, and granulocytes were made to determine the pattern of MN presence in HIV+ patients. Significant differences were observed between HIV+ patients and healthy controls regarding alcohol consumption ($p = 0.004 < 0.05$) and smoking ($p = 0.041 < 0.05$). The relationship between micronucleus and VL is substantial. After calculating the linear regression model, it was discovered that the VL ratio of HIV-positive patients could predict the micronucleus cells (R-Sq = 55%, $p < 0.000$). In conclusion, HIV VL shows increased genomic instability. These findings are relevant to understanding the mechanisms of cellular damage and developing potential strategies to mitigate carcinogenesis in HIV+ patients.**

***Index Terms*—Chromosome instability, DNA damage, HIV, Micronucleus, Viral load.**

I. Introduction

Preserving genome stability is crucial for ensuring optimal cell function and preventing disease. Accumulated DNA damage speeds up the aging process by interfering with cellular metabolism, which can trigger senescence, immune system decline, programmed cell death, stem cell loss, and inflammation. These detrimental effects heighten the risk of age-related illnesses (Ellwanger, et al., 2023). Genomic instability refers to the genome's susceptibility to chemical modification or mutations (Drews, et al., 2022) and can arise from factors such as replication stress, errors in chromosome segregation during faulty mitosis, defective homologous recombination, environmental exposures, and lifestyle habits such as diet, exercise, alcohol consumption, and smoking. This instability can trigger gene amplifications or deletions, structural rearrangements, extrachromosomal DNA formation, and micronuclei (MN) development, all of which contribute to various pathological outcomes, including different forms of cancer (Valverde and Rojas, 2009; Fenech and Bonassi, 2011).

Acquired immunodeficiency syndrome is an infectious disease caused by the HIV, at present, there are 42.3 million people globally who have HIV infection (World Health Organization, 2024). Despite efforts to prevent, diagnose, and treat HIV, mortality rates remain higher than those of the general population. In addition, people living with HIV have an increased risk of developing cancer (Gutierrez-Sevilla, et al., 2021; Poetsch, 2020). HIV-positive individuals are now approximately 500 times more likely to acquire Kaposi sarcoma, 12 times more likely to develop non-Hodgkin lymphoma, and, in the case of women, 3 times the risk of developing cervical cancer when compared to the general population (Hernández-Ramírez, et al., 2017). Furthermore, individuals infected with HIV face an increased risk of various other cancer types. This includes cancers of the liver, oral cavity, and pharynx, as well as the lungs. In addition, those living with HIV are 3 times more likely to receive a liver cancer diagnosis, approximately twice as likely to be diagnosed with oral cavity or pharyngeal cancer, and roughly twice as likely to be identified with lung cancer compared to the general population (Wang, Silverberg and Abrams, 2014; Silverberg, et al., 2015). The impact of HIV infection on oral cancer development is not yet understood (Pradeep, et al., 2014). The presence of the accessory gene Vpr from HIV virus can be attributed to the viral HIV infection in neoplastic processes, causing disruptions in the cell cycle and resulting in changes in ploidy due to accumulation in the G2/M cell division phase. As a result, it is recommended to biomonitor HIV+ patients for early signs of oral squamous cell carcinoma (OSCC), with the potential use of the micronucleus test (Caponio, et al., 2024). The MN test is commonly utilized for

---

ARO-The Scientific Journal of Koya University
Vol. XIII, No. 1 (2025), Article ID: ARO.12035. 5 pages
DOI: 10.14500/aro.12035
Received: 05 February 2025; Accepted: 11 May 2025
Regular research paper; Published: 25 May 2025

†Corresponding author's e-mail saifadin.khder@koyauniversity.org

biomonitoring and risk assessment of populations exposed to various genotoxic agents, as it aids in detecting the early stages of carcinogenesis. During the anaphase of mitosis, MNs are created when fragments of delayed chromatin or chromosomes with abnormalities separate from the nucleus. They apparently reflect chromosomal aberrations that occurred during the proliferation of the basal layer (Luzhna, Kathiria, and Kovalchuk, 2013).

The amount of HIV in the blood that can be detected through testing is referred to as the HIV viral load (VL). VL is a major factor affecting HIV transmission. Many studies have demonstrated that higher VL is associated with a significantly greater risk of HIV transmission compared to lower VL levels (Eisinger, Dieffenbach, and Fauci, 2019). HIV infects the immune system cells of the host and mainly targets monocytes/macrophages and CD4+ T lymphocytes, leading to gradual destruction. Ongoing viral replication results in a gradual decrease in CD4+ cells, leading to weakened immune defenses and heightened vulnerability to opportunistic infections (Veenhuis, et al., 2023). Moreover, there are data indicating that HIV infection causes an imbalance between the production of reactive oxygen species and antioxidants, causing OS (Dravid, et al., 2022). OS can cause genomic instability, increased risk of mutations, disruption of cell cycle control and DNA repair, chromosome rearrangements, and aneuploidy, which can contribute to the onset of specific cancer types (Poetsch, 2020).

This is the first MN analysis conducted in Northern Iraq. The purpose of this study is to examine the effect of HIV infection on the formation of MN in the oral mucosa of HIV-positive patients.

II. METHODOLOGY

A. Sample Collection

The study involved the enrollment of 38 HIV-infected patients with 44 controls. Patients with documented HIV infection older than 24 years of age were included in this study. The stages of HIV infection were not included because they were not recorded in the patients’ profiles. As a result, it was not conceivable to precisely report or analyze the stages in this study. Patients who agreed to participate answered a questionnaire about general data and habits. Lymphocytes (10^9/L), granulocyte (10^9/L), and VL values were registered.

A wooden tongue depressor is used for the collection of the buccal mucosa of the participants. A buccal mucosa sample was collected through swabbing the mucosa from the left and right sides of the cheek. The collected cells are then spread on a clean slide to create a smear, which is then stained with a 5% methylene blue. The smears are then examined under a microscope with a magnification of ×100. Cells were evaluated in a zigzag pattern from one side of the smear to the other, counting solely distinct, nucleated, non-overlapping cells that were not folded. Blinding and inter-observer variability were not applied because of practical limitations. Both male and female participants were included to ensure a comprehensive representation, as HIV affects individuals of both genders. The process of identification of MN involves the counting of 100 cells per slide.

B. Statistical Analysis

The statistical program statistica software was used to analyze the data. The association between the affiliation between factors was carried out utilizing the t-test, which could be a measurable theory test to decide the goodness of fit of whether a variable has a place in a specific dispersion. $p < 0.05$ was considered statistically significant.

C. Ethical Approval

The study was conducted at the protect and Transmission Disease Hospital in Erbil, Kurdistan Region, Iraq, in collaboration with the Department of Medical Microbiology, Faculty of Sciences and Health, Koya University, Iraq. The Ethical Committee of the Faculty of Science and Health, Koya University, Iraq, approved the study. Approval number (021Bio).

III. RESULTS

38 HIV-infected patients and 44 healthy controls admitted at the Infectious Diseases Hospital (Erbil, Iraq) were recruited in this study. To study whether there is homogeneity in the patient group with the healthy group in terms of demographic and clinical characteristics, the differences between the HIV+ patients and the control group are illustrated in Table I. For HIV patients and healthy controls, highly significant differences were observed for smokers ($p = 0.041 < 0.05$), alcohol ($p = 0.004 < 0.05$), and other diseases ($p = 0.02 < 0.05$). However, there is no significant difference in gender ($p = 0.85 > 0.05$). All HIV patients are

TABLE I
DEMOGRAPHIC AND CLINICAL CHARACTERISTICS BETWEEN HIV+PATIENTS AND THE CONTROL GROUP

	Control (n=44)	Patient (n=38)	p-value	Other diseases treatment	HIV treatment
Male	34	30	0.85 >0.05		Tenofovir+Lamivudine+Dolutegravir (300:300:50)
Female	10	8			
Smoke	19	25	0.04 <0.05		
Alcohol	7	17	0.004 <0.05		
Other diseases	5	12	0.02 <0.05		
Diabetes	2	3		Metformin 500 mg and Glimepiride 2 mg	
Blood pressure	3	4		Valsartan 40 mg	
Anxiety	0	5		Mirtazapine 30 mg	

treated with the same medication (Tenofovir + Lamivudine + Dolutegravir [TLD] [300:300:50]).

Table II illustrates the data provide insights into six variables across a sample size of 38, including their means, standard deviations, and 95% confidence intervals. The mean age of participants is 33.42 years (±5.21), indicating a relatively young group, with an age range estimated between 31.71 and 35.13 years. The mean duration of observation is 42.32 months (±10.90), with a confidence interval of 38.73–45.90 months, suggesting moderate variability in study duration. Micronucleate cell counts average at 11.29 (±4.88), with a range from 9.69 to 12.89, reflecting some degree of cellular variability among the participants. VL shows a significantly high mean of 136,645 IU/mL (±209,376), but its wide confidence interval (33,965–67,825) indicates high dispersion, likely skewed by extreme values. Lymphocyte counts average 2.30 × 10^9/L (±1.14), within a confidence range of 1.92–2.67 × 10^9/L, suggesting relatively low variability. Granulocyte counts are slightly higher, with a mean of 3.66 × 10^9/L (±1.97) and a confidence interval of 3.01–4.31 × 10^9/L. These results reveal differences in variability among the variables, with VL showing the highest dispersion, indicating potential outliers or heterogeneity in the dataset. Further analyses, such as correlation or regression, could explore relationships between these variables.

The results regarding age, Micronucleated cells/100, lymphocyte, and granulocyte (means, standard deviation, standard error, t-value, and p-value) and the comparisons between both groups (patients and control) are shown in Table III.

No significant differences were observed between HIV patients and healthy controls in terms of age and granulocytes with p = 0.777 and p = 0.534, respectively. However, a significant difference was found in the comparison of MN frequency in the oral mucosa and lymphocyte count between HIV patients and controls (Table III). In addition, patient hematological characteristics in the control group and HIV+ patients are shown in Fig. 1.

The study involved counting 100 buccal cells of each of the participants. The presence of MN in these cells was further noted to determine the pattern of existence of MN in the cells of HIV patients and healthy controls (Fig. 1a). It was found that MN were more prominent in the buccal cells of the HIV+ patients. Also, our statistical analysis showed that the granulocyte count was slightly higher in HIV+ patients compared to the control group (Fig. 1b). However, our statistical analysis illustrated that the lymphocyte count is higher in the control group than in HIV patients (Fig. 1c).

To study whether there is a significant relationship between MN and VL, a linear regression model was calculated, and it was found that (R-Sq = 55%, $p < 0.000$), the VL ratio of HIV-positive patients can predict the MN cells (Fig. 2).

TABLE II

Illustrate Mean, Standard Deviation, and 95% Confidence Interval for Patients Group. IU/ml stands for logarithm ($\log_{10}$) international units per milliliter

Sample size (38)	Mean	Standard deviation	95% confidence interval (C.I.)	
			Lower limit	Upper limit
Age/year	33.421	5.207	31.709	35.133
Duration/month	42.320	10.900	38.73	45.90
Micronucleate cell	11.289	4.876	9.687	12.892
Viral load IU/mL	136,645	209,376	33965.0	67825
Lymphocyte 0.9–5×10^9/L	2.297	1.136	1.924	2.671
Granulocyte 1.2–8×10^9/L	3.661	1.971	3.013	4.308

TABLE III

Age, micronucleated cells, and Laboratory values: Comparison between the Control Group as Healthy Individuals and HIV+Patient Samples

	Sample Size	Mean	SD	SE	t	p-value
Age/year						
Control	44	33	7.76	1.2	−0.28	0.777
Patients	38	33.42	5.21	0.84		
Micronucleated cells/100						
Control	44	0.386	0.655	0.099	−14.69	0
Patients	38	11.29	4.88	0.79		
Lymphocyte 0.9–5×10^9/L						
Control	44	3.14	1.01	0.15	3.53	0
Patients	38	2.3	1.14	0.18		
Granulocyte 1.2–8×10^9/L						
Control	44	3.44	1.24	0.19	−0.62	0.534
Patients	38	3.66	1.97	0.32		

SD: Standard deviation, SE: Standard error

IV. Discussion

This study aimed to evaluate the impact of HIV infection on cytogenetic damage in the oral mucosa, considering that DNA damage could lead to oral cancer. For this purpose, two groups were analyzed: The study group, comprising HIV-positive patients, and the control group, consisting of patients without HIV infection. Fortunately, patients in the Kurdistan region of Iraq, start treatment as soon as they are diagnosed. Therefore, all HIV+ patients in this research were treated with the same antiretroviral TLD (300:300:50). This is a significant step for a developing nation. On the other hand, Ellwanger et al. (2023) and Ivanov et al. (2016) suggest that HIV medications can also contribute to chromosome instability. In Brazil, Lima et al. (2017) examined MN in exfoliated oral cells from HIV+ individuals undergoing antiretroviral therapy and non-infected controls, with 30 participants in each group. The MN were divided into two categories: (I) single MN and (II) multiple MN. There was no significant difference in the total number of micronucleated cells or the number of MN between the groups, nor any correlation with CD4+ T cell counts. However, the study found a significantly higher mean number of single MN in the control group compared to the HIV-positive individuals. The occurrence of multiple MN was also reported in the HIV group compared to the controls, though the difference was not significant.

This is one of the first studies in northern Iraq that focused on identifying individuals posing a high risk of forming MN due to having HIV or a HIV VL. In this study, we found

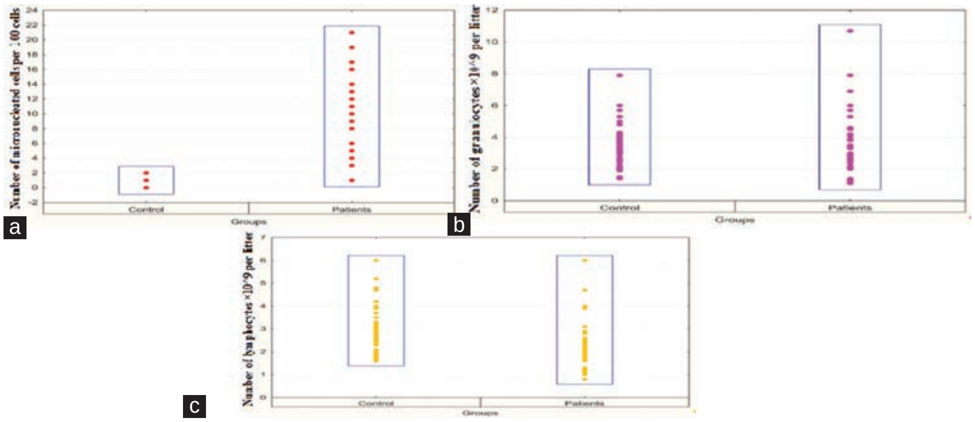

Fig. 1. (a-c) Patient characteristics of micronuclei, granulocytes, and lymphocytes, between the control group and HIV+ patients.

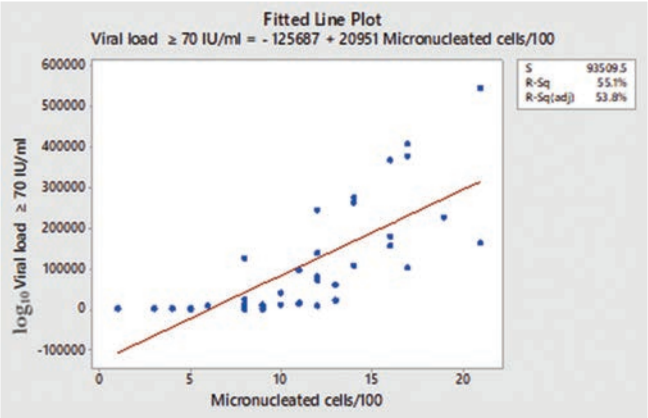

Fig. 2. Graphic representation of the regression analysis between micronucleated cells per 100 cells and the $\log_{10}$ viral load ≥70 IU/mL in HIV-positive patients.

that the VL was associated with the occurrence of MN. A significant correlation was observed between the VL and MN ($p < 0.05$). This indicated that VL might influence the clinical characteristics of patients with HIV. To better understand chromosome instability, we investigated whether VLs are associated with DNA damage. Overall, we concluded there is a modest and consistent linear relationship between VL and MN. However, causality cannot be inferred from cross-sectional data alone. Longitudinal studies are needed to determine whether changes in VL directly contribute to increased MN formation over time. Current clinical observation suggests that VL is a risk factor in the susceptibility to cytogenetic damage. In addition, previous studies have reported that HIV plays a crucial role in the development of MN (Faig Lima, et al., 2017; Zizza, et al., 2019).

Significant differences were observed between HIV patients and healthy controls regarding smoking and alcohol consumption, with $p = 0.041$ ($p < 0.05$) and 0.004 ($p < 0.05$), respectively. Jung and Yoon (2022), and Mohammed et al. (2020), have strongly suggested that the distribution of smoking and alcohol has been correlated with genotoxic effects and acts as a genetic risk factor for different diseases, such as malignancies. Although the exact connection between HIV infection and the development of oral cancer has yet to be determined, the resulting immunosuppression makes individuals more vulnerable to carcinogens and the formation of MN (Lima, et al., 2017). Therefore, HIV-positive patients should be regularly monitored for the early onset of OSCC, for which the MN test is a useful tool. According to Luzhna, Kathiria, and Kovalchuk (2013), the MN test has been widely adopted in biomonitoring and risk assessment of populations exposed to various genotoxic agents, as it serves as an effective method for identifying the initial alterations associated with carcinogenesis.

In our study, 38 HIV-positive patients were evaluated, with 100 buccal cells counted for each participant. Granulocyte and lymphocyte levels were also recorded to help identify the pattern of MN presence in the cells of HIV-positive patients. Our statistical result revealed no significant differences in granulocyte count between healthy individuals and HIV+ patients ($p = 0.534$) (Fig. 1b). On the other hand, there were significant differences in lymphocyte count between the control group and HIV patients ($p = 0.000$) (Fig. 1c). The lack of a significant difference in granulocyte levels ($p = 0.534$) suggests that granulocytes may not play a central role in reflecting HIV-related DNA damage. Unlike lymphocytes, which are more directly affected by HIV infection and are commonly used in genotoxicity assessments due to their higher mitotic activity and susceptibility to DNA damage (Nacher, et al., 2018). Lymphocytes and macrophages, key parts of the immune system, are primarily affected by HIV, which gradually damages these cells. The levels of CD4+ cells decrease gradually as the virus continues to replicate, resulting in a slow deterioration of the host's immune defense system and increased susceptibility to opportunistic infections (Vijayan, et al., 2017).

The MN formation may be associated with various chromosome-breaking events that have a direct impact on the cell cycle (Luzhna, Kathiria, and Kovalchuk, 2013). The existence of HIV accessory genes and infection by oncoviruses derived from human herpesviruses and human papillomavirus (HPV) have been the subject of numerous theories in recent years. The action of the HIV virus accessory gene Vpr, which causes disruptions in the cell cycle, can be used to explain the oncogenic process. Although there is considerable evidence linking the effects of HPV to HIV infection, leading to DNA alterations, this connection is primarily associated with oropharyngeal cancer (Proulx, et al., 2022; Haworth, et al., 2018) and does not pertain to our study design.

V. Conclusion

Our research lends credence to the idea that HIV infection causes DNA damage, but further research in this area is required. Furthermore, even if the exact period of exposure is unknown, our results indicate that exposure to the virus is a significant factor in the development of chromosome-breaking. Further investigation is required to elucidate the relationship between HIV stages and MN, as the absence of stage data in this study constrained the inclusion of this critical contextual information. Last but not least, many unresolved questions remain regarding the relationship between HIV and MN. In addition, understanding the mechanism of DNA damage is essential for developing therapies aimed at reducing the cancer risk in HIV patients.

Acknowledgments

We are grateful to all members of the Transmission Disease Hospital in Erbil, Kurdistan Region – F.R. Iraq.

References

Caponio, V.C.A., Silva, F.F., Popolo, F., Giugliano, S., Spizzirri, F., Lorenzo-Pouso, A.I., Padín-Iruegas, M.E., Zhurakivska, K., Muzio, L.L., and López-Pintor, R.M., 2024. State of the art of micronuclei assay in exfoliative cytology as a clinical biomarker of genetic damage in oral carcinogenesis: A systematic review and meta-analysis. *Mutation Research Reviews in Mutation Research*, 794, p.108508.

Dravid, A., Morkar, D., Prasad, D., Ramapuram, J.T., Patel, K.V., Naik, K.S., Bhrusundi, M., Kulkarni, M., Hegde, S., Anuradha, S., Nageswaramma, S., Madan, S., Jayaprakash, T., and Kulkarni, V., 2022. A phase IV study on safety, tolerability, and efficacy of dolutegravir, lamivudine, and tenofovir disoproxil fumarate in treatment naive adult Indian patients living with HIV-1. *Pragmatic and Observational Research,* 13, pp.75-84.

Drews, R.M., Hernando, B., Tarabichi, M., Haase, K., Lesluyes, T., Smith, P.S., Morrill Gavarró, L., Couturier, D.L., Liu, L., Schneider, M., Brenton, J.D., Van Loo, P., Macintyre, G., and Markowetz, F., 2022. A pan-cancer compendium of chromosomal instability. *Nature*, 606, pp.976-983.

Eisinger, R.W., Dieffenbach, C.W., and Fauci, A.S., 2019. HIV viral load and transmissibility of HIV infection: Undetectable equals untransmittable. *JAMA,* 321, pp.451-452.

Ellwanger, J.H., Kulmann-Leal, B., Ziliotto, M., and Chies, J.A.B., 2023. HIV infection, chromosome instability, and micronucleus formation. *Viruses,* 15, p.155.

Faig Lima, C., Alves, M.G.O., Furtado, J.J.D., Marcelo, M., Ivan, B., and Almeida, J.D., 2017. Effect of HIV infection in the micronuclei frequency on the oral mucosa. *Journal of Oral Pathology and Medicine*, 46(8), pp.644-648.

Fenech, M., and Bonassi, S., 2011. The effect of age, gender, diet and lifestyle on DNA damage measured using micronucleus frequency in human peripheral blood lymphocytes. Mutagenesis, 26, pp.43-49.

Gutierrez-Sevilla, J.E., Cardenas-Bedoya, J., Escoto-Delgadillo, M., Zúniga-Gonzalez, G.M., P´erez-Ríos, S.M., Gomez-Meda, B.C., Gonzalez-Enríquez, G.V., Figarola-Centurion, I., Chavarría-Avila, E., and Torres-Mendoza, B.M., 2021. Genomic instability in people living with HIV'. *Mutation Research Genetic Toxicology and Environmental Mutagenesis,* 865, p.503336.

Haworth, K.G., Schefter, L.E., Norgaard, Z.K., Ironside, C., Adair, J.E., and Kiem, H.P., 2018. HIV infection results in clonal expansions containing integrations within pathogenesis-related biological pathways. *JCI Insight*, 3(13), p.e99127.

Hernández-Ramírez, R.U., Shiels, M.S., Dubrow, R., and Engels, E.A., 2017. Cancer risk in HIV-infected people in the USA from 1996 to 2012: A population-based, registry-linkage study. *The Lancet HIV*, 4(11), pp.e495-e504.

Ivanov, A.V., Valuev-Elliston, V.T., Ivanova, O.N., Kochetkov, S.N., Starodubova, E.S., Bartosch, B., and Isaguliants, M.G., 2016. Oxidative stress during HIV infection: Mechanisms and consequences. *Oxidative Medicine and Cellular Longevity*, 2016, p.8910396.

Jung, Y.S., and Yoon, S.J., 2022. Burden of cancer due to cigarette smoking and alcohol consumption in Korea. *International Journal of Environmental Research and Public Health*, 19(6), p.3493.

Lima, C.F., Alves, M.G.O., Furtado, J.J.D., Marcucci, M., Balducci, I., and Almeida, J.D., 2017. Effect of HIV infection in the micronuclei frequency on the oral mucosa. Journal of Oral Pathology and Medicine, 46(7), pp.644-648.

Luzhna, L., Kathiria, P., and Kovalchuk, O., 2013. Micronuclei in genotoxicity assessment: From genetics to epigenetics and beyond. Frontiers in Genetics, 4, p.131.

Mohammed, A.M., Hussen, D.F., Rashad, H., and Hasheesh, A., 2020. The micronuclei scoring as a biomarker for early detection of genotoxic effect of cigarette smoking. *Asian Pacific Journal of Cancer Prevention*, 21(1), pp.87-92.

Nacher, M., Huber, F., Adriouch, L., Djossou, F., Adenis, A., and Couppié, P., 2018. Temporal trend of the proportion of patients presenting with advanced HIV in French Guiana: Stuck on the asymptote? *BMC Research Notes*, 11(1), p.831.

Poetsch, A.R., 2020. The genomics of oxidative DNA damage, repair, and resulting mutagenesis. *Computational and Structural Biotechnology Journal*, 18, pp.207-219.

Pradeep, M.R., Guruprasad, Y., Jose, M., Saxena, K., Deepa, K., and Prabhu, V., 2014. Comparative study of genotoxicity in different tobacco related habits using micronucleus assay in exfoliated buccal epithelial cells. *Journal of Clinical and Diagnostic Research,* 8(5), p.ZC21-ZC24.

Proulx, J., Ghaly, M., Park, I., and Borgmann, K., 2022. HIV-1-mediated acceleration of oncovirus-related non-AIDS-defining cancers. *Biomedicines*, 10(4), p.768.

Silverberg, M.J., Lau, B., Achenbach, C.J., Jing, Y., Althoff, K.N., D'Souza, G., Engels, E.A., Hessol, N.A., Brooks, J.T., Burchell, A.N., Gill, M.J., Goedert, J.J., Hogg, R., Horberg, M.A.,… & Dubrow, R., 2015. Cumulative incidence of cancer among persons with HIV in North America: A cohort study. *Annals of Internal Medicine,* 163(7), pp.507-518.

Valverde, M., and Rojas, E., 2009. Environmental and occupational biomonitoring using the Comet assay. Mutation Research, 681, pp.93-109.

Veenhuis, R.T., Abreu, C.M., Costa, P.A.G., Ferreira, E.A., Ratliff, J., Pohlenz, L., Shirk, E.N., Rubin, L.H., Blankson, J.N., Gama, L., and Clements, J.E., 2023. Monocyte-derived macrophages contain persistent latent HIV reservoirs. *Nature Microbiology*, 8, pp.833-844.

Vijayan, K.K.V., Karthigeyan, K.P., Tripathi, S.P., and Hanna, L.E., 2017. Pathophysiology of CD4+ T-cell depletion in HIV-1 and HIV-2 infections. *Frontiers in Immunology*, 8, p.580.

Wang, C.C., Silverberg, M.J., and Abrams, D.I., 2014. Non-AIDS-defining malignancies in the HIV-infected population. *Current Infectious Disease Reports*, 16(6), pp.406.

World Health Organization., 2024. *HIV and AIDS*. Avialable from: https://www.who.int/news-room/fact-sheets/detail/hiv-aids [Last accessed on 2024 Oct 09].

Zizza, A., Grima, P., Andreassi, M.G., Tumolo, M.R., Borghini, A., Donno, D.E., Negro, P., and Guido, M., 2019. HIV infection and frequency of micronucleus in human peripheral blood cells. *Journal of Preventive Medicine and Hygiene*, 60(3), pp.E191-E196.

Hybrid Cryptosystem with Computational Ghost Imaging Based on Integer Wavelet Transform and Chaotic Maps

Khalid T. Alnidawi[1†], and Ali M. Sagheer[2]

[1]Department of Computer Science, College of Computer Science and IT, University of Anbar,
Ramadi, Iraq

[2]Department of Computer Networks System, College of Computer Science and IT, University of Anbar,
Ramadi, Iraq

***Abstract*—Computational ghost imaging encryption (CGIE) has gained increasing attention from researchers in the field of optical cryptography due to its unique phenomenon. However, traditional CGIE suffers from long imaging time, inherent system linearity, and an enormous number of random phase masks that must be transmitted as secret keys, which limits its application in practical communication. In this paper, a hybrid optical image encryption approach is proposed using CGIE based on integer wavelet transform and chaotic maps. In addition, Hadamard basis patterns are employed to reduce sampling times and improve reconstructed image quality. Simulation results demonstrate that the proposed system is robust against different types of attacks with high key sensitivity and low execution times of 0.03 s for encryption and 0.14 s for decryption. This approach will ensure broader adoption of this technology by facilitating its integration into cryptosystems.**

***Index Terms*—Chaotic maps, Cryptography, Ghost imaging, Optical image encryption, Wavelet transform.**

I. INTRODUCTION

The amazing phenomenon of computational ghost imaging (CGI) led us to focus on incorporating it more widely in image encryption systems (Liu, Wang and Zhao, 2022). Due to the special properties of CGI, such as non-local imaging by encoding the image into intensity correlation between the original image and the projected random patterns, make it a valuable technique in optical cryptography (Zhang, Wang and Zhang, 2022). CGI is a new technique that has been widely used since it appeared. This technique has a simple structure. The specialized light source continuously generates a changing laser speckle pattern and projects it onto an object, then uses a lens to direct the light that passes the object to a bucket detector to record the total intensity with no spatial information. The image is then constructed by using a simple linear operation between the bucket values and the total intensity recorded by the reference arm that calculates the total intensity of the speckle patterns alone (Zhang, et al., 2019). However, for encryption purposes, CGI encryption (CGIE) has serious limitations that the researchers are aiming to solve, such as the need for an enormous number of random patterns to encode and reconstruct the image. This will take a lot of time and consume high computational power. Another issue is the need for transmitting all the random patterns to the receiver side to reconstruct the image. To address these challenges, this work incorporates advanced techniques to improve the efficiency and security of CGIE. By leveraging the orthogonality and structured nature of the Hadamard matrix (HM) that generates unique and non-repetitive Hadamard basis patterns (HBPs) through its scrambling with chaotic maps, the need for transmitting large pattern sets is eliminated and the number of measurements required for image reconstruction is significantly reduced. Integer wavelet transform (IWT) ensures a lossless, integer-to-integer transformation, enabling faster encryption with XOR operations. I addition, the strong properties of the chaotic maps enhance both the security and efficiency of the system, ensuring improved resilience and optimized performance. The rest of this paper is organized as follows. The related works are described in Section 2. In Section 3, the theoretical background of the proposed system is introduced. In section 4, the proposed model framework is explained. Section 5 contains the quantitative measures used to evaluate the system. The simulation results and security analysis are performed in section 6, the conclusion is given in section 7.

II. RELATED WORKS

The CGI technique was first introduced by (Shapiro, 2008). In which the reference beam is computed offline using a computer instead of using a charged-coupled device. On the basis of this foundational work, (Clemente, et al., 2010) introduced a new approach in optical cryptography utilizing CGI for image encryption by using the random phase masks (RPMs) as a

ARO-The Scientific Journal of Koya University
Vol. XIII, No.1(2025), Article ID: ARO.12153. 12 pages
DOI: 10.14500/aro.12153
Received: 27 March 2025; Accepted: 22 May 2025
Regular research paper; Published: 05 June 2025

[†]Corresponding author's e-mail: kha23c1009@uoanbar.edu.iq

secret key. This approach paved the way for the researchers to enhance and develop CGI techniques for cryptography. However, the reconstruction quality is poor and the complexity of the system is high. To address these limitations, (Duran, 2011). introduced a new method by incorporating compressed sensing with CGI to reduce the complexity of the system while improving reconstruction quality. However, the system's linearity issue remains unresolved. To address this issue, (Chen and Chen, 2015) proposed an optical encryption technique by utilizing CGIE with labyrinth-like phase modulation patterns. The method employs a single phase-only mask (POMs), which optimizes storage and transmission efficiency of system keys while introducing highly randomness patterns. Similarly, in the same year, (Zhao, et al., 2015). incorporated CGIE with QR code improving image reconstruction quality and resisting cropping attack due to the high error tolerance in QR code. In a subsequent development, (Li, et al., 2016). developed a multiple image encryption scheme by using CGIE based on compressive ghost imaging leveraging the DCT domain and generating random patterns using a modified logistic map (LM) to reduce key transmission. Subsequently, (Yi, Leihong and Dawei, 2018). combined CGI with RSA algorithm to solve the problem with key distribution among the parties and add a high level of security to the system. In the same year, (Jiang, et al., 2017). Proposed a new approach using computational temporal ghost imaging to extend the concept to the time domain for encrypting temporal data in the time domain to improve the security and robustness against noise attack. Further enhancing security, (Zhu, et al., 2018). introduced a CGIE technique based on fingerprint phase mask to encrypt and decrypt the image using off-axis digital holography to add an additional layer of security besides the CGIE. Recently, (Guo, et al., 2024). proposed an optical image encryption and authentication scheme with CGI based on 4D chaotic system and DNA encoding using dual channels for encryption and authentication that alleviates the burden of key transmission need. In the same year, (Huang and Han, 2024). proposed CGIE technique using improved RSA algorithm and cake-cutting HM and discrete wavelet transform (DWT) to reduce the sampling times and eliminate RPMs transmission using a private channel. Building on previous advancements, (Miao, et al., 2025). proposed an image encryption and authentication scheme utilizing CGIE and lifting wavelet transform (LWT), employing the Knuth-Durstenfeld shuffling algorithm and chaotic maps. This approach ensures the enhancement of system's security and reduces the computational complexity of the wavelet transform due to the straightforward transformation of LWT.

However, most of these studies focused on performing CGIE on small-sized grayscale images to demonstrate the feasibility of CGIE. In this study, we have developed a low-complexity version that significantly reduces processing requirements. Our proposed system is designed to perform CGIE on a large-scale RGB image dataset with the aim of enabling the seamless adoption of this technology more widely within cryptographic frameworks. First, a two-level decomposition IWT is performed on the secret image. Second, a unique HM is generated and then scrambled using chaotic LM indices to eliminate POMs transmission needs. Then, HBPs are extracted from HM and projected on the LL sub-band to get the bucket signal. Firstly, a two-level decomposition IWT is performed on the secret image, generating four sub-bands: Low-Low (LL), High-Low (HL), Low-High (LH), and High-High (HH). LL serves as the approximation sub-band, preserving the most important structural details of the image, while the other sub-bands, known as detail sub-bands, capture edge and texture information. Finally, the other IWT sub-bands (HL, LH, HH) are shuffled with a piecewise linear chaotic map (PWLCM) then XORed with a second LM to achieve permutation-substitution. In addition, using another chaotic map to substitute the bucket signal to break the linearity of the system and improve the security. Simulation results show that our encryption system has a high level of security robustness against different attacks with perfect reconstruction quality compared to other methods.

III. Theoretical Background

A. CGIE

In the optical security field, instead of converting an image into a complex-valued matrix, CGI encrypts the image into correlated intensity values of the image and the HBPs, which makes CGI widely studied (Leihong, et al., 2018).

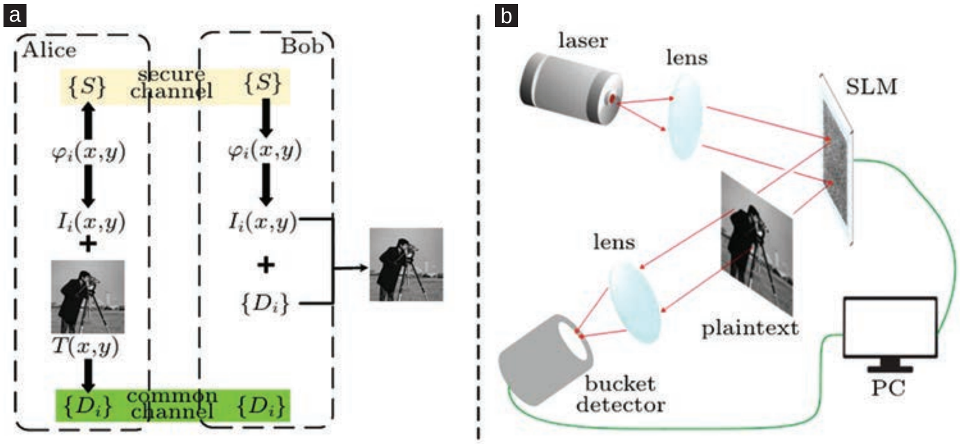

Fig. 1. (a). the block diagram of computational ghost imaging encryption encryption/decryption process, (b) The experimental setup of Computational Ghost Imaging (Kang, et al., 2021).

The structure of computational ghost imaging is very simple. As shown in Fig. 1a. Alice wants to encrypt the secret image $I(x, y)$ and transmit it to Bob using the public channel. Alice uses the CGI structure as shown in Fig. 1b. the specialized light source is passed through a lens to the spatial light modulator to regularly generate RPMs denotes $\emptyset(x, y)$ with values uniformly distributed between [0-2π] then project them onto an image $I(x, y)$ to record the total intensity with no spatial information. The resulting light intensity is directed by a lens to a bucket detector (B_i) using the equation as follows:

$$B_i = \sum_{i=1}^{m} \sum_{j=1}^{n} \varnothing(x, y).I(x, y) \tag{1}$$

Then, Alice sends the (B_i) as a cipher image using the public channel and transmits all the RPMs using the secured channel to Bob to decrypt the image. On the receiving side, Bob uses a simple linear operation between the bucket values and the secret patterns to reconstruct the image (Tao, et al., 2020), by calculating the average sum of B_i denotes AVB, and the average sum of the RPMs denotes AVI, the image can be reconstructed by performing *image* = (*AVB* × *AVI*) – *AVI* × *AVB* to reconstruct the image $I(x, y)$. The equation is mathematically described as follows:

$$I(x, y) = \langle BI(x, y)\rangle - \langle B\rangle.\langle\emptyset(x, y)\rangle \tag{2}$$

Where ⟨•⟩ denotes the mean operation,
$\langle B\rangle$ is the mean of the bucket values B_i,
$\langle\emptyset(x, y)\rangle$ is the mean of the RPMs,
$BI(x, y)$ is the scalar product between B_i and $\emptyset(x, y)$,
$I(x, y)$ is the reconstructed image.

The CGIE can be implemented either with specialized hardware devices or through software simulation as we used in this paper.

B. HM and HBPs

Significant types of POMs are used in CGI, which is considered as a key to collect the measured intensities to encrypt and reconstruct the image in high quality. However, POMs with values between [0-2π] require a more complex representation (at least 8 bits per pixel), making the initialization more complex and the storage and transmission of these masks less efficient, which limits the adoption of CGI in practical applications (Liansheng, et al., 2019). In addition, because of the random nature of generating these masks, the redundancy is very high. To address these problems, an orthogonal HM with binary representation of values (+1, −1) is used to generate HBPs that serve as POMs (Zhang, et al., 2017). Because of the orthogonality of HM, the redundancy between these masks is decreased, which results in reconstructing the image with high quality by using fewer measurements (Wang and Zhao, 2016). In addition, HBPs are more efficient and require 8 times less storage than POMs for initialization due to their binary representation (1 bit per pixel). To encrypt an image with the size of (N, N) pixels, HM with order 2^k is constructed (Yu, 2019), where the condition ($N \times N = 2^k$) should be satisfied. The HM with 2nd-order is mathematically defined as:

$$H_{2^2} = \begin{bmatrix} 1 & 1 \\ 1 & -1 \end{bmatrix} \tag{3}$$

Then, the HM with order 2^k can be calculated with the recursive formula is mathematically defined as:

$$H_{2^k} = \begin{bmatrix} H_{2^{k-1}} & H_{2^{k-1}} \\ H_{2^{k-1}} & -H_{2^{k-1}} \end{bmatrix} \tag{4}$$

After obtaining the desired HM, 2^k HBPs can be extracted by rearranging each row into a 2D pattern with $N \times N$ pixels (Yu, et al., 2022). For example, as illustrated in Fig. 2. From our code, to encrypt and reconstruct an image with size (8, 8) pixels, 64 × 64 HM is generated to extract 64 HBPs with size (8, 8).

C. IWT

In cryptosystems, using traditional wavelet transform may result in distortion during the reconstruction, especially when using multilevel wavelet decomposition, resulting in quality degradation of the reconstructed image because the binary representation for the floating-point numbers is limited. Eventually, there will be energy loss during reconstruction. Even when representing the pixel values of the image in integer form, the coefficients obtained from the wavelet transform are not represented as an integer (Yunus, Firmansyah and Subiono, 2024). The significance of IWT provides an optimal solution. IWT is an integer-to-integer

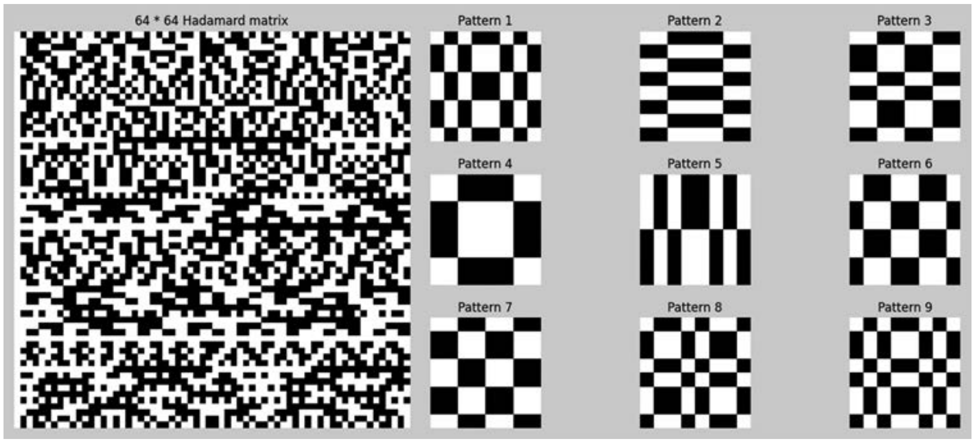

Fig. 2. Hadamard matrix and hadamard basis patterns generation and visualization from our code.

transformation, so there will be no degradation even after using multilevel decomposition.

IWT is implemented using a lifting scheme (LS) that replaces the convolution-based filter banks that used in the traditional wavelet transform, such as DWT with more computationally efficient and lossless transformation by performing simple operations (split, predict, update and merge), producing integer coefficients (Sweldens, 1996). In addition, IWT is preferable over DWT when performing XOR operation in cryptosystems because XOR only operates on integer values. DWT produces floating-point coefficients, requiring an additional step to convert them into integers, which increases computational time and may lead to precision loss, potentially reducing overall quality. By using IWT, this conversion is avoided, leading to more efficient processing and improved accuracy. In this paper, LS is performed on the Haar wavelet, and its implementation steps are detailed in the following section and illustrated in Fig. 3. On Haar wavelet, the implementation steps are outlined as follows:

Split the original image $A(i)$ into a disjoint two sequences based on odd and even indices as follows:

$$split(A(i)) = (even_i), (odd_i) \tag{5}$$

Then, the even sequence is used to predict the odd sequence that serves as high-pass filter to obtain detail signal $D(i)$ as follows:

$$D_{i+1} = odd_i - p[even_i] \tag{6}$$

Where $p[even_i]$ is the predicted value of odd_i based on $even_i$.

The idea is to find how much the original odd sequence differs from the even sequence.

Then, the detail signal $D(i)$ is used to update the even sequence that serves as low-pass filter to obtain the approximation signal $S(i)$ as follows:

$$S_{i+1} = even_i + u[odd_i] \tag{7}$$

For the inverse IWT, the $even_i$ can be obtained as follows:

$$even_i = S_{i+1} - u[D_{i+1}] \tag{8}$$

Then, odd_i can be recovered as follows:

$$odd_i = D_{i+1} - peven_i] \tag{9}$$

Finally, merge odd_i and $even_i$ to obtain A_i as follows:

$$A_i = merge\ (even_i, odd_i) \tag{10}$$

This scheme ensures lossless reconstruction with lowest calculation time and less memory taken by the system compared to the other wavelet schemes (Ananthi, et al., 2024).

D. Chaotic Maps

Chaotic maps are a field of study of mathematics where non-linear dynamic systems generate a set of random numbers that are absolutely disordered and appear irregular but are controlled by the initial seed conditions. It examines how minor variations in initial conditions can result in major different outcomes. This phenomenon is often called the "butterfly effect" (Shen, 2023).

The inherent nature of non-linear chaotic characteristics led to an increasing use of chaotic maps for image encryption, such as sensitivity to the initial conditions, pseudo-randomness, and non-periodicity (Zhang and Huo, 2019). These features motivated the researchers to propose a variety of chaotic maps with a particular focus on creating a strong random sequence for information encryption. There are two chaotic maps that we used in our system.

LM

The most popular one-dimensional chaotic LM was implemented in cryptography by (May, 1978) which led to its rise in popularity. The mathematical equation of the LM is as follows:

$$x_{n+1} = r * x_n * (1 - x_n) \tag{11}$$

The initial condition X_0 where ($X_0 \in [0, 1]$) and the control parameter r, where $0 < r \leq 4$ to control the chaotic phenomena. It has been proved by researchers that the LM exhibits the best chaotic dynamics behavior. When $r \geq 3.87$, the map becomes highly sensitive to initial conditions and exhibits strong randomness, producing non-repetitive and unpredictable sequences. For $r < 3.57$, the map enters a periodic window, and for $r > 3.57$ the system enters chaos, but there are three periodic windows within this chaotic regime as shown in Fig. 4.

The LM is an efficient, highly secured chaotic map with low computational complexity. Making it well-suited

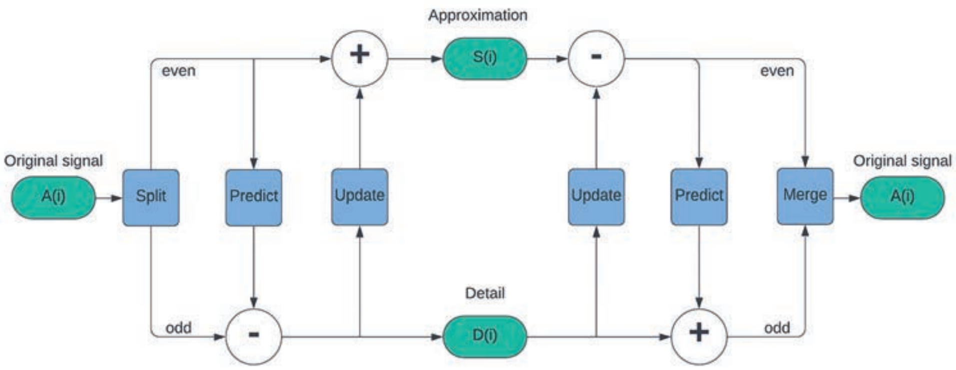

Fig. 3. The block diagram of lifting scheme.

for resource-constrained environments. The simplicity of this map ensures efficient processing without demanding significant computational resources (İnce, İnce and Hanbay, 2024).

PWLCM

PWLCM was first proposed by (Li, Chen and Mou, 2005). It is a map that is composed of multiple linear segments, allowing for a limited number of breakpoints (Wang and Chen, 2013). The mathematical equation of PWLCM is as follows:

$$G(x)=\begin{cases}\dfrac{x}{p}, & x\in[0,p]\\[2ex] \dfrac{1-x}{1-p}, & x\in[p,1]\end{cases} \tag{12}$$

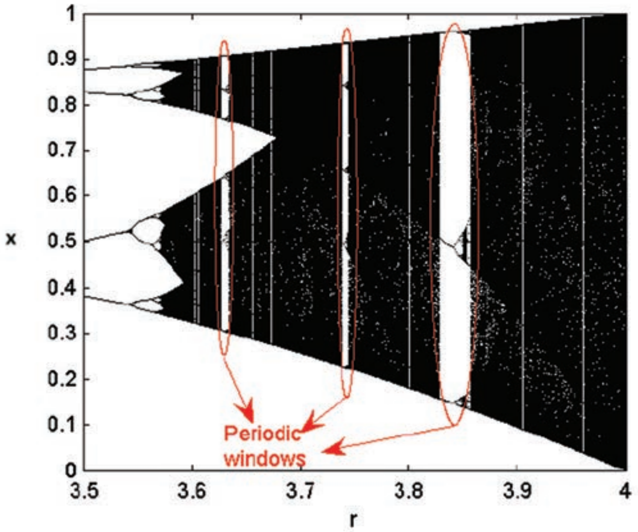

Fig. 4. The bifurcation diagram of the logistic map (Arroyo, et al., 2009).

Where p is the control parameter with values (0–1), X is the initial parameter with values (0–1).

PWLCM is linear but exhibits strong chaotic behavior with different initial conditions that make it sensitive to initial conditions, making it deterministic but unpredictable. In addition, it is simple in implementation and computationally lightweight, making it suitable for real-time applications (Chen, Tang and Yi, 2020).

IV. The Proposed Model

The proposed cryptosystem leverages the strength of advanced techniques to ensure robust and efficient encryption and decryption of large images. Optical CGI encryption technology based on wavelets and chaos theory is proposed. Below are the encryption and decryption processes as well as the algorithms used in the system.

A. Encryption Scheme

As shown in Fig. 5. The image channels are first separated, and then a two-level decomposition IWT is performed on the secret image to get the approximation sub-band (LL) and the detail sub-bands (HL, LH, HH). Second, HM with LL dimensions is generated. Subsequently, generate PWLCM sequence using LL dimensions. The indices of PWLCM sequence are used to shuffle HM. Then, taking each row of the shuffled HM and form it into a 2D array to extract HBPs and project them on the LL sub-band to get the bucket values. The bucket values are then substituted using XOR operation with the generated LM sequence. The other detail sub-bands are first substituted with a second LM then scrambled using a second PWLCM. The new two matrices are appended to form the final cipher image.

This process is repeated 3 times to encrypt image channels with different initial parameters to reach a high level of security.

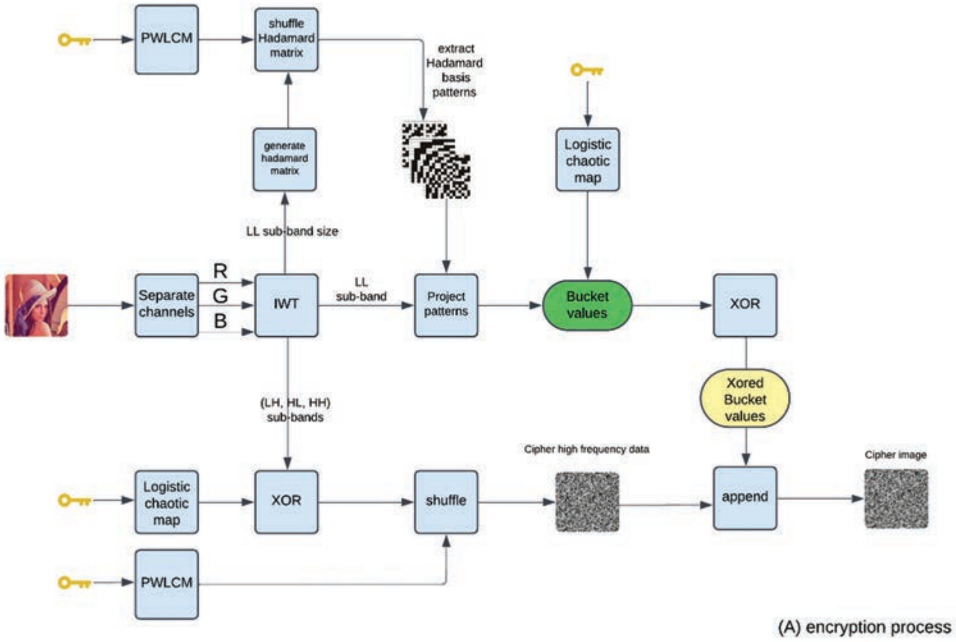

Fig. 5. The block diagram for the encryption process of the proposed system.

Channel-wise processing is performed to avoid predictable patterns across channels and minimizing ciphertext correlation.

Algorithm 1: Encryption process

```
Input: original image (A), parameters of chaotic maps as a seed of the key such as($p_0$=0.51, $r_1$= 3.991, $r_2$=3.992, $x_{0r}$=0.565, $x_{0g}$=0.566, $x_{0b}$=0.567).
Output: Cipher image(C).
Steps:
1. Read input image (A).
2. Separate (R, G, B) channels.
3. For each channel in (R, G, B):
    A. Perform $S = IWT(A)$.
    B. Separate Low frequency coefficients (LL) and the other coefficients (HL, LH, HH) as (OC).
    C. Generate HM as a measurement matrix (H).
    D. Generate chaotic map (C1) using PWLCM with ($p_0$, $x_0$) initial parameters.
    E. Scramble H using C1 indices to generate $H_{new}$.
    F. Extract HBPs from $H_{new}$ by taking each row and convert it to 2D matrix.
    G. Project HBPs on (LL) to get the bucket values ($B_i$) for each channel as follows: $B[i] = HBP[i] \times LL$.
    H. Generate chaotic map (C2) using logistic chaotic map with ($r_1$, $x_0$) initial parameters.
    I. Perform bitwise XOR on the (OC) using C2 as follows $sub(OC) = OC \wedge C2$.
    J. Generate chaotic map (C3) using PWLCM with ($p_0$, $x_0$) initial parameters.
    K. Shuffle the substituted OC with C3 to get $SH(OC)$.
    L. Generate chaotic map (C4) using logistic map with ($r_2$, $x_0$) initial parameters.
    M. Perform bitwise XOR on bucket values $S(B_i) = B_i \wedge C4$.
    N. Append $S(B_i)$ and $SH(OC)$ to get the cipher image (C).
4. Append cipher image (C) for (R, G, B) channels.
5. Transmit C to the receiving side.
```

B. Decryption Scheme

The process of retrieving the secret image begins by separating the cipher image into two parts, as illustrated in Fig. 6. The cipher image is separated into two parts. The top left part is XORed with the LM using the same shared parameters as a secret key to get the bucket values. Then, perform the CGIE scheme on the result to retrieve the LL sub-band. The detail sub-bands are retrieved using the same parameters of LM and PWLCM on the remaining information of the cipher image. Finally, appending the results and performing inverse IWT to get the secret image.

Algorithm 2: Decryption process

```
Input: cipher image (C), parameters of chaotic maps as a seed of the key such as ($p_0$=0.51, $r_1$= 3.991, $r_2$=3.992, $x_{0r}$=0.565, $x_{0g}$=0.566, $x_{0b}$=0.567).
Output: Original image(A).
Steps:
1. Read cipher image (C).
2. Separate $S(B_i)$ and $SH(OC)$..
3. Separate (R, G, B) channels.
4. For each channel in (R, G, B):
    A. Generate chaotic map (C1) using logistic map with ($r_2$, $x_0$) initial parameters.
    B. Perform bitwise XOR to get the bucket values $B_i = S(B_i) \wedge C1$.
    C. Generate chaotic map (C2) using PWLCM with ($p_0$, $x_0$) initial parameters.
    D. Scramble H using C2 indices to generate $H_{new}$.
    E. Extract HBPs from $H_{new}$ by taking each row and convert it to 2D matrix.
    F. Perform a simple linear operation on $B_i$ using HBPs to get the low frequency coefficients (LL).
    G. Generate chaotic map (C3) using PWLCM with ($p_0$, $x_0$) initial parameters.
    H. Reshuffle $SH(OC)$ to get $sub(OC)$ as follows: $sub(OC) = SH(OC) \wedge C3$.
    I. Generate chaotic map (C4) using logistic chaotic map with ($r_1$, $x_0$) initial parameters.
    J. Perform bitwise XOR on the $sub(OC)$ to get the other coefficients $OC$ as follows: $OC = sub(OC) \wedge C4$
    K. Append LL and OC to get the original signal (S).
    L. Perform $A = IIWT(S)$.
5. Merge (R, G, B) channels to get the original image (A).
```

V. QUANTITATIVE MEASURES

A. Correlation Coefficient

Correlation coefficient is a statistical measure with values between (−1 and 1), it is used to assess how strongly and in what direction the two variables are linearly related. In security, it used to measure the similarity between the contents of the images to determine how much the the encrypted image or the reconstructed image differs from the original image (Elashry, et al., 2009), 1 indicates a perfect correlation (identical images) in the same direction, zero indicates no correlation and no linear relationship between the original image and the encrypted or reconstructed image, and −1 indicates a perfect negative correlation (different images) in opposite directions.

The correlation coefficient for two different images can be calculated using the following equation:

$$C = \frac{(\sum_{i=1}^{n}((Xi - uXi) \times (Yi - uYi)}{\sqrt{\sum_{i=1}^{n}(Xi - uXi)^2} \times \sqrt{\sum_{i=1}^{n}(Yi - uYi)^2}} \tag{13}$$

Where C is the correlation coefficient value, the two images variables are (X, Y), μ is the mean of X and Y.

B. Mean Square Error (MSE)

In cryptography, MSE is a measurement used to evaluate the quality of the encryption algorithm by calculating the average squared difference between the original image and the reconstructed image to determine how much information is lost or altered during the encryption and reconstruction

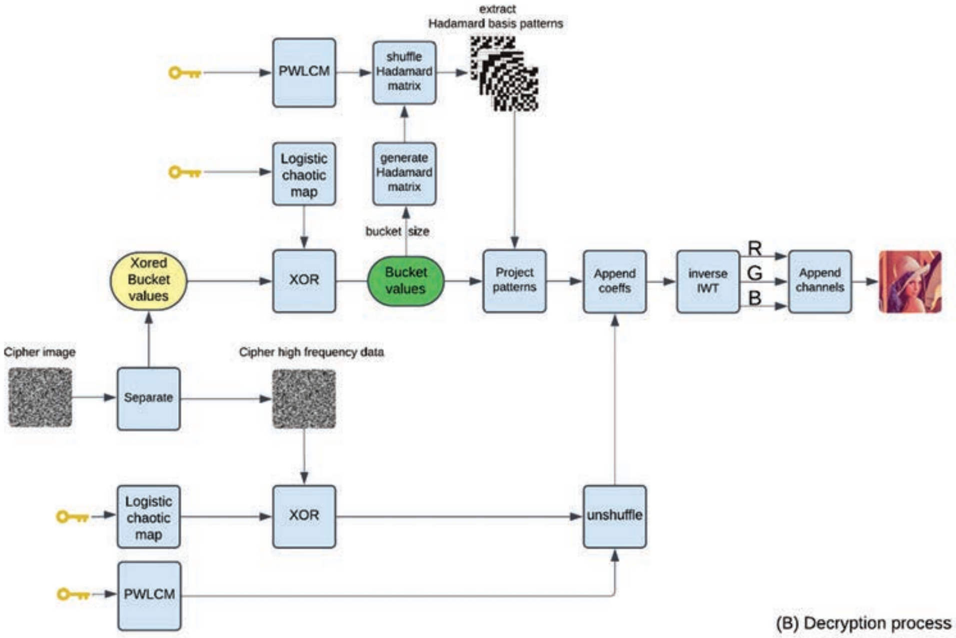

Fig. 6. The block diagram of the decryption process of the proposed system.

processes (Alghamdi, Munir and Ahmad, 2022). Lower MSE indicates better reconstruction.

The equation of MSE is as follows:

$$MSE = \frac{1}{n}\sum_{i=1}^{n}(O_i - R_i)^2 \tag{14}$$

Where (o_i) is the original image, (R_i) is the reconstructed image, (n) is the number of pixels in an image.

C. Peak Signal-to-Noise Ratio (PSNR)

In cryptography, PSNR is a widely used measurement that is used to evaluate the quality of the reconstructed image compared with the original image by measuring the ratio between the maximum possible pixel value (peak signal) and the unwanted noise that appeared in the reconstructed image (MSE).

The equation of PSNR is as follows:

$$\mathrm{PSNR} = 20.\ \log_{10}(\max_i) - 10.\ \log_{10}(MSE) \tag{15}$$

Where (Max_i) is the maximum possible pixel value of the image.

A higher PSNR value indicates better reconstruction and lower noise in the reconstructed image (Mali, Chakraborty and Roy, 2015).

D. Number of Changing Pixel Rate (NPCR)

NPCR is a measurement especially used in image encryption to evaluate the diffusion strength in the algorithm by measuring the percentage of changing pixels between two encrypted images by changing only 1 bit in the secret key (Chowdhary, et al., 2020). A higher NPCR value indicates better diffusion.

By creating a new empty matrix D(i, j) that has the same dimensions as the encrypted image. The result matrix is as follows:

$$D(i,\ j) = \begin{cases} 0 & C1(i,\ j) = C2(i,\ j) \\ 1 & C1(i,\ j) \neq C2(i,\ j) \end{cases} \tag{16}$$

Then, using the new matrix D(i, j) to calculate NPCR as follows:

$$NPCR = \frac{\sum_{i=1}^{m}\sum_{j=1}^{n} D(i,\ j)}{n \times m} \times 100\% \tag{17}$$

Where C1 is the first encrypted image, C2 is the second encrypted image, and (m, n) are the dimensions of the encrypted images.

The best NPCR value is typically >99.50%, meaning that almost all pixels in C1 differ from C2 (Saidi, et al., 2020).

E. Unified Averaged Changing Intensity (UACI)

UACI is a measurement especially used in image encryption to calculate the average intensities modified between two encrypted images by changing only 1 bit in the secret key. It gives insight about the strength of the algorithm (Khanzadi, Eshghi and Borujeni, 2014).

The UACI between two encrypted images can be calculated as follows:

$$UACI = \frac{1}{m \times n}\left[\frac{\sum_{i=1}^{m}\sum_{j=1}^{n}(C1(i,\ j) - C2(i,\ j))}{255}\right] \times 100\% \tag{18}$$

Where C1 is the first encrypted image, C2 is the second encrypted image, and (m, n) are the dimensions of the two encrypted images.

F. Entropy Analysis

In cryptography, entropy analysis is used to measure the randomness or unpredictability in the encrypted image. Higher entropy indicates a highly random distribution of

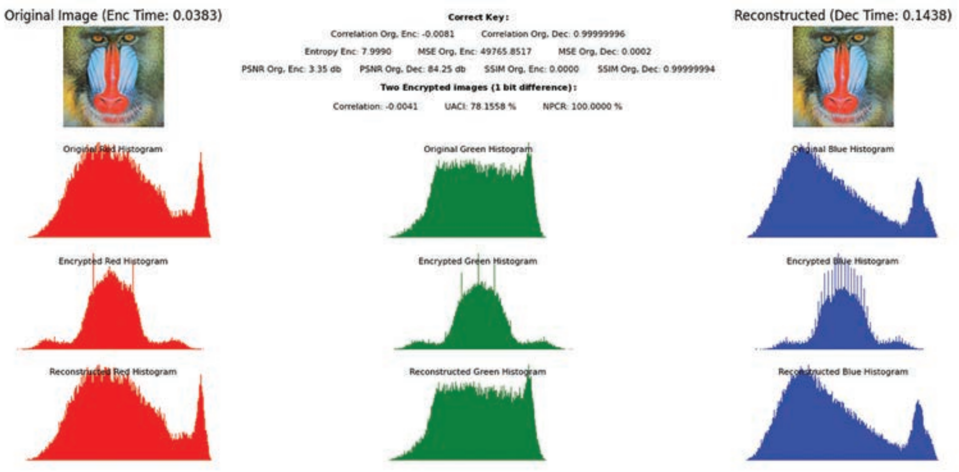

```
Correct Key:
Correlation Org, Enc: -0.0081      Correlation Org, Dec: 0.99999996
Entropy Enc: 7.9990      MSE Org, Enc: 49765.8517      MSE Org, Dec: 0.0002
PSNR Org, Enc: 3.35 db      PSNR Org, Dec: 84.25 db      SSIM Org, Enc: 0.0000      SSIM Org, Dec: 0.99999994
Two Encrypted images (1 bit difference):
Correlation: -0.0041      UACI: 78.1558 %      NPCR: 100.0000 %
```

Fig. 7. Output visualization with correct keys.

image pixels. This indicates better complexity and high security in the encryption system. While lower entropy indicates that the pixel values of the encrypted image are less random and contain predictable patterns (Dick, 2014).

The equation for calculating Entropy is as follows:

$$H(x) = -\sum_{i=1}^{N} p(x_i) log_2 p(x_i) \tag{19}$$

Where H(x) is the summation of the entropy of all discrete random variables (x_i), p(x_i) is the existence probability of the randomness in (x_i).

The negative sign before summation is to ensure that the entropy value is non-negative (Ye, Zhou and Gong, 2020).

G. Structural Similarity Index Measure (SSIM)

In cryptography, SSIM is used to measure how far the cipher image is deviated from the original image according to the structural properties. By measuring the luminance, contrast, and structural properties changes (Yuan, et al., 2019). SSIM values fall within the ranges of (−1, 1), where 1 indicates perfect similarity. 0 indicates no similarity. The formula of SSIM is as follows:

$$L(o,e) = \frac{2\mu_a\mu_c + C1}{\mu_a^2 + \mu_c^2 + C1} \tag{20}$$

$$C(o,e) = \frac{2\sigma_a\sigma_c + C2}{\sigma_a^2 + \sigma_c^2 + C2} \tag{21}$$

$$S(o,e) = \frac{\sigma_{ac} + C3}{\sigma_a\sigma_c + C3} \tag{22}$$

Where O is the original image, C is the encrypted image, μ_a and μ_c are the means of the original and encrypted images, σ_a and σ_c are the standard deviation of the original and encrypted images, σ_{ac} is the covariance of the original and encrypted images, and c1, c2, and c3 are constants used to avoid the multiplication by zero where $C1 = (K1.R1)^2$, $C2 = (K2.R1)^2$ and $C3 = K2/2$.

K1 and K2 are small variables, and R1 is the dynamic range of pixel values.

TABLE I
IMAGE DATASET

Image name	Color	Type	Dimensions
Lena	Color	tiff	512×512
Baboon	Color	tiff	512×512
Peppers	Color	tiff	512×512
Jellybeans	Color	tiff	256×256
Female	Color	tiff	256×256
Airplane	Color	tiff	512×512
Couple	Color	tiff	256×256
Female 2	Color	tiff	256×256
House	Color	tiff	256×256
House 2	Color	tiff	512×512
Sailboat	Color	tiff	512×512
Tree	Color	tiff	256×256

Finally, the SSIM can be calculated as follows:

$$SSIM = L(a,c).C(a,c).S(a,c) \tag{22}$$

VI. EXPERIMENTAL RESULTS AND ANALYSIS

To verify the feasibility and security of our encryption system, numerical experiments were carried out on this method. The proposed image encryption technique was implemented with a visual studio code environment using Python. The computer CPU was an AMD Ryzen 7 4700U, 16 GB RAM, Win 11 64-bit. A sample of output visualization of our code, as shown in Fig. 7. Contains all the measures used and the histogram analysis for the original, encrypted, and reconstructed images. The selected image dataset from the USC-SIPI Image Database is shown in Table I.

A. Security Analysis

The above-mentioned measures are used to evaluate the security and reconstruction quality of our system. To evaluate the security strength of the system, the test results as shown in Table II demonstrate that the key sensitivity of the system is very high, with only 1-bit difference between encryption keys resulting in two different cipher images with <0.006 correlation. To further validate these results, Table III provides a 95%

confidence interval analysis after performing 10 independent runs with different initial parameters for each tested image. Fig. 8. shows the output visualization using the wrong key (only 1 bit difference). To evaluate the reconstruction quality of the system, the test results presented in Table IV demonstrate that the system achieves perfect image reconstruction, indicating that it operates in a lossless manner. In addition, the XOR implementation with chaotic maps is completely reversible when the exact same parameters are used by both parties, ensuring that the original data can be accurately retrieved. This reversibility guarantees the integrity of the cryptosystem.

B. Key Space Analysis

Here we take a (256, 256) image as an example. With our system, we used a chaotic PWLCM with initial parameters (x, p). These parameters are securely exchanged between

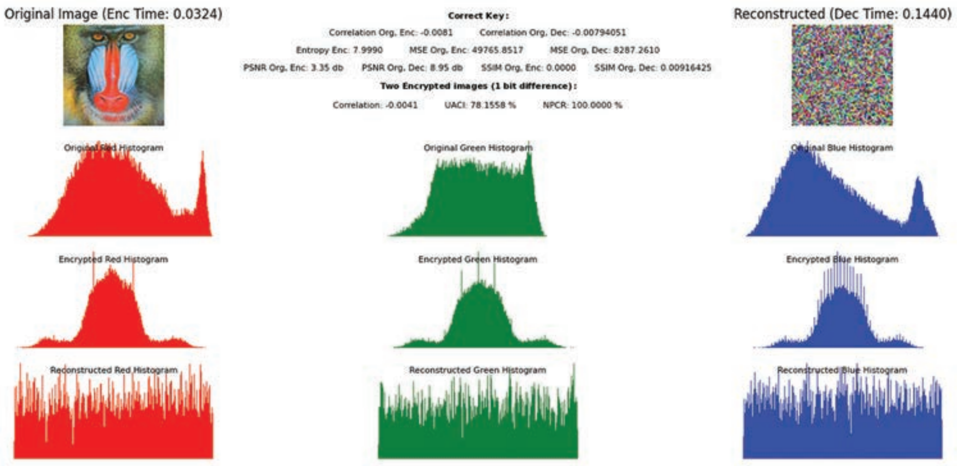

Fig. 8. Output visualization with wrong keys.

TABLE II
SECURITY TEST RESULTS

Images	**Entropy Enc**	**CC Org, Enc**	**CC Enc1, Enc2**	**MSE Org, Enc**	**PSNR Org, Enc**	**SSIM Org, Enc**	**UACI Enc1, Enc2**	**NPCR Enc1, Enc2 (%)**
Lena	7.9989	0.0013	0.0039	49175	5.43 DB	−0.000002	76.9823	100
Baboon	7.9990	−0.0081	−0.0041	49765	3.35 DB	0.000001	78.1558	100
Female	7.9988	0.0016	0.0063	35265	7.95 DB	0.000003	77.6543	100
Jellybeans	7.9983	0.0011	0.0014	39771	6.76 DB	−0.000001	78.2313	100
Peppers	7.9990	0.0008	−0.0001	41431	3.54 DB	0.000001	79.1012	100
Airplane	7.9997	0.0068	0.0001	35210	4.53 DB	−0.000001	59.4187	100
Couple	7.9989	0.0073	0.0011	35211	7.41 DB	0.000003	68.3211	100
Female2	7.9991	0.0006	0.0023	47561	3.31 DB	0.000001	78.6661	100
House	7.9984	0.0021	0.0084	31231	6.59 DB	−0.000002	73.5832	100
House2	7.9991	0.0009	−0.0011	38574	4.32 DB	0.000001	77.4390	100
Sailboat	7.9990	0.0003	0.0041	41854	5.21 DB	−0.000001	73.5832	100
Tree	7.9993	−0.0004	0.0012	47571	3.47 DB	0.000001	79.1211	100

TABLE III
RESULTS WITH A 95% CONFIDENCE INTERVAL FOR THE TESTED IMAGES WITH DIFFERENT INITIAL PARAMETERS

Images	**Entropy Enc**	**CC Org, Enc**	**CC Enc1, Enc2**	**MSE Org, Enc**	**PSNR Org, Enc**	**SSIM Org, Enc**	**UACI Enc1, Enc2**	**NPCR Enc1, Enc2 (%)**
Lena	±0.0005	±0.00075	±0.00131	±1384	±0.11	±0	±1.34	±0
Baboon	±0.0007	±0.00029	±0.00117	±1628	±0.09	±0	±1.11	±0
Female	±0.0011	±0.00092	±0.00311	±956	±0.33	±0	±2.04	±0
Jellybeans	±0.0006	±0.00106	±0.00152	±889	±0.13	±0	±2.87	±0
Peppers	±0.002	±0.00126	±0.00084	±1053	±0.21	±0	±3.25	±0
Airplane	±0.0009	±0.00191	±0.00114	±759	±0.12	±0	±2.01	±0
Couple	±0.0005	±0.00073	±0.00135	±931	±0.19	±0	±1.71	±0
Female2	±0.0009	±0.00095	±0.00127	±1355	±0.05	±0	±3.01	±0
House	±0.0005	±0.00115	±0.00232	±1249	±0.01	±0	±1.14	±0
House2	±0.002	±0.00109	±0.00301	±958	±0.29	±0	±1.31	±0
Sailboat	±0.001	±0.0007	±0.0023	±1633	±0.05	±0	±1.34	±0
Tree	±0.0009	±0.0011	±0.0008	±1282	0.19	±0	±1.29	±0

communicating parties using public key cryptography, ensuring robust security against unauthorized access. Then, the chaotic sequence generated is used to scramble the HM rows to generate a unique HM. For an image with a size of (256, 256) pixels, the LL sub-band extracted after performing two-level decomposition IWT is (64, 64) pixels. Since HM size should be equal to the power of rows and columns for the LL sub-band, this will need to generate HM with size =(2^{64}, 2^{64}) = (4096, 4096). Suppose that the attacker attempts to directly manipulate the HM by rearranging its rows and trying to reach the correct sorting of the HM to obtain all the HBPs using brute-force cracking. The probability is (2^{4096}) to obtain only the LL sub-band. This will take an enormous amount of time due to the complexity and size of the matrix. The vast number of possible rearrangements makes it extremely time-consuming for an attacker to identify any hidden patterns through brute force methods. However, the attacker may seek alternative strategies to bypass direct guessing on HM by attempting to extract the initial parameters of PWLCM. Since each parameter is encoded with 64-bit precision, the probability of obtaining the parameters (x, p) is 2^{128}. In addition, this is only one layer of the system. The attacker still needs to break the substitution layer with a probability of 2^{128} for the parameter (x, u) of the chaotic LM to get only the LL sub-band of the secret image. The other coefficients are also encoded with two chaotic maps that need to be extracted with probability of 2^{128} for each map.

TABLE IV
Reconstruction Quality Test Results

Images	Correlation Org, Dec	MSE Org, Dec	PSNR Org, Dec	SSIM Org, Dec
Lena	0.99999997	0.0002	84.79 DB	0.99999995
Baboon	0.99999996	0.0002	84.25 DB	0.99999994
Female	0.99999995	0.0003	83.94 DB	0.99999994
Jellybeans	0.99999999	0.0001	85.15 DB	0.99999997
Peppers	0.99999992	0.0004	82.11 DB	0.99999991
Airplane	0.99999994	0.0002	83.21 DB	0.99999995
Couple	0.99999995	0.0002	84.76 DB	0.99999996
Female 2	0.99999992	0.0004	81.32 DB	0.99999993
House	0.99999996	0.0001	84.98 DB	0.99999996
House 2	0.99999998	0.0001	84.79 DB	0.99999998
Sailboat	0.99999994	0.0002	82.56 DB	0.99999995
Tree	0.99999996	0.0002	84.35 DB	0.99999995

MSE: Mean square error, PSNR: Peak signal-to-noise ratio, SSIM: Structural similarity index measure

C. System's Linearity Analysis

In CGIE, ensuring the system's security against unauthorized parties is important. Even if they manage to obtain partial information of the secret key, also called the Eavesdropping Ratio (ER). To test the linearity of the system, we conducted another experimental approach by removing the substitution layer to validate the impact of this layer within our system. As shown in (Fig. 9a), if the

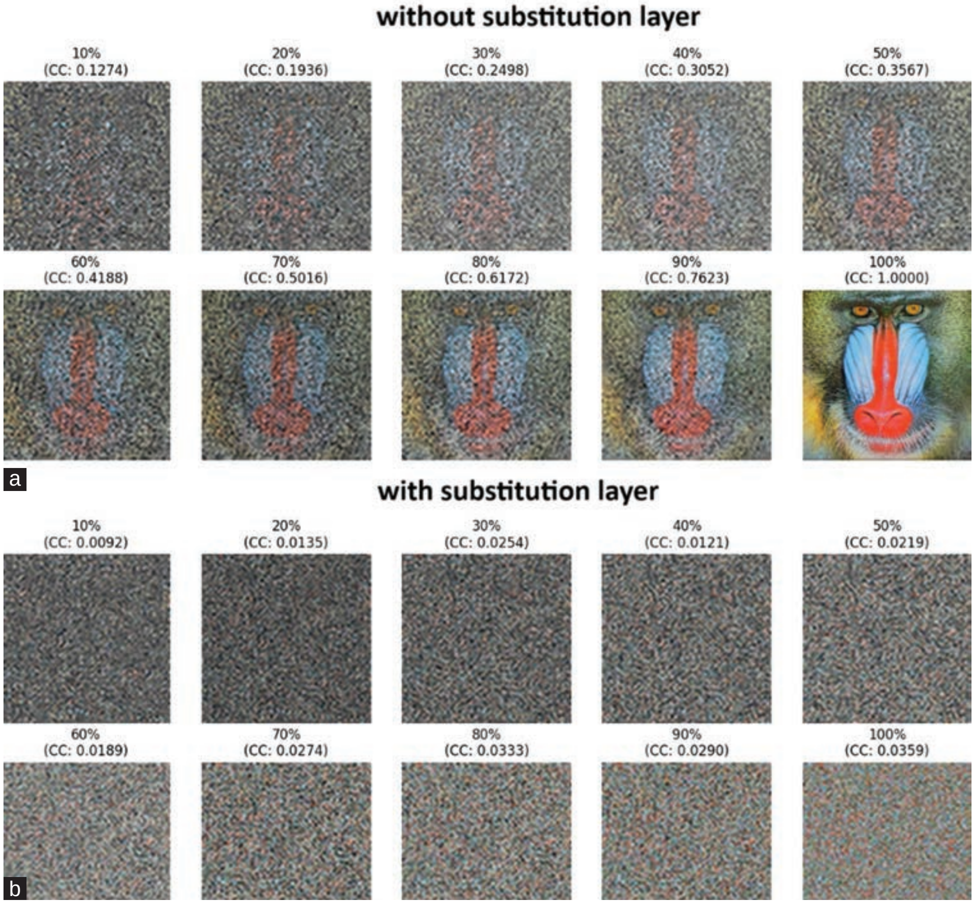

Fig. 9. Percentage of correct Hadamard basis patterns obtained by the eavesdropper. (a) Without the substitution layer, (b). With the implementation of the substitution layer.

attacker was able to get a percentage of HBPs randomly and wishes to decrypt only the LL sub-band. With ER = 30%, the secret image still appears distorted, with a correlation coefficient of 0.2498. The reconstructed image information remains incomplete. With ER = 50%, the image will become more recognizable with a correlation coefficient of 0.3567, and the hacker starts to recognize a small amount of image information, demonstrating improved approximation.

ER has further been promoted to 55%, 80% in (Chen and Chen, 2015; Zhao, et al., 2015) by Chen and Zhao, respectively. The problem still exists. Earlier, in the study by Huang and Han, a comparison was conducted between their method, which utilizes Cake-Cutting HM, and other transforms, such as DCT and HM. Notably, at ER = 60, the image information begins to be visible (Huang and Han, 2024). In contrast, as shown in (Fig. 9b), our proposed system ensures no information is obtained. Even with ER = 100%, the correlation coefficient is only 0.0359 due to the implementation of the second security layer (substitution layer).

VII. CONCLUSION AND FUTURE RECOMMENDATIONS

In this paper, we designed a new hybrid CGIE scheme to enhance encryption efficiency while significantly reducing computational complexity. By leveraging the orthogonality of Hadamard matrices, the limitation requiring the transmission of all the patterns is eliminated, and the number of measurements used for both encryption and reconstruction is minimized due to the non-repetitive HBPs. In addition, IWT preserves an integer-to-integer mapping, allowing lossless transformation and enabling more efficient encryption. Since XOR operations are inherently faster when applied to integer values, this approach significantly reduces computational overhead compared to methods that require floating-point conversions, making the encryption process both quicker and more efficient. Our approach strategically achieves a balance between security strength and low computational complexity while preserving the robust encryption strength of CGIE. The optimized framework not only improves computational feasibility but also enhances the adaptability of CGIE within cryptosystems, paving the way for broader adoption in encryption applications where efficiency and resilience are critical. However, the presented algorithm lies in the use of HM, which requires the input dimensions to be power of two (e.g., 64, 128, 256, etc.). Consequently, if the LL sub-band obtained from two-level IWT does not meet this criterion, the encryption process cannot be directly applied without resizing or padding.

Future recommendations include exploring a new alternative transform that supports arbitrary-sized dimensions, such as another orthogonal transform or custom-sized Hadamard-like matrices. In addition, replacing chaotic maps with a stochastic approach may enhance security while improving computational efficiency, offering a more secure and flexible framework.

REFERENCES

Alghamdi, Y., Munir, A., and Ahmad, J., 2022. A lightweight image encryption algorithm based on chaotic map and random substitution. *Entropy*, 24(10), p. 1344.

Ananthi, A., Subathra, M.S., Thomas George, S., and Sairamya, N.J., 2024. Entropy-based feature extraction for classification of EEG signal using lifting wavelet transform. *Przeglad Elektrotechniczny*, 9, pp. 146-150.

Arroyo, D., Alvarez, G., Li, S.J., Li, C.Q., and Fernandez, V., 2009. Cryptanalysis of a new chaotic cryptosystem based on ergodicity. *International Journal of Modern Physics B*, 23, pp. 651-659.

Chen, W., and Chen, X., 2015. Ghost imaging using labyrinth-like phase modulation patterns for high-efficiency and high-security optical encryption. *Europhysics Letters*, 109(1), p. 14001.

Chen, Y., Tang, C., and Yi, Z., 2020. A novel image encryption scheme based on PWLCM and standard map. *Complexity*, 23, p. 3026972.

Chowdhary, C.L., Virenbhai Patel, P., Kathrotia, K.J., Attique, M., Perumal, K., and Ijaz, M.F., 2020. Analytical study of hybrid techniques for image encryption and decryption. *Sensors*, 20(18), p. 5162.

Clemente, P., Durán, V., Torres-Company, V., Tajahuerce, E., and Lancis, J., 2010. Optical encryption based on computational ghost imaging. *Optics Letters*, 35, pp. 2391-2393.

Dick, B., 2014. Inverting ion images without Abel inversion: Maximum entropy reconstruction of velocity maps. *Physical Chemistry Chemical Physics*, 16(2), pp. 570-580.

Duran, V., 2011. Optical encryption with compressive ghost imaging. In: *The European Conference on Lasers and Electro-Optics*. Optica, United States, p. CH3-4.

Elashry, I.F., Farag Allah, O.S., Abbas, A.M., El-Rabaie, S., and Abd El-Samie, F.E., 2009. Homomorphic image encryption. *Journal of Electronic Imaging*, 18(3), p. 033002.

Guo, Z., Chen, S.H., Zhou, L., and Gong, L.H., 2024. Optical image encryption and authentication scheme with computational ghost imaging. *Applied Mathematical Modelling*, 131, pp. 49-66.

Huang, H., and Han, Z., 2024. Computational ghost imaging encryption using RSA algorithm and discrete wavelet transform. *Results in Physics*, 56, p. 107282.

İnce, C., İnce, K., and Hanbay, D., 2024. Novel image pixel scrambling technique for efficient color image encryption in resource-constrained iot devices. *Multimedia Tools and Applications*, 83(29), pp. 72789-72817.

Jiang, S., Wang, Y., Long, T., Meng, X., Yang, X., Shu, R., and Sun, B., 2017. Information security scheme based on computational temporal ghost imaging. *Scientific Reports*, 7(1), p. 7676.

Yi, K., Leihong, Z., Dawei, Z., 2018. Optical encryption based on ghost imaging and public key cryptography. *Optics and Lasers in Engineering*, 111, pp. 58-64.

Kang, Y., Zhang, L., Ye, H., Zhang, D., and Zhuang, S., 2021. Ghost imaging-based optical cryptosystem for multiple images using integral property of the Fourier transform. *Chinese Physics B*, 30(12), p. 124207.

Khanzadi, H., Eshghi, M., and Borujeni, S.E., 2014. Image encryption using random bit sequence based on chaotic maps. *Arabian Journal for Science and Engineering*, 39(2), pp. 1039-1047.

Leihong, Z., Xiao, Y., Dawei, Z., and Jian, C., 2018. Research on multiple-image encryption scheme based on Fourier transform and ghost imaging algorithm. *Current Optics and Photonics*, 2(4), pp. 315-323.

Li, S., Chen, G., and Mou, X., 2005. On the dynamical degradation of digital piecewise linear chaotic maps. *International Journal of Bifurcation and Chaos*, 15(10), pp. 3119-3151.

Li, X., Meng, X.F., Yang, X., Yin, Y., Wang, Y., Peng, X., He, W., Dong, G., and Chen, H., 2016. Multiple-image encryption based on compressive ghost imaging and coordinate sampling. *IEEE Photonics Journal*, 8(4), pp. 1-1.

Liansheng, S., Cong, D., Minjie, X., Ailing, T., and Anand, A., 2019. Information encryption based on the customized data container under the framework of computational ghost imaging. *Optics Express*, 27(12), pp. 16493-16506.

Liu, J., Wang, L., and Zhao, S., 2022. Secret sharing scheme based on spread spectrum ghost imaging. *Applied Optics*, 61(24), pp. 7102-7107.

Mali, K., Chakraborty, S., and Roy, M., 2015. A study on statistical analysis and security evaluation parameters in image encryption. *International Journal of Scientific and Engineering Research,* 3, pp. 339-343.

May, R.M., 1978. *Exploiting Natural Populations in an Uncertain World*. Elsevier, North Holland.

Miao, M.K., Gong, L.H., Zhang, Y.J., and Zhou, N.R., 2025. Image encryption and authentication scheme based on computational ghost imaging and lifting wavelet transform. *Optics and Lasers in Engineering*, 184, p. 108560.

Saidi, R., Cherrid, N., Bentahar, T., Mayache, H., and Bentahar, A., 2020. Number of pixel change rate and unified average changing intensity for sensitivity analysis of encrypted insar interferogram. *Ingenierie des Systemes d'Information*, 25(5), pp. 601-607.

Shapiro, J.H., 2008. Computational ghost imaging. *Physical Review Atomic*, 78(6), p. 061802.

Shen, B.W., 2023. *Attractor Coexistence, Butterfly Effects, and Chaos (ABC): A Review of Lorenz and Generalized Lorenz Models (published) Attractor Coexistence, Butterfly Effects, and Chaos (ABC): A Review of Lorenz's Models from 1960 to 2008*.

Sweldens, W., 1996. The lifting scheme: A custom-design construction of biorthogonal wavelets. *Applied and Computational Harmonic Analysis*, 3, pp. 186-200.

Tao, Y., Yang, X., Meng, X.F., Wang, Y., Yin, Y., and Dong, G., 2020. Plaintext-related multiple-image encryption based on computational ghost imaging. *Journal of Modern Optics*, 67(5), pp. 394-404.

Wang, L., and Zhao, S., 2016. Fast reconstructed and high-quality ghost imaging with fast Walsh-Hadamard transform. *Photonics Research*, 4(6), p. 240.

Wang, X., and Chen, D., 2013. A parallel encryption algorithm based on piecewise linear chaotic map. *Mathematical Problems in Engineering*, 2013, p. 537934.

Ye, H.S., Zhou, N.R., and Gong, L.H., 2020. Multi-image compression-encryption scheme based on quaternion discrete fractional Hartley transform and improved pixel adaptive diffusion. *Signal Processing*, 175, p. 107652.

Yu, W.K., 2019. Super sub-nyquist single-pixel imaging by means of cake-cutting hadamard basis sort. *Sensors (Switzerland)*, 19(19), p. 4122.

Yu, W.K., Cao, C., Yang, Y., Wei, N., Wang, S.F., and Zhu, C.X., 2022. Single-pixel imaging based on weight sort of the Hadamard basis. *Image and Video Processing*, 2203, p. 04659.

Yuan, X., Zhang, L., Chen, J., Wang, K., and Zhang, D., 2019. Multiple-image encryption scheme based on ghost imaging of Hadamard matrix and spatial multiplexing. *Applied Physics B*, 125(9), p. 174.

Yunus, M., Firmansyah, M.I.D., and Subiono., 2024. A cryptography using lifting scheme integer wavelet transform over min-max-plus algebra. *Kybernetika*, 60(5), pp. 576-602.

Zhang, J., and Huo, D., 2019. Image encryption algorithm based on quantum chaotic map and DNA coding. *Multimedia Tools and Applications*, 78, pp. 15605-15621.

Zhang, L., Wang, Y., and Zhang, D., 2022. Research on multiple-image encryption mechanism based on Radon transform and ghost imaging. *Optics Communications*, 504, p. 127494.

Zhang, L., Yuan, X., Wang, K., and Zhang, D., 2019. Multiple-image encryption mechanism based on ghost imaging and public key cryptography. *IEEE Photonics Journal,* 11(4), pp. 1-14.

Zhang, Z., Wang, X., Zheng, G., and Zhong, J., 2017. Hadamard single-pixel imaging versus Fourier single-pixel imaging. *Optics Express*, 25(16), pp. 19619-19639.

Zhao, S., Wang, L., Liang, W., Cheng, W.W., and Gong, L., 2015. High performance optical encryption based on computational ghost imaging with QR code and compressive sensing technique. *Optics Communications*, 353, pp. 90-95.

Zhu, J., Yang, X., Meng, X., Wang, Y., Yin, Y., Sun, X., and Dong, G., 2018. Computational ghost imaging encryption based on fingerprint phase mask. *Optics Communications*, 420, pp. 34-39.

Enhanced Pneumonia Detection from Chest X-rays Using Machine Learning and Deep Neural Architectures

Kamal Upreti[1†], Anju Singh[2], Divakar Singh[3], Preety Shoran[1], Uma Shankar[4],
Meenakshi Yadav[5] and Rituraj Jain[6]

[1]Department of Computer Science, CHRIST (Deemed to be University),
Delhi NCR Campus, Ghaziabad, India

[2]Department of Computer Science and Engineering, Lakshmi Narain College of Technology, Kalchuri Nagar,
Raisen Road, Bhopal, Madhya Pradesh, India

[3]Department of Computer Science and Engineering, university Institute of Technology, Barkatullah University,
Bhopal, Madhya Pradesh, India

[4]Department of Management, Faculty of Management and Social Sciences, Qaiwan International University,
Sulaimanyah, Kurdistan, Iraq

[5]Department of Information Technology, Galgotias College of Engineering and Technology,
Greater Noida, India

[6]Department of Information Technology, Marwadi University,
Rajkot, Gujarat, India

***Abstract*—*Pneumonia* is a major worldwide health concern, particularly for vulnerable groups such as babies and the elderly. Despite advances in medical imaging, diagnosing pneumonia using a chest X-ray remains difficult, due to the subtle presentation of symptoms and the variety in picture interpretation. This study utilizes modern machine learning can improve the accuracy and speed of diagnosing pneumonia using chest X-ray images. Utilizing a comprehensive dataset from the Kaggle online repository, consisting of over 5,000 annotated images, we evaluate the efficacy of various machine learning models including deep convolutional neural networks (CNN) and ensemble learning techniques. Our findings indicate that models like the Fuzzy opponent histogram filter combined with Logistic model trees (LMT) achieved the highest accuracy at 96.97%, while the deep learning-based Lenet (CNN) with LMT closely followed at 95.85%. The study aims to improve diagnostic precision, reduce interpretation discrepancies, and facilitate faster clinical decision-making by identifying the most effective machine learning approaches for real-world applications in healthcare settings.**

***Index Terms*—Artificial intelligence, Chest X-rays, Fuzzy opponent histogram filter, Machine learning, Pneumonia.**

ARO-The Scientific Journal of Koya University
Vol. XIII, No. 1 (2025), Article ID: ARO.12174. 10 pages
DOI: 10.14500/aro.12174
Received: 05 April 2025; Accepted: 18 May 2025
Regular research paper; Published: 10 June 2025
[†]Corresponding author's e-mail: kamal.upreti@christuniversity.in

I. INTRODUCTION

Pneumonia is a major health concern across the world, accounting for the majority of illnesses and deaths, particularly among young children and the elderly. Chest X-ray imaging is commonly used for diagnosis; however, it can be difficult to interpret, especially if the symptoms are mild. Recent breakthroughs demonstrated that the application of machine learning algorithms considerably enhances the capacity of chest X-ray imaging to identify pneumonia; hence, it accelerates the diagnostic process and leads to dramatically better patient outcomes (Singh, et al., 2024). Another kind of pneumonia is acinetobacter baumannii, which is notable for its resistance to strong antibiotics such as carbapenems and colistin. This resistance complicates therapy, highlighting the need for more effective therapeutic procedures. Although utilizing a mixture of antibiotics has been somewhat successful, the outcomes vary and are not always constant (Shein, et al., 2024). Pneumonia is a serious respiratory disease that can take many different forms, including bacterial pneumonia, virus-induced pneumonia, mycoplasma-caused pneumonia, and others that may be parasitic or fungal in origin. This illness can also be classified according to where it was acquired: In a hospital, in the community, or by aspiration. Every year, this condition causes over a million hospital admissions in the United States, as well as half a million fatalities.

Globally, the effect is even more striking, with the World Health Organization stating in 2019 that pneumonia is the main cause of mortality among children under five, accounting for 14% of all fatalities in this age range (Yang, et al., 2020). This highlights the crucial need for improved diagnostic and treatment options.

An X-ray picture is the most trustworthy diagnostic tool due to its low cost and comprehensive nature when compared to other traditional diagnostic procedures. X-rays are valuable because they offer good pictures of the lungs, allowing healthcare personnel to better diagnose and assess the severity of the infection (Rajpurkar, et al., 2017). In reality, radiologists devote a significant amount of time and attention to scrutinizing and interpreting X-ray pictures, which may be exhausting and can lead to dispute among physicians over the outcome. Early pneumonia identification using deep learning-based algorithms would considerably simplify the procedure and assist deliver treatment more quickly, thereby lowering mortality and saving lives (Hasan, et al., 2021). Even now, pneumonia remains the most frequent illness in areas such as Sub-Saharan Africa and South Asia, affecting both the elderly and the young. Artificial intelligence (AI), especially the use of neural networks and deep learning technologies, has transformed how medical pictures are processed (Pant, et al., 2020). In the health industry, AI and machine learning are increasingly being used for biomedical image processing to improve diagnosis accuracy and efficiency (Racic, et al., 2021). Computer vision is an excellent high-speed, objective evaluation technique for all types of pneumonia, whether viral, bacterial, or fungal, to improve diagnosis and therapy. Furthermore, the COVID-19 pandemic has expedited the development of computer-aided diagnosis techniques. These mostly use convolutional neural networks (CNN) and deep learning approaches to improve pneumonia detection and classification. It emphasizes its involvement in global health emergencies (Szepesi and Szilágyi, 2022). Machine learning techniques are increasingly being used to enhance pneumonia detection with chest X-rays. Deep learning algorithms are effective at detecting specific patterns such as alveolar or interstitial infiltration, which frequently indicate bacterial and viral pneumonia, respectively. Sufficiency in terms of data used for training aided in the development of distinctions and distinguishing between bacterial and viral causes (Rahman, et al., 2020). Transfer learning has also shown to be a valuable method for biological picture categorization. This strategy includes adapting and reusing a model developed on a big dataset, such as imagenet, to fit other but related objectives. Furthermore, ensemble approaches, which combine judgments from several classifiers, are utilized to harness discriminative information that all base classifiers may possess, hence enhancing prediction accuracy (Kundu, et al., 2021). The major goal of this research is to use machine learning and AI to improve the identification and categorization of pneumonia from chest X-ray images, ultimately improving treatment results and decreasing death rates. The study is designed to begin by introducing the literature on hassle detection and evaluation, followed by an in-depth methodological section that explains statistics pre-processing, feature extraction strategies, and model assessment methodologies. The repercussions section provides a comparative evaluation of the overall performance metrics among unique machine learning models, which leads into a full discussion of the findings' significance for medical exercise and future research possibilities.

II. Literature Review

The biggest problem of overfitting in computer-assisted vision applications occurs, especially when working with limited labeled data. This is compensated for by applying augmentation techniques such as image data augmentation, which add new samples to the dataset, increase its size and diversity, and help the network learn generalizable features. Such techniques have been well-tested across a range of applications including image classification, object recognition, and semantic segmentation (Kumar, et al., 2024). In addition, the latest research (Li, et al., 2023) has been conducted on the potential applications of artificial general intelligence models in medical imaging and healthcare. This paper discusses the capabilities of large language models, large vision models, and large multimodal models, which are discussed in detail along with their key features, enabling technologies, and development trajectories. It also indicates a roadmap for their evolution and practical application in the medical field by discussing future research directions and possible impacts on health care.

Another study by (Sailunaz, et al., 2024) describes a statistical deformation model-based data augmentation technique for volumetric medical picture segmentation. This approach considerably enhances the automatic segmentation of organs at risk in computed tomography (CT) scans, solving the issue of restricted data availability. It utilizes varied and enhanced data manipulation on CT scans from a limited number of patients in improving the approach's precision in treatment planning, with minimized adverse impacts of radiation on non-targeted organs. The "Healthcare Federated Ensemble Internet of Learning Cloud Doctor System" is a worldwide cloud-based diagnostic machine learning system that uses Internet of Things (IoT) devices to produce precise and reliable diagnoses. It applies a federated ensemble learning strategy for creating a decentralized global prediction model from local healthcare models, which ensures biomedical security and integrity of the patient data. In performance validations, the proposed approach achieved exceptional accuracies of 99.24% with Chest X-ray data and 99.0% with magnetic resonance imaging (MRI) brain tumor data, thus proving its adequacy for precise diagnostics in IoT-enabled healthcare environments (Khan et al., 2024).

Another proposal for a hybrid deep learning model was put forth for pediatric pneumonia detection based on the architecture of EfficientNetV2. It extracts features from radiographic images and then combines them through the use of a combined classifier using SVM and RFT. Its accuracy improves 4% better than earlier approaches and has also performed well with unknown datasets (Ravi, 2024). Cardiovascular diseases are the leading cause of death worldwide, accounting for 31% of all deaths annually, so early detection is critical for proper treatment (Selvanandhini and Karthikeyan, 2024). Combining medical research with machine learning provides holistic views of treatment outcomes and important risk factors. Advanced classification techniques developed using machine learning can be used to detect diseases early on, enabling customized preventive measures.

The collaboration of data scientists, medical professionals, and regulatory bodies is important to deal with issues of data privacy and interpretability of models. Furthermore, the number of innovative research is produced to the development of the Hybrid Deep Neural Network (VGG16-PCA-PB3C), which has dramatically increased the accuracy and speed of leukemia genomes (Kaur and Singh, 2024). In this model, feature extraction is done with the help of the Visual Geometry Group and dimensionality reduction is done by the help of principal component analysis, and training it is done by parallel Big-Bang-Big-Crunch optimization technique. The algorithm has been tested on the Classification of Normal versus Malignant Cells dataset and achieved 95% accuracy and 94% precision, thereby helping clinicians to improve the accuracy of the classification of leukemia.

Further, research into transfer learning techniques aims at verifying how successful it will be for various forms of brain tumor detection; more so on early diagnosis based on the usage of pre-trained models, such as VGG-16, VGG-19, Inception-v3, ResNet-50, DenseNet, and MobileNet on classifying MRI data with good precision. Such efforts again mark an area that recognizes how new-generation ML tools and methodologies contribute toward streamlining medical diagnostic methods. The study in reference (Shamshad, et al., 2024) is aimed to improve the accuracy of treatment planning and patient outcomes by using the best possible approaches for accurate and automated analysis of brain tumors. It is noted that the model VGG-16 surpasses earlier methods, yielding the highest accuracy at 97% while it only consumes 22% of the processing time used by previous techniques.

In another study, (Venkatraman and Reddy, 2024) uses the SVM and VGG16 classifiers to improve the outcome of lung cancer detection. By using a hybrid approach on the dataset "IQ-OTH/NCCD," this model efficiently distinguishes between aggressive, benign, and normal cases, showing how combining traditional machine learning with deep learning addresses the issues of accuracy and efficiency and renders it a significant improvement on present approaches. Further medical imaging innovations are presented in (El-Ghandour and Obayya, 2024), where a new pneumonia classification approach uses three optimized pre-trained CNN models combined with the XGBoost algorithm. Bayesian optimization is used to fine-tune each CNN model so that the feature representation is optimized while general features are lost to the minimum. Excellent results of the technique were achieved with a correct classification rate of 99.15%, accuracy of 99.53%, sensitivity of 99.30%, and an area under the curve (AUC) of 0.9972%, which can aid radiologists in confirming pneumonia diagnoses more reliably.

Moreover, the deep learning model "PneuCoNet," which is proposed by (Dasgupta and Sen, 2024), detects pneumonia, COVID-19, or normal cases with 93% accuracy through chest X-rays. The present model has been improved to treat critical respiratory disorders. The CNNs used in (Deepak, 2024) are to aid in the earlier detection of pneumonia. It is done using the transfer learning to process datasets to develop a multi-classification model that includes SqueezeNet, ResNet-50, and EfficientNet-b0. This model classifies chest X-rays into Normal/Abnormal and specific types of pneumonia, with an astonishing 99% accuracy in the detection of Normal/Abnormal X-rays and a 97% accuracy in the identification of specific bacterial or viral pneumonia conditions, ultimately enhancing the precision of diagnosis and response time in medical environments.

Using medical imaging has revealed the challenges in diagnosis, mainly due to the variable presentation of pneumonia, which often closely mimics other respiratory conditions and easily leads to diagnostic errors. Although such studies are listed in Table I, more yet to be tapped potential from combining ensemble methods and transfer learning in machine learning models to further enhance accuracy and reliability into real settings. This research bridges this gap by systematically evaluating the efficacy of these integrated machine learning approaches on a diverse clinical dataset, thereby enhancing the precision and dependability of pneumonia diagnoses and potentially improving patient outcomes in clinical practice.

III. METHODOLOGY

This research uses an image mining technique to classify X-ray images as either showing pneumonia or normal. Image mining is the process of extracting valuable patterns and insights from image data, which can be particularly useful in medical diagnostics. The study focuses on two distinct categories of X-ray images. Fig. 1 in the study illustrates the types of images analyzed:

- Pneumonia infected Fig. 1 is an X-ray image that demonstrates typical characteristics of pneumonia, such as consolidation or infiltration patterns in the lungs. Such visual cues are vital for the diagnosis of pneumonia; thus, the healthcare provider will be able to identify the infected patients promptly.
- Normal image: They are X-rays that show no pneumonia or abnormalities. They help to establish control in the study. This will set the accuracy of the image mining technique in its ability to discriminate between healthy lung tissues and those affected.

A. Dataset

Dataset description

The study utilizes a comprehensive dataset sourced from the Kaggle online repository, consisting of 5,216 chest X-ray images. These images are categorized into four distinct classes, reflecting various diagnostic categories relevant to the study.

Class distribution

The dataset contains 3,875 images from patients diagnosed with pneumonia, which were the main target

TABLE I
EXISTING STUDIES RELATED TO THE CONTRIBUTION OF AI AND ML IN THE HEALTHCARE ENVIRONMENT

References	Focus area	Techniques	Key features	Outcomes	Application
(Kumar, et al., 2024)	Computer vision	Data augmentation	Enhances variety, reduces overfitting	Effective in object recognition and segmentation	Image processing
(Li, et al., 2023)	Artificial general intelligence in healthcare	Large language models, large vision/multimodal models	Broad AI integration	Potential revolution in medical AI applications	Medical imaging
(Sailunaz, et al., 2024)	Medical imaging	Statistical deformation model	Realistic data augmentation	Improved organ segmentation accuracy	CT scans
(Khan et al., 2024)	IoT in healthcare	FDEIoL, federated learning	Combines IoT for global model accuracy	High accuracy in diagnostics	IoT healthcare systems
(Ravi, 2024)	Pediatric pneumonia	EfficientNetV2, SVM, RFT	Integrates features into a stacked classifier	Outperforms previous models by 4% in accuracy	Pediatric diagnostics
(Selvanandhini and Karthikeyan, 2024)	CVD early detection	Machine learning and medical research	Combines clinical and data science	Enhances early detection and interventions	Cardiovascular health
(Kaur and Singh, 2024)	Leukemia diagnosis	Hybrid deep NN (VGG16-PCA-PB3C)	Feature extraction and dimensionality reduction	Accuracy of 95%, precision of 94%	Leukemia detection
(Shamshad, et al., 2024)	Brain tumor analysis	VGG-16, transfer learning	Optimal approaches for automated analysis	Best accuracy (97%) and efficiency	Brain tumor diagnosis
(Venkatraman and Reddy, 2024)	Lung cancer detection	SVM, VGG16	Hybrid model, distinguishes case types	Improves accuracy and efficiency	Lung cancer diagnosis
(El-Ghandour and Obayya, 2024)	Pneumonia classification	Optimized CNNs, XGBoost	Bayesian optimization for feature representation	High classification rate and accuracy	Pneumonia diagnosis
(Dasgupta and Sen, 2024)	Critical condition diagnosis	PneuCoNet	Classifies X-rays with deep learning	Accuracy of 93% in identifying conditions	Diagnostic imaging
(Deepak, 2024)	Pneumonia detection	CNNs, transfer learning	Multiclassification model	Accurate detection of pneumonia phases	Pneumonia screening

FDEIoL: Federated ensemble internet of learning cloud doctor system, CVD: Cardiovascular diseases, PCA: Principal component analysis, CNNs: Convolutional neural networks, IoT: Internet of Things

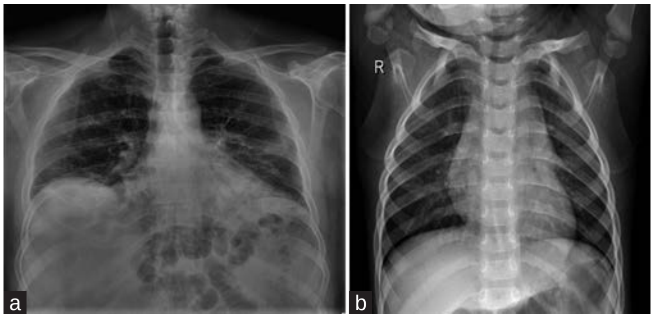

Fig. 1. (a) Pneumonia infected. (b) Normal. Examples of X-ray images used in the study, with (a) showing a pneumonia-infected image and (b) displaying a normal image.

of the study for the detection of pneumonia and 1,341 images of healthy people, used as control samples to help develop the classification models. Despite an imbalanced distribution between pneumonia cases (3,875) and healthy individuals (1,341), the dataset still enabled model training with reasonable class separation. However, due to the class skew toward pneumonia, the model's learning is biased toward the majority class, and the detection process may favor pneumonia classification. To mitigate this, class weights and performance metrics such as precision, recall, and F1-score were used for a more holistic evaluation of robustness.

B. Data Representation

The dataset in Fig. 2 is treated as a collection of features, which are the X-ray images; every image would be considered as a transaction of the features in this approach. This simplifies the analysis since it considers repeatable and recognizable patterns in images. Every single image is represented by a code of the sort which describes classification; "A" for an infected pneumonia status, and "D" indicates the normal kind. This descriptive type of classification method helps keep organized the dataset such that it does not require unnecessary lengthy processing as well as subsequent analysis.

This study treats the images as transactional features using a method, which is equivalent to the way an item is considered in market basket analysis, as every item of the transaction would be analyzed according to its frequency and association with other features of the transaction that is the image. This approach enables the use of data mining techniques, such as classification and pattern recognition to differentiate between pneumonia-infected and normal images based on their inherent characteristics. This methodology not only improves the efficiency of the diagnostic process but also enhances the accuracy with which these conditions are identified and classified.

C. Feature Extraction

The raw X-ray images are subjected to a series of feature extraction techniques to reduce the data dimensionality and

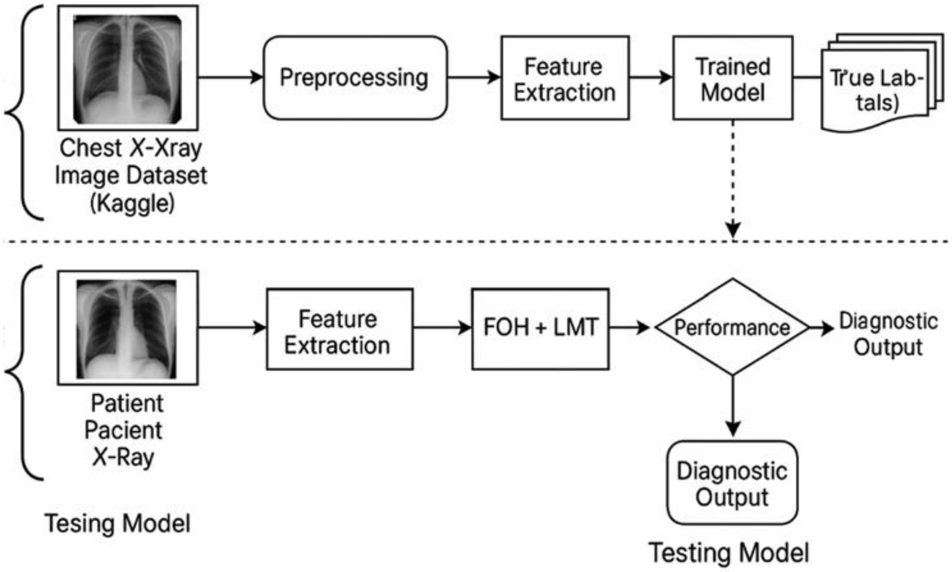

Fig. 2. Illustration of the proposed methodology for creating and evaluating the classification model.

enhance relevant features for classification. This process involves compressing and altering the visual information into a compact feature vector that captures essential diagnostic information.

D. Dataset Preparation

The dataset accommodates an identical distribution of pneumonia-infected and normal chest X-ray pictures. These images undergo pre-processing to ensure they may be as it should be formatted for the following device learning steps. During pre-processing, all images were carefully reviewed for artifacts or annotations (e.g., text labels, and markers such as “R”) that could introduce class-specific biases. We verified that the presence of such markers was not unique to any single class (normal or pneumonia) and ensured that models learned from medically relevant features rather than superficial visual cues. If such markers were found consistently in only one class, they were either cropped out or excluded from training to prevent unintentional model bias.

E. Model Training and Validation

The feature vectors were used to train the classification model using the Weka machine learning platform. It involves the training process as described below:

In addition, to ensure fair evaluation, the model performance was assessed on unseen test data. A 10-fold stratified cross-validation technique was employed, wherein each fold, the model was trained on 90% of the data and validated on the remaining 10%, ensuring that no sample used for training appeared in the corresponding test set. This approach ensures generalization performance is not inflated by data leakage.

F. Classification Model

This model classifies every image as either pneumonia-infected or normal using the processed feature vectors. Results from the training set form the basis of the model, which then applies to the test set.

G. Diagnostic Evaluation

The final stage includes the diagnostic testing of the model on unseen data from the test set. Here, the actual image labels are compared with the output of the model to test its accuracy and effectiveness. The performance of various models is statistically analyzed to conclude which one produces the most accurate classification.

H. Algorithm

This study effectively makes use of both feature extraction and classification algorithms, which classify and detect pneumonia using chest X-rays. It assimilates different algorithms with these advanced features to enable an amalgamation of textural, and color properties from images with deep machine learning concepts for enhanced diagnostics.

Feature extraction methods

The feature extraction techniques utilized include:

Fuzzy opponent histogram (FOH) filter: The color histograms are processed using fuzzy logic in opponent color spaces, hence enhancing the capacity to detect even minute differences between image intensities and colors. It is very advantageous in medical imaging operations, such as the detection of pneumonia.

FCTH filter (Texture Histogram and Fuzzy Color): Combines texture and color information using fuzzy logic to create a comprehensive feature set that captures critical characteristics of the images essential for accurate classification.

Classification methods

The classification of images is performed using several robust methods:

The ensemble learning approach in the case of random forest (RF), it generates as many decision trees as the number of trees on training to increase the accuracy and control the overfitting of the model (Mittal and Kumar, 2023)

Logistic model tree (LMT): Combines decision tree learning with logistic regression, allowing the handling of both linear and non-linear data relationships, with logistic regression functions at the tree's leaves (Pacal, et al., 2020).

Lenet CNN: A deep learning architecture specifically designed for image recognition tasks, which uses layers of convolution, pooling, and full connection to automatically extract and learn hierarchical features necessary for classification (Ahishakiye, et al., 2021).

Algorithm implementation

The study evaluates various combinations of feature extraction and classification methods:

FOH Filter + RF
FOH Filter + LMT
FCTH Filter + RF
FCTH Filter + LMT
Lenet (CNN) + RF
Lenet (CNN) + LMT

Each combination is meticulously applied to extract features from the X-ray images, which are then classified as either normal or pneumonia-affected. These methods are tested for their effectiveness in accurately categorizing chest X-ray images into the respective classes.

Ensemble framework and workflow

An ensemble framework that incorporates deep features from CNN is created to enhance the classification process (Thibault, et al., 2007). The workflow, illustrated in Fig. 3, outlines how deep features extracted from various layers of the pre-trained LeNet model, trained on our datasets, are concatenated to form a robust feature set. The model is evaluated using standard pneumonia datasets, including the Kaggle online dataset, employing classification methods such as RF and LMTs to ensure robust validation.

This ensemble approach allows the integration of diverse classification techniques and deep learning features, resulting in a highly accurate diagnostic tool for pneumonia detection based on chest X-ray images.

Evaluation metrics

To assess the performance of the proposed classification models, we used standard evaluation metrics including Accuracy, Precision, Recall, F1-score, and receiver operating characteristic (ROC)-AUC. These are defined as follows:

- Accuracy measures the overall correctness of the model:

$$\text{Accuracy} = TP + TN/TP + TN + FP + FN$$

- Precision evaluates how many of the predicted positive cases were actually positive:

$$\text{Precision} = TP/TP + FP$$

- Recall (Sensitivity) indicates how many actual positive cases were correctly predicted:

$$\text{Recall} = TP/TP + FN$$

- F1-score is the harmonic mean of precision and recall:

$$\text{F1-score} = 2\times\frac{\text{precision}\times\text{Recall}}{\text{Precision}+\text{Recall}}$$

ROC-AUC measures the trade-off between true positive rate and false positive rate across different thresholds, providing an aggregate measure of classification performance. Where:

- *TP* = True positives
- *TN* = True negatives
- *FP* = False positives
- *FN* = False negatives.

IV. RESULTS AND DISCUSSION

The goal of Table II is to identify pneumonia using a chest X-ray. A comprehensive evaluation of the performance of different combinations of feature extraction and classification methods on pneumonia detection is depicted in Fig. 4, which is presented in terms of five important metrics, namely, Pneumonia Accuracy (%), Precision, Recall, F-measure, and ROC. The shaded region around each line corresponds to the standard deviation or error margin within the shaded region which reflects the model's stability for multiple runs or folds for that particular combination of feature extractor and classifier.

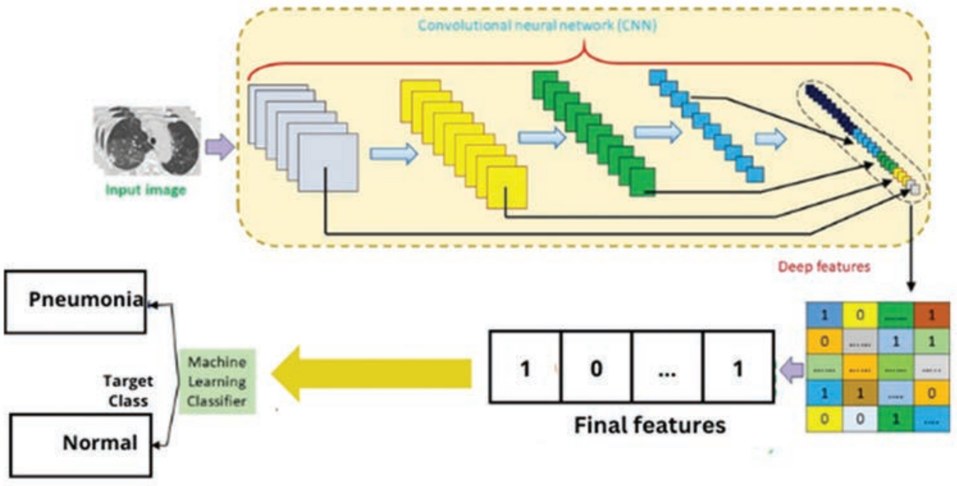

Fig. 3. Workflow of the proposed convolutional neural networks-based feature extraction approach for pneumonia detection.

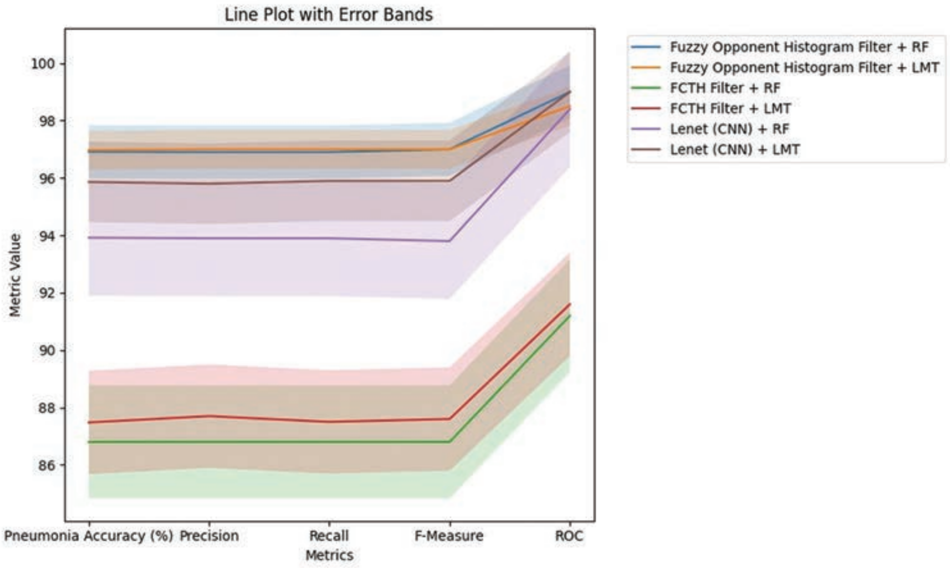

Fig. 4. Line plot with error bands for comparative evaluation of pneumonia detection models.

The combinations evaluated include:

- FOH filter with RFand LMT,
- FCTH Filter with both RF and LMT, and
- The RF and LMT are combined with LeNet (CNN).

As can be seen from the plot, the FOH Filter was combined with LMT and RF and outperformed the rest of the combinations in regard to all of the metrics, as the average values were high with very skinny error bands, meaning accurate and consistent. Like with the Lenet (CNN) combinations, the results for these too used the deep learning-based feature extractor well with a suitable classifier. Compared to these combinations, metric values of the FCTH Filter combinations with less metric values and wider error bands, representing a larger variability and less diagnostic precision.

Effectively highlighting the advantage of fuzzy logic-based feature extraction with either ensemble or hybrid classification model for enabling pneumonia detection accuracy in chest x-ray imagery, this visualization puts the focus on how fuzzy logic-based feature extraction methods will improve classifier performance for this area of study.

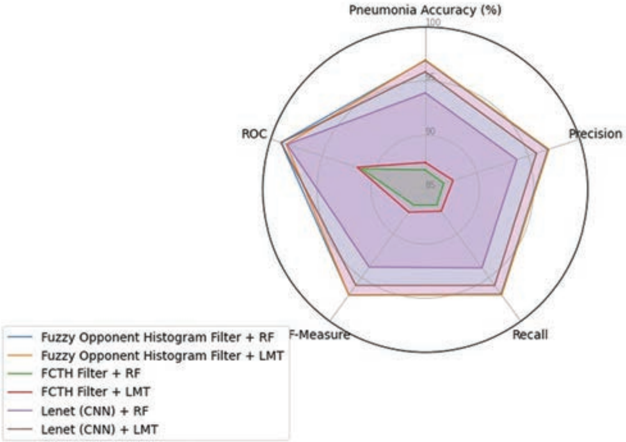

Fig. 5. Comparative radar plot of evaluation metrics for artificial intelligence-based pneumonia classification.

Fig. 5 shows the radar chart of model effectiveness in terms of five critical evaluation metrics. From the least to most expansive and balanced polygon the one that forms is the Lenet (CNN) + LMT one, this one having consistently high performance on all the metrics. The performance of both the FOH Filter + LMT method and the proposed one are strong and uniform. On the other hand, FCTH-based combinations feature also quite smaller coverage areas, indicating that they are less well-performing in metrics, such as accuracy, recall, and ROC AUC.

A comparison of six different method combinations when pneumonia is detected across the five essential performance metrics: Pneumonia accuracy (%), Precision, Recall, F-Measure, and ROC is illustrated in Fig. 6. Specific combinations are of three feature extraction technique (FOH Filter, FCTH Filter, and Lenet [CNN]), two classifiers RF and LMT. As can be seen clearly in the chart, whatever combinations using the FOH Filter have performed better across all metrics when compared to other combinations. More specifically, the combination of this filter with LMT results in the highest overall values; Pneumonia Accuracy, Precision, Recall, and F-Measure go up to 98%, and ROC reaches 98.5%. Furthermore, the performance with RF is nearly the same as with its combination, ROC is a bit higher with a score of 99%.

The Lenet (CNN)-based combinations also perform very well (especially in conjunction with LMT) with all metrics over 95.9 for Pneumonia Accuracy, with the exception of: Details accuracy (95.8), Prognosis accuracy (95.3), and Healed_Pneumonia Accuracy (94.5). They indicate that CNN-derived deep features provide strength in helping with accurate medical image classification. On the other hand, the performance of the FCTH based methods is comparatively lower with respect to all metrics. The accuracy values for Pneumonia in which FCTH and RF or LMT have been used

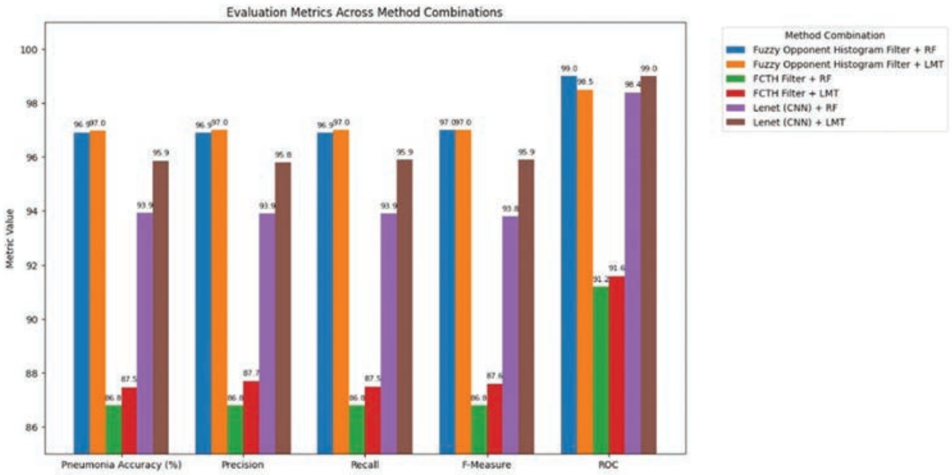

Fig. 6. Comparing evaluation metrics across feature extraction and classification techniques.

as an additive feature that is, 86.8% and 87.5% with its corresponding lower values in Precision, Recall, F-Measure and ROC.

The superior performance of the FOH Filter combined with LMT can be attributed to the complementary strengths of the two components. The FOH filter extracts color-texture information in opponent color spaces using fuzzy logic, which allows it to capture subtle gradations and variations in medical images—particularly important for detecting pneumonia patterns that may not be starkly visible. LMT, on the other hand, offers the interpretability and flexibility of decision trees with the generalization power of logistic regression, allowing it to model both linear and non-linear relationships. Together, this combination exploits both nuanced image characteristics and robust classification boundaries, leading to higher and more consistent performance compared to other methods tested.

Comparative Evaluation with VGG-16:

While numerous studies have reported high accuracy using deep learning models such as VGG-16 for pneumonia detection, we performed a comparative assessment based on literature-reported metrics. VGG-16-based models typically report accuracies in the range of 97–99% using transfer learning approaches on large datasets. In contrast, our hybrid approach combining the FOH Filter and LMT (FOH + LMT) achieved a close accuracy of 96.97% with the added advantage of reduced training time and improved interpretability. Unlike the black-box nature of VGG-16, the LMT-based approach allows for rule-based understanding of classification outcomes, which is highly valuable in clinical applications requiring transparency. This trade-off between slightly lower accuracy and higher transparency, combined with computational efficiency, makes our proposed method a practical and reliable solution in real-time diagnostic environments.

Fig. 7 shows the diagnostic accuracy and the confusion matrix, and they show that the combination of the FOH Filter with LMT and the same filter with RF have the highest classification accuracy of 96.97% and 96.91%, respectively. For both the normal and pneumonia cases, these combinations achieved the lower number of misclassifications.

As opposed to these, the FCTH Filter combinations yielded the lowest performance, that is with accuracy scores of 86.80% (FCTH + RF) and 87.48% (FCTH + LMT) for both false positives and false negatives. The Lenet (CNN) models in combination with RF and LMT form a strong middle ground, especially when Lenet + LMT reached 95.85% accuracy for the classification of normal and pneumonia-contaminated cases.

The results have proved that it was the ones including FOH Filter with the classifiers LMT and RF that yield the highest accuracy values, also proving substantial difference-making between images containing normal versus pneumonia-infected X-rays, as the application of deep learning through Lenet, which works based on a CNN, provides significant performance regarding differentiating image features.

While prior studies on brain tumor detection using VGG-16 and other pre-trained models, such as SqueezeNet, ResNet-50, and EfficientNet-b0 have achieved impressive accuracies ranging from 97% to 99%, our study focuses on pneumonia detection using chest X-ray datasets. The diagnostic nature of pneumonia and brain tumor imaging tasks differs significantly in terms of feature distribution and radiological presentation. In our study, although the absolute accuracy improvement over existing methods is marginal (peaking at 96.97%), the novelty lies in the hybrid combinations of fuzzy logic-based feature extraction with ensemble classifiers (e.g., FOH filter + LMT). Unlike deep CNNs alone, this framework demonstrates interpretability, reduced computational complexity, and comparable diagnostic power – making it more practical in resource-limited clinical environments.

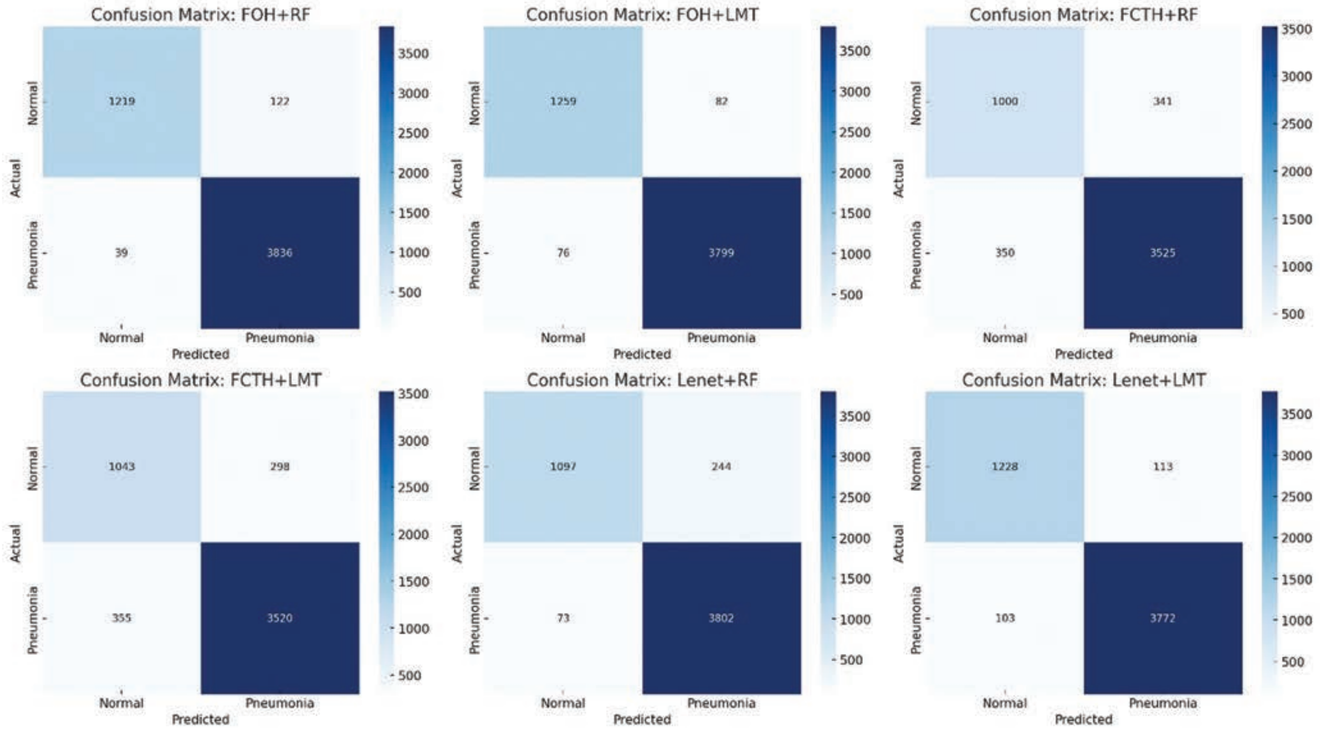

Fig. 7. Confusion matrices showing classification performance of feature extraction and classifier combinations for pneumonia detection.

TABLE II
Performance Metrics by Technique

Method combination	Pneumonia accuracy (%)	Precision %	Recall %	F-measure %	ROC%
Fuzzy opponent histogram filter + RF	96.91	0.969	0.969	0.97	0.99
Fuzzy opponent histogram filter + LMT	96.97	0.97	0.97	0.97	0.985
FCTH filter + RF	86.8	0.868	0.868	0.868	0.912
FCTH filter + LMT	87.48	0.877	0.875	0.876	0.916
Lenet (CNN) + RF	93.92	0.939	0.939	0.938	0.984
Lenet (CNN) + LMT	95.86	0.958	0.959	0.959	0.99

CNNs: Convolutional neural networks, RF: Random forest, LMT: Logistic model trees, ROC: Receiver operating characteristic

V. Conclusion

In this research, the significant capacity of adding advanced techniques of machine learning and AI over traditional methods to increase the diagnostic accuracy and precision of pneumonia which is detected in chest X-ray images has been realistically proven. Finally, our experiments demonstrate that deep learning models (especially CNNs) and ensemble methods significantly improve the precision and reliability of diagnosis and at its peak achieve 96.97% accuracy in the case of FOH Filter along with LMT. These technologies help in the better identification of pneumonia and also decrease the time it takes to identify the disease, which is vital for the proper administration of the treatment. More than that, Lenet (CNN) combined with LMT achieved great results with 95.85% accuracy, demonstrating excellent performance in medical imaging tasks. The involvement of AI in the field of medical imaging to support pneumonia diagnosis significantly reduces the subjectivity and variation inherent in the interpretation of radiographs and potentially lowers the error rate of diagnostic findings. Moving forward, these models need to be extended with larger and more diverse datasets to further test their effectiveness in different populations and clinical settings. Future research will also be important in integrating these machine learning models into real-time diagnostic platforms in the hospital setting, where their practical utility and effects on patient outcomes can be ascertained.

References

Ahishakiye, E., Van Gijzen, M.B., Tumwiine, J., Wario, R., and Obungoloch, J., 2021. A survey on deep learning in medical image reconstruction. *Intelligent Medicine*, 1(3), pp.118-127.

Dasgupta, D., and Sen, H., 2024. PneuCoNet: A deep learning model for early detection of pneumonia & amp; COVID-19. In: *Interdisciplinary Research in Technology and Management*. United States, CRC Press, pp.223-227.

Deepak, G.D., 2024. Optimization of deep neural network for multiclassification of Pneumonia. *Computer Methods in Biomechanics and Biomedical Engineering Imaging and Visualization*, 12(1), p.2292072.

El-Ghandour, M., and Obayya, M.I., 2024. Pneumonia detection in chest x-ray images using an optimized ensemble with XGBoost classifier. *Multimedia Tools and Applications*, 84(9), pp.5491-5521.

Hasan, M.D.K., Ahmed, S., Abdullah, Z.M.E., Monirujjaman Khan, M., Anand, D., Singh, A., AlZain, M., and Masud, M., 2021. Deep learning approaches for detecting pneumonia in COVID-19 patients by analyzing chest X-ray images. *Mathematical Problems in Engineering*, 2021, pp.1-8.

Kaur, N., and Singh, A., 2024. VGG16-PCA-PB3C: A hybrid PB3C and deep neural network based approach for leukemia detection. *International Journal of Information Technology*, 16(6), pp.3605-3615.

Khan, R., Taj, S., Ma, X., Noor, A., Zhu, H., Khan, J., Khan, Z.U., and Khan, S.U., 2024. Advanced federated ensemble internet of learning approach for cloud based medical healthcare monitoring system. *Scientific Reports*, 14(1), p.26068.

Kumar, T., Brennan, R., Mileo, A., and Bendechache, M., 2024. Image data augmentation approaches: A comprehensive survey and future directions. *IEEE Access*, 12, pp.187536-187571.

Kundu, R., Das, R., Geem, Z.W., Han, G.T., and Sarkar, R., 2021. Pneumonia detection in chest X-ray images using an ensemble of deep learning models. *PLOS ONE*, 16(9), p.e0256630.

Li, X., Zhao, L., Zhang, L., Wu, Z., Liu, Z., Jiang, H., Cao, C., Xu, S., Li, Y., Dai, H., Yuan, Y., Liu, J., Li, G., Zhu, D., and Shen, D., 2023. *Artificial General Intelligence for Medical Imaging Analysis*. Carolina Digital Repository (University of North Carolina at Chapel Hill, United States.

Mittal, V., and Kumar, A., 2023. COVINet: A hybrid model for classification of COVID and Non-COVID pneumonia in CT and X-Ray imagery. *International Journal of Cognitive Computing in Engineering*, 4, pp.149-159.

Pacal, I., Karaboga, D., Basturk, A., Akay, B., and Nalbantoglu, U., 2020. A comprehensive review of deep learning in colon cancer. *Computers in Biology and Medicine*, 126, p.104003.

Pant, A., Jain, A., Nayak, K.C., Gandhi, D., and Prasad, B.G., 2020. Pneumonia detection: An efficient approach using deep learning. *2020 11th International Conference on Computing, Communication and Networking Technologies (ICCCNT)*, pp.1-6.

Racic, L., Popovic, T., Cakic, S., and Sandi, S., 2021. Pneumonia detection using deep learning based on convolutional neural network. *2021 25th International Conference on Information Technology (IT)*, pp.1-4.

Rahman, T., Chowdhury, M.E.H., Khandakar, A., Islam, K.R., Islam, K.F., Mahbub, Z.B., Kadir, M.A., and Kashem, S., 2020. Transfer learning with deep convolutional neural network (CNN) for pneumonia detection using chest x-ray. *Applied Sciences*, 10(9), p.3233.

Rajpurkar, P., Irvin, J., Zhu, K., Yang, B., Mehta, H., Duan, T., Ding, D., Bagul, A., Langlotz, C., Shpanskaya, K., Lungren, MP., and Ng, Ay., 2017. *CheXNet: Radiologist-Level Pneumonia Detection on Chest X-Rays with Deep Learning*. arXiv (Cornell University), United States.

Ravi, V., 2024. Deep fine-tuned efficientNetV2 ensemble deep learning approach for pediatric pneumonia detection using chest radiographs. *Journal of Intelligent and Fuzzy Systems*, pp.1-18.

Sailunaz, K., Alhajj, S., Özyer, T., Rokne, J., and Alhajj, R., 2024. A survey on brain tumor image analysis. *Medical and Biological Engineering and Computing*, 62(1), pp.1-45.

Selvanandhini, B., and Karthikeyan, R., 2024. Ensemble heartguard: Integrating svm and random forest for robust heart disease prediction. *Educational Administration Theory and Practices*, 30, pp.13091-13099.

Shamshad, N., Sarwr, D., Almogren, A., Saleem, K., Munawar, A., Rehman, A.U., and Bharany, S., 2024. Enhancing brain tumor classification by a comprehensive study on transfer learning techniques and model efficiency using MRI datasets. *IEEE Access*, 12, pp.100407-100418.

Shein, A.M.S., Hongsing, P., Smith, O.K., Phattharapornjaroen, P., Miyanaga, K., Cui, L., Ishikawa, H., Amarasiri, M., Monk, P.N., Kicic, A., Chatsuwan, T., Pletzer, D., Higgins, P.G., Abe, S., and Wannigama, D.L., 2024. Current and novel therapies for management of *Acinetobacter baumannii*-associated pneumonia. *Critical Reviews in Microbiology*, 51, pp.441-462.

Singh, S., Kumar, M., Kumar, A., Verma, B.K., Abhishek, K., and Selvarajan, S., 2024. Efficient pneumonia detection using vision transformers on chest X-rays. *Scientific Reports*, 14(1), p.2487.

Szepesi, P., and Szilágyi, L., 2022. Detection of pneumonia using convolutional neural networks and deep learning. *Biocybernetics and Biomedical Engineering*, 42(3), pp.1012-1022.

Thibault, J., Sauer, K.D., Bouman, C.A., and Hsieh, J., 2007. A three□dimensional statistical approach to improved image quality for multislice helical CT. *Medical Physics*, 34(11), pp.4526-4544.

Venkatraman, K., and Reddy, S.N.P.S., 2024. Augmenting clinical decisions with deep learning lung cancer image abnormality segmentation. *2024 14th International Conference on Cloud Computing, Data Science & Engineering (Confluence)*, pp.674-678.

Yang, J., Zheng, Y., Gou, X., Pu, K., Chen, Z., Guo, Q., Ji, R., Wang, H., Wang, Y., and Zhou, Y., 2020. Prevalence of comorbidities and its effects in patients infected with SARS-CoV-2: A systematic review and meta-analysis. *International Journal of Infectious Diseases*, 94, pp.91-95.

Predicting the Unconfined Compressive Strength of Rice Husk Ash – Treated Fine-grained Soils

Rizgar A. Blayi[1], Jamal I. Kakrasul[1†] and Samir M. Hamad[2]

[1]Department of Civil and Environmental Engineering, Faculty of Engineering, Soran University,|
Soran 44008, Kurdistan Region – F.R. Iraq

[2]Scientific Research Centre, Soran University,
Soran, Kurdistan Region – F.R. Iraq

***Abstract*—This study aims to develop novel and accurate data-driven predictive models to replace labor-intensive laboratory testing for estimating the unconfined compressive strength (UCS) of problematic soils treated with rice husk ash (RHA) Full Quadratic, Interaction, M5P-tree, and Artificial Neural Network (ANN) were trained and evaluated using a dataset of 211 samples that involved seven key geotechnical parameters, including RHA content (0–30%), liquid limit (22–108%), plasticity index (1.3–82%), maximum dry density (1.2–1.9 g/cm^3), optimum moisture content (10.5–42.6%), and curing time (CT) (0–112 days). Among all these models, the ANN model demonstrated superior performance ($R^2 = 0.97$, RMSE = 24 kPa, MAE = 17 kPa, SI = 0.10). Sensitivity analysis revealed CT as the most influence factor (21.9%), followed by moisture content (16.1%) and RHA content (15.3%). The findings present that these predictive models provide a hybrid empirical–machine learning approach, and an accurate alternative to traditional UCS testing, significantly reducing the need for laboratory experiments. They also emphasize enhanced geotechnical performance and the sustainable reuse of agricultural waste. Furthermore, the models can offer a time-efficient solution with practical applications in areas such as highway development and foundation engineering.**

***Index Terms*—Modeling techniques, Rice husk ash stabilization, Soil properties, Unconfined compressive strength prediction**

I. INTRODUCTION

Clay soils are among the most common soil types in earthwork projects. These soils are usually susceptible to volume changes, which can cause shrinkage, swelling, and differential settlements (Estabragh, Moghadas, and Javadi, 2013). These volume changes can significantly impact the structural stability of underlying infrastructures such as pavements and foundations. Mechanical and chemical approaches have been used to address problems of clayey soil (Abbey, Eyo and Ng'ambi, 2020; Ahmed, 2013; Blayi, et al., 2024; Lin and Cerato, 2012). Over last decades, integrating industrial and agricultural waste materials (e.g., rice husk ash [RHA]) has gained substantial attention as alternative soil stabilizer, attributable to their sustainability and easy availability (Behak and Musso, 2016; Canakci, Aziz and Celik, 2015; Choobbasti, et al., 2010; Eberemu Adrian, Amadi Agapitus and Sule, 2012). RHA, which is a byproduct of rice milling, is an eco-friendly solid waste material with high amorphous silica content, making it an alternative to traditional soil stabilizers, including cement and lime. Replacing one ton of cement with RHA reduces CO_2 emissions by 0.9 tons, offering a cost-effective and sustainable alternative for geotechnical projects (Khan, et al., 2012; Rahman, 1987).

One of the geotechnical parameters used as a measurement of soil improvement is unconfined compressive strength (UCS). Studies found that the UCS of natural and treated soil can varies with physical properties of soil, including the addition of RHA and other combined agents, the liquid limit (LL), plasticity index (PI), maximum dry density (MDD), optimum moisture content (OMC), and the curing times (CT) (Anwar Hossain Khandaker, 2011; Behak and Musso, 2016; Canakci, Aziz and Celik, 2015; Choobbasti, et al., 2010; Eberemu Adrian, Amadi Agapitus and Sule, 2012; Zivari, Siavoshnia and Rezaei, 2023). In addition, studies have shown that combining RHA with additional stabilizers, including lime, cement, and calcium chloride can further improve soil properties (Ashango and Patra, 2014; Choobbasti, et al., 2010; Maithili, Nagakumar, and Shashishankar, 2024; Pushpakumara and Mendis, 2022). Using RHA as a soil additive not only improves its mechanical properties but also aligns with sustainable development goals by utilizing industrial byproducts to stabilize soil (Ashango and Patra, 2014; Choobbasti et al., 2010; Maithili, Nagakumar, and Shashishankar, 2024; Pushpakumara and Mendis, 2022).

In addition, Free swelling (FS) index, as a measure of soil swelling potential, can complement UCS in evaluating soil stability for predicting soil behavior under varying moisture conditions. Traditional UCS testing is often time-consuming,

ARO-The Scientific Journal of Koya University
Vol. XIII, No. 1 (2025), Article ID: ARO.11967. 14 pages
DOI: 10.14500/aro.11967
Received: 23 December 2024; Accepted: 13 April 2025
Regular research paper; Published: 15 June 2025

[†]Corresponding author's e-mail: jamal.kakrasul@soran.edu.iq

labor-intensive, and unusable for large-scale projects. Therefore, studies have explored alternative methods, including predictive modeling to evaluate UCS of soils (Goktepe, et al., 2008; Mawlood et al., 2021 (Mohammed and Vipulanandan, 2015; Mozumder and Laskar, 2015; Mohammed, 2018; Sharma and Singh, 2018; Vipulanandan and Mohammed, 2020). Precise prediction of the UCS is important to obtain the desired improved properties. Soft computing models, including full quadratic (FQ), Interaction (IA), M5P-tree, and ANN models, are commonly used for predicting soil properties. These models can handle difficult conditions in large datasets (Ali, et al., 2024; Mohammed et al., 2021). Recent studies revealed that ANN can be highly effective under certain conditions (Hossain and Kim, 2015; Mozumder and Laskar, 2015; Sharma and Singh, 2018), while FQ, linear, or multilinear regression models may be more suitable in others. Studies use statistical indicators such as R^2, RMSE, MAE, and SI to assess prediction model performance (Mousavi et al., 2011; Westerberg et al., 2015; Zaimoglu, 2015). These measures evaluate the accuracy and reliability of models (Blayi et al., 2021; Baghbani, et al., 2023; Cabalar and Omar, 2023; Baghbani, et al., 2023).

Based on the literature analysis, no prediction models have been developed specifically for estimating the UCS of fine-grain soils treated with RHA. Therefore, this study aims to develop various machine learning and statistical methods to predict the UCS of RHA-treated soil based on easily measurable input parameters (McBratney et al., 2000; Wattanapanich et al., 2024; Zhang et al., 2024). This approach addresses the challenge of conducting geotechnical testing at every site, which can be particularly difficult for small-scale projects. The models investigated include Artificial Neural Networks (ANN), M5P-tree, FQ, and IA models. These models can predict UCS values given sufficient data, relevant input parameters, and a wide range of UCS values. The study employs multiple evaluation techniques to assess the performance and accuracy of each model in predicting UCS for RHA-stabilized soils. ANN models are particularly interesting for their ability to capture complex, nonlinear IAs between material characteristics, stabilization parameters, and performance results, even in high-dimensional data forms. FQ and IA models take IA effects into account when interpreting data, while M5P-tree dividers datasets in an interpretable method. This comparison emphasizes on each model's prediction accuracy and practicality for optimizing RHA content and stabilization strategies. Ultimately, the study presents a novel application of FQ, IA, M5P-tree, and ANN models for predicting the UCS of RHA-stabilized soils, representing a highly accurate, data-driven alternative to traditional labor-intensive and time-consuming testing methods (Emad et al., 2022; Gautam et al., 2023; Nasir Amin et al., 2023).

II. Objectives of the Study

This work aims to develop different models and correlations to predict the UCS of RHA-treated soil utilizing laboratory test results found in the published literature. Four various models, including FQ, IA, M5P-tree, and ANN were developed to predict UCS based on the addition of waste by-product materials and geotechnical properties of the soils. In addition, linear and Vipulanandan model relationships were employed between UCS and FS values. The main objectives of this study are as follows:

1. Develop and compare predictive models to predict the UCS and establish correlations with FS index of the natural and RHA-stabilized soils
2. Evaluate the performance of the models with statistical assessment metrics (R^2, RMSE, MAE, and SI), to identify the most accurate approach
3. Analyze the impact of the additives and soil properties on UCS by conducting a sensitivity analysis to identify the most significant parameters influencing UCS values
4. Establish a sustainable framework for soil improvement by promoting the use of RHA in geotechnical applications and advance the state-of-the-art in geotechnical engineering through AI-driven methods for predicting soil properties.

III. Methodology

This study focuses on developing soft computing and statistical models to predict the UCS of natural and RHA-treated soils and evaluate the impact of other geotechnical properties of soil on UCS values. 211 datasets were collected from various published research and randomly divided into training (70% of data) and testing (30% of data). The training datasets were employed to develop models to predict the UCS values. The models were evaluated using the testing datasets. The retaining 30% for testing assists in defining the model's capacity to generalize to newly introduced data. Moreover, the dataset comprises main geotechnical properties impacting UCS, including RHA content (0–30%), LL (22–108%), PI (1.3–82%), MDD (1.2–1.9 g/cm^3), OMC (10.5–42.6%), and CT (0–112 days). The collected data were preprocessed by removing irregularities and standardizing values to guarantee the best model performance. The models include two learning machine approaches, ANN and M5P-tree, and two statistical regression models: FQ and IA. AI and FQ were chosen for their interpretability, while M5P-tree was included for its ability to combine decision-tree structures with regression. ANN was selected for its capability to capture complex, nonlinear relationships. The ANN architecture consisted of three hidden layers with 64, 32, and 16 neurons, respectively, using ReLU activation.

Table I shows the details of the datasets collected from various studies. The table includes the measured (UCS) kPa ranges, which are compared to the predicted values from the models later. These input parameters were used to develop the models, and their performance was evaluated using the actual values of the output parameters. Fig. 1 shows a flowchart of the study's research approach, which consists of five steps. During the initial stage, data were gathered from numerous sources. In the second stage, input and output parameters were correlated to find potential relationships. In the third stage, the data was divided into two groups: training (70%) and testing (30%). In the fourth stage, models were

TABLE I
The number and the range of used input and output datasets

Authors	Data ranges								
	No. data	RHA (%)	Additives (%)	LL (%)	PI (%)	MDD (g/cm^3)	OMC (%)	Curing (days)	UCS (kPa)
Rahman (1986)	5	0–16	0	50–53.4	18.2–27.2	1.39–1.56	22–25.7	0	211.2–371.6
Muntohar (2004)	4	0–12.5	0	64–74	25–43	1.18–1.32	34–37.9	0	219–268
Muntohar (2004)	4	0–12.5	6 Lime	54–74	5–23	1.15–1.32	26.5–34	0	238–269
Basha, et al. (2005)	5	0–20	0	35.6–46.5	11.2–14	1.45–1.68	15–24	0	100–140
Alhassan (2008)	1	0	0	49.5	25.1	1.48	18.38	7	180
Murty and Praveen (2008)	5	0–8	0	63–108	32–82	1.50–1.58	24–28.3	0	186–321
Murty and Praveen (2008)	44	0–8	0.25–1 CaCl$_2$	44–76	14–47	1.45–1.61	22–28.5	0–14	181–481
Anwar Hossain Khandaker (2011)	1	0	0	39	19	1.63	21.58	7	94
Yadu, Tripathi and Singh, (2011)	5	6–15	0	52–74	5–10	1.62–1.76	14.4–19.6	0	128–180
Sarkar, et al. (2012)	5	0–12.5	0	46–56	20–24	1.42–1.55	21.4–30.2	0	58–255
Fattah, Rahil and Al-Soudany (2013)	4	0–9	0	56.9–63	28.1–37.2	1.53–1.76	22–25	0	81.9–128.2
Anupam, Kumar and Ransingchung (2014)	1	0	0	46	25	1.68	16.91	7	83.28
Adhikary and Jana (2016)	11	0–20	0	48–63.5	17.8–22	1.29–1.61	20–30.8	0–28	93–235
Kumar Yadav, et al. (2017)	6	0–12.5	0	34.5–36.1	6.2–12.4	1.55–1.64	17–23.3	0	110.9–216.9
Nahar, et al. (2021)	1	0	0	37.5	7.8	1.7	18.7	0	42
Adajar, et al. (2019)	11	0–25	0	48–75	18–53	1.19–1.42	27.3–40.2	7–28	90–320
Jalal, et al. (2021)	35	0–12	0	30.7–36.3	14.6–20.5	1.48–1.7	19.8–26	3–112	75–665
Ordoñez Muñoz, et al. (2021)	14	0–15	2–5 Cement	45.9–51.7	6.9–15	1.34–1.40	25–33	7–90	350–815
Hossain, et al. (2022)	4	0–9	0	35–42	10.5–12	1.56–1.77	15.9–20.1	0	82.7–193.1
Pushpakumara and Mendis (2022)	4	0–20	0	51–66.5	29–33.4	1.37–1.48	26.3–42.6	0	75–87
Pushpakumara and Mendis (2022)	10	0–30	10–20 Lime	38–55	16.5–33	1.23–1.43	26–42	0	79–106
Zivari, Siavoshnia and Rezaei, (2023)	14	0–10	1–4 Lime	22–31.3	1.3–5	1.72–1.84	12.2–16.2	7–28	125–625
Charyulu, et al. (2023)	4	0–15	0–15	63.2–75	34–38	1.3–1.9	22–30	0	72–104
Ingabire and Kumar (2023)	5	0–15	6 Sawdust ash	25–40	10.2–21.1	1.38–1.56	17.8–19.7	0	13.1–24.6
Maithili, Nagakumar and Shashishankar (2024)	3	5–15	5–15	32–35	7.5–16	1.63–1.84	13–16.8	0	92–128
Abdulrahman, et al. (2024)	5	0–10	0–10	55–62	14–41	1.6–1.74	10.5–15	0	65–100

RHA: Rice husk ash, LL: Liquid limit, PI: Plasticity index, MDD: Maximum dry density, OMC: Optimum moisture content, UCS: Unconfined compressive strength

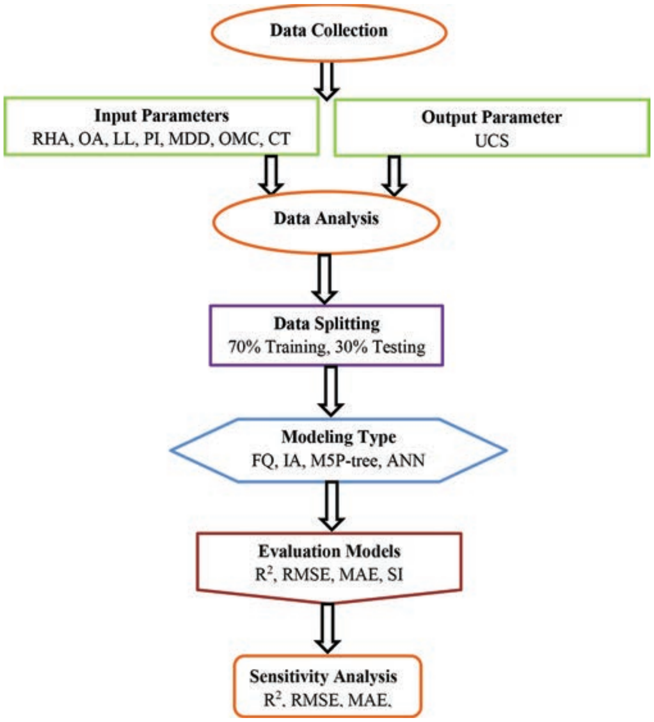

Fig. 1. The process of the work by a flow chart diagram.

developed based on input characteristics to estimate UCS. In the fifth stage, the models were evaluated based on testing data to establish their accuracy in predictions. Finally, in the sixth stage, sensitivity analysis was performed to determine the highest impact of input parameters.

IV. Correlations Between Input and Output Parameters

Figs. 2 and 3 showed the correlation and matrix plots between the input parameters and UCS values. Among all the parameters, CT showed a moderate positive relationship with UCS (r = 0.58). Other parameters, such as LL, PI, and dry density, showed weak or negative correlations. CT supports pozzolanic reactions in RHA-treated soil, resulting in cementitious products that increase strength. Insufficient curing causes incomplete reaction and reduced UCS. While LL and PI affect soil workability and water retention, they do not strongly correlate with UCS unless combined with density, moisture content, and CT.

Table II shows descriptive statistics for each variable. Kurtosis and skewness describe the form of a distribution. In numerical analysis, kurtosis denotes a distribution's peak

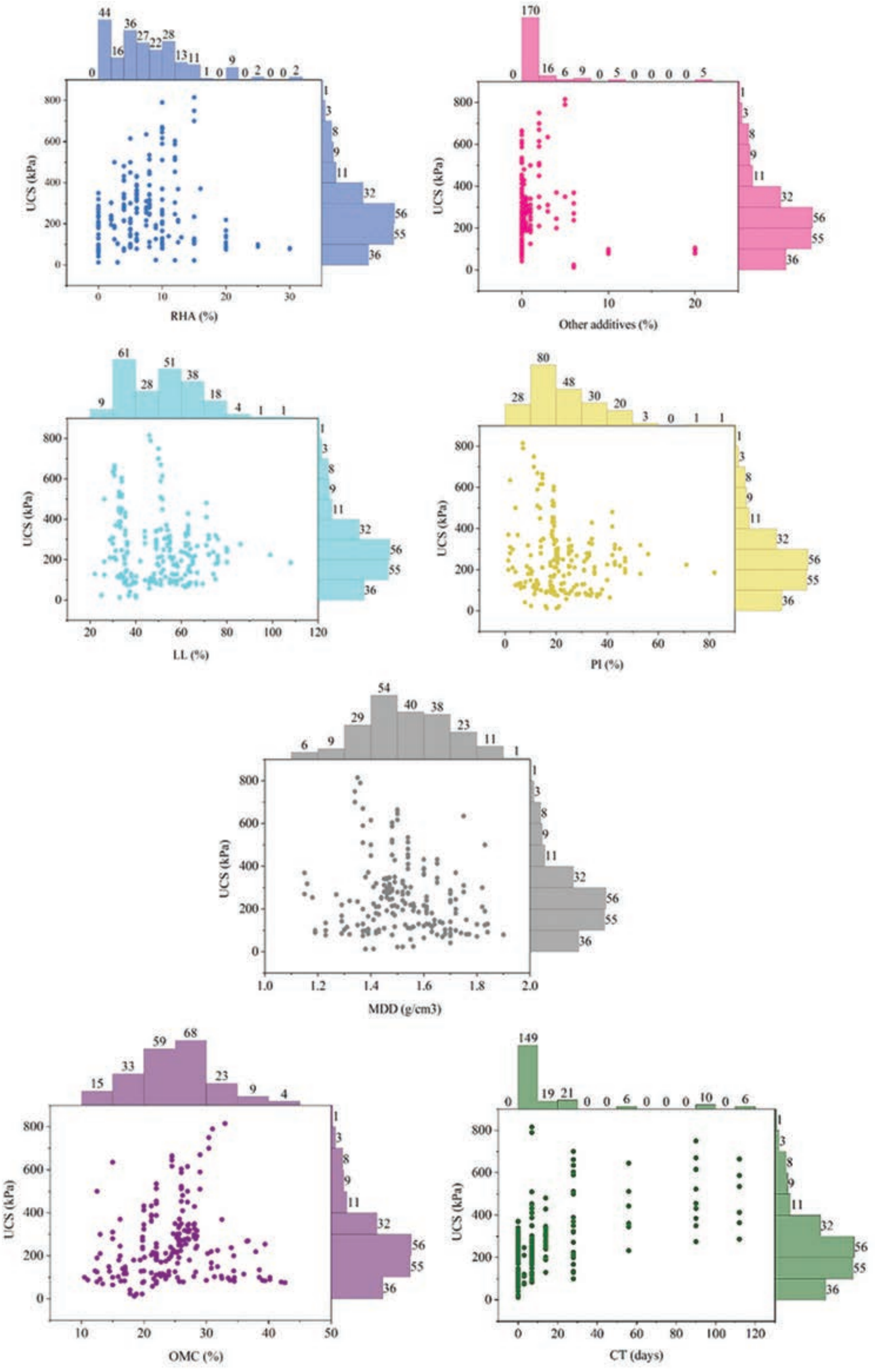

Fig. 2. Matrix plot between the input parameters and the unconfined compressive strength.

or flatness, whereas skewness refers to asymmetry. Negative kurtosis indicates shorter and thinner tails than normal distributions. A positive kurtosis value suggests lengthier and fatter tails than a normal distribution. Generally, a normal distribution has a kurtosis value of 0 (nearly zero in LL, MDD, and OMC). A distribution with high negative kurtosis may imply that there are lesser extreme values. Hence, input and output values should be chosen to avoid extreme distribution ends. A negative skewness number proposes a longer left tail, while a positive skewness value indicates a longer right tail. Similarly, LL, MDD, and OMC have the smallest values. This is illustrated in Figs. 2c, 2e, and 3f. Overall, negative skewness and kurtosis in MDD and OMC suggest that the dataset contains uniformly distributed soil properties with a tendency to higher values. This distribution helps consistent and predictable UCS outputs in fine-grained soils.

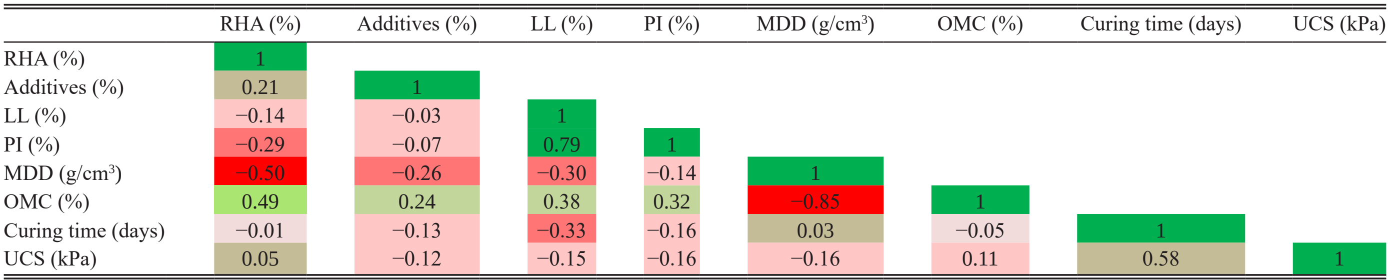

	RHA (%)	Additives (%)	LL (%)	PI (%)	MDD (g/cm³)	OMC (%)	Curing time (days)	UCS (kPa)
RHA (%)	1							
Additives (%)	0.21	1						
LL (%)	−0.14	−0.03	1					
PI (%)	−0.29	−0.07	0.79	1				
MDD (g/cm³)	−0.50	−0.26	−0.30	−0.14	1			
OMC (%)	0.49	0.24	0.38	0.32	−0.85	1		
Curing time (days)	−0.01	−0.13	−0.33	−0.16	0.03	−0.05	1	
UCS (kPa)	0.05	−0.12	−0.15	−0.16	−0.16	0.11	0.58	1

RHA: Rice husk ash, LL: Liquid limit, PI: Plasticity index, MDD: Maximum dry density, OMC: Optimum moisture content, UCS: Unconfined compressive strength

Fig. 3. Correlation matrix between the input and output parameters.

TABLE II

Statistical Measures for Input and Output Variables

	RHA (%)	OA (%)	LL (%)	PI (%)	MDD (g/cm³)	OMC (%)	CT (days)	UCS (kPa)
Min	0	0	22	1.3	1.2	10.5	0	13.1
Max	30.0	20	108	82	1.9	42.6	112.0	815
Mean	6.9	1.4	50.3	22.4	1.5	24.4	14.6	249.8
Median	6.0	0	51	19.4	1.5	24.7	7	219
Mode	0.0	0	51	25	1.5	22	0	130
Variance	35.4	12.6	239.1	166.5	0	42.3	725.2	26521.4
Standard deviation	5.9	3.5	15.5	12.9	0.2	6.5	26.9	162.9
Skewness	1.1	3.9	0.4	1.1	0	0.3	2.5	1.2
Kurtosis	1.7	16.6	0.1	2.2	−0.2	0.2	5.2	1.2
Sum	1462.5	295	10611.3	4734	321.3	5141.1	3088	52699.8
Count	211	211	211	211	211	211	211	211

RHA: Rice husk ash, LL: Liquid limit, PI: Plasticity index, MDD: Maximum dry density, OMC: Optimum moisture content, UCS: Unconfined compressive strength, CT: Curing time

V. Modeling

This section evaluates the predictive performance of four models – FQ, IA, M5P-tree, and ANN – using standard metrics on the UCS dataset. Models are employed to forecast UCS, and their performance is assessed compared to the measured data using valuation standards, including proportion difference between investigated and predicted data, R^2 value, RMSE, MAE, and SI values. The least squares method is used in Excel and soft computing, such as WEKA to calculate parameter coefficients in all models. It includes minimizing the sum of squared variances between the observed data points and the predicted values of the line of best fit. Overall, the models show that non-linear correlations, IAs, and complicated variable dependencies must all be considered when predicting UCS (Vipulanandan et al., 2012).

A. FQ Model

The mathematical FQ model uses various input parameters to predict UCS values for natural and treated soils. This model can capture non-linear correlations between input parameters and UCS values (Ali, 2024; Hoque, et al., 2023; Meskini, et al., 2022; Wang, et al., 2023). The FQ model equation is as follows:

$$UCS = \beta_0 + \beta_1 * (RHA) + \beta_2 * (OA) + \beta_3 * (LL) + \beta_4 * (PI) + \beta_5 * (MDD) + \beta_6 * (OMC) + \beta_7 * (CT) + \beta_8 * (RHA * OA) + \beta_9 * (RHA * LL) + \beta_{10} * (RHA * PI) + \beta_{11} * (RHA * MDD) + \beta_{12} * (RHA * OMC) + \beta_{13} * (RHA * CT) + \beta_{14} * (OA * LL) + \beta_{15} * (OA * PI) + \beta_{16} * (OA * MDD) + \beta_{17} * (OA * OMC) + \beta_{18} * (OA * CT) + \beta_{19} * (LL * PI) + \beta_{20} * (LL * MDD) + \beta_{21} * (LL * OMC) + \beta_{22} * (LL * CT) + \beta_{23} * (PI * MDD) + \beta_{24} * (PI * OMC) + \beta_{25} * (PI * CT) + \beta_{26} * (MDD * OMC) + \beta_{27} * (MDD * CT) + \beta_{28} * (OMC * CT) + \beta_{29} * (RHA)^2 + \beta_{30} * (OA)^2 + \beta_{31} * (LL)^2 + \beta_{32} * (PI)^2 + \beta_{33} * (MDD)^2 + \beta_{34} * (OMC)^2 + \beta_{35} * (CT)^2 \quad (1)$$

The model parameters are defined as β_0–β_{35} values. The clarification of coefficients in the FQ model can be more composite than the multilinear linear regression model.

B. IA Model

IA multivariable models consider non-linear IAs among input and output parameters to predict UCS (Ahmed, et al., 2021; Ghafor, et al., 2022; Tahr, Mohammed, and Ali, 2022). The general equation for an IA multivariable model is as follows:

$$UCS = \beta_0 + \beta_1 * (RHA) + \beta_2 * (OA) + \beta_3 * (LL) + \beta_4 * (PI) + \beta_5 * (MDD) + \beta_6 * (OMC) + \beta_7 * (CT) + \beta_8 * (RHA * OA) + \beta_9 * (RHA * LL) + \beta_{10} * (RHA * PI) + \beta_{11} * (RHA * MDD) + \beta_{12} * (RHA * OMC) + \beta_{13} * (RHA * CT) + \beta_{14} * (OA * LL) + \beta_{15} * (OA * PI) + \beta_{16} * (OA * MDD) + \beta_{17} * (OA * OMC) + \beta_{18} * (OA * CT) + \beta_{19} * (LL * PI) + \beta_{20} * (LL * MDD) + \beta_{21} * (LL * OMC) + \beta_{22} * (LL * CT) + \beta_{23} * (PI * MDD) + \beta_{24} * (PI * OMC) + \beta_{25} * (PI * CT) + \beta_{26} * (MDD * OMC) + \beta_{27} * (MDD * CT) + \beta_{28} * (OMC * CT) \quad (2)$$

Model parameters range from β_0 to β_{28}. The IA term indicates that the impact of one interpreter variable on the output variable is dependent on the values of another predictor variable.

C. M5P-tree Model

Fig. 4 shows the M5P-tree analysis tree for input and output parameters in a geotechnical context, almost certainly related to

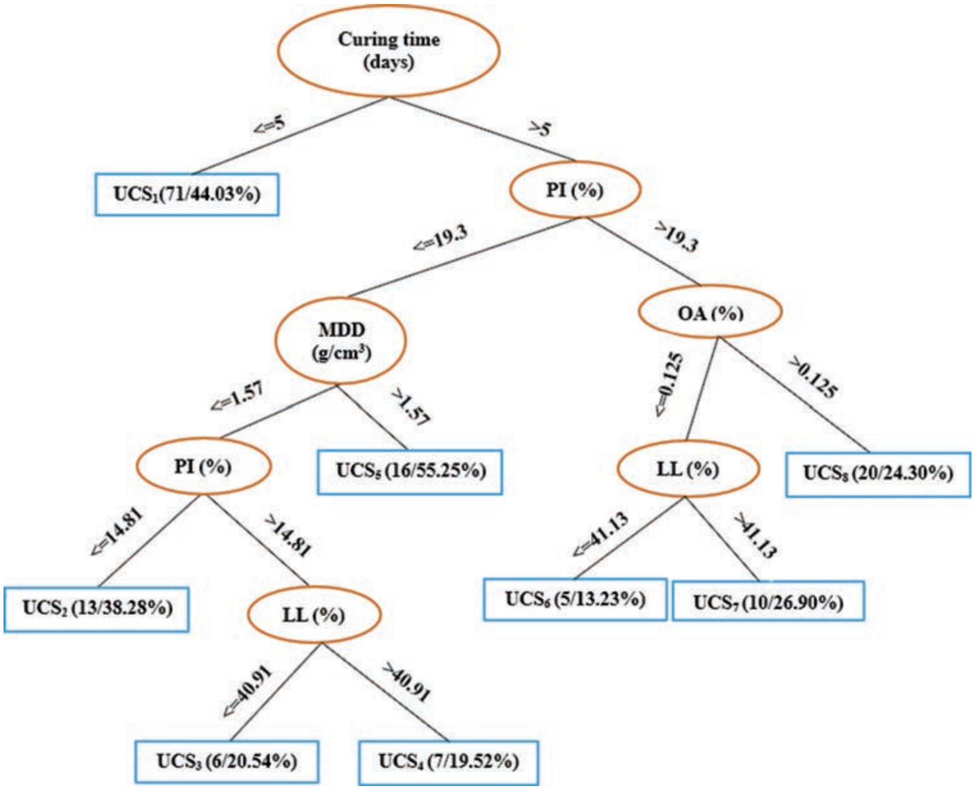

Fig. 4. M5P-tree analysis tree of input and output parameters.

soil stabilization using UCS values. The M5P-tree model offers both a logical structure for decision-making and the ability to model numerical data in a divided linear method. The UCS is organized into modules (UCS_1-UCS_8), with each branch corresponding to specific combinations of input parameters. In addition, this analysis reveals the complexities of parameters affecting soil strength and the systematic identification of their roles (Ahmad et al., 2022; Gnananandarao et al., 2022; Gnananandarao et al., 2023; Mahmood & Mohammed, 2022; Mohammed et al., 2020; Mohanty et al., 2019; Sihag et al., 2021; Suthar, 2020). The M5P-tree model equation is as follows:

$$UCS_1 = -6.56OA + 1.665LL - 0.412PI - 279.55MDD + 0.58CT + 525.78 \tag{3}$$

$$UCS_2 = 4.25RHA + 33.44OA - 4.40LL - 9.80PI - 294.66MDD + 2.39CT + 1032.67 \tag{4}$$

$$UCS_3 = -RHA + 22.41OA - 5.87LL - 9.80PI - 294.66MDD + 1.89CT + 1156.28 \tag{5}$$

$$UCS_4 = -1.54RHA + 22.41OA - 5.80LL - 9.80PI - 294.66MDD + 1.89CT + 1144.56 \tag{6}$$

$$UCS_5 = 11.25RHA + 9.65OA - 3.38LL - 0.39PI - 363.15MDD + 1.72CT + 913.91 \tag{7}$$

$$UCS_6 = 12.37OA - 1.20LL + 1.35PI - 88.77MDD + 1.21CT + 380.60 \tag{8}$$

$$UCS_7 = 12.37OA - 0.31LL + PI - 88.77MDD + 1.21CT + 333.294 \tag{9}$$

$$UCS_8 = -27.48OA + 0.27LL - 0.39\ PI - 88.77MDD + 7.85OMC + 3.65CT + 177.97 \tag{10}$$

D. ANN Model

ANN is an influential simulation program designed to process and analyze data evidence equally to a human brain. This mechanism learning technique is commonly used in construction engineering to predict how many numerical problems will behave in the future (Verma and Kumar, 2021; Wang and Huang, 1984). In this research, a multilayer feed-forward Network is assembled using proportions, weight/bias, and parameters (RHA, OA, LL, PI, MDD, OMC, and CT) as inputs, whereas the output ANN is the UCS values. There is no conventional method to structure Network architecture; the ideal network construction procedure includes selecting the optimal number of training periods to achieve low MAE and RMSE while maintaining a high R-value (Mohammed, et al., 2021; Sharma and Singh, 2018; Zeng, et al., 2021). Multiple transfer functions and ANN architectures with hidden layers and neurons were tested to optimize the Network structure and forecast UCS. Fig. 5 represents the best Network architectures for estimating UCS of natural and treated soils. Overall, the architecture of three hidden layers with six neurons per layer is likely a viable compromise to meet the problem's complexity while minimizing processing overhead.

VI. Model Valuation Tools

Model accuracy was assessed using R^2, RMSE, MAE, and SI, summarized in Table III and Figs. 6-9. ANN consistently outperformed others, while FQ and IA performed better in lower UCS ranges. The formulas below can be used to calculate the following metrics:

TABLE III
Comparative Analysis of Models Based on Ease of Use, Computational Efficiency, Interpretability and Accuracy

Models	Ease of use	Computational efficiency	Interpretability	Accuracy (R^2)
Full quadratic	High	High	High	Moderate
Interaction model	High	Moderate	Moderate	Moderate
M5P-Tree	Moderate	High	Moderate	High
ANN	Low (requires expertise)	Low	Low	Very high

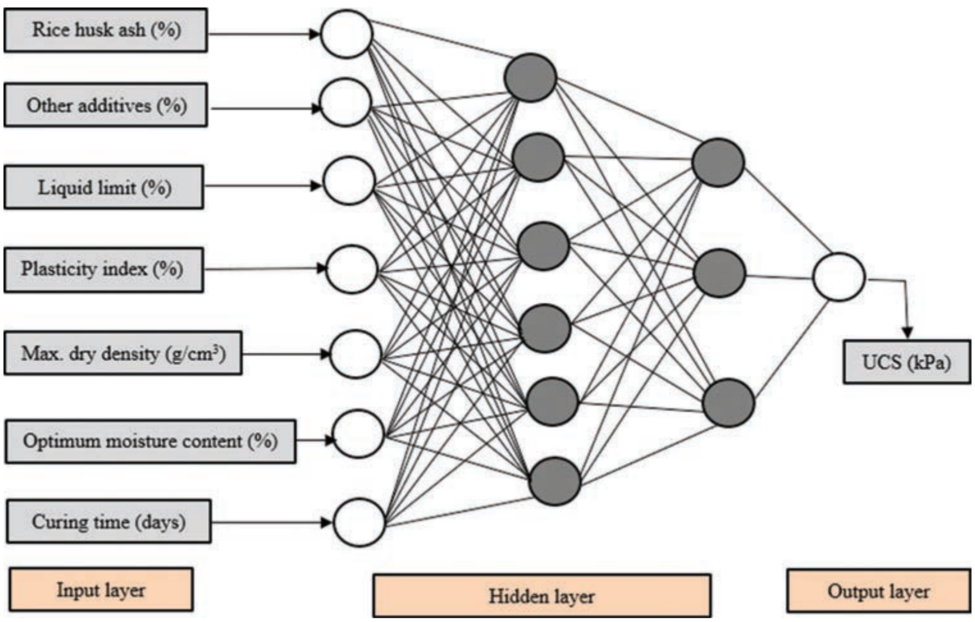

Fig. 5. The architecture of the used artificial neural network models and unconfined compressive strength.

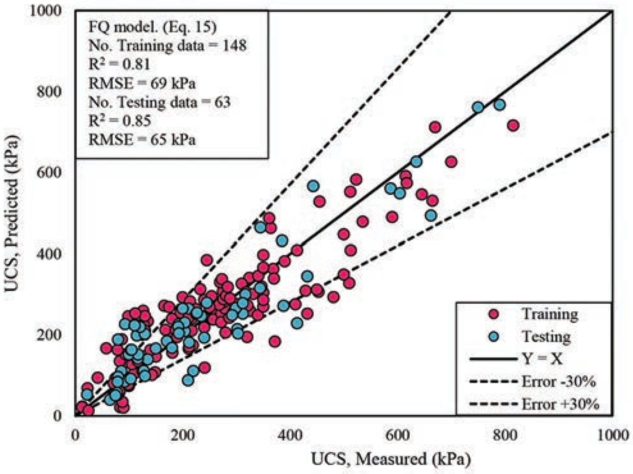

Fig. 6. Correlation between unconfined compressive strength and free swelling of natural and treated soil (Belabbaci, Mamoune, and Bekkouche, 2013).

$$R^2 = \left(\frac{\sum_{p=1}^{p}(yi - yi')(yp - yp')}{\sqrt{\left[\sum_{P=1}^{P}(yi - yi')^2\right]\left[\sum_{P=1}^{P}(yi - yi')^2\right]}} \right)^2 \quad (11)$$

$$RMSE = \sqrt{\frac{\sum_{p=1}^{p}(yp - yi)^2}{p}} \quad (12)$$

$$MAE = \frac{\sum_{p=1}^{p}|yp - yi|}{p} \quad (13)$$

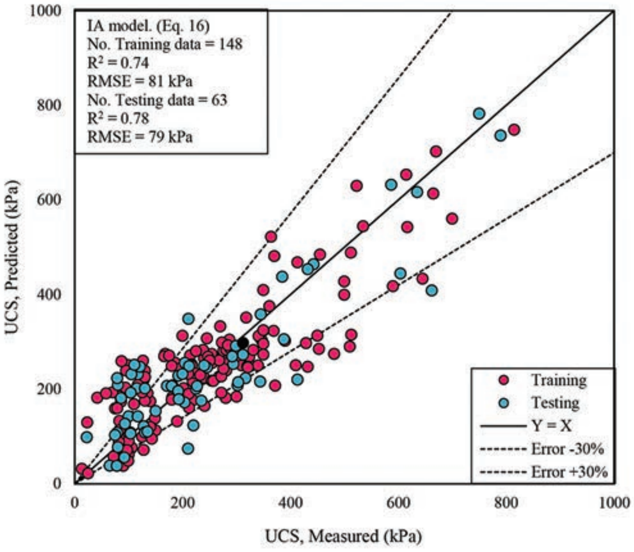

Fig. 7. The R2 values of unconfined compressive strength for all four models.

$$SI = \frac{RMSE}{y'} \quad (14)$$

VII. Results and Discussion

Table III presents a qualitative comparison of the models' accuracy, ease of use, and interpretability. Among

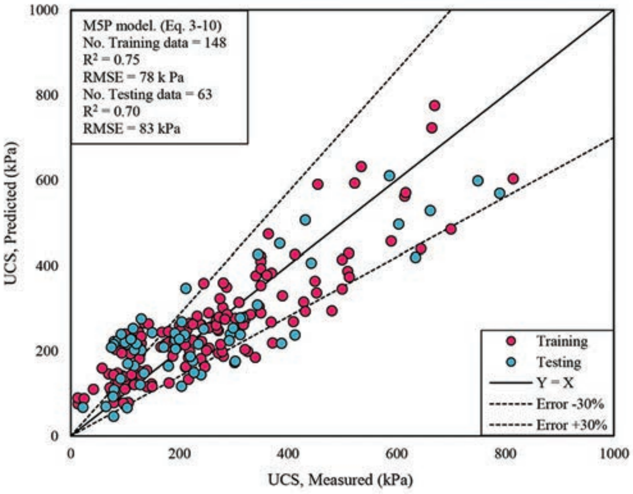

Fig. 8. The RMSE values of unconfined compressive strength for all four models.

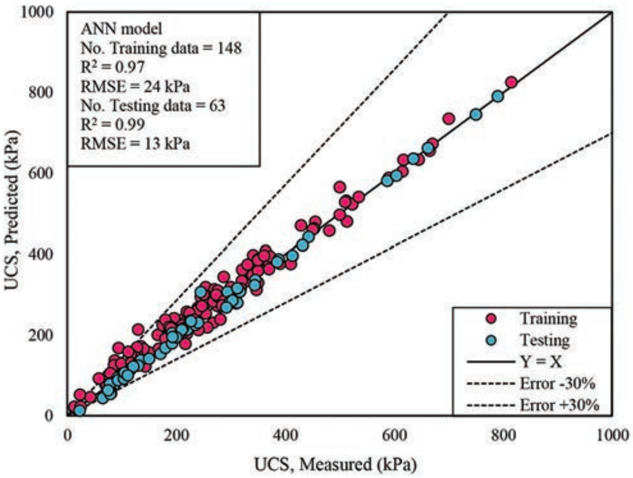

Fig. 9. The MAE values of unconfined compressive strength for all four models.

the evaluated models, the ANN approach demonstrated the highest predictive accuracy for UCS, outperforming M5P-tree, FQ, and IA models. While the FQ model was more interpretable, it lacked precision in nonlinear cases, which the ANN addressed effectively.

A. FQ Model

The FQ model achieved R^2 values of 0.81 (training) and 0.85 (testing) in predicting UCS. The training and testing datasets have RMSE values of 69 and 65 kPa, respectively. Fig. 10 compares the actual and expected UCS values. FQ provides equations incorporating linear, quadratic, and IA terms for input parameters. The coefficients in the equations represent how each parameter affects the result. Equation 15 shows UCS models with assigned weights for each parameter (Hama Ali, 2023; Li et al., 2021; Mawlood et al., 2022).

$$\mathrm{UCS} = -3403.37 - 77.337\mathrm{RHA} - 19.438\mathrm{OA} - 28.439\mathrm{LL} + 4.817\mathrm{PI} + 2905.378\mathrm{MDD} + 204.959\mathrm{OMC} - 13.088\mathrm{CT} + 0.917(\mathrm{RHA}\ast\mathrm{OA}) - 0.172(\mathrm{RHA}\ast\mathrm{LL}) + 0.035(\mathrm{RHA}\ast\mathrm{PI}) + 47.791(\mathrm{RHA}\ast\mathrm{MDD}) + 1.138(\mathrm{RHA}\ast\mathrm{OMC}) + 0.321(\mathrm{RHA}\ast\mathrm{CT}) + 1.172(\mathrm{OA}\ast\mathrm{LL}) - 0.901(\mathrm{OA}\ast\mathrm{PI}) - 25.778(\mathrm{OA}\ast\mathrm{MDD}) + 0.181(\mathrm{OA}\ast\mathrm{OMC}) + 2.504(\mathrm{OA}\ast\mathrm{CT}) + 0.089(\mathrm{LL}\ast\mathrm{PI}) + 14.655(\mathrm{LL}\ast\mathrm{MDD}) + 0.275(\mathrm{LL}\ast\mathrm{OMC}) - 0.091(\mathrm{LL}\ast\mathrm{CT}) - 4.920(\mathrm{PI}\ast\mathrm{MDD}) + 0.133(\mathrm{PI}\ast\mathrm{OMC}) - 0.003(\mathrm{PI}\ast\mathrm{CT}) - 82.853(\mathrm{MDD}\ast\mathrm{OMC}) + 13.817(\mathrm{MDD}\ast\mathrm{CT}) + 0.003(\mathrm{OMC}\ast\mathrm{CT}) - 0.834(\mathrm{RHA})^2 - 0.216(\mathrm{OA})^2 - 0.003(\mathrm{LL})^2 - 0.112(\mathrm{PI})^2 - 681.150(\mathrm{MDD})^2 - 2.121(\mathrm{OMC})^2 + -0.050(\mathrm{CT})^2 \tag{15}$$

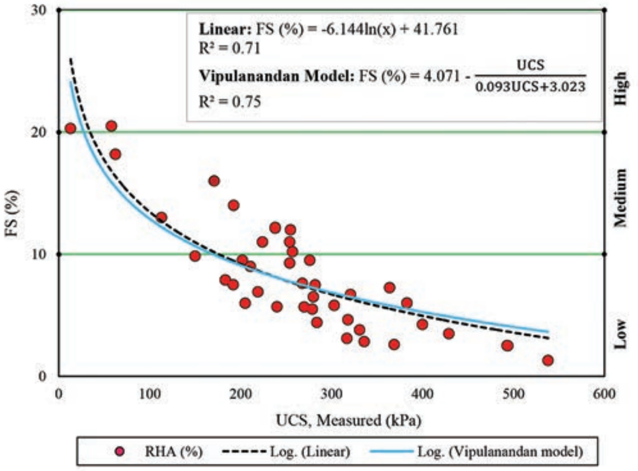

Fig. 10. Comparison between measured and predicted values of unconfined compressive strength for full quadratic model.

The parameters with a considerable positive effect on UCS are PI, MDD, and OMC, with coefficients of 4.8, 2905.4, and 205, respectively. RHA, OA, LL, and CT negatively affect UCS, with values of −77.3, −19.4, −28.4, and −13.1.

B. IA Model

Fig. 11 compares actual and predicted UCS values using the IA model. The IA model offered similar interpretability to the FQ but with slightly lower accuracy ($R^2 = 0.74$ training, 0.78 testing). In addition, the training and testing data have RMSEs of 81 and 79 kPa. Therefore, the IA model may yield a satisfactory prediction for UCS values (Ali & Mohammed, 2024; Ali et al., 2024; Eyo et al., 2022). Equation 16 shows the mathematical formula of the IA model for UCS.

$$\mathrm{UCS} = -1007.088 - 1.391(\mathrm{RHA}) + 0.021(\mathrm{OA}) + 19.370(\mathrm{LL}) + 37.216(\mathrm{PI}) + 360.966(\mathrm{MDD}) + 4.433(\mathrm{OMC}) - 26.413(\mathrm{CT}) + 0.930(\mathrm{RHA}*\mathrm{OA}) - 0.258(\mathrm{RHA}*\mathrm{LL}) + 0.704(\mathrm{RHA}*\mathrm{PI}) + 15.510(\mathrm{RHA}*\mathrm{MDD}) - 0.990(\mathrm{RHA}*\mathrm{OMC}) + 0.443(\mathrm{RHA}*\mathrm{CT}) + 1.232(\mathrm{OA}*\mathrm{LL}) - 1.015(\mathrm{OA}*\mathrm{PI}) - 31.099(\mathrm{OA}*\mathrm{MDD}) - 0.492(\mathrm{OA}*\mathrm{OMC}) + 1.817(\mathrm{OA}*\mathrm{CT}) + 0.086(\mathrm{LL}*\mathrm{PI}) - 11.081(\mathrm{LL}*\mathrm{MDD}) - 0.082(\mathrm{LL}*\mathrm{OMC}) + 0.029(\mathrm{LL}*\mathrm{CT}) - 18.231(\mathrm{PI}*\mathrm{MDD}) - 0.797(\mathrm{PI}*\mathrm{OMC}) + 0.017(\mathrm{PI}*\mathrm{CT}) + 18.769(\mathrm{MDD}*\mathrm{OMC}) + 14.153(\mathrm{MDD}*\mathrm{CT}) + 0.115(\mathrm{OMC}*\mathrm{CT}) \tag{16}$$

C. M5P Model

Fig. 12 depicts a scatter plot of measured and predicted UCS values for natural and treated soils, using an M5P model. It performed moderately well ($R^2 = 0.75$ training, 0.70 testing) but exhibited higher RMSE in predicting UCS >500 kPa. The figure shows ±30% error bands, indicating the model's

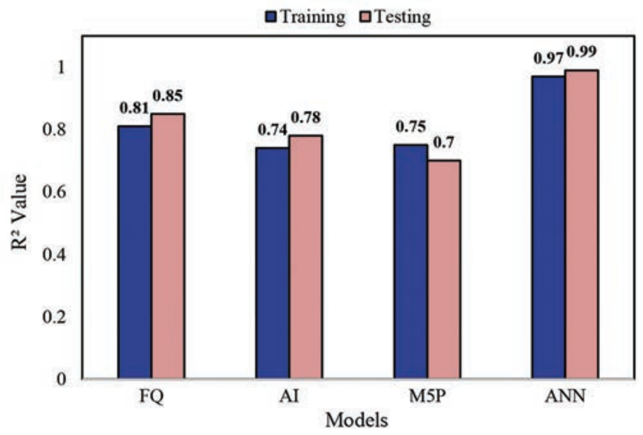

Fig. 11. Comparison between measured and predicted values of unconfined compressive strength for the interaction model.

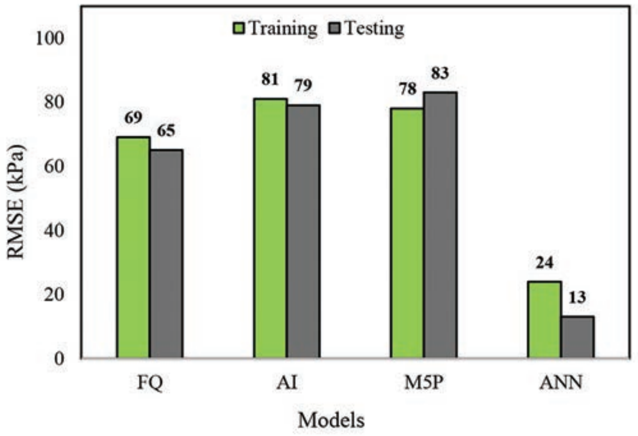

Fig. 12. Comparison between measured and predicted values of unconfined compressive strength for M5P model.

predicted accuracy. Most data points, particularly those with lower UCS values, fit inside these bands, indicating high model performance in this range. Points beyond the ±30% error range indicate considerable deviations between the model's predictions and actual results, especially for higher UCS values, which were similar to (Ahmad, et al., 2024; Ghanizadeh and Naseralavi, 2023; Pandey and Aggarwal, 2022; Sihag, Suthar, and Mohanty, 2021). The performance variance between training and testing data is small, implying that the M5P model generalizes reasonably well. Overall, while the M5P model displays satisfactory predictive capabilities with a low performance decrease between training and testing, improving the model for higher UCS values and experimenting with new modeling strategies may improve overall accuracy and strength.

D. ANN Model

Table IV compares various ANN designs to find the best model for UCS values. ANN using three hidden layers, six neurons on the left side (Fig. 5), 0.1 momentum, 0.1 learning rate, and 50000 iterations produces the best UCS prediction. Fig. 13 compares predicted and actual UCS values for training and testing datasets. The ANN model significantly outperformed all others in accuracy and generalizability. It achieved RMSE values of 24 kPa (training) and 13 kPa (testing), with minimal bias across the full UCS range. Similar results were achieved by (Ghorbani and Hasanzadehshooiili, 2018; Jalal, et al., 2021; Mohammed, Hummadi, and Mawlood, 2022; Pham, et al., 2021). The training and testing datasets for UCS have SI values of 0.1 and 0.07, respectively, as shown in Fig. 14. Also, the ANN model excels at predictive accuracy but faces limitations such as overfitting risks, computational complexity, reliance on massive datasets, low interpretability, and difficult hyperparameter tuning. Addressing these challenges through regulation, cross-validation, and simplified model integration can increase its practical applicability.

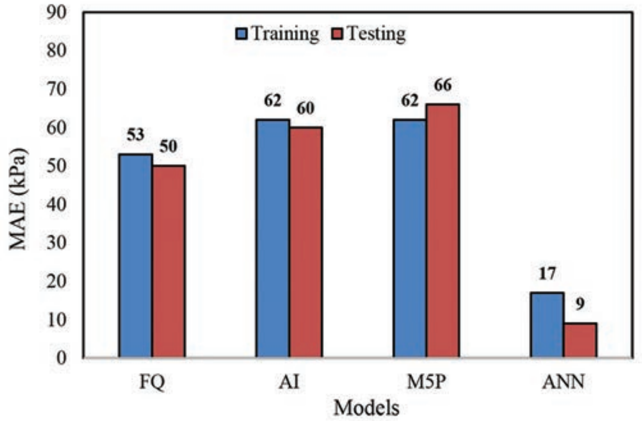

Fig. 13. Evaluation between measured and predicted values of unconfined compressive strength for artificial neural network model: training data and testing data.

TABLE IV
ANN Testing Architecture for UCS

No. of hidden layers	No. of neurons in hidden layers			R-Square	MAE (kPa)	RMSE (kPa)
	Left	Middle	Right			
1	3	0	0	0.78	55.58	70.68
1	5	0	0	0.84	43.39	59.57
1	6	0	0	0.82	46.69	63.72
1	8	0	0	0.88	35.47	52.05
1	9	0	0	0.89	36.36	47.77
2	5	0	5	0.94	25.77	37.01
2	6	0	6	0.94	25.75	48.20
2	7	0	7	0.96	21.78	30.46
3	**7**	**6**	**3**	**0.97**	**16.75**	**24.16**
3	7	5	2	0.96	17.65	28.08
3	5	4	2	0.93	35.41	46.35
3	5	5	5	0.91	32.28	43.47

Bold values indicate the best ANN model with highest R-square and lowest MAE and RMSE.

E. The Linear and Vipulanandan Correlations between UCS, and FS

Fig. 6 represents the relationship between UCS and swelling potential, as measured by the free swell index (FS). For both natural and RHA-treated soils, two models are used

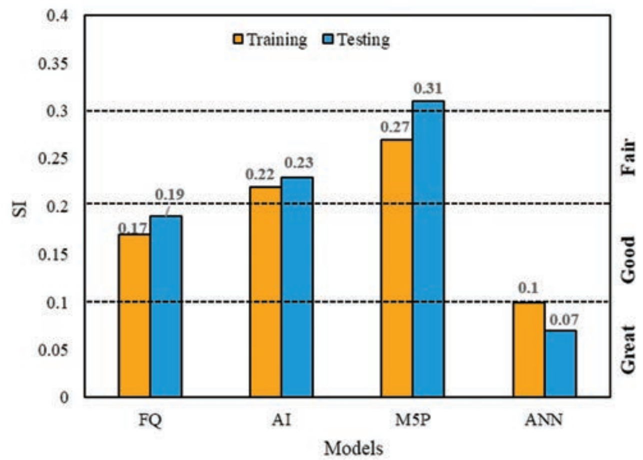

Fig. 14. The SI values of unconfined compressive strength for all four models.

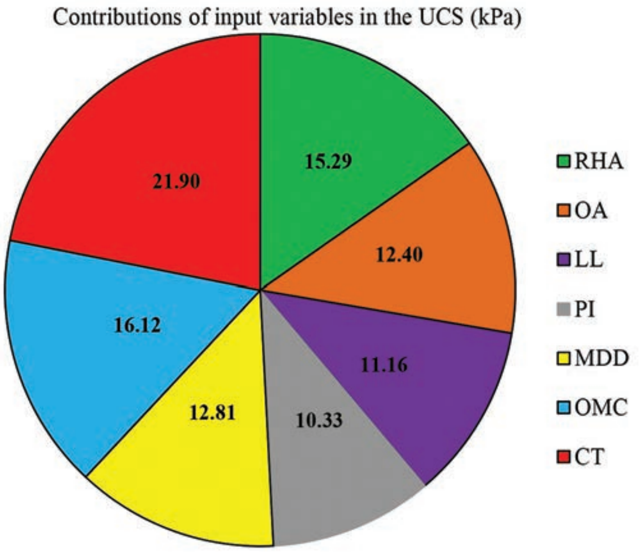
Contributions of input variables in the UCS (kPa)

Fig. 15. The production of the sensitivity analysis for the main parameters' effect on the unconfined compressive strength.

to represent this relationship. The negative slope reveals an inverse relationship between UCS and FS, implying that as UCS increases, FS decreases. This suggests that stronger soil, as indicated by greater UCS values, has a reduced swelling potential, which is beneficial for the stabilization process. The R^2 value of 0.71 proposes a moderate to strong correlation, representing that the UCS describes 71% of the variance in FS in this linear model. Moreover, the Vipulanandan correlation model (2014) has an R^2 of 0.75, showing 75% of the variance in FS. The improved fit implies that the Vipulanandan model may better reflect the behavior of soil swelling as UCS changes, mainly at higher UCS values (Mawlood, et al., 2022; Mohammed, 2024; Rabat, Cano, and Tomás, 2020; Vipulanandan and Mohammed, 2020). Overall, The Vipulanandan model's higher R^2 value shows a more accurate depiction of the UCS-FS relationship for the natural and RHA-treated soils, specifically when predicting FS behavior is required. The linear and Vipulanandan correlation model equations are as follows:

$$\text{FS (\%)} = -6.144\ln(x) + 41.761 \text{ (Linear)} \tag{17}$$

$$\text{FS }(\%) = 4.071 - \frac{\text{UCS}}{0.093\text{UCS} + 3.023}(\text{Vipulanandan Model}) \tag{18}$$

VIII. COMPARISON MODELS

The study compares the employment of four multivariable models (FQ, IA, M5P, and ANN) in predicting UCS properties. The effectiveness of the models was assessed using four quantitative tools: R^2, RMSE, MAE, and SI, and the results were displayed in Figs. 7-9,14, respectively. These Figures show that the ANN model consistently outperformed others in all categories, particularly in reducing prediction error and residual spread The findings show that the ANN model has the greatest R^2 value for UCS in training (0.97) and testing (0.99) data sets, and the lowest RMSE values for UCS in training (24 kPa) and testing (13 kPa) data sets, followed by FQ, IA, and M5P models. In addition, SI measures data scatter about the regression line. Lower SI values recommend a better fit of the model to the data. The results show that the ANN model has the lowest SI values for UCS in training (0.1) and testing (0.07) data sets, followed by FQ, IA, and M5P models. Overall, Figs. 7-9,14 shows that while simpler models like FQ and IA offer interpretability, they fall short in generalizing over wide UCS ranges or under varying soil conditions.

IX. SENSITIVITY ANALYSIS

A sensitivity analysis was performed to identify the most influential input variables affecting UCS predictions. The analysis employed a variable-exclusion approach: each input (RHA, OA, LL, PI, MDD, OMC, and CT) was individually removed, and changes in RMSE, R^2, and MAE were used to quantify its relative importance. The most comprehensive and precise model (the ANN model) was chosen to identify the parameter with the highest impact on UCS of natural and treated soils. The most common statistical measures (RMSE) were performed, as input parameter has a greater impact on RMSE values than other factors. Fig. 15 shows the results of the sensitivity analysis. The figure shows that CT had the highest influence (21.9%), followed by OMC (16.1%), RHA content (15.3%), MDD (14.3%), and PI (12.6%). The study found, when CT was excluded, the RMSE increased from 24 to 53 kPa. Excluding OMC or RHA content also caused significant accuracy losses, while LL and PI had marginal effects.

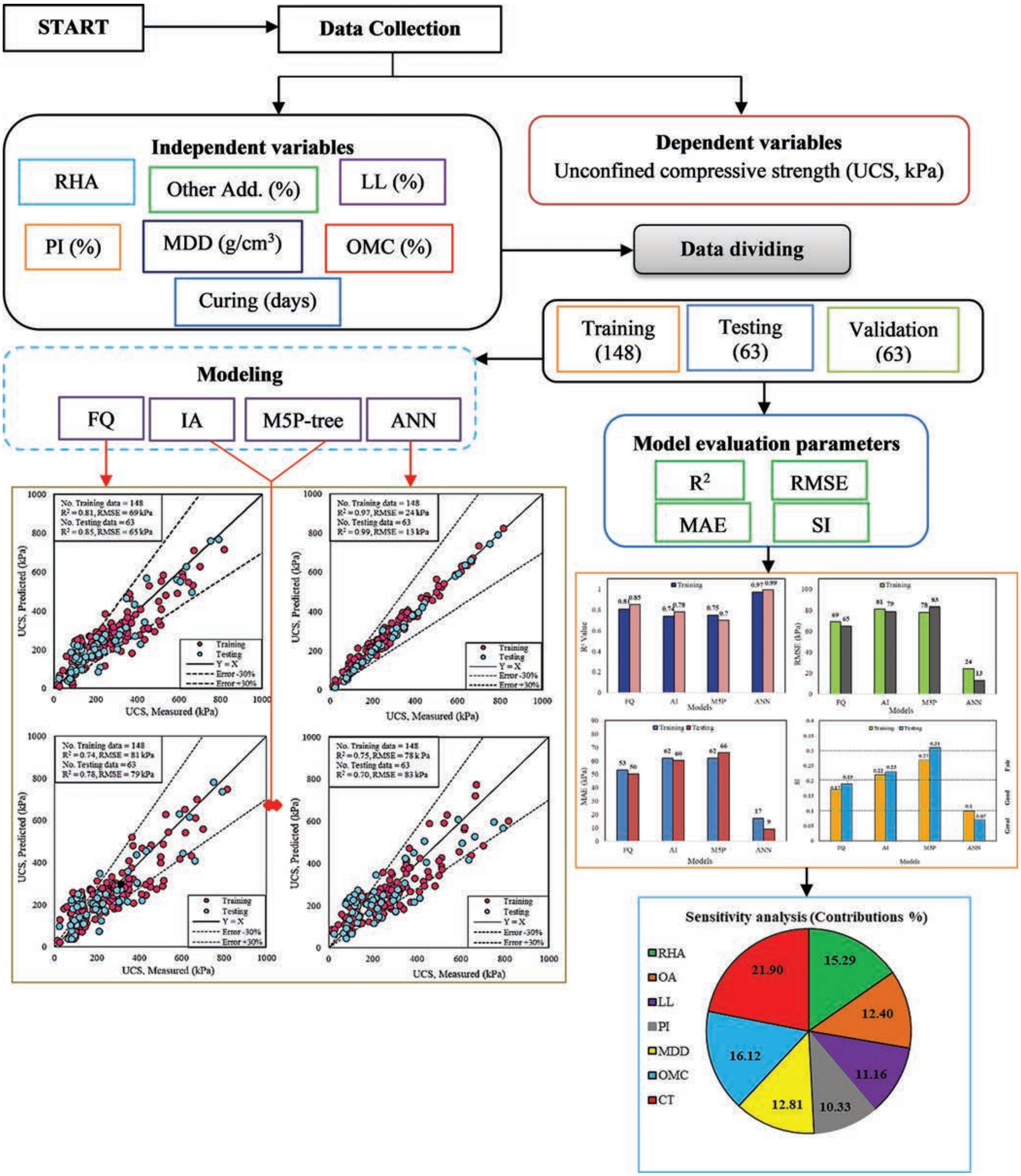

Fig. 16. Summary of the research framework and findings.

X. CONCLUSIONS

A. Findings

This study utilized various predictive models, including ANN and M5P-tree, along with FQ and IA, to predict the UCS of fine-grained soils stabilized with RHA. The overall modeling framework, comparative performance, and key findings are visually synthesized and provided in Fig. 16. The followings are the main findings of this study:

1. Out of the four models tested, the ANN gave the most accurate and reliable UCS predictions.
2. Both ANN and FQ models exhibited strong predictive performance for UCS, with SI values below 0.2. The IA model had fair accuracy with SI values between 0.2 and

0.3, while the M5P model showed weak accuracy with SI values of 0.3 and above.

3. The ANN model achieved the highest accuracy with an R^2 of 0.97, RMSE of 24 kPa, and MAE of 17 kPa, using inputs such as RHA, OA, LL, PI, MDD, OMC, and CT.
4. CT, OMC, and RHA content were the most important factors in predicting UCS.
5. ANN is great for accurate predictions but hard to interpret. FQ is more user-friendly because it provides clear equations.
6. Sensitivity analysis indicated that the CT (21.90%) had the biggest impact on UCS, followed by moisture content (16.12%) and RHA (15.29%).
7. Both the linear and Vipulanandan models demonstrated an inverse relationship between UCS and FS, showing that as UCS increases, FS decreases – indicating that stronger soils exhibit lower FS values

B. Research Limitations

1. The dataset involves 211 UCS test results, whereas wide may not fully capture the variability of soil structures across various topographical areas. A larger dataset integrating field-scale UCS tests would improve model generalizability.
2. The model was trained on laboratory-scale data and has not been validated in field conditions.
3. The study focuses on UCS prediction only; other parameters such as durability, swelling potential, or long-term behavior were not considered.
4. ANN models require computational resources and expertise, which may limit their direct application by practitioners without technical support.

C. Future Work Recommendations

1. Apply additional machine learning techniques, including ensemble models and deep learning, to boost accuracy and compare with traditional models such as M5P and ANN.
2. Study the durability and behavior of treated soils under varying environmental conditions over time.
3. Use soils with a wide range of LLs from different regions to enhance the model's adaptability and generalizability.
4. Perform large-scale real-world tests to confirm the reliability of ANN and other predictive models in actual geotechnical projects.

References

Abbey, S.J., Eyo, E.U., and Ng'ambi, S., 2020. Swell and microstructural characteristics of high-plasticity clay blended with cement. *Bulletin of Engineering Geology and the Environment, 79*(4), pp.2119-2130.

Abdulrahman, S.M., Al-Kaream, A., Khalid, W., and Ihsan, E.A., 2024. Enhancing soil with low-cost pozzolanic materials: Rice husk ash and groundnut shell ash compared to cement. *Mathematical Modelling of Engineering Problems, 11*(4), pp.1115-1122.

Adajar, M.A.Q., Aquino, C.J.P., Martin, C.P.H., and Urieta, D.K.G., 2019. Investigating the effectiveness of rice husk ash as stabilizing agent of expansive soil. *GEOMATE Journal, 16*(58), pp.33-40.

Adhikary, S., and Jana, K., 2016. Potentials of rice husk ash as a soil stabilizer. *International Journal of Latest Research in Engineering and Technology, 2*(2), pp.40-42.

Ahmad, M., Al-Mansob, R.A., Ramli, A.B.B., Ahmad, F., and Khan, B.J., 2024. Unconfined compressive strength prediction of stabilized expansive clay soil using machine learning techniques. *Multiscale and Multidisciplinary Modeling, Experiments and Design, 7*(1), pp.217-231.

Ahmad, M., Alsulami, B.T., Al-Mansob, R.A., Ibrahim, S.L., Keawsawasvong, S., Majdi, A., and Ahmad, F., 2022. Predicting subgrade resistance value of hydrated lime-activated rice husk ash-treated expansive soil: A comparison between M5P, support vector machine, and gaussian process regression algorithms. *Mathematics, 10*(19), p.3432.

Ahmed, A., 2013. Recycled bassanite for enhancing the stability of poor subgrades clay soil in road construction projects. *Construction and Building Materials, 48*, pp.151-159.

Ahmed, C., Mohammed, A., and Saboonchi, A., 2022. ArcGIS mapping, characterisations and modelling the physical and mechanical properties of the Sulaimani City soils, Kurdistan Region, Iraq. *Geomechanics and Geoengineering, 17*(2), pp.384-397.

Ahmed, H.U., Mohammed, A.S., and Mohammed, A.A., 2022. Multivariable models including artificial neural network and M5P-tree to forecast the stress at the failure of alkali-activated concrete at ambient curing condition and various mixture proportions. *Neural Computing and Applications, 34*(20), pp.17853-17876.

Ahmed, H.U., Mohammed, A.S., Mohammed, A.A., and Faraj, R.H., 2021. Systematic multiscale models to predict the compressive strength of fly ash-based geopolymer concrete at various mixture proportions and curing regimes. *PLoS One, 16*(6), pp.e0253006.

Alhassan, M., 2008. *Potentials of Rice Husk Ash for Soil Stabilization*. Available from: https://www.thaiscience.info/journals/article/aujt/10290698.pdf

Ali, H.F.H., 2024. Utilizing several multivariable mathematical and M5P-tree models to predict uniaxial compressive strength of rocks. *Multiscale and Multidisciplinary Modeling, Experiments and Design, 7*(3), pp.1737-1753.

Ali, H.F.H., and Mohammed, A.S., 2024. Modeling the effect of chemical additives on clay soil plasticity: Novel analysis of oxide contributions in fly ash and cement treatments. *Modeling Earth Systems and Environment*, 10, pp.7049-7078.

Ali, H.F.H., Omer, B., Mohammed, A.S., and Faraj, R.H., 2024. Predicting the maximum dry density and optimum moisture content from soil index properties using efficient soft computing techniques. *Neural Computing and Applications, 36*(19), pp.11339-11369.

Anupam, A.K., Kumar, P., and Ransingchung, R.N.G.D., 2014. Performance evaluation of structural properties for soil stabilised using rice husk ash. *Road Materials and Pavement Design, 15*(3), pp.539-553.

Anwar Hossain Khandaker, M., 2011. Stabilized soils incorporating combinations of rice husk ash and cement kiln dust. *Journal of Materials in Civil Engineering, 23*(9), pp.1320-1327.

Ashango, A.A., and Patra, N.R., 2014. Static and cyclic properties of clay subgrade stabilised with rice husk ash and Portland slag cement. *International Journal of Pavement Engineering, 15*(10), pp.906-916.

Baghbani, A., Soltani, A., Kiany, K., and Daghistani, F., 2023. Predicting the strength performance of hydrated-lime activated rice husk ash-treated soil using two grey-box machine learning models. *Geotechnics, 3*(3), pp.894-920.

Basha, E.A., Hashim, R., Mahmud, H.B., and Muntohar, A.S., 2005. Stabilization of residual soil with rice husk ash and cement. *Construction and Building Materials, 19*(6), pp.448-453.

Behak, L., and Musso, M., 2016. Performance of low-volume roads with wearing course of silty sand modified with rice husk ash and lime. *Transportation Research Procedia, 18*, pp.93-99.

Belabbaci, Z., Mamoune, S.M.A., and Bekkouche, A., 2013. Laboratory study of the influence of mineral salts on swelling (KCl, MgCl^ sub 2^). *Earth Science Research, 2*(2), p.135.

Blayi, R.A., Omer, B., Sherwani, A.F.H., Hamadamin, R.M., and Muhammed, H.K., 2024. Geotechnical characteristics of fine-grained soil with wood ash. *Cleaner Engineering and Technology, 18*, p.100726.

Blayi, R.A., Sherwani, A.F.H., Mahmod, F.H.R., and Ibrahim, H.H., 2021. Influence of rock powder on the geotechnical behaviour of expansive soil. *International Journal of Geosynthetics and Ground Engineering, 7*(1), p.14.

Cabalar, A.F., and Omar, R.A., 2023. Stabilizing a silt using waste limestone powder. *Bulletin of Engineering Geology and the Environment, 82*(8), p.300.

Canakci, H., Aziz, A., and Celik, F., 2015. Soil stabilization of clay with lignin, rice husk powder and ash. *Geomechanics and Engineering*, 8(1), pp.67-79.

Charyulu, S.V., Akhila, C., Vineetha, C., and Akanksha, A., 2023. Stabilisation of soil using rice husk ash (RHA) and cement. *E3S Web Conf., 391*, p.01201.

Choobbasti, A.J., Ghodrat, H., Vahdatirad, M.J., Firouzian, S., Barari, A., Torabi, M., and Bagherian, A., 2010. Influence of using rice husk ash in soil stabilization method with lime. *Frontiers of Earth Science in China, 4*(4), pp.471-480.

Eberemu Adrian, O., Amadi Agapitus, A., and Sule, J., 2012. Desiccation effect on compacted tropical clay treated with rice husk ash. In: *Geo-Frontiers 2011*. Geo-Frontiers, Karnataka, pp. 1192-1201.

Emad, W., Salih Mohammed, A., Kurda, R., Ghafor, K., Cavaleri, L., Qaidi, S.M.A., Hassan, A.M.T., and Asteris, P.G., 2022. Prediction of concrete materials compressive strength using surrogate models. *Structures, 46*, pp.1243-1267.

Estabragh, A.R., Moghadas, M., and Javadi, A.A., 2013. Effect of different types of wetting fluids on the behaviour of expansive soil during wetting and drying. *Soils and Foundations, 53*(5), pp.617-627.

Eyo, E.U., Abbey, S.J., and Booth, C.A., 2022. Strength predictive modelling of soils treated with calcium-based additives blended with eco-friendly pozzolans-a machine learning approach. *Materials* (*Basel*), *15*(13), pp.4575.

Fattah, M.Y., Rahil, F.H., and Al-Soudany, K.Y., 2013. Improvement of clayey soil characteristics using rice husk ash. *Journal of Civil Engineering and Urbanism, 3*(1), pp.12-18.

Gautam, N., Gupta Kritesh, K., Bhowmik, D., and Dey, S., 2023. Probing the stochastic unconfined compressive strength of lime-RHA mix treated clayey soil. *Journal of Materials in Civil Engineering, 35*(3), p.04022469.

Ghafor, K., Ahmed, H.U., Faraj, R.H., Mohammed, A.S., Kurda, R., Qadir, W.S., Mahmood, W., and Abdalla, A.A., 2022. Computing models to predict the compressive strength of engineered cementitious composites (ECC) at various mix proportions. *Sustainability, 14*(19), p.12876.

Ghanizadeh, A.R., and Naseralavi, S.S., 2023. Intelligent prediction of unconfined compressive strength and young's modulus of lean clay stabilized with iron ore mine tailings and hydrated lime using gaussian process regression. *Journal of Soft Computing in Civil Engineering, 7*(4), pp.1-23.

Ghorbani, A., and Hasanzadehshooiili, H., 2018. Prediction of UCS and CBR of microsilica-lime stabilized sulfate silty sand using ANN and EPR models; application to the deep soil mixing. *Soils and Foundations, 58*(1), pp.34-49.

Gnananandarao, T., Dutta, R.K., Khatri, V.N., and Kumar, M.S., 2022. Soft computing based prediction of unconfined compressive strength of fly ash stabilised organic clay. *Journal of Soft Computing in Civil Engineering, 6*(4), pp.43-58.

Gnananandarao, T., Onyelowe, K.C., Dutta, R.K., and Ebid, A.M., 2023. Chapter sixteen - sensitivity analysis and estimation of improved unsaturated soil plasticity index using SVM, M5P, and random forest regression. In: Basetti, V., Shiva, C.K., Ungarala, M.R., and Rangarajan, S.S., Eds. *Artificial Intelligence and Machine Learning in Smart City Planning*. Elsevier, Netherlands, pp. 243-255.

Goktepe, A.B., Altun, S., Altintas, G., and Tan, O., 2008. Shear strength estimation of plastic clays with statistical and Neural approaches. *Building and Environment*, *43*(5), pp.849-860.

Hama Ali, H.F., 2023. Utilizing multivariable mathematical models to predict maximum dry density and optimum moisture content from physical soil properties. *Multiscale and Multidisciplinary Modeling, Experiments and Design, 6*(4), pp.603-627.

Hoque, M.I., Hasan, M., Islam, M.S., Houda, M., Abdallah, M., and Sobuz, M.H.R., 2023. Machine learning methods to predict and analyse unconfined compressive strength of stabilised soft soil with polypropylene columns. *Cogent Engineering, 10*(1), p.2220492.

Hossain, M.S., and Kim, W.S., 2015. Estimation of subgrade resilient modulus for fine-grained soil from unconfined compression test. *Transportation Research Record, 2473*(1), pp.126-135.

Hossain, Z., Bulut, R., Tarhuni, F., and Al-Dakheeli, H., 2022. *Using Rice Husk Ash (RHA) as Stabilizing Agent for Problematic Subgrade Soils and Embankments*. Retrieved from: https://repository.lsu.edu/transet_pubs/141/

Ingabire, D., and Kumar, S., 2023. Enhancement of engineering properties of black cotton soil using rice husk and sawdust ash. *E3S Web Conf., 391*, p.01023.

Jalal, F.E., Mulk, S., Memon, S.A., Jamhiri, B., and Naseem, A., 2021. Strength, hydraulic, and microstructural characteristics of expansive soils incorporating marble dust and rice husk ash. *Advances in Civil Engineering, 2021*(1), p.9918757.

Jalal, F.E., Xu, Y., Iqbal, M., Javed, M.F., and Jamhiri, B., 2021. Predictive modeling of swell-strength of expansive soils using artificial intelligence approaches: ANN, ANFIS and GEP. *Journal of Environmental Management, 289,* p.112420.

Khan, R., Jabbar, A., Ahmad, I., Khan, W., Khan, A.N., and Mirza, J., 2012. Reduction in environmental problems using rice-husk ash in concrete. *Construction and Building Materials, 30*, pp.360-365.

Kumar Yadav, A., Gaurav, K., Kishor, R., and Suman, S.K., 2017. Stabilization of alluvial soil for subgrade using rice husk ash, sugarcane bagasse ash and cow dung ash for rural roads. *International Journal of Pavement Research and Technology, 10*(3), pp.254-261.

Li, C., Su, L., Liao, H., Zhang, C., and Xiao, S., 2021. Modeling of rapid evaluation for seismic stability of soil slope by finite element limit analysis. *Computers and Geotechnics, 133,* pp.104074.

Lin, B., and Cerato, A.B., 2012. Prediction of expansive soil swelling based on four micro-scale properties. *Bulletin of Engineering Geology and the Environment, 71*(1), pp.71-78.

Mahmood, W., and Mohammed, A., 2022. Performance of ANN and M5P-tree to forecast the compressive strength of hand-mix cement-grouted sands modified with polymer using ASTM and BS standards and evaluate the outcomes using SI with OBJ assessments. *Neural Computing and Applications, 34*(17), pp.15031-15051.

Maithili, K.L., Nagakumar, M.S., and Shashishankar, A., 2024. Laboratory assessment of the effectiveness of rice husk ash, rice husk, and groundnut shells in soil improvement. *Indian Geotechnical Journal*, 54, pp.2143-2157.

Mawlood, Y., Mohammed, A., Hummadi, R., Hasan, A., and Ibrahim, H., 2022. Modeling and statistical evaluations of unconfined compressive strength and compression index of the clay soils at various ranges of liquid limit. *Journal of Testing and Evaluation, 50*(1), pp.551-569.

Mawlood, Y., Salih, A., Hummadi, R., Hasan, A., and Ibrahim, H., 2021. Comparison of artificial neural network (ANN) and linear regression modeling with residual errors to predict the unconfined compressive strength and compression index for Erbil City soils, Kurdistan-Iraq. *Arabian Journal of Geosciences, 14*(6), p.485.

McBratney, A.B., Odeh, I.O.A., Bishop, T.F.A., Dunbar, M.S., and Shatar, T.M., 2000. An overview of pedometric techniques for use in soil survey. *Geoderma, 97*(3), pp.293-327.

Meskini, S., Remmal, T., Ejjaouani, H., and Samdi, A., 2022. Formulation and optimization of a phosphogypsum - fly ash - lime composite for road construction: A statistical mixture design approach. *Construction and Building Materials, 315*, p.125786.

Mohammed, A., 2024. Property correlations and statistical variations in the geotechnical properties of (CH) clay soils. *Geotechnical and Geological Engineering, 42*(1), p.843-858.

Mohammed, A., and Vipulanandan, C., 2015. Testing and modeling the short-term behavior of lime and fly ash treated sulfate contaminated CL soil. *Geotechnical and Geological Engineering, 33*(4), pp.1099-1114.

Mohammed, A., Burhan, L., Ghafor, K., Sarwar, W., and Mahmood, W., 2021. Artificial neural network (ANN), M5P-tree, and regression analyses to predict the early age compression strength of concrete modified with DBC-21 and VK-98 polymers. *Neural Computing and Applications, 33*(13), pp.7851-7873.

Mohammed, A., Hummadi, R.A., and Mawlood, Y.I., 2022. Predicting the chemical and mechanical properties of gypseous soils using different simulation technics. *Acta Geotechnica, 17*(4), pp.1111-1127.

Mohammed, A., Rafiq, S., Sihag, P., Kurda, R., Mahmood, W., Ghafor, K., and Sarwar, W., 2020. ANN, M5P-tree and nonlinear regression approaches with statistical evaluations to predict the compressive strength of cement-based mortar modified with fly ash. *Journal of Materials Research and Technology, 9*(6), pp.12416-12427.

Mohammed, A.S., 2018. Property correlations and statistical variations in the geotechnical properties of (CH) clay soils. *Geotechnical and Geological Engineering, 36*(1), pp.267-281.

Mohanty, S., Roy, N., Singh, S.P., and Sihag, P., 2019. Estimating the strength of stabilized dispersive soil with cement clinker and fly ash. *Geotechnical and Geological Engineering, 37*(4), pp.2915-2926.

Mousavi, S.M., Alavi, A.H., Gandomi, A.H., and Mollahasani, A.L.I., 2011. Nonlinear genetic-based simulation of soil shear strength parameters. *Journal of Earth System Science, 120*(6), pp.1001-1022.

Mozumder, R.A., and Laskar, A.I., 2015. Prediction of unconfined compressive strength of geopolymer stabilized clayey soil using artificial neural network. *Computers and Geotechnics, 69*, pp.291-300.

Muntohar, A.S., 2004. Utilization of uncontrolled burnt rice husk ash in soil improvement. *Civil Engineering Dimension, 4*(2), pp.100-105.

Murty, V.R., and Praveen, G.V., 2008. Use of chemically stabilized soil as cushion material below light weight structures founded on expansive soils. *Journal of Materials in Civil Engineering, 20*(5), pp.392-400.

Nahar, N., Owino, A.O., Khan, S.K., Hossain, Z., and Tamaki, N., 2021. Effects of controlled burn rice husk ash on geotechnical properties of the soil. *Journal of Agricultural Engineering, 52*(4). Doi: 10.4081/jae.2021.1216

Nasir Amin, M., Iftikhar, B., Khan, K., Faisal Javed, M., Mohammad AbuArab, A., and Faisal Rehman, M., 2023. Prediction model for rice husk ash concrete using AI approach: Boosting and bagging algorithms. *Structures, 50*, pp.745-757.

Ordoñez Muñoz, Y., Luis dos Santos Izzo, R., Leindorf de Almeida, J., Arrieta Baldovino, J., and Lundgren Rose, J., 2021. The role of rice husk ash, cement and polypropylene fibers on the mechanical behavior of a soil from Guabirotuba formation. *Transportation Geotechnics, 31*, pp.100673.

Pandey, P.K., and Aggarwal, Y., 2022. ANN and M5P Approaches with Statistical Evaluations to Predict Compressive Strength of SCC Containing Silicas. In: *Proceedings of the International Conference on Paradigms of Communication, Computing and Data Sciences*, Singapore.

Pham, V.N., Huu-Dao, D., Erwin, O., and Ong, D.E.L., 2021. Prediction of unconfined compressive strength of cement-stabilized sandy soil in Vietnam using artificial neural networks (ANNs) model. *International Journal of Geotechnical Engineering, 15*(9), pp.1177-1187.

Pushpakumara, B.H.J., and Mendis, W.S.W., 2022. Suitability of rice husk ash (RHA) with lime as a soil stabilizer in geotechnical applications. *International Journal of Geo-Engineering, 13*(1), p.4.

Rabat, Á., Cano, M., and Tomás, R., 2020. Effect of water saturation on strength and deformability of building calcarenite stones: Correlations with their physical properties. *Construction and Building Materials, 232*, p.117259.

Rahman, M.A., 1987. Effects of cement-rice husk ash mixtures on geotechnical properties of lateritic soils. *Soils and Foundations, 27*(2), pp.61-65.

Rahman, M.D.A., 1986. The potentials of some stabilizers for the use of lateritic soil in construction. *Building and Environment, 21*(1), pp.57-61.

Sarkar, G., Islam, M.R., Alamgir, M., and Rokonuzzaman, M., 2012. Interpretation of rice husk ash on geotechnical properties of cohesive soil. *Global Journal of Researches in Engineering Civil and Structural Engineering, 12*(2), pp.1-7.

Sharma, L.K., and Singh, T.N., 2018. Regression-based models for the prediction of unconfined compressive strength of Artificially structured soil. *Engineering with Computers, 34*(1), pp.175-186.

Sihag, P., Suthar, M., and Mohanty, S., 2021. Estimation of UCS-FT of dispersive soil stabilized with fly ash, cement clinker and GGBS by artificial intelligence. *Iranian Journal of Science and Technology, Transactions of Civil Engineering, 45*(2), pp.901-912.

Suthar, M., 2020. Applying several machine learning approaches for prediction of unconfined compressive strength of stabilized pond ashes. *Neural Computing and Applications, 32*(13), pp.9019-9028.

Tahr, Z., Mohammed, A., and Ali, J.A., 2022. Surrogate models to predict initial shear stress of clay bentonite drilling fluids incorporated with polymer under various temperature conditions. *Arabian Journal of Geosciences, 15*(17), pp.1449.

Verma, G., and Kumar, B., 2021. Multi-layer perceptron (MLP) neural network for predicting the modified compaction parameters of coarse-grained and fine-grained soils. *Innovative Infrastructure Solutions, 7*(1), p.78.

Vipulanandan, C., Ahossin Guezo, Y.J., and Bilgin, Ö., 2012. Geotechnical properties of marine and deltaic soft clays. In: *Advances in Measurement and Modeling of Soil Behavior*. United States: ASCE, pp.1-13.

Vipulanandan, C., and Mohammed, A., 2020. Characterizing the index properties, free swelling, stress-strain relationship, strength and compacted properties of polymer treated expansive CH clay soil using vipulanandan models. *Geotechnical and Geological Engineering, 38*(5), pp.5589-5602.

Wang, M.C., and Huang, C.C., 1984. Soil compaction and permeability prediction models. *Journal of Environmental Engineering, 110*(6), pp.1063-1083.

Wang, X., Kim, S., Wu, Y., Liu, Y., Liu, T., and Wang, Y., 2023. Study on the optimization and performance of GFC soil stabilizer based on response surface methodology in soft soil stabilization. *Soils and Foundations, 63*(2), p.101278.

Wattanapanich, C., Imjai, T., Kefyalew, F., Aosai, P., Garcia, R., Vapppangi, S., and Noguchi, T., 2024. Integration of internet of things (IoT) and machine learning for management of ground water banks in drought-prone areas: A case study from imjai organic garden, Thailand. *Engineered Science, 31*, p.1248.

Westerberg, B., Müller, R., and Larsson, S., 2015. Evaluation of undrained shear strength of Swedish fine-grained sulphide soils. *Engineering geology, 188*, pp.77-87.

Yadu, L., Tripathi, R.K., and Singh, D., 2011. Comparison of fly ash and rice husk ash stabilized black cotton soil. *International Journal of Earth Sciences and Engineering, 4*(6), pp.42-45.

Zaimoglu, A.S., 2015. Optimization of unconfined compressive strength of fine-grained soils modified with polypropylene fibers and additive materials. *KSCE Journal of Civil Engineering, 19*(3), pp.578-582.

Zeng, J., Asteris, P.G., Mamou, A.P., Mohammed, A.S., Golias, E.A., Armaghani, D.J., Faizi, K., and Hasanipanah, M., 2021. The effectiveness of ensemble-neural network techniques to predict peak uplift resistance of buried pipes in reinforced sand. *Applied Sciences, 11*(3), p.908.

Zhang, L., Liu, Z., Zhou, Y., Wu, T., and Sun, J., 2024. *Grounding Large Language Models in Real-World Environments using Imperfect World Models*. [Authorea Preprints].

Zivari, A., Siavoshnia, M., and Rezaei, H., 2023. Effect of lime-rice husk ash on geotechnical properties of loess soil in Golestan province, Iran. *International Journal of Geo-Engineering, 14*(1), p.20.

A Systematic Survey on Large Language Models for Static Code Analysis

Hekar A. Mohammed Salih[1†] and Qusay I. Sarhan[2]

[1]Department of Computer Science, College of Science, University of Duhok,
Zakho Street 38 AJ, Duhok, Kurdistan Region - Iraq

[2]Department of Computer Science, College of Science, University of Duhok,
Zakho Street 38 AJ, Duhok, Kurdistan Region - Iraq

***Abstract—Static* code analysis plays a pivotal role in improving software quality, security, and maintainability by detecting vulnerabilities, errors, and programming issues in source code without executing it. Recent advancements in artificial intelligence, especially the development of large language models (LLMs), such as ChatGPT, have enabled transformational opportunities in this domain. Thus, it is essential to explore this emerging field of research from many perspectives. This systematic survey focuses on the use of LLMs for static code analysis, detailing their applications, advantages, contexts, limitations, etc. The study examines research papers published on the topic from reputable literature databases to answer several research questions regarding the state-of-the-art use of LLMs in static code analysis. In addition, different research gaps and challenges were identified and discussed alongside many directions. The results of this study demonstrate how LLMs can enhance static code analysis and address existing limitations, paving the way for developers and researchers to employ LLMs for a more affordable and effective software development process.**

***Index Terms*—Large language models, Software metrics, Software quality, Static code analysis.**

I. Introduction

Static code analysis is a crucial activity in software development, which is aimed at detecting possible vulnerabilities, defects, or other issues related to code quality without executing the program (Louridas, 2006). Traditional static analysis techniques are based on rules and heuristics defined to analyze the source code; however, they often face challenges with modern complex systems and new coding styles. Static code analysis is essential in several domains including software engineering, cybersecurity, and the Internet of Things (IoT, henceforth). For example, in software engineering, static code analysis is critical for the prompt resolution of potential code threats, which in turn makes it easy to develop software programs that are competent, high-quality, reliable, and error-free (Ramamoorthy, et al., 2024). In the area of cybersecurity, it helps locate and understand vulnerabilities in sensitive information systems, such as banking and healthcare systems (Hassan, Sarhan and Beszédes, 2024). In the field of IoT, where interconnected devices are used extensively in critical areas, such as healthcare, smart cities, and automated industry, the risk is higher than ever. With the diverse resource and connection constraints, static code analysis ensures that IoT applications meet high performance and security needs. Static code analysis helps to a system's robustness and effectiveness, thereby enhancing the overall safety and efficiency of contemporary digital ecosystems (Kotenko, Izrailov and Buinevich, 2022).

Large language models (LLMs, henceforth), such as ChatGPT and many others have triggered a new interest in their application for improving static code analysis. LLMs have a unique feature that allows them to understand source code because they are trained on extensive code and natural language datasets. In addition to that, LLMs can recognize many different types of code issues, especially those that require an in-depth comprehension of context or intricate reasoning. Furthermore, by synthesizing information from multiple code snippets, LLMs may be able to recognize several issues that offer a great deal of information on the code's readability, maintainability, and compliance with software design paradigms. On the other hand, traditional methods, such as abstract syntax tree (AST, henceforth) analysis, data flow analysis, and static symbolic execution may not be able to identify certain types of faults compared to LLMs.

By incorporating more advanced artificial intelligence (AI) models, especially LLMs, there is a remarkable transformation in the methods of software development in the fast-evolving field of software engineering. Generative AI technologies are widely adopted because they have clear advantages, such as high productivity, high accuracy, and rapid development cycles. Industry research suggests that by 2027, around 70% of professional software

ARO-The Scientific Journal of Koya University
Vol. XIII, No. 1 (2025), Article ID: ARO.12082. 15 pages
DOI: 10.14500/aro.12082
Received: 03 March 2025; Accepted: 27 May 2025
Regular review paper; Published: 22 June 2025

†Corresponding author's e-mail hekar.mohammedsalih@uod.ac

developers will use AI-assisted coding tools for standard programming activities, such as code creation, debugging, and optimization (Sikand, et al., 2024). The use of LLMs for static code analysis, or in combination with traditional methods, holds great potential for developing new tools in the software industry. Given their knowledge of natural and programming languages, LLMs can find bugs, provide specific suggestions in code, and even improve a developer's productivity.

This systematic survey represents the first comprehensive review focused exclusively on LLM-based static code analysis. Through rigorous examination of many related studies, the survey provides insights and establishes a novel taxonomy for this rapidly evolving field, while identifying critical limitations and proposing actionable research directions.

Summing up, the key contributions of this survey are listed below:

- First dedicated survey: This survey provides the first dedicated, systematic examination of LLMs for static code analysis, establishing a comprehensive foundation for understanding their applications, capabilities, and limitations in this specific domain. Unlike broader surveys of LLMs in software engineering, our work focuses exclusively on static code analysis tasks.
- Systematic methodology: This survey concentrates on the research that were recently published on the topic by using systematic techniques for inclusion and exclusion of the criteria set by the clearly articulated questions.
- Identification of critical challenges: This survey highlights the limitations of LLMs in static analysis, such as (high false positive rates, context window constraints, and computational costs as key adoption barriers).
- Statistical synthesis of LLMs applications in static code analysis: The survey provides a comprehensive statistical synthesis of prior research, including the prevalence of LLMs, such as ChatGPT-4 and its alternatives, as well as traditional static code analysis tools that have been widely used. It also covers programming language distribution, software engineering tasks coverage, evaluation metrics, and prompting strategies in significant detail.
- Future research directions: This survey identifies many possible research directions that need to be studied and addressed by researchers. Thus, this work serves as a quality reference for researchers and developers, bridging the gap between LLMs and static code analysis while setting a foundation for future advancements.

This systematic survey was prompted by the reasons listed below:

- Traditional static code analysis constraints: Traditional approaches, such as AST analysis, data flow analysis, and symbolic execution often fail to detect coding errors and coding quality issues as they are not designed to understand codes. Such techniques may be enhanced by LLMs which offer improved comprehension and reasoning capabilities over the code.
- LLMs for static code analysis: The use of LLMs in coding activities is rapidly increasing, making it necessary to evaluate their effectiveness in performing static code analysis in terms of functional correctness, security, and maintainability. A survey would facilitate the evaluation of their strengths, limitations, and potential areas for development in this area.
- Gaps in existing research: A significant deficiency exists in survey research that particularly examines the application of LLMs in static code analysis. A systematic survey would address this gap by aggregating insights on how LLMs might improve static code analysis and pinpointing areas for further advancement.

The remainder of this survey paper is structured as follows: Section II presents the related works for this survey. Section III describes the details of the research methodology that has been used to conduct this survey systematically. Section IV presents the results and outcomes of this survey. Section V presents the future directions of research in the selected topic. Section VI outlines threats to validity and the measures taken to address them. Finally, the conclusions of the survey are provided in Section VII.

II. Related Works

The use of LLMs in software engineering has transformed several research areas, including static code analysis, code creation, optimization, testing, maintenance, and security. This section summarizes the progress and related works that have been performed in the literature divided in several categories, as follows:

A. Code Generation and Optimization

The application of LLMs to the generation and completion of code has gained significant attention in recent years. The authors (Zheng, et al., 2023a) offer a comprehensive review of the development of LLMs for code generation and their astounding success in this task. In addition, they discussed the impact of model size and the quality of data on code generation, and called for more comprehensive ways to enhance these models. In (Zheng, et al., 2023b), the incorporation of LLMs into software engineering and their efficiency in code summarization or repair tasks were discussed significantly. The study highlights the innovative changing possibilities of LLMs in boosting developer efficiency and automating mundane coding tasks, while calling for further research to solve issues, such as model explainability and optimization for specific tasks. LLMs have proven to be useful in the area of code optimization as well as by increasing the overall efficiency of the code, such as in the cases of execution duration and memory use. The authors (Gong, et al., 2025), provide a systematic literature review pinpointing different trends and obstacles in LLMs-based code optimization. The paper emphasizes the superiority of general-purpose LLMs, such as GPT-4 for general optimization tasks, although other models excel in specific optimization tasks. The primary issues include reconciling model complexity with practical applicability and attaining cross-linguistic generalizability. The authors suggest further research avenues, including model reduction and multilingual optimization, to improve the efficiency and resilience of LLM-based code optimization methods for more dependable and scalable solutions.

B. Software Testing and Debugging

The application of LLMs in automating software testing activities, including test case development, program repair, and bug detection, has been thoroughly investigated in many studies. The authors (Wang, et al., 2024), conducted a comprehensive review on the applications of LLMs in activities, such as unit test case development and test oracle creation. While noting the effective capabilities of LLMs for the generation of diverse test inputs and their use in testing, they identified the obstacles that hinder achieving appropriate coverage and the test oracle challenge. They also discussed automating and optimizing software testing and debugging processes with the novel capabilities of LLMs while noting the imperfection of existing studies, such as the lack of integration into actual developer's work and lack of tools for deeper evaluation.

C. Software Maintenance and Management

LLMs have been put to use for the automation of several tasks within software maintenance and management, including rewriting code, creating documentation, and managing the software's lifecycle. The authors (Zhang, et al., 2023a), discussed the impact of LLMs on coding tasks, such as code creation, summarization, and program repair. The author vividly describes the increasing LLM-based software engineering research, driven by deep learning and the availability of open-source code on repositories. The authors (Hou, et al., 2023), conducted a systematic review and identified 85 distinct software engineering jobs in which LLMs have demonstrated efficacy, notably in software development and maintenance. These studies provide evidence that different tasks can be automated using LLMs, which drives software quality improvement, but at the same time creates new challenges, such as data dependence, model size, and generalization. The authors suggest the focus should move toward developing domain-oriented LLMs, along with more detailed evaluation processes.

D. Security and Vulnerability Detection

The utilization of LLMs for detecting and addressing security issues in software systems is a rapidly growing area of study. The authors (Chen, et al., 2024) provided a systematic analysis that classifies the types of attacks and how LLMs can be used to detect them. Furthermore, they provided several defense strategies that can be used to prevent such attacks. The authors (Zhou, et al., 2024) conducted a literature review on the employment of LLMs for discovering and fixing software vulnerabilities. This study shows that encoder-only models, such as CodeBERT, performed best for detection tasks, while decoder-only models, such as GPT-4 excelled at repair tasks. These papers jointly highlight the ability of LLMs for enhancing software security.

E. Natural Language Processing in Software Engineering

Like many domains, the intersection of natural language processing (NLP, henceforth) and software engineering has been very promising with respect to research for different activities, such as code summarization, code translation, and even code repair. The authors in (Zhang, et al., 2023b), provided a detailed understanding of processes related to coding by reviewing work on language model-based processing of code, including modern changes that improve performance, such as moving from statistical models to pre-trained transformers and LLMs. The research focuses on the efficiency of LLMs, such as Codex and GitHub Copilot, within the scope of code generation and comprehension. Moreover, it tackles issues, such as the need for thorough evaluation strategies, benchmarks, and the need for better practical features for codes. The authors in (Salem, et al., 2024), investigated the role of language models in the intersection of spoken languages and computer languages, particularly in automated processes that include writing of code, code refactoring, and debugging. Such studies together demonstrate the promise the application of LLMs has for changing the workflow of software engineering to foster higher productivity of software developers and enable the automation of complex processes.

F. Sustainability and Reusability in Software Engineering

The environmental impact and the sustainability of using LLMs in software engineering have also been addressed in many studies. The authors (Hort, Grishina and Moonen, 2023), examined the diffusion of software source codes and other studies artifacts and found out that only 27% of relevant studies provide sufficient artifacts for reuse. The paper highlights the significant energy consumption associated with training such large models and argues for more transparency regarding hardware specifications and training durations. The authors advocate for the dissemination of pre-trained models to mitigate unnecessary training and foster sustainable methods in software engineering. This research highlights the necessity of mitigating the environmental effect of LLMs and enhancing model reusability to promote sustainability in the domain.

In recent years, the incorporation of LLMs into software engineering has attracted considerable research interest, with various surveys investigating their applications in tasks, such as code generation, optimization, and testing. However, this systematic survey differentiates itself by providing a concentrated, thorough, and rigorous analysis of LLMs specifically for static code analysis, highlighting their applications, challenges, and other aspects often overlooked in general surveys. Thus, this survey represents a significant contribution to the field of software engineering, particularly in the niche area of static code analysis. To achieve this, the survey follows a systematic approach making the analysis of the related works to be relevant and accurate, which in return increases the trustworthiness of the obtained results. Thus, this study can be considered as the most comprehensive and up-to-date study on the use of LLMs in static code analysis, which is beneficial for developers and researchers alike.

III. Research Methodology

This survey follows established guidelines for conducting systematic literature surveys which were presented in (Petersen, Vakkalanka and Kuzniarz, 2015). Fig. 1 illustrates the five steps in the study's process. The first step defines the purpose and scope of the study and defines its objectives along with the research questions (RQs) to be answered. The second step termed the search strategy, focuses on devising a method for searching relevant articles related to the topic under investigation. In the third step, the identified papers are screened and filtered. The fourth step involves data extraction, whereby the selected papers are reviewed and relevant data that meets the objectives of the research is collected. The results are documented during the fifth step of the process. Subsequently, the following sections explain these steps in detail.

A. Identification of Research Objectives and Questions

1. Research objectives: This systematic survey seeks to examine the published works on involving static code analysis with LLMs by searching, assessing, and categorizing state-of-the-art contributions. This is done so that developers and researchers can understand the answers to particular questions and subsequently enhance their efforts in development and research.
2. RQs: Several primary RQs have been defined and answered in this survey. Each RQ deals with a different dimension of the topic of the study, as follows:
   - RQ1: What are the most frequently used LLMs for static code analysis tasks?
   - RQ2: What are the traditional static code analysis tools that are used to assess the quality of LLMs for static code analysis?
   - RQ3: What are the major programming languages used in research for specific static code analysis tasks that involve the use of LLMs?
   - RQ4: What is the range of software engineering activities that have been targeted by static code analysis with LLMs?
   - RQ5: Which evaluation metrics are most used in quantifying the accuracy and utility of LLMs in static code analysis?
   - RQ6: What prompt design strategies are most effective for optimizing LLMs performance in static code analysis?
   - RQ7: What are the common challenges and limitations in leveraging LLMs for static code analysis?

B. Search Strategy

1. Literature sources: Well-known standard online databases, such as IEEE Xplore, Elsevier Science Direct, and ACM Digital Library. that index most of the papers relevant to the scope of this survey were selected as literature sources.

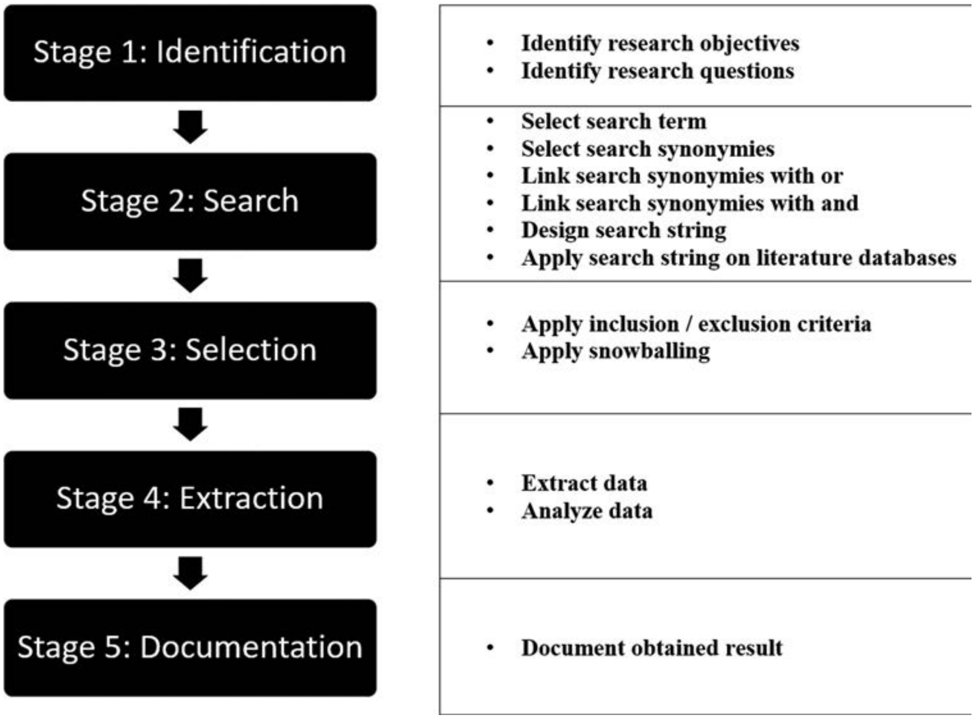

Fig. 1. The employed survey process.

2. Search string: Using the database literature sources, the following search string was used to locate the papers relevant to this survey:

   "(*Generative AI OR LLM OR Large Language Model) AND (static code analysis*)"

All terms of the search string were linked with each other using Boolean operators (Brereton, et al., 2007). The Boolean "OR" was employed to link synonyms or related terms that refer precisely or broadly to different aspects of the study topic and the Boolean "AND" was used to link the major terms.

C. Paper Selection

1. Paper inclusion/exclusion criteria: A set of inclusion and exclusion criteria were established and employed to decide whether a paper is relevant to this study or not. These criteria, which are listed below, have been applied based on the titles, abstracts, and full-text reading of the collected papers.
   a. Inclusion criteria:
   - Papers related directly to static code analysis using LLMs.
   - Papers published over the past 2 years (2023–2024). According to our search and exploration of the literature, papers on static code analysis using LLM started in 2023.

   b. Exclusion criteria:
   - Papers not published in English
   - Papers not peer reviewed (e.g., grey literature)
   - Papers not published electronically
   - Papers that are duplicates of other papers
   - Papers without clear results and evidence.
2. Snowballing: To reduce the risk of missing some relevant papers, the snowballing search technique (Wohlin, 2014) was applied to the remaining papers. In snowballing, the reference list of each paper is checked with the inclusion/exclusion criteria. Then, the paper selection process is applied recursively to the papers that have been found. Fig. 2 shows the number of included and excluded papers at each stage of the paper selection process.

All the papers used in this study are listed below: (Sikand, et al., 2024), (Amburle, et al., 2024), (Li, et al., 2023), (Rahmaniar, 2024), (Hajipour, et al., 2024), (Wadhwa, et al., 2024), (AlOmar and Mkaouer, 2024), (Yuan, et al., 2024), (Mahyari, 2024), (Fang, et al., 2023), (Mathews, et al., 2024), (Li and Shan, 2023), (Hossain, et al., 2024), (Mohajer, et al., 2023), (Gonzalez-Barahona, 2024), (Omar and Shiaeles, 2023), (Guo, et al., 2023a), (Ságodi, Siket and Ferenc, 2024), (Venkatesh, et al., 2024), (Moratis, et al., 2024), (Souma, et al., 2023), (Pearce, et al., 2023), (Bajpai, et al., 2024), (Yin, Ni and Wang, 2024), (Bairi, et al., 2024), (Akuthota, et al., 2023), (Ignatyev, et al., 2024), (Gupta, et al., 2023), (Liu, Yang and Liao, 2024), (Villmow, et al., 2023), (Jesse, et al., 2023), (Guo, et al., 2023b), (Di, et al., 2023), (Haindl and Weinberger, 2024), (Ardito, Ballario and Valsesia, 2023), (Purba, et al., 2023).

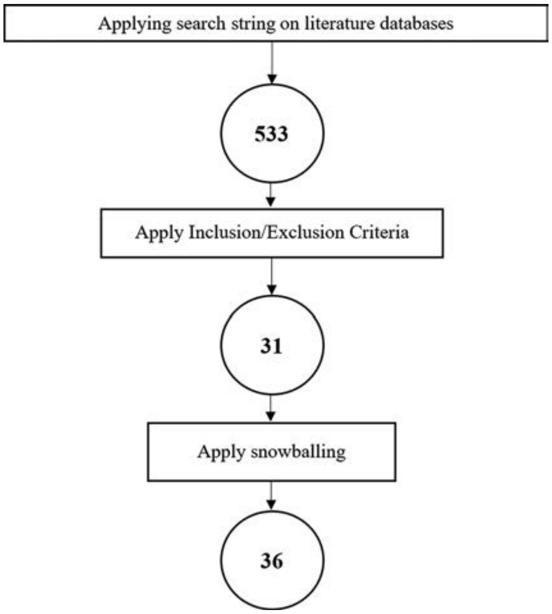

Fig. 2. Results of the paper selection process.

D. Data Extraction and Analysis

To address the RQs, data were taken from the chosen papers and thoroughly examined. An Excel document with several fields was made, especially for this study to include the extracted data. As presented in Table I, each field contains a data item and a value. It is worth mentioning that the Excel document can be accessed by clicking on the link given here: Extraction form (Google Drive).

IV. RESULTS

All of the papers selected were thoroughly examined to address the RQs that were identified for this survey. Based on the results, each RQ is represented by a brief title and is covered in the next subsections.

A. Popular LLMs for Static Code Analysis (RQ1)

Table II presents the most used LLMs in research. It is clear that OpenAI's models, such as ChatGPT-4 and ChatGPT-3.5-turbo, lead the academic landscape, with ChatGPT-4 being referenced in 16 studies, underscoring its versatility and widespread adoption. ChatGPT models, particularly ChatGPT-4 and ChatGPT-3.5-turbo, are popular LLMs because they are the best performers at tasks, are easy to reach through OpenAI APIs, and have better contextual understanding and reasoning. With researchers, working on AI-powered static analysis and software engineering, they remain a top choice especially when economical options, such as ChatGPT-3.5-turbo are available (Gupta, et al., 2023; Acl, 2024). This is because the researchers can find fairly priced options for a variety of tasks including bug detection, code generation, and even vulnerability scans. LLMs are known to have a wide range of applications in static code analysis. They aid in enhancing error detection, warning verification, as well as static analysis test translations across programming languages. LLMs are also known to enhance precision and efficacy by reducing false positives and false negatives in bug detection, malicious code detection, and even vulnerability detection. Their scope of usage expands within programming education for real-time error checking and explanation purposes and even cybersecurity for aiding in the detection and remediation of vulnerabilities.

TABLE I
Data Extraction Form

Data item	Value	RQs
Paper number	Paper ID.	None
Paper title	Title of the study.	None
Used LLMs	LLMs used in the studies.	RQ1
Static code analysis tools	Static code analysis tools used in the studies with LLMs for code evaluation.	RQ2
Programming languages	Programming languages involved in the studies utilizing LLMs for static code analysis.	RQ3
Type of tasks	Tasks of static code analysis performed in the studies using LLMs.	RQ4
Evaluation metrics	Metrics used to assess the effectiveness of LLMs for static code analysis.	RQ5
Prompt designs	Strategies of effective prompt designs for LLMs used in static code analysis tasks.	RQ6
Limitations and challenges	Limitations and Challenges of performing static code analysis using LLMs.	RQ7

LLMs: Large language models, RQs: Research questions

Fig. 3 displays the companies that contributed toward LLMs development which suggests the scope of activity and engagement. OpenAI is leading the list by boosting 8 LLMs, much higher than the other prominent companies including Google, Hugging Face, Meta Microsoft, and Salesforce who have only made 2 LLMs each. This highlight gap clearly indicates openness toward capital and optimism toward supporting the research and development of LLMs. Hence, further solidifying the statement of America being proactive on AI research. The data reveals the rapid changing competitive landscape of LLMs development where OpenAI holds the front line in production, and the other groups have a significantly lesser but steady presence. This gap could mean a change in primary research objectives, budgetary spending, or competitive practices for progressing AI technology.

B. Baseline Static Code Analysis Tools (RQ2)

Table III presents the use of different static code analysis tools outlined in the academic articles, with a particular focus on their application and frequency. Programming mistake

Table II
Popular LLMs for Static Code Analysis

S. No.	LLM	Corresponding papers	Total papers
1.	ChatGPT-4	(Amburle, et al., 2024), (Li, et al., 2023), (Rahmaniar, 2024), (Hajipour, et al., 2024), (Wadhwa, et al., 2024), (AlOmar and Mkaouer, 2024), (Sikand, et al., 2024), (Yuan, et al., 2024), (Mahyari, 2024), (Fang, et al., 2023), (Mathews, et al., 2024), (Li and Shan, 2023), (Hossain, et al., 2024), (Mohajer, et al., 2023), (Gonzalez-Barahona, 2024), (Omar and Shiaeles, 2023)	16
2.	ChatGPT-3.5-turbo	(Guo, et al., 2023a), (Mahyari, 2024), (Fang, et al., 2023), (Ságodi, Siket and Ferenc, 2024), (Mohajer, et al., 2023), (Gonzalez-Barahona, 2024), (Venkatesh, et al., 2024), (Omar and Shiaeles, 2023), (Moratis, et al., 2024)	9
3.	ChatGPT-3.5	(Amburle, et al., 2024), (Souma, et al., 2023), (Hajipour, et al., 2024), (Yuan, et al., 2024), (Pearce, et al., 2023), (Li and Shan, 2023), (Hossain, et al., 2024)	7
4.	CodeLlama	(Amburle, et al., 2024), (Fang, et al., 2023), (Bajpai, et al., 2024), (Li and Shan, 2023), (Yin, Ni and Wang, 2024), (Omar and Shiaeles, 2023)	6
5.	ChatGPT-2	(Bairi, et al., 2024), (Pearce, et al., 2023), (Akuthota, et al., 2023)	3
6.	GitHub Copilot	(Rahmaniar, 2024), (AlOmar and Mkaouer, 2024), (Ságodi, Siket and Ferenc, 2024)	3
7.	CodeGen	(AlOmar and Mkaouer, 2024), (Ignatyev, et al., 2024), (Venkatesh, et al., 2024)	3
8.	ChatGPT-3	(Bairi, et al., 2024), (Wadhwa, et al., 2024)	2
9.	Mixtral	(Li, et al., 2023), (Bajpai, et al., 2024)	2
10.	Google Bard	(Rahmaniar, 2024), (Gupta, et al., 2023)	2
11.	Codex	(Liu, Yang and Liao, 2024), (Ignatyev, et al., 2024)	2
12.	Polycoder	(Liu, Yang and Liao, 2024), (Ignatyev, et al., 2024)	2
13.	DeepSeek-Coder	(Bajpai, et al., 2024), (Yin, Ni and Wang, 2024)	2
14.	WizardCoder	(Yin, Ni and Wang, 2024), (Omar and Shiaeles, 2023)	2
15.	Mistral	(Yin, Ni and Wang, 2024), (Omar and Shiaeles, 2023)	2
16.	ChatGPT-1	(Bairi, et al., 2024)	1
17.	StarCoder	(Amburle, et al., 2024)	1
18.	CodeQL	(AlOmar and Mkaouer, 2024)	1
19.	CodeFuse	(Pearce, et al., 2023)	1
20.	AI21 Jurassic-1	(Liu, Yang and Liao, 2024)	1
21.	BERT	(Villmow, et al., 2023)	1
22.	CODEDOCTOR	(Jesse, et al., 2023)	1
23.	INCODER	(Jesse, et al., 2023)	1
24.	GRAPHCODEBERT	(Jesse, et al., 2023)	1
25.	StarChat-Beta	(Fang, et al., 2023)	1
26.	Phi-2	(Yin, Ni and Wang, 2024)	1
27.	OpenAI Davinci	(Venkatesh, et al., 2024)	1
28.	Vicuna	(Omar and Shiaeles, 2023)	1

LLMs: Large language models

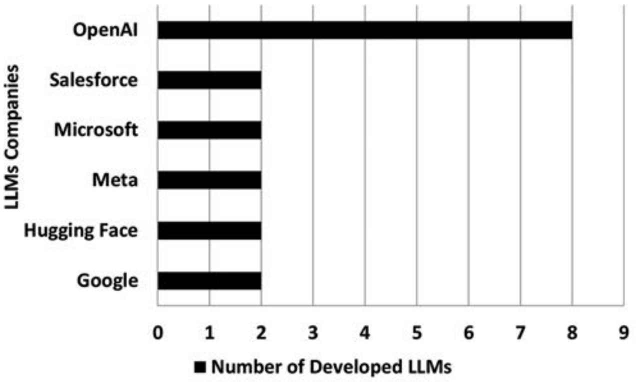

Fig. 3. Company contributing to large language models development.

TABLE III
STATIC CODE ANALYSIS TOOLS

S. No.	Tool	Corresponding papers	Total papers
1.	PMD	(Souma, et al., 2023), (Sikand, et al., 2024), (Guo, et al., 2023b)	3
2.	SonarQube	(Guo, et al., 2023b), (Mohajer, et al., 2023)	2
3.	Simian	(Souma, et al., 2023)	1
4.	Custom static analysis tool	(Di, et al., 2023)	1
5.	Static analyzer	(Haindl and Weinberger, 2024)	1
6.	PyTorch	(Haindl and Weinberger, 2024)	1
7.	LLB	(Li and Shan, 2023)	1
8.	FindBugs	(Guo, et al., 2023b)	1
9.	Coverity	(Guo, et al., 2023b)	1
10.	TECA	(Guo, et al., 2023b)	1
11.	Rust-code-analysis	(Ardito, Ballario and Valsesia, 2023)	1
12.	CodeQL	(Mohajer, et al., 2023)	1
13.	Infer	(Gonzalez-Barahona, 2024)	1
14.	PyCG	(Omar and Shiaeles, 2023)	1
15.	HeaderGen	(Omar and Shiaeles, 2023)	1
16.	TypeEvalPy	(Omar and Shiaeles, 2023)	1

detector (PMD, henceforth) emerges as the most widely cited tool, appearing in three papers, suggesting its effectiveness in code analysis and bug detection. SonarQube, cited in two papers, illustrates its capability in continuously monitoring of code quality. Simian, Static Analyzer, and Pytorch receive single mentions, reflecting their specialized use cases. More advanced tools, such as PyCG and HeaderGen indicate growing attention toward domain and language-specific static analysis, especially in Python and C++.

PMD is considered one of the most widely used static code analysis tools due to several critical factors. It covers a number of programming languages, such as Java, JavaScript, Apex, and PLSQL, which makes it very flexible and appropriate for a wide range of tasks. Another factor is that PMD is highly configurable which allows a great deal of customization enabling developers to create new rule sets or change existing ones to particular coding standards and best practices (AlOmar and Mkaouer, 2024). This flexibility ensures that each development team can adjust the processes according to their specific needs. In addition, PMD is available as an open-source tool which enables people to improve it and make it better and more sophisticated than ever. The ability to detect code duplication, dead variables, and potential bugs assists to improve the quality and longevity of the code. PMD also works with other popular build tools and IDEs, which makes it easy to use in various development environments. Together, all these factors combined with an active community and frequent releases increase PMD's recognition as one of the best static code analysis tools.

C. Target Programming Languages (RQ3)

Table IV presents the focus of research regarding the target programming languages for static code analysis using LLMs. The Java language was noted more often than other languages, as it appeared in 22 of the examined papers, while Python appeared in 17 and the C language in 14. Other languages, such as C++ had a moderate representation, 10 papers.

In contrast, languages, such as Swift, Kotlin, and Go appear in only 2 papers each, while niche or specialized languages, including Solidity, Ruby, Rust, Verilog, PHP, Objective-C, SQL, Perl, Scala, and R, are mentioned in just 1 paper each. These findings highlight the prominence of widely adopted languages, such as Java and Python in research contexts, particularly in leveraging LLMs for tasks, such as bug detection, vulnerability identification, and code comprehension through static code analysis. Java and Python are the most studied programming languages in static code analysis due to their widespread use, mature ecosystems, and suitability for analysis. Java's prevalence in enterprise systems and Android development, coupled with Python's dominance in data science, Machine Learning, and web development, ensures their relevance in improving code quality and security (Rahmaniar, 2024). Comprehensive static code analysis tools, including PMD and SonarQube for Java, as well as Pylint and Bandit for Python, bolstered by engaged communities and enormous resources, enhance both languages. The object-oriented structure and strong typing of Java enable correct interpretation and analysis of the program under consideration. In comparison, Python's dynamic features create unique challenges that nurture the ingenuity of researchers. Furthermore, the active interest from industry and academia, underlines the importance of these programming paradigms for static code analysis research. The limited scope of representation of the other general languages or domain-specific languages suggests a reasonable avenue for subsequent research regarding the potential of LLMs in using them.

D. Common Static Code Analysis Tasks (RQ4)

Numerous tasks in the collected papers have been identified regarding the static code analysis and applied LLMs are presented in Table V. The greatest number of papers that is 12, has been published in the area of security weaknesses and the attempts that are done to discover and resolve these issues in the code. Static behavior analysis and code quality estimation and control are fundamental parts of 10 papers that concern the understanding of program behavior and

TABLE IV
Programming Language used in Studies

S. No.	Programming language	Corresponding papers	Total Papers
1.	Java	(Amburle, et al., 2024), (Li, et al., 2023), (Souma, et al., 2023), (Rahmaniar, 2024), (Gupta, et al., 2023), (Di, et al., 2023), (Wadhwa, et al., 2024), (Sikand, et al., 2024), (Yuan, et al., 2024), (Pearce, et al., 2023), (Mahyari, 2024), (Jesse, et al., 2023), (Ignatyev, et al., 2024), (Bajpai, et al., 2024), (Li and Shan, 2023), (Ságodi, Siket and Ferenc, 2024), (Guo, et al., 2023b), (Ardito, Ballario and Valsesia, 2023), (Mohajer, et al., 2023), (Gonzalez-Barahona, 2024), (Akuthota, et al., 2023), (Moratis, et al., 2024)	22
2.	Python	(Amburle, et al., 2024), (Souma, et al., 2023), (Rahmaniar, 2024), (Gupta, et al., 2023), (Di, et al., 2023), (Hajipour, et al., 2024), (Wadhwa, et al., 2024), (AlOmar and Mkaouer, 2024), (Pearce, et al., 2023), (Liu, Yang and Liao, 2024), (Guo, et al., 2023a), (Jesse, et al., 2023), (Fang, et al., 2023), (Hossain, et al., 2024), (Mohajer, et al., 2023), (Venkatesh, et al., 2024), (Omar and Shiaeles, 2023)	17
3.	C	(Amburle, et al., 2024), (Gupta, et al., 2023), (Wadhwa, et al., 2024), (AlOmar and Mkaouer, 2024), (Liu, Yang and Liao, 2024), (Guo, et al., 2023a), (Mahyari, 2024), (Villmow, et al., 2023), (Fang, et al., 2023), (Hossain, et al., 2024), (Guo, et al., 2023b), (Yin, Ni and Wang, 2024), (Venkatesh, et al., 2024), (Akuthota, et al., 2023)	14
4.	C++	(Wadhwa, et al., 2024), (Guo, et al., 2023a), (Mahyari, 2024), (Jesse, et al., 2023), (Bajpai, et al., 2024), (Ságodi, Siket and Ferenc, 2024), (Guo, et al., 2023b), (Yin, Ni and Wang, 2024), (Venkatesh, et al., 2024), (Akuthota, et al., 2023)	10
5.	JavaScript	(Souma, et al., 2023), (Rahmaniar, 2024), (Wadhwa, et al., 2024), (Mahyari, 2024), (Fang, et al., 2023), (Hossain, et al., 2024)	6
6.	C#	(Haindl and Weinberger, 2024), (Mahyari, 2024), (Bajpai, et al., 2024), (Mathews, et al., 2024)	4
7.	Swift	(Wadhwa, et al., 2024), (Mahyari, 2024)	2
8.	Kotlin	(Wadhwa, et al., 2024), (Mahyari, 2024)	2
9.	Go	(Mahyari, 2024), (Venkatesh, et al., 2024)	2
10.	Solidity	(Amburle, et al., 2024)	1
11.	Ruby	(Wadhwa, et al., 2024)	1
12.	Rust	(Wadhwa, et al., 2024)	1
13.	Verilog	(Liu, Yang and Liao, 2024)	1
14.	PHP	(Mahyari, 2024)	1
15.	Objective-C	(Mahyari, 2024)	1
16.	SQL	(Mahyari, 2024)	1
17.	Perl	(Mahyari, 2024)	1
18.	Scala	(Mahyari, 2024)	1
19.	R	(Mahyari, 2024)	1

TABLE V
Addressed Tasks in Academic Paper on Static Code Analysis using LLMs

S. No.	Type of task	Corresponding papers	Total papers
1.	Security vulnerability detection	(Li, et al., 2023), (AlOmar and Mkaouer, 2024), (Liu, Yang and Liao, 2024), (Guo, et al., 2023a), (Villmow, et al., 2023), (Mathews, et al., 2024), (Li and Shan, 2023), (Hossain, et al., 2024), (Yin, Ni and Wang, 2024), (Venkatesh, et al., 2024), (Akuthota, et al., 2023), (Moratis, et al., 2024)	12
2.	Static behavior analysis	(Amburle, et al., 2024), (Di, et al., 2023), (Fang, et al., 2023), (Bajpai, et al., 2024), (Hossain, et al., 2024), (Guo, et al., 2023b), (Ardito, Ballario and Valsesia, 2023), (Mohajer, et al., 2023), (Gonzalez-Barahona, 2024), (Omar and Shiaeles, 2023)	10
3.	Code quality assurance	(Souma, et al., 2023), (Di, et al., 2023), (Sikand, et al., 2024), (Yuan, et al., 2024), (Pearce, et al., 2023), (Jesse, et al., 2023), (Ságodi, Siket and Ferenc, 2024), (Guo, et al., 2023b), (Ardito, Ballario and Valsesia, 2023), (Mohajer, et al., 2023)	10
4.	Bug detection	(Gupta, et al., 2023), (Sikand, et al., 2024), (Liu, Yang and Liao, 2024), (Ignatyev, et al., 2024), (Bajpai, et al., 2024), (Purba, et al., 2023)	6
5.	Syntax understanding	(Amburle, et al., 2024)	1
6.	Variable misuse detection	(Haindl and Weinberger, 2024)	1
7.	Adherence to green coding rules	(Rahmaniar, 2024)	1
8.	Logical reasoning in error detection	(Hajipour, et al., 2024)	1
9.	Identifying violations (naming conventions)	(Jesse, et al., 2023)	1

the quality control standards, respectively. Six papers are dedicated to bug detection highlighting the ongoing approach of seeking errors in different phases of software development and correcting them.

There are relatively few studies looking at other more specific issues, such as understanding syntax, detecting variable misuses, and reasoning for errors. These suggest very specific research areas. It also shows research activities, such as compliance with the green coding initiative, breaches of naming conventions, and the reasoning logic behind error detection, all of which are performed by individual researchers. These definitional boundaries mark some of the newer and broader static code analysis challenges where researchers are exploring sustainable coding practices and improving sustainability and maintainability in software development. The complex nature of static code analysis and its importance in various software engineering fields is exhibited in these different sets of tasks.

E. Evaluation Metrics (RQ5)

Table VI presents the common metrics used to evaluate the abilities of LLMs for static code analysis. Accuracy is the most often reported metric, cited in 11 papers, which illustrates its importance in measuring the effectiveness of these AI models. Several papers refer to the F1 Score, manual verification, precision, and false positive rate as terms of importance each in the balance of capturing problems and warnings. The specific metrics, such as recall, match rate, and true positive rate provide deeper insight into how well these models perform in detecting important issues (Liu, Yang and Liao, 2024). Some metrics are domain-specific metrics, such as Green Code Compliance Percentage, Rule Satisfaction Rates, and Security Correctness that focus on sustainability and security. Syntax error counts, repair success rates, and functional correctness measures highlight the significance of evaluating code quality and the effectiveness of automatic code repair. The complexity metrics, such as Cyclomatic Complexity, Cognitive Complexity, and Weighted Methods per Class assess the structural and maintainability aspect of the code. Novel approaches to code comparison and evaluation are captured by distinctive measures, such as the DiffBLEU score, Levenshtein Distance, and Jaccard Index. As for the measurement, the most frequent usage is for the F1 score and accuracy, which can provide a relatively objective and comprehensive evaluation. Accuracy is defined as the number of correctly identified issues (including both true positives and true negatives) divided by all predictions made, thus offering a complete picture of a tool's effectiveness.

The datasets used in static code analysis often show an uneven distribution between genuine issues and non-problems because they contain many more instances of the latter (negatives). This disparity renders accuracy inadequate since a tool could achieve elevated accuracy by only predicting the majority class (non-issues) and fail to detect actual problems (Ignatyev, et al., 2024). The F1 score addresses this challenge because it merges both accuracy and recall into one single value (Yin, Ni and Wang, 2024). The precision metric defines the ratio of actual problem instances correctly identified from total expected problem instances to address false positives; recall defines the ratio of correctly detected real issues to prevent false negatives. The F1 score serves as the harmonic mean of precision and recall and provides a good balance between them, which makes it particularly valuable for evaluating static code analysis tools since both types of errors (false positives and negatives) can produce major consequences. The integrated use of accuracy and the F1 score together can be used to assess both the reliability and effectiveness of static code analysis. The range of metrics applied shows both the extensive research in static code analysis and its broad application to every field of software engineering.

Fig. 4 highlights how academic papers are distributed across research categories, with performance-related studies leading the way due to 51 papers focusing on tool and model efficiency assessment. Code quality ranks as the second most investigated domain, with 18 papers, indicating a significant focus on maintainability and adherence to best practices. Categories, such as code analysis, code complexity, and code structure, each represented by 5–7 papers, highlight targeted efforts to understand software behavior and architecture. Less commonly addressed topics, including similarity, security, code size, process success, bug analysis, and test coverage, each account for fewer than five papers, indicating niche but essential areas of study. This distribution underscores the diverse priorities within the field of static code analysis and software engineering research.

F. Common Prompting Strategies (RQ6)

Table VII categorizes various prompting strategies for LLMs across the collected papers. Among the prompting techniques, Structured Prompting is the most widely used, appearing in 8 papers. This technique likely involves designing prompts with a defined structure to enhance a model's performance. Standardized or Basic Prompting follows closely, with 7 associated papers, highlighting its role as a fundamental approach in prompt design. Few-shot

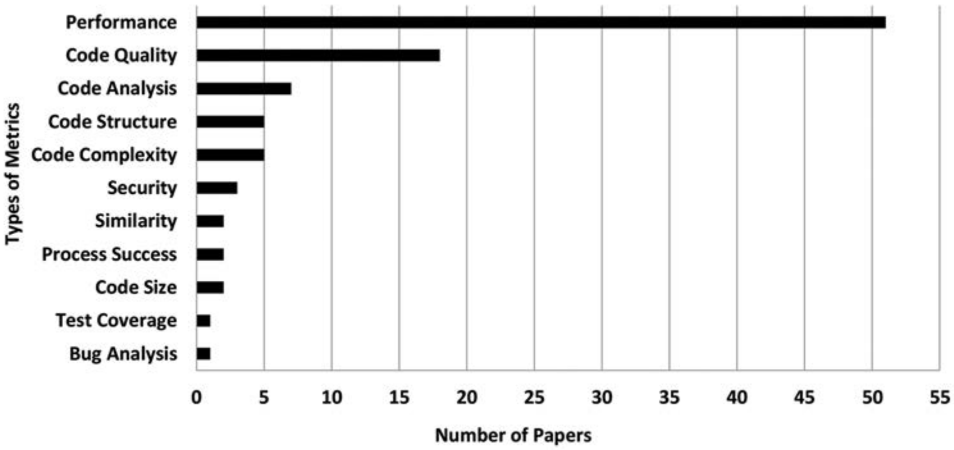

Fig. 4. Number of papers categorized by type of evaluation metrics.

TABLE VI
Commonly used evaluation metrics

S. No.	Metric	Corresponding papers	Total papers
1.	Accuracy	(Amburle, et al., 2024), (Gupta, et al., 2023), (Hajipour, et al., 2024), (Wadhwa, et al., 2024), (Haindl and Weinberger, 2024), (Guo, et al., 2023a), (Villmow, et al., 2023), (Yin, Ni and Wang, 2024), (Gonzalez-Barahona, 2024), (Akuthota, et al., 2023), (Moratis, et al., 2024)	11
2.	F1 score	(Amburle, et al., 2024), (Hajipour, et al., 2024), (Guo, et al., 2023a), (Bajpai, et al., 2024), (Yin, Ni and Wang, 2024), (Gonzalez-Barahona, 2024), (Venkatesh, et al., 2024), (Akuthota, et al., 2023)	8
3.	Manual verification	(Li, et al., 2023), (Gupta, et al., 2023), (Sikand, et al., 2024), (Pearce, et al., 2023), (Mathews, et al., 2024), (Ságodi, Siket and Ferenc, 2024), (Mohajer, et al., 2023)	7
4.	Precision	(Guo, et al., 2023a), (Bajpai, et al., 2024), (Hossain, et al., 2024), (Yin, Ni and Wang, 2024), (Gonzalez-Barahona, 2024), (Venkatesh, et al., 2024), (Akuthota, et al., 2023)	7
5.	False positive	(Haindl and Weinberger, 2024), (Li and Shan, 2023), (Guo, et al., 2023b), (Yin, Ni and Wang, 2024), (Mohajer, et al., 2023), (Venkatesh, et al., 2024)	6
6.	Recall	(Guo, et al., 2023a), (Yin, Ni and Wang, 2024), (Gonzalez-Barahona, 2024), (Venkatesh, et al., 2024), (Akuthota, et al., 2023)	5
7.	Match rate	(Mahyari, 2024), (Fang, et al., 2023), (Ignatyev, et al., 2024), (Bajpai, et al., 2024), (Omar and Shiaeles, 2023)	5
8.	Number of rule violations	(Souma, et al., 2023), (Yuan, et al., 2024), (Mohajer, et al., 2023)	3
9.	Time to fix issues	(Sikand, et al., 2024), (Mathews, et al., 2024), (Li and Shan, 2023)	3
10.	True positive	(Li and Shan, 2023), (Guo, et al., 2023b), (Venkatesh, et al., 2024)	3
11.	Syntax error counts	(Di, et al., 2023), (Gonzalez-Barahona, 2024)	2
12.	Success rate of LLM	(Sikand, et al., 2024), (Hossain, et al., 2024)	2
13.	False negative	(Haindl and Weinberger, 2024), (Venkatesh, et al., 2024)	2
14.	Security correctness	(Liu, Yang and Liao, 2024), (Li and Shan, 2023)	2
15.	Soundness	(Omar and Shiaeles, 2023)	1
16.	Completeness	(Omar and Shiaeles, 2023)	1
17.	Jaccard index	(Amburle, et al., 2024)	1
18.	Number of prompts	(Souma, et al., 2023)	1
19.	Green code compliance percentage	(Rahmaniar, 2024)	1
20.	Rule satisfaction rates	(Di, et al., 2023)	1
21.	Plagiarism detection	(Di, et al., 2023)	1
22.	Pass@k	(Hajipour, et al., 2024)	1
23.	Number of discovered vulnerabilities	(AlOmar and Mkaouer, 2024)	1
24.	Top-k accuracy	(Yin, Ni and Wang, 2024)	1
25.	Cyclomatic complexity	(Yuan, et al., 2024)	1
26.	Cognitive complexity	(Yuan, et al., 2024)	1
27.	Correctness metrics	(Pearce, et al., 2023)	1
28.	Coverage metrics	(Pearce, et al., 2023)	1
29.	Functional correctness	(Liu, Yang and Liao, 2024)	1
30.	Repair success rate	(Liu, Yang and Liao, 2024)	1
31.	BLEU	(Mahyari, 2024)	1
32.	Mean	(Jesse, et al., 2023)	1
33.	Bug/patch ratio	(Ignatyev, et al., 2024)	1
34.	Logical lines of code	(Ságodi, Siket and Ferenc, 2024)	1
35.	Number of statements	(Ságodi, Siket and Ferenc, 2024)	1
36.	McCabe cyclomatic complexity	(Ságodi, Siket and Ferenc, 2024)	1
37.	Nesting level	(Ságodi, Siket and Ferenc, 2024)	1
38.	Coding smells	(Ságodi, Siket and Ferenc, 2024)	1
39.	ABC metric	(Ardito, Ballario and Valsesia, 2023)	1
40.	Weighted methods per class	(Ardito, Ballario and Valsesia, 2023)	1
41.	Number of public methods	(Ardito, Ballario and Valsesia, 2023)	1
42.	Number of public attributes	(Ardito, Ballario and Valsesia, 2023)	1
43.	Class operation accessibility	(Ardito, Ballario and Valsesia, 2023)	1
44.	Class data accessibility	(Ardito, Ballario and Valsesia, 2023)	1
45.	Area under the curve	(Akuthota, et al., 2023)	1

TABLE VII
Distribution prompting strategies

S. No.	Prompt type	Corresponding papers	Total papers
1.	Structured prompting	(Souma, et al., 2023), (Liu, Yang and Liao, 2024), (Fang, et al., 2023), (Ignatyev, et al., 2024), (Mathews, et al., 2024), (Mohajer, et al., 2023), (Venkatesh, et al., 2024), (Moratis, et al., 2024)	8
2.	Standardized/basic prompting	(Hajipour, et al., 2024), (Guo, et al., 2023a), (Mahyari, 2024), (Fang, et al., 2023), (Bajpai, et al., 2024), (Li and Shan, 2023), (Ságodi, Siket and Ferenc, 2024)	7
3.	Few-shot prompting	(Amburle, et al., 2024), (Wadhwa, et al., 2024), (AlOmar and Mkaouer, 2024), (Sikand, et al., 2024), (Li and Shan, 2023), (Gonzalez-Barahona, 2024)	6
4.	Zero-shot prompting	(Amburle, et al., 2024), (Wadhwa, et al., 2024), (Sikand, et al., 2024), (Gonzalez-Barahona, 2024)	4
5.	Iterative prompting	(Souma, et al., 2023), (Pearce, et al., 2023), (Purba, et al., 2023), (Omar and Shiaeles, 2023)	4
6.	One-shot prompting	(Sikand, et al., 2024), (Gonzalez-Barahona, 2024), (Omar and Shiaeles, 2023)	3
7.	Task-specific prompting	(Rahmaniar, 2024), (Yin, Ni and Wang, 2024)	2
8.	CoT prompting	(Hajipour, et al., 2024), (Guo, et al., 2023a)	2
9.	Natural language descriptions	(Pearce, et al., 2023), (Ignatyev, et al., 2024)	2
10.	High-level query language	(Di, et al., 2023), (Bajpai, et al., 2024)	2
11.	Temporal and spatial context	(Bajpai, et al., 2024)	1
12.	Retrieval-augmented generation	(Li and Shan, 2023)	1
13.	Scenario-based prompting	(Mahyari, 2024)	1
14.	Correction prompt	(Hajipour, et al., 2024)	1

Prompting, where the model is given limited examples, is addressed in 6 papers, while Zero-shot Prompting, where the model is given no examples, is used in 4 papers. Iterative Prompting, which involves multi-step refinement, appears in 4 papers. One-Shot Prompting has 3 associated papers, indicating a growing interest in specific task-tailored or stepwise reasoning approaches. Less frequently studied techniques include Task-Specific Prompting, Chain-of-Thought (CoT, henceforth) Prompting, Natural Language Descriptions, and High-Level Query Language, each appeared in 2 papers. Niche methods, such as Temporal and Spatial Context, Retrieval-Augmented Generation, Scenario-Based Prompting, and Correction Prompts are mentioned in 1 paper each, reflecting emerging or specialized areas of research in LLM prompting strategies in the case of static code analysis.

Structured Prompting, Standardized/Basic Prompting, and Few-shot Prompting are the most widely used prompting strategies due to their effectiveness, simplicity, and adaptability to the static code analysis unique challenges. Structured Prompting is advantageous as it offers a coherent, systematic framework for directing models in code analysis, which corresponds effectively with the ordered characteristics of programming languages. This approach enables the breakdown of complex code analysis tasks into smaller components, which improve the model's ability to detect issues, such as syntax errors, code smells, or security vulnerabilities (Jesse, et al., 2023). Standardized/Basic Prompting is chosen because it is straightforward and can be duplicated because it involves specific directions that apply from one codebase to another and from one analytical task to another (Mathews, et al., 2024). This sets up a trustworthy standard for evaluating static code analysis techniques. The method is exceptionally effective for static code analysis because it allows models to learn from limited examples, which makes it very useful when datasets are small or when shifting between coding languages or styles. These strategies together meet the needs for static code analysis precision, scalability, and adaptability, which make them the most common approaches in research. This distribution shows the scope and distinctiveness of prompt engineering strategies that are being studied in the related works.

G. Common Limitations and Challenges (RQ7)

In this survey, the following challenges and constraints on the use of LLMs in static code analysis are identified:

1. High false positive rates: In the static code analysis, LLMs tend to produce many false positives that require a thorough human verification process to detect actual issues. Some of the related challenges include; how to detect Null Dereferences and Resource Leaks among others (AlOmar and Mkaouer, 2024), (Guo, et al., 2023b), (Mohajer, et al., 2023), (Gonzalez-Barahona, 2024), (Venkatesh, et al., 2024).
2. Token and context limitations: LLMs have limitations on the input size which makes them not very effective in handling large codebases or complex dependencies at a time. For example, dealing with imported module code or checking through large files is challenging (Amburle, et al., 2024), (Wadhwa, et al., 2024), (Sikand, et al., 2024), (Yuan, et al., 2024), (Liu, Yang and Liao, 2024), (Jesse, et al., 2023), (Fang, et al., 2023), (Mathews, et al., 2024), (Li and Shan, 2023), (Mohajer, et al., 2023), (Gonzalez-Barahona, 2024).
3. Data limitations: It is a common issue to find that the quality and diversity of training data sets directly impact the model's generality and accuracy. The reliance on databases, such as CVE, which are prone to errors, decreases the accuracy of vulnerability detection (Amburle, et al., 2024), (Rahmaniar, 2024), (Hajipour, et al., 2024), (Haindl and Weinberger, 2024), (Guo, et al., 2023a).
4. Non-deterministic outputs: Uncertainty about how many times LLMs will produce different outcomes from multiple executions for the same input creates problems when integrating them into static code analysis frameworks. For instance, making coding integration and development workflows deterministic is difficult due to the variability result (Rahmaniar, 2024), (Bajpai, et al., 2024).

5. Computational costs: The high resource requirements pose a significant problem for implementing large-scale code analysis with LLMs and the need for fine-tuning that complicates this issue further. Flow-sensitive pointer information and extensive call graphs demand substantial processing resources to address them (Bajpai, et al., 2024), (Venkatesh, et al., 2024), (Omar and Shiaeles, 2023).
6. Model hallucinations and assumptions: Sometimes LLMs produce wrong or overconfident outcomes because of built-in biases and limited understanding of context. For instance, when doing bug detection tasks, they frequently hallucinate or miss dependencies (Amburle, et al., 2024), (Li and Shan, 2023), (Gonzalez-Barahona, 2024).
7. Scalability and adaptability issues: LLMs struggle to generalize across different languages, ecosystems, or complex design patterns. For instance, they have a limited capacity to preserve language-specific semantics while doing cross-language analysis (Gupta, et al., 2023), (Villmow, et al., 2023).

V. Future Directions of Research

Examining the collected papers reveals that there are many research gaps to be addressed in using LLMs for static code analysis, which can be summarized as follows:

1. Improving prompt engineering
    - Researchers can develop automated prompt generating strategies to tailor prompts for certain activities (such as vulnerability detection and bug fixing) (Li, et al., 2023).
    - To increase accuracy and reasoning in challenging tasks, researchers can investigate iterative prompting and CoT prompting (Li, et al., 2023).
    - Researchers can examine task-specific prompt templates for various analytical tasks and programming languages (Liu, Yang and Liao, 2024).
2. Fine-tuning LLMs for specific tasks
    - To enhance the performance, researchers can fine-tune LLMs using domain-specific datasets (such as code vulnerabilities and static analysis warnings) (Hossain, et al., 2024).
    - To improve accuracy and efficiency, researchers can develop hybrid models that incorporate LLMs in traditional static analysis techniques (Omar and Shiaeles, 2023).
    - To allow LLMs to manage several static code analysis tasks at once, researchers can investigate multi-task learning (Yin, Ni and Wang, 2024).
3. Handling complex and obfuscated code
    - Researchers can develop techniques to de-obfuscate code before analysis using LLMs (Fang, et al., 2023).
    - Researchers can integrate graph-based representations (e.g., control flow graphs and data flow graphs) to help LLMs understand complex code structures (Hossain, et al., 2024).
    - Researchers can explore multi-agent systems where LLMs collaborate with other tools to analyze interconnected code components (Bajpai, et al., 2024).
4. Reducing false positives and improving precision
    - Researchers can combine LLMs with rule-based systems or ML classifiers to filter out false positives (Guo, et al., 2023b).
    - Researchers can use ranking mechanisms to prioritize the most likely true positives for developer review (Mohajer, et al., 2023).
    - Researchers can develop explainable AI techniques to help developers understand why a particular issue was flagged (Wadhwa, et al., 2024).
5. Expanding language and framework support
    - Researchers can extend LLM-based static analysis to less common programming languages (e.g., Rust, Kotlin, Swift, Arduino, etc.) (Guo, et al., 2023a).
    - Researchers can develop cross-language LLMs-based analysis tools that can handle multi-language projects (Guo, et al., 2023a).
    - Researchers can explore support for domain-specific languages (e.g., solidity for smart contracts) (Ardito, Ballario and Valsesia, 2023).
6. Integration with development workflows
    - Researchers can develop IDE plugins that leverage LLMs for real-time code analysis and feedback (Bajpai, et al., 2024).
    - Researchers can create automated tools for continuous monitoring of code quality and vulnerabilities using LLMs (Akuthota, et al., 2023).
    - Researchers can explore collaborative workflows where LLMs assist developers in debugging, refactoring, and code review (Bajpai, et al., 2024).
7. Addressing ethical and security concerns
    - Researchers can develop secure coding guidelines for LLM-generated code to prevent vulnerabilities (Purba, et al., 2023).
    - Researchers can investigate adversarial training to make LLMs more robust against malicious inputs (Li and Shan, 2023).
    - Researchers can ensure data privacy by avoiding the use of proprietary or sensitive code in LLM training datasets (Akuthota, et al., 2023).
8. Scaling to large codebases
    - Researchers can develop chunking strategies to break down large codebases into manageable segments for analysis (Bairi, et al., 2024).
    - Researchers can use hierarchical models that analyze code at multiple levels of granularity (e.g., file-level, function-level, etc.) (Ignatyev, et al., 2024).
    - Researchers can explore distributed computing techniques to scale LLM-based analysis to enterprise-level projects (Venkatesh, et al., 2024).
9. Benchmarking and standardization
    - Researchers can produce uniform datasets and metrics that enable effective assessment of LLM performance in static code analysis tasks (Yin, Ni and Wang, 2024).
    - Researchers can establish assessment tools that report on both primary product behavior and secondary qualities including code readability and maintainability (Ságodi, Siket and Ferenc, 2024).

- Researchers can foster open-source contributions to aggregate research data and materials (Omar and Shiaeles, 2023).

10. Enhancing explainability and developer trust
    - Researchers can design tools that give thorough explanations for the LLM-produced analysis findings (Wadhwa, et al., 2024).
    - Researchers can use interactive interfaces where developers can request further context or clarification from LLMs (Bajpai, et al., 2024).
    - Researchers can study how human-loop systems function to cooperate between developers and LLMs to improve analysis product accuracy (Mohajer, et al., 2023).
11. Exploring hybrid approaches
    - Researchers can improve precision by integrating LLMs with symbolic execution, abstract interpretation, or formal methods (Omar and Shiaeles, 2023).
    - Researchers can integrate LLMs with graph-based models (e.g., GraphCodeBERT) for better representation of code dependencies (Hossain, et al., 2024).

The future of static code analysis using LLMs lies in improving prompt engineering, fine-tuning models for specific tasks, reducing false positives, and integrating LLMs into development workflows. By combining LLMs with traditional static analysis tools and exploring hybrid approaches, researchers can unlock the full potential of LLMs for different static code analysis tasks.

VI. Threat to Validity

The results of surveys may be impacted by many factors. Thus, to prevent validity risks, the following steps were taken into consideration for this paper:

- Finding related papers: The availability of all relevant papers cannot be guaranteed. To find the related papers, a search string containing several word synonyms was employed, and many well-known literature databases were employed. There could yet be some missing papers, though. The snowballing search strategy was used to mitigate this issue by lowering the likelihood of missing related papers.
- Accuracy of data extraction: When extracting data from the chosen papers, several errors might happen. The data extraction procedure was carried out by hand to address this threat. The spreadsheet also made advantage of Microsoft Excel's automatic mining and filtering features. After that, the outcomes of the two approaches were contrasted to identify any differences and create a final Excel document with all the correct extracted data.
- Study reproducibility: A further threat is that if this study is carried out or replicated, other researchers could get similar findings. Every stage of the research approach used and carried out in this study was thoroughly explained to address this threat (see Section III).

VII. Conclusion

This survey highlights the transformative role of LLMs in static code analysis, offering a fresh perspective on leveraging LLMs to address longstanding challenges in software quality, security, and maintainability. By synthesizing insights from a diverse range of studies, we identified how LLMs excel in tasks, such as vulnerability detection, bug fixing, and code quality assurance, often complementing or surpassing traditional static analysis tools. Key strengths include their ability to understand complex code semantics and adapt to diverse programming languages and contexts. However, integrating LLMs into static code analysis workflows is not without challenges. High false positive rates, token size constraints, and computational costs remain significant barriers to widespread adoption. Looking ahead, future research should focus on refining prompt engineering, exploring underrepresented programming languages and niche tasks, and improving scalability to support large codebases. In addition, expanding benchmarks and real-world case studies will further validate the practical utility of LLMs in static code analysis. As the field evolves, LLMs have the potential to redefine software engineering practices, making development processes more efficient, secure, and adaptive to the complexities of modern codebases and software applications. By bridging the gap between traditional static code analysis methods and AI-driven solutions, this study aims to inspire researchers and practitioners to unlock the full potential of LLMs, contributing to the ongoing advancement of secure and high-quality software development.

References

Acl, A., 2024. *An Empirical Study of LLM for Code Analysis : Understanding Syntax and Semantics*. *ACL ARR*. Available from: https://openreview.net/forum?id=yezazwj1yf> [Last assessed on 2025 Jan 04].

Akuthota, V., Kasula, R., Sumona, S.T., Mohiuddin, M., Reza, M.T., and Rahman, M.M., 2023. Vulnerability detection and monitoring using LLM. In: *Proceedings of 2023 IEEE 9th International Women in Engineering (WIE) Conference on Electrical and Computer Engineering, WIECON-ECE 2023*, IEEE, United States, pp.309-314.

AlOmar, E.A., and Mkaouer, M.W., 2024. Cultivating software quality improvement in the classroom: An experience with chatGPT. In: *2024 36th International Conference on Software Engineering Education and Training (CSEE&T)*. IEEE, United States, pp.1-10.

Amburle, A., Almeida, C., Lopes, N., and Lopes, O., 2024. AI based code error explainer using gemini model. In: *2024 3rd International Conference on Applied Artificial Intelligence and Computing (ICAAIC)*. IEEE, United States: pp.274-278.

Ardito, L., Ballario, M., and Valsesia, M., 2023. Research, Implementation and Analysis of Source Code Metrics in Rust-Code-Analysis. In: *2023 IEEE 23rd International Conference on Software Quality, Reliability, and Security (QRS)*. IEEE, United States, pp.497-506.

Bairi, R., Sonwane, A., Kanade, A., Vageesh, D.C., Iyer, A., Parthasarathy, S., Rajamani, S., Ashok, B., and Shet, S., 2024. Codeplan: Repository-level coding using LLMs and planning. *Proceedings of the ACM on Software Engineering*, 1, pp.675-698.

Bajpai, Y., Chopra, B., Biyani, P., Aslan, C., Coleman, D., Gulwani, S., Parnin, C., Radhakrishna, A., and Soares, G., 2024. Let's fix this together: Conversational debugging with github copilot. In: *2024 IEEE Symposium on Visual Languages and Human-Centric Computing (VL/HCC)*. IEEE, United States, pp.1-12.

Brereton, P., Kitchenham, B.A., Budgen, D., Turner, M., and Khalil, M., 2007. Lessons from applying the systematic literature review process within the software engineering domain. *Journal of Systems and Software*, 80(4), pp.571-583.

Chen, Y., Sun, W., Fang, C., Chen, Z., Ge, Y., Han, T., Zhang, Q., Liu, Y., Chen, Z., and Xu, B., 2024. *Security of Language Models for Code: A Systematic Literature Review*. Vol. 1. Available from: https://arxiv.org/abs/2410.15631 [Last assessed on 2025 Jan 04].

Di, P., Li, J., Yu, H., Jiang, W., Cai, W., Cao, Y., Chen, C., Chen, D., Chen, H., Chen, L., Fan, G., Gong, J., Gong, Z., Hu, W.,… & Zhu, X., 2023. CodeFuse-13B: A pretrained multi-lingual code large language model. *Proceedings of the 46th International Conference on Software Engineering: Software Engineering in Practice*. ICSE, New Delhi, pp.418-429.

Fang, C., Miao, N., Srivastav, S., Liu, J., Zhang, R., Fang, R., Asmita, Tsang, R., Nazari, N., Wang, H., and Homayoun, H., 2023. *Large Language Models for Code Analysis: Do LLMs Really do Their Job*? Available from: https://arxiv.org/abs/2310.12357 [Last assessed on 2025 Jan 04].

Gong, J., Voskanyan, V., Brookes, P., Wu, F., Jie, W., Xu, J., Giavrimis, R., Basios, M., Kanthan, L., and Wang, Z., 2025. *Language Models for Code Optimization: Survey, Challenges and Future Directions*. Vol. 1. ACM Computing Surveys. [arxiv Preprint]. Available from: https://arxiv.org/abs/2501.01277 [Last assessed on 2025 Jan 04].

Gonzalez-Barahona, J.M., 2024. Software development in the age of LLMs and XR. In: *Proceedings of the 1st ACM/IEEE Workshop on Integrated Development Environments*. ACM, New York, USA, pp.66-69.

Guo, Q., Cao, J., Xie, X., Liu, S., Li, X., Chen, B., and Peng, X., 2023a. Exploring the potential of chatGPT in automated code refinement: An empirical study. In: *Proceedings of the IEEE/ACM 46th International Conference on Software Engineering*. pp.1-13.

Guo, Z., Tan, T., Liu, S., Liu, X., Lai, W., Yang, Y., Li, Y., Chen, L., Dong, W., and Zhou, Y., 2023b. Mitigating false positive static analysis warnings: Progress, challenges, and opportunities. *IEEE Transactions on Software Engineering*, 49(12), pp.5154-5188.

Gupta, N.K., Chaudhary, A., Singh, R., and Singh, R., 2023. ChatGPT: Exploring the capabilities and limitations of a large language model for conversational AI. In: *2023 International Conference on Advances in Computation, Communication and Information Technology (ICAICCIT)*. IEEE, United States, pp.139-142.

Haindl, P., and Weinberger, A.G., 2024. Does chatGPT help novice programmers write better code? Results from static code analysis. *IEEE Access*, 12, pp.114146-114156.

Hajipour, H., Hassler, K., Holz, T., Schönherr, L., and Fritz, M., 2024. CodeLMSec benchmark: Systematically evaluating and finding security vulnerabilities in black-box code language models. In: *2024 IEEE Conference on Secure and Trustworthy Machine Learning (SaTML)*. IEEE, United States, pp.684-709.

Hassan, H.B., Sarhan, Q.I., and Beszédes, Á., 2024. Evaluating python static code analysis tools using FAIR principles. *IEEE Access*, 12, pp.173647-173659.

Hort, M., Grishina, A., and Moonen, L., 2023. An exploratory literature study on sharing and energy use of language models for source code. In: *2023 ACM/IEEE International Symposium on Empirical Software Engineering and Measurement (ESEM)*. IEEE, United States, pp.1-12.

Hossain, A.A., Mithun Kumar, P.K., Zhang, J., and Amsaad, F., 2024. Malicious code detection using LLM. In: *NAECON 2024 - IEEE National Aerospace and Electronics Conference*. IEEE, United States, pp.414-416.

Hou, X., Zhao, Y., Liu, Y., Yang, Z., Wang, K., Li, L., Luo, X., Lo, D., Grundy, J., and Wang, H., 2023. *Large Language Models for Software Engineering: A Systematic Literature Review*. pp.1-79. Available from: https://arxiv.org/abs/2308.10620 [Last assessed on 2025 Jan 04].

Ignatyev, V.N., Shimchik, N.V., Panov, D.D., and Mitrofanov, A.A., 2024. Large language models in source code static analysis. In: *2024 Ivannikov Memorial Workshop (IVMEM)*. IEEE, United States, pp.28-35.

Jesse, K., Ahmed, T., Devanbu, P.T., and Morgan, E., 2023. Large language models and simple, stupid bugs. In: *2023 IEEE/ACM 20th International Conference on Mining Software Repositories (MSR)*. IEEE, United States, pp.563-575.

Kotenko, I., Izrailov, K., and Buinevich, M., 2022. Static analysis of information systems for IoT cyber security: A survey of machine learning approaches. *Sensors (Basel)*, 22(4), p.1335.

Li, H., and Shan, L., 2023. LLM-based vulnerability detection. In: *2023 International Conference on Human-Centered Cognitive Systems (HCCS)*. IEEE, United States, pp.1-4.

Li, H., Hao, Y., Zhai, Y., and Qian, Z., 2023. Assisting static analysis with large language models: A chatGPT experiment. In: *Proceedings of the 31st ACM Joint European Software Engineering Conference and Symposium on the Foundations of Software Engineering*. ACM, New York, USA, pp.2107-2111.

Liu, Z., Yang, Z., and Liao, Q., 2024. Exploration on prompting LLM with code-specific information for vulnerability detection. *Proceedings - 2024 IEEE International Conference on Software Services Engineering, SSE 2024*. IEEE, United States, pp.273-281.

Louridas, P., 2006. Static code analysis. *IEEE Software*, 23(4), pp.58-61.

Mahyari, A.A., 2024. Harnessing the power of LLMs in source code vulnerability detection. In: *MILCOM 2024 - 2024 IEEE Military Communications Conference (MILCOM)*. IEEE, United States, pp.251-256.

Mathews, N.S., Brus, Y., Aafer, Y., Nagappan, M., and McIntosh, S., 2024. *LLbezpeky: Leveraging Large Language Models for Vulnerability Detection*. Available from: https://arxiv.org/abs/2401.01269 [Last assessed on 2025 Jan 04].

Mohajer, M.M., Aleithan, R., Harzevili, N.S., Wei, M., Belle, A.B., Pham, H.V., and Wang, S., 2023. *SkipAnalyzer: A Tool for Static Code Analysis with Large Language Models*. Available from: https://arxiv.org/abs/2310.18532 [Last assessed on 2025 Jan 04].

Moratis, K., Diamantopoulos, T., Nastos, D.N., and Symeonidis, A., 2024. Write me this code: An analysis of chatGPT quality for producing source code. In: *Proceedings - 2024 IEEE/ACM 21st International Conference on Mining Software Repositories, MSR 2024*, pp.147-151.

Omar, M., and Shiaeles, S., 2023. VulDetect: A novel technique for detecting software vulnerabilities using language models. In: *2023 IEEE International Conference on Cyber Security and Resilience (CSR)*. IEEE, United States, pp.105-110.

Pearce, H., Tan, B., Ahmad, B., Karri, R., and Dolan-Gavitt, B., 2023. Examining zero-shot vulnerability repair with large language models. In: *2023 IEEE Symposium on Security and Privacy (SP)*. IEEE, United States, pp.2339-2356.

Petersen, K., Vakkalanka, S., and Kuzniarz, L., 2015. Guidelines for conducting systematic mapping studies in software engineering: An update. *Information and Software Technology*, 64(5), pp.1-18.

Purba, M.D., Ghosh, A., Radford, B.J., and Chu, B., 2023. Software vulnerability detection using large language models. In: *2023 IEEE 34th International Symposium on Software Reliability Engineering Workshops (ISSREW)*. IEEE, United States, pp.112-119.

Rahmaniar, W., 2024. ChatGPT for software development: Opportunities and challenges. *IT Professional*, 26(3), pp.80-86.

Ramamoorthy, J., Gupta, K., Kafle, R.C., Shashidhar, N.K., and Varol, C., 2024. A novel static analysis approach using system calls for linux IoT malware detection. *Electronics*, 13(15), p.2906.

Ságodi, Z., Siket, I., and Ferenc, R., 2024. Methodology for code synthesis evaluation of LLMs presented by a case study of chatGPT and copilot. *IEEE*

Access, 12, pp.72303-72316.

Salem, N., Hudaib, A., Al-Tarawneh, K., Salem, H., Tareef, A., Salloum, H., and Mazzara, M., 2024. A survey on the application of large language models in software engineering. *Computer Research and Modeling*, 16(7), pp.1715-1726.

Sikand, S., Mehra, R., Sharma, V.S., Kaulgud, V., Podder, S., and Burden, A.P., 2024. Do generative AI tools ensure green code? An investigative study. In: *Proceedings of the 2nd International Workshop on Responsible AI Engineering*. ACM, New York, USA, pp.52-55.

Souma, N., Ito, W., Obara, M., Kawaguchi, T., Akinobu, Y., Kurabayashi, T., Tanno, H., and Kuramitsu, K., 2023. Can chatGPT correct code based on logical steps. In: *Proceedings - Asia-Pacific Software Engineering Conference, APSEC*, pp.653-654.

Venkatesh, A.P.S., Sabu, S., Mir, A.M., Reis, S., and Bodden, E., 2024. The emergence of large language models in static analysis: A first look through micro-benchmarks. In: *Proceedings of the 2024 IEEE/ACM First International Conference on AI Foundation Models and Software Engineering*. ACM, New York, USA, pp.35-39.

Villmow, J., Campos, V., Petry, J., Abbad-Andaloussi, A., Ulges, A., and Weber, B., 2023. How well can masked language models spot identifiers that violate naming guidelines? In: *2023 IEEE 23rd International Working Conference on Source Code Analysis and Manipulation (SCAM)*. IEEE, United States, pp.131-142.

Wadhwa, N., Pradhan, J., Sonwane, A., Sahu, S.P., Natarajan, N., Kanade, A., Parthasarathy, S., and Rajamani, S., 2024. CORE: Resolving code quality issues using LLMs. In: *Proceedings of the ACM on Software Engineering*. Vol. 1. ACM, United States, pp.789-811.

Wang, J., Huang, Y., Chen, C., Liu, Z., Wang, S., and Wang, Q., 2024. Software testing with large language models: Survey, landscape, and vision. *IEEE Transactions on Software Engineering*, 50(4), pp.911-936.

Wohlin, C., 2014. Guidelines for snowballing in systematic literature studies and a replication in software engineering. In: *ACM International Conference Proceeding Series*. ACM, United States.

Yin, X., Ni, C., and Wang, S., 2024. Multitask-based evaluation of open-source LLM on software vulnerability. *IEEE Transactions on Software Engineering*, 50(11), pp.3071-3087.

Yuan, Z., Liu, M., Ding, S., Wang, K., Chen, Y., Peng, X., and Lou, Y., 2024. Evaluating and improving chatGPT for unit test generation. *Proceedings of the ACM on Software Engineering*. 1(FSE), pp.1703-1726.

Zhang, Q., Fang, C., Xie, Y., Zhang, Y., Yang, Y., Sun, W., Yu, S., and Chen, Z., 2023a. *A Survey on Large Language Models for Software Engineering*. Available from: https://arxiv.org/abs/2312.15223 [Last assessed on 2025 Jan 04].

Zhang, Z., Chen, C., Liu, B., Liao, C., Gong, Z., Yu, H., Li, J., and Wang, R., 2023b. *Unifying the Perspectives of NLP and Software Engineering: A Survey on Language Models for Code*. pp.1-99. Available from: https://arxiv.org/abs/2311.07989 [Last assessed on 2025 Jan 04].

Zheng, Z., Ning, K., Wang, Y., Zhang, J., Zheng, D., Ye, M., and Chen, J., 2023a. A survey of large language models for code: Evolution, benchmarking, and future trends. *ACM Transactions on Software Engineering and Methodology*, 31(2), pp.1-44.

Zheng, Z., Ning, K., Zhong, Q., Chen, J., Chen, W., Guo, L., Wang, W., and Wang, Y., 2023b. Towards an understanding of large language models in software engineering tasks. *Empirical Software Engineering*, 30(2), p.50.

Zhou, X., Cao, S., Sun, X., and Lo, D., 2024. *Large Language Model for Vulnerability Detection and Repair: Literature Review and the Road Ahead*. Vol. 1. Available from: https://arxiv.org/abs/2404.02525 [Last assessed on 2025 Jan 04].

Artificial Intelligence - Based Digital Pathology Assessment of CD44s Expression in Breast Cancer: Association with Clinicopathological Features and Survival Outcomes

Avan S. Mohammed[1†], Ramadhan T. Othman[2] and Rafil T. Yaqo[3]

[1]Department of Biology, Faculty of Science, University of Duhok,
Duhok, Kurdistan Region – F.R. Iraq

[2]Department of Medicine, College of Medicine, University of Duhok,
Duhok, Kurdistan Region – F.R. Iraq

[3]Department of Pathology, College of Medicine, University of Duhok,
Duhok, Kurdistan Region – F.R. Iraq

***Abstract*—Breast cancer (BC) exhibits considerable molecular and clinical heterogeneity, complicating prognostic evaluation. The cluster of differentiation 44 standard (CD44s) isoform has been proposed as a prognostic marker in various cancers; however, its role in BC remains unclear. This study evaluated CD44s expression in BC tissues and its association with clinicopathological features and survival outcomes using an artificial intelligence (AI)-based digital pathology scoring method. A retrospective analysis of 98 BC tissue samples is conducted, with CD44s cell membrane protein expression assessed through both manual and AI-based immunohistochemical (IHC) scoring. Statistical analyses included Pearson's chi-square test, Kaplan-Meier (log-rank), and Cox regression. CD44s expression was observed in 65.31% of patients. No significant associations are found between CD44s expression and clinicopathological characteristics, including age, tumor size, lymph node metastasis, histological grade, lymphovascular invasion (LVI), or hormone receptor status (all $p > 0.05$). Survival analysis reveals no significant association between CD44s expression and overall survival (OS, $p = 0.1345$) or progression-free survival ($p = 0.0669$). While CD44s expression is prevalent in BC samples, it is not an independent prognostic factor; LVI is the only significant predictor of OS ($p = 0.036$). Finally, the moderate agreement between AI and manual scoring (Cohen's Kappa = 0.4337, $p < 0.0001$) supports the potential of AI-assisted methods for biomarker quantification, warranting further validation in larger cohorts.**

***Index Terms*—Artificial intelligence, Breast cancer stem cells, Breast cancer, CD44s, Immunohistochemistry, QuantCenter.**

ARO-The Scientific Journal of Koya University
Vol. XIII, No. 1 (2025), Article ID: ARO.12248. 9 pages
DOI: 10.14500/aro.12248
Received: 04 May 2025; Accepted: 02 June 2025
Regular research paper; Published: 22 June 2025

†Corresponding author's e-mail: avan.mohammed@uod.ac

I. INTRODUCTION

Breast cancer (BC) is the primary cause of mortality among females. Global figures indicate that around 9.7 million new cancer cases were diagnosed in females in 2022, with BC comprising 23.8% of all cases, far surpassing lung cancer at 9.4% (Bray, et al., 2024). In Iraq, BC exhibits a 23.1% incidence rate, and a 15.7% mortality rate compared to other malignancies, making it the country with the highest prevalence and fatality rates for BC in the Middle East (Zahwe, et al., 2025). The occurrence of BC and the potential for later recurrence or metastasis are caused by several risk factors. These include age, genetic profile, reproductive characteristics, obesity, alcohol consumption, smoking, and general lifestyle choices. In addition, intrinsic molecular subtypes of BC, based on tumor gene expression and phenotypes, are also considered risk factors in the disease etiology (Barnard, Boeke and Tamimi, 2015; Winters, et al., 2017; Lee, et al., 2019). BC is a heterogeneous disease with variability in both clinical and molecular characteristics, which results in differing responses to treatments (Turner, et al., 2021).

Cancer stem cells (CSCs) represent a small subset of cancer cells that exhibit self-renewal, differentiation, and tumorigenic capabilities. They also have the ability to undergo epithelial-to-mesenchymal transition, which substantially contributes to tumor heterogeneity, leading to therapeutic resistance and an increased chance of local recurrences and metastasis (Walcher, et al., 2020; Wilson, et al., 2020). The cluster of differentiation 44 (CD44) is a transmembrane glycoprotein expressed on several human cell types, including embryonic stem cells, immune cells, and connective tissues (Goodison, Urquidi and Tarin, 1999). CD44 is recognized as a molecular marker of CSCs (Al-Hajj, et al., 2003; Schmitt, et al., 2012). This gene regularly undergoes alternative splicing, which results in the standard (CD44s) and variable (CD44v) isoforms (Wilson, et al., 2020). CD44 interaction with extracellular ligand activates various signaling pathways leading to cell proliferation, survival, adhesion, invasion, and migration (Herrera-Gayol and Jothy, 1999; Senbanjo and Chellaiah, 2017).

In BC, CD44 plays an essential role in tumor aggressiveness, progression, and the induction of CSC traits (Lopez, et al., 2005; Vadhan, et al., 2022; Gu, et al., 2022; Zhang, et al., 2019). Despite the recent advancements in BC therapy, certain patients experience disease recurrence. This may be attributed to the existence of BC stem cells (BCSCs) that withstand chemotherapy and radiotherapy (Steinbichler, et al., 2018; Clark, et al., 2022). Nevertheless, conflicting results concerning stemness and carcinogenesis were observed based on various splice variants of CD44 (Cho, et al., 2015; Zhang, et al., 2019). A study reported that the lack of CD44s correlates with a high incidence of lymph node metastases and poorer prognoses in BC patients (Gong, et al., 2005). In the triple-negative BC (TNBC) molecular subtype, CD44 was found to be related to the aggressiveness and resistance to the targeted therapy when transformed from the standard isoform into the variant isoform (Bei, et al., 2020). The mechanisms through which CD44s influence BC remain ambiguous. Precise histological diagnosis, molecular subtyping, and further classification are essential to better understand the causes of mortality and morbidity associated with this disease. In recent years, the application of artificial intelligence (AI) has attracted increasing interest in BC diagnostics, particularly in the evaluation of immunohistochemistry (IHC) and molecular markers. Conventional IHC assessments depend heavily on manual evaluation by pathologists, a process that is inherently subjective and prone to inter- and intra-observer variability. AI-driven approaches provide a more objective, consistent, and high-throughput alternative for interpreting IHC results (Rakha, Vougas and Tan, 2022; Pati, et al., 2024). These systems have shown promise in analyzing key biomarkers such as estrogen receptor (ER), progesterone receptor (PR), human epidermal growth factor receptor 2 (HER2), and the Ki-67 index, as well as BCSC markers, such as CD44, thereby enhancing diagnostic accuracy and assisting clinicians in selecting the most appropriate treatment in a timely manner (Wu, et al., 2023; McCaffrey, et al., 2024; Xiong, et al., 2025). Therefore, this study was designed to apply AI-based digital pathology (DP) to evaluate CD44s IHC expression in BC patients, aiming to assess its correlation with clinicopathological features, molecular subtypes, and survival, as well as to examine its prognostic and predictive value.

II. Materials and Methods

A. Sample Collection

The present retrospective study was approved by the Directorate of Health Research Ethics Committee through the College of Science-Biology Department, University of Duhok (Number: 21082022-6-5). A total of 105 formalin-fixed paraffin-embedded (FFPE) BC tissue blocks of patients who underwent surgery (from 2013 to 2019) were collected from the Histopathology Departments of both the Central Laboratory and Vajeen Private Laboratory in Duhok Province. Medical records and histopathological data were retrieved from both laboratories' databases and the medical oncology department at Azadi Cancer Center/Duhok/Iraq. All patients received routine chemotherapy, radiotherapy, and/or hormonal therapy following surgery according to the stage of the disease. The retrieved clinicopathological data were the age at diagnosis, pathological diagnosis of BC, histological grade, tumor size, axillary lymph node metastasis status, tumor stage, distance metastasis, and hormonal status such as ER and PR, HER2 expression, and the proliferative marker (Ki-67).

The classification of BC molecular subtypes was conducted according to the IHC profile, based on ER, PR, HER2, and the Ki-67 index, using a 20% cutoff to distinguish between high and low expression levels (Dai, et al., 2015; Bustreo, et al., 2016). In this study, the defined molecular subtypes of BC were as follows: luminal A (ER+, PR+, HER2-, Ki-67 <20%), luminal B HER2-negative (ER+, PR+, HER2-, Ki-67 ≥20%), luminal B HER2-positive (ER+, PR+, HER2+, any Ki-67), HER2-enriched (ER-, PR-, HER2+, Ki-67 ≥20%), and TNBC (ER-, PR-, HER2, Ki-67 ≥20%) (Vallejos, et al., 2010; Somal, et al., 2023).

In this study, the exclusion criteria included fine needle aspiration samples and core biopsies; only cases with excisional biopsies were included. Patients diagnosed with stage IV disease and those who were lost to follow-up were also excluded. All patients were followed every 6 months during the study period through phone calls, and survival data were validated using hospital records, pathology reports, and oncology follow-up records. Tumor grading was defined according to the combined Bloom–Richardson grading system (Elston and Ellis, 1991), and tumor staging was based on the International Union Against Cancer–American Joint Committee on Cancer TNM criteria (Giuliano, Edge and Hortobagyi, 2018). Overall survival (OS) was defined as the time from the date of surgery to death, while progression-free survival (PFS) was defined as the time from diagnosis to the first progression event.

B. IHC Staining of CD44s

IHC slides were prepared from three-micron sections cut from corresponding FFPE blocks. Heat-induced epitope retrieval was used for dewaxing and hydration at 50–60°C overnight (Paulsen, Dimke and Frische, 2015). Antigen retrieval was then performed using a water bath method (Dako, PT Link). Slides were placed in a water bath containing 1.5 L of low pH (×50) Target Retrieval Solution (Dako, EnVision™ FLEX; K8005, Glostrup, Denmark), following a specific protocol with a pre-heat temperature of 65°C and antigen retrieval at 97°C for 20 min. Afterward, the slides were immediately transferred to the PT Link Rinse Station containing diluted wash buffer (PBS ×20) (Dako, EnVision™ FLEX; K8000, Glostrup, Denmark) at room temperature for 1–5 min to prevent dehydration.

The IHC staining was performed using the Dako Autostainer Link 48 and a polymer-based detection system, following the recommended antibody protocol. All reagents were from the Dako EnVision™ FLEX Visualization Kit (K8000). To detect the CD44s cell membrane protein, a monoclonal mouse anti-human CD44s antibody (clone DF1485; Dako, Glostrup, Denmark) was used at a dilution of 1:50, prepared by mixing 1 μL of the concentrated antibody with 49 μL of antibody diluent.

The staining procedure consisted of several steps. First, endogenous peroxidase activity and non-specific binding were blocked using a peroxidase blocking reagent for 5 min. The primary antibody was then applied and incubated for 20 min. This was followed by rinsing in wash buffer and incubation with the secondary FLEX+ Mouse (LINKER) reagent for 15 min. After another rinse, slides were incubated in EnVision FLEX/HRP for 20 min, followed by two additional washes. To visualize antigen staining, 3,3'-diaminobenzidine was applied, and the slides were counterstained with hematoxylin. Finally, the slides were dehydrated through graded ethanol (70–100%) and mounted using Dibutyl-phthalate Polystyrene Xylene. Human urinary bladder tissue was used as a positive control for each sample.

C. Digitizing the Slides and Utilizing AI for Evaluation through DP/3DHISTECH

The prepared CD44s IHC slides were initially digitized using the Pannoramic® Desk II DW scanner from 3DHISTECH (Budapest, Hungary). SlideViewer 2.5, a digital microscopy tool, was subsequently used to examine the scanned slides. The certified QuantCenter 2.3 Image Analyzer was then employed to quantify the CD44s transmembrane protein (User Guide, June 3, 2021; MembraneQuant Image Analyzer) (Acs, et al., 2019; Braun, et al., 2020). The "PatternQuant" module was first selected to identify specific malignant and stromal regions. Subsequently, "MembraneQuant" color deconvolution was applied within the delineated malignant regions, based on the chromogen color of the marker.

The image analysis procedure uses quantitative algorithms that mimic the pathologist's assessment, producing semiquantitative outcomes on a non-standardized scoring system. Cell membranes are colored blue, yellow, orange, or red, corresponding to final scores of 0–+3, respectively. The final score is determined based on both the percentage of positive cells within the malignant area and the staining intensity (Aeffner, et al., 2018; Liu, et al., 2023). To validate the AI-based scoring by DP/3DHISTECH, the IHC slides were also manually evaluated by two pathologists.

D. Manual Scoring

Manual scoring was performed on the same digitized slides by two pathologists who were blinded to the patients' clinicopathological data. For each slide, five fields were examined using SlideViewer 2.5 at ×20 magnification. CD44s expression was evaluated based on the percentage of positive cells (0 points: <5%; 1 point: 6–25%; 2 points: 26–50%; 3 points: 51–75%; and 4 points: 76–100%) and the staining intensity of the cell membrane (0 points: no staining; 1 point: weak staining; 2 points: moderate staining; and 3 points: strong staining). The final score was calculated by multiplying the percentage score by the intensity score, yielding a total score ranging from 0 to 12. A score of ≥3 was considered positive (Wu, et al., 2015).

E. Statistical Methods

The general and medical characteristics of BC patients were presented as mean (SD), median (median absolute deviation [MAD]), or percentages. The association between CD44s protein expression and clinicopathological data was examined using the Pearson Chi-square test. The Kaplan-Meier method was used for OS and PFS analysis. Comparisons of OS and PFS across different general and medical characteristics were performed using the Wilcoxon/Kruskal–Wallis test (rank sums test). Cox regression analysis, based on the proportional hazards model, was conducted to identify factors associated with OS and PFS, considering mortality as the outcome. The strength and precision of these associations were expressed as hazard ratios (HR) with 95% confidence intervals (CI). Cohen's Kappa test was used to assess the agreement between manual scoring and AI-based scoring of CD44s protein expression. A $p < 0.05$ was considered statistically significant. All statistical analyses were performed using JMP®, Version 18.0 (SAS Institute Inc., Cary, NC, 1989–2023).

III. Results

A. Patient Baseline Characteristics

In this study, a total of 105 BC samples were obtained, of which 98 were included in the analysis, while 7 cases were excluded due to loss to follow-up. All of the included samples were invasive ductal carcinoma. The patients' clinicopathological characteristics are listed in Table I. The mean age at diagnosis was 48.36 ± 11.28 years (range: 28–75 years), with the majority of patients (72.45%) being over 40 years old. Regarding tumor size, 68.37% of patients had tumors measuring >2 cm to ≤5 cm, 18.37% had tumors >5 cm, and 13.27% had tumors ≤2 cm. Histological grading revealed that 54.08% of patients had Grade III tumors, 41.84% had Grade II, and 4.08% had Grade I. TNM cancer staging results were as follows: Stage II (50%), Stage III (39.8%), and Stage I (10.2%). Lymph node metastasis was present in 65.31% of patients, while 34.69% had no lymph node involvement. Lymphovascular invasion (LVI) was observed in 74.23% of cases. In addition, 11.22% of patients developed local recurrence, and 13.27% developed distant metastases. Metastatic patterns were identified in the bone and vertebrae (3 cases), head and brain (5 cases), liver (2 cases), peritoneum (1 case), skin (1 case), and one case with an unidentified metastatic site.

In the present study, the ER, PR, and HER2 status of BC patients was categorized into positive and negative groups. The ER and PR status results were identical, with

70.41% of patients testing positive and 29.59% testing negative. Regarding HER2 status, 30.61% of patients were HER2-positive, while 69.39% were HER2-negative. Fifty-three patients (54.08%) had a Ki-67 index score of ≥20, while forty-five patients (45.92%) had a score of <20. The molecular classification of BC cases identified Luminal A as the most prevalent subtype, comprising 38 cases (38.78% of the cohort). This was followed by Luminal B HER2-negative with 21 cases (21.65%) and HER2-enriched with 18 cases (18.56%). The remaining subtypes included Luminal B HER2-positive (11 cases, 11.34%) and TNBC, the least common subtype, with 9 cases (9.28%).

B. CD44s Protein Expression

CD44s is predominantly expressed in the cell membranes of BC tissues, as illustrated in Fig. 1. CD44s protein expression, as determined by AI scoring, was positive in 65.31% of patients and negative in 34.69%. The agreement between AI and manual scoring was moderate, with a Cohen's Kappa value of 0.4337 (p < 0.0001).

C. Association between CD44s Expression and Clinicopathological Features

This study analyzed the association between clinicopathological characteristics and the expression of the CD44s cell membrane protein (Table I). CD44s positivity was higher in patients over 40 years of age (74.07%) compared to those aged ≤40 years (61.97%), although this difference was not statistically significant (p = 0.2608). Similarly, CD44s expression showed no significant association with tumor size, lymph node metastasis, histological grade, LVI, or disease stage (p = 0.8904; p = 0.2126; p = 0.7385; p = 0.1789; p = 0.6946, respectively).

In terms of hormone receptor status, CD44s positivity was higher in ER-negative and PR-negative patients (75.86%) compared to ER-positive and PR-positive patients (60.87%); however, these differences were not statistically significant (p = 0.1547 for both). For HER2 status, CD44s positivity was greater in HER2-positive patients (73.33%) than in HER2-negative patients (61.76%), but this difference was not statistically significant (p = 0.2675). The Ki-67 index showed that CD44s positivity was higher in patients with a Ki-67 index ≥20% (73.58%) than in those with <20% (55.56%), although the difference was not statistically significant (p = 0.0617).

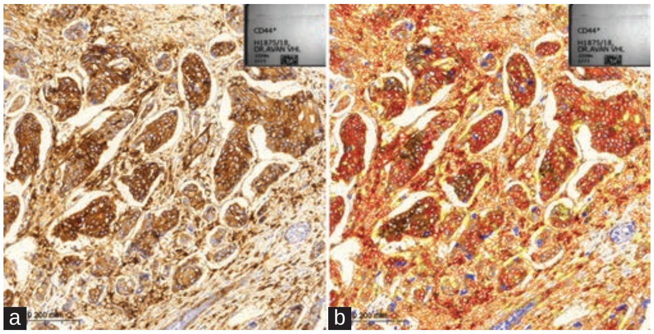

Fig. 1. Representative digital pathology images (3DHISTECH). (a) Scanned IHC slide illustrating CD44s protein expression in breast cancer tissue, visualized using SlideViewer. (b) QuantCenter software performing color deconvolution of immunohistochemical staining for CD44s cell membrane protein expression. Blue indicates absence of membrane staining (score 0), while yellow, orange, and red represent increasing staining intensities, corresponding to scores of +1, +2, and +3, respectively.

Regarding molecular subtypes, CD44s expression varied among subtypes but did not reach statistical significance (p = 0.251). Notably, the highest expression was observed in the HER2-Enriched subtype (78.95%) and Luminal-B HER2-negative (76.19%), followed by TNBC (66.67%) and Luminal-B HER2-positive (63.64%), while the lowest expression was seen in the Luminal-A subtype (52.63%).

Progression events such as local recurrence, distant metastasis, or death were more frequent in CD44s-positive cases (74.36%) compared to those with no progression (59.32%), although the difference was not statistically significant (p = 0.126). Local recurrence specifically demonstrated a higher rate of CD44s expression (90.91%) compared to non-recurrent cases (62.07%), though this difference also did not reach statistical significance (p = 0.058). Similarly, distant metastasis showed no significant association with CD44s expression (61.54% in metastatic cases vs. 65.88% in non-metastatic cases; p = 0.759). Finally, no significant survival difference was observed between CD44s-positive and CD44s-negative groups (p = 0.202).

D. Survival Analysis

Kaplan-Meier analysis, including the log-rank test, was used to assess OS and PFS across various BC patient characteristics. Median OS and median PFS are reported in months, along with the MAD (Table II). Patients with tumors measuring >2–≤5 cm had a median OS of 86.47 months (MAD = 15.86), which was significantly longer than that of patients with tumors >5 cm (median OS = 53.42 months, MAD = 25.39; p = 0.0229). Similarly, PFS was significantly longer for patients with tumors ≤2 cm (median PFS = 86.7 months, MAD = 18.53) compared to those with tumors >5 cm (median PFS = 17.85 months; p = 0.0023).

Stage I disease was associated with the longest survival, with a median OS of 87.05 months (MAD = 20.44) and a median PFS of 87.05 months (MAD = 20.44). A significant difference in PFS was observed across disease stages (p = 0.0199). In addition, ER and PR status significantly impacted both OS and PFS. ER-positive and PR-positive patients had longer median OS (86.33 months) and PFS (75.9 months) compared to ER-negative and PR-negative patients (median OS = 69.4 months, p = 0.0198; median PFS = 61.23 months, p = 0.0392).

Among the molecular subtypes of BC, Luminal-B HER2-negative tumors demonstrated the longest median OS at 87.4 months (MAD = 11.4), whereas HER2-Enriched tumors exhibited the shortest median OS at 68.5 months (MAD = 27.27), although this difference approached but did not reach statistical significance (p = 0.0982). Similarly, PFS was longer in Luminal-B HER2-negative cases, with a

TABLE I
General Medical and Clinicopathological Characteristics of BC Patients and their Association with AI-based Scores of CD44s Protein Expression

Characteristics	Categories, n (%)		CD44s protein expression, n (%)		p-value
			Negative 34 (34.69)	Positive 64 (65.31)	
Age (Years)	Mean±SD	48.36±11.28	-	-	-
	Median (Range)	48 (28–75)	-	-	
	≤40	27 (27.55)	7 (25.93)	20 (74.07)	0.2608
	>40	71 (72.45)	27 (38.03)	44 (61.97)	
Tumor size	>2–≤5 cm	67 (68.37)	23 (34.33)	44 (65.67)	0.8904
	>5 cm	18 (18.37)	7 (38.89)	11 (61.11)	
	≤2	13 (13.27)	4 (30.77)	9 (69.23)	
Lymph node metastasis	No	34 (34.69)	9 (26.47)	25 (73.53)	0.2126
	Yes	64 (65.31)	25 (39.06)	39 (60.94)	
Histological grading	Grade I	4 (4.08)	2 (50.00)	2 (50.00)	0.7385
	Grade II	41 (41.84)	13 (31.71)	28 (68.29)	
	Grade III	53 (54.08)	19 (35.85)	34 (64.15)	
Lymphovascular invasion	Negative	25 (25.77)	6 (24.00)	19 (76.00)	0.1789
	Positive	72 (74.23)	28 (38.89)	44 (61.11)	
Staging	Stage I	10 (10.20)	4 (40.00)	6 (60.00)	0.6946
	Stage II	49 (50.00)	15 (30.61)	34 (69.39)	
	Stage III	39 (39.80)	15 (38.46)	24 (61.54)	
ER	Negative	29 (29.59)	7 (24.14)	22 (75.86)	0.1547
	Positive	69 (70.41)	27 (39.13)	42 (60.87)	
PR	Negative	29 (29.59)	7 (24.14)	22 (75.86)	0.1547
	Positive	69 (70.41)	27 (39.13)	42 (60.87)	
HER2	Negative	68 (69.39)	26 (38.24)	42 (61.76)	0.2675
	Positive	30 (30.61)	8 (26.67)	22 (73.33)	
Ki-67 index (Cutoff 20%)	<20	45 (45.92)	20 (44.44)	25 (55.56)	0.0617
	≥20	53 (54.08)	14 (26.42)	39 (73.58)	
BC molecular subtypes	Luminal-A	38 (39.18)	18 (47.37)	20 (52.63)	0.2511
	Luminal-B Her2-ve	21 (21.65)	5 (23.81)	16 (76.19)	
	HER2-Enriched	19 (18.56)	4 (21.05)	15 (78.95)	
	Luminal-B Her2+ve	11 (11.34)	4 (36.36)	7 (63.64)	
	TNBC	9 (9.28)	3 (33.33)	6 (66.67)	
Progression event	No	59 (60.20)	24 (40.68)	35 (59.32)	0.1258
	Yes	39 (39.80)	10 (25.64)	29 (74.36)	
Local recurrence	No	87 (88.78)	33 (37.93)	54 (62.07)	0.0583
	Yes	11 (11.22)	1 (9.09)	10 (90.91)	
Distance metastasis	No	85 (86.73)	29 (34.12)	56 (65.88)	0.7593
	Yes	13 (13.27)	5 (38.46)	8 (61.54)	
Survival	Alive	70 (71.43)	27 (38.57)	43 (61.43)	0.2023
	Died	28 (28.57)	7 (25.00)	21 (75.00)	
OS in months	Mean±SD	78.26±30.03	-	-	-
	Median (Range)	53.3 (2.8–141.8)	-	-	-

ER: Estrogen receptor, PR: Progesterone receptor, HER2: Human epidermal growth factor receptor 2, OS: Overall survival

median of 82.03 months (MAD = 22.03), compared to HER2-Enriched subtypes, which had a median of 48.13 months (MAD = 21.07). Nonetheless, no statistically significant differences in time to progression were observed between the groups (p = 0.1616).

Local recurrence did not have a statistically significant impact on OS (p = 0.2418). However, patients without distant metastasis had a significantly longer median OS of 86.47 months (MAD = 16.87) compared to those with distant metastasis, whose median OS was 59.43 months (MAD = 25.66, p = 0.0009). In addition, patients with negative CD44s protein expression exhibited longer median OS (87.64 months, MAD = 13.7) and PFS (86.64 months, MAD = 18.14) compared to those with positive CD44s protein expression; nevertheless, the differences were not statistically significant (p = 0.1345 for OS, p = 0.0669 for PFS). Furthermore, no other clinicopathological prognostic factors were found to be significantly associated with OS or PFS in BC patients.

Fig. 2 shows Kaplan-Meier survival curves for OS and PFS of BC patients with respect to CD44s protein expression. Although patients with CD44-negative tumors demonstrated better prognosis and improved OS and PFS compared to those with CD44-positive tumors, the differences were not statistically significant. The median survival times were longer in the CD44-negative group, but the log-rank test yielded p-values of 0.1776 for OS and 0.2274 for PFS, respectively.

TABLE II
Kaplan-Meier (log-rank test) Analysis for OS and PFS

Characteristics	Categories	OS in Months	p-value	PFS in Months	p-value
		Med (MAD)		Med (MAD)	
Age category	≤40	75.6 (16.23)	0.2104	72.33 (24.2)	0.4105
	>40	86.47 (17.5)		72.57 (25.9)	
Tumor size	>2–≤5 cm	86.47 (15.86)	**0.0229**	75.27 (20.5)	**0.0023**
	>5 cm	53.42 (25.39)		17.85	
	≤2 cm	86.7 (18.53)		86.7 (18.53)	
Lymph node metastasis	No	85.52 (15.42)	0.2224	74.84 (18.52)	0.2085
	Yes	81.53 (20.22)		70.12 (27.15)	
Histological grading	I	80.85 (9.83)	0.8578	80.85 (9.83)	0.4466
	II	81.03 (16.56)		75.3 (20.83)	
	III	86.33 (19.14)		69.4 (29.07)	
Lymphovascular invasion	Negative	72.57 (12.7)	0.4529	72.57 (13.9)	0.3664
	Positive	86.4 (19.27)		72.44 (29.09)	
Staging	I	87.05 (20.44)	0.1017	87.05 (20.44)	**0.0199**
	II	86.47 (15.07)		75.3 (20.47)	
	III	75.27 (30.6)		59.63 (26.7)	
ER	Negative	69.4 (26.37)	**0.0198**	61.23 (26.2)	**0.0392**
	Positive	86.33 (15.7)		75.9 (22.37)	
PR	Negative	69.4 (26.37)	**0.0198**	61.23 (26.2)	**0.0392**
	Positive	86.33 (15.7)		75.9 (22.37)	
HER2	Negative	86.215 (14.89)	0.1269	78.47 (19.79)	0.1030
	Positive	70.04 (28.01)		59.67 (26.3)	
Ki-67 index (Cutoff 20%)	<20%	85.33 (19.57)	0.5493	75.9 (23.23)	0.1802
	≥20%	82.03 (15.87)		69.4 (26.37)	
BC molecular subtypes	Luminal-B Her2-ve	87.4 (11.4)	0.0982	82.03 (22.03)	0.1616
	Luminal-B Her2+ve	86.47 (27.56)		75.3 (38.73)	
	Luminal-A	85.83 (16.37)		78.47 (20.52)	
	TNBC	73.77 (18.06)		73.77 (18.06)	
	HER2-Enriched	68.5 (27.27)		48.13 (21.07)	
Local recurrence	No	82.03 (16.83)	0.2418	-	-
	Yes	86.47 (19.4)		-	
Distance metastasis	No	86.47 (16.87)	**0.0009**	-	-
	Yes	59.43 (25.66)		-	
CD44s protein expression	Negative	87.64 (13.7)	0.1345	86.64 (18.14)	0.0669
	Positive	75.75 (21.09)		69.54 (26)	

MAD: Median absolute deviation, ER: Estrogen receptor, PR: Progesterone receptor, HER2: Human epidermal growth factor receptor 2, OS: Overall survival, PFS: Progression-free survival. The bold values indicate p-values < 0.05.

E. Cox Regression Analysis of Survival in BC Patients

In the present study, patients with LVI had a 2.37-fold higher risk of death compared to those without LVI, making it the only significant predictor of poor OS (HR = 2.37, 95% CI = 1.06–5.29; p = 0.036). LVI-positive tumors also showed a higher risk of progression (HR = 2.19, 95% CI = 0.95–5.03), though this did not reach statistical significance (p = 0.064) (Table III).

Although patients with Stage II disease exhibited a higher risk of progression (HR = 3.28, 95% CI = 0.75–14.28), the association was not statistically significant (p = 0.122). A tumor size greater than 5 cm also showed worse survival outcomes for both OS (HR = 1.74, 95% CI = 0.37–8.21) and PFS (HR = 1.97, 95% CI = 0.37–10.47), yet the associations were not statistically significant (OS: p = 0.701; PFS: p = 0.709). Finally, other variables (e.g., ER status, lymph node metastasis, age, HER2, Ki-67, CD44s protein expression) did not show significant correlations with survival (all p > 0.05).

IV. Discussion

In this study, IHC analysis using AI-based scoring methods was employed to investigate the expression of CD44s cell membrane protein in BC patients and its potential prognostic value. Our analysis revealed that 65.31% of patients exhibited positive CD44s protein expression, while 34.69% were negative, consistent with previous studies on CSC markers in BC tissues (Mohamed, et al., 2019; Wu, et al., 2015). However, despite the high rate of CD44s protein expression, we found no significant correlation between CD44s protein expression and key clinicopathological factors such as age, tumor size, lymph node metastasis, or hormone receptor status. The lack of association with clinicopathological factors aligns with studies reporting no significant correlation between CD44s protein expression and clinical outcomes (Abraham, et al., 2005). This may suggest that the standard isoform of CD44 cell membrane protein contributes to tumor initiation, warranting further

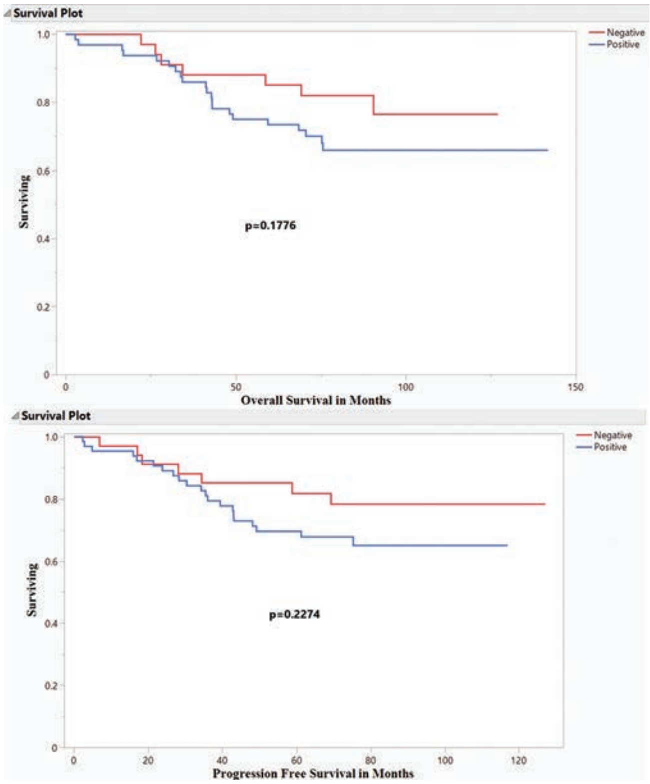

Fig. 2. Kaplan-Meier survival curves with log-rank test results. Comparison of overall survival between patients with positive and negative CD44s protein expression (top); comparison of progression-free survival between patients with positive and negative CD44s protein expression (bottom).

investigation into its role in both primary and metastatic tissues in BC patients.

Nevertheless, conflicting results from other studies regarding the association of CD44s with clinicopathological characteristics highlight the complexity of CD44s as a prognostic and predictive biomarker (Wu, et al., 2015). These discrepancies may be due to differences in study populations, methodologies, or the biological heterogeneity of BC subtypes. Furthermore, the specific CD44 isoform selected in various studies may demonstrate distinct roles in BC initiation and progression (Yang, et al., 2019; Brown, et al., 2011; Guo, et al., 2021).

Kaplan-Meier survival analysis showed that CD44s protein expression did not significantly affect OS or DFS, which may be due to the short follow-up period of the cohort. Notably, similar clinical outcomes were reported in a study by Abraham, et al. (Abraham, et al., 2005). However, a meta-analysis suggested that CD44 serves as a negative prognostic marker for OS and PFS (Gu, et al., 2022). It is possible that CD44v isoforms play a more prominent role in BC progression (Hu, et al., 2017). Since our study focused on CD44s, future research should include CD44v isoforms and a larger cohort to better clarify the prognostic significance of CD44.

Interestingly, our analysis identified LVI as the only independent predictor of both OS and PFS, underscoring its importance as a key prognostic factor in BC. This finding aligns with other studies that have associated LVI with more aggressive BC subtypes, higher recurrence rates, and lower survival outcomes (Lee, et al., 2023; Nishimura, et al., 2022; Song, et al., 2011).

TABLE III
COX REGRESSION ANALYSIS FOR OS AND PFS IN BC PATIENTS

Predictors (n=98)	OS in months		PFS in Months	
	HR (95% CI)	p-value	HR (95% CI)	p-value
Age category		0.37404		0.78630
>40 versus ≤40	0.74 (0.38–1.43)		1.10 (0.56–2.16)	
Tumor size		0.70059		0.70915
>2–≤5 cm versus ≤2	1.64 (0.50–5.33)		1.36 (0.40–4.61)	
>5 cm versus ≤2	1.74 (0.37–8.21)		1.97 (0.37–10.47)	
Lymph node metastasis		0.34261		0.55337
Yes versus No	1.50 (0.65–3.47)		1.31 (0.54–3.18)	
Histological grading		0.60362		0.77761
II versus I	0.82 (0.25–2.65)		0.79 (0.24–2.56)	
III versus I	0.59 (0.16–2.19)		0.64 (0.17–2.41)	
Lymphovascular invasion		**0.03565**		0.06433
Positive versus Negative	2.37 (1.06–5.29)		2.19 (0.95–5.03	
Staging		0.50417		0.12226
II versus I	1.92 (0.50–7.31)		3.28 (0.75–14.28)	
III versus I	1.51 (0.28–8.28)		2.19 (0.36–13.39)	
ER		0.31812		0.81644
Positive versus Negative	0.66 (0.29–1.49)		0.91 (0.41–2.03)	
PR		0.31812		0.81644
Positive versus Negative	0.66 (0.29–1.49)		0.91 (0.41–2.03)	
HER2		0.80453		0.90197
Positive versus Negative	1.15 (0.39–3.36)		0.93 (0.31–2.84)	
Ki-67 (20%)		0.95403		0.73258
≥20% versus <20%	1.02 (0.50–2.10)		1.13 (0.56–2.30)	
CD44s protein expression		0.99849		0.95663
Positive versus Negative	1.00 (0.54–1.86)		0.98 (0.51–1.90)	

ER: Estrogen receptor, PR: Progesterone receptor, HER2: Human epidermal growth factor receptor 2, OS: Overall survival, PFS: Progression-free survival

The integration of an AI-based scoring method for IHC slide quantification represents a significant advancement in BC diagnostics. In this study, we observed moderate agreement between the AI-based scoring method and manual scoring of CD44s cell membrane protein expression, highlighting the potential of AI to complement traditional approaches, particularly in reducing interobserver variability.

Despite its strengths, this study has several limitations. These include its retrospective design, relatively short follow-up period, and relatively small sample size, particularly within stratified subgroups, which may limit the statistical power to detect subtle associations. Another potential limitation is recall bias, especially for data obtained directly from patients. However, most clinical and follow-up information was sourced from hospital records, including patient registries, the oncology clinic, and the cancer center database at Azadi Teaching Hospital, helping to reduce this risk. For the small portion of data collected through patient phone calls, no more practical or reliable method was available. Future studies should aim to validate these findings in larger, prospective cohorts and explore the distinct roles of CD44s and CD44v isoforms in BC progression and survival outcomes. Moreover, the development and refinement of AI-based scoring systems warrant further exploration to establish standardized protocols for clinical application.

V. Conclusion

This study contributes to the growing body of literature on CD44s cell membrane protein expression in BC, providing insights into its role in disease characterization. While some results align with prior studies, others contradict established findings, underscoring the complexity of CD44s cell membrane protein expression as a biomarker. Future research with larger cohorts and integrated molecular profiling is needed to clarify the prognostic and therapeutic relevance of CD44s cell membrane protein expression in BC. The moderate concordance between AI-based and manual scoring methods highlights the promise of AI in enhancing pathological assessments. Further research is essential to elucidate the prognostic value of CD44s cell membrane protein expression and to optimize AI tools alongside manual pathology, ensuring robustness and accuracy for routine clinical use.

REFERENCES

Abraham, B.K., Fritz, P., McClellan, M., Hauptvogel, P., Athelogou, M., and Brauch, H., 2005. Prevalence of CD44+/CD24−/low cells in breast cancer may not be associated with clinical outcome but may favour distant metastasis. *Clinical Cancer Research*, 11(3), pp.1154-1159.

Acs, B., Pelekanou, V., Bai, Y., Martinez-Morilla, S., Toki, M., Leung, S.C., Nielsen, T.O., and Rimm, D.L., 2019. Ki-67 reproducibility using digital image analysis: An inter-platform and inter-operator study. *Laboratory Investigation*, 99(1), pp.107-117.

Aeffner, F., Adissu, H.A., Boyle, M.C., Cardiff, R.D., Hagendorn, E., Hoenerhoff, M.J., Klopfleisch, R., Newbigging, S., Schaudien, D., Turner, O., and Wilson, K., 2018. Digital microscopy, image analysis, and virtual slide repository. *ILAR journal*, 59(1), pp.66-79.

Al-Hajj, M., Wicha, M.S., Benito-Hernandez, A., Morrison, S.J., and Clarke, M.F., 2003. Prospective identification of tumorigenic breast cancer cells. *Proceedings of the National Academy of Sciences*, 100(7), pp.3983-3988.

Barnard, M.E., Boeke, C.E., and Tamimi, R.M., 2015. Established breast cancer risk factors and risk of intrinsic tumour subtypes. *Biochimica Biophysica Acta (BBA)-Reviews on Cancer*, 1856(1), pp.73-85.

Bei, Y., Cheng, N., Chen, T., Shu, Y., Yang, Y., Yang, N., Zhou, X., Liu, B., Wei, J., Liu, Q., Zheng, W., Zhang, W., Su, H., Zhu, W., Ji, J., and Shen, P., 2020. CDK5 inhibition abrogates TNBC stem-cell property and enhances anti-PD-1 therapy. *Advanced Science*, 7(22), p.2001417.

Braun, M., Piasecka, D., Bobrowski, M., Kordek, R., Sadej, R., and Romanska, H.M., 2020. A 'Real-Life' experience on automated digital image analysis of FGFR2 immunohistochemistry in breast cancer. *Diagnostics(Basel)*, 10(12), p.1060.

Bray, F., Laversanne, M., Sung, H., Ferlay, J., Siegel, R.L., Soerjomataram, I., and Jemal, A., 2024. Global cancer statistics 2022: GLOBOCAN estimates of incidence and mortality worldwide for 36 cancers in 185 countries. *CA: A Cancer Journal for Clinicians*, 74(3), pp.229-263.

Brown, R.L., Reinke, L.M., Damerow, M.S., Perez, D., Chodosh, L.A., Yang, J., and Cheng, C., 2011. CD44 splice isoform switching in human and mouse epithelium is essential for epithelial-mesenchymal transition and breast cancer progression. *The Journal of Clinical Investigation*, 121(3), pp.1064-1074.

Bustreo, S., Osella-Abate, S., Cassoni, P., Donadio, M., Airoldi, M., Pedani, F., Papotti, M., Sapino, A., and Castellano, I., 2016. Optimal Ki-67 cut-off for luminal breast cancer prognostic evaluation: A large case series study with a long-term follow-up. *Breast Cancer Research and Treatment*, 157, pp.363-371.

Cho, Y., Lee, H.W., Kang, H.G., Kim, H.Y., Kim, S.J., and Chun, K.H., 2015. Cleaved CD44 intracellular domain supports activation of stemness factors and promotes tumorigenesis of breast cancer. *Oncotarget*, 6(11), pp.8709-8721.

Clark, G.C., Hampton, J.D., Koblinski, J.E., Quinn, B., Mahmoodi, S., Metcalf, O., Guo, C., Peterson, E., Fisher, P.B., Farrell, N.P., Wang, X.Y., and Mikkelsen, R.B., 2022. Radiation induces ESCRT pathway dependent CD44v3+ extracellular vesicle production stimulating pro-tumor fibroblast activity in breast cancer. *Frontiers in Oncology*, 12, p.913656.

Dai, X., Li, T., Bai, Z., Yang, Y., Liu, X., Zhan, J., and Shi, B., 2015. Breast cancer intrinsic subtype classification, clinical use and future trends. *American Journal of Cancer Research*, 5(10), pp.2929-2943.

Elston, C.W., and Ellis, I.O., 1991. Pathological prognostic factors in breast cancer. I. The value of histological grade in breast cancer: Experience from a large study with long-term follow-up. *Histopathology*, 19(5), pp.403-410.

Giuliano, A.E., Edge, S.B., and Hortobagyi, G.N., 2018. Eighth edition of the AJCC cancer staging manual: Breast cancer. *Annals of Surgical Oncology*, 25, pp.1783-1785.

Gong, Y., Sun, X., Huo, L., Wiley, E.L., and Rao, M.S., 2005. Expression of cell adhesion molecules, CD44s and E-cadherin, and microvessel density in invasive micropapillary carcinoma of the breast. *Histopathology*, 46(1), pp.24-30.

Goodison, S., Urquidi, V., and Tarin, D., 1999. CD44 cell adhesion molecules. *Molecular Pathology*, 52(4), pp.189-196.

Gu, J., Chen, D., Li, Z., Yang, Y., Ma, Z., and Huang, G., 2022. Prognosis assessment of CD44^{+}/CD24^{-} in breast cancer patients: A systematic review and meta-analysis. *Archives of Gynecology and Obstetrics*, 306(4), pp.1147-1160.

Guo, Q., Liu, Y., He, Y., Du, Y., Zhang, G., Yang, C., and Gao, F., 2021. CD44 activation state regulated by the CD44v10 isoform determines breast cancer proliferation. *Oncology Reports*, 45(4), p.7.

Herrera-Gayol, A., and Jothy, S., 1999. Adhesion proteins in the biology of breast cancer: Contribution of CD44. *Experimental and Molecular Pathology*, 66(2), pp.149-156.

Hu, J., Li, G., Zhang, P., Zhuang, X., and Hu, G., 2017. A CD44v+ subpopulation of breast cancer stem-like cells with enhanced lung metastasis capacity. *Cell Death Disease*, 8(3), p.e2679.

Lee, K., Kruper, L., Dieli-Conwright, C.M., and Mortimer, J.E., 2019. The impact of obesity on breast cancer diagnosis and treatment. *Current Oncology Reports*, 21, p.41.

Lee, S.J., Go, J., Ahn, B.S., Ahn, J.H., Kim, J.Y., Park, H.S., Kim, S.I., Park, B.W., and Park, S., 2023. Lymphovascular invasion is an independent prognostic factor in breast cancer irrespective of axillary node metastasis and molecular subtypes. *Frontiers in Oncology*, 13, p.1269971.

Liu, Y., Han, D., Parwani, A.V., and Li, Z., 2023. Applications of artificial intelligence in breast pathology. *Archives of Pathology and Laboratory Medicine*, 147(9), pp.1003-1013.

Lopez, J.I., Camenisch, T.D., Stevens, M.V., Sands, B.J., McDonald, J., and Schroeder, J.A., 2005. CD44 attenuates metastatic invasion during breast cancer progression. *Cancer Research*, 65(15), pp.6755-6763.

McCaffrey, C., Jahangir, C., Murphy, C., Burke, C., Gallagher, W.M., and Rahman, A., 2024. Artificial intelligence in digital histopathology for predicting patient prognosis and treatment efficacy in breast cancer. *Expert Review of Molecular Diagnostics*, 24(5), pp.363-377.

Mohamed, S.Y., Kaf, R.M., Ahmed, M.M., Elwan, A., Ashour, H.R., and Ibrahim, A., 2019. The prognostic value of cancer stem cell markers (Notch1, ALDH1, and CD44) in primary colorectal carcinoma. *Journal of Gastrointestinal Cancer*, 50, pp.824-837.

Nishimura, R., Osako, T., Okumura, Y., Nakano, M., Ohtsuka, H., Fujisue, M., and Arima, N., 2022. An evaluation of lymphovascular invasion in relation to biology and prognosis according to subtypes in invasive breast cancer. *Oncology Letters*, 24(2), p.245.

Pati, P., Karkampouna, S., Bonollo, F., Compérat, E., Radić, M., Spahn, M., Martinelli, A., Wartenberg, M., Kruithof-de Julio, M., and Rapsomaniki, M., 2024. Accelerating histopathology workflows with generative AI-based virtually multiplexed tumor profiling. *Nature Machine Intelligence*, 6(9), pp.1077-1093.

Paulsen, I.M.S., Dimke, H., and Frische, S., 2015. A single simple procedure for dewaxing, hydration and heat-induced epitope retrieval (HIER) for immunohistochemistry in formalin fixed paraffin-embedded tissue. *European Journal of Histochemistry EJH*, 59(4), p.2532.

Rakha, E.A., Vougas, K., and Tan, P.H., 2022. Digital technology in diagnostic breast pathology and immunohistochemistry. *Pathobiology*, 89(5), pp.334-342.

Schmitt, F., Ricardo, S., Vieira, A.F., Dionísio, M.R., and Paredes, J., 2012. Cancer stem cell markers in breast neoplasias: Their relevance and distribution in distinct molecular subtypes. *Virchows Archiv*, 460, pp.545-553.

Senbanjo, L.T., and Chellaiah, M.A., 2017. CD44: A multifunctional cell surface adhesion receptor is a regulator of progression and metastasis of cancer cells. *Frontiers in Cell and Developmental Biology*, 5, p.18.

Somal, P.K., Sancheti, S., Sharma, A., Sali, A.P., Chaudhary, D., Goel, A., Dora, T.K., Brar, R., Gulia, A., and Divatia, J., 2023. A clinicopathological analysis of molecular subtypes of breast cancer using immunohistochemical surrogates: A 6-year institutional experience from a tertiary cancer center in north India. *South Asian Journal of Cancer*, 12(02), pp.104-111.

Song, Y.J., Shin, S.H., Cho, J.S., Park, M.H., Yoon, J.H., and Jegal, Y.J., 2011. The role of lymphovascular invasion as a prognostic factor in patients with lymph node-positive operable invasive breast cancer. *Journal of Breast Cancer*, 14(3), pp.198-203.

Steinbichler, T.B., Dudás, J., Skvortsov, S., Ganswindt, U., Riechelmann, H., and Skvortsova, I.I., 2018. December. Therapy resistance mediated by cancer stem cells. In: *Seminars in Cancer Biology*. Vol. 53. Academic Press, United States, pp.156-167.

Turner, K.M., Yeo, S.K., Holm, T.M., Shaughnessy, E., and Guan, J.L., 2021. Heterogeneity within molecular subtypes of breast cancer. *American Journal of Physiology Cell Physiology*, 321(2), pp.C343-C354.

Vadhan, A., Hou, M.F., Vijayaraghavan, P., Wu, Y.C., Hu, S.C.S., Wang, Y.M., Cheng, T.L., Wang, Y.Y., and Yuan, S.S.F., 2022. CD44 promotes breast cancer metastasis through AKT-mediated downregulation of nuclear FOXA2. *Biomedicines*, 10(10), p.2488.

Vallejos, C.S., Gómez, H.L., Cruz, W.R., Pinto, J.A., Dyer, R.R., Velarde, R., Suazo, J.F., Neciosup, S.P., León, M., De La Cruz, M.A., and Vigil, C.E., 2010. Breast cancer classification according to immunohistochemistry markers: Subtypes and association with clinicopathologic variables in a peruvian hospital database. *Clinical Breast Cancer*, 10(4), pp.294-300.

Walcher, L., Kistenmacher, A.K., Suo, H., Kitte, R., Dluczek, S., Strauß, A., Blaudszun, A.R., Yevsa, T., Fricke, S., and Kossatz-Boehlert, U., 2020. Cancer stem cells-origins and biomarkers: Perspectives for targeted personalized therapies. *Frontiers in Immunology*, 11, p.1280.

Wilson, M.M., Weinberg, R.A., Lees, J.A., and Guen, V.J., 2020. Emerging mechanisms by which EMT programs control stemness. *Trends in Cancer*, 6(9), pp.775-780.

Winters, S., Martin, C., Murphy, D., and Shokar, N.K., 2017. Breast cancer epidemiology, prevention, and screening. *Progress in Molecular Biology and Translational Science*, 151, pp.1-32.

Wu, Q., Yang, Y., Wu, S., Li, W., Zhang, N., Dong, X., and Ou, Y., 2015. Evaluation of the correlation of KAI1/CD82, CD44, MMP7 and β-catenin in the prediction of prognosis and metastasis in colorectal carcinoma. *Diagnostic Pathology*, 10, p.176.

Wu, S., Yue, M., Zhang, J., Li, X., Li, Z., Zhang, H., Wang, X., Han, X., Cai, L., Shang, J., Jia, Z., Wang, X., Li, J., and Liu, Y., 2023. The role of artificial intelligence in accurate interpretation of HER2 immunohistochemical scores 0 and 1+ in breast cancer. *Modern Pathology*, 36(3), p.100054.

Wu, X.J., Li, X.D., Zhang, H., Zhang, X., Ning, Z.H., Yin, Y.M., and Tian, Y., 2015. Clinical significance of CD44s, CD44v3 and CD44v6 in breast cancer. *Journal of International Medical Research*, 43(2), pp.173-179.

Xiong, X., Zheng, L.W., Ding, Y., Chen, Y.F., Cai, Y.W., Wang, L.P., Huang, L., Liu, C.C., Shao, Z.M., and Yu, K.D., 2025. Breast cancer: Pathogenesis and treatments. *Signal Transduction and Targeted Therapy*, 10(1), p.49.

Yang, C., Cao, M., Liu, Y., He, Y., Du, Y., Zhang, G., and Gao, F., 2019. Inducible formation of leader cells driven by CD44 switching gives rise to collective invasion and metastases in luminal breast carcinomas. *Oncogene*, 38(46), pp.7113-7132.

Zahwe, M., Bendahhou, K., Eser, S., Mukherji, D., Fouad, H., Fadhil, I., Soerjomataram, I., and Znaor, A., 2025. Current and future burden of female breast cancer in the Middle East and North Africa region using estimates from GLOBOCAN 2022. *International Journal of Cancer*, 156, pp.2320-2329.

Zhang, H., Brown, R.L., Wei, Y., Zhao, P., Liu, S., Liu, X., Deng, Y., Hu, X., Zhang, J., Gao, X.D., Kang, Y., Mercurio, A.M., Goel, H.L., and Cheng, C., 2019. CD44 splice isoform switching determines breast cancer stem cell state. *Genes and Development*, 33(3-4), pp.166-179.

Levofloxacin Determination in Pharmaceutical Tablets by Sensitive Spectrofluorometric Method with L-Tryptophan as a Fluorescent Probe

Kurdo A. Abdullah and Aryan F. Qader†

Department of Chemistry, Faculty of Science and Health, Koya University,
Koya, KOY45, Kurdistan Region – F.R., Iraq

Abstract—**Proper dosage, therapeutic effectiveness, patient safety, and quality control throughout manufacture and storage can only be achieved by closely monitoring the concentration of pharmaceutical products. A precise and reliable spectrofluorometric approach for quantitative analysis and detection of levofloxacin (LEVO) in various pharmaceutical products was developed in this work using the fluorescent reagent L-tryptophan. When L-tryptophan, which has its inherent fluorescence signal quenched by LEVO, is mixed with Britton-Robinson buffer solution (pH 9.0), a stable ion-associated complex forms. The fluorescence intensity of L-tryptophan decreased at 365 nm after excitation at 281 nm. The method showed linearity for LEVO concentrations from 0.3 to 18.0 μg/mL, with a minimum detectable value of 0.10 μg/mL. An effective linear relationship ($R^2 = 0.9985$) between the concentration and fluorescence intensity (ΔF) was obtained. This technique has been well-proven to be minimally affected by impurities commonly found in pharmaceutical formulations. The results were validated through comparative analyses with high-performance liquid chromatography. The study revealed that both equivalence levels and analytical quality (as measured by precision and accuracy) are very satisfactory. This study addresses the increasing demand for established and reliable methods in the quality control of pharmaceutical products.**

Index Terms—**L-tryptophan, Levofloxacin, Pharmaceuticals, Quenching, Spectrofluorometric.**

I. Introduction

Levofloxacin (LEVO) is a 3rd-generation fluorine class antibiotic. It works extremely well against a lot of germs (El-Yazbi, et al., 2020). The molecular mass is 361.37°g/mL as represented in Fig. 1 9-fluoro-2,3-dihydro-3-methyl-1,2,3-de-10-(4-methyl-1-piperazinyl)-7-oxo-7H-pyrido. It has strong antibacterial properties, such as inhibiting the growth of pathogens outside and within body cavities *in vitro* (in a test tube). It is effective to treat urinary tract infections (UTIs), lung infections, and gastrointestinal problems (Bano, et al., 2014). LEVO is one of the most commonly administered bacterial infection-specific medications in hospital outpatient settings. LEVO is used to treat acute and moderate illness, chronic bacterial prostatitis, infections of the skin and soft tissue with the UTIs, community-acquired pneumonia, and other mild-to-severe diseases (Elgendy, et al., 2024). A subgroup of quinolones designated fluoroquinolones is characterized by a fluorine substituent present on the sixth position of the naphthyridine ring (Bano, et al., 2014)

In the United States, LEVO is the only Food and Drug Administration -accepted respiratory fluoroquinolone for the treatment of patients with nocomial pneumonia. LEVO, the optical S-(-) isomer of ofloxacin, was created by Daiichi Seiyaku Pharmaceutical Co., Ltd. of Japan. Despite the fact that the two form a racemic mixture, the S-isomer of ofloxacin is 32–128 times more efficient against bacteria than the R-isomer; hence, the S-isomer is primarily responsible for the drug's antibacterial activities. Combining the strong antibacterial properties of ofloxacin with the relatively moderate toxicity profile of LEVO suggests that the former may be equally effective at half the usual dose (Une, et al., 1988; Tanaka, et al., 1992; Inage, et al., 1992; Nakamori, et al., 1995). The antibacterial spectrum of the novel broad-spectrum antibiotic LEVO surpasses that of the more recognized quinolones, including ciprofloxacin and norfloxacin. Anaerobes, atypical pathogens, and specific species among microorganisms that are Gram positive and Gram negative (Bano, et al., 2014).

Accurate quantification of LEVO is critically important to ensure the safety, efficacy, and regulatory compliance of pharmaceutical formulations. Over the years, numerous analytical techniques have been developed and refined for this purpose. Among them, ultraviolet (UV) spectrophotometry, fluorescent methods, and high-performance liquid chromatography (HPLC) have been widely employed (Ashour and Bayram, 2020; Da Silva, et al., 2012; Radi and El-Sherif, 2002; Devi and Chandrasekhar, 2009; Koeppe, et al., 2011; Ocaña, Callejón and Barragán, 2001; González, Mochón and De La Rosa, 2000).

ARO-The Scientific Journal of Koya University
Vol. XIII, No. 1 (2025), Article ID: ARO.12197. 11 pages
DOI: 10.14500/aro.12197
Received: 14 April 2025; Accepted: 04 June 2025
Regular research paper; Published: 24 June 2025

†Corresponding author's e-mail: aryan.qader@koyauniversity.org

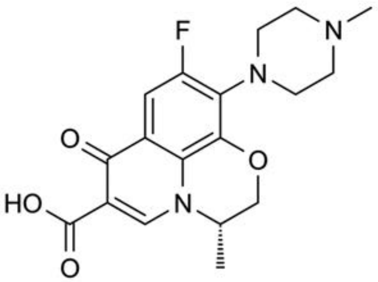

Fig. 1. Structure of levofloxacin in chemical terms.

In addition to pharmaceutical formulations, the analysis of LEVO in biological matrices such as blood, bile, soft tissues, and bones has been performed using microbiological tests and HPLC methods to determine drug concentrations (Aman, et al., 2010; Maurya, et al., 2021; Böttcher, et al., 2001). High-performance thin-layer chromatography (HPTLC) has also been explored for LEVO quantification in pharmaceutical samples (Davit, et al., 2009; Meyyanathan, et al., 2003). More recently, HPLC coupled with tandem mass spectrometry has been applied for precise measurement of LEVO levels in human plasma, providing enhanced sensitivity and specificity (Une, et al., 1988; Lu, et al., 2022; Szerkus et al., 2017; Zheng et al., 2020; Notario, et al., 2017). A considerable body of research has also addressed the detection of LEVO metabolites and its presence in various biological fluids (Elgendy, et al., 2024).

Despite these advances, many existing methods face practical limitations because of the complexity of mobile phases (buffers) and detection techniques, such as fluorescence and HPTLC, which restrict their routine applicability. Furthermore, while numerous analytical procedures have been established for LEVO in biological samples, there is a notable lack of stability-indicating methods designed for bulk LEVO samples contaminated with degradation products and process-related impurities (Nakamori, et al., 1995; Parys, Dołowy and Pyka-Pająk, 2022; Mehta, et al., 2010; Szerkus, et al., 2017; Elgendy, et al., 2024; Maurya, et al., 2021; Notario, et al., 2017). Our work addresses this gap by developing a reliable, stability-indicating analytical method that can accurately quantify LEVO in bulk samples, thereby enhancing quality control and ensuring pharmaceutical safety.

These accomplishments underscore the ongoing need for sensitive and versatile analytical techniques in pharmaceutical quality control. The objective of this study is to develop a simple, sensitive, and cost-effective spectrofluorometric method for quantifying LEVO in pharmaceutical tablets. By utilizing L-tryptophan as a novel fluorescent reagent, this approach aims to offer an efficient and reliable alternative to existing fluorescence probes and standard methods, enhancing the accuracy and practicality of LEVO analysis in quality control applications.

II. Materials and Methods

A. Instruments

Fluorescence spectra were recorded using a Cary Eclipse Fluorescence Spectrophotometer equipped with instrumentation from Agilent Technologies, USA. The system featured a xenon lamp as the light source and a grating monochromator for excitation and emission measurements. Both the excitation and emission monochromators utilized slits with a width of 5.0 nm, and measurements were carried out in a 1.0 cm quartz cell. The pH of the buffer solutions was measured using a digital pH meter (EUTECH, Thermo Fisher Scientific, USA).

B. Chemicals and Reagents

The study exclusively used high-purity chemical compounds provided by the suppliers, without any further purification performed. The tests were carried on with solutions prepared as solvents by using pure water, methanol, and sodium hydroxide.

To prepare a 0.1 moL/L NaOH solution, 0.2 g of NaOH (Merck, Germany) was dissolved in 50 mL of distilled water. The aqueous solution of L-Tryptophan 4.0 × 10^{-4} moL/L (Sigma-Aldrich) was prepared by dissolving 8.2 mg in 50 mL of 0.1 moL/L NaOH.

To make the Carbonate-Bicarbonate buffer (pH 9.2–10.6), 0.1 moL/L sodium bicarbonate ($NaHCO_3$) (Schallau, Spain) was mixed with sodium carbonate (Na_2CO_3) (Schallau, Spain) in the proper proportions. More carbonate increases pH, whereas more bicarbonate reduces it.

To prepare an ammonia-ammonium chloride buffer (pH 9–12) in water. The components were 0.1 moL/L ammonium chloride (NH_4Cl) and 0.1 moL/L ammonia solution (NH□OH) from Scharlau, Spain. They use an ammonia solution to elevate the pH, and ammonium chloride to lower it.

The Britton-Robinson buffer solution consists of a combination of 0.04 moL/L acetic acid (Scharlau, Spain), 0.04 moL/L boric acid (Sigma-Aldrich, USA), (Qader and Fakhre, 2017), 0.04 moL/L phosphoric acid (Merck, Germany). The addition of sodium hydroxide at a concentration of 0.2 moL/L is used to adjust the pH levels by using the pH meter (Abd Ali, et al., 2019).

C. Standard Stock Solution

The standard for LEVO was made in the Erbil-Kurdistan Region of Iraq, by Kurdistan Medical Control Agency (KMCA). A solution with a concentration of 100 μg/mL of LEVO is prepared by dissolving 5 mg of the drug in 50 mL of methanol, and the container should be stored in the refrigerator (Kaczmarek, Staninski and Stodolny, 2021).

D. Sample Preparation

Six different brands of medicinal pills were investigated. The weight of 10 individual pills from each brand was measured. The pills were then crushed into a fine powder using a mortar. The average weight of a single pill was calculated. Exactly 500 mg of LEVO was dissolved in 40 mL of methanol in a beaker. To enhance solubility, the mixture was stirred for 15 min. After filtration, the solution was transferred to a 50 mL volumetric flask, and the volume was adjusted to 50 mL precisely. This resulted in a solution with a concentration of 10,000 μg/mL. The initial solution was then diluted stepwise to obtain a final concentration of 100 μg/mL. The same procedure was applied to all six brands of pills. Finally, the proposed method was used to analyze the diluted solutions.

Each LEVO tablet contains 500 mg, were received from a local pharmacy, and included the following brands: Brand 1: Levobest (Syria); Brand 2: Levoneer (Iraq); Brand 3: Levoking (Ukraine); Brand 4: Nevotek (Turkey); Brand 5: Levopyx (India); Brand 6: Advaquin (Oman).

E. Spectrofluorometric Assay for the Quantification of LEVO

Preparing all the standard and sample solutions separately, 0.235 mL of L-tryptophan solution was placed into a 10-mL volumetric flask. Next, 1.0 mL of Britton-Robinson buffer solution (pH 9.0) was added. Then, distilled water was added to complete the volume to 10 mL. The mixture was stirred for 15 min at 25 ± 5°C. A 1.0 cm quartz cell was used to measure the intensity difference of the fluorescence signal at λex = 281 nm and λem = 365 nm for each sample, standard solution, and blank solution (Tahir, et al., 2019).

III. Results and Discussion

A. Optical Response Spectroscopy

A 10 mL volumetric flask was employed to dilute 0.15 mL of the fluorescent reagent L-tryptophan (4.0×10^{-4} mol/L), and the emission spectra showed significant fluorescence at excitation 281 nm. Figure 2 shows A new ion-associated complex is formed along with its interaction with the target analyte, LEVO (5.0 μg/mL). The formation of this complex resulted in the complete loss of fluorescence intensity of L-Tryptophan. Consequently, to ascertain the quantity of LEVO, fluorometric studies were conducted at 365 nm after excitation at 281 nm, which involved quenching the fluorescence spectra of L-Tryptophan. The data from the spectrofluorometric analysis demonstrate a progressive reduction in L-Tryptophan fluorescence with increasing concentrations of LEVO, thereby validating the establishment of a stable complex.

The unique absorption outcome of the UV-visible spectrophotometry experiment is indicative of Bell-shaped dose–response curve of L-Tryptophan, LEVO, and their combination (Fig. 3). The L-Tryptophan molecule shows a significant peak in the UV-V range, especially between 250 and 300 nm, with a maximum absorbance of approximately 0.40.

In addition, there is another peak at approximately 230 nm, though this is less pronounced. In contrast, LEVO presented a small peak at 250 nm and a high absorption in between 270 and 300 nm. Absorbance increases dramatically from 270 to 300 nanometers due to interactions between the two chemicals. Based on spectrophotometric studies, the interaction of L-Tryptophan and LEVO is significant with time, which has been fluorescently evidence from a stable complex formation. It strongly suggests that L-Tryptophan may be used as a LEVO test reagent.

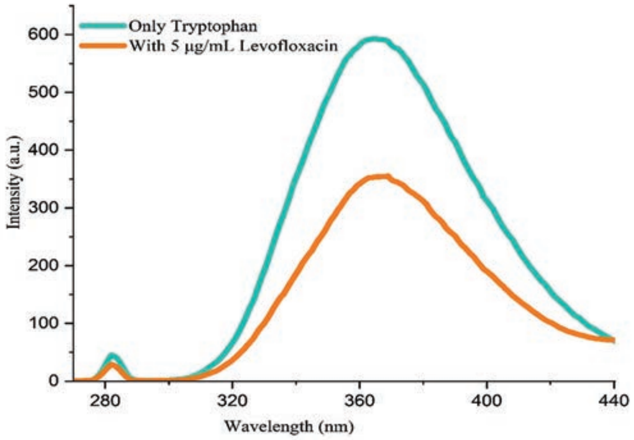

Fig. 2. Demonstrates the emission spectra of L-Tryptophan (0.15 mL) with a concentration of 4.0×10^{-4} mol/L and the reaction product of L-Tryptophan with levofloxacin (5.0 μg/mL) after being excited at 281 nm.

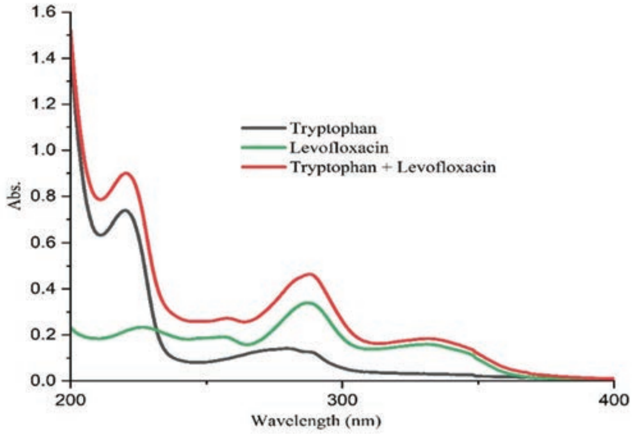

Fig. 3. The absorption spectra of L-Tryptophan, levofloxacin, as well as the combination of the two chemicals, emphasizing the different interactions and ultraviolet-visible features of both chemicals.

B. Optimization of Experimental Conditions

Chemical parameters associated with the reaction were systematically assessed for standardizing optimum sensitivity. Several different types of scenarios were considered to determine the most useful criteria for the proposed strategy. To obtain the maximal quenching fluorescence intensity (ΔF), the experimental conditions for fluorescence reactions were optimized. We meticulously varied the pH of the medium, concentration of L-Tryptophan, reaction duration, and the presence or absence of coexisting materials to acquire the optimal conditions for the proposed strategy.

C. Effects of Varied Buffers and Buffer Volume

LEVO (5.0 μg/mL) and fluorescent L-Tryptophan reagent (0.15 mL from 4.0×10^{-4} moL/L) were tested in several buffer solutions, including ammonia-ammonium, carbonate-bicarbonate, and Britton-Robinson buffers, to determine the best pH buffer for the fluorescence quenching. Fig. 4a shows that the fluorescence intensity was optimally quenched using

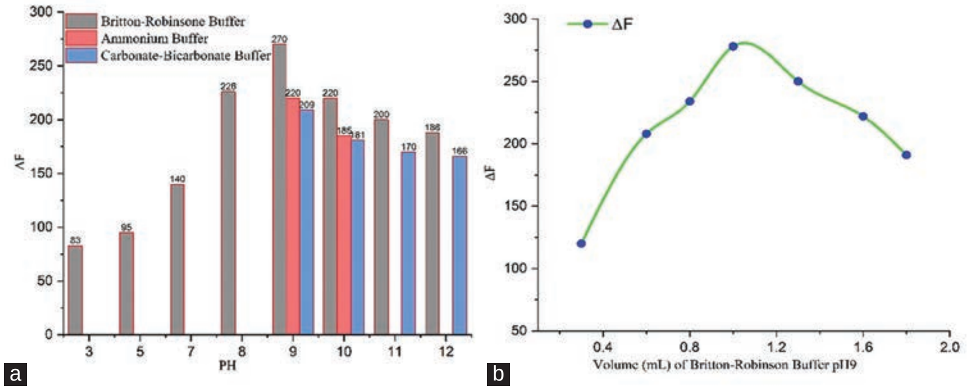

Fig. 4. (a) Different buffer solutions affect the ΔF intensity of L-Tryptophan and levofloxacin (5.0 µg/mL), (b) Changes in the volumes of Britton-Robinson buffer solutions influence the ΔF intensity of L-Tryptophan and levofloxacin.

the Britton-Robinson buffer solution at pH 9.0. Consequently, the following investigations will employ the Britton-Robinson solution, which has a pH of 9.0. This pH promotes a favorable ion-association complex between L-tryptophan and LEVO, diminishing the fluorescence response (Üçer, Ertekin, and Dinç 2024). The best buffer quantities were carefully examined; several amounts of Britton-Robinson buffer (0.3, 0.6, 0.8, 1.0, 1.3, 1.6, and 1.8 mL) were added to 5.0 µg/mL LEVO (Fig. 4b). The fluorescence signal produced for 1.0 mL of Britton-Robinson medium solution shows the most notable difference. This volume was chosen for additional experimental examination as a consequence.

D. Effect of L-Tryptophan Concentrations

To evaluate the effect of varying L-tryptophan reagent concentrations, the quenching signal was examined for volumes of 0.050, 0.100, 0.150, 0.200, and 0.235 mL from (4.0×10^{-4} moL/L). Fig. 5 shows the maximum fluorescence response, indicating that 0.235 mL of L-tryptophan was determined to be the most effective amount for further tests. This resulted in quenching because, following the addition of L-tryptophan, the two substances combine to create an ion-association complex that does not fluoresce and lowers the L-tryptophan fluorescence.

E. Impact of Response Duration

The effect of reaction time on fluorescence response was studied at room temperature (25.0 ± 5.0°C). After completely combining all of the reactants, the quenching signal gradually decreased (Fig. 6). The findings show that the quenching of the fluorescence signal decreased gradually over time, peaking at 15 min after mixing and remaining stable for at least 70 min. As a result, the quenching fluorescence signal for this process was examined 15 min later.

F. Analysis of Materials that Coexist

To determine how effectively the proposed fluorescence approach functioned analytically with real samples examined the impacts of common coexisting components, such as those found in medication tablets. LEVO and 0.235 mL of (4.0×10^{-4} moL/L) L-Tryptophan were introduced to 10.0 mL of a volumetric flask holding a number of coexisting compounds at concentrations of 500 µg/mL under optimum experimental conditions. After 15 min of stimulation at 281 nm, the decrease in L-Tryptophan fluorescence intensity was measured at 365 nm. Fig. 7 illustrates the results. With the permitted limit established at the concentration of the coexisting species, the quantitative examination of the quantity of LEVO revealed an error of no more than 3.0%. (Average of five determinations). Based on the data gathered, it was determined that there was no interference or influence since the ingredients – starch, lactose, stearic acid, magnesium stearate, cellulose, and silicon dioxide – were present in the standard ratios used to manufacture pharmaceutical tablets.

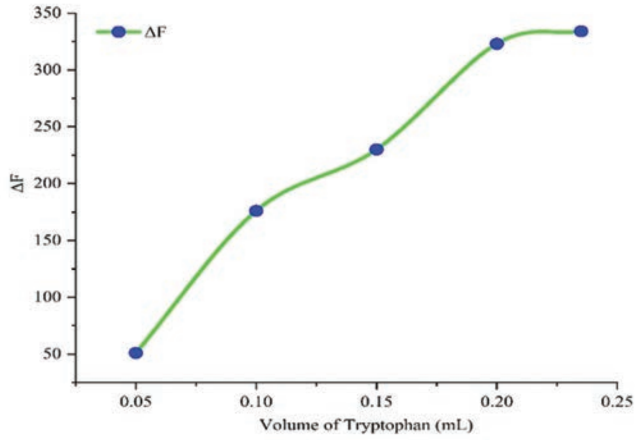

Fig. 5. The effect of different doses of L-Tryptophan on the ΔF fluorescence intensity reaction between L-Tryptophan and levofloxacin (5.0 µg/mL) at pH 9.0.

G. LEVO Detection and the Calibration Graph

Fig. 8a depicts the fluorescence intensity interaction of L-tryptophan with varying amounts of LEVO after optimal circumstances have been established. The results showed that when the quantity of LEVO in the solution increased, the fluorescence signal gradually decreased, with the intensity of the quenched signal exactly proportional to the concentration of LEVO. As a result, the L-Tryptophan reagent serves as a fluorescent agent for the quantitative assessment of LEVO. Fig. 8b shows a calibration curve based on the fluctuation in different fluorescence intensity (ΔF) versus LEVO concentration under optimum circumstances. The calibration curve showed a linear correlation ($\Delta F = 40.888\ C_{Levo}$ (μg/mL) + 47.139) at concentrations ranging from 0.3 to 18.0 μg/mL, with a correlation value of 0.9985. The International Union of Pure and Applied Chemistry standards specify that the limit of detection (LOD) is computed as LOD = 3.3 standard deviation (SD)/P, while the limit of quantification (LOQ) is established as LOQ = 10 SD/P (Qader, 2024). In this case, SD is the SD obtained from five reagent blank measurements, whereas P represents the slope of the calibration curve. The limits of detection (LOD) and LOQ for LEVO were established at 0.100 μg/mL and 0.294 μg/mL, respectively.

H. Exactness and Correctness of the Fluorometric Technique

The calculation of the SD, which measures the degree of variance or dispersion within a collection of values, was part of the assessment of the precision and accuracy of the fluorometric approach. Five repeated aliquots of three standard solutions of LEVO at concentrations of 0.3, 8.0, and 18.0 μg/mL were used to compute the relative SD (RSD %) and percentage error. Table I presents the results. The method exhibits a great degree of accuracy, with the defined ranges of RSD % being 0.48%, 1.01%, and 1.28%. Furthermore, it was found that the percentage error ranged from 3.33 to −1.7, suggesting that the established approach exhibits a high degree of accuracy.

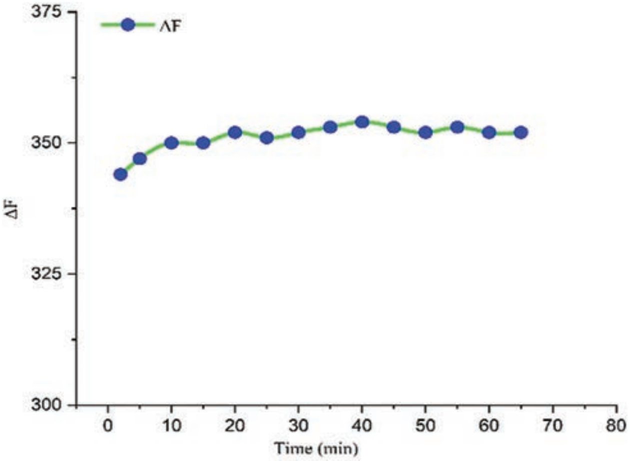

Fig. 6. The duration of the reaction influences the ΔF intensity in the fluorescence reaction involving 0.235 mL of (4.0×10^{-4} moL/L) L-Tryptophan and 5.0 μg/mL of levofloxacin at pH 9.0.

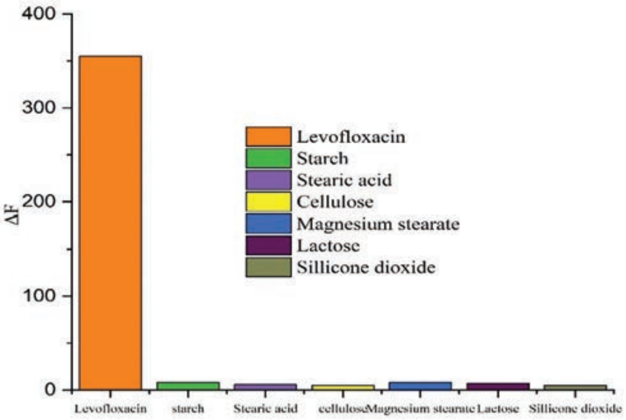

Fig. 7. The impact of standard excipients in pharmaceutical tablets on the fluorescence detection of levofloxacin reveals interference from coexisting substances, including lactose, starch, stearic acid, magnesium stearate, cellulose, and silicon dioxide.

I. Fluorometric Reaction Stoichiometry

To determine the stoichiometry reaction between the fluorescent reagents L-tryptophan and LEVO, the limiting logarithmic approach was applied (Qader and Fakhre, 2017; Tahir, et al., 2019). Fig. 9a illustrates a graph depicting the relationship between log (LEVO) and log ΔF, with L-Tryptophan concentration held constant. Conversely, (Fig. 9b) depicts log (L-Tryptophan) in relation to log ΔF while maintaining a constant concentration of LEVO. The analysis of both plots revealed linear segments, and by evaluating the slopes of these lines, the results indicated that the LEVO -L-tryptophan complex had a 1:1 reaction ratio (Fig. 10).

J. Fluorescence Quenching Mechanism

Fluorescence quenching refers to the interaction of fluorescent compounds with quenching agents. Two basic mechanisms impact the decline in fluorescence intensity: static quenching and dynamic quenching. When the fluorescent species in its ground state interacts with the quencher species, a complex structure forms in a static quenching mechanism. Dynamic quenching, on the other hand, occurs as a result of interactions between excited fluorescent species and quencher species, which are aided by collisions (Abd Ali, et al., 2019). The study findings reveal that the process of fluorescence quenching may be quantitatively examined using the Stern-Volmer equation (Park, et al., 2009; Duan, et al., 2017; Gökoğlu, Kıpçak and Seferoğlu, 2014; Yang et al., 2018).

$$F_0/F=1+K_{SV}\ C_{que}$$

The words F and F_0 relate to the intensity of the fluorescence signals generated by L-Tryptophan when employed as a fluorescence reagent, both when the quencher (C_{que}) is present and when it is not. The Stern-Volmer equation is used to

TABLE I
Data Gathered for The Suggested Fluorometric Measurement of Levofloxacin Utilizing L-Tryptophan as the Fluorescent Reagent in Order to Ensure Precision and Accuracy

Contained value (μg/mL)	Found value (μg/mL)	SD	RSD%	Error[1]%
0.3	0.31	1.42	0.15	3.33
8.0	8.21	1.63	0.35	2.62
18.0	17.68	−1.58	0.79	−1.70

SD: Standard deviation, RSD %: Relative standard deviation. [1] Mean value derived from five separate measurements

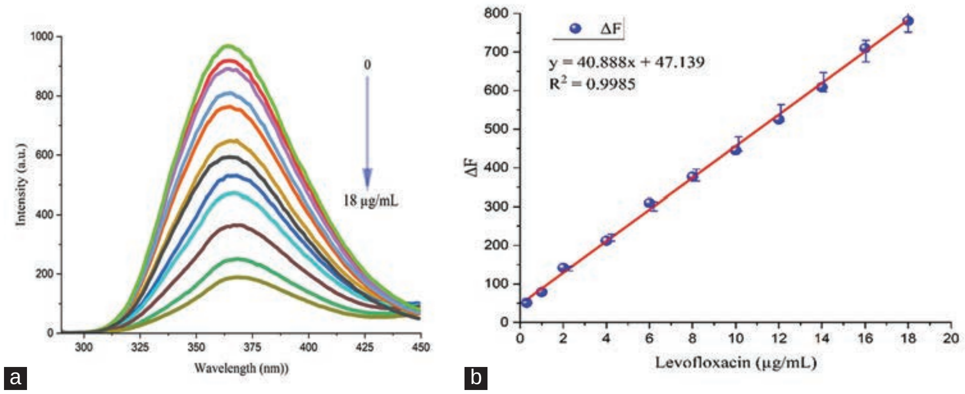

Fig. 8. (a) The influence of various Levofloxacin concentrations (0.3, 1.0, 2.0, 4.0, 6.0, 8.0, 10.0, 12.0, 14.0, 16.0, and 18.0 μg/mL) on the fluorescence intensity of the L-Tryptophan reagent at pH 9.0 was examined (b) Calibration graph for the fluorometric quantitative measurement of levofloxacin utilizing L-Tryptophan as the fluorescent reagent.

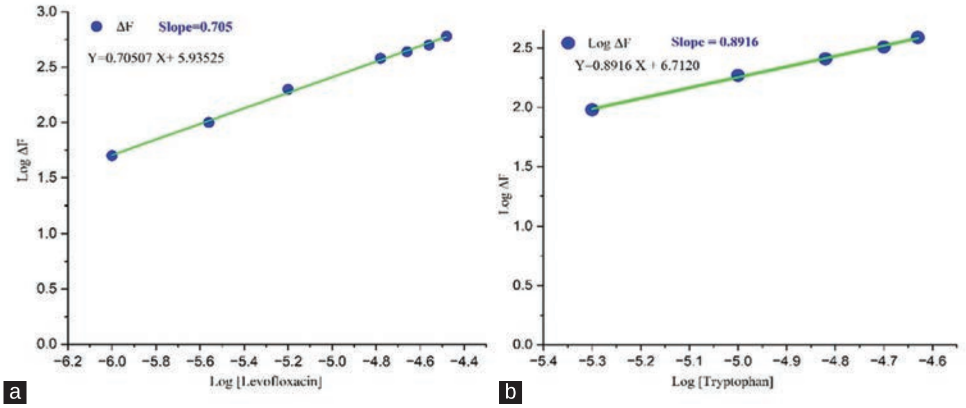

Fig. 9. Illustrates the stoichiometric ratio of the fluorometric reaction involving the L-Tryptophan reagent and levofloxacin (LEVO) (a). Graphing log (LEVO) against log ΔF (b), Graphing log (L-Tryptophan) against log ΔF.

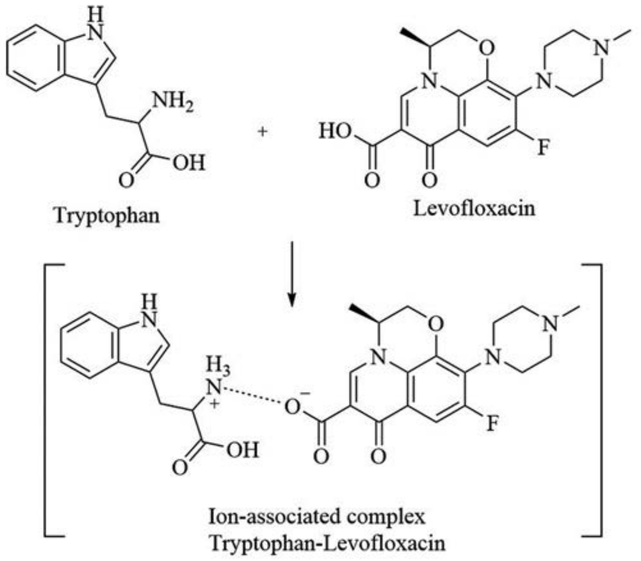

Fig. 10. The formulation of an L-Tryptophan-levofloxacin ion-associated combination.

study fluorescence quenching and to distinguish between static and dynamic quenching at various temperatures. At this stage, the Stern-Volmer quenching constant (K_{SV}) is utilized (Duan, et al., 2017). The equation was used to examine fluorescence quenching at two different temperatures (298.0 and 308.0 K) (Yang, et al., 2018). Fig. 11 shows Stern-Volmer graphs of F_0/F versus C_{que} (LEVO concentration) at two temperatures. A static quenching process is characterized by a reduction in the Stern-Volmer quenching constant (K_{SV}) with increasing temperature, while an increase indicates a dynamic quenching process. The data indicates a linear connection between F_0/F and C_{que}, suggesting a mathematical link (Fig. 11 at both temperatures). This suggests that the findings were made mostly through quenching (Park, et al., 2009; Duan, et al., 2017). As temperature rises, the K_{SV} value decreases, suggesting static quenching as the primary cause of fluorescence quenching.

K. Analysis using the Fluorometric Method

In a structured analysis, the fluorometric technique provides a method for quantifying LEVO in pharmaceutical tablets, utilizing L-tryptophan as a fluorescent reagent. To evaluate the reliability of this approach, the results are compared with those obtained from a standard HPLC method provided by the KMCA in Erbil, Iraqi Kurdistan. As shown in Table II, the findings demonstrate a strong degree of agreement between the proposed fluorometric method and

TABLE II

The examination of commercial pharmaceutical tablets containing levofloxacin was carried out utilizing the suggested fluorometric method with L-Tryptophan reagent in conjunction with the standard HPLC method

Pharmaceutical tablets	Observed Values (mg)	Proposed Procedure (mg)	HPLC Procedure (mg)	Recovery %	Error[1]%
Brand 1	500	493.5	506.0	97.5	-2.47
Brand 2	500	491.0	492.0	99.8	-0.20
Brand 3	500	498.5	506.5	98.4	-1.58
Brand 4	500	508.5	520.5	97.7	-2.30
Brand 5	500	488.5	471.5	103.6	3.61
Brand 6	500	501.0	491.5	101.9	1.93

[1]Mean value calculated from five measurements

TABLE III

Comparison of the Analytical Performance Metrics of the Present Research with Other Relevant Techniques

Reagent	Methods	LOD (µg/mL)	Linear ranges (µg/mL)	References
Terbium (III) ions were used to oxidize a subset of fluoroquinolones using potassium bromate	Spectrofluorometric	0.11	0.3–13	Kaczmarek, Staninski and Stodoln, 2021
Graphene oxide composites coated with silver nanoparticles (GO@AgNPs)	Voltammetric	0.012	0.0154–788.38	Chinnaraj, et al., 2021
HPLC method with fluorescence detection	HPLC-fluorescence	6.3×10^{-4}	0.0025–0.5	Toker, Kızılçay and Sagirli, 2021
The carbon paste electrode (CPE) is produced from a film created via the electropolymerization of α-cyclodextrin (CPEα-CD).	Spectrofluorometric	0.21	1–90	Hashmi, et al., 2021
Graphene quantum dots, magnetite (Fe3O4) nanoparticles, and porous graphene form a selective molecularly imprinted polymer for levofloxacin detection	Spectrofluorometric	0.3×10^{-3}	0.00010–0.0250	Chansud, Longnapa and Bunkoed, 2021
This method is grounded on the fact that levofloxacin can still quench the intrinsic fluorescence signal of L-Tryptophan and they can be combined to form a stable complex by introducing ions as a bridge.	Spectrofluorometric	0.100	0.3–18	Present work

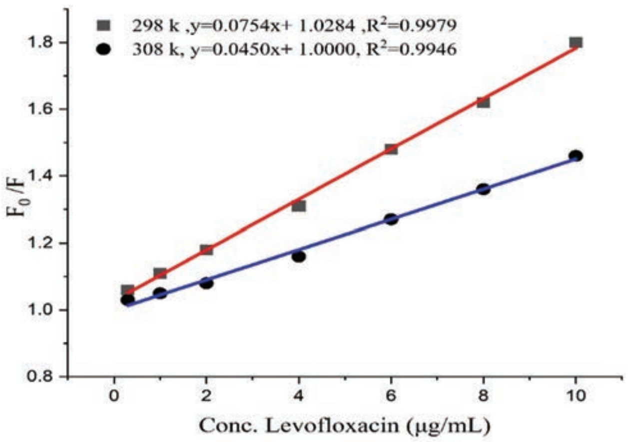

Fig. 11. Exhibits the fluorescence quenching process via a Stern-Volmer plot at temperatures of 298.0 K and 308.0 K.

the HPLC reference method. The recovery percentages for all brands range from 97.5% to 103.6%, indicating the proposed method's accuracy and reliability in detecting LEVO content close to the labeled 500 mg. The error percentage values also remain within an acceptable range, further supporting the method's precision. For instance, Brand 2 shows a nearly negligible error of −0.20%, while Brand 5 exhibits a slightly higher positive error of 3.61%, yet still within acceptable pharmaceutical analytical limits. These results confirm that the fluorometric method is suitable for routine analysis of LEVO in commercial formulations.

L. Comparison with other Reported Methods

Other methods for measuring LEVO have been compared to the present one. Table III compares the LEVO LOD and linear ranges obtained in this study with those reported in previously published methods. Although the LOD of the proposed spectrofluorometric method (0.100 µg/mL) is only slightly lower than that of some other fluorometric techniques, such as the method using terbium (III) ions (0.110 µg/mL) (Kaczmarek, Staninski and Stodolnym, 2021), this improvement reflects the enhanced sensitivity achieved through method optimization. Importantly, the suggested technique eliminates the need for sample pre-extraction, a limitation in some analytical procedures with lower LODs. In addition, the proposed method offers several advantages over older techniques, such as HPLC and voltammetry, including simplicity, higher sensitivity, shorter analysis time, and lower cost. These features make the present method highly suitable for routine analysis of LEVO in pharmaceutical formulations.

IV. Conclusion

The present study conducted a quantitative investigation of levofloxacin using L-Tryptophan as a fluorescence-quencher agent. The method demonstrated an excellent linear fit (R^2 = 0.9985) and a minimum detectable concentration of 0.100 µg/mL over a range of 0.3–18 µg/mL. This method is used for accurate and reliable measurement of LEVO in pharmaceutical compositions. Offering significant advantages owing to its straightforwardness and the ability to immediately quantify the ion-associated complex. This eliminates the need for further processing or extraction methods. This method demonstrates good specificity, as common pharmaceutical excipients found in tablet formulations – such as starch, lactose, stearic acid, magnesium stearate, cellulose, and silicon dioxide – produce negligible interference, typically causing signal changes of <3%. This underscores the reliability of L-tryptophan as an innovative fluorescence quenching reagent with promising implications for drug analysis.

V. Acknowledgment

We thank the directors of the chemistry departments of Koya University of Iraq for giving us permission to carry out our research study in their laboratories.

References

Abd Ali, L.I., Qader, A.F., Salih, M.I., and Aboul-Enein, H.Y., 2019. Sensitive spectrofluorometric method for the determination of ascorbic acid in pharmaceutical nutritional supplements using acriflavine as a fluorescence reagent. *Luminescence*, 34, pp.168-174.

Aman, S.F., Hassan, F., Naqvi, B.S., and Hasan, S.M.F., 2010. Studies of food drug interactions. *Pakistan Journal of Pharmaceutical Sciences*, 23, pp.313-320.

Ashour, S., and Bayram, R., 2020. New sensitive derivatization methodology of levofloxacin antibiotic from its dosage formulations: Kinetic spectrophotometric methods for determination. *Analytical Chemistry Letters*, 10, pp.562-576.

Bano, R., Arsalan, A., Ahmad, I., and Shad, Z., 2014. *Levofloxacin: A Potent Antibiotic*. Baqai Medical University, Baqai Institute of Pharmaceutical Sciences, Pakistan.

Böttcher, S., Baum, H., Hoppe-Tichy, T., Benz, C., and Sonntag, H.G., 2001. An HPLC assay and a microbiological assay to determine levofloxacin in soft tissue, bone, bile and serum. *Journal of Pharmaceutical and Biomedical Analysis,* 25, pp.197-203.

Chansud, N., Longnapa, N., and Bunkoed, O., 2021. A nanohybrid magnetic sensing probe for levofloxacin determination integrates porous graphene, selective polymer and graphene quantum dots. *Journal of Pharmaceutical and Biomedical Analysis,* 205, p.114316.

Chinnaraj, S., Palani, V., Yadav, S., Arumugam, M., Sivakumar, M., Maluventhen, V., and Singh, M. 2021. Green synthesis of silver nanoparticle using goniothalamus wightii on graphene oxide nanocomposite for effective voltammetric determination of metronidazole. *Sensing and Bio-Sensing Research,* 32, p.100425.

Da Silva, A.P., Luna, A.S., Da Silva Costa, T., Aucelio, R.Q., Braga, J., Boqué, R., and Ferré, J., 2012. Spectrofluorimetric determination of levofloxacin in pharmaceuticals and human urine. *International Journal of Life science and Pharma Research,* 2, pp.147-158.

Davit, B.M., Nwakama, P.E., Buehler, G.J., Conner, D.P., Haidar, S.H., Patel, D.T., Yang, Y., Yu, L.X., and Woodcock, J., 2009. Comparing generic and innovator drugs: A review of 12 years of bioequivalence data from the United States Food and Drug Administration. *Annals of Pharmacotherapy,* 43, pp.1583-1597.

Devi, M.L., and Chandrasekhar, K., 2009. A validated stability-indicating RP-HPLC method for levofloxacin in the presence of degradation products, its process related impurities and identification of oxidative degradant. *Journal of Pharmaceutical and Biomedical Analysis*, 50, pp.710-717.

Duan, R., Jiang, J., Liu, S., Yang, J., Zhu, J., Qiao, M., Yan, J., and Hu, X., 2017. Spectrofluorometric determination of ascorbic acid using thiamine and potassium ferricyanide. *Instrumentation Science and Technology,* 45, pp.312-323.

Elgendy, K.H., Zaky, M., Altorky, A.E.M.M., and Fadel, S., 2024. Determination of levofloxacin, norfloxacin, and moxifloxacin in pharmaceutical dosage form or individually using derivative UV spectrophotometry. *BMC Chemistry,* 18, p.115.

El-Yazbi, A.F., Khamis, E.F., Youssef, R.M., El-Sayed, M.A., and Aboukhalil, F.M., 2020. Green analytical methods for simultaneous determination of compounds having relatively disparate absorbance; application to antibiotic formulation of azithromycin and levofloxacin. *Heliyon*, 6, p.e04819.

Gökoğlu, E., Kıpçak, F., and Seferoğlu, Z., 2014. Studies on the interactions of 3, 6-diaminoacridine derivatives with human serum albumin by fluorescence spectroscopy. *Luminescence*, 29, pp.872-877.

González, J.A.O., Mochón, M.C., and De La Rosa, F.J.B., 2000. Spectrofluorimetric determination of levofloxacin in tablets, human urine and serum. *Talanta*, 52, pp.1149-1156.

Hashmi, S.Z.H., Dhiman, T.K., Chaudhary, N., Singh, A.K., Kumar, R., Sharma, J.G., Kumar, A., and Solanki, P.R., 2021. Levofloxacin detection using l-cysteine capped MgS quantum dots via the photoinduced electron transfer process. *Frontiers in Nanotechnology*, 3, p.616186.

Inage, F., Kato, M., Yoshida, M., Akahane, K., and Takayama, S., 1992. Lack of nephrotoxic effects of the new quinolone antibacterial agent levofloxacin in rabbits. *Arzneimittel-Forschung*, 43, pp.395-397.

Kaczmarek, M., Staninski, K., and Stodolny, M., 2021. New chemiluminescent method of levofloxacin and ofloxacin determination based on terbium (III)-sensitized fluoroquinolone-KBrO3 reaction. *Luminescence*, 36, pp.1945-1952.

Koeppe, M.O., Cristofoletti, R., Fernandes, E.F., Storpirtis, S., Junginger, H.E., Kopp, S., Midha, K.K., Shah, V.P., Stavchansky, S., and Dressman, J.B., 2011. Biowaiver monographs for immediate release solid oral dosage forms: Levofloxacin. *Journal of Pharmaceutical Sciences*, 100, pp.1628-1636.

Lu, W., Pan, M., Ke, H., Liang, J., Liang, W., Yu, P., Zhang, P., and Wang, Q. 2022. An LC-MS/MS method for the simultaneous determination of 18 antibacterial drugs in human plasma and its application in therapeutic drug monitoring. *Frontiers in Pharmacology*, 13, pp.1044234.

Maurya, P., Kumar, A., Singh, S., Nisha, R., Pal, R.R., Chourasia, M.K., and Saraf, S.A., 2021. Bio-analytical method development for estimation of levofloxacin: Application in estimation of drug in nano-formulations and pharmacokinetic studies. *Indian Journal of Pharmaceutical Education and Research*, 55, pp.S814-824.

Mehta, J., Pancholi, Y., Patel, V., Kshatri, N., and Vyas, N., 2010. Development and validation of a sensitive stability indicating method for quantification of levofloxacin related substances and degradation products in pharmaceutical dosage form. *International Journal of PharmTech Research,* 2, pp.1932-1942.

Meyyanathan, S., Ramasarma, G., and Suresh, B., 2003. Analysis of levofloxacin in pharmaceutical preparations by high performance thin layer chromatography. *Journal of Separation Science*, 26, pp.1698-1700.

Nakamori, Y., Miyashita, Y., Nakatani, I., and Nakata, K., 1995. Levofloxacin: penetration into sputum and once-daily treatment of respiratory tract infections. *Drugs*, 49, pp.418-419.

Notario, D., Martono, S., Ikawati, Z., Hakim, A.R., Jannah, F., and Lukitaningsih, E., 2017. A rapid and simple high-performance liquid chromatographic method for determination of levofloxacin in human plasma. *Indonesian Journal of Chemistry*, 17, pp.54-62.

Ocaña, J.A., Callejón, M., and Barragán, F.J., 2001. Determination of trovafloxacin in human serum by time resolved terbium-sensitised luminescence. *European Journal of Pharmaceutical Sciences*, 13, pp.297-301.

Park, H.W., Alam, S.M., Lee, S.H., Karim, M.M., Wabaidur, S.M., Kang, M., and Choi, J.H., 2009. Optical ascorbic acid sensor based on the fluorescence quenching of silver nanoparticles. *Luminescence: The Journal of Biological and*

Chemical Luminescence, 24, pp.367-371.

Parys, W., Dołowy, M., and Pyka-Pająk, A., 2022. Significance of chromatographic techniques in pharmaceutical analysis. *Processes*, 10, p.172.

Qader, A.F., 2024. Validated spectrofluorometric assay for folic acid determination in pure and pharmaceutical forms via basic fuchsin fluorescence quenching. *Luminescence*, 39, p.e70022.

Qader, A.F., and Fakhre, N.A., 2017. Spectrofluorometric determination of furosemide in some pharmaceutical product using acriflavine as a reagent. *AIP Conference Proceedings,* 1888, p.020042.

Radi, A., and El-Sherif, Z., 2002. Determination of levofloxacin in human urine by adsorptive square-wave anodic stripping voltammetry on a glassy carbon electrode. *Talanta*, 58, p.319-324.

Szerkus, O., Jacyna, J., Gibas, A., Sieczkowski, M., Siluk, D., Matuszewski, M., Kaliszan, R., and Markuszewski, M., 2017. Robust HPLC-MS/MS method for levofloxacin and ciprofloxacin determination in human prostate tissue. *Journal of Pharmaceutical and Biomedical Analysis*, 132, pp.173-183.

Tahir, T.F., Qader, A.F., Salih, M.I., and Rashid, E.Q., 2019. L-tryptophan as fluorescent probe for determination of folic acid in some pharmaceutical products. *Aro-The Scientific Journal of Koya University*, 7, pp.19-26.

Tanaka, K., Iwamoto, M., Maesaki, S., Koga, H., Kohno, S., Hara, K., Sugawara, K., Kaku, M., Kusano, S., and Sakito, O., 1992. Laboratory and clinical studies on levofloxacin. *The Japanese Journal of Antibiotics,* 45, pp.548-556.

Toker, S.E., Kızılçay, G.E., and Sagirli, O., 2021. Determination of levofloxacin by HPLC with fluorescence detection in human breast milk. *Bioanalysis*, 13, pp.1063-1070.

Üçer, A., Ertekin, Z.C., and Dinç, E., 2024. A comparative application of spectrophotometric and spectrofluorimetric methods to estimate levofloxacin-DNA and ofloxacin-DNA interactions. *Journal of Fluorescence*, 35, p.123-134.

Une, T., Fujimoto, T., Sato, K., and Osada, Y., 1988. *In vitro* activity of DR-3355, an optically active ofloxacin. *Antimicrobial Agents and Chemotherapy*, 32, pp.1336-1340.

Yang, H., Ran, G., Yan, J., Zhang, H., and Hu, X., 2018. A sensitive fluorescence quenching method for the detection of tartrazine with acriflavine in soft drinks. *Luminescence*, 33, pp.349-355.

Zheng, X., Jongedijk, E.M., Hu, Y., Kuhlin, J., Zheng, R., Niward, K., Paues, J., Xu, B., Forsman, L.D., and Schön, T., 2020. Development and validation of a simple LC-MS/MS method for simultaneous determination of moxifloxacin, levofloxacin, prothionamide, pyrazinamide and ethambutol in human plasma. *Journal of Chromatography B,* 1158, p.122397.

Assessment of Leakage Radiation and Radiobiological Impacts in Gamma Knife Radiosurgery: Dosimetric and Biological Analysis

Bazhdar N. Mohammed[1†], Asaad H. Ismail[1] and Edrees M. Tahir[1,2]

[1]Department of Physics, College of Education, Salahaddin University-Erbil,
Erbil, Kurdistan Region – F.R. Iraq

[2]Department of Medical Technical Radiology, Erbil Technical Health and Medical College, Erbil Polytechnic University,
Erbil, Kurdistan Region – F.R. Iraq

***Abstract*—Gamma Knife radiosurgery is a non-invasive radiotherapy technique for brain lesions. However, radiation leakage from collimators and high-dose exposure may alter blood parameters, potentially increasing the risk of secondary cancers and other complications. The purpose of this study is to measure the leakage radiation produced during trigeminal neuralgia and meningiomas lesion treatments and impact on various radiosensitive organs. In addition, the radiobiological impact on patients' blood parameters is investigated for both short-term and long-term treatment exposure. Scatter radiation was measured using dosimeters placed at various body regions. Blood samples were collected from 20 patients at three different times. Changes in parameters were statistically analyzed using one-way analysis of variance, to assess significant differences across the time points. The highest scatter radiation levels were recorded at the face and neck significantly exceeding other body regions about 110 µSv and 350 µSv, respectively. Statistical analysis revealed that long-term exposure (58.2 min at 80 Gy) in trigeminal neuralgia cases resulted in significantly greater blood parameter changes ($p \leq 0.05$) compared to short-term exposure (19.4 min at 20 Gy) in meningiomas. These findings reveal dose-dependent blood changes and highlight the importance of radiation protection measures to enhance patient safety, particularly during high-dose treatments.**

***Index Terms*—Gamma knife radiosurgery, Leakage radiation, Patient Safety, Radiation dose, Radiobiological impacts.**

I. Introduction

Gamma Knife radiosurgery (GKRS) is a non-invasive procedure that administers accurate, high-dose radiation to specific areas of the brain, making it an effective treatment for a range of neurological conditions, such as brain tumors, vascular malformations, and functional disorders (Stone, et al., 2025). It utilizes multiple cobalt-60 (^{60}Co) sources that converge at a single focal point, using an internal collimator to direct the photon beams generated by the decay of ^{60}Co toward the tumor or abnormality. The system contains 192 sources, distributed across 8 sectors, with each sector holding approximately 24 capsules, each with an activity of 3,000 curies from the date of neutron activation (Ismail et al., 2025). The amount of the prescribed dose during GKRS planning depends on the type of lesion being treated, as different lesions require different dosages to achieve optimal therapeutic effects, such as trigeminal patients, one of the highest suggested dosages for GKRS treatments is 85–85 Gy (Verheul, et al., 2010; Barzaghi, et al., 2021). Meanwhile, certain cases, such as meningiomas, often require lower doses of radiation, typically around 20 Gy, for effective treatment (Le, et al., 2017). As the radiation dose increases, the risk of radiation-induced side effects also increases, as recognized by international organizations, such as the United Nations Scientific Committee on the Effects of Atomic Radiation and International Commission on Radiological Protection (ICRP) (Wijma, et al., 2024 ; Wojcik, 2022; Charles, 2008). This is because higher doses not only intensify the primary radiation but also increase scatter radiation, which can affect surrounding healthy tissues (Albano, et al., 2021; Ismail, et al., 2024). On the other hand, according to the World Health Organization, ensuring radiation safety in radiotherapy is essential to protect patients and must include justification of procedures, dose optimization, and adherence to established safety protocols to minimize unnecessary exposure (World Health Organization, 2008).

Several studies conducted both *in vitro* and *in vivo* on humans and rats have shown that gamma rays significantly affect blood cells. Ismail, Hamad and Harki, (2012) observed a notable decrease in red blood cell (RBC), white blood cell (WBC), and platelet (PLT) counts when exposed to a radiation dose rate of 1.1 mSv/h, with statistically significant differences. In another study, by Abojassim, Jaffat and Hassan, (2015) exposure to 6 Gy of X-rays was found to significantly reduce RBC, hemoglobin (HGB), hematocrit (HCT), mean corpuscular volume (MCV), and

ARO-The Scientific Journal of Koya University
Vol. XIII, No.1(2025), Article ID: ARO.12194. 7 pages
DOI: 10.14500/aro.12194
Received: 13 April 2025; Accepted: 31 May 2025
Regular research paper; Published: 25 June 2025

[†]Corresponding author's e-mail: bazhdar.sh.mohammed@su.edu.krd

mean corpuscular hemoglobin (MCH), with statistically significant differences ($p \leq 0.05$). Similarly, in the study by Taqi, et al. (2018) long-term exposure to X-rays in diagnostic technicians resulted in a significant ($p < 0.05$) decrease in RBC, lymphocytes (LYM), HGB, and HCT compared to the control group. Furthermore, Surniyantoro, et al. (2019) reported that while WBC, HCT, MCV, and LYM levels were significantly lower in radiation-exposed individuals compared to controls, RBC and Monocyte counts were notably higher. In addition, RBC levels showed a significant correlation with the equivalent dose ($p = 0.001$). In addition, Gul, Sengul and Demir, (2024) demonstrated that exposure to 16 Gy and 32 Gy of X-rays, both as a single dose and in fractionated form, led to a significant decrease in WBC, RBC, HGB, and PLT, with a statistically significant probability of occurrence ($p < 0.05$). Furthermore, in a study done by Ismail, et al. (2024) the effect of gamma radiation exposure and duration of exposure produce a great impact on WBC, RBC, LYM, LYM percentage (LYM%), and Granulocyte, with significant changes ($p \leq 0.05$). Berpan and Janhom, (2025) analyzed data from cancer patients undergoing radiotherapy at a dose of 10 Gy, considering treatment location and complete blood count (CBC), WBC count, PLT, and Neutrophils (NEU). Regression analysis during therapy explained approximately 10%, 30%, and 40% of the variance in WBC count, NEU, and PLT count, respectively. However, no studies have specifically examined the effects of high-dose gamma radiation on blood parameters during GKRS, nor have they compared the impact of exposure duration between different dose levels. While GKRS is highly targeted, and the primary focus of its calibration is to ensure precise dose delivery to intracranial lesions, standard calibration protocols do not address scatter or leakage radiation to other body organs.

This study evaluated extracranial absorbed dose, effective dose, and side effects in patients with trigeminal neuralgia who receives 80 Gy and meningiomas who receives 20 Gy in average, allowing for a comparison between these treatment doses. Scatter radiation exposure to various body regions was measured too by using a Radiacode 103 dosimeter. Blood samples were collected before, after, and about 20 days post-treatment to assess effects on blood parameters. The findings provide insights into short- and long-term health risks, highlighting differences in the impact of the two radiation doses.

II. MATERIALS AND METHODS

A. Study Area and Participants

A prospective analysis was studied on patients diagnosed with meningiomas and trigeminal neuralgia, who underwent frame-based ^{60}Co stereotactic radiosurgery at Erbil Teaching Hospital in the Kurdistan region of Iraq. The treatments were administered using the Leksell Gamma Knife ELEKTA Perfexion™ system (Fig. 1). Patients who received the lowest recommended dosage (meningiomas) and those who received the highest suggested dosage (trigeminal neuralgia) have been taken according to protocols (Gong, et al., 2022, Barzaghi, et al., 2021). A total of 20 patients have been taken, equally divided into two groups, receiving dosages of 20 Gy (median age 41 years; range 25–71 years) and 80 Gy (median age 43 years; range 36–77 years) from June 15, 2024 to December 6, 2024 (Table I). Blood samples of 3 mL were collected from each patient before treatment, after treatment, and again 20 days following treatment. All procedures involving these consecutive patients were conducted in accordance with the guidelines of the Salahaddin University Human Ethics Committee (approval number 4S/269, dated June 30, 2024), based in Erbil, Kurdistan region, Iraq.

B. Nuclear Radiation Dosimeter and Spectrometer

For measuring leaking radiation three same models of the RadiaCode (RC) 103 nuclear radiation detector and spectrometer – RC-103-004240, RC-103-004284, and RC-103-004378 – were utilized to measure leakage radiation exposure from the GKRS. These devices have an energy measurement range for gamma radiation from 0.02 MeV to 3 MeV and a dose rate range of 0.02–20 mSv/h. The dosimeters were calibrated in a certified reference laboratory in line with the ISO 4037–1:2020 standard (Qian, et al., 2021). Calibrations were conducted in July 2024 using Cesium-137 (^{137}Cs) as the reference source with 8.2 ± 0.4% full-width height maximum (Hussein, Salih and Sedeeq, 2021). The background radiation dose rate (μSv/h) inside the GKRS room (560×700 cm^2) was first measured at a height of 110 cm from the floor. The dose rate was averaged and recorded for each square

Fig. 1. The Gamma knife ELEKTA perfexion™ 2006.

TABLE I
FEATURES OF THE POPULATION IN THE STUDY. GY=GRAY

Characteristics	Highest dosage lesions	Lowest dosage lesions
Number of patients	10 cases (3 males and 7 females)	10 cases (4 males and 6 females)
Median age (year range)	43 (36–77)	41 (25–71)
BMI (kg/cm^2) Median (range)	23.5 (23.8–29.8)	25.5 (18.1–30.2)
Place of residency	Erbil (40%), Mosul (30%), Salahaddin (20%), Duhok (10%)	Erbil (40%), Sulaymaniyah (%20), Mosul (20%), Salahaddin (10%), Kerkuk (10%)
Prescription dose at 100% Gy Median (range) Standard (limit)	80 Gy at 100% 80 (only 80 Gy used) Standard (80–85 Gy) (Boling, et al., 2019)	20-28 Gy at 100% 20 (20–28) Standard (20–28) (Lee, et al., 2017)
Median time exposure in minutes (range)	58.2 (41–66.8)	19.4 (7.7–39)

BMI: Body mass index

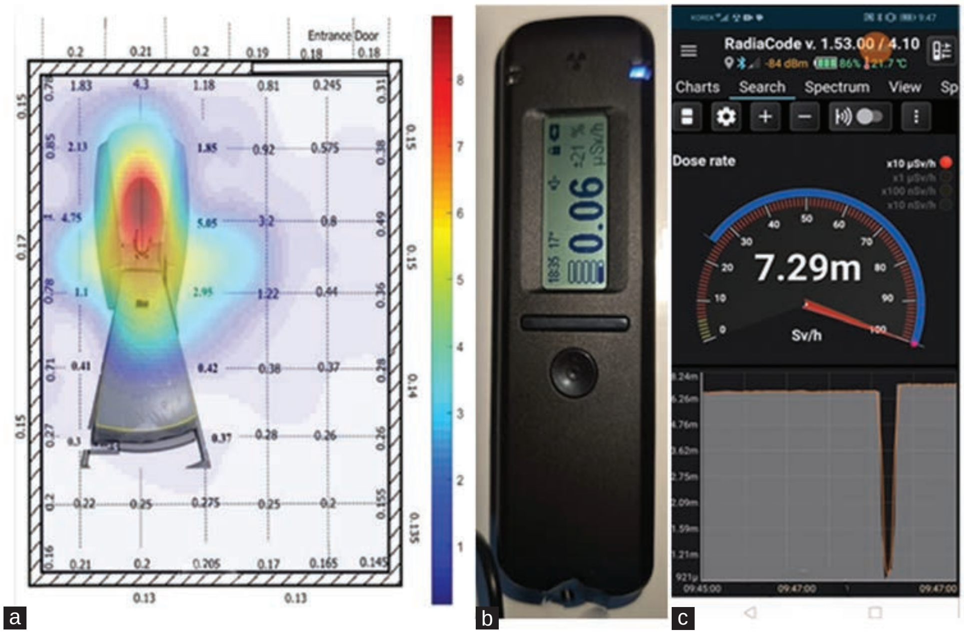

Fig. 2. The map of treatment room and related measurements: (a) Room layout showing background radiation levels recorded at one-meter intervals, (b) RadiaCode 103 nuclear radiation detector and spectrometer, and (c) Huawei mobile screen used for monitoring dose and absorbed dose rate.

meter, as shown in (Fig. 2). In (Fig. 2a), the heatmap uses a color gradient, with blue indicating lower radiation levels and red representing higher radiation levels measured by RCs dosimeters (Fig. 2b). As can be seen, there is a notable concentration of radiation near the central treatment gate. Approximately 1 m away from the gate, the dose distribution decreases exponentially, showing a low value that falls within the safety range as per ICRP guidelines (Boice, et al., 2020). In addition, the dosimeters were controlled and read through a mobile system through a Bluetooth connection, allowing for real-time tracking of the dose and dose rate outside the treatment room during the treatments (Fig. 2c).

According to previous research, phantom measurements demonstrate that there is no significant difference in the absorbed dose at various depths (Hasanzadeh, et al., 2006). Therefore, we can estimate the depth (organ) dose by placing dosimeters at the surface of the patient's skin, as the surface dose is comparable to the depth dose. Then, the average scatter dose rate was measured using an 8 mm collimator. Each patient had radiation doses measured at seven specific anatomical positions to capture dose variation across the body. The targeted measurement sites included the Face (A), Neck (B), Chest (C), Abdomen (D), Gonad (E), Knee (F), and Feet (G) (Fig. 3).

C. CBC Tests and Blood Analysis

A 3 mL of blood were collected from all individuals a few minutes before treatment to serve as control samples. The samples were collected in vacutainer tubes containing the anticoagulant ethylenediamine tetraacetic acid and gently inverted to prevent clot formation (Elmali, et al., 2024). The same amount of blood was extracted after about 2 h from the treatment. The obtained blood samples were stored in the refrigerator at 4–8°C until measured (Van Balveren, et al., 2017; Amini, et al., 2021). The blood sample was tested using the MEDONIC M32M cell counter and analyzer, which provides 22 hematological blood parameters, such as WBC, RBC, HGB, HCT, and PLT. Other indices, such as MCH, Mean platelet volume, Red cell distribution width (RDW), Plateletcrit, Mean corpuscular hemoglobin concentration, and Platelet distribution width were also reported (Ismail and Abdulla, 2021; Mustafa, Yaba and Ismail, 2020).

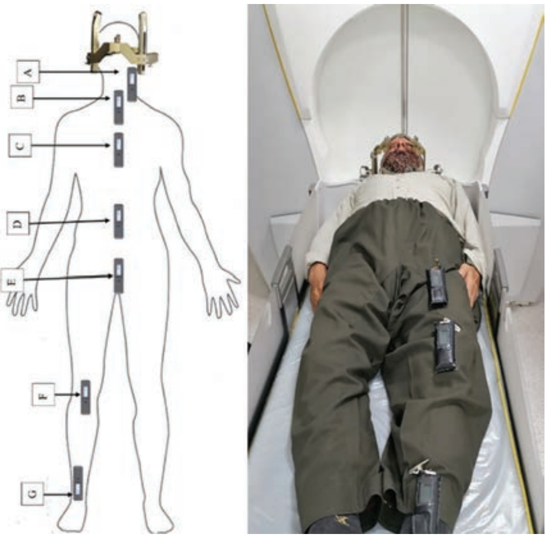

Fig. 3. Patient positioning and dosimeters placements. Left: Schematic representation highlighting dosimeter placement sites: A (head), B (neck), C (chest), D (abdomen), E (gonads), F (knee), and G (feet). Right: A patient secured in the gamma knife radiosurgery frame with dosimeters applied to different body regions.

D. Statistical Analysis Method

Variation of blood parameters were calculated based on comparison with control sample as well as the results are presented as the average (Ave.) ± standard deviation, and statistical significance is evaluated using a repeated measurement one-way analysis of variance followed by Dunnett multiple comparison test for *post hoc* comparisons to compare the ratio of changes in blood components between the 20 Gy group and the 80 Gy group with control (Uthirapathy and Tahir, 2021). A p-value below 0.05 is regarded as statistically significant. All statistical analyses were performed using GraphPad Prism software version 8.

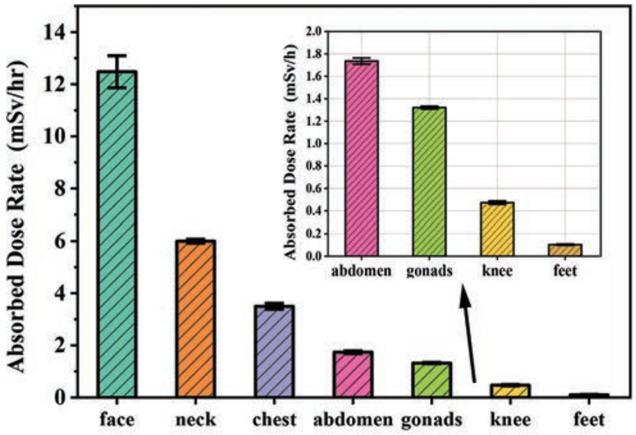

Fig. 4. Absorbed dose rate for different body parts received from scatter radiation of an 8 mm collimator.

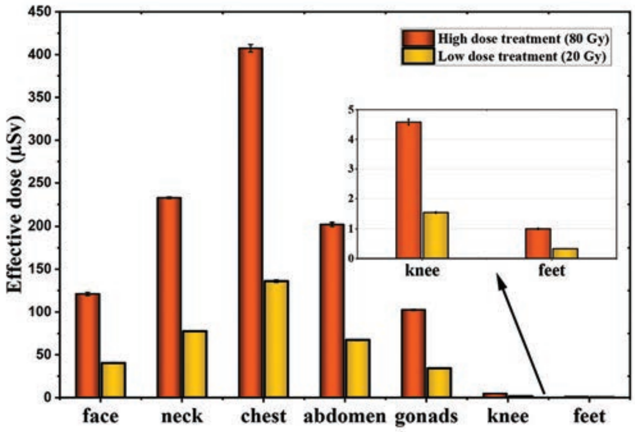

Fig. 5. Comparison of effective dose distribution across different body parts for 80 Gy and 20 Gy treatment cases of trigeminal neuralgia and meningiomas brain lesions.

III. Results and Discussion

Table II shows the radiation dose rates at various distances when using an 8 mm treatment beam collimator for different patient body parts undergoing GKRS for high-dose treatment cases, such as trigeminal neuralgia and low-dose treatment cases, such as meningiomas. It illustrates the radiation received by each body part during treatment. The highest dose rates are observed at the face and neck, significantly higher than those received by other body parts. In contrast, the abdomen, pelvis, knee, and feet receive progressively lower doses. Effective dose values were also calculated following the ICRP 103 guidelines (Nenot, et al., 2009; Charles, 2008).

(Fig. 4) illustrates the scattering of the gamma beam across the patient's body, following an exponential decrease with increasing distance from the source to extracranial body sections. The absorbed dose rates, presented from the face to the furthest body parts, highlight the minimal and maximal values measured in mSv. The inset plot emphasizes the lower dose regions, showing a clear reduction in absorbed dose with increasing distance from the prescribed dose because radiation intensity decreases exponentially with distance due to attenuation and the inverse square law, resulting in higher absorbed dose rates closer to the source.(Fig. 5) presents a comparison of the effective dose (μSv) measured at different body regions following GKRS under two treatment conditions: High-dose (80 Gy) and low-dose (20 Gy). Across all body sites, the effective dose is higher in high-dose treatments because greater photon flux produces more scatter radiation, and each organ has its own sensitivity to radiation, influencing how much dose contributes to overall risk. The effective dose for high-dose treatments is typically 3 times greater than that for low-dose treatments across all body regions. The chest exhibits the highest effective dose among all regions, exceeding 407 μSv in the high-dose group while receiving 136 μSv in the low-dose group. Similarly, the neck receives a substantially higher dose under the high-dose treatment, exceeding 230 μSv, while the low-dose group remains below 100 μSv. The abdomen and gonads also follow this trend, with effective doses in the high-dose group being significantly greater than those in the low-dose group. In contrast, the knee and feet receive considerably lower doses compared to other body regions, with values remaining below 5 μSv. Despite their low exposure, the high-dose

TABLE II

Measurements of the Mean Leakage Gamma Radiation dose from 8 mm Collimator for Extracranial Body Organs in Patients Undergoing Gkrs

Body parts	**Average dose rate (Average±SD) in (μSv/h)**	**Average absorbed dose (high-dose, 58.2 min [μSv])**	**Average absorbed dose (low-dose, 19.4 min [μSv])**	**Tissue weighting factors**	**Effective dose in high-dose treatment (μSv)**	**Effective dose in low-dose treatment (μSv)**
Face	12476±205	12102±199	4034±66	0.01	121±2	40±0.7
Neck	5996±26	5816±25	1939±8	0.04	233±1	77±0.3
Chest	3499±37	3395±37	1132±12	0.12	407±4	136±1.5
Abdomen	1736±18	1684±18	561±6	0.12	202±2	67±0.7
Gonads	1320±9	1280±8	427±3	0.08	102±0.7	34±0.2
Knee	472±10	458±10	153±3	0.01	5±0.1	1.5±0.03
Feet	103±3	100±3	33±1	0.01	1±0.03	0.3±0.01

SD: Standard deviation

treatment still leads to a relatively greater dose than the low-dose treatment at these sites.(Table III and Fig. 6) represents bar graphs to compare the effects of radiation exposure on hematological parameters based on short-term change (STC) and long-term change (LTC) for both doses. As can be seen, WBC, RBC, PLT, LYM, LYM%, HGB, HCT, RDW%, platelet large cell count (p-LCC), and platelet large cell ratio (p-LCR). Low-dose exposure induces minimal changes, with most parameters remaining comparable to the control. In contrast, high-dose exposure (80 Gy) leads to significant alterations. RBC, WBC, and HCT decrease notably, particularly in LTC80 Gy, indicating a stronger impact with prolonged exposure. PLT-related parameters show mixed responses: PLT, p-LCC, and p-LCR increase significantly in LTC80 Gy, suggesting a compensatory response, while RDW% also rises in LTC80 Gy, indicating increased variability in RBC size. LYM counts rise significantly in STC80 Gy and LTC80 Gy, with a stronger effect in long-term exposure, and LYM% also increases in LTC80 Gy. HGB levels remain stable across most groups but show a slight

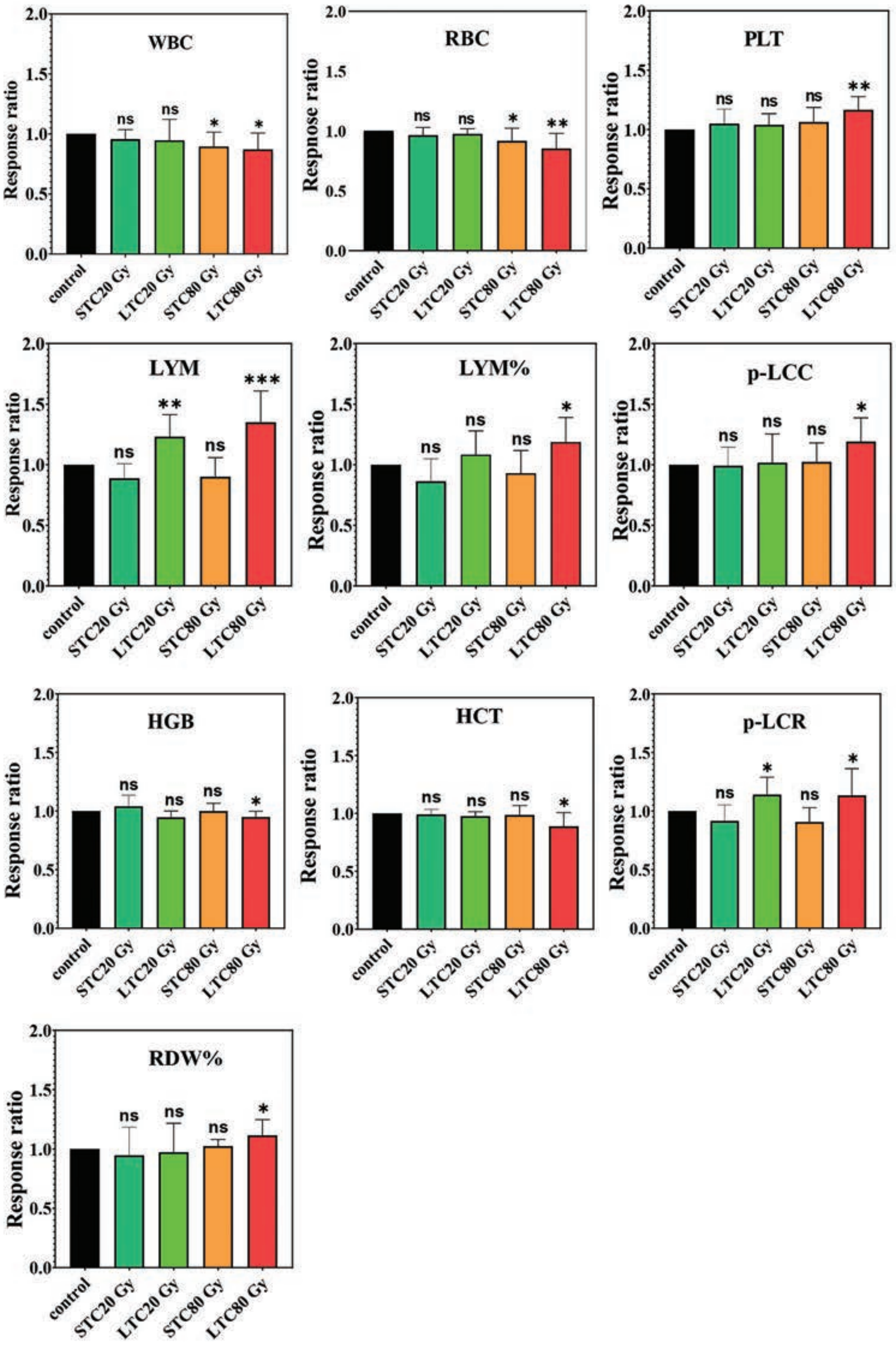

Fig. 6. Short term change and Long-term Change of blood parameters at different radiation doses versus control ($p \leq 0.05$).

TABLE III
Blood Parameter Changes in Response to stc and ltc Radiation Exposure

parameters	STC20 (Average±SD)	p-value[1]	LTC20 (Average±SD)	p-value	STC80 (Average±SD)	p-value	LTC80 (Average±SD)	p-value
WBC	0.95±0.08	ns	0.95±0.18	ns	0.9±0.12	*	0.87±0.14	*
LYM	0.89±0.12	ns	1.23±0.18	**	0.9±0.16	ns	1.35±0.26	***
LYM%	0.87±0.16	ns	1.12±0.21	ns	0.93±0.15	ns	1.12±0.2	*
MID	0.86±0.14	ns	1.11±0.22	ns	0.95±0.14	ns	1.04±0.7	ns
MID%	0.87±0.13	ns	1.06±0.27	ns	1.01±0.23	ns	1.08±0.32	ns
GRA	1.02±0.14	ns	0.95±0.19	ns	1.00±0.20	ns	0.89±0.17	ns
GRA%	1.05±0.07	ns	0.97±0.10	ns	1.12±0.26	ns	1.08±0.46	ns
RBC	0.98±0.04	ns	0.97±0.05	ns	0.94±0.08	*	0.89±0.10	**
HGB	1.05±0.11	ns	0.94±0.06	ns	0.99±0.08	ns	0.95±0.05	*
HCT	0.98±0.04	ns	0.97±0.03	ns	0.98±0.07	ns	0.91±0.09	*
MCV	0.99±0.02	ns	1.01±0.03	ns	0.98±0.03	ns	0.97±0.05	ns
MCH	0.99±0.05	ns	0.97±0.05	ns	0.99±0.03	ns	1.00±0.06	ns
MCHC	1.02±0.04	ns	0.97±0.05	ns	1.01±0.03	ns	1.06±0.15	ns
RDWa	0.94±0.13	ns	1.05±0.11	ns	1.01±0.07	ns	1.06±0.12	*
RDW%	1.04±0.35	ns	1.03±0.09	ns	1.02±0.06	ns	1.04±0.14	ns
PLT	1.03±0.12	ns	1.04±0.08	ns	1.05±0.09	*	1.12±0.11	*
MPV	0.97±0.06	ns	1.04±0.09	ns	0.99±0.06	ns	1.03±0.10	ns
PDWa	0.97±0.12	ns	0.96±0.09	ns	1.00±0.10	ns	1.00±0.11	ns
PDW%	1.02±0.07	ns	1.00±0.05	ns	1.04±0.11	ns	1.04±0.10	ns
PCT	1.02±0.16	ns	1.01±0.13	ns	1.06±0.09	ns	1.08±0.13	ns
p-LCR	0.98±0.07	ns	1.02±0.19	*	0.93±0.09	ns	1.12±0.15	*
p-LCC	1.01±0.13	ns	1.04±0.14	*	1.05±0.14	ns	1.14±0.18	*

[1] ns: Non-significant, ***** = Significant ($p \leq 0.05$), ****** = More significant ($p \leq 0.01$), ******* = Highly significant ($p \leq 0.001$). LTC: Long-term change, STC: Short-term change, SD: Standard deviation, WBC: White blood cell, LYM: Lymphocytes, RBC: Red blood cell, HGB: Hemoglobin, HCT: Hematocrit, MCV: Mean corpuscular volume, MCH: Mean corpuscular hemoglobin, MCHC: Mean corpuscular hemoglobin concentration, RDW: Red cell distribution width, PLT: Platelet, MPV: Mean platelet volume, PDW: Platelet distribution width, PCT: Plateletcrit, p-LCR: Platelet large cell ratio, p-LCC: Platelet large cell count

decline in LTC80 Gy. Overall, hematological parameters are more sensitive to high radiation because radiation severely affects the bone marrow, where blood cells are produced.

As can be seen, in the cases of 20 Gy rescripted dose resulted in a smaller percentage change in blood parameters compared to 80 Gy, which required a higher dose of radiation for treatment. The results are in agreement with most previous works done by (Ismail, Hamad and Harki, 2012; Abojassim, Jaffat and Hassan, 2015; Taqi, et al., 2018; Surniyantoro, et al., 2019; Gul, Sengul and Demir, 2024; Ismail, et al., 2025; Berpan and Janhom, 2025) which show that increase does and exposure time produces high impact on blood components. The effective doses in high-dose and low-dose treatments across all assessed body regions ranged from 1.5 μSv to 407 μSv, all of which remain substantially lower than the ICRP's recommended dose limit for the general public. On average, the effective doses in high-dose treatments were approximately 3 times higher than those in low-dose treatments, reflecting the extended treatment duration and radiation exposure in the high-dose group (Charles, 2008; World Health Organization, 2008). It is important to note that while patients also received additional diagnostic radiation through computed tomography scans and X-rays for stereotactic planning, these doses were not included in the present analysis, which focuses solely on the radiation exposure resulting from GKRS.

IV. Conclusion

The study assessed the safety of dose-staged GKRS on organs by calculating effective doses across different body regions and analyzing the short- and long-term radiation effects on blood components. We observed that the scattering of the gamma beam from the 8 mm collimator within the patient's body follows an exponential pattern based on the distance from the source to extracranial regions. Across all body regions, leakage radiation is higher in high-dose treatments (80 Gy) compared to low-dose treatments (20 Gy) due to the increased radiation output and intensity used for higher doses. Most hematological parameters showed significant changes that were dependent on high-dose and long-term exposure. This finding is important for GKRS staff to consider when treating patients receiving high radiation doses, emphasizing the need for precise treatment planning and shielding to ensure the radiation remains both effective and safe.

Acknowledgment

The authors would like to extend their sincere thanks to the Salahaddin University-Erbil for their invaluable support and collaboration. Special thanks also go to Dr. Hoshanc S. Rashid, head of the Gamma Knife unit at Erbil Teaching Hospital, Kurdistan Region, Iraq, and his staff for their assistance and contributions.

References

Abojassim, A.A., Jaffat, H.S., and Hassan, A.B., 2015. Effects of gamma radiation on some hematological parameters in female rats. *Theoretical and Applied Science*, 25, pp. 101-109.

Albano, D., Benenati, M., Bruno, A., Bruno, F., Calandri, M., Caruso, D., Cozzi, D., De Robertis, R., Gentili, F., Grazzini, I., Micci, G., Palmisano, A., Pessina, C., Scalise, P.,…& Young SIRM Working Group., 2021. Imaging side effects and complications of chemotherapy and radiation therapy: A pictorial review from head to toe. *Insights into Imaging,* 12(1), p.76.

Amini, F., Auma, E., Hsia, Y., Bilton, S., Hall, T., Ramkhelawon, L., Heath, P.T., and Le Doare, K., 2021. Reliability of dried blood spot (DBS) cards in antibody measurement: A systematic review. *PLoS One,* 16(3), p.e0248218.

Barzaghi, L.R., Albano, L., Scudieri, C., Gigliotti, C.R., Del Vecchio, A., and Mortini, P., 2021. Factors affecting long-lasting pain relief after gamma knife radiosurgery for trigeminal neuralgia: A single institutional analysis and literature review. *Neurosurgical Review,* 44, pp.2797-2808.

Berpan, A., and Janhom, N., 2025. Linear regression analysis for complete blood count parameters during radiotherapy. *Strahlentherapie und Onkologie*, 201(5), pp.561-566.

Boice, J. Jr., Dauer, L.T., Kase, K.R., Mettler F.A Jr., and Vetter, R.J., 2020. Evolution of radiation protection for medical workers. *The British Journal of Radiology,* 93(1112), p.20200282.

Boling, W., Song, M., Shih, W., and Karlsson, B., 2019. Gamma Knife radiosurgery for trigeminal neuralgia: A comparison of dose protocols. *Brain Sciences,* 9(6), p.134.

Charles, M.W., 2008. *ICRP Publication 103: Recommendations of the ICRP*. Oxford University Press, Oxford.

Elmali, A., Guler, O.C., Demirhan, B., Yavuz, M., and Onal, C., 2024. Long-term analysis of hematological parameters as predictors of recurrence patterns and treatment outcomes in cervical cancer patients undergoing definitive chemoradiotherapy. *Strahlentherapie and Onkologie,* 200(11), pp.949-957.

Gong, X., Ding, J., Knisely, J.P.S., Wang, E., Pan, L., Wang, B., Zhang, N., Wu, H., Dai, J., Yu, T., and Tang, X., 2022. Dose-staged gamma knife radiosurgery for meningiomas: A retrospective study in a single center. *Frontiers in Neurology*, 13, p.893480.

Gul, O.V., Sengul, A., and Demir, H., 2024. Effects of radiation at different dose rates on hematologic parameters in rats. *Journal of Radiation Research and Applied Sciences*, 17(2), p.100873.

Hasanzadeh, H., Sharafi, A., Verdi, M.A., and Nikoofar, A., 2006. Assessment of absorbed dose to thyroid, parotid and ovaries in patients undergoing gamma knife radiosurgery. *Physics in Medicine and Biology*, 51(17), pp.4375-4383.

Hussein, Z.A., Salih, N.F., and Sedeeq, S.Z., 2021. Assessment the natural radioactivity of radionuclides (226Ra, 232Th, 40K, and 137Cs) in wheat grain. *ARO-The Scientific Journal of Koya University*, 9(1), pp.95-102.

Ismail, A.H., and Abdulla, K.N., 2021. Biochemical and hematological study of the effects of annual exposure radiation doses on the operators of X-ray and CT-scan in some Erbil hospitals. *Radiation Physics and Chemistry*, 184, p.109466.

Ismail, A.H., Hamad, M.A., and Harki, E.M.T., 2012. Radiation exposure of leukemia blood samples and its impacts on the density of RBC, WBC, and PLT: *In vitro*. *Open Journal of Biophysics*, 2(4), pp.130-136.

Ismail, A.H., Rashid, H.S., Omar, A.A., Alomari, A.H., Al-Qahtani, S.M., Alnaemi, T.A., Todorović, N., Pehlivanoglu, S.A., Guida, M., and Mancini, S., 2025. Radiobiological evaluation of the impact of the treatment with the gamma knife radiosurgery technique on the body parts of patients with different brain lesions: Does the radiation exposure affect also the patient's blood components? *Radiation Physics and Chemistry*, 226, p.112267.

Le, Z., Niu, X., Chen, Y., Ou, X., Zhao, G., Liu, Q., Tu, W., Hu, C., Kong, L., and Liu, Y., 2017. Predictive single nucleotide polymorphism markers for acute oral mucositis in patients with nasopharyngeal carcinoma treated with radiotherapy. *Oncotarget*, 8(38), pp.63026-63037.

Lee, C.C., Sheehan, J.P., Kano, H., Akpinar, B., Martinez-Alvarez, R., Martinez-Moreno, N., Guo, W.Y., Lunsford, L.D., and Liu, K.D., 2017. Gamma knife radiosurgery for hemangioma of the cavernous sinus. *Journal of Neurosurgery*, 126(5), pp.1498-1505.

Mustafa, B.T., Yaba, S.P., and Ismail, A.H., 2020. Moderate range static magnetic field promoted variation of blood parameters: An *in vitro* study. *ARO The Scientific Journal of Koya University*, 8(1), pp.55-64.

Nenot, J.C., Brenot, J., Laurier, D., Rannou, A., and Thierry, D., 2009. ICRP Publication 103. The 2007 recommendations of the international commission on radiological protection. *International Committe for Radiological Protection*, 127(4), pp.2-7.

Qian, Y.K., Feng, P., Yin, G.L., Zhang, S., Wei, B., Mao, B.J., and Liu, Y.X., 2021. Monte carlo simulation investigation on the minimum dimension of gamma reference radiation regulated by ISO 4037-1. *The European Physical Journal Plus,* 136(8), p.855.

Stone, P.H., Lay, L.M., Ramirez, R., Neck, D., Chu, C., Dey, J., and Solis, D., 2025. A 3D superposition approximation for gamma knife dose calculation. *Radiation*, 5(1), p.6.

Surniyantoro, H., Rahardjo, T., Lusiyanti, Y., Rahajeng, N., Sadewa, A., Hastuti, P., and Date, H., 2019. Assessment of ionizing radiation effects on the hematological parameters of radiation-exposed workers. *Atom Indonesia*, 45(2), pp.123-129.

Taqi, A.H., Faraj, K.A., Zaynal, S.A., Hameed, A.M., and Mahmood, A.A.A., 2018. Effects of occupational exposure of x-ray on hematological parameters of diagnostic technicians. *Radiation Physics and Chemistry,* 147, pp. 45-52.

Uthirapathy, S., and Tahir, T.F., 2021. Withania somnifera: Correlation of phytoconstituents with hypolipidemic and cardioprotective activities. *ARO The Scientific Journal of Koya University*, 9(2), pp.15-21.

Van Balveren, J.A., Huijskens, M.J., Gemen, E.F., Péquériaux, N.C., and Kusters, R., 2017. Effects of time and temperature on 48 routine chemistry, haematology and coagulation analytes in whole blood samples. *Annals of Clinical Biochemistry*, 54(4), pp.448-462.

Verheul, J.B., Hanssens, P.E.J., Te Lie, S., Leenstra, S., Piersma, H., and Beute, G.N., 2010. Gamma Knife surgery for trigeminal neuralgia: A review of 450 consecutive cases. *Journal of Neurosurgery,* 113 Suppl, pp.160-167.

Wijma, I.N., Casal, R.F., Cheng, G.Z., Einsiedel, P.F., Fantin, A., Hall, D.J., Herth, F.J.F., Ng, C.S.H., Pritchett, M.A., Shah, P.L., Steinfort, D.P., Trisolini, R., Verhoeven, R.L.J., and Van Der Heijden, E.H.F.M., 2024. Radiation principles, protection, and reporting for interventional pulmonology: A world association of bronchology and interventional pulmonology white paper. *Respiration*, 103(11), pp.707-722.

Wojcik, A., 2022. Reflections on effects of low doses and risk inference based on the UNSCEAR 2021 report on 'biological mechanisms relevant for the inference of cancer risks from low-dose and low-dose-rate radiation'. *Journal of Radiological Protection*, 42(2), p.023501.

World Health Organization, 2008. *PRIMA-EF: Guidance on the European Framework for Psychosocial Risk Management: A Resource for Employer and Worker Representatives.* World Health Organization, Geneva. Available from: https://iris.who.int/handle/10665/43966Leka: PRIMA-EF-Guidance on the European Framework... - Google Scholar

General Information

ARO's Mission: ARO seeks to publish those papers that are most influential in their fields or across fields and that will significantly advance scientific understanding. Selected papers should present novel and broadly important data, syntheses, or concepts. They should merit the recognition by the scientific community and general public provided by publication in ARO, beyond that provided by specialty journals.

We welcome submissions from all fields of natural science and technology, and from any source. We are committed to the prompt evaluation and publication of submitted papers. ARO is published biannually; selected papers are published online ahead of print.

Submission

Manuscripts should be submitted by the correspondent authors of the manuscript via the on-line submission page. Regardless of the source of the word-processing tool, only electronic Word (.doc, .docx, .rtf) files can be submitted on-line. There is no page limit. Only online submissions are accepted to facilitate rapid publication and minimize administrative costs. Submissions by any other one but the authors will not be accepted. The submitting author takes responsibility for the paper during submission and peer review. If for some technical reason submission through the email is not possible, the author can contact aro.journal@koyauniversity.org for support. Before submitting, please check ARO's guide to authors thoroughly to avoid any delay in the review and publication process.

Authors are explicitly responsible for the language of their texts. Paper should be submitted in a well written in understandable English. Authors should not expect the editor or editorial board to rewrite their paper. Prior to submission, authors should have their paper proofread by a possible academic native speaker of English.

- Submit the Article with contact Information
- File name should be your article title
- Don't submit your article in multiple journals, we are taking only minimum time for the review process. please don't waste our time
- Once the paper is accepted, it can't be withdrawn
- Please follow publication ethics and regulation
- Avoid plagiarism and copied material
- Strictly Follow ARO's template

Terms of Submission

Papers must be submitted on the understanding that they have not been published elsewhere and are not currently under consideration by another journal or any other publisher. ARO accepts original articles with novel impacts only. Post conference papers are not accepted "as is", however, regular papers on the same topic but with a different title can be submitted. The new paper should contain significant improvements in terms of extended content, analysis, comparisons with popular methods, results, figures, comments, etc. Please do not forget that the publication of the same or similar material in ARO constitutes the grounds for filing an (auto) plagiarism case.

The submitting author is responsible for ensuring that the article's publication has been approved by all the other co-authors. It is also the authors' responsibility to ensure that the articles emanating from a particular institution are submitted with the approval of the necessary institution. Only an acknowledgement from the editorial office officially establishes the date of receipt. Further correspondence and proofs will be sent to the author(s) before publication unless otherwise indicated. It is a condition of submission of a paper that the authors permit editing of the paper for readability. All enquiries concerning the publication of accepted papers should be addressed to aro.journal@koyauniversity.org.

Peer Review

All manuscripts are subject to peer review and are expected to meet standards of academic excellence. Submissions will be considered by an editor and "if not rejected right away" by peer-reviewers, whose identities will remain anonymous to the authors.

Guide to Author

We welcome submissions from all fields of science and from any source. We are committed to the prompt evaluation and publication of submitted papers. Selected papers are published online ahead of print. Authors are encouraged to read the instructions below before submitting their manuscripts. This section is arranged into an overview of the of the speedy guidelines below and is more detailed in the bottom section of this page.

Manuscript Preparation

Submitting your manuscript will be in two stages namely before final acceptance and after.

Stage One:

For the initial submission, the manuscript should be prepared electronically in Microsoft Word (.doc, .docx, .rtf) and PDF formats. Submit it through the online submission system after completing the registration. The Word file should be in a single-column format, double-spaced, with Times New Roman font, and 12-point font size. The authors' names and affiliations should be removed from the manuscript for the double-blind review process. Referencing and citation should follow the Harvard/ARO system. You can download the stage-one manuscript template by clicking here.

Stage Two:

Once the manuscript is accepted, the production team of ARO Journal will prepare the camera-ready paper.

Units of Measurement

Units of measurement should be presented simply and concisely using System International (SI) units.

Title and Authorship Information

The following information should be included;

- Paper title.
- Full author names.
- Affiliation.
- Email addresses.

Abstract

The manuscript should contain an abstract. The abstract should be self-contained and citation-free and should not exceed 250 words.

Introduction

This section should be succinct, with no subheadings.

Materials and Methods

This part should contain sufficient detail so that all procedures can be repeated. It can be divided into subsections if several methods are described.

Results and Discussion

This section may each be divided by subheadings or may be combined.

Conclusions

This should clearly explain the main conclusions of the work highlighting its importance and relevance.

Acknowledgements

All acknowledgements (if any) should be included at the very end of the paper before the references and may include supporting grants, presentations, and so forth.

References

References must be included in the manuscript and authors are responsible for the accuracy of references. Manuscripts without them will be returned. ARO is following Harvard System of Referencing. (Learn how to import and use Harvard Styling in your Microsoft Office by following this link:
http://bibword.codeplex.com/releases/view/15852)

Preparation of Figures

Upon submission of an article, authors are supposed to include all figures and tables in the PDF file of the manuscript. Figures and tables should be embedded in the manuscript. Figures should be supplied in either vector art formats (Illustrator, EPS, WMF, FreeHand, CorelDraw, PowerPoint, Excel, etc.) or bitmap formats (Photoshop, TIFF, GIF, JPEG, etc.). Bitmap images should be of 300 dpi resolution at least unless the resolution is intentionally set to a lower level for scientific reasons. If a bitmap image has labels, the image and labels should be embedded in separate layers.

Preparation of Tables

Tables should be cited consecutively in the text. Every table must have a descriptive title and if numerical measurements are given, the units should be included in the column heading. Vertical rules should not be used.

Copyright

Open Access authors retain the copyrights of their papers, and all open access articles are distributed under the terms of the Creative Commons Attribution License, which permits unrestricted use, distribution and reproduction in any medium, provided that the original work is properly cited.
The use of general descriptive names, trade names, trademarks, and so forth in this publication, even if not specifically identified, does not imply that these names are not protected by the relevant laws and regulations.

While the advice and information in this journal are believed to be true and accurate on the date of its going to press, neither the authors, the editors, nor the publisher can accept any legal responsibility for any errors or omissions that may be made. The publisher makes no warranty, express or implied, with respect to the material contained herein.

ARO Reviewer/Associate Editor Application Form

ARO is a scientific journal of Koya University (p-ISSN: 2410-9355, e-ISSN: 2307-549X) which aims to offer a novel contribution to the study of Science. The purpose of ARO is twofold: first, it will aim to become an ongoing forum for debate and discussion across the sciences and Engineering. We hope to advance our problem-solving capacity and deepen our knowledge regarding a comprehensive range of collective actions. Second, ARO accepts the challenges brought about by multidisciplinary scientific areas and aspires to expand the community of academics who are able to learn from and help to produce advances in a variety of different disciplines.

The Journal is seeking reviewers who can provide constructive analysis of papers thus enhancing the overall reputation of the Journal. If any expert is interested in participating in the review process, we highly encourage you to sign up as a reviewer for our Journal and help us improve our presence in the domain of your expertise. Appropriate selection of reviewers who have expertise and interest in the domain relevant to each manuscript are essential elements that ensure a timely, productive peer review process. We require proficiency in English.

How to apply

To apply for becoming a reviewer of ARO, please submit the application form by following the link:
https://aro.koyauniversity.org/user/register

To apply for becoming a member of the Editorial Board of ARO, please submit the application form by completing the application form.

Both Associate Editor and Reviewers should specify their areas of research and expertise. Applicants must have a doctorate (or an equivalent degree), and if Master degree they need to have significant publishing experience. Please note that;

- You will need to write your full official name.
- Please provide an email which reflects your official name, such as nameOne.NameTwo@... , or your institute's official email.
- All data need to be written in English.

Note: For more information, kindly visit the following websites:

1. aro.koyauniversity.org.
2. http://libweb.anglia.ac.uk/referencing/harvard.htm.
3. http://bibword.codeplex.com/releases/view/15852.

Journal Citation Reports
Clarivate
2024

PRESERVED IN CLOCKSS

PRESERVED IN LOCKSS

PKP
PUBLIC KNOWLEDGE PROJECT

DOAJ SEAL

INDEXED IN DOAJ

Journal TOCs
The latest Journals Tables of Contents

ingenta

Dimensions

ZDB ZEITSCHRIFTEN DATENBANK

SHERPA RoMEO

scinapse

Scilit

ScienceGate

ROAD DIRECTORY OF OPEN ACCESS SCHOLARLY RESOURCES

ResearchGATE scientific network

OAJSE

Microsoft Academic

OCLC WorldCat

Google Scholar

Crossref

BASE

publons

ACADEMIA

KOYA UNIVERSITY

Koya University is a young University established in 2003 and it is located in the city of Koya (Koysinjaq), short distance to the East of regional capital city of Erbil (Arbil, Hewlêr) in Kurdistan Region of Iraq. It is on the foothills of beautiful High Mountain. Its campus has been carefully laid out to embrace the beautiful mountainous nature. The Koya University has a Faculty system which enhances the interactions between similar academic fields. Today, Koya University has four Faculties: Engineering, Science and Health, Humanities and Social Sciences and Education in addition to the School of Medicine, which all consist of twenty-five scientific departments in different fields, such as Petroleum Engineering, Geotechnical Engineering, Software Engineering, Physics, Chemistry, Clinical Psychology, Social Science, Medical Microbiology and Sport Education.

ARO-The Scientific Journal of Koya University is a biannual journal of original scientific research, global news, and commentary in the areas of Science and Technology. ARO is a Peer-reviewed Open Access journal with CC BY-NC-SA 4.0 license. It provides immediate, worldwide and barrier-free access to the full text of research articles without requiring a subscription to the journal, and has no article processing charge (APC). ARO Journal seeks to publish those papers that are most influential in their fields or across fields and that will significantly advance scientific understanding. ARO Journal is a member of ROAD and Cross-ref agencies and has got ESCI, DOAJ seal, SHERPA/RoMEO deposit policy, and

ARO

The Scientific Journal of Koya University

Koya University (KOU)
University Park
Danielle Mitterrand Boulevard
Koya KOY45, Kurdistan Region - Iraq

DOI: 10.14500/2307-549X p-ISSN: 2410-9355 e-ISSN: 2307-549X